

REPORT DOCUMENTATION PAGE

Form Approved
OMB No. 0704-0188

Public reporting burden for this collection of information is estimated to average 1 hour per response, including the time for reviewing instructions, searching existing data sources, gathering and maintaining the data needed, and completing and reviewing the collection of information. Send comments regarding this burden estimate or any other aspect of this collection of information, including suggestions for reducing this burden, to Washington Headquarters Services, Directorate for Information Operations and Reports, 1215 Jefferson Davis Highway, Suite 1204, Arlington, VA 22202-4302 and to the Office of Management and Budget, Paperwork Reduction Project (0704-0188), Washington, DC 20503.

1. AGENCY USE ONLY (Leave blank)		2. REPORT DATE July 1, 1997		3. REPORT TYPE AND DATES COVERED FINAL	
4. TITLE AND SUBTITLE Processing and Design Issues in High Temperature Materials				5. FUNDING NUMBERS F49620-96-1-0203	
6. AUTHOR(S) N.S. Stoloff and R. H. Jones					
7. PERFORMING ORGANIZATION NAME(S) AND ADDRESS(ES) Engineering Foundation 435 E. 47th St. New York, NY 10017				8. PERFORMING ORGANIZATION REPORT NUMBER 96-AF	
9. SPONSORING / MONITORING AGENCY NAME(S) AND ADDRESS(ES) AFOSR/DPE 110 Duncan Ave. Rm. 115 Bolling AFB, DC 20332-8050 NA				10. SPONSORING / MONITORING AGENCY REPORT NUMBER 96-1-0203	
11. SUPPLEMENTARY NOTES					
12a. DISTRIBUTION / AVAILABILITY STATEMENT The Minerals, Metals & Materials Society 420 Commonwealth Drive Warrendale, PA 15086				12b. DISTRIBUTION CODE Unlimited	
13. ABSTRACT (Maximum 200 words) The Engineering Foundation Conference on Processing and Design Issues in High Temperature Materials was held in Davos, Switzerland, 19-24, 1996. Approximately fifty participants represented academic institutions, industrial research laboratories and government organizations. The goal of the conference was to exchange areas of common concern among developers and users of high temperature materials of differing types, including superalloys, ceramics, intermetallics and composites. Levels of design ranging from atomic theory to processing techniques were covered in nine oral technical sessions and a poster session. The keynote lecture, entitled "Implementation Challenges for High Temperature Composites" was followed by 26 invited and 15 contributed papers, of which four were poster presentations. The participants were noteworthy for the wide range of their technical specialties. It was evident that many participants were exposed to relatively unfamiliar materials and topics as a result of efforts by the organizing committee to have an extremely diverse group of conferees. Since superalloys dominate current high temperature applications in the 800-1100 C range, it was considered be important to discuss alloy design principles, microstructures and mechanical properties of potentially competitive materials such as ceramics and intermetallics, as well as their composites. Environmental effects on mechanical properties were highlighted; it was shown, for example, that water vapor can be detrimental to both intermetallics at low temperatures and ceramics at high temperatures. Oxidation of high temperature materials was another environmental issue of great importance that was discussed in several papers.					
14. SUBJECT TERMS Advanced metallics, micromechanics				15. NUMBER OF PAGES 445	
				16. PRICE CODE	
17. SECURITY CLASSIFICATION OF REPORT none	18. SECURITY CLASSIFICATION OF THIS PAGE none	19. SECURITY CLASSIFICATION OF ABSTRACT none	20. LIMITATION OF ABSTRACT none		

PROCESSING
and
DESIGN ISSUES
in
HIGH TEMPERATURE
MATERIALS

N.S. Stoloff and R.H. Jones

19971002 127

THIS QUALITY INSPECTED 3

PROCESSING
and
DESIGN ISSUES
in
HIGH TEMPERATURE
MATERIALS

N.S. Stoloff and R.H. Jones

A Publication of
TMS
Minerals • Metals • Materials

A Publication of The Minerals, Metals & Materials Society
420 Commonwealth Drive
Warrendale, Pennsylvania 15086
(412) 776-9000

The Minerals, Metals & Materials Society is not responsible for statements or opinions and is absolved of liability due to misuse of information contained in this publication.

Printed in the United States of America
Library of Congress Catalog Number 96-80050
ISBN Number 0-87339-357-0

Authorization to photocopy items for internal or personal use, or the internal or personal use of specific clients, is granted by The Minerals, Metals & Materials Society for users registered with the Copyright Clearance Center (CCC) Transactional Reporting Service, provided that the base fee of \$3.00 per copy is paid directly to Copyright Clearance Center, 27 Congress Street, Salem, Massachusetts 01970. For those organizations that have been granted a photocopy license by Copyright Clearance Center, a separate system of payment has been arranged.

TMS
Minerals • Metals • Materials

© 1996

If you are interested in purchasing a copy of this book, or if you would like to receive the latest TMS publications catalog, please telephone 1-800-759-4867 (U.S. only), or 412-776-9000, Ext. 270.

PREFACE

The Engineering Foundation Conference on Processing and Design Issues in High Temperature Materials was held in Davos, Switzerland, 19–24 May 1996. It followed by three years a similar conference entitled "Critical Issues in the Design of High Temperature Materials" held in Kona, Hawaii, and published by TMS. In the current conference approximately fifty participants represented academic institutions, industrial research laboratories and government organizations. The goal of the conference was to exchange areas of common concern among developers and users of high temperature materials of differing types, including superalloys, ceramics, intermetallics and composites. Levels of design ranging from atomic theory to processing techniques were covered in nine oral technical sessions and a poster session.

The keynote lecture, entitled "Implementation Challenges for High Temperature Composites" was followed by 26 invited and 15 contributed papers, of which four were poster presentations. These proceedings contain the texts of most of the invited and contributed papers to the Conference.

The participants were noteworthy for the wide range of their technical specialties. It was evident that many participants were exposed to relatively unfamiliar materials and topics as a result of efforts by the organizing committee to have an extremely diverse group of conferees. Since superalloys dominate current high temperature applications in the 800–1100°C range, it was considered to be important to discuss alloy design principles, microstructures and mechanical properties of potentially competitive materials such as ceramics and intermetallics, as well as their composites. Environmental effects on mechanical properties were highlighted; it was shown, for example, that water vapor can be detrimental to both intermetallics at low temperatures and ceramics at high temperatures. Oxidation of high temperature materials was another environmental issue of great importance that was discussed in several papers.

The organizers are grateful to the Engineering Foundation for enabling this conference to occur. Barbara Hickernell, Conferences Director, was especially helpful in providing assistance with respect to local arrangements before and during the Conference and in providing rapid responses to inevitable problems of conference organization and communications. The staff of the Cresta Hotel, under the direction of Mr. Jagi, went to great lengths to assure excellent food and service during the Conference. All requests for changes in normal routine were met swiftly and cheerfully.

Financial support came from several sources in the United States and Europe, as listed on the following page. Without this support many conferees could not have attended. We are particularly grateful for the efforts of many individuals to seek out sources of funding from their respective organizations.

We anticipate that these proceedings will provide an important source of information on the most recent developments in the design and manufacture of high temperature metals, ceramics, composites and intermetallics. Further, we look forward to scheduling another conference in this series in two or three years.

N. S. Stoloff
Rensselaer Polytechnic
Institute
Troy, New York

R H. Jones
Pacific Northwest
National Laboratory
Richland, Washington

Conference Co-Chairmen
August 1996

ORGANIZING COMMITTEE

K.K. Chawla
A.G. Evans
R.H. Jones
B. Moudgil
M. Nazmy
N.S. Stoloff
R. Wagner
M.Yoo

We wish to thank the following organizations for their support of this conference:

AFOSR
Asea Brown Boveri - Power Generation Ltd.
Pacific Northwest National Laboratory
GKSS
ONR
U.S. Department of Energy
TMS

TABLE OF CONTENTS

Preface	V
Organizing Committee	VII
Sponsors	VII

KEYNOTE

Implementation Challenges for High Temperature Composites	3
<i>A.G. Evans</i>	

MICROMECHANICS

Universal Behavior in Adhesion of Some High Temperature Materials	37
<i>J.R. Smith, J.E. Raynolds, E.R. Roddick and D.J. Srolovitz</i>	
Atomic-Scale Calculations of Mechanical Behavior of Intermetallic Alloys	49
<i>M.S. Daw and M.J. Mills</i>	
Role of Interfaces in Deformation and Fracture: Titanium Aluminides	57
<i>M.H. Yoo and C.L. Fu</i>	
Constitutive Relationships of Plasticity and Texture Development	67
<i>H. Mecking</i>	

ADVANCED METALLICS, SUPERALLOYS

Unique Single Crystal Superalloys for Industrial Gas Turbine Application	75
<i>G.L. Erickson</i>	
The Aging Alloys Have Matured	91
<i>C.H. Lund</i>	
Development of Advanced Steels for Steam Turbine Applications	107
<i>R.B. Scarlin</i>	
Materials for Advanced Power Plant	123
<i>T.B. Gibbons</i>	

INTERMETALLICS

Design of Ni ₃ Al Alloys for Structural Use	139
<i>C.T. Liu, E.P. George, V.K. Sikka and S.C. Deevi</i>	
Processing, Microstructural Design and Properties of γ -Titanium Aluminides for Industrial Applications	159
<i>M. Nazmy, C. Nosedo, M. Staubli and B. Phillipsen</i>	

Processing and Design Issues in High Temperature Materials – Some Issues in TiAl - Based Alloys	169
<i>M.H. Loretto</i>	
Intermetallics Research in Japan - With Particular Emphasis on TiAl	175
<i>M. Yamaguchi and D.R. Johnson</i>	
Challenges in the Development and Application of β -NiAl as a Structural Material	185
<i>V.I. Levit, J. Hu, I.A. Bul, J.S. Winton and M.J. Kaufman</i>	
Fatigue and Fracture of High Temperature Intermetallics	195
<i>N.S. Stoloff</i>	
Damage Tolerance in Intermetallic and Ceramic Materials at Ambient and Elevated Temperatures: Role of Extrinsic vs. Intrinsic Mechanisms	209
<i>K.T. Venkateswara Rao, C.J. Gilbert and R.O. Ritchie</i>	
Development of a New Series of Nb Aluminides for Elevated Temperature Applications	221
<i>R. Wheeler, IV, S.S. Yang, D.-H. Hou and H.L. Fraser</i>	

CERAMICS AND COMPOSITES

Oxide Fiber/Oxide Matrix Composites	235
<i>K.K. Chawla, H. Schneider, M. Schmücker and Z.R. Xu</i>	
Directionally Solidified High Temperature In-Situ Composites	247
<i>B.P. Bewlay, M.R. Jackson and H.A. Lipsitt</i>	
Biasing Reaction Pathways in In-Situ Composites	263
<i>S.G. Fishman</i>	
Interfacial Structure and Properties for the Design of Fiber-Reinforced Metal Matrix Composites	227
<i>D.B. Miracle, D.B. Gundel and S. Warrior</i>	
High Frequency Fatigue of Continuous Fiber Reinforced Ceramic Matrix Composites	287
<i>N. Chawla and J.W. Holmes</i>	
The Effect of Temperature, in the Range 750°C–1500°C, on the Flow Stress of Polycrystalline Diamond	301
<i>E.J. Brookes, T. Harris, R.L. Wallis and A. Al-Watban</i>	
Strength of Particulate Composites with a High Content of High-Melting Point Filler	311
<i>L.L. Mishnaevsky, Jr., and S. Schmauder</i>	

Hydrogen Effects and Microstructure in Titanium Aluminide Alloys	319
<i>A.W. Thompson</i>	
Hydrogen and Oxygen Effects on Composites Containing a Continuous Carbon Phase	331
<i>A.J. Eckel and J.D. Cawley</i>	
Environmental Effects on the High Temperature Crack Growth of SiC/SiC Composites	343
<i>R.H. Jones, C.H. Henager, Jr., C.F. Windisch, Jr., and C.A. Lewinsohn</i>	
Limitations and Benefits to the Use of Structural Silicides Under Combustion Conditions	359
<i>P. Lipetzky and W.B. Hillig</i>	
Effects of Processing and Environment on Properties of SiC/SiC Composites	369
<i>P. Lipetzky, N.S. Stoloff and G.J. Dvorak</i>	

PROCESSING AND DESIGN

Processing Issues Related to Environmental Effects in Superalloys, Composites and Intermetallics	379
<i>F.S. Pettit and G.H. Meier</i>	
Boron-Modified and Germanium-Doped Silicide Diffusion Coatings for Ti-Al-Nb, Nb-Ti-Al, Nb-Cr and Nb-Base Alloys	391
<i>B.V. Cockeram and R.A. Rapp</i>	
Purity and Processing Effects on the Microstructure and Oxidation of MoSi ₂	403
<i>A. Newman, S. Sampath and H. Herman</i>	
Design and Synthesis of Functionally Graded Composites: The TiB ₂ /NiAl System	413
<i>R.D. Torres, I.E. Reimanis, J.J. Moore and G.W. Mustoe</i>	
Ductility Improvement of Al-Rich Ni ₃ Al by Unidirectional Solidification	425
<i>T. Hirano and T. Mawari</i>	
Fatigue Life Prediction of Titanium Matrix Composites Under Mission Spectrum Loading	433
<i>T. Nicholas and A.H. Rosenberger</i>	
Subject Index	441
Author Index	445

KEYNOTE

IMPLEMENTATION CHALLENGES FOR HIGH TEMPERATURE COMPOSITES

A. G. Evans
Harvard University
Division of Engineering and Applied Sciences
Cambridge, MA 02138

Abstract

Some issues that influence the implementation of ceramic (CMC) and titanium (TMC) matrix composites in high temperature systems are addressed. Commonalities and differences are brought out by comparing and contrasting their thermomechanical characteristics, with examples. Emphasis is given to the role of design and the use of mechanism-based models of material behavior. Factors addressed include the relative significance of toughness and ductility for thermostructural applications, including their manifestation in the notch sensitivity. The detriments caused by anisotropy are examined, through discussions of mechanisms such as delamination in CMCs and transverse debonding in TMCs.

Introduction

The implementation of new high-temperature materials involves an integration of manufacturing, design and life prediction that attains improved system performance at costs lower than existing systems. In turbines for propulsion and power generation, various composite materials, intermetallics, ceramics and coatings are all vying for implementation. Each promotes specific performance benefits, mostly based on reduced weight or higher gas temperatures. The rationale for evaluating this spectrum of materials is described. Among these, only polymer matrix composites (PMCs) and ceramic thermal barrier coatings (TBCs) are in routine implementation. Technological issues restricting wide implementation are discussed.

An underlying *technical theme* is the relative sensitivity of many candidate materials to strain concentrators: particularly, manufacturing flaws, holes, impact sites, fretting contacts. This sensitivity is reflected in the *toughness* and *ductility* and manifest in the engineering notch performance[1-9]. The mechanisms involved are those governing inelastic strains. Such strains enable *redistribution* of the stresses and diminish their peak magnitudes[6-9]. These mechanisms are described and used to address the relative importance of toughness and ductility.

Fatigue, oxidation, stress corrosion, creep and rupture are dominant considerations for long life applications. They determine the reliability and life expectancy. Implementation requires that these phenomena be understood at levels needed to devise a robust life prediction methodology: preferably mechanism-based. The status of these models is assessed.

Manufacturing costs are dominated by small production volumes, as well as complex manufacturing procedures with long cycle times[10,11]. These factors distinguish high-temperature materials and their applications from those used in mass production. This distinction provides openings for new materials. Analytical approaches that clarify these opportunities are described and illustrated.

Materials Selection

The current rationale for developing new high temperature materials resides in property advantages that provide a *manufacturing cost benefit at superior performance*. Frequently, stiffness and density are the dominant performance drivers [11]. Creep strength and thermal diffusivity are important in other instances. Throughout, *notch sensitivity* has a defining role. These property advantages can be displayed with Materials Selector software[12]. They rationalize why certain materials have progressed furthest toward implementation.

Modulus/density charts(Fig.1) with superposed design indices provide one rationale. Most propulsion components have stiffness and weight constraints, subject to cost objectives. There are also geometric requirements. These lead to three primary structural indices: E_L/ρ (strut), E_L^2/ρ (beam), E_L^3/ρ (plate), with E_L being the longitudinal modulus and ρ the density[11,12]. Intermetallics and ceramics have preferred stiffness/density combinations, suggesting TiAl, Be/Al, Si₃N₄ and SiC as the preferred monolithic materials. But, as elaborated below, creep strength and notch sensitivity limit their performance. Instead *composites* emerge as more relevant candidates, because they combine favorable structural indices with acceptable notch

properties. The application of charts to composites requires definition of the fiber architecture. There are two situations. (i) In polymer (PMC) and ceramic (CMC) matrix materials, weaves and plies are generally used, with a relatively high volume fraction of fibers (0.4 to 0.6). These are organized in at least two orientations. Such reinforcement schemes are necessary because of low transverse properties. The structural attributes realized with PMCs are indicated on Fig. 1a

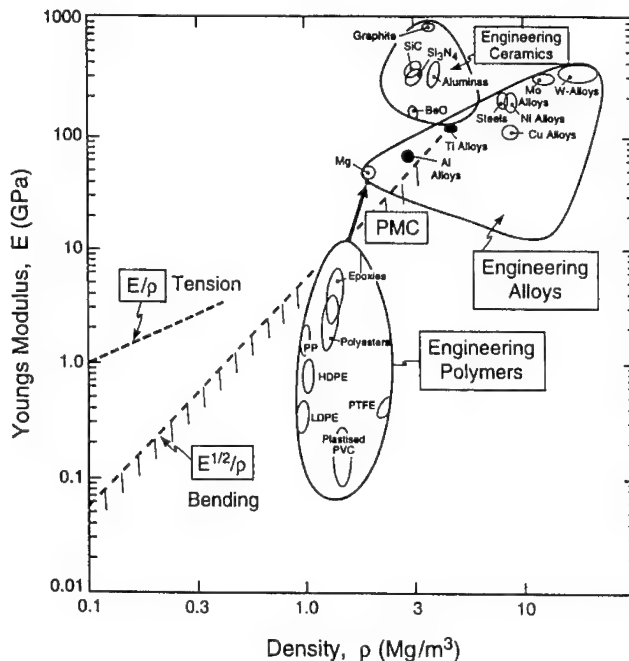


Fig. 1. Modulus/density charts. (a) The benefits achieved with PMCs relative to alloys, especially in bending.

(ii) Ti matrix composites (TMCs) can only be fabricated with relatively low fiber volume fractions(0.3). Thus, favorable structural indices require *unidirectional reinforcement* schemes(Fig.1b)

Implementation with this architecture is feasible, because TMCs have adequate transverse properties that suffice in some basic designs.

Ceramic matrix composites have been devised to obviate the prime limitation of monolithic ceramics. That is, they acquire acceptable notch performance through the introduction of stress redistribution mechanisms. The goal is to realize a stress redistribution capability comparable to that for Al or Ti alloys, without compromising high-temperature durability, at acceptable cost. These objectives can be appreciated with the use of a toughness, density chart (fig 2)

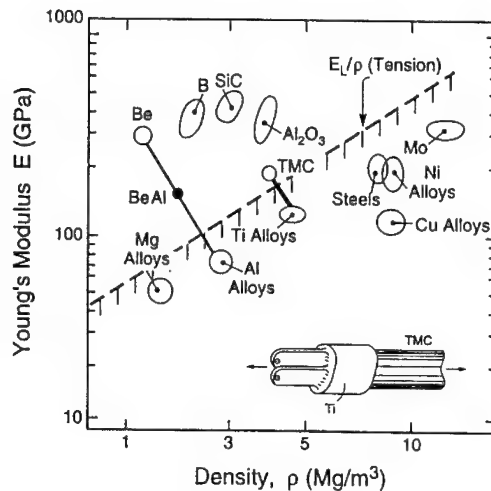


Fig. 1.b) The location of unidirectional TMCs and the benefit that derives from using them in tension loaded components. The line E/ρ refers to tension and $E^{1/2}/\rho$ is for bending.

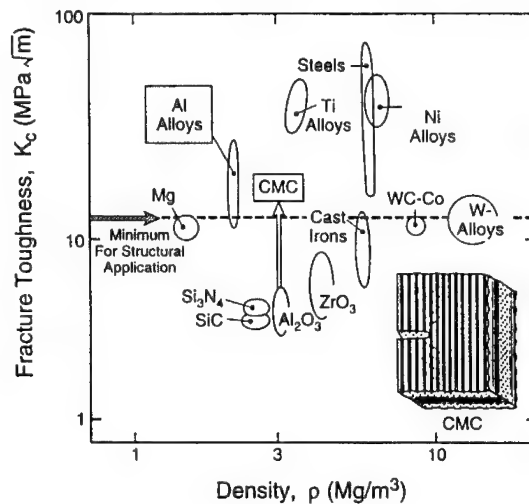


Fig. 2 A toughness/density chart showing CMCs relative to structural alloys and engineering ceramics. Experience indicates that a toughness of 15-20 MPa \sqrt{m} or greater is needed for structural use.

Toughness does not enter as an explicit design parameter, but it has an indirect relationship with notch performance. Experience has indicated that acceptable thermostructural characteristics arise when the toughness exceeds about 15-20 MPa \sqrt{m} . This toughness establishes one CMC property goal.

A thermal conductivity(k)/thermal expansion coefficient(α) chart (Fig.3)

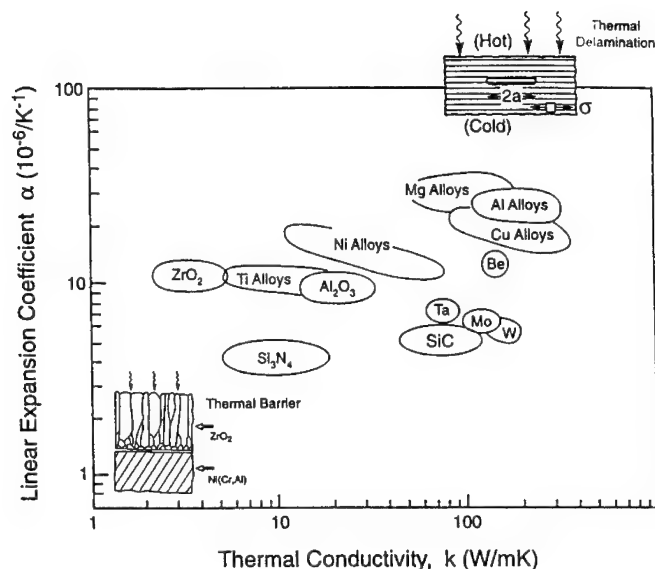


Fig. 3 A thermal expansion, thermal conductivity chart for the constituent materials used in MMCs and CMCs.

provides additional materials selection input. *Expansion mismatches* ($\Delta\alpha$) between components exceeding about 5ppmC^{-1} lead to severe thermal fatigue. Even smaller differences are demanded for composite constituents: $\Delta\alpha < 2\text{ppmC}^{-1}$. Otherwise, ratcheting or cracking occur upon thermal cycling[13, 14]. This requirement severely constrains the selection of fiber reinforcements and of protective coatings. For example, *high-temperature* TMC applications require Al_2O_3 fibers. The SiC fibers used now are unacceptable. Yet, the fabrication of such TMCs has not yet been possible because of reactivity problems during consolidation. In CMCs, the same issues dictate preferences for SiC/SiC or mullite/ Al_2O_3 over SiC/ Al_2O_3 . *Thermal conductivity* is important for materials with limited ductility, because low k elevates both the transient thermal strains and the temperatures reached in operation. High k materials are thus preferred, such as SiC.

Design Issues

Inelastic Strain and Toughness

Inelastic deformation with attendant "ductility" enables stresses to be redistributed and thereby, diminishes stress concentrations[8,9,15]. This peak stress reduction is particularly crucial to notch performance. In monolithic alloys, this effect is achieved through plasticity[16]. In CMCs, multiple matrix cracking with internal friction is the responsible mechanism[8,9]. In TMCs and PMCs, matrix plasticity is

predominant[17]. Moreover, materials exhibiting inelastic deformation are amenable to *well-established design strategies*. [18,21] That is, an inelastic constitutive law is devised, preferably mechanism-based. Stresses are calculated by numerical methods and a failure criterion implemented. The peak tensile stress is equated to a critical stress, such as the ultimate tensile strength (UTS) measured on test coupons.

The notch strength of a material is a good engineering indicator of its stress redistribution capacity: whereby, a notch sensitivity index establishes the relative importance attached to the design of holes and other strain concentrators [19]. There is a well-established methodology for assessing the notch performance of conventional materials. At the experimental level, it involves instrumented Charpy tests. At the mechanism level, it entails the use of FEM with plasticity to calculate peak stresses and to equate these to the critical stress [16]. Moreover, since the plastic zone around the notch is similar to that around a crack, the notch behavior scales with the fracture toughness. This connection allows the toughness to be used as materials selection input (Fig.2).

For composites, the toughness is non-unique, because of large-scale inelastic deformation effects, such as bridging (LSB) and yielding (LSY) [20-22]. The notch sensitivity is then a more robust and useful measure of performance. Among composite materials the trend in notch sensitivity, from least to greatest is, surprisingly: CMC > PMC > TMC (fig 4). The latter are quite notch-sensitive, because of plastic localization [23]. By contrast, CMCs combine a large inelastic zone with stochastic scaling effects to eliminate stress concentrations [9] (Fig.4).

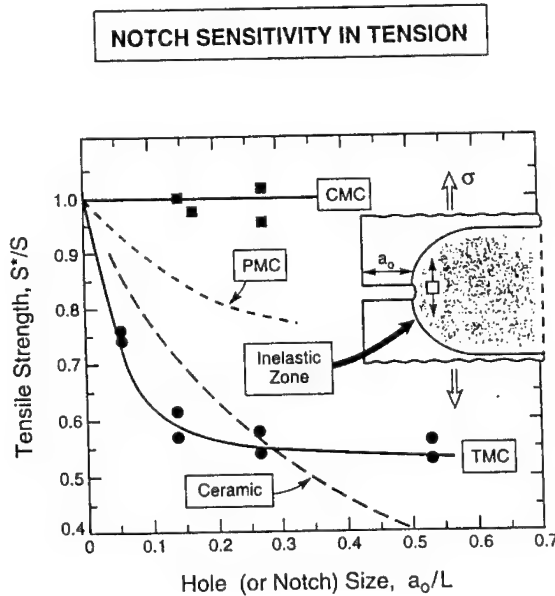


Fig. 4 The relative notch sensitivities of various composite systems. The inset shows the inelastic zone that dictates the stress redistribution occurring around the notch. The notch length a_0 is normalised by L , the inelastic zone length that develops upon localisation of the failure process on the notch plane.

In ceramics and intermetallics, large stress concentrations persist because inelastic deformation mechanisms do not operate on a sufficiently macroscopic scale. They only occur in the 1-100 μm range around cracks, where they cause toughening[18,24-26]. Consequently, notches cause a dramatic reduction in strength (Fig. 4). Moreover, the UTS is scale (size) dependent because of weakest-link statistics, and the distributions are often extreme value[27,28]. These problems compromise robust design practices [18,26].

Anisotropy

When reinforcements are used to provide a performance advantage, there are corresponding detriments associated with the *anisotropy*. The issues differ for PMCs/CMCs compared with TMCs. For the former, out-of-plane stresses can cause delamination and interlaminar shear cracking[8,29-31]. These phenomena are dominated by the matrix properties, subject to manufacturing flaws and to weakest-link scaling. Incomplete understanding of the effects has resulted in the use of "knock-down factors" in conjunction with elastic analysis. Often, such conservatism discounts the advantage of the composite relative to competing monolithic materials. The limitations of this design strategy are ameliorated by the stable nature of the damage. That is, delamination and shear cracks invariably *arrest* as the stresses redistribute upon cracking, such that some load carrying capacity is retained[31]. These non-catastrophic modes provide a crucial thermostructural "safety factor".

A different anisotropy issue arises in TMCs [17]. These materials have moderate transverse strength and toughness, as well as sufficient ductility to facilitate stress redistribution (fig 5).

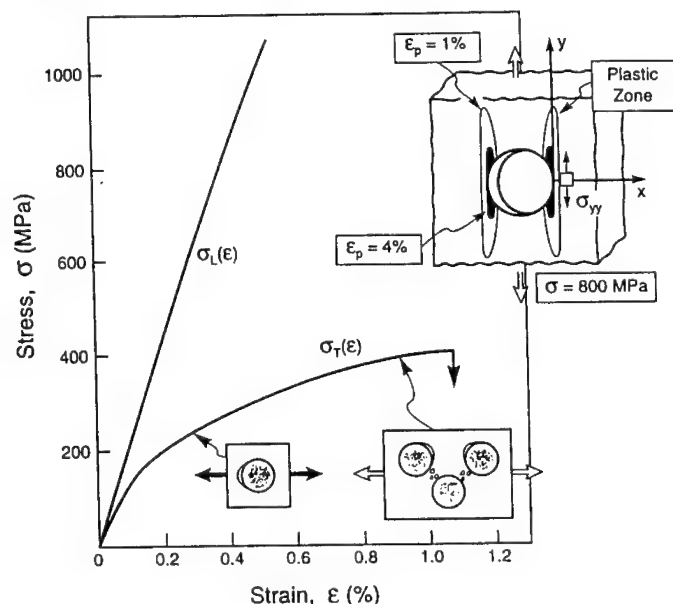


Fig. 5 The anisotropic stress/strain behaviour of TMCs. The inset indicates the plastic zone that develops around a hole at a 800 MPa. The contours indicate the plastic strain levels.

But, design flexibility is still limited, because TMCs only have structural benefit when *unidirectional reinforcements* are embedded in monolithic Ti alloys [18,32]. The designs are configured in such a way that the loads enter the TMC through the monolith with minimal transverse stresses [32-34] (Fig.6).

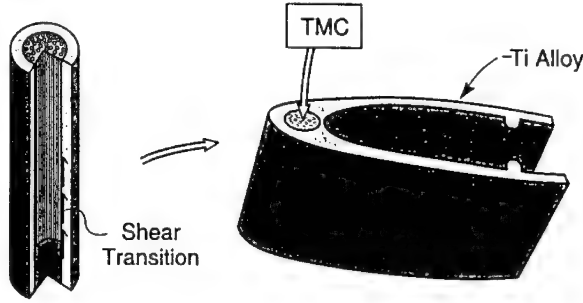


Fig 6 A schematic of a TMC within a bonded monolith that transmits the stress into the TMC with minimal transverse loads.

However, many potential applications are excluded by this constraint.

Manufacturing Challenges

Manufacturing problems and associated costs often dominate implementation strategies. Simple process and cost models highlight the key issues. A straightforward expression for the cost per component, designated \$, is

$$\text{\$} = \text{\$}_m + \sum_{\text{All}} \left(\frac{\text{\$}_R^\circ}{\tau_s} \right) \quad (1)$$

where $\text{\$}_m$ is the raw material price per component. The summation is over all manufacturing steps. The throughput τ_s is the ratio of the number of components passing through the manufacturing process, N_s , divided by the cycle time t_s . The cost-rate $\text{\$}_R^\circ$ includes power usage, capital and replacement costs, labor costs, and so on,

$$\text{\$}_R^\circ = \bar{Q}\phi_u + C_c/t_L + C_e/t_e + \phi_L(\Delta t/t_s) + \dots \quad (2)$$

Here, \bar{Q} is the average power used in a cycle, and ϕ_U its cost (in\$ per kWh). C_C is the equipment price and t_L the depreciation period, C_e is the cost of tooling, heating elements and other parts that must be replaced with periodicity, t_e ; Δt is that portion of the cycle time that requires labor, ϕ_L (in\$/h). The goal is to reduce S_R and increase τ_s such that S approaches S_m . For most high-temperature components, this goal is not realized, because of manufacturing complexity and the small throughput. Moreover, most manufacturing operations involve multiple steps. Those steps that dominate the cost need to be identified and addressed through process understanding and by the use of process models. While such models are incompletely developed and not broadly available, some general conclusions can still be reached.

Small volume production is an overriding non-technical factor that can only be rectified by either diversifying the range of products or by writing off the development costs. Technical factors arise from the important contributions to the costs originating with long cycle times for the high temperature steps in the production, expensive chemicals/powders and high capital costs. These can be systematically addressed through combinations of modeling, process optimization, lower cost ingredients and the matching of capital costs to product volumes.

For composites, the costs of the fibers and the fiber coatings often dominate [35] (Fig. 7).

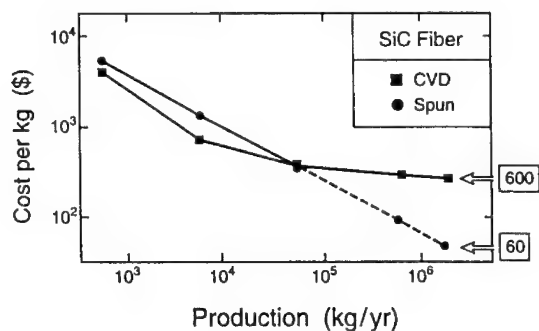


Fig 7 The effect of production volume on the manufacturing cost for two types of SiC fiber. The dotted region for the polymer derived fiber assumes a reduction in the price of the organic precursors, below present prices, as the production volume becomes large.

One clear implication is that fiber reinforcement should be used judiciously and selectively. That is, composite regions should be embedded in monolithic material through a complete redesign, wherein the benefits provided by the fibers are

introduced only in critical regions. This strategy has been used with TMCs for struts, fan blades, etc. with the TMC emplaced selectively within an otherwise cast Ti alloy product [36]. Here, the TMC is used to enhance the overall bending stiffness. This extra stiffness enables a weight reduction. Then, the performance advantages of the TMC/Ti system are in balance with the manufacturing costs.

Comparable strategies are less tractable with CMCs and PMCs, because of design problems with the surrounding monolithic material. Hence, for these materials, manufacturing strategies focus on low cost methods for introducing the fiber coatings and the matrix in order to minimize the overall cost (beyond that for the woven fiber preform)[37]. Transfer molding and its derivatives are preferred, because of the diminished number of processing steps, with a consequent reduction in overall cycle time and labor costs. Processes with inherently long cycle times (such as CMC production by chemical vapor infiltration) are disadvantaged.

Property Profiles

Ultimate Tensile Strength

Key issues associated with the UTS are its scale dependence and its statistical variability. All materials subject to stress-controlled fracture are susceptible to such effects. They arise from weakest link considerations. Such scale dependence is frequently associated with an extreme value distribution [27,28]. These factors present important design challenges. Monolithic brittle materials subject to small-scale toughening are particularly challenging, because it is imperative that the scaling behavior be *well calibrated*, as well as manufacturing *invariant* [15]. The associated costs are often prohibitive. By introducing inelastic mechanisms that stabilize damage, through plasticity, internal friction, etc., progressive reduction in the scale sensitivity can be achieved. Eventually, as the inelastic mechanisms are made more effective and the number density of active inelastic strain sites is increased, macroscopic inelastic strain can be induced prior to the UTS [8,38,39]. Such deformations profoundly change the design philosophy. With sufficient inelastic deformation, the scale dependence is virtually eliminated, the UTS distribution is essentially Gaussian, and design strategies used for metals can be applied.

When size scaling of the UTS obtains, it is vividly manifest upon testing specimens that have vastly different stressed volumes; for example, tension relative to bending [27]. The goal of the testing is to characterize the population of defects that control the strength, S (Fig. 8a).

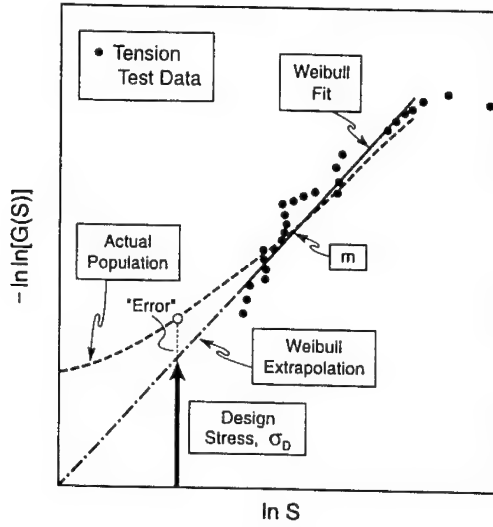


Fig 8 a The cumulative flaw strength distribution estimated by using tension test data. The data and the region of extrapolation are indicated. The Weibull fit does not represent the actual flaw population in this case, resulting in an overestimate of the strength in that part of the population relevant to the design.

This population can be represented by a frequency distribution, designated, $g(S)dS$ [28]; the fraction of defects per unit volume (or per unit surface area for surface flaws) that cause failure when the stresses are between S and $S + dS$. Then, the survival probability of a small volume element, ΔV , subject to uniaxial stress σ is [28]

$$1 - \delta\phi = \Delta V \int_0^{\sigma} g(S) dS$$

$$\equiv \Delta V G(\sigma)$$
(3)

where $\delta\phi$ is the failure probability. This relates to the overall failure probability Φ through [27,28],

$$1 - \Phi = \Pi_N (1 - \delta\phi)$$
(4)

where N is the number of volume elements in the component and Π refers to the product over all elements. $G(S)$ for each flaw population can be fit by a power law,

$$G(S) = \left(\frac{S - S_u}{S_o} \right)^m \quad (5)$$

where m is the shape parameter, S_o the scale parameter and S_u the offset parameter. However, the strength is affected by more than one defect population and $G(S)$ is not normally single valued. That is different m , S_o and S_u are needed to represent the defect populations over the full stress range relevant to specimen testing and design. This presents stringent testing requirements for the acquisition of accurate design data.

When inelastic deformation mechanisms operate around the defects, $G(S)$ can be dramatically modified. These mechanisms include plastic yielding and internal friction. The most comprehensive illustration is for fiber-reinforced composites that exhibit large-scale debonding and friction, such as CMCs and TMCs. These mechanisms "blunt" and stabilize the damage emanating from failed fibers, by redistributing stresses in the surrounding material, thereby reducing the stress concentrations in the nearest fibers [41-43]. The consequence is that multiple fiber failures can occur before the UTS is reached [44], often allowing other inelastic mechanisms to be activated in the matrix. The stabilization efficiency increases as the interface debond and friction stresses decrease [43-46]. A practical measure of the efficacy of these mechanisms is the width of the unload/reload hysteresis loops measured upon tensile testing [47-49]: wide loops correspond with small friction and debond stresses (Fig. 9).

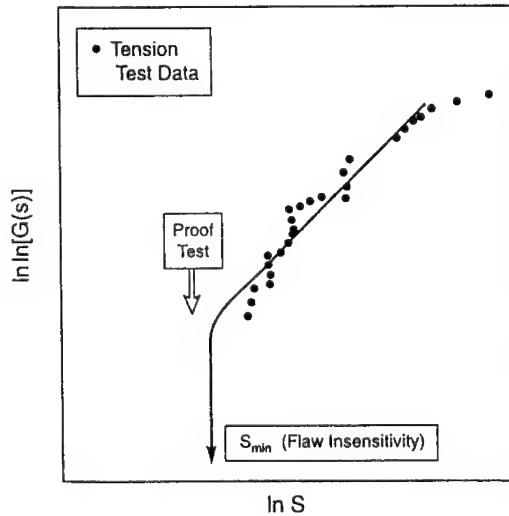


Fig. 8 b. Truncation of the strength at a minimum achieved either by proof testing or by developing inelastic mechanisms in the material that provide stress redistribution with an attendant insensitivity to large manufacturing flaws.

As these mechanisms come into operation, there is a markedly diminished scale dependence of the UTS.

Friction at the interfaces dictates the dimension over which stress concentrations around failed fibers are eliminated. This dimension becomes an *internal* scale parameter, which allows fiber failures to occur in a spatially uncorrelated manner. When this happens, global load sharing (GLS) ensues with an associated UTS given by

$$S = S_u + (1 - f)\sigma_o \quad (6)$$

where

$$S_u = F(m)S_g \left(\tau L_o / R S_g \right)^{1/(m+1)}$$

and

$$F(m) = [2/(m+1)]^{1/(m+1)} [(m+1)/(m+2)] \quad (7)$$

with L_o being a reference gauge length (normally 25 mm), τ is the friction stress, R the fiber radius, f the fiber volume fraction and S_g the tensile strength at length L_o . The first term is that contributed by the fibers. The second is provided by the matrix. For TMCs, σ_o is the matrix yield strength. For CMCs, $\sigma_o = 0$, because of multiple matrix cracking. The main features described by this result are as follows. (i) The UTS is affected by friction. (ii) There is a weak dependence on the shape parameter, m , characterizing the individual fiber strengths. (iii) There is a strong effect of the mean reinforcement strength, S_g .

Usually, low friction is not sufficient to realize GLS conditions. Concentrated stresses persist upon fiber failure, resulting in local load sharing (LLS) [51,52]. The ensuing UTS *decreases below that given by (6) and becomes scale dependent*. But, the effects are not especially deleterious. In practice, the UTS scales in accordance with (3) to (5), subject to a large effective shape parameter, m^* [51]. More importantly, the behavior is insensitive to the occurrence of large manufacturing flaws, because of the existence of a robust strength minimum, S_{min} (Fig. 8b).

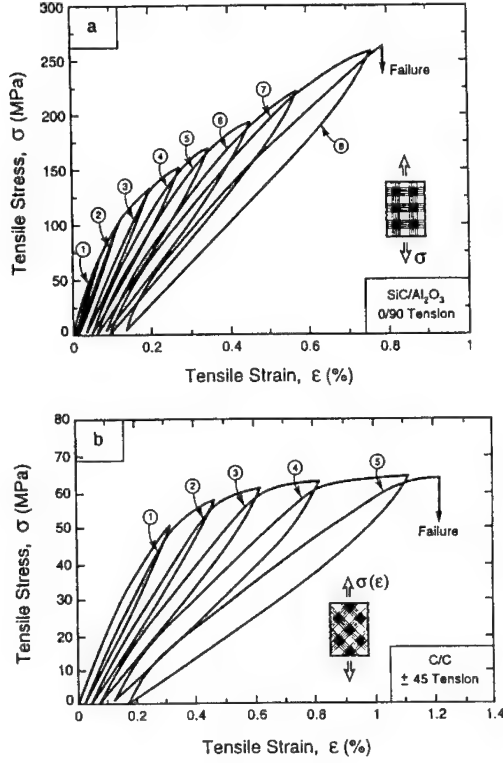


Fig 9. Hysteresis loops measured upon the tensile testing of CMCs: (a) 0/90 (b) ± 45 .

This attribute is understood upon examining the stress concentrations induced by large flaws. Two effects are involved. (i) One is associated with large scale fiber bridging (LSB), governed by the index [52]:

$$\eta = \frac{\pi f^2 E_f E a \tau}{(1-f)^2 E_m^2 R S A} \quad (8)$$

where a is the size of the flaw, E is Young's modulus, A is an anisotropy coefficient of order unity, with the subscript f and m referring to the fibers and matrix, respectively. Based on this index, the strength contributed by the fibers through LSB is [52,53]:

$$S/S_u \equiv (1 + \eta^{2/3})^{-1/2} \quad (9)$$

Note that, when τ is small, $\eta \rightarrow 0$, and the flaws have no effect on the strength. (ii) The second effect is related to the notch performance enabled by large scale inelastic strains[4,6,8,9]. These dominate at larger τ . Such strains diminish the stress concentrations around the manufacturing flaws, leading to tensile behavior independent of the flaw size, analogous to the notch insensitivity.

Inelastic Strain and Ductility

When the number density and the potency of the inelastic deformation sites increases, macroscopic inelasticity initiates at stresses below the UTS. This typically causes a marked increase in the failure strain, or ductility. The inelastic strain now allows *stress redistribution*. An illustration for a mechanical attachment to a CMC is presented in Fig. 10,

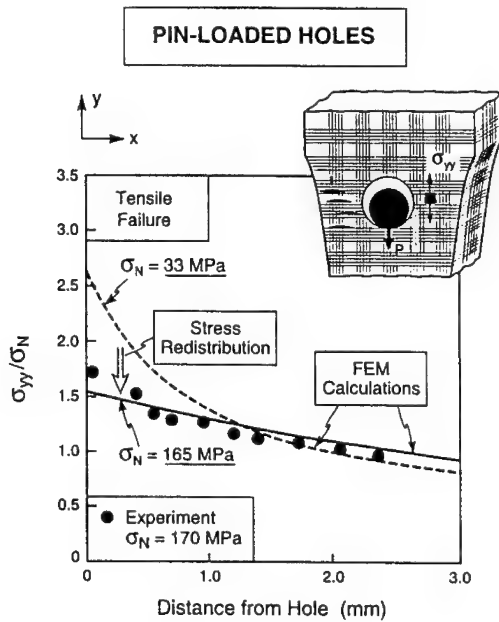


Fig 10 Stress redistribution effects around a pin loaded hole. The experimental results have been obtained by Moire interferometry. The constitutive law used for the FEM calculations is based on (12). Note that the stress concentration factor decreases as the net section stress, σ_N increases.

along with an experimental validation, obtained using Moire interferometry [5,9]. The key feature is that the stress concentration factor around the hole diminishes upon increasing the load, as an inelastic zone develops. This diminished stress concentration combines with an elevation in the local UTS arising from volume scaling[52,54]. The overall effect is a *component performance unaffected by the presence of the hole*. These characteristics originate with the inelastic strain mechanisms, manifest in the stress/strain curves.

(i) Brittle Matrix Composites

For CMCs, multiple matrix cracking with interface debonding and friction enable appreciable inelastic strain in tension and shear [8] (Fig.9). Two cell models represent most of the important physical relationships between the inelastic strains and the mechanisms of matrix cracking, friction and debonding. One model applies to cracks that first form on the 90° plies (Fig.11)[55,56]. The other represents cracks that penetrate the 0° plies (Fig.11) [41]. Cracks in the 90° plies tunnel with an associated inelastic strain (Fig.11)

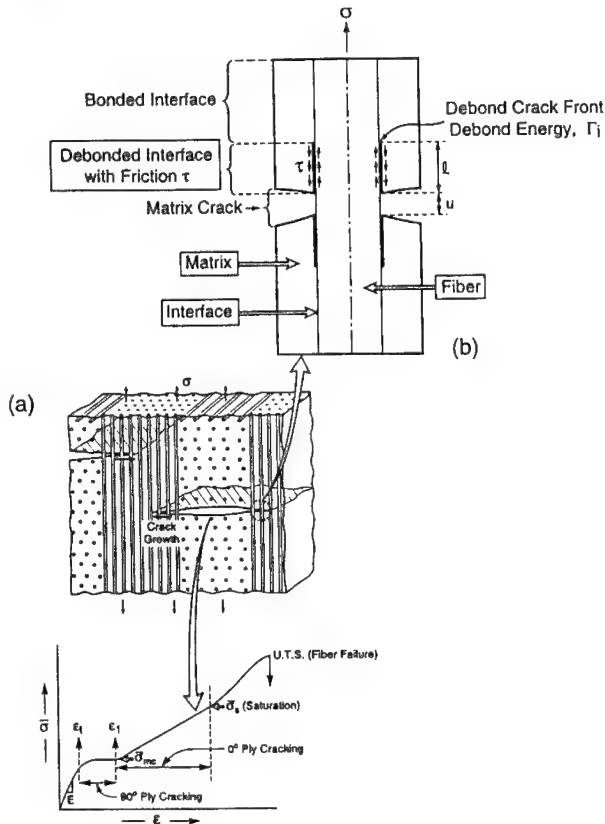


Fig 11. Schematic of matrix cracking in CMCs and the associated cell models. The corresponding stress/strain curve is indicated.

Upon subsequent loading, as the cracks penetrate the 0° plies, they interact with the fibers and the coatings. When debonding and slip occur *within the coating*, two stresses characterize the inelastic strain: a friction stress τ , and a debond stress σ_i (Fig. 11).

The latter is related to the debond toughness for the coating and the residual stress [41]. The consequent inelastic tensile strain ϵ depends on the stress σ acting on the 0° plies. It has linear and parabolic terms, given by

$$\epsilon = (1 + \Sigma^T) \sigma / E + 2L\sigma^2(1 - \Sigma_i)(1 + \Sigma_i + 2\Sigma^T) - \sigma / E_* \quad (10)$$

where Σ_i is the non-dimensional debond stress, ($\Sigma_i = \sigma_i / \sigma$), E_* is the diminished elastic modulus caused by matrix cracking, Σ^T is the residual stress ($\Sigma^T = \sigma^T / \sigma$) and L is an interface friction index, given by

$$L = \frac{(1-f)^2 R}{4f^2 \tau d E_m} \quad (11)$$

with d being the crack spacing. The parameters, E_* , L , and Σ_i , evaluated from hysteresis loops (Fig.9) provide understanding about the separate influences of debonding, friction and matrix cracking on the inelastic strain [58]. They also provide the insight needed to develop a constitutive law compatible with finite element codes [9,59]. Simulations, as well as hysteresis measurements, have established the influence of friction and debonding on the stress/strain behavior of CMCs [57-59]. The principal effects associated with (10) are as follows. The inelastic strain and the hysteresis loop width increase as the friction stress τ decreases (or L increases). Small τ accounts for the wide hysteresis loops in SiC/CAS [58]. A large debond stress σ_i limits the role of friction and diminishes both the inelastic strain and hysteresis. Large σ_i accounts for the narrow hysteresis loops in SiC/SiC and SiC/MAS [58]. These insights have lead to the formulation of a constitutive law [9,59]. The plane stress relation for the stresses and strains in directions (1,2) obtained by expressing the inelasticity through the stress drops that occur upon matrix cracking is [93],

$$\begin{aligned} \sigma_1 &= \frac{E_o}{1-\nu_o^2} (\epsilon_1 + \nu_o \epsilon_2) + \Delta\sigma_1 \cos^2 \theta + \Delta\sigma_{11} \sin^2 \theta \\ \sigma_2 &= \frac{E_o}{1-\nu_o^2} (\epsilon_1 + \nu_o \epsilon_1) + \Delta\sigma_1 \sin^2 \theta + \Delta\sigma_{11} \cos^2 \theta \\ \tau &= \frac{E_{45}}{2(1-\nu_{45})} \gamma_{12} - (\Delta\sigma_1 - \Delta\sigma_{11}) \sin \theta \cos \theta \end{aligned} \quad (12)$$

where τ is now the macroscopic shear stress, $\epsilon_{1,2}$ the normal strains and γ_{12} the shear strain: $\Delta\sigma_{I,II}$ are the stress drops upon matrix cracking at fixed strain, parallel and normal to the fiber directions, θ is the angle between (1) and the fiber direction. This constitutive law has been used to calculate the results presented on fig 10, which vividly illustrate the role of ductility in design.

(ii) Ductile Matrix Composites

The stress/strain response of unidirectional TMCs is quite different (Fig.5). These materials are anisotropic [17]. They are almost linear in longitudinal tension, but exhibit some ductility in transverse tension and shear, controlled by matrix yielding and plastic hole coalescence. This anisotropy causes problems in longitudinal performance, in addition to the issues that arise upon transverse loading, elaborated below.

Implementation of a constitutive law to calculate stress concentrations at holes and slots [17] (Fig.12)

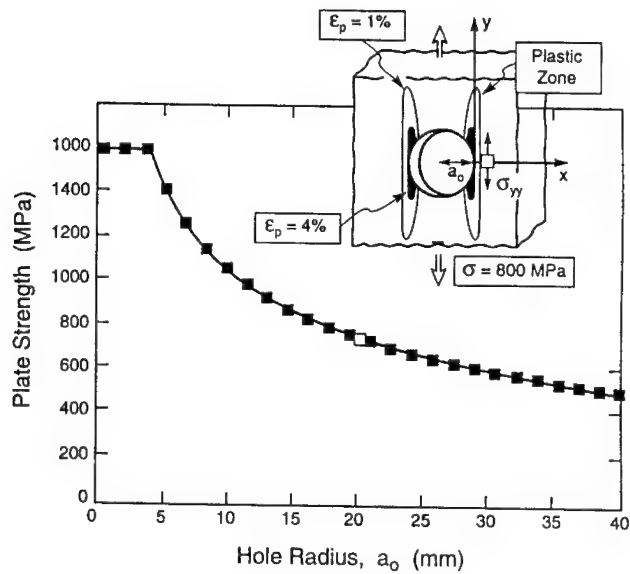


Fig 12 Stress concentrations around holes in unidirectional TMCs calculated using the constitutive law obtained from fig 5. Also shown are the post-localisation effects that enable bridging by the intact matrix that leads to the notch insensitivity found at larger notch sizes.

indicates that the stresses in axially loaded configurations are *unaffected by the plastic deformation* [60-62]. That is, elastic stress concentrations are retained and even exacerbated by anisotropy, despite the extensive plastic zone in the matrix. This behavior is typical of that found for anisotropic materials that respond linearly in one direction: as previously elaborated for layered materials and coatings [43,61,62]. This effect accounts for the relative notch sensitivity found for TMCs; differing dramatically from that for metals in which isotropic plastic deformation greatly diminishes stress concentrations.

But, the extreme notch sensitivity that might be expected from the stress concentrations is ameliorated in TMCs by inelasticity arising *after localization by fiber bundle failure*. The effect is depicted in Fig.12. When the fiber bundle at the notch front attains the UTS, it fails but transfers the load to the intact matrix. This causes the matrix to yield in a band contiguous with the notch. This plastic band acts as a bridging zone subject to tractions which provide the extra toughness needed to prevent unstable fracture. Composite failure only occurs when the matrix in the plastic band stretches to its rupture strain. This constitutes a large scale bridging (LSB) phenomenon, which can be analyzed using standard LSB mechanics [19-21]. The results for TMCs are indicated on Fig.6 [23]. That is, notch degradation is ameliorated at larger notch sizes. But there is still a strong sensitivity of TMC performance to small notches. This problem can be obviated in design, but re-emerges as an issue in fatigue, through its effect on the fatigue threshold.

Transverse Properties

Low transverse strengths constrain designs and limit application. An understanding of the transverse responses is essential to effective implementation. These properties are dominated by the matrix and the interfaces. They have monolith counterparts. Cracking and delamination occur in CMCs [8, 31]. Yielding and plastic straining obtain in TMCs [17]. But, in both cases, the fibers and the interfaces require that new factors be addressed.

For TMCs, there are two principal factors. (i) The interface has minimal tensile strength, such that debonding occurs when the transverse stress exceeds the residual compression induced by thermal expansion mismatch [17,63,64]. At this "elastic limit", σ_e , there is a reduction in the transverse modulus to about half its initial value [17,63]. (ii) At larger strains, matrix yielding occurs: but the hydrostatic tensions in the matrix induced by the fibers are an appreciable fraction of the matrix yield strength, despite interface debonding. This stress state accentuates plastic hole growth and leads to low transverse ductility (relative to monoliths having the same composition and microstructure) [17]. The elastic limit has been a design constraint, because the diminished modulus causes *stress amplification*. An illustration is presented for a drum rotor [65] (Fig.13).

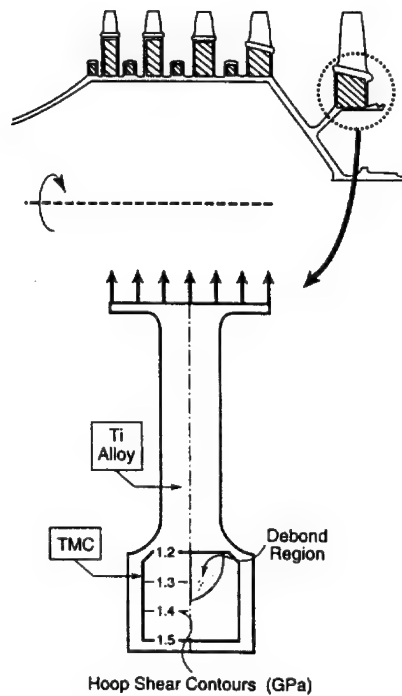


Fig 13 FEM calculations for a drum rotor with a TMC annulus. The debonded regions within the TMC, caused by the transverse loads, are indicated on the right, while the hoop stresses in the TMC are on the left. Note that debonding has elevated the hoop stresses in neighbouring regions of the TMC. These stresses would cause premature failure.

Transverse stresses are induced by the rotations. When these exceed the elastic limit of the TMC closest to the center of rotation, the hoop stresses increase on the remainder of the TMC. This stress elevation causes the UTS to be reached at lower rotational velocities as σ_e diminishes. This factor is of particular concern upon thermal cycling. Beyond a thermal range ΔT_c , dependent on the transverse stress, ratchetting occurs [13] and the residual stress decreases, causing σ_e to diminish and eventually approach zero. This phenomenon results in a maximum temperature range allowing shakedown [13], plotted on Fig 14.

The transverse responses in CMCs are quite different. The major concern is delamination, particularly in attachments and transitions [31,66-68] (Fig.15).

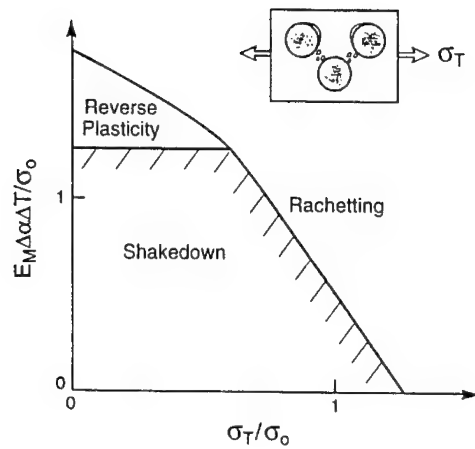


Fig 14 The shake down and ratchetting regions in a TMC subject to transverse loads, σ_T and cyclic temperature, ΔT : here σ_0 is the matrix yield strength.

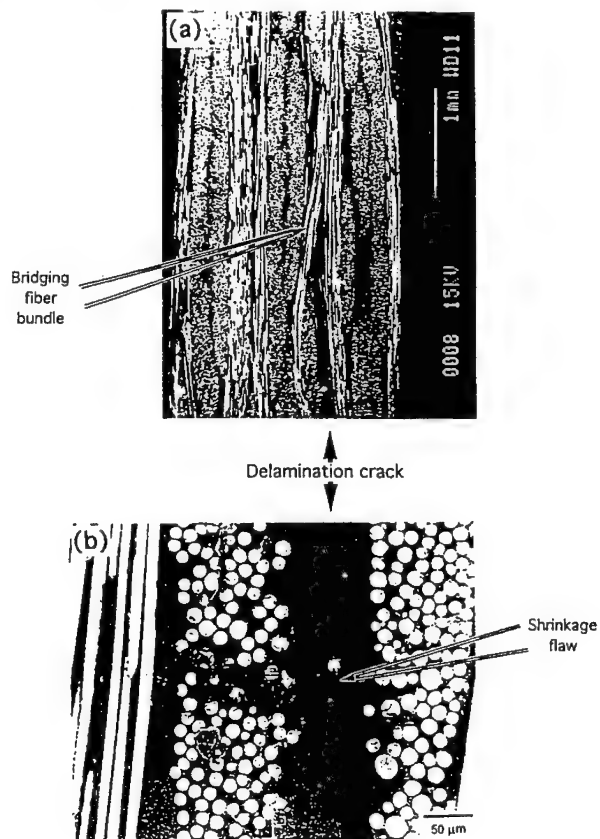


Fig 15 Delaminations induced in I-sections by applied bending moments. The load deflection response is indicated.

There are two motivating forces: one caused by the loads and the other by the heat flux [68]. Manufacturing flaws interact with these forces to initiate cracks, which then extend along interlaminar planes. Usually, the delaminations arrest, because they extend into regions that diminish the energy release rate. Some load bearing capacity is thus retained[31]. The non-catastrophic nature of delamination is an attribute, but the remnant load bearing capacity is small. Designing to this remnant strength would lead to excessive mass in the attachments and transitions. This factor requires that designs be made based on the initiation loads. Then, the key issue is that delaminations initiate subject to weakest link scaling, with extreme variability arising from manufacturing flaws; that is, in this orientation, CMC performance is dominated by the low toughness matrix.

Manufacturing flaws and other transverse cracks induce local temperature variations. The temperature gradients create an energy release rate, through the thermal strains, even when there are no applied loads. This phenomenon has a steady-state, wherein the energy release rate is independent of the flaw size. The steady-state result is [69]:

$$EG_s / H(\alpha\Delta T)^2 = \lambda(h/H) \quad (13)$$

where H is the CMC thickness, ΔT_0 the temperature drop through the CMC, h the flaw location and λ the function plotted on Fig.16

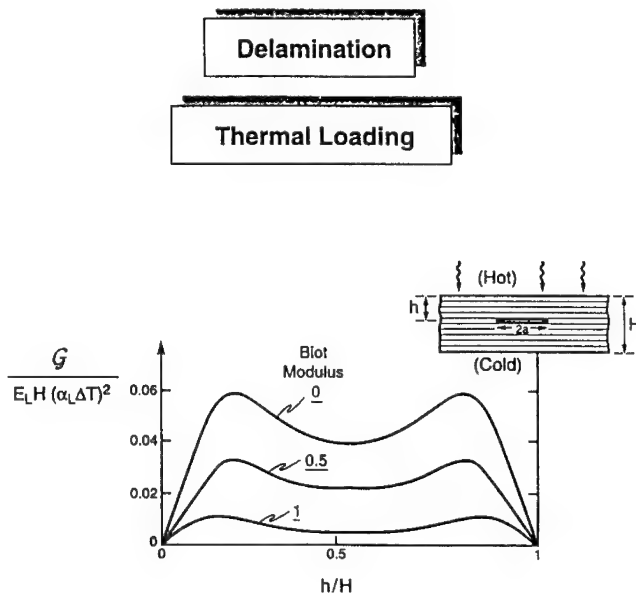


Fig 16 Delamination caused by a through thickness thermal gradient in a CMC. Also shown are the steady-state energy release rates. Here ΔT_0 is the temperature difference across the CMC and α is its thermal expansion coefficient.

Thermal delamination occurs when G_s reaches the matrix toughness, Γ_m

The design implications are so debilitating that a delamination strategy is needed to enable successful implementation. There are no evident mechanisms for elevating the matrix toughness, subject to the constraints of affordable processing. Moreover, there are only limited means for ameliorating the manufacturing flaws. A preferred approach is to use braiding or cross stitching of the fibers in the attachments and in sections subject to high heat flux. The fibers that cross over the delamination plane have a major effect on the transverse toughness, though large scale bridging[67]. Order of magnitude improvements in toughness are induced by a relatively small fraction of fibers (< 0.1) in the thickness orientation[69]. While the benefits are clear, there has been minimal technical progress. The limitation has been the difficulty in weaving ceramic fibers with high modulus into the required configurations, without either fracturing or inducing large bending stresses.

Life Limiting Mechanisms

Fatigue

Cyclic degradation occurs in both CMCs and TMCs [23,70-74]. At ambient temperature, the degradation is minimal for CMCs, but substantial for TMCs: a consequence of their relative notch sensitivities[73]. However, CMCs have problems at *intermediate temperatures*, where corrosion fatigue mechanisms operate, as elaborated in 6.2[75]. Composites are subject to a diminishing friction stress upon load cycling. The changes can be diagnosed using hysteresis loop measurements[70] (Fig.17).

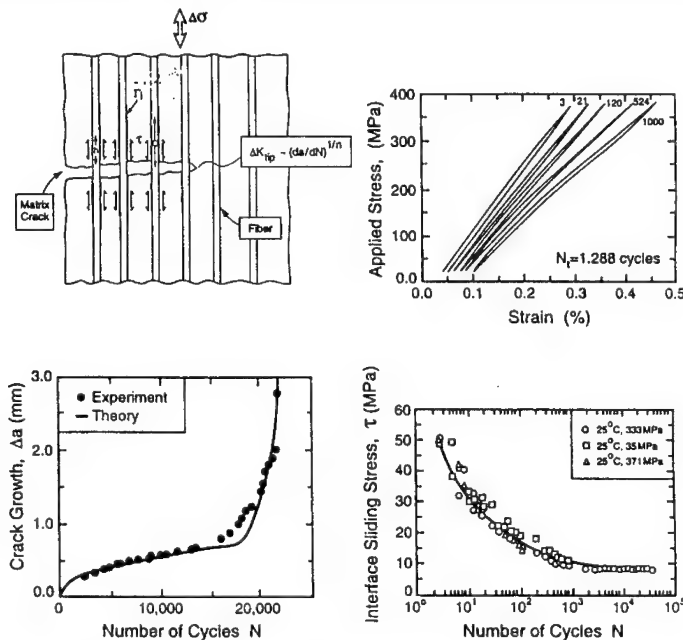


Fig 17 Cyclic loading effects found in TMCs. There are changes in the friction stress diagnosed using hysteresis loops. But the crack growth rates are still much lower than those in the matrix without the fibers.

The reductions in τ are attributed to interface wear. This process is not understood, but it exhibits a *limiting friction*, τ_s [23]. The diminished τ increases the stress intensity range at the matrix crack tip, ΔK_{tip} [72,73], as well as the mean value, \bar{K}_{tip} . The consequences differ for TMCs and CMCs. For TMCs, the ΔK_{tip} causes the crack to extend in accordance with a Paris Law [72](Fig.17). But, even though τ diminishes and increases ΔK_{tip} , the crack growth rates are considerably lower than those for the monolithic alloy, because of the strong fiber bridging (LSB) effect [72,73]. The principal problem arises from the notch sensitivity of TMCs, because they are embedded within a monolith. The TMC is subject to residual compression, whereas the monolith is in tension. This increases the R-ratio in the monolith, which accelerates crack formation. Should such a crack extend through the monolith and penetrate the TMC, the composite notch sensitivity becomes a factor [23]. The implications become apparent upon equating the monolith thickness, h , to the notch size and the peak stress, σ_{max} , to that from the combined residual and cyclic stresses. When h and σ_{max} are small, the stresses on the fibers in the TMC never reach their UTS and the cracks extend benignly, only in the matrix. Conversely, at larger stresses, the outer fibers in the TMC fail. This causes the entire bridging zone to rupture, resulting in rapid crack acceleration. This fiber failure transition thus represents a design limit, or threshold. Life prediction methods require that the parameters governing the fatigue limit are manufacturing insensitive and well-controlled.

For CMCs, there is no mechanism for cyclic growth of matrix cracks. A more important factor is the increase in \bar{K}_{tip} , which causes cracks to extend upon reaching the matrix toughness [70,71]. However, this is a benign phenomenon, since matrix cracking is *stable* and, moreover, is the source of the inelastic strain that imparts stress redistribution capacity to the material.

Corrosion Fatigue

High-temperature forms of stress corrosion with attendant embrittlement pose major materials development and life prediction challenges [75,76]. When one or more material constituent is susceptible to oxidation, a rapid degradation in performance may ensue, particularly when the process is accelerated by stress. The clearest illustration is oxidation embrittlement in non-oxide CMCs. In this case, oxidation decreases the fiber strength and increases the interface friction stress. These effects act synergistically to cause premature fiber failure at small cracks in the matrix. The consequence is rapid crack growth, with diminished crack “blunting,” resulting in low rupture life. The behavior has all of the characteristics exhibited by stress corrosion, with the active species now being oxygen. The phenomenon is illustrated on Fig 18.

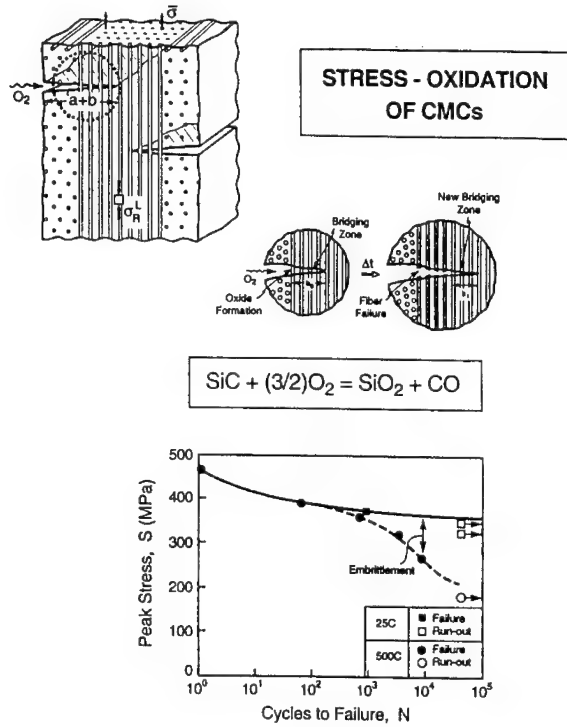


Fig 18 A schematic illustrating the stress oxidation effect. Oxygen penetrates the material through the matrix cracks. Local oxidation interacts with the stress concentrations on the fibers to diminish their failure strength, causing the fibers to fail at the matrix crack. This process repeats and the crack extends in a manner analogous to stress corrosion.

Matrix cracks created upon loading become pathways for the relatively rapid ingress of oxygen. The oxygen reacts to form solid and gaseous products. There is a threshold stress below which the phenomenon does not occur, given by [76]

$$S_{th} = \sqrt{\frac{2E_m \Gamma_m}{\pi h}} \quad (14)$$

This stress is typically small, of order 10-15 MPa, and too low to enable efficient, lightweight design. Degradation when $\sigma < S_{th}$ occurs according to two rate-limiting phenomena. (i) When the oxygen flow within the cracks is relatively rapid, all reinforcements bridging surface-connected cracks oxidize and weaken

simultaneously. When they have degraded sufficiently to fail, the surface cracks extend across the weakened zone and form a *new crack segments* bridged by pristine reinforcements (Fig.18).

This new bridged region again gradually weakens and fails. The process continues in a manner resembling reaction-controlled, stress corrosion cracking. This is the more important regime, because it *governs the rupture life at long times*. (ii) When the matrix crack opening is narrow, oxygen gradients develop along the crack, resulting in a degradation front that progresses into the material. This process is similar to diffusion controlled, stress corrosion cracking.

In order to provide a life prediction methodology, three principal phenomena must be addressed. (a) The reduced strength of the reinforcements with an oxide reaction layer. (b) The stress concentration on the reinforcements at the perimeters of unbridged crack segments. (c) The oxygen concentration within the matrix cracks, which is coupled with the thickness of the oxide reaction product on the reinforcements. Analysis of these effects leads to an expression for the failure time, Δt_c [76]

$$\Delta t_c \approx t_o \left[\frac{S_L^4 \sqrt{E \Gamma_m} R^{2/3}}{(\sigma^{13} \tau^2)^{1/3} h_L^{7/6}} \right] \quad (15)$$

The features emphasized by (15) are the explicit role of the applied stress and the friction stress as well as the fiber strength. But, the major issues related to the chemistry, which determines the reference time t_o . The basic kinetic factors are presently unresolved.

The crack growth rates found in composites reinforced with available SiC- based fibers have been inexplicably high, especially at intermediate temperatures, such as 500-800C. This problem is related to the fiber chemistry. Improved chemistry diminishes their sensitivity to degradation, but does not eliminate the effect. It has yet to be established that the kinetic limitation of stress oxidation in non-oxide CMCs can be an effective life enhancing strategy. This difficulty does not exist in all-oxide composites, suggesting that these materials be given preference in oxidizing situations. The life assurance problem then becomes management of creep and rupture. The creep susceptibility of the available polycrystalline oxide fibers limits oxide CMCs to temperatures below 1200C. Exploitation of some newly discovered effects would be needed to overcome this limitation. These effects include creep enhancements enabled by yttria doping or by nanoparticle incorporation.

Concluding Comments

An implementation strategy for TMCs is well-developed. It recognizes that these materials provide stiffness benefits when used as unidirectional reinforcements in selected areas of stiffness-critical components. Redesigns that enhance performance while minimizing the amount of TMC addresses cost objectives. However, more widespread implementation is limited by two problems. (i) The interior transverse properties constrain the design by requiring minimal transverse loads in the TMC

sections. (ii) The use of SiC fibers limit higher temperature applications because of thermal fatigue, caused by the thermal expansion mismatch. New developments in fibers and fiber coatings are needed to obviate these limitations. There are also some concerns brought about by the notch sensitivity of TMCs. In particular, fatigue cracks that penetrate the TMC from the surrounding Ti alloy result in severe LCF degradation. There are no obvious solutions to this problem, because the notch sensitivity is inherent to the anisotropy. It must be taken into account in the design and the life prediction methodology.

The implementation of CMCs is dictated by material short comings as well as manufacturing cost issues, having commonality with polymer matrix composites (PMCs). Delamination at transitions and around hot spots presents major challenges. Unlike PMCs, the feasibility of suppressing delamination by substantially enhancing the matrix toughness and by "eliminating" manufacturing flaws is restricted by processing requirements for the matrix. The only reasonable approach appears to be the use of braiding or cross-stitching. This technology has yet to be demonstrated because of the problems associated with the weaving of stiff ceramic fibers.

There are additional materials problems. For non-oxide CMCs, it has yet to be demonstrated that stress oxidation can be suppressed to an extent that allows acceptable thermomechanical fatigue life. Fiber/fiber coating combinations having chemistries that inhibit stress-enhanced oxidation are needed. Oxide CMCs are not susceptible to embrittlement. But, polycrystalline oxide fibers have inferior creep strength. New approaches for creep strengthening of oxide polycrystals must be implemented in order to create oxide CMCs having desirable creep resistance above 1200C. Relatively low thermal conductivity, especially at high temperatures, remains a problem. But there are no obvious solutions to enhancing thermal conductivity while also trying to attain good creep resistance. Design strategies that disperse heat fluxes and control the temperature excursions, such as thermal barrier coatings, may be required.

REFERENCES

1. H. R. Bakis, N. R. Yih, W. W. Stinchcomb, and K. L. Reifsnider. ASTM STP 1012 (American Society of Testing and Materials, Philadelphia, PA., 66-83 (1989).
2. W. W. Stinchcomb and E. Bakis, in "Fatigue of Composite Materials", edited by K.L. Reifsnider, Elsevier Science, NY, 105-80 (1990)
3. T. J. Mackin, K. E. Perry, J. S. Epstein, C. Cady and A. G. Evans, *J. Amer. Ceram Soc.*, **79**, , 65-73 (1996).
4. T.J. Mackin, T.E. Purcell, M.Y. He and A.G. Evans, *J. Amer. Ceram. Soc.*, **78**, 1719-1728 (1995)
5. C. Cady, A.G. Evans and K.E. Perry, Jr., *Composites*, **26**, 683-690 (1995).
6. C. M. Cady, T. J. Mackin and A. G. Evans, *J. Amer. Ceram. Soc.*, **78**, 77-82 (1995).
7. F. E. Heredia, S. M. Spearing, T. J. Mackin, M. Y He, A. G. Evans, P. Mosher and P. Brondsted, *J. Amer. Ceram. Soc.*, **77**, 2817-2827 (1994)
8. A. G. Evans and F. W. Zok, *Solid State Physics*, **47**, 177-286 (1994)
9. G.Genin and J. W. Hutchinson, High Temperature Ceramic Matrix Composites II. (Ed. R. Naslain and A. G. Evans), *J. Amer. Ceram. Soc.* (1994)
10. T. J. Lu, J. W. Hutchinson, and A. G. Evans, *J. Amer. Ceram Soc.*, in press.
11. M. F. Ashby, Materials Selection in Mechanical Design, Pergamon Press (1988).
12. Cambridge Materials Selector, Granta Design, Cambridge, UK. (1994)

13. A. C. F. Cocks, S. Jansson, and F. A. Leckie, *J. Therm. Stress*, **15**, (1992)
14. T. C. Lu, J. Yang, Z. Suo, A. G. Evans, R. Hecht and R. Mehrabian, *Acta Metall. mater.* **39**, 1883-1890 (1991)
15. A. G. Evans, *Phil. Trans. Roy Soc. Lond. A* **315**, 511 (1995)
16. J. W. Hutchinson, Non-Linear Fracture Mechanics, Technical University Denmark, (1980)
17. S. R. Gunawardena, S. Jansson and F. A. Leckie, *Acta Metall. Mater.*, **41** (1993).
18. F. A. Leckie, *Phil Trans. Roy. Soc. Lond.*, **A315**, 611-623 (1995).
19. G. Bao and Z. Suo, *Appl. Mech. Rev.*, **45**, 355 (1992).
20. B. N. Cox, *Acta Metall. Mater*, **39**, 1189 (1991).
21. B. N. Cox and C. S. Lo, *Acta Metall. Mater*, **40**, 60 (1992).
22. D. B. Marshall, B. N. Cox, and A. G. Evans, *Acta Metall.*, **33**, 2013 (1985).
23. F. W. Zok, Z. Z. Du and S. J. Connell, *Mat. Sci. Eng.*, **A200**, 103-113 (1995)
24. A.G. Evans, *J Amer. Ceram. Soc.*, **73**, 187-206 (1990)
25. B. R. Lawn, *Fracture of Brittle Solids*, Cambridge Press (1993)
26. A. G. Evans, *Acta Metall. Mater.*, in press.
27. A. Freudenthal, in "Fracture", edited by H. Liebowitz , Academic Press, 341-345 (1967).
28. J. R. Matthews, W. J. Shack and F. A. McClintock, *J. Amer. Ceram. Soc.*, **59**, 304 (1976).
29. D. A. W. Kaute, J. R. Shercliff and M. F. Ashby, *Acta Metall. Mater.*, (1993)
30. S. M. Spearing and A. G. Evans, *Acta Metall. Mater*, **40**, 2191 (1992).
31. F. A. Heredia, M. Y. He, and A. G. Evans, *Composites*, (1996), in press.
32. S. Jansson and F. A. Leckie, *Mech. of Materials*, **18**, (1994).
33. A. Burr, J. Yang, C. G. Levi, and F. A. Leckie, *Acta Metall. Mater.*, **43**, 3361-3373 (1995).
34. F. W. Zok, F. A. Leckie, M. Y. He and A. G. Evans, *Composites*, (1996), in press.
35. J. Busch, IBIS Associates, private communication.

36. R. Anderson, Pratt and Whitney, private communication.
37. W. Tu, F. F. Lange and A. G. Evans., *J. Amer. Ceram. Soc.*, **79**, 417-24 (1996).
38. W. A. Curtin, *J. Amer. Ceram. Soc.*, **74**, 2837-2845 ,(1991)
39. Z. Z. Du and R. M. McMeeking, *J. Computer-Aided Materials Design*, **1**, 243-264 (1993).
40. W. Weibull, *Ingeniversvelenskopsakad. Handl.*, **151**, 1-45 (1939).
41. J. W. Hutchinson, and H. Jensen, *Mech. Mater.*, **9**, 139 (1990).
42. W. A. Curtin, *J. Mech. Phys. Solids*, **41**, 217-245 (1993).
43. M.Y. He, A. G. Evans and W. A. Curtin, *Acta Metall. Mater.*, **41**, 871-878 (1993).
44. S. L. Phoenix, *Comp. Sci. Tech.*, **48**, 65-80 (1994).
45. R. B. Henstenburg and S. L. Phoenix, *Polym. Compos.*, **10**, 389 (1989).
46. S. L. Phoenix and R. Raj, *Acta Metall. Mater.*, **40**, 2813 (1992).
47. T. J. Kotil, J. W. Holmes and M. Comninou, *J. Amer. Ceram. Soc.*, **73**, 1879 (1990).
48. J.M. Domergue, E. Vagaggini and A. G. Evans, *J. Amer. Ceram. Soc.*, **78**, 2721-2731 (1995)
49. A. G. Evans, J. M. Domergue and E. Vagaggini, *J. Amer. Ceram. Soc.*, **77**, 1425-1435 (1994)
50. S. J. Zhou and W. A. Curtin, *Acta Metall. Mater.*, **43**, 3093-3104 (1995).
51. M. Ibnabdeljalil and W. A. Curtin, to be published.
52. Z. C. Xia, J. W. Hutchinson, A. G. Evans and B. Budiansky, *J. Mech. Phys. Solids*, **42**, 1139-1158 (1994)
53. B. Budiansky and Y. L. Cui, *Mechanics of Materials*, **21**, 139-146 (1995).
55. C. Xia, R. R. Carr, and J. W. Hutchinson, *Acta Metall. Mater.*, **41**, 2365 (1993).
56. C. Xia and J. W. Hutchinson, *Acta Metall. Mater.*, **42**, 1935-45 (1994).
57. M. Y. He, B.-X. Wu, A. G. Evans and J. W. Hutchinson, *Mechanics of Materials*, **18**, 213-229, (1994)
58. J.-M. Domergue, F.E. Heredia and A.G. Evans. *J. Amer. Ceram.* **79**, 161-179 (1996)
59. F. Hild, A. Burr, and F. A. Leckie, *Int'l. J. Solids and Struct.*, **33**, 1209-1220 (1996)

60. J. W. Hutchinson, S. K. Chan and M. Y. He., *Materials Science and Engineering*, **A167**, 57-664 (1993).
61. D. K. Leung, M. Y. He and A. G. Evans, *J. Mater. Res.*, **10**, 1693-1699 (1995).
62. M. C. Shaw, D. B. Marshall, B. J. Dalgleish, M. S. Dadkhah, M. Y. He and A. G. Evans. *Acta Metall. Mater.*, **42**, 4091-4099 (1994)
63. R. P. Nimmer, R. J. Bankert, E. S. Russell and G. A. Smith, *ASM Materials Conf.*, Indianapolis, In., October (1989).
64. S. Jansson, H. Deve and A. G. Evans., *Metallurgical Trans.* , **22A**, 2975-2984 (1991).
65. S. Jansson and F. A. Leckie, to be published.
66. J. W. Hutchinson, T. J. Lu and Z. C. Xia, *Materials Science and Engineering*, **A188**, 103-112 (1994).
67. J. W. Hutchinson and T. J. Lu, *J. Amer. Ceram. Soc.*, **78**, 251-253 (1995).
68. J. W. Hutchinson and T. J. Lu, *J. Engineering Materials and Technology*, **117**, 386-390 (1995).
69. B. N. Cox, R. Massabó and K. T. Kedward, *Composites*, (1995) in press.
70. A. G. Evans, F. W. Zok and R. M. McMeeking, *Acta Metall. Mater.*, **43**, 859 (1995).
71. D. Rouby and P. Reynaud, *Compos. Sci. Technol.*, **48**, 109-118 (1993).
72. R. M. McMeeking and A. G. Evans., *Mechanics of Materials*, **9**, 217-227 (1990).
73. M. Sensmeier and K. Wright, *Proceedings TMS Fall Meeting*, (eds. P. K. Law and M. N. Gungor), ASM , Pittsburgh, 441, (1989).
75. F. E. Heredia, J. C. McNulty, F. W. Zok and A. G. Evans, *J. Amer. Ceram. Soc.*, **78**, 2097-2100 (1995).
76. D. R. Walls, M. McNulty and F. W. Zok, *Metall. Mater. Trans. A*, (1996) in press.
77. A. G. Evans., F. W. Zok, Z. Z. Du and R. M. McMeeking, *J. Amer. Ceram. Soc.*, in press.

MICROMECHANICS

UNIVERSAL BEHAVIOR IN ADHESION

OF SOME HIGH TEMPERATURE MATERIALS

John R. Smith¹, J. E. Raynolds², E. R. Roddick², and D. J. Srolovitz²

¹*Physics Department, GM Research and Development Center, Warren, MI 48090-9055*

²*Department of Materials and Engineering, University of Michigan, Ann Arbor, MI 48109-2136*

Abstract

Processing and design of materials often involves issues of adhesion. The nature of the strong bonds which can form between materials in intimate contact is therefore of considerable interest. Because of the variety of materials found in these interfaces (metals, ceramics, intermetallics, and impurities), adhesion computations must be first-principles, self-consistent quantum-mechanical calculations. A number of years ago, the first such computations revealed an unexpected universality. It was found that the total energy versus interfacial spacing for a number of different metal contacts could be simply scaled onto a single curve. Subsequently it was found that this universality extended to a variety of materials in cohesion, chemisorption, and to diatomic molecules. More recently, it was shown that the universal behavior extends to Mo/MoSi₂ adhesion with and without monolayers of C, O, B, S, and Nb interfacial impurities. Impurity effects were found to be large and strongly dependent on impurity atom type. For example, S lowered the adhesive energy by approximately a factor of two. For the ceramic/metal interfaces MgO/Ag and MgO/Al with and without C and S impurities, universal behavior was again observed as were substantial impurity effects. For Al₂O₃/Cu, surface relaxation effects were found to be substantial, lowering the work of adhesion by a factor of three. The bimetallic interface NiAl/Cr accurately exhibited universal behavior, as expected. In all these cases electron density distributions help to illustrate the nature of the bonding, which varies from pure metallic to partially ionic - partially covalent.

Introduction

Bimaterial adhesion is a subject which brings together engineers and scientists because of its technological significance and its substantial but interesting scientific challenges. A knowledge of and the ability to control adhesion is important to a number of technologies. While there are many examples, we will give just a few in the following. Adhesion is critical to the functioning of coatings for wear and corrosion resistance as well as coatings for electrical and thermal insulation. Adhesion between the matrix material and the strengthening material is crucial to the appropriate functioning of composites. Another example of the importance of adhesion can be found in the packaging and functioning of electronic circuits. Finally, tribologists are well aware of the role adhesion can play in friction and wear.

While it is generally agreed that adhesion is important technologically, the science of adhesion has been limited by several factors. The probing of an internal interface is, by its nature, difficult experimentally. Further, impurities can segregate to the interface, and we will see in the following that impurities can significantly affect adhesion. The control and analysis of interfacial impurities is a challenging experimental problem.

It is no less difficult on the theoretical side. There are a variety of types of atoms and bonds that can be found in a bimaterial interface. Consider, e.g., a metal/ceramic interface including interfacial impurities, with its mixture of metallic, covalent, and ionic bonds. Because of this complexity, there is no simple, semiempirical method that is adequate to treat this problem. This means that first principles solutions of the Schrödinger equation are required. That, coupled with the relatively low symmetry associated with interfaces makes studies of adhesion challenging indeed for the theorist.

We will see that the situation is not quite as difficult as one might think, because of some unexpected universal behavior. A number of years ago, one of us was working with Rose¹ and Ferrante, computing from first principles quantum mechanical total energies as a function of interfacial spacing for a variety of bimetallic contacts. Adhesive interactions were being computed for all combinations of Al, Zn, Mg, and Na, yielding 10 different curves of total energy $E(d)$ versus interfacial spacing d . Looking for systematics, the authors tried scaling these curves, and found that the following scaling caused all 10 curves to fall accurately on one, universal, adhesion curve $E^*(d^*)$, where $E^*(d^*)$ is the scaled energy and d^* is the scaled interfacial spacing:

$$E(d) = \Delta E E^*(d^*) \quad , \quad (1)$$

$$d^* = (d - d_m)/l \quad , \quad (2)$$

and

$$l = \sqrt{\Delta E / [d^2 E(d)/d^2]_{d_m}} \quad . \quad (3)$$

Here ΔE is equilibrium binding energy (ΔE is the surface energy for adhesion between identical metals), and d_m is the equilibrium interfacial separation.

Subsequently, it was found that this universality is not limited to adhesion between metals. It was found to extend to metallic and covalent bonds in chemisorption, cohesion, and diatomic molecular energetics. This universality also found applications in equations of state for solids² and nuclear matter³ (for a review, see Ref. 4). Fig. 1 is a plot of the scaled energy E^* versus the scaled interatomic separation d^* for the H_2^+ diatomic molecule, Al/Zn adhesion, oxygen chemisorbed on Al, and cohesion in bulk Mo. These results are representative, and one can see that there is indeed a universal form. The solid curve in Fig. 1 is the following simple form:

$$E^*(d^*) = -(1 + d^*)e^{-d^*} \quad . \quad (4)$$

One can see that the curve in Fig. 1 represents well the numerically-determined universal points plotted there. Henceforth we will use this simple form to represent the universal energy relation. $E(a)$, obtained by multiplying this simple function by ΔE as in Eq. 1, is the universal function plotted as the curves in the upper half of Fig. 2 and in Figs. 5 and 7.

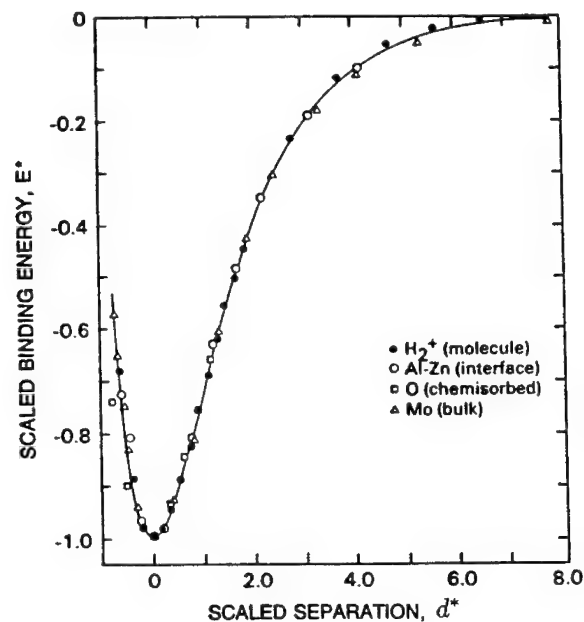


Figure 1 - Scaled binding energy E^* plotted against the scaled separation d^* for representative cases of cohesion, bimetallic adhesion, chemisorption, and a diatomic molecule. The solid curve is a plot of the function in Eq. 4. The sources of the unscaled results are listed in Ref. 5.

Those readers interested in following up on this universal behavior in its full generality are invited to read Refs. 1-4 and references therein. Because of the particular interests of those at this conference in high temperature materials, we will investigate universal behavior in adhesion of high temperature materials throughout the rest of this manuscript. In these initial computations of adhesive energetics, we will not consider the effects of plastic or elastic deformations. As such, we will establish the baseline energetics associated with the making and breaking of atomic bonds across the interface, and leave plastic and elastic effects for future work.

Adhesion Results

MoSi₂/Mo with Impurities

MoSi₂ has been a candidate material for high-temperature structural applications. Since MoSi₂ is brittle at low temperatures, it is often combined with another metallic phase to provide ductile phase toughening. MoSi₂/Mo was chosen as a model interface to investigate MoSi₂/Mo composites. The lattice mismatch for (100) planes of the two materials is less than 2%, so the interface is chosen for this first calculation to be epitaxial. In addition to the clean interface, we⁶ consider interfacial impurity monolayers of C, O, B, Nb, and S. Thus when we add impurities, each interface contains 3 different elements and a mixture of metallic and covalent bonds. This kind of complexity is beyond semiempirical many-

atom methods, and requires a fully self-consistent solution of the Schrödinger equation. To accomplish this, we employ the self-consistent local-orbital (SCLO) method⁷.

We first compute the electron density distributions for the MoSi_2/Mo interface at equilibrium interfacial separation and at very large interfacial separation (solid-vacuum interface), and subtract. Any nonzero difference is due then to the adhesive interaction, and as such is a map of the interaction. The density difference plot for the clean MoSi_2/Mo interface is shown in the left panel of Fig. 2. Where the adhesive interaction causes an increase in electron density, we have solid contours. An electron density decrease is indicated by dashed contours. The contours in the left panel show that effectively the adhesive interaction is limited to within a few atomic layers of the interface. Also, it is banded across the interface, as is typical of metallic adhesion. Note that there is a directional accumulation of electrons between atoms across the interface. According to the Hellmann- Feynman theorem, this is consistent with bonds forming across the interface, i.e., adhesive bonds.

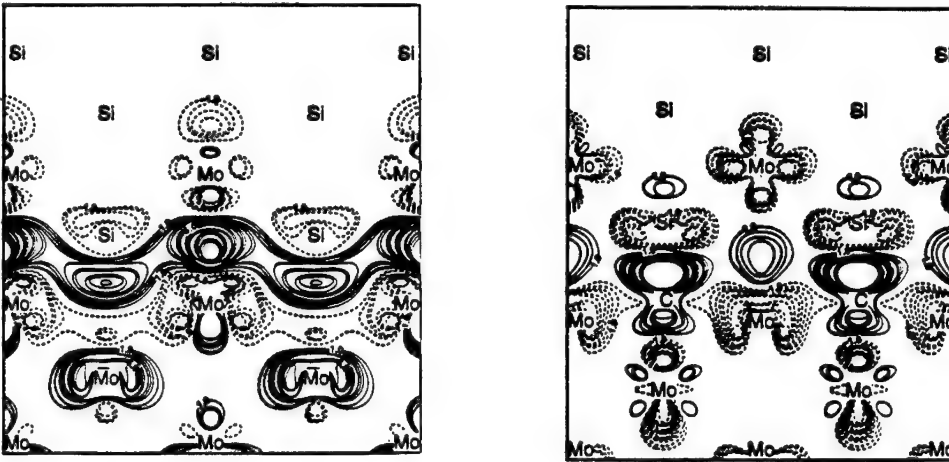


Figure 2 - Electron density difference contours due to adhesion between (001) surfaces of Mo and MoSi_2 . The left panel is for the impurity free case, while the right panel is for the case of a C monolayer in the interface. Solid contours indicate electron accumulation, while dashed contours indicate electron depletion.

Next, let us introduce a carbon monolayer at interstitial sites in the interface, as shown in the right panel of Fig. 2. One can see that the aforementioned electron density accumulations in the adhesive bonds of the clean interface are significantly reduced by the presence of the C monolayer. This is a strain effect, i.e., the two surfaces are pushed apart by 0.82\AA due to the C (see Fig. 3), thereby weakening the MoSi_2/Mo bonds. In fact, we found⁶ that the equilibrium interfacial spacings were accurately a linear function of the Pauling covalent or metallic radii of the impurities, for all impurities investigated: O, C, B, S, and Nb. At the same time, it is clear from the right panel of Fig. 2 that new bonds are formed from the C atoms across the interface, thereby strengthening the interface. These two effects compete, and one has to compute total energies and forces to find which one wins.

The results for the total energy (upper panel) and interfacial strengths (lower panel - force per unit cross sectional area) as a function of interfacial spacing are given in Fig. 3. The adhesive energy is defined as the total energy at large interfacial separation minus the total energy at equilibrium separation, divided by the surface area of the two surfaces. That is, the adhesive energy is the well depth of the adhesion curve, which we defined earlier as ΔE

in Eq. 1. Alternatively, the work of adhesion, W_{ad} , is twice the adhesive energy because W_{ad} is defined as the total energy difference per cross sectional area.

First, note that in all cases - impurity free and all 5 different impurities - the adhesion points are well represented by the universal energy relation given by Eqs. 1-4 and plotted as the curves in Fig. 3. Secondly, one can see in the upper panel of Fig. 1 that in this case all impurities lower the adhesive energy.

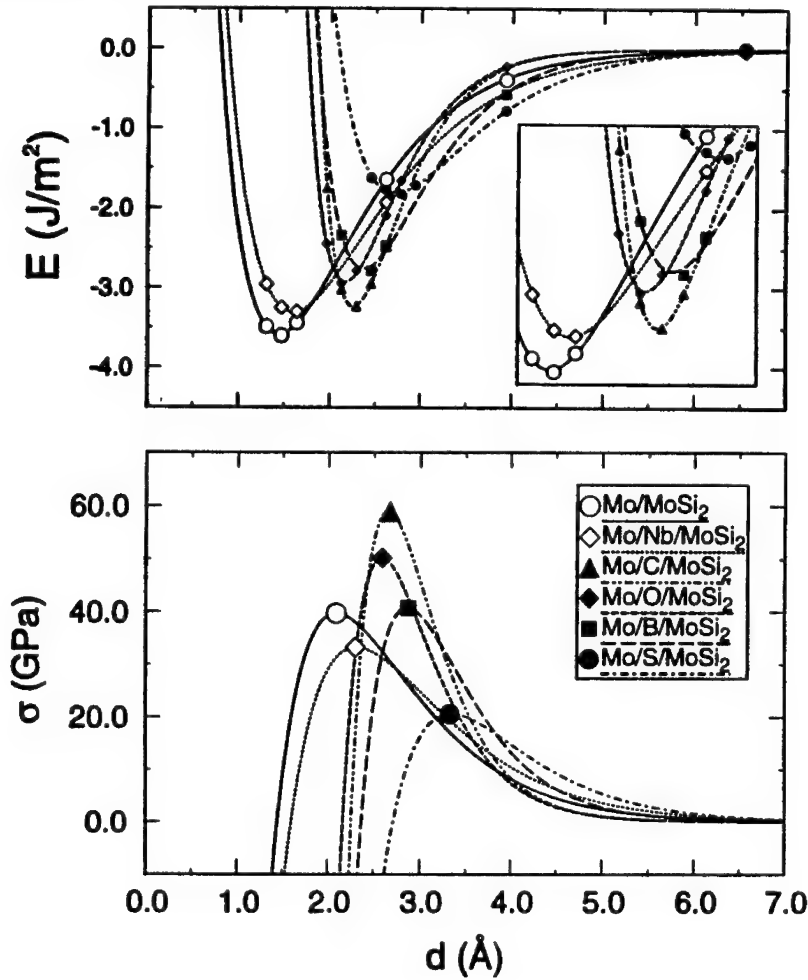


Figure 3 - The upper panel is a plot of the total energy $E(d)$ per unit surface area as a function of the interfacial spacing d between interfaces as denoted by the insert in the lower panel. The lower panel contains the calculated interfacial strengths (force per unit cross sectional area) vs d . The curves are the universal forms represented by Eqs. 1-4.

The appropriate measure of the width in this case is the scaling length l of Eqs. 2 and 3. In fact, from Third, note that impurity affects on adhesion are strong, with S lowering the adhesive energy by nearly a factor of 2. One can easily find the interfacial strengths or forces by differentiating $E(d)$ with respect to d . These are plotted in the lower panel of Fig. 3. Here we see that C and O clearly *increase* the peak interfacial strength, while Nb and S

decrease it. This ordering is qualitatively different from that just shown for the adhesive energies. That is, even though the depth of the energy curve (adhesive energy) is lowered by the introduction of the impurities, the maximum slope (peak interfacial strength) can nevertheless be increased if the width of the curve is also decreased sufficiently. Eqs. 1 and 4 we have for the peak interfacial strength σ_{max} :

$$\sigma_{max} = 2\Delta E / le \quad , \quad (5)$$

where e is the base of the natural logarithm and ΔE is the adhesive energy.

MgO/Ag and MgO/Al with Impurities

Next we move on to the subject of ceramic/metal interfaces. In this section we will consider MgO, and in the next section Al_2O_3 . MgO offers certain computational advantages. First it is cubic, like many metals, which leads to higher symmetry in MgO/metal interfaces and correspondingly lower computational requirements. Secondly, Trampert⁹ et al. have grown Ag on MgO(100) by molecular beam epitaxy in ultra high vacuum. This allows for careful control of impurities in the interface, which we've seen in the preceding section could have a substantial affect on adhesion. Further, their high resolution transmission electron microscopy results indicate that the epitaxial Ag atoms are either on top of the Mg atoms or the O atoms. This geometry information is a help to us, because it limits the number of geometric configurations we have to consider to two. We¹⁰ did computations for both configurations and found that the lower energy configuration was obtained for Ag on top of the O atoms.

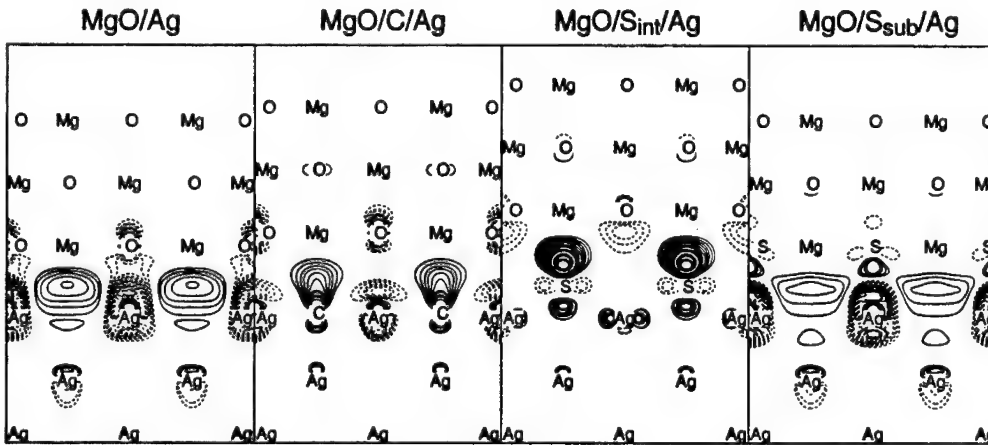


Figure 4 - Electron density rearrangements due to adhesion between the (100) surfaces of Ag and MgO. Solid lines denote electron accumulation, while dashed lines denote electron depletion. Interfacial monolayers of impurities are added as denoted over the panels.

The electron density difference plots for the MgO/Ag(001) interface, clean and containing interfacial monolayers of C, interstitial S, and substitutional S are shown in Fig. 4. The first thing to note is that these plots are qualitatively different from what we saw for the $MoSi_2/Mo$ interface in Fig. 2. In the left panel of Fig. 2 we saw a band of electron density accumulation in the interface which was reasonably continuous. In the left panel of Fig. 4, however, the electron density accumulation is much more localized. We see an accumulation of electrons in the Ag surface near the (positively charged) Mg ions.

Similarly, we see a diminution of electrons (i.e., the electron density was lowered compared to the free surface values), in the Ag surface near the (negatively charged) O ions. This is highly suggestive of a significant ionic component to the MgO/Ag adhesive bond. We found similar results for the MgO/Al adhesive bond. While the clean (impurity free) charge rearrangements due to adhesion in Mg/Ag and MgO/Al are qualitatively different than those for MoSi₂/Mo, the results for impurity effects appear similar. The remainder of the panels in Fig. 4 are devoted to MgO/C/Ag, MgO/S_{int}/Ag, and MgO/S_{sub}/Ag, where the last two refer to interstitial and substitutional S respectively. Note that both interstitial C and S lead to less lowering of the electron density in the Ag surface near the O ions. This suggests a weakening of the clean-interface adhesive bonds. There is also evidence of new bonds forming across the interface from the impurity atoms. Both of these impurity effects were seen in the MoSi₂/Mo interface. The right panel in Fig. 4 is for S substituted for O, and the results look similar to the clean MgO/Ag interface, as one might expect given the similarity of S and O.

Next let us look at results for total energies as a function of interfacial spacing as shown in Fig. 5. First, note that the computed points fall very closely on the universal energy relation given by the curves, which are plots of Eqs. 1-4. This suggests a significant metallic/covalent component of this metal/ceramic adhesive bond, because of the exponential form of Eq. 4. Recall that Fig. 4 had suggested a significant ionic component of this adhesive bond. Thus the adhesive bond is a complicated mix of metallic, covalent, and ionic bonding. Secondly, note that again the impurity effects are strong. Interstitial S lowers the MgO/Ag adhesive energy by over 60%. Third, note that generally the impurities lower the adhesive energies, but that C in MgO/Al actually increases it. As in MoSi₂/Mo, C increases the peak interfacial strength in both MgO/Al and MgO/Ag, while S decreases it.

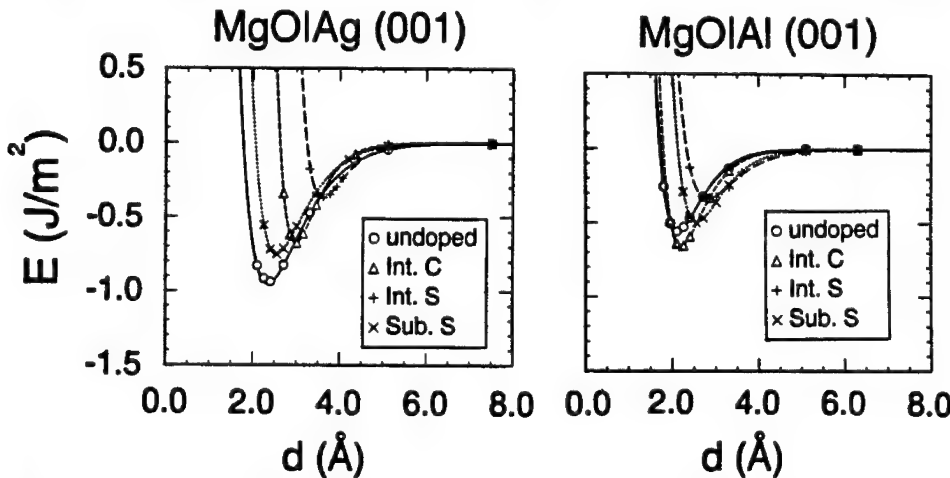


Figure 5 - Total energy E per surface area as a function of interfacial spacing d for contacts as indicated. The curves are the universal forms represented by Eqs. 1-4.

Alumina/Cu

No treatment of ceramic/metal interfaces would be complete without considering alumina. Alumina is perhaps the most common oxide or ceramic in composites, and it also finds significant useage in electronic packaging and exhaust gas catalysis. Alumina presents difficulties for anyone who wants to do first principles computations of alumina/metal adhesion, because alumina is not cubic and therefore the computational time required is

significantly higher than required for, e.g., MgO/Ag. The Al_2O_3 /Cu interface is a good one to probe the fundamentals of ceramic/metal adhesion because atomically sharp interfaces have been produced by internal oxidation, solid state bonding, and vapor deposition¹¹. Further, Dehm¹¹ et al. prepared an epitaxial Cu film on (0001)-oriented single crystal sapphire wafers by molecular beam epitaxy. Their TEM observations on this clean interface indicated a preferred (111) Cu on (0001) sapphire orientational relationship. This is a major help to us in locating the atoms and therefore limits the amount of computer time required. For computational simplicity, we assume that the Cu(111)/ Al_2O_3 (0001) interface is coherent (commensurate), even though that was not seen experimentally¹¹. Early work¹² in the case of bimetallic adhesion suggests that this assumption would introduce errors in adhesive energies of no more than of order 10-20%.

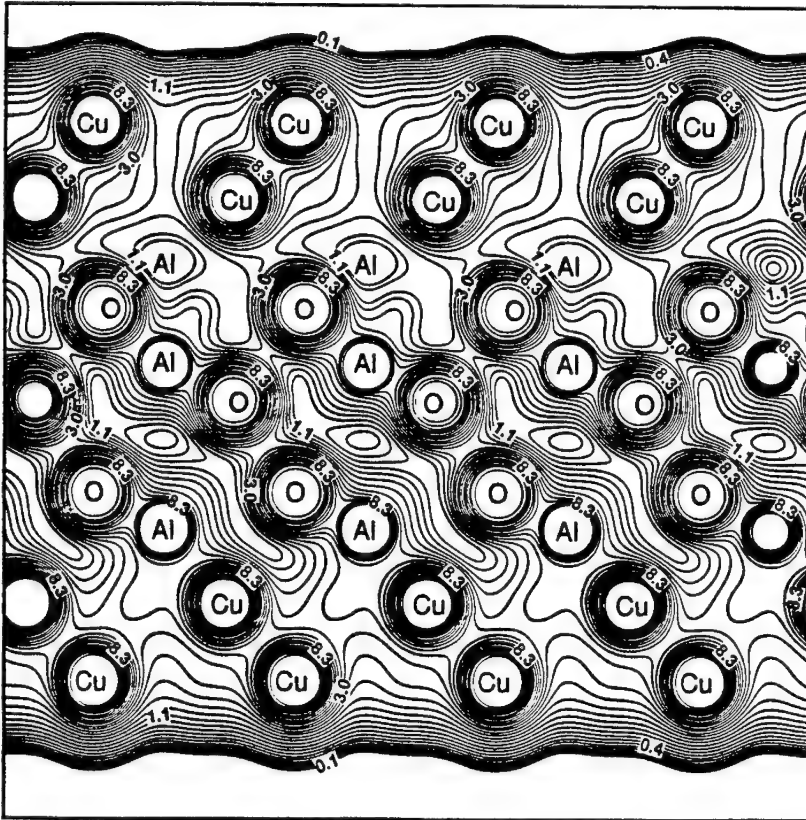


Figure 6 - The total electron density contours (not a difference contour) on a plane perpendicular to the Cu(111)/ Al_2O_3 (0001) interface.

In Fig. 6 we¹³ show electron density contours for a sandwich formed with Cu on the outside and Al_2O_3 on the inside. These contours are plotted on a plane perpendicular to the interface. They suggest strong bonds between the Al and O atoms, as expected from the relatively high surface energy of Al_2O_3 (0001), as we will see. There is some indication of bonding between Cu and O as well, but not much indication of bonding between Al and Cu. One might think at first that the Al_2O_3 (0001) /Cu(001) adhesive strength would be determined by a competition between Cu and Al for bonding with the O. This would be easily won by Al, since¹⁴ the oxide formation energy of Al is an order of magnitude larger

than that for Cu, suggesting that the Al₂O₃ /Cu adhesive bond should be weak. We will see in the following that unfortunately it is not that simple.

We will first test our computational methods for the free surface. Table I shows the surface energy of Cu(111) as computed here (present work), as computed by earlier authors¹⁵, and as measured¹⁶ for polycrystalline Cu. One can see that all three results agree well. Table II shows our results for the α-Al₂O₃(0001) surface energy. Again one can see that the results of our present work agree well with results computed earlier¹⁷⁻¹⁸. Manassidis¹⁸ and Gillan reported a relatively large planar relaxation of the atomic layers near the free surface of Al₂O₃(0001) , lowering the surface energy by over a factor of two, as shown in Table II. We will see that this has important implications for the work of adhesion of Cu(111)/Al₂O₃(0001) .

Table I. Surface energy of Cu(111) in J/m².

Unrelaxed Surface:		
Reported results	2.1	(a)
	2.016	(b)
Present work	2.07	

(a) Ref. 15
(b) Ref. 16

Table II. Surface energy of α-Al₂O₃(0001) in J/m².

Unrelaxed Surface:		
Reported results	3.7	(a)
	3.77	(b)
Present work	3.68	

Relaxed Surface:

Reported result	1.76	(b)
------------------------	------	-----

(a) Ref. 17
(b) Ref. 18

Table III. Work of adhesion for Cu/Al₂O₃ in J/m².

Present work:		
	2.9	(unrelaxed)
	0.9	(relaxed)
Experiment:		
	0.71	(a)
	0.441	(b)

(a) Ref. 19
(b) Ref. 14

Our computed work of adhesion for Cu(111)/Al₂O₃(0001) is given in Table III. The first

result of 2.9 J/m^2 is for the case where we do not allow the $\text{Al}_2\text{O}_3(0001)$ to relax. Recalling that by convention the work of adhesion (W_{ad}) is given in units of energy per cross sectional area, while surface energies are given in energy per surface area, to compare the two we must consider $W_{ad}/2 = 1.45 \text{ J/m}^2$. This value is smaller than either the surface energy of $\text{Cu}(111)$ or (unrelaxed) $\text{Al}_2\text{O}_3(0001)$. This perhaps due in part to, as mentioned earlier, the fact that the oxide formation energy of Al is an order of magnitude larger than that of Cu. That is, the $\text{Cu}/\text{Al}_2\text{O}_3$ adhesive bonding is weakened by the fact that Cu atoms loose out to the Al atoms in trying to bond to the O atoms. Moreover, if we allow for the free $\text{Al}_2\text{O}_3(0001)$ surface relaxation reported in Ref. 18, we see in Table III that the W_{ad} lowers to 0.9 J/m^2 . Now if we compare $W_{ad}/2 = 0.45 \text{ J/m}^2$ to the corresponding surface energies, we see that $W_{ad}/2$ is roughly 4 times smaller. That is, the $\text{Al}_2\text{O}_3(0001)$ surface relaxation lowers W_{ad} by over a factor of 3, making the $\text{Cu}(111)/\text{Al}_2\text{O}_3(0001)$ adhesion even weaker.

Finally, we compare our computed W_{ad} with experimental values. The experimental value of 0.71 J/m^2 of Ref. 19 for a faceted, solid Cu particle on $\text{Al}_2\text{O}_3(0001)$ agrees perhaps fortuitously well with our prediction of 0.9 J/m^2 . The other experimental value¹⁴ listed in Table III is for a molten Cu drop on an alumina surface. Since our calculations are for solid Cu, one would expect the results of Ref. 19 to be more relevant to our predictions.

NiAl/Cr

As our last example, we will consider NiAl-Cr in-situ composites. NiAl with bcc-metal-rich phases are being researched for potential use in high temperature structural applications. For example, NiAl-Cr containing, say, 6 atomic percent Mo can, by directional solidification processing, be made to have the Cr-rich phases to grow in lamellar morphology with the lamellae aligned. The idea is to produce higher fracture toughness and higher elevated-temperature strength through the formation of a composite. Of course, for the composite to function properly, the two phases will have to adhere, and hence our interest in determining properties important to the NiAl/Cr adhesive bond.

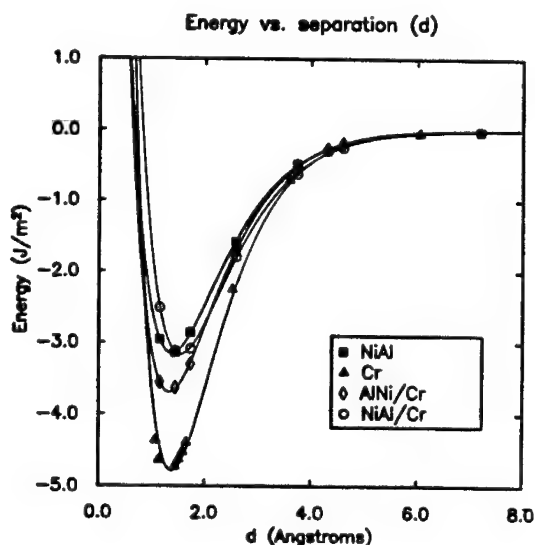


Figure 7 - Calculated total energy (per surface area) versus interfacial spacing d for contacts denoted in the insert. The solid curves are the universal forms represented by Eqs. 1-4.

The NiAl has a cubic (CsCl) type of structure, which matches well the bcc structure of

the Cr. The lattice constants of both materials are approximately 2.88 Å, so we assume an epitaxial (100) interface for our computations. We found electron density difference contours typical of bimetallic interfaces, not unlike what we showed in the left panel of Fig. 2. Our adhesion energetics are shown in Fig. 7. There we show results for four metallic (100) contacts: NiAl/NiAl, Cr/Cr, AlNi/Cr, and NiAl/Cr. The notation AlNi/Cr means that the Ni is in direct contact (atomically contiguous) with the Cr while NiAl/Cr denotes that the Al is in direct contact. Note first, as we have shown throughout this paper, that the computed adhesion points fall accurately on the curves computed from the universal form given by Eqs. 1-4. Secondly, the AlNi/Cr has a higher adhesive energy than the NiAl/Cr, and therefore AlNi/Cr is the preferred configuration energetically. The ordering of the adhesive energies is Cr/Cr > AlNi/Cr > NiAl/Cr \approx NiAl/NiAl. The peak interfacial stresses have the same ordering. Thus the adhesive energetics of these contacts appear to be well behaved.

Summary

We have examined the making and breaking of adhesive bonds at the atomic level and in the absence of elastic and plastic deformation for a variety of interfaces involving high temperature materials. The universal behavior in total energy versus interfacial spacing, originally discovered in bimetallic adhesion and found to extend to chemisorption, cohesion, and molecular energetics, was accurately obeyed for all interfaces considered here. Evidence of strong metallic adhesive bonding was found, as expected, for Mo/MoSi₂ and NiAl/Cr interfaces. AlNi/Cr adhesion results suggested that the Ni rather than the Al would be contiguous to the Cr on the atomic level in the interface. There was in addition evidence of directional adhesive bonding in these systems, reminiscent of what one might find in covalent bonding. Electron density profiles suggested a significant ionic component to the MgO/Ag and MgO/Al adhesive bonding, as expected. The universal (exponential) form of the adhesive energy curves for these ceramic/metal interfaces indicated that there is also a metallic-covalent component to that bond. Atomic monolayer interfacial impurity effects were found to be strong for the bimetallic and metal/ceramic interfaces studied. The impurities introduce a strain effect on the interface, pushing the surfaces apart and thereby weakening adhesive bonding. The impurities strengthen adhesive bonding by forming new bonds across the interface. The resultant impurity effects are determined by a competition between the strain and new bonding effects. It was found that typically the impurities decreased the adhesive energies, but C in MgO/Al actually increased the adhesive energy. Peak interfacial strengths were increased by C in the cases investigated, while S decreased peak interfacial strengths. The alumina/copper adhesion was decreased by a factor of 3 due to free alumina surface relaxation. The resultant work of adhesion was weak compared to the surface energy of either alumina or copper and in good agreement with experiment.

Acknowledgements

The authors are grateful to Professor Tony Evans for suggesting that adhesion in ceramic/metal interfaces would be a fruitful area for computations and for numerous discussions of how our results relate to experiment. The metal/ceramic work was supported by the U.S. Office of Naval Research, Grant N00014-91-J4019. The MoSi₂/Mo and NiAl/Cr work was supported by the U.S. Air Force Office of Scientific Research. Computational resources were provided by the San Diego, Lawrence Livermore and NASA-Lewis Supercomputing Facilities.

References

1. J. H. Rose, J. Ferrante, and J. R. Smith, "Universal Binding Energy Curves for Metals and Bimetallic Interfaces," Phys. Rev. Lett., **47** (1981), 675-8; J. Ferrante and J. R. Smith, "Theory of the Bimetallic Interface," Phys. Rev. B, **31** 3427 (1985), 3427-34.
2. P. Vinet, J. H. Rose, J. Ferrante, and J. R. Smith, "Universal Features of the Equation of State of Solids," J. Phys.:Condens. Matter, **1** (1989), 1941-63.
3. J. H. Rose, J. P. Vary, and J. R. Smith, "Nuclear Equation of State from Scaling Relations for Solids," Phys. Rev. Letters, **53** (1984), 344-7.
4. A. Banerjee and J. R. Smith, "Origins of the Universal Binding Energy Relation," Phys. Rev. B, **37** (1988), 6632-45.
5. J. H. Rose, J. R. Smith, and J. Ferrante, "Universal Features of Bonding in Metals," Phys. Rev. B, **28** 1835-45 (1983).
6. T. Hong, J. R. Smith, and D. J. Srolovitz, "Impurity Effects on Adhesion: Nb, C, O, B, and S at a Mo/MoSi₂ Interface,"
7. J. R. Smith, J. G. Gay, and F. J. Arlinghaus, "Self-Consistent Local-Orbital Method for Calculating Surface Electronic Structure: Application to Cu(100)," Phys. Rev. B, **21** 2201-2221 (1980). Phys. Rev. B, **47**, 13 615 - 13 625 (1993).
8. Linus Pauling, The Nature of the Chemical Bond (Cornell University Press, Ithaca, 1960), 225-8 and 256.
9. A. Trampert, F. Ernst, C. P. Flynn, H. F. Fischmeister, and M. Rühle, "High Resolution Transmission Electron Microscopy Studies of the Ag/MgO Interface," Acta metall. mater., **40** S227-36 (1992).
10. T. Hong, J. R. Smith, and D. J. Srolovitz, "Theory of Metal-Ceramic Adhesion," Acta metall. mater., **43** 2721-30 (1995).
11. G. Dehm, M. Rühle, G. Ding, and R. Raj, "Growth and Structure of Copper Thin Films Deposited on (0001) Sapphire by Molecular Beam Epitaxy," Phil. Mag. B, **71** 1111-24 (1995).
12. J. Ferrante and J. R. Smith, "A Theory of Adhesion at a Bimetallic Interface: Overlap Effects," Surface Sci., **38** 77-92 (1973).
13. G. L. Zhao, J. R. Smith, J. Reynolds, and D. J. Srolovitz, "First-Principles Study of the α -Al₂O₃(0001) /Cu(111) Interface," Interface Science, **3** 289-302 (1996).
14. D. Chatain, L. Coudurier, and N. Eustathopoulos, "Wetting and Interfacial Bonding in Ionocovalent Oxide-Liquid Metal Systems," Revue Phys. Appl., **23** 1055-64 (1988).
15. J. A. Appelbaum and D. R. Hamann, "Electronic Structure of the Cu(111) Surface," Solid State Commun., **27** 881 (1978).
16. H. Wawra, "The Surface Energy of Solid Materials as Measured by Ultrasonic and Conventional Test Methods," Z. Metallk., **66** 395-401, 492-98 (1975).
17. J. Guo, D. E. Ellis, and D. J. Lam, "Electronic Structure and Energetics of Sapphire (0001) and (1102) Surfaces," Phys. Rev. B, 13647-56 (1992).
18. I. Manassidis and M. J. Gillan, "Structure and Energetics of Alumina Surfaces Calculated from First Principles," J. Am. Ceram. Soc., **77** 335-8 (1994).
19. R. M. Pilliar and J. Nutting, "Solid-Solid Interfacial Energy Determinations in Metal-Ceramic Systems," Phil. Mag., **16** 181-8 (1967).

Atomic-Scale Calculations of Mechanical Behavior of Intermetallic Alloys

Murray S. Daw

Department of Physics and Astronomy, Clemson University, Clemson, SC, 29634

Michael J. Mills

Department of Materials Science and Engineering, The Ohio State University, Columbus, OH 43210

(July 2, 1996)

Abstract

It is now possible to resolve directly the atomic-scale structure of dislocations in metals and intermetallics. This experimental break-through has provided strong motivation for further theoretical investigations of structure and its relationship to mechanical properties. For example, detailed theoretical studies of dislocation complexes can be compared to parallel experimental studies to reveal the atomic-scale structure of dislocations. Furthermore, various theoretical tools, from atomic-scale simulations to macroscopic scale models, can be used to explore the dynamical behavior of these defects beyond what is accessible directly by experiment. Through this approach, a comprehensive picture of the deformation mechanisms in intermetallic alloys can be pieced together. A particular example is discussed: the $a(110)$ dislocations in $NiAl$, which are responsible for deformations at high temperatures. These dislocations are observed to decompose. A mechanism for the decomposition is proposed and analyzed by atomic-scale calculation.

Support by the National Science Foundation (grant number DMR-9510259) and the Department of Energy (OBES) (contract number DE-FG02-96ER45550).

Our understanding of mechanical properties on a fundamental scale has increased greatly in the last few years. With High Resolution Transmission Electron Microscopy (*HRTEM*), it is now possible to resolve directly the atomic-scale structure dislocations. Theoretical techniques have also advanced, aided in no small part by increased computing speeds. These combined improvements have provided strong motivation for further fundamental investigations mechanical properties. For example, detailed theoretical studies of dislocation complexes can be compared to parallel experimental studies to reveal the atomic-scale structure of dislocations. Furthermore, various theoretical tools, from atomic-scale simulations to macroscopic scale models, can be used to explore the dynamical behavior of these defects beyond what is accessible directly by experiment. By combining results of experimental and theoretical work under the umbrella of atomistic science, a comprehensive picture of the deformation mechanisms in intermetallic alloys can be pieced together.

The atomic-scale science of mechanical properties is especially fruitful when the core structure of dislocations dominates their behavior. Dislocation mobility in intermetallics, for example, is often determined by the atomic-scale structure near the core. In this case, we can begin a fundamental understanding of deformation by careful experimental and theoretical work at the atomic scale.

The atomistic approach is quite useful, both in developing conceptual images of the physical mechanisms, as well as providing quantitative information regarding those mechanisms. But it is useful to understand the practical limitations of the approach. Some of the limitations include level of approximation, time-scale, and length-scale, as is discussed next.

The information derived from atomic-scale calculations is based on knowing the energy of a system. From the energy, one can calculate (in principal) the thermodynamic functions. Or one can calculate the forces on the particles and follow their motion. It has been known for some time [1] that the energy of a system of nuclei and electrons adds together: $E_{tot} = E_{nuc} + E_{elec}$. The nuclei can be treated as classical particles which experience forces created by the chemical bonds that the electrons form between the nuclei. The electrons must be treated on a quantum mechanical basis.

All calculations of the electronic structure in the solid state are approximate. The best calculation we can imagine involves solving the Schrödinger's Equation, which is solved in a space of $3N_e$ variables, where N_e , the number of electrons in the system, is on the order of Avogadro's Number (10^{23})! This is clearly impractical. A very common approximation is to assume that each electron interacts with a "field" created by the other electrons. This "field" is made self-consistent, in that it both determines and yet depends on the solutions for the electronic states. Then one is solving for the state of one electron at a time, in a self-consistent field. This single-electron approach is much more tractable than the full electron problem; but it is an approximation, which must be justified.

The single-electron problem is the origin of the solid-state band theory [2]. In solving for the states of the single-electron in a self-consistent field, one finds that the electronic energy levels may be grouped into bands. These continuous bands help to distinguish the properties of the solid from those of small molecules where the energy levels are discrete.

Calculations at this level can still be challenging for complex defects such as dislocations. Further levels of approximation are commonly made to retain the qualitative features of the band structure, while allowing for some simplification of the calculations. Some approaches retain more details of the band structure, while others make only very crude estimates of

the band's width and shape. The Embedded-Atom Method (*EAM*) [3–6] is in this latter category. These days, the *EAM* is the most common method for dealing with complex defects in metals.

On the bottom of this chain of approximations would lie the “pair potential” scheme, which retains little or no information about the quantum mechanics as described by the Schrödinger's Equation. When a pair of atoms form a bond, the strength of that bond depends on what other bonds those atoms have formed. But the pair potential neglects that dependence: each bond is of the same strength, regardless of the number of bonds each atom has formed.

The interested reader is referred to the review of the *EAM* for more discussion of solid state calculations. [6]

At some level of approximation, one has determined the energy of the electronic states, E_{elec} . Even with the best approximation we can make, atomic-scale calculations treat systems of a finite size. A very large calculation [7], recently done at Los Alamos, employed the *EAM* to treat crack propagation in a *Cu* slab of a few million atoms, or a few hundred atoms on a side: impressive to the purist, not so impressive to those trying to unravel processes taking place on a much larger scale.

Similarly, the time scale in molecular dynamics calculations is puny. The basic unit of time is set by the natural vibrational period in the lattice, which is on the order of $10^{-12}sec$. To simulate one second of lab time takes at least 10^{14} iterations of the molecular dynamics! A fast computer and program with an iteration time of $10^{-6}CPU-sec/iteration$ still would take $3CPU-years$ to complete the calculation.

Clearly, atomic-scale calculations cannot be used brute-force to study systems of interest, even if one could overcome difficulties with various approximations made in the electronic structure calculations. Instead, such calculations should be just one tool in the set.

Having delineated what is reasonable to expect from atomic-scale calculations, we now consider a recent example.

The deformation mechanisms and mechanical properties of *NiAl* (*B2* structure) have been studied extensively [8]. A striking feature of deformation in single crystals is the large anisotropy of the mechanical properties. Deformation occurs principally by the motion of $a\langle 100 \rangle$ dislocations for most orientations (*i.e.*, non- $\langle 100 \rangle$ axes, defined as “soft” orientations). The yield strength for “soft” orientations is relatively low above room temperature and increases moderately below. Coupled with this relatively weak temperature dependence is a mild strain rate dependence at lower temperatures. When deformed along a $\langle 100 \rangle$ axis (defined as the “hard” orientation), there is no resolved shear stress on $a\langle 100 \rangle$ dislocations. At lower temperatures, single crystals deformed in tension are brittle, and a brittle-to-ductile transition temperature occurs at about 400C. Yielding in the “hard” orientation at room temperature occurs at a stress approximately ten times larger than in the “soft” orientation. Above the brittle-to-ductile transition temperature, $a\langle 110 \rangle$ dislocations begin to operate, and the yield strength decreases sharply with temperature and increases with strain rate.

These macroscopic observations suggest that the anisotropy of the mechanical properties of *NiAl* single crystals might be due to a difference in the mobility of $a\langle 100 \rangle$ and $a\langle 110 \rangle$ dislocations, which are operative in the “soft” and “hard” orientations, respectively.

The $a\langle 100 \rangle$ dislocation cores were found to be compact, with no apparent dissociation. These dislocations are predicted by theory [9] to be relatively mobile on $\{100\}$ slip planes,

which is consistent with the characteristics of flow in the “soft” orientations.

Two different $a\langle 110 \rangle$ core structures were observed in HRTEM [10,11]: a dissociated configuration and a decomposed structure. The dissociated structure arises from the reaction $a[110] \rightarrow \frac{a}{2}[111] + \text{fault} + \frac{a}{2}[11\bar{1}]$, where the fault is an Anti-Phase Boundary. The decomposed structure (shown in Fig. 1) occurs by the reaction $a[110] \rightarrow a[100] + a[010]$, where no fault is formed. Atomistic calculations of the dissociated configurations in the *bulk* showed such core structures to be unstable, converting to the decomposed structure. However, when the calculations were performed in thin slabs of about the same thickness as the experimental samples, the dissociated configuration was stabilized. The theory predicts that *both* types of dislocations may exist in thin slabs, but only the decomposed structure exists in the bulk. Thus, only the decomposed core is believed to be relevant to bulk deformation.

The decomposition is observed to be incomplete. That is, some segments of the dislocation appear perfect, while others are widely decomposed, as in Fig. 2.

The decomposed core, which consists of two $a\langle 100 \rangle$ dislocations with orthogonal Burger’s vectors, has no possibility for conservative glide in the “hard” orientation. The decomposition effectively locks the edge portions of $a\langle 110 \rangle$ dislocations, suggesting that motion is instead accomplished by the lateral movement of non-edge segments, via transfer of vacancies [12,13]. To accomplish glide, vacancies must be transferred from one leg of the decomposed pair to the other, along the dislocation line through the vertex where the decomposed segments join. This diffusion-mediated glide model appears to be in reasonable agreement with the observed kinetics of deformation, as well as the strong temperature and strain-rate dependence. In particular, one expects that the activation energy for the process is that for the pipe-diffusion of vacancies. This suggests that there may also be a strong stoichiometric effect on the mobility of $a\langle 110 \rangle$ dislocations.

With a combined analysis of experimental and theoretical results, we conclude that the core structure determines the mobility of dislocations in *NiAl*.

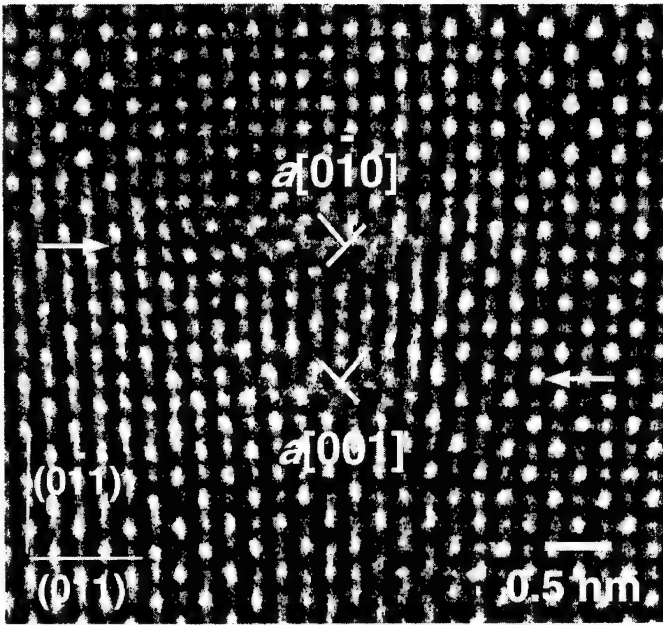


FIG. 1. HRTEM micrograph of an end-on $a[0\bar{1}1]$ edge dislocation in $NiAl$ which has decomposed into two separate $a\langle 010 \rangle$ edge dislocations. The arrows indicate discontinuities in the nominal (022) slip plane for the complete dislocation. The decomposition reaction has occurred *normal* to the (022) slip plane. This image was obtained using conditions (JEOL 4000EX; defocus = -60 nm; thickness = 7 nm) for which the image intensities correspond to atomic column positions in a perfect crystal.

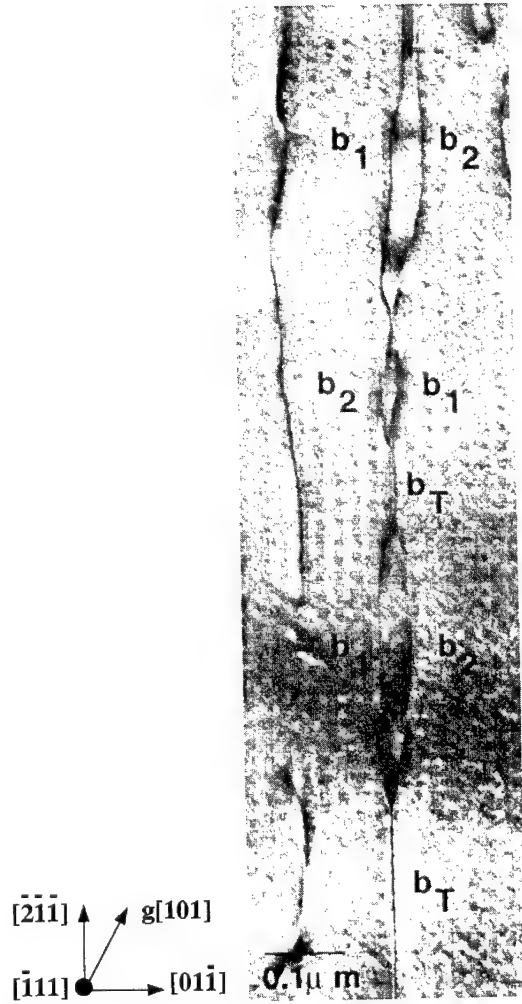


FIG. 2. Bright-field ($g = [101]$) TEM image of an $a[011]$ dislocation in which some segments of the dislocation appear perfect (labelled " b_T "), while other segments are widely decomposed into $a[011]$ (labelled as " b_1 ") and $a[010]$ (labelled as " b_2 ") dislocations. The beam direction is parallel to $[\bar{1}11]$, so that the decomposed segments clearly lie out of the $(01\bar{1})$ glide plane for the overall $a[011]$ dislocation.

REFERENCES

- [1] J. C. Slater, *Quantum Theory of Matter* (McGraw-Hill, New York, 1968), note1.
- [2] C. Kittel, *Solid State Physics* (John Wiley & Sons, New York, 1976), note1.
- [3] M. S. Daw and M. I. Baskes, Phys Rev Lett **50**, 1285 (1983).
- [4] M. S. Daw and M. I. Baskes, Phys Rev B **29**, 6443 (1984).
- [5] S. M. Foiles, M. I. Baskes, and M. S. Daw, Phys Rev B **33**, 7983 (1986).
- [6] M. S. Daw, S. M. Foiles, and M. I. Baskes, Materials Science Reports **9**, 251 (1993).
- [7] S. Zhou *et al.*, MRS Bulletin **21**, cover (1996).
- [8] D. B. Miracle, Acta metall. mater. **41**, 649 (1993).
- [9] T. A. Parthasarathy, S. I. Rao, and D. M. Dimiduk, Phil. Mag. A **67**, 643 (1993).
- [10] M. J. Mills, M. S. Daw, S. M. Foiles, and D. B. Miracle, in *HRTEM Observation and EAM Calculation of Dislocation Cores in NiAl*, Vol. 288 of *Mat. Res. Soc. Symp. Proc.*, MRS (MRS, Pittsburgh, 1993), p. 257.
- [11] M. J. Mills, M. S. Daw, and S. M. Foiles, Ultramicroscopy **56**, 79 (1994).
- [12] M. J. Mills, M. S. Daw, J. E. Angelo, and D. B. Miracle, in *High Temperature Ordered Intermetallic Compounds V*, Vol. 364 of *Mat. Res. Soc. Symp. Proc.*, MRS, edited by J. A. Horton *et al.* (MRS, Pittsburgh, 1995), p. 401.
- [13] M. J. Mills, S. Ragagopalan, J. E. Angelo, and M. S. Daw, submitted May 1996 (unpublished).

ROLE OF INTERFACES IN DEFORMATION AND FRACTURE:

TITANIUM ALUMINIDES*

M. H. Yoo and C. L. Fu

Metals and Ceramics Division
Oak Ridge National Laboratory
Oak Ridge, TN 37831, USA

Abstract

Available experimental data on deformation and fracture behavior of polysynthetically twinned (PST) TiAl crystals are analyzed on the basis of the calculated results of bulk and defect properties and shear fault, cleavage and interfacial energies of TiAl and Ti₃Al. The extent of dissociation width of an ordinary dislocation is calculated to be larger at α_2/γ and γ/γ interfaces by about two-fold as compared to the bulk of γ -phase, suggesting the enhanced slip along the interfaces when the crystal is at a soft orientation. Propagation of (111) cleavage cracks is influenced by the mixed mode (II and III) of external loading applied to the coplanar deformation twinning and ordinary slip, leading to translamellar fracture. According to the calculated interfacial fracture energies, cleavage cracking is to occur on α_2/γ boundaries and least likely on true-twin boundaries. Discussion is given on the roles of misfit dislocations, kinetics of dislocation-interface interactions, and hydrogen embrittlement in deformation and fracture processes.

*Research sponsored by the Division of Materials Sciences, U.S. Department of Energy, under contract number DE-AC05-96OR22464 with Oak Ridge National Laboratory, managed by Lockheed Martin Energy Research Corporation.

"The submitted manuscript has been authored by a contractor of the U.S. government under contract NO. DE-AC05-96OR22464. Accordingly, the U.S. Government retains a nonexclusive, royalty-free license to publish or reproduce the published form of this contribution, or allow others to do so, for U.S. Government purposes."

Processing and Design Issues
in High Temperature Materials
Edited by N.S. Stoloff and R.H. Jones
The Minerals, Metals & Materials Society, 1997

Introduction

Microcomposite structures resulting from phase separation or decomposition can offer many unique microstructural advantages in thermodynamic stability, directional alignment, and fine dispersion of component phases. For examples, γ'/γ phases in Ni-base superalloys, α/β or β'/β in Ni-Al-X ternary (X = Cr or Ti) system, and α_2/γ in Ti-Al binary system are the outstanding cases in point. In the case of Ti-rich two-phase TiAl-Ti₃Al alloys, significant advances have been made recently in understanding the role of interfaces in deformation and fracture behavior of fully lamellar microstructure, due largely to controlled experimental investigations using the so-called polysynthetically twinned (PST) crystals, e.g., [1,2]. Quantitative interpretation of these experimental results, such as the anisotropic yield strength and tensile elongation [1,3] and fracture behavior [2,4] with respect to the lamellar orientation in PST TiAl crystals, requires fundamental information on the bulk and defect properties of the two constituent phases and the surface and interfacial energies of various γ/γ interfacial variants and α_2/γ boundary. It is this fundamental aspect of deformation and fracture in two-phase TiAl alloys which is the focus of this paper.

Phase stability and elastic constants [5-7], elastic incompatibility and misfit strain [8], bonding mechanisms [7,9], point defects in TiAl [9], shear fault energies [5,7], twin boundaries in TiAl [10], and cleavage and interfacial fracture energies [11,12] have been determined from total energy calculations using the full potential linearized augmented plane wave (FLAPW) method within the framework of the local density functional (LDF) theory. The purpose of this paper is to discuss available experimental data on the role of interfaces in deformation and fracture of PST TiAl crystals on the basis of the calculated results mentioned above [5-12].

Shear Fault Energies and Deformation Modes

TiAl

Plastic deformation of γ -TiAl by slip or twinning occurs primarily on {111} planes. Figure 1 (a) shows the atom stacking sequence on the (111) plane of the L1₀ structure viewed on the (111) plane, wherein the three different fault vectors, \mathbf{b}_i , are described. An ordinary dislocation is expected to dissociate into a pair of Shockley partials, with Burgers vectors of $\mathbf{b}_1 = [\bar{2}11]/6$ and $-\mathbf{b}_2 = [1\bar{2}1]/6$, forming a strip of complex stacking fault (CSF) ribbon,

$$[\bar{1}10]/2 \rightarrow [\bar{2}11]/6 + \text{CSF} + [1\bar{2}1]/6. \quad (1)$$

The four-fold dissociation of a superdislocation consists of two sets of $\mathbf{b}_3 = [11\bar{2}]/6$ and $-\mathbf{b}_2 = [1\bar{2}1]/6$ partial dislocations,

$$[01\bar{1}] \rightarrow [11\bar{2}]/6 + \text{SISF} + [1\bar{2}1]/6 + \text{APB} + [11\bar{2}]/6 + \text{CSF} + [1\bar{2}1]/6, \quad (2)$$

where SISF and APB are superlattice intrinsic stacking fault and anti-phase boundary, respectively. According to the classical Peierls concept of dislocation mobility, which says that the wider the planar dissociation configuration of a dislocation, the more mobile the dislocation is, the values of these fault energies provide a relative measure for the ease of gliding.

Ti₃Al

Plastic deformation of α_2 -Ti₃Al of the DO₁₉ structure is known to occur by three slip systems, viz., the prism slip, {1100}<11 $\bar{2}$ 0>, the basal slip, (0001)<11 $\bar{2}$ 0>, and the pyramidal slip, {11 $\bar{2}$ 1}<11 $\bar{2}$ 6>. The crystallographic aspects of the APB formation on these slip planes are well described by Umakoshi and Yamaguchi [13].

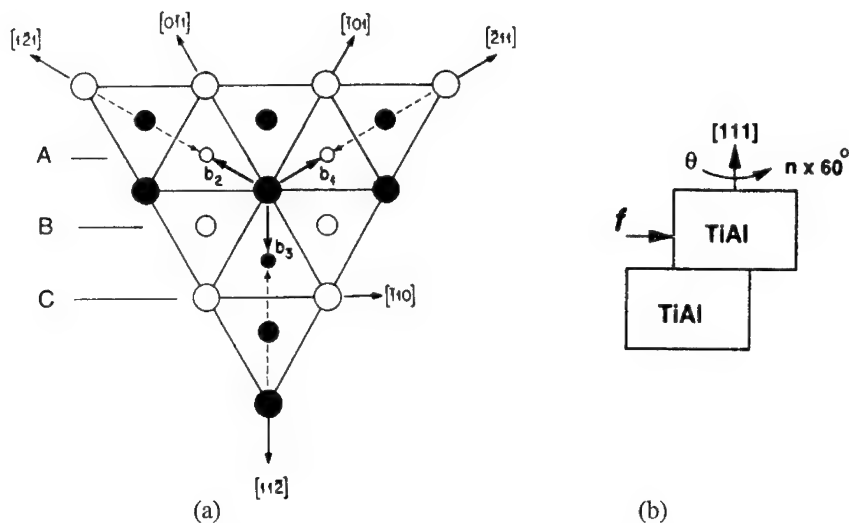


Figure 1. (a) Atomic stacking (ABC) sequence on the (111) plane of the L1₀ structure, and (b) Schematic illustration of translation and rotation operations.

Structure and Energies of Interfaces

γ/γ Interfaces

Figure 1 (b) shows schematically how three different types of planar faults are created at three different types of γ/γ interfaces. When the angle of rotation, θ , and the fault shift vector, \mathbf{f} , are both zero, the top and bottom halves together constitute the reference state of a single crystal, i.e., the total internal energy is set to zero.

All the calculated interfacial energies in Table I are the values obtained after atomic relaxation. Fault energies calculated for the three types on the (111) plane, i.e., APB with $\mathbf{f} = \mathbf{b}_1 - \mathbf{b}_3$ or $\mathbf{b}_2 - \mathbf{b}_3 = \langle 101 \rangle / 2$, SISF with $\mathbf{f} = \mathbf{b}_3 = [11\bar{2}] / 6$, and CSF with $\mathbf{f} = \mathbf{b}_1$ or $\mathbf{b}_2 = \langle \bar{2}11 \rangle / 6$, are listed in the first row ($\theta = 0^\circ$). The APB, SISF, and true-twin boundary energies of $E_{\text{APB}} = 560$, $E_{\text{SISF}} = 90$, and $\Gamma_T = 60$ mJ/m², respectively, are similar to the results reported earlier [5]. It should be noted that in the earlier paper [5] the relaxation effect was included only for the APB. Since there is no change in the nearest-neighbor atomic coordination at the SISF, superlattice extrinsic stacking fault (SESF), and true-twin interfaces, atomic relaxation at these fault interfaces is assumed to be negligibly small. According to a more refined calculation, the present result gives an APB energy which is slightly increased from the previously reported value. With the inclusion of relaxation energy, the CSF energy is reduced from $E_{\text{CSF}} = 600$ mJ/m² to 530 mJ/m². Consequently, the hierarchy of the fault energies remains as $E_{\text{CSF}} \approx E_{\text{APB}} > E_{\text{SISF}} > E_{\text{SESF}} > \Gamma_T$, which is consistent with the recent experimental and simulation analysis in Ti-54at.%Al by Wiezorek and Humphreys [14].

Interfacial energies calculated for the three different types, i.e., pseudo-twin ($\theta = 60^\circ$), "rotational" ($\theta = 120^\circ$), and true-twin ($\theta = 180^\circ$) boundaries, are listed in the first column ($\mathbf{f} = 0$) of Table I. The pseudo-twin boundary energy of $\Gamma_P = 300$ mJ/m² [10] is reduced to 270 mJ/m² after relaxation. At the pseudo-twin ($\theta = 60^\circ$) and rotational ($\theta = 120^\circ$) boundaries, while both E_{APB} and E_{CSF} are reduced markedly, by factors of about two, as compared to those in the bulk, E_{SISF} is increased by a factor of three. At the true-twin boundary, on the other hand, changes in the fault energies are relatively small, with slight increases in both E_{APB} and E_{CSF} and a decrease in E_{SISF} .

Table I. Interfacial Energies of γ/γ Lamellar Boundaries in TiAl (in Units of mJ/m²)

Interface type	θ	$\mathbf{f} = 0$ Γ_i	$\frac{1}{2}\langle\bar{1}01\rangle$ APB	$\frac{1}{6}[11\bar{2}]$ SISF	$\frac{1}{6}\langle\bar{2}11\rangle$ CSF
Bulk	0°	0	560	90	530
Pseudo-twin	60°	270	270	270	270
Rotational	120°	250	250	280	280
True-twin	180°	60	550	60	550

Degeneracies of fault energies noted in Table I are due to geometrically equivalent characteristic patterns of interfaces resulting from certain combinations of rigid-body translations and rotations according to the O-lattice theory [15]. An example of these degeneracies can be described with the aid of Fig. 2, where the C-layer of atoms have been rotated and translated with reference to the B-layer. Figure 2(b) shows the geometric pattern of interfaces by $\theta = 60^\circ$ and $\mathbf{f} = 0$, and Fig. 2(c) shows that by $\theta = 60^\circ$ and $\mathbf{f} = \mathbf{b}_2$. These two operations result in a geometrically equivalent pattern between two atomic rows of the adjacent B and C layers. Because of the assumption that $c/a = 1$, the magnitude of $\mathbf{b}_1 = \mathbf{b}_2$ are equal to that of \mathbf{b}_3 , and the atomic lattices shown in Figs. 1 and 2 are equilateral triangles. With the actual value of $c/a = 1.02$ for γ -TiAl, this symmetry and the degeneracies are broken, thus giving rise to long-range coherency stresses and interfacial dislocations to accommodate the misfit strain across the interface. A contribution of misfit dislocation content to the determination of interfacial fracture energy is discussed below.

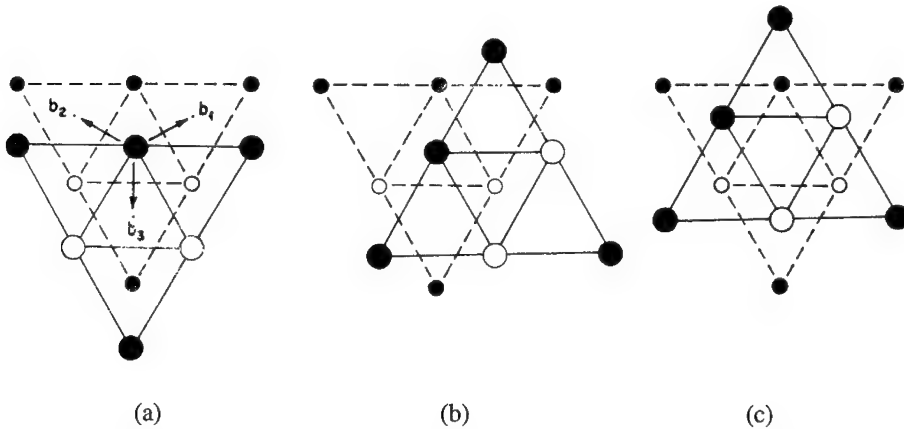


Figure 2. Degeneracy of the shear faults at a pseudo-twin interface, (a) reference state, (b) $\theta = 60^\circ$, $\mathbf{f} = 0$, and (c) $\theta = 60^\circ$, $\mathbf{f} = \mathbf{b}_2$

α_2/γ Interface

At an α_2/γ interface with the crystallographic habit relationship₂ of (0001)[11 $\bar{2}$ 0]-Ti₃Al and (111)[1 $\bar{1}$ 0]-TiAl, the interfacial energy is calculated to be 100 mJ/m² (the reference energy in this case is the sum of TiAl and Ti₃Al bulk energies). Significant reductions of E_{APB} and E_{CSF} in α_2 phase to those (280 and 220 mJ/m², respectively) at the Ti₃Al/TiAl interface were reported recently [7], which are summarized in Table II.

Table II. Calculated Shear Fault Energies at the TiAl/Ti₃Al Interface (in Units of mJ/m²)

Plane	APB	SISF	CSF
(111) TiAl	560	90	530
(0001) Ti ₃ Al	300		320
TiAl/Ti ₃ Al	280	20	220

Inhomogeneous Slip and Plastic Anisotropy

Possible roles of various interfaces in the slip system, $\{111\}\langle 1\bar{1}0\rangle/2$, can be discussed with the aid of Figure 3 which schematically illustrates true-twin (TT, γ_1/γ_2), pseudo-twin (PT, γ_1/γ_3), rotational (RB, γ_1/γ_4), and α_2/γ (Ti₃Al/TiAl) boundaries. Domain boundaries of other γ/γ -type that are roughly perpendicular to the (111) plane are neglected here for simplicity. The crystallographic orientation shown in Fig. 3 is with reference to the γ_1 domain. A screw ordinary dislocation of Burgers vector, $[1\bar{1}0]/2$, is dissociated on either the (111) or $(\bar{1}\bar{1}1)$ slip plane according to Eq. (1), where $E_{\text{CSF}} = 530 \text{ mJ/m}^2$ in the γ_1 bulk gives the equilibrium width of $w = 0.23 \text{ nm}$ [16]. The calculated values of E_{CSF} at the γ/γ -type interfaces (the last column of Table I) and at the α_2/γ interface [7] are shown in Fig. 3, which schematically depicts relatively wider dissociations at interfaces, the widest being at the α_2/γ interface with $w \approx 0.55 \text{ nm}$. According to the simple criterion for the ease of gliding that the wider the dissociation configuration of a dislocation, the more mobile the dislocation is [16], the mobility of $[1\bar{1}0]/2$ screw dislocation is expected to be slightly reduced along a true-twin boundary, but significantly enhanced along all other types of the interfaces.

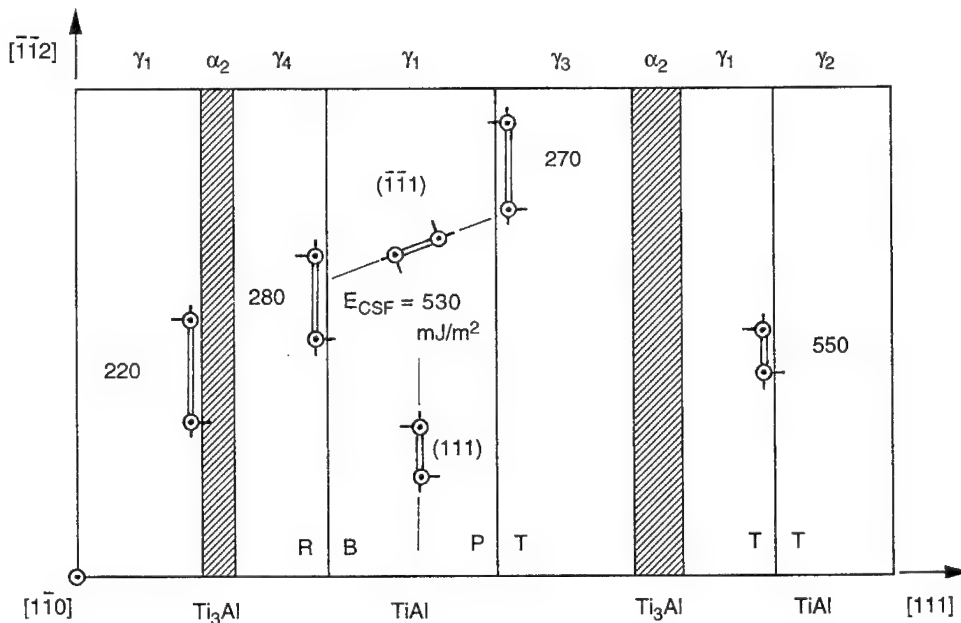


Figure 3. CSF energies and dissociation of screw $[1\bar{1}0]/2$ dislocations in PST crystals.

Because of more complex dissociation configuration involving all three types of the planar faults, Eq. (2), the role of interfaces in the relative mobility of superdislocations is more complicated than of ordinary dislocations. As listed in Table I, while E_{APB} and E_{CSF} in the bulk of γ -phase are both reduced, by about a half, at pseudo-twin and 120° rotational boundary interfaces, E_{SISF} is increased about threefold.

As far as ordinary dislocations are involved, the enhanced mobility along these lamellar interfaces supports the notion of "channeled dislocation motion" [17] or "supersoft deformation mode" [15] in lamellar TiAl, which may be a contributing factor to the strong orientation dependence of yield strength in PST TiAl crystals [1]. The recent experiment purported to examine the role of α_2/γ interfaces in plastic deformation at the soft orientation (shear parallel to the lamellar interfaces) revealed, however, that plastic shear strain occurred mostly away from the α_2/γ interfaces [3]. Though Inui et al. [3] concluded that shear strain in the soft orientation was due to twinning and slip in the bulk of γ lamellae, possibility of inhomogeneous flow by ordinary dislocations along γ/γ interfaces cannot be ruled out from this experimental observation. Presumably, misfit dislocations and ledges on an α_2/γ interface significantly influence the parallel slip process along the interface.

Cleavage and Interfacial Fracture

Once a cleavage crack is initiated on a (111) plane, which is of the lowest cleavage energy in TiAl [8], it may propagate across a series of γ/γ interfaces under the influence of mode-II and mode-III components of external loading applied to the coplanar (111)[11 $\bar{2}$] twinning (edge) and (111)[1 $\bar{1}$ 0] ordinary slip (screw), leading to translamellar fracture. This effect of mode mixity was illustrated in terms of crack-tip stress fields [8] and observed in an electron microscopy study [18].

Using the ideal cleavage energies, G_c , calculated earlier [8] and the interfacial energies, Γ_i , obtained recently [12], one can evaluate interfacial fracture energy, the work of adhesion, by

$$G_i = G_c - \Gamma_i - E_m, \quad (3)$$

where E_m is the misfit energy estimated using the Frank and van der Merwe method [19] and the calculated lattice parameters of TiAl and Ti_3Al [5-7]. The calculated results are summarized in Table III. Because of the approximations involved in determining the interfacial and misfit energies, the final interfacial fracture energies are only estimates. Nevertheless, these results, indicating that the interfacial work of adhesion is slightly larger for α_2/γ and true-twin boundaries than for other types of γ/γ interfaces, enable us to set a relative measure of interfacial fracture mode.

Table III. Interfacial Fracture Energies in Two-Phase TiAl
(in Units of J/m²)

Interface	G_c	Γ_i	E_m	G_i
γ/γ				
PT (60°)	4.5	0.27		~4.2
RB (120°)	4.5	0.25	0.03	4.2
TT (180°)	4.5	0.06		~4.4
α_2/γ	4.65	0.10	0.07	4.5

Fracture behavior and toughness of PST TiAl crystals at room temperature were investigated using three-point bending tests of Chevron-notched crystals in five different lamellar orientations [4]. While the preliminary results suggest that delamination-type separation occurs in α_2 lamellae, examinations to clarify whether fracture occurs along γ/γ , α_2/γ , or in α_2 lamellae have not been completed. On the other hand, in the fracture tests using microcompact tension specimens of TiAl PST crystals [2], it was found that a microcrack was initiated on the α_2 plate and easily developed into a main crack on the (0001) plane, finally leading to failure because of the hydrogen embrittlement of the α_2 phase. Though the intrinsic cleavage energy of the (0001) plane in the α_2 phase is, $G_c = 4.8 \text{ J/m}^2$ [8], higher than those of any other interfaces listed in Table III, it could be reduced appreciably, due probably to the relatively high solubility of interstitials (hydrogen, in this case) in the α_2 phase. In fact, our recent study of the effect of atomic hydrogen on the interfacial cohesion indicates that hydrogen preferentially segregates to the α_2/γ boundaries and also to the α_2 phase. The (0001) surface energy of Ti_3Al is reduced by $\approx 15\%$ with a hydrogen coverage of ≈ 0.2 on the surface. Environmental embrittlement can have a pronounced effect on the fracture mode in TiAl alloys.

Figure 4 shows a schematic diagram illustrating the experimental results by Oh et al. [20] on the fracture mode changes in PST crystals in response to the applied strain rate under a hydrogen producing environment. When the strain rate was $\dot{\epsilon} = 2 \times 10^{-4} \text{ s}^{-1}$, the fracture mode was an interlamellar type along the (111) γ/γ interfaces parallel to the α_2/γ interfaces as shown by Fig. 4 (a), and the tensile elongation was 16%. When the strain rate was raised to $\dot{\epsilon} = 1 \times 10^{-1} \text{ s}^{-1}$, the fracture mode was changed to a translamellar type, Fig. 4 (b), which occurred with nearly a factor of two increase in ductility of $\epsilon_f = 30\%$. The authors [20] concluded that (a) the interfacial (γ/γ with $\theta = 60^\circ$ and 120°) cleavage was initiated due to the reduced interfacial energy by hydrogen segregation, and (b) at the higher strain rate diffusion time for the atomic hydrogen was too short to effect the interlamellar fracture.

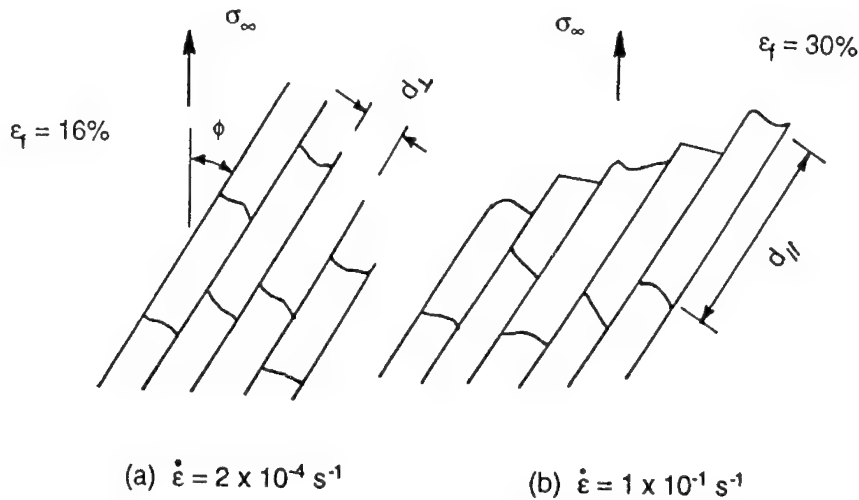


Figure 4. Schematic illustration (based on Ref. [20]) of fracture mode change in PST crystals ($\phi = 31^\circ$) with two different strain rates under environmental embrittlement at room temperature.

Two additional viewpoints regarding interpretation of these experimental results [20] were offered based on the energetic and kinetic aspects of nucleation and propagation of cracks [21]. First, in Fig. 4 (a), once nucleated, the propagation of an interfacial crack can be promoted by the mixed-mode (I+II) effect, together with the enhanced slip along the interface. Second, in Fig. 4 (b), because of the relatively large interspacing of the γ/γ domain boundaries, d_{\parallel} , as compared to the average interlamellar spacing, d_{\perp} , translamellar crack nucleation at a γ/γ domain boundary may occur due to a pile-up of soft-mode ordinary dislocations under the high strain rate.

Discussion

The ratio of γ/γ -type interfacial energies calculated for true-twin, pseudo-twin, and rotational boundaries ($\Gamma_T : \Gamma_P : \Gamma_R$) is 1 : 4.5 : 4.2. This is consistent with more frequent observation of true-twin type lamellar interfaces, in two-phase TiAl alloys of binary compositions, compared with the 120°-rotational and pseudo-twin types [22]. On the other hand, the reason why the lamellar domain boundaries of higher energies than that of the true-twin type, by factors of more than four, do appear in the TiAl phase is not entirely clear. One possible explanation for the formation of these lamellar domain boundaries may be closely related to the preexisting anti-phase domain boundaries (APBs) of Ti_3Al before the $\alpha_2 \rightarrow \alpha_2 + \gamma$ transformation [23].

Misfit dislocations present at semicoherent α_2/γ and γ/γ interfaces are often the sites for generation of slip dislocations and deformation twinning [24]. When a dislocation pile-up occurs against an interface, stress concentration at the interface may reach a level sufficiently high for either initiation of slip or twinning into the adjacent domain leading to a Hall-Petch type relationship, or crack nucleation by the Stroh mechanism. Using Hall-Petch and Stroh mechanisms, Hazzledine and Kad [25] discussed the orientation dependent yield and fracture stresses reported in PST TiAl crystals [1]. In light of the fact that all the deformation modes in γ -TiAl occur on {111} planes and the ideal cleavage energy is lowest on these planes, the importance of mode-mixity was emphasized earlier not only in crack-tip plasticity, but also in nucleation of slip, twinning, or cracking by stress concentration due to a dislocation pile-up [8].

Most of modeling analyses for the stress concentration associated with a pile-up of dislocations, including the above two papers [8,25], are based on a static equilibrium condition, and as such these cannot be applied to treat dynamic or quasi-static aspects of deformation and fracture processes. Regarding the stress concentration associated with a dislocation pile-up against an interface, the role of energetic barriers estimated on the basis of linear elasticity is relatively unimportant as compared to that of kinetics of the dislocation reaction resulting from the leading dislocation [21]. In other words, how efficiently the reaction products (resulting from incorporation of a slip dislocation into a semicoherent interface containing interfacial dislocations) glide/climb away from the site of intersection is far more crucial to whether or not the following dislocations can be incorporated into the interface. This kinetic barrier of slip-interface interaction will be lowered with increasing temperature, which may be one of the reasons for a sharp drop in the yield stresses for the hard ($\phi = 0^\circ$ and $\phi = 90^\circ$) orientations [3]. Another possible contribution to the softening at elevated temperatures (> 1073 K) may be from deformation twinning in non-stoichiometric Ti_3Al alloy at the elevated temperatures [26].

According to the recent review by Wiezorek and Humphreys [14], the hierarchy of planar fault energies in Ti-54%Al is $E_{\text{CSF}} > E_{\text{APB}} > E_{\text{SISF}}$, and the values for TiAl are $E_{\text{APB}} > 250 \text{ mJ/m}^2$ and $E_{\text{SISF}} = 140 \text{ mJ/m}^2$. Our calculated results of $E_{\text{APB}} = 560 \text{ mJ/m}^2$ and $E_{\text{SISF}} = 90 \text{ mJ/m}^2$ for TiAl (at stoichiometry) at 0K indicate that temperature and composition dependencies of planar fault energies in TiAl may be very substantial. Further theoretical and experimental studies are needed to assess the dependencies of planar fault energies on temperature and composition in order to better understand the role of interfaces in mechanical behavior of Ti-rich two-phase alloys.

Summary

The intrinsic values of interfacial energies based on first-principles calculations, including atomic relaxation, were obtained for the three types of γ/γ interfaces and the α_2/γ lamellar boundary in two-phase TiAl alloy. The pseudo-twin boundary energy is highest, $\Gamma_P = 270 \text{ mJ/m}^2$, and the true-twin boundary energy is lowest, $\Gamma_T = 60 \text{ mJ/m}^2$. Planar fault energies at pseudo-twin and 120° rotational interfaces are markedly different from those in the bulk of γ -phase, i.e., approximately, E_{APB} and E_{CSF} decreases by a half and E_{SISF} increases by a threefold. Enhanced mobility of ordinary dislocations along α_2/γ and γ/γ interfaces (except true twin boundaries) is predicted based on the reduced E_{CSF} values. Interfacial fracture energies are estimated to be slightly higher for the α_2/γ and true-twin boundaries than for other γ/γ type interfaces. Crack nucleation at γ/γ domain boundaries and the mode mixity together with the enhanced slip along the interfaces are suggested as contributing factors involved in the reported environmental embrittlement effects on PST TiAl crystals.

References

1. T. Fujiwara, A. Nakamura, M. Hosomi, S. R. Nishitani, Y. Shirai, and M. Yamaguchi, "Deformation of PST Crystals of TiAl with a Nearly Stoichiometric Composition," *Phil. Mag. A* **61** (1990), 591-606.
2. T. Nakano, T. Kawanaka, H. Y. Yasuda, and Y. Umakoshi, "Effect of Lamellar Structure on Fracture Behavior of TiAl PST Crystals," *Mater. Sci. Eng. A* **194** (1995), 43-51.
3. H. Inui, K. Kishida, M. Misaki, M. Kobayashi, Y. Shirai, and M. Yamaguchi, "Temperature Dependence of Yield Stress, Tensile Elongation and Deformation Structures in PST Crystals of TiAl," *Phil. Mag. A* **72** (1995), 1609-1631.
4. S. Yokoshima and M. Yamaguchi, "Fracture Behavior and Toughness of PST Crystals of TiAl," *Acta Mater.* **44** (1996), 873-883.
5. C. L. Fu and M. H. Yoo, "Elastic Constants, Fault Energies, and Dislocation Reactions in TiAl: A First-Principles Total-Energy Investigation," *Phil. Mag. Lett.* **62** (1990), 159-165.
6. J. Zou, C. L. Fu, and M. H. Yoo, "Phase Stability of Intermetallics in the Al-Ti System: A First-Principles Total-Energy Investigation," *Intermetallics* **3** (1995) 265-269.
7. C. L. Fu, J. Zou, and M. H. Yoo, "Elastic Constants and Planar Fault Energies of Ti_3Al and Interfacial Energies at the $\text{Ti}_3\text{Al}/\text{TiAl}$ Interface by First-Principles Calculations," *Scr. Metall. Mater.* **33** (1995), 885-891.
8. M. H. Yoo, J. Zou, and C. L. Fu, "Mechanistic Modeling of Deformation and Fracture Behavior in TiAl and Ti_3Al ," *Mater. Sci. Eng. A* **192/193** (1995), 14-23.
9. C. L. Fu and M. H. Yoo, "Bonding Mechanisms and Point Defects in TiAl," *Intermetall.* **1** (1993), 59-63.
10. M. H. Yoo, C. L. Fu, and J. K. Lee, "Elastic Properties of Twin Dislocations in Titanium Aluminides," *Twinning in Advanced Materials*, ed. M. H. Yoo and M. Wuttig, (TMS Symp. Proc., Warrendale, PA, 1994), 97-106.
11. M. H. Yoo and C. L. Fu, "Cleavage Fracture of Ordered Intermetallic Alloys," *Mater. Sci. Eng. A* **153** (1992), 470-478.
12. C. L. Fu and M. H. Yoo, "Interfacial Energies in Two-Phase TiAl- Ti_3Al Alloy," *Scr. Mater.* (submitted).
13. Y. Umakoshi and M. Yamaguchi, "The Stability and Energies of Planar Faults in D_{019} Ordered Structure," *Phys. Stat. Sol. (a)* **68** (1981), 457-468.
14. J.M.K. Wiezorek and C. J. Humphreys, "On the Hierarchy of Planar Fault Energies in TiAl," *Scr. Metall. Mater.* **33** (1995), 451-458.
15. S. Rao, C. Woodward, and P. M. Hazzledine, "The Interaction between Dislocations and Lamellar Grain Boundaries in PST $\gamma\text{-TiAl}$," *Defect-Interface Interactions*, ed. E. P. Kvam, A. H. King, M. J. Mills, T. D. Sands, and V. Vitek, (MRS Symp. Proc. Vol. 319, Pittsburgh, PA, 1994), 285-292.
16. M. H. Yoo and C. L. Fu, "Strength of Intermetallic Compounds: TiAl," *Intermetallic Compounds for High-Temperature Structural Applications*, ed. M. Yamaguchi and H. Fukutomi, (Proc. 3rd Japan Int. SAMPE Symp., 1993), 1286-1293.

17. B. K. Kad, P. M. Hazzledine, and H. L. Fraser, "Lamellar Interfaces and Their Contribution to Plastic Flow Anisotropy in TiAl-Based Alloys," High-Temperature Ordered Intermetallic Alloys V, ed. I. Baker, R. Darolia, J. D. Whittenberger, and M. H. Yoo, (MRS Symp. Proc. Vol. 288, MRS, Pittsburgh, PA, 1993), 495-500.
18. F. Appel, U. Christoph, and R. Wagner, "An Electron Microscope Study of Deformation and Crack Propagation in (α_2 + γ) Titanium Aluminides," *Phil. Mag. A* **72** (1995), 341-360.
19. J. W. Mathews, "Misfit Dislocations in Screw Orientation," *Phil. Mag.* **29** (1974), 797-802.
20. M. H. Oh, H. Inui, M. Misaki, and M. Yamaguchi, "Environmental Effects on the Room Temperature Ductility of PST Crystals of TiAl," *Acta Metall. Mater.* **41** (1993), 1939-1949.
21. M. H. Yoo, "Time-Dependent Stress Concentration and Microcrack Nucleation in TiAl," *Int. Symp. on Gamma Titanium Aluminides*, ed. Y.-W. Kim, R. Wagner, and M. Yamaguchi, (TMS Symp. Proc., Warrendale, PA, 1995), 259-266.
22. D. M. Dimiduk, Y. Sun, and P. M. Hazzledine, "Interfacial Structure and Lattice Mismatch in Lamellar TiAl Alloys," High-Temperature Ordered Intermetallic Alloys VI, ed. J. H. Horton, I. Baker, S. Hanada, R. D. Noebe, and D. S. Schwartz, (MRS Symp. Proc. Vol. 364, Pittsburgh, PA, 1995), 599-604.
23. Y. S. Yang and S. K. Wu, "Orientation Faults of γ Lamellae in a Ti-40%Al Alloys," *Scr. Metall. Mater.* **25** (1991), 255-260.
24. F. Appel, P. A. Beaven, and R. Wagner, "Deformation Processes related to Interfacial Boundaries in Two-Phase γ -Titanium Aluminides," *Acta Metall. Mater.* **41** (1993), 1721-1732.
25. P. M. Hazzledine and B. K. Kad, "Yield and Fracture of Lamellar γ/α_2 TiAl Alloys," *Mater. Sci. Eng. A* **192/193** (1995), 340-346.
26. J. W. Lee, S. Hanada, and M. H. Yoo, "Deformation Twinning in Non-Stoichiometric Ti_3Al Alloys," *Scr. Metall. Mater.* **33** (1995), 509-514.

Note: Recently, after the completion of this manuscript, the authors learned of the experimental results by Kad and Asaro (unpublished research, University of California, San Diego) on deformation inhomogeneities in PST-TiAl crystals. They observed γ/γ interface sliding in PST-TiAl deformed in compression at room temperature by means of offset displacement of the fiducial lines. In addition to this evidence of coarse slip parallel to the laminates, localized at the γ/γ and/or α_2/γ interfaces, they also observed transition from the coarse slip to mode II cracking parallel to lamellar interfaces, and then to mixed mode (I+II) across the interfaces. These experimental findings are entirely consistent with the present results predicting inhomogeneous slip along the lamellar interfaces (60° pseudo-twin and 120° rotational γ/γ , and α_2/γ) and translamellar crack nucleation due to a pileup of soft mode ordinary dislocations.

CONSTITUTIVE RELATIONSHIPS OF PLASTICITY AND TEXTURE DEVELOPMENT

H. Mecking

Materials Physics and Technology, Technical University Hamburg-Harburg
21071 Hamburg, Eissendorfer Str. 42, Germany

Abstract

Conventional models of plastic flow in polycrystals are based on the assumption, that every grain deforms homogeneously and thus can be characterized by a single crystallographic orientation. Under these circumstances the conditions of material continuity and stress equilibrium across the grain boundaries cannot be fulfilled simultaneously. The compromises introduced by the different models and their implications for the fluctuation of internal stresses set up between grains as well as for the strain fluctuations from grain to grain will be discussed. The validity range of the various models is strongly influenced by the topography of the single-crystal yield-surfaces of the constituent phases as will be exemplified for the case of intermetallic γ -TiAl. Needs for finite element simulations will be given and it will also be shown, to what extent FEM results can be utilized for the adaption of the parameters of grain interaction in continuous models and for the description of strain inhomogeneities and structure evolution within individual grains.

Work supported by DFG in the special research program „Micromechanics of Multiphase Materials (SFB 371)“.

Introductory Remarks

This paper is a discussion of the present state of understanding and modeling of plastic flow in crystalline aggregates and is a summary of our recent publications in this area. Here only a short outline of the general aspects of this work will be presented. For details the reader is referred to the original papers [1-4] where also comprehensive reference lists are given.

For ductile polycrystals a proper description of plastic deformation has to consider the following two facts:

- Material continuity is generally observed in the whole sample-volume up to strain levels which are by orders of magnitude larger than the elastic strains.
- General mechanical principles require stress equilibrium everywhere, in particular across grain boundaries.

By assuming unique behavior in a grain volume i.e. by assuming no stress and no strain variation within an individual grain both of the above requirements cannot be fulfilled simultaneously so that simplifications have to be made. The following is an assessment of the capability of different approaches and a discussion of general conclusions based on FEM results.

Crystallites in a homogeneous environment

By far the most successful and most extensively applied approach for modeling plastic flow in polycrystals is the Taylor model. It is based on the straight-forward assumption that compatibility is the ruling principle and that this is achieved by an unique plastic strain being the same in all grains of a sample. The crystallographic nature of the material then demands that the prescribed strain is achieved by polyslip on possible slips systems in such a way that the sum of shears is minimized, individually in each grain according to its specific orientation.

Bishop and Hill have shown that this minimum shear criterion is identical with the validity of the Schmid law and they have defined the stress states which in each grain activate the demanded polyslip. It has been shown by various authors that the Bishop-Hill stress-states build up when the elastic interaction stresses are determined for a crystalline inclusion in a homogeneous medium with the average properties of the polycrystalline aggregate according to Kröner's equation.

$$\sigma_v - \Sigma_v = \sum_{\varphi} G_{v\varphi} (\epsilon_{\varphi} - E_{\varphi}) \quad (1)$$

Here σ_v and ϵ_{φ} are the local values of the stresses and strain components while Σ_v and E_{φ} are the average values and $G_{v\varphi}$ is the corresponding matrix of elastic constants.

In the framework of this approach a Taylor factor M is commonly defined which links the macroscopic quantities with the atomistic parameters by $\sigma = M\tau^s$ and $\delta\Gamma = M\delta\epsilon$. τ^s is the CRSS of the active systems in a crystallite and $\delta\Gamma$ is the average sum of their individual shear contributions. The necessary requirement for these simple relationships, with only a single

factor M , to apply is that the CRSS τ^* is the same for all active deformation systems. In cases where various physically different systems are involved, one may define two separate Taylor factors, M_σ and M_ϵ , by

$$\sum_s \delta\gamma^s \equiv \delta\Gamma = M_\epsilon \delta\epsilon \quad (2)$$

where $d\Gamma$ is the average sum of shear increments and

$$\sigma = M_\sigma \tau_{\text{ref}} \quad (3)$$

where the standard strength τ_{ref} is defined as the strength of a reference slip system, which can be chosen arbitrarily [3].

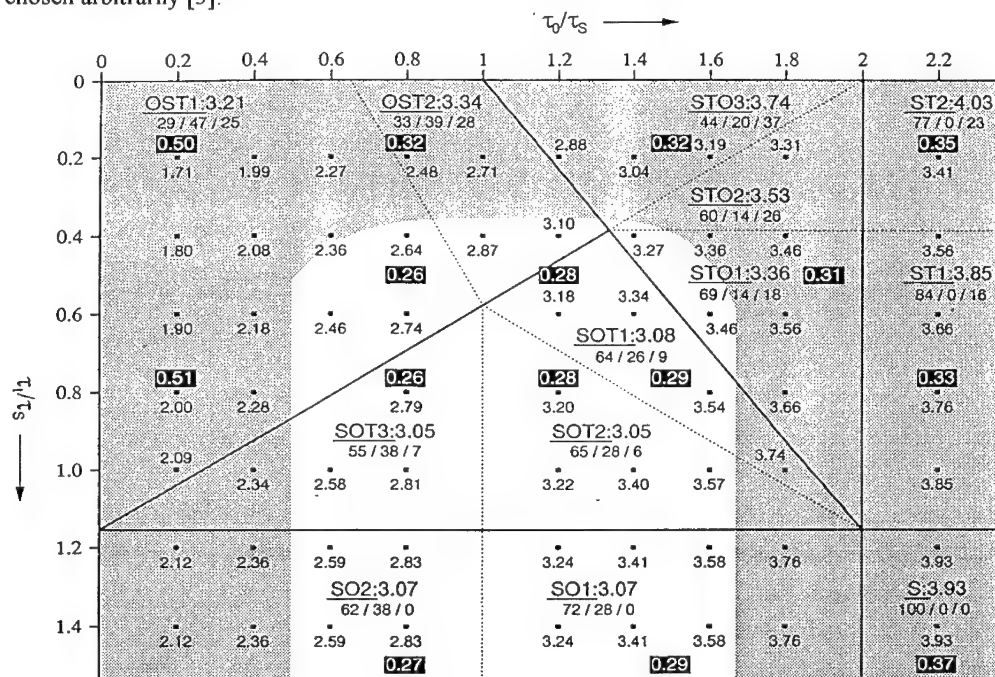


Figure 1: Deformation mode map for TiAl [3]. Parameters as derived by the Taylor model for the deformation of polycrystals with random orientation distribution. For each regime of the deformation mode map the Taylor factor M_ϵ is constant and is given together with the slip distribution (always in the order $\delta\gamma_s > \delta\gamma_o > \delta\gamma_i$) among super-, ordinary- and twinning-systems which is also constant for each regime. The notation of each field relates to the slip activities in the order of the amount contributed by each system (e.g. OST means that $\delta\gamma_o > \delta\gamma_s > \delta\gamma_i$). The stress related quantities vary continuously in each regime. The value of the Taylor factor M_σ is given for each point of a 0.2 by 0.2 grid of the coordinate system by characters in a dark frame. The average internal stresses between grains are given for some points as standard deviations in fractions of the applied stress. The white area is the validity range of the Taylor model where the standard deviation is below 0.3.

TiAl can serve as an example of a case where different slip modes can be activated, namely twinning-shear, shear by slip of ordinary dislocation and of superdislocations i.e. the slip systems $(111)[11\bar{2}]$, $(111)(110)$ and $(111)(101)$ resp.. Under these conditions a suitable choice for τ_{ref} is the critical resolved shear stress of superdislocations since this mode always has to be activated in order to provide 5 independent slip systems.

Figure 1 is a deformation mode map for TiAl in the coordinate system of the relative strength of the twinning system τ_t/τ_s and the ordinary system τ_o/τ_s . Notations and numbers are inserted referring to specific quantities which were derived with the help of the Taylor theory for deformation in uniaxial compression of a polycrystal with random texture. The notation is chosen so as to reflect the slip distribution among the three slip modes: OST, if the relative contribution is in the sequence ordinary, super-slip and twinning or STO: when the sequence is super-slip, twin, and ordinary slip a.s.o. For a regime where a mode does not contribute like ST where ordinary slip is not activated or S if neither ordinary slip nor twinning occurs. Regimes with equal sequence of slip distribution are additionally numbered like STO1, STO2, etc..

The factor M_σ is listed right after the regime identifier. Note that M_σ is a constant for each regime and, interestingly, is always close to 3 except for the extreme cases when deformation would be exclusively carried by superdislocations and twins.

While all the above strain related quantities are characteristics of the general topography of the single crystal yield surface and thus are constants for each regime (in the limit of rate independency, i.e. of athermal flow), the stress related values change strongly since they are affected additionally by the size of the yield surface. Therefore in Fig. 1 the values of M_σ are plotted in a 0.2 by 0.2 grid. Also for some points in the diagram the standard deviation of the stress components in the crystallites are given in units of the average stress. These deviations are a reliable measure of the limits of confidence for applicability of the Taylor-Bishop-Hill theory of polycrystal deformation and these limits are marked in Fig. 1 by the white area where the standard deviation stays below 0.3. It is seen that the validity range expands into practically all regimes of the deformation mode map except for the ST- and S-area where ordinary dislocations are not active.

This example has been chosen in order to demonstrate that the Taylor model provides an excellent basis for interpretation of polycrystal deformation on grounds of crystallographic deformations modes and their critical resolved shear stresses.

The Taylor model however is only applicable when the stress states in the individual crystallites do not deviate to strongly from the average value which however is the case if the single crystal yield surface is very anisotropic (hatched area in Fig. 1) or in multiple phase materials.

In these cases viscoplastic models with adequately adapted parameters for the grain interaction may be successfully employed. The interaction equation of a grain with the average in environment reads now.

$$\sigma_v - \Sigma_v = \sum_{\varphi} A_{v\varphi} (\dot{\epsilon}_{\varphi} - \dot{\bar{\epsilon}}) \quad (4)$$

$A_{v\varphi}$ follows from a selfconsistent interaction scheme and comparison of experimental results with theoretical predictions [1] show that the interaction is grossly underestimated in numerical treatments on the basis of equation (4). An adaption of this promising approach is in progress

which is expected to lead to realistic interaction forces between the microstructural elements of a material.

Crystallites in an individual environment

Efforts that combine finite element methods with crystal plasticity models have been applied either on a grain scale (to each mesh point the properties of a different crystallite are ascribed) or below this scale (to address gradients in the deformation field of individual grains). In the latter case also strain gradients occurring in the crystallites can be investigated. Fig. 2 is the result of such a calculation for a very specific arrangement of grains namely 8 grains of the 4 equivalent positions of the S-orientation which were arranged such that the sample had the same symmetry as the strain tensor in plane strain compression. The differently shaded areas reflect the orientation distribution which developed in a crystallite at 82 % thickness reduction.

In the crystals narrow bands of strong orientation gradients occur. These are assumed to present preferred sites for recrystallization nuclei to form upon annealing and the orientations typically spread towards the cube position in these bands.

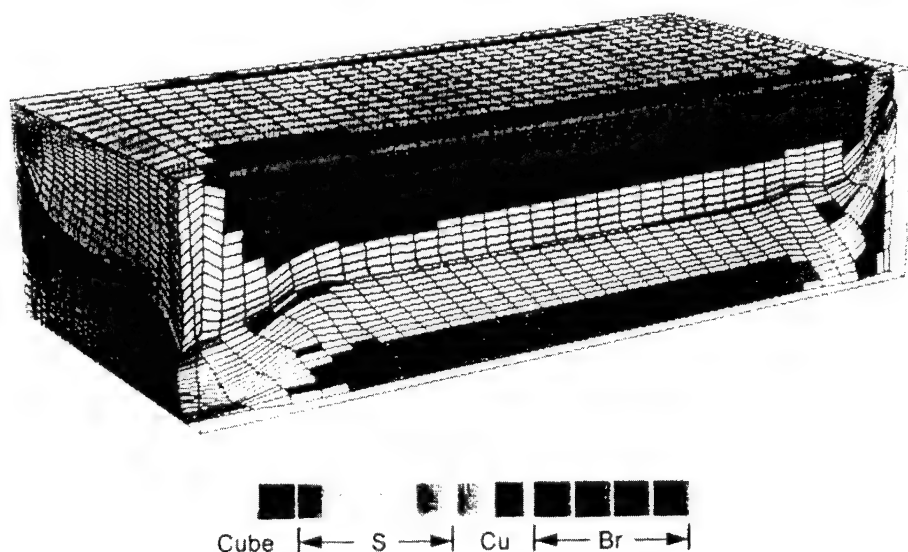


Figure 2:
Orientation distribution in two grains of the S-array (8 grains of the position $\{123\} \langle 634 \rangle$) after 82 % thickness reduction in plane strain. Image is scaled by a factor of 30 in the thickness direction [2].

Another important consequence of this investigation for the general problem of polycrystal deformation is following:

The conventional view is that each orientation after deformation is unambiguously linked to its initial orientation. Of course, the track of an orientation may be influenced also by the grain's environment, so a more adequate picture might be that an initial orientation ends up in an area around the main orientation.

This concept may have to be fundamentally changed in view of the results exhibited in Fig. 2. Although calculations were performed only for one specific position of the rolling texture, i.e. the four equivalent orientations of the S position $\{123\}\langle 634\rangle$, an orientation spread occurred along the whole skeleton line of the texture. Thus, the main characteristics of the texture of a polycrystalline aggregate developed in the volume of a single crystallite. This spread would certainly change by changing boundary conditions according to a different local environment of a grain. These findings suggest that during deformation a grain develops a microtexture which becomes more and more dictated by the environment of the grain volume, i.e. by the overall texture, so that, as deformation proceeds, the grains lose identity in that the memory of their origin fades continuously. If this should be a general phenomenon, it bears on the general interpretation of the evolution of microstructure during deformation: evolution becomes rather insensitive to the details of the initial microstructure such as grain size and grain shape and is basically controlled by the overall texture as a characteristic of the average environment.

Literature

- [1] D. Dunst and H. Mecking
Simulation of Rolling Textures of Two-Phase ($\alpha + \beta$)-Titanium Alloys
Z. Metallkunde, June 1996 (in press)
- [2] A. J. Beaudoin, Jr., H. Mecking and U. F. Kocks
Development of Localized Orientation Gradients in FCC Polycrystals,
submitted to Phil. Mag. 1996
- [3] H. Mecking and U. F. Kocks
Deformation Modes in γ -TiAl as Derived from the Single Crystal Yield Surface,
Acta , mater. 44, 1309, 1996
- [4] H. Mecking, U. F. Kocks and Ch. Hartig
Taylor Factors in Materials with Many Deformation Modes,
Scripta Met. in press 1996

**ADVANCED METALLICS,
SUPERALLOYS**

UNIQUE SINGLE CRYSTAL SUPERALLOYS
FOR INDUSTRIAL GAS TURBINE APPLICATION

G. L. Erickson
Cannon-Muskegon Corporation
(a subsidiary of SPS Technologies)
P.O. Box 506
Muskegon, MI 49443-0506 U.S.A.

Abstract

Two different, non-Re containing single crystal (SX) superalloys are defined primarily for industrial turbine application. The alloys, CMSX®-11B and CMSX®-11C, contain respective chromium levels of about 12.5% and 14.5%. Both materials develop unique and extremely good blends of hot corrosion and oxidation resistance. They exhibit extremely good castability, employ relatively simple solution heat treatments and provide creep strength which is as good or better in comparison to other first generation SX materials such as CMSX-2/3, PWA 1480 and René N4. Moreover, at certain engine-pertinent temperature/stress conditions, and particularly in long-term tests, the alloys appear to exhibit density corrected strengths which are similar or better than CMSX-4® and other second generation SX casting superalloys.

CM 247 LC®, CM 186 LC®, CMSX-2®, CMSX-3®, CMSX-4®, CMSX-6®, CMSX®-10,
CMSX®-11B AND CMSX®-11C
are registered trademarks of the Cannon-Muskegon Corporation.

Introduction

The land-based, combustion turbine industry is experiencing tremendous growth, in part due to public utility commission rulings and environmental considerations. Prevailing rulings appear inconsistent with the long term, high capital expenditure associated with coal and nuclear power projects, thereby making the utility industry increasingly reliant on combustion turbine technology for its power generation requirements.

Forecast International predicts that 9,958 industrial and marine gas turbine units will be manufactured during the 1994-2003 period. This represents about 7.9% of the total combustion turbine engine market predicted during the period, and is expected to result in an approximate 550 GW electric power capacity expansion being realized throughout the world (1). See Table I.

Table I Anticipated Electric Power Capacity Additions (GW)
Occurring During the Period 1994-2003 (1).

	FI*	UDI**
Asia/Pacific	245 - 266	249
Europe (inc CIS)	90 - 98	113
North America	95 - 100	94
Central/South America	50 - 58	51
Middle East & Africa	42 - 44	40

* Forecast International, 1994-2003
** Utility Data Institute, 1993-2002

Of the anticipated power capacity increase, a significant portion of the turbines manufactured will utilize fossil fuels (Figure 1). Additionally, the new industrial and marine gas turbines are expected to be sized as indicated in Figure 2.

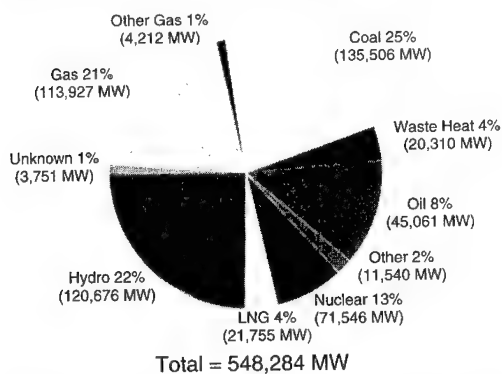


Figure 1 - Worldwide electric power generating capacity additions predicted for the period 1994-2003. Data presented on the basis of fuel type employed (1).

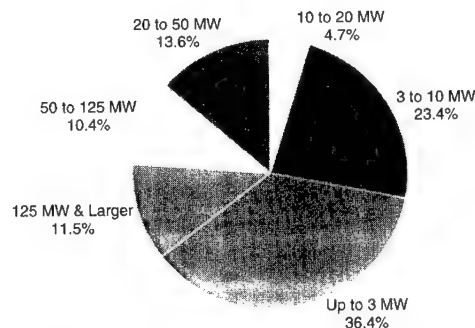


Figure 2 - Anticipated world gas turbine industry power generation machine market for period 1994-2003. Data presented in terms of production by power class (1).

Complementary to the Forecast International predictions, the General Electric Company forecasts that base-load electric power generation combustion turbines (CT) and combined cycle (CC) plants will account for about 45% of the new global orders and 66% of the new orders placed in the United States through the year 2001 (2). Advances in turbine design, materials, cooling technology and coatings have helped develop this market. Current advanced combustion turbines

typically achieve more than 35% efficiency in the simple cycle mode and greater than 50% efficiency in the combined cycle mode. For example, the recent definition of its new gas turbine machine characteristics by Asea Brown Boveri (ABB) reveals that a simple cycle efficiency of 37.8% and combined cycle efficiency of 58.5% are anticipated for their GT 26 model; this being achieved through increasing power density and mass flow by doubling the pressure ratio (up from 15.0 in the GT 13E2 to 30.0) combined with sequential combustion at a relatively low maximum firing temperature (3).

And still another industry giant, Siemens, appears to rely on a more moderate increase to engine pressure ratio (eg., 16.0 for the Siemens V84.3 model versus 10.8 in its V84.2 machine) albeit in tandem with increased firing temperature, mass flow, compressor and turbine efficiencies. It's reported that the V84.3 firing temperature is expected to be 1310°C (2350°F) in contrast to the model V84.2 at 1120°C (2050°F). Furthermore, vane cooling increases from three to four stages while blade cooling is similarly increased from two to three stages (4). Further design improvements incorporated in the Siemens V84.3A engine are reported to allow an additional increase to firing temperature of about 22°C (40°F) while continuing to maintain acceptable NOx level (5).

In order to achieve these increased firing temperatures which result in thermal efficiency improvement, large industrial turbine designers are beginning to utilize higher technology materials in their respective engine hot sections than previously applied. Where alloys such as IN 738 LC and IN 939 were previously employed, the search for greater engine efficiency has led the industrial turbine community to adopt technologies which have already been commercially applied within the aero-turbine and small industrial engine community, eg., directionally solidified columnar grain and single crystal components, serpentine and film cooling designs, as well as certain advanced coatings technology. While Siemens is apparently the first large frame turbine producer to announce the usage of SX components within their new turbines (6), it is also accepted that most other large turbine producers have designed SX components into their new products.

Complementary to the internal engine company R&D efforts toward improving industrial turbine efficiencies, industry collaborative programs targeted toward developing and commercializing ultra-high efficiency, environmentally superior, cost-competitive gas turbine systems for base-load applications [with a 1427°C (2600 °F) or greater firing temperature] such as the U.S. Department of Energy (DOE) Advanced Turbine Systems (ATS) Program (7) are extremely active. While the ATS Program continues on target toward achieving the goals of greater than 60% net efficiency for utility scale combined cycles and a 15% jump in efficiency for small industrial machines (8), similarly aimed activities of the Collaborative Advanced Gas Turbine (CAGT) Program encompassing joint efforts between 17 parties in North America and Europe (9) further complement the the efforts of the COST program in Europe and the DOE sponsored ATS program.

To similar end, this narrative reports on the development of two single crystal casting alloys exhibiting characteristics which are hoped attractive to the industrial turbine community. Specifically, both alloys provide 738 LC - type hot corrosion resistance in tandem with CM 186 LC level oxidation resistance. The alloys' capability to exhibit good hot corrosion resistance concurrent to providing extremely good oxidation resistance is thought unique in the industry, as most alloys exhibit only one or the other. Combined with this positive characteristic, the alloys exhibit extremely good castability (in small or large components), are able to be solution heat treated in a relatively short period and provide extremely good creep-rupture strength. In certain engine-significant temperature/stress conditions, the alloys exhibit creep-strength, on a density-

corrected basis, which is similar to second generation Re-containing alloys such as CMSX-4 and PWA 1484. Furthermore, the alloys appear to exhibit greater long-term rupture strength than CMSX-4 alloy. Moreover, since the alloys do not contain Re, they are at least 50% cheaper per pound of alloy purchased, in comparison to 3 wt.% Re-containing alloys.

Alloy Design

Industrial gas turbine engines have historically operated in temperature/pressure regime where Type II hot corrosion attack was the dominating environmental issue (Fig. 3). However, as the industry has sought to improve engine efficiency, engine firing temperatures have generally increased, thereby creating need for materials more able to endure exposures where a blending of Type I hot corrosion and oxidation predominates.

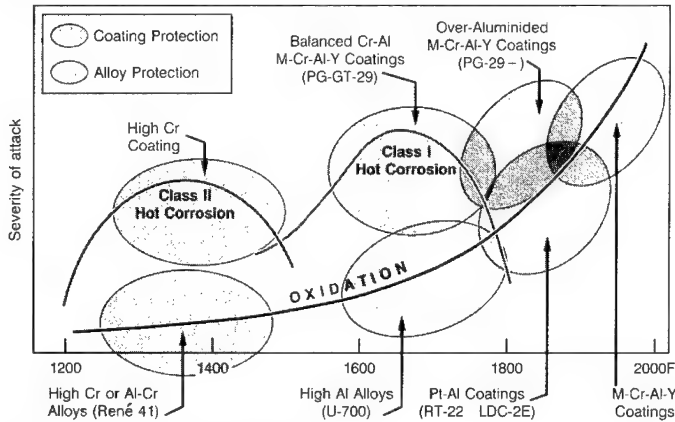


Figure 3 - The Protection Scene (10).

To best achieve the perceived environmental need, moderate alloy chromium levels must be utilized in an alloy's design. As it appears that each turbine producer requires different blends of hot corrosion/oxidation/strength characteristic, two different chromium levels were used as starting points for the CMSX-11B (12.5%) and CMSX-11C (14.5%) alloy designs.

Along with relatively high chromium contributing to alloy environmental properties, other considerations applied to the designs include the selection of low molybdenum level, moderate Ta and elevated Ti: Al ratio. Relatively high Al+Ti levels are employed, which in tandem with moderate alloy Ta level, helps provide the high strength achieved.

Similarly, the alloy systems employ moderate tungsten levels for solid solution strengthening, however, the alloys also engage Ta: W ratios greater than unity to assist with SX component castability. Partly necessitated by the relatively high chromium levels employed, and the desired levels of W + Ta content, alloy cobalt levels are set relatively low to ensure adequate microstructural stability.

An overview of these alloy design considerations are provided in Figure 4, while more specific chemistry detail is provided in Table II, where the CMSX-11B and CMSX-11C alloy nominal compositions are compared to other first, second and third generation SX superalloys which have gained some commercial significance, albeit mostly in aero-turbine application. Note that the CMSX-11 derivatives do not rely on Re additions for strength attainment and that the alloys may,

therefore, exhibit more desirable long-term lives and utility in certain components due to their inherently lower tendency for phasial instability in the temperature regime where Re containing alloys tend to form Topologically-Close-Packed (TCP) phase.

The CMSX-11 alloy derivatives are moderate density materials due to their high chromium and Al+Ti levels. The density of CMSX-11B is 8.44 kg/dm³ while it is 8.36 kg/dm³ for CMSX-11C; this in comparison to CMSX-3 at 8.56 kg/dm³, CMSX-4 at 8.70 kg/dm³ and CMSX-10 at 9.05 kg/dm³.

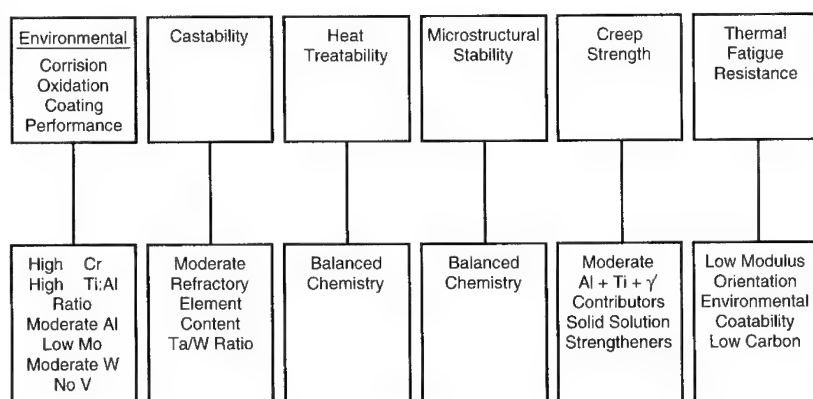


Figure 4 - Alloy design criteria.

Table II Nominal Compositions of Three Generations of Single-Crystal Superalloys (Wt%)

Alloy	Cr	Co	Mo	W	Ta	Re	V	Nb	Al	Ti	Hf	Ni	Density (kg/dm ³)	Ref.
First Generation														
PWA 1480	10	5	—	4	12	—	—	—	5.0	1.5	—	Bal.	8.70	11
PWA 1483	12.8	9	1.9	3.8	4	—	—	—	3.6	4.0	—	Bal.	—	32
René N4	9	8	2	6	4	—	—	0.5	3.7	4.2	—	Bal.	8.56	12, 13
SRR 99	8	5	—	10	3	—	—	—	5.5	2.2	—	Bal.	8.56	14, 15
RR 2000	10	15	3	—	—	—	1	—	5.5	4.0	—	Bal.	7.87	14, 15
AM1	8	6	2	6	9	—	—	—	5.2	1.2	—	Bal.	8.59	16
AM3	8	6	2	5	4	—	—	—	6.0	2.0	—	Bal.	8.25	17
CMSX-2®	8	5	0.6	8	6	—	—	—	5.6	1.0	—	Bal.	8.56	18
CMSX-3®	8	5	0.6	8	6	—	—	—	5.6	1.0	0.1	Bal.	8.56	18
CMSX-6®	10	5	3	—	2	—	—	—	4.8	4.7	0.1	Bal.	7.98	19
AF 56 (SX 792)	12	8	2	4	5	—	—	—	3.4	4.2	—	Bal.	8.25	20
SC 16	16	—	3	—	3.5	—	—	—	3.5	3.5	—	Bal.	8.21	21
CMSX®-11B	12.5	7	0.5	5	5	—	—	0.1	3.6	4.2	0.04	Bal.	8.44	22
CMSX®-11C	14.9	3	0.4	4.5	5	—	—	0.1	3.4	4.2	0.04	Bal.	8.36	23
Second Generation														
CMSX-4®	6.5	9	0.6	6	6.5	3	—	—	5.6	1.0	0.1	Bal.	8.70	24
PWA 1484	5	10	2	6	9	3	—	—	5.6	—	0.1	Bal.	8.95	25
SC 180	5	10	2	5	8.5	3	—	—	5.2	1.0	0.1	Bal.	8.84	26
MC2	8	5	2	8	6	—	—	—	5.0	1.5	—	Bal.	8.63	27
René N5	7	8	2	5	7	3	—	—	6.2	—	0.2	Bal.	NA	28
Third Generation														
CMSX®-10	2	3	.4	5	8	6	—	.1	5.7	.2	.03	Bal.	9.05	29
René N6	4.2	12.5	1.4	6	7.2	5.4	—	—	5.75	—	.15	Bal.	8.98	30

Alloy Manufacture

The CMSX-11B and CMSX-11C alloys are VIM produced according to the process consideration detailed in Reference 31. Due to the relatively high alloy chromium contents employed, judicious Cr raw material selection is required to achieve the low levels of residual sulfur and phosphorus desired in the alloy product. Similarly, since low master alloy gas contents are always preferred, and high chromium and titanium containing alloys notoriously exhibit higher residual nitrogen

levels, careful raw material selection in tandem with proper VIM procedure development are paramount to quality attainment.

Approximately twenty developmental 136 kg. heats have been produced through the development process. Consistency of major element heat chemistries are easily achieved, and typical tramp element levels prevailing in the CMSX-11 derivatives are illustrated in Table III. The levels achieved, except for gas content, are typical of those predominating in other SX alloys, such as CMSX-4 and CMSX-10. The abnormally high level of nitrogen in the CMSX-11 derivatives (4 ppm vs. 1 ppm) is a function of alloy chromium content, while the 4 ppm oxygen level (vs. 1 ppm in other CM product) is thought attributable to the alloys' relatively high Ti content. Although the developmental heat gas contents are higher than the other CM experience, they nonetheless have not adversely affected SX casting yields when measured in terms of defect formation tendency and/or non-metallic inclusion content. Furthermore, production alloy manufacture will likely provide improvement to each characteristic.

Table III Typical Tramp Element Levels in Development Heats of the CMSX-11B and CMSX-11C Alloys

Alloy	Element/Concentration						
	C ppm	B ppm	Zr ppm	S ppm	N ppm	O ppm	Si wt. %
CMSX®-11B	20	<20	<10	1	4	4	<.01
CMSX®-11C	20	<20	<10	1	4	4	<.01

Foundry and Heat Treatment Characteristics

Through February 1996, the CMSX-11B and CMSX-11C alloys have been cast successfully in six investment casting foundries located throughout the world. Items cast include test bars to 26 mm diameter, test slabs of varying size, plus both aero-turbine and industrial turbine blade components. Better than forty investment cast molds have been produced.

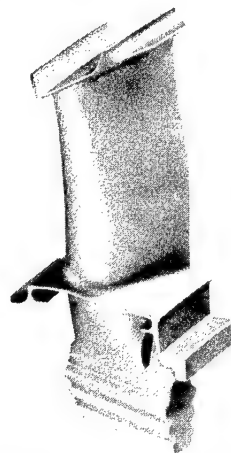
Through this experience, it is clear that both CMSX-11 alloy derivatives provide excellent SX castability. The alloys are not prone to formation of SX process defects such as freckles, slivers, high or low angle boundaries and/or stray grain formation. High production product yields are anticipated since every developmental mold produced has output nearly 100% satisfactory product. Moreover, no cleanliness problems, as measured through zygo dye penetrant inspection and metallographic observation, have been experienced. An example of one of the test casting configurations utilized in the development is provided in Figure 5. The industrial turbine blade test configurations are considerably larger, with heavy platform/root-section blades to about 250mm length being successfully cast.

The test articles and components produced are solution heat treated and given a three step aging treatment. Slightly different peak solution heat treatment temperatures are employed for the CMSX-11B and CMSX-11C alloys. Both treatments, however, can be accomplished in 10 hours or less. Primary aging (pseudo coating treatment aging) is undertaken at 1121°C/5 Hr./AC condition for both alloys. Similarly, both alloys are further aged at 871°C/24 Hrs./AC + 760°C/30 Hrs./ AC condition.

The typical CMSX-11B and CMSX-11C fully heat treated microstructures are illustrated in Figures 6 and 7, as well as the specific respective solution heat treatments currently utilized. The

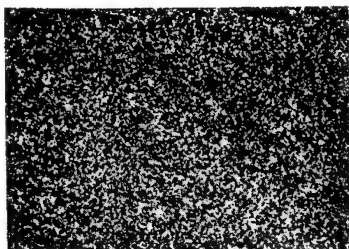
respective solution heat treatments effect nearly 100% γ' and eutectic γ - γ' dissolution, while the primary aging treatments result in γ' growth and arrangement into fairly regularly aligned, cubic γ' precipitates of about 0.4 - 0.5 μm edge dimension. The secondary and tertiary aging treatments, as shown in Figure 8 for CMSX-11B, tend to promote the formation of relatively fine matrix channel γ' precipitates which likely enhance strength in blade root sections, since root section temperature exposures are generally lower than 760°C.

Figure 5 - One of the several turbine blade configurations used to characterize the CMSX-11B and CMSX-11C alloy castability.

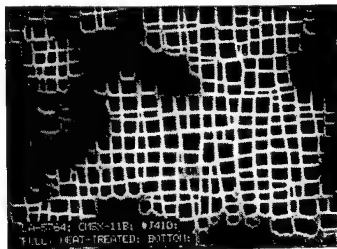


Allison AE 2100
2nd Stage Blade.

Solution: 1227°C/1 Hr.
+ 1249°C/1 Hr.
+ 1260°C/2 Hrs.
+ 1264°C/4 Hrs./AC.
Age: 1121°C/ 5 Hrs./AC.
871°C/24 Hrs./AC.
760°C/30 Hrs./AC.



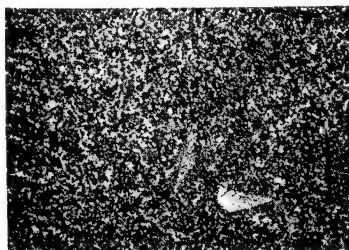
0.25 μm



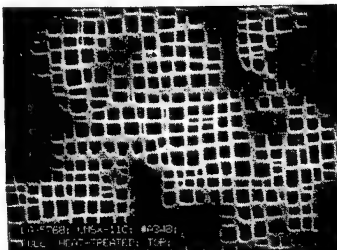
1 μm

Figure 6 - Two views of fully heat treated CMSX-11B alloy.

Solution: 1204°C/1 Hr.
+ 1227°C/1 Hr.
+ 1250°C/2 Hrs.
+ 1256°C/4 Hrs./AC.
Age: 1121°C/ 5 Hrs./AC.
871°C/24 Hrs./AC.
760°C/30 Hrs./AC.



0.25 μm



1 μm

Figure 7 - Two views of fully heat treated CMSX-11C alloy.

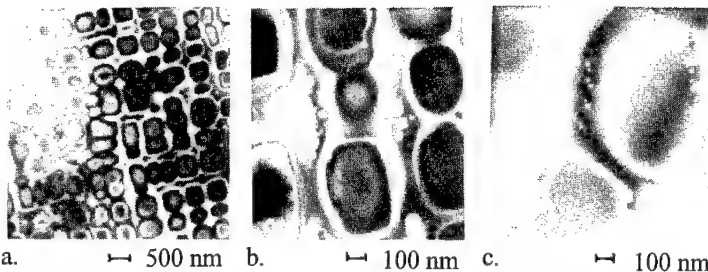


Figure 8 - The CMSX-11B alloy aged at (a) 1121°C, (b) 1121°C + 871°C, and (c) 1121°C + 871°C + 760°C.

Mechanical Properties

Fairly extensive creep-rupture tests with temperature ranging 760-1038°C confirms the CMSX-11B and CMSX-11C alloys develop impressive respective strength levels. Alloy strengths are at least as good as commercialized SX casting alloys such as CMSX-2/3, PWA 1480 and René N4, plus as good or better, in certain tests, than creep-rupture strengths typically exhibited by the second generation, 3 wt. % Re containing CMSX-4, PWA 1484 and René N5 alloys.

Figure 9 illustrates the typical CMSX-11B/11C alloy strength in comparison to the DS René 80 and equiaxed IN 939 alloys. For a running stress of about 138 MPa, the CMSX-11 derivatives exhibit about 92°C greater strength than IN 939. Also indicated are the 871°C and 982°C capabilities of the PWA 1483 alloy (32).

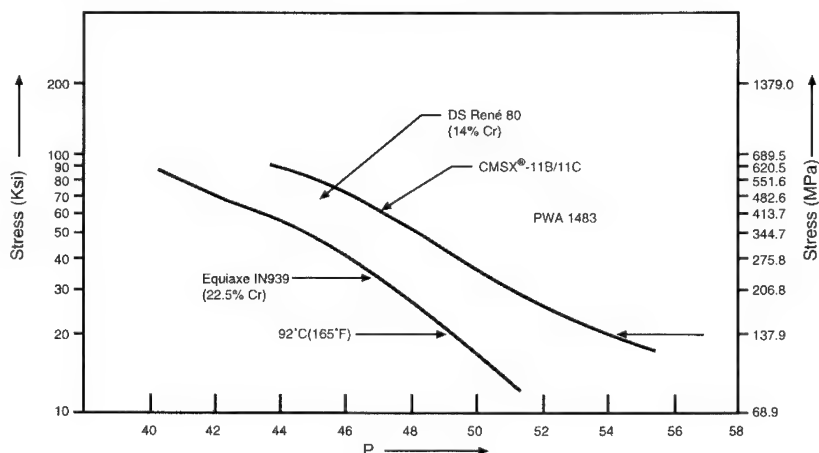


Figure 9 - Average longitudinal Larson-Miller stress-rupture strength of several alloys.

While Figure 9 compared the CMSX-11B/11C materials to IN 939, DS René 80 and PWA 1483, Figure 10 illustrates the materials' advantage over the SC 16 alloy, an IN 738 SX alloy derivative developed by ONERA for the European Community Collaborative COST program (21). At about 207 MPa stress, the SC 16 alloy deficit is about 44°C and at 138 MPa, approximately 64°C. If compared on the basis of 1% creep strength, the SC 16 alloy exhibits an even greater deficit. Others have shown the SC 16 creep strength to be similar to equiaxed IN 738 (33).

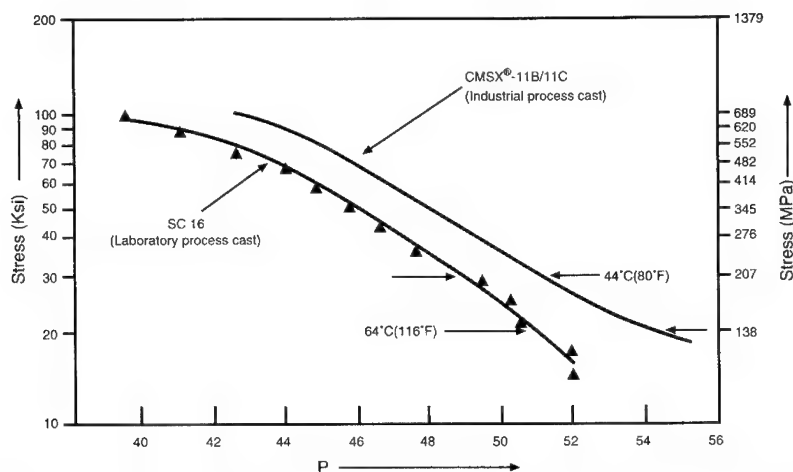


Figure 10 - Average longitudinal Larson-Miller stress-rupture strength of three alloys.

As illustrated in Table II, the densities of the CMSX-11B and CMSX-11C alloys are moderately low in comparison to other commercially utilized DS and SX casting alloys. Figure 11 illustrates the specific or density corrected strengths of several commercial alloys in comparison to the CMSX-11 materials. Perhaps of most significance, the CMSX-11B alloy's strength is shown to equal or exceed that of CMSX-4, while the higher Cr containing CMSX-11C alloy appears superior to CMSX-4 only at higher temperatures such as 982-1038°C.

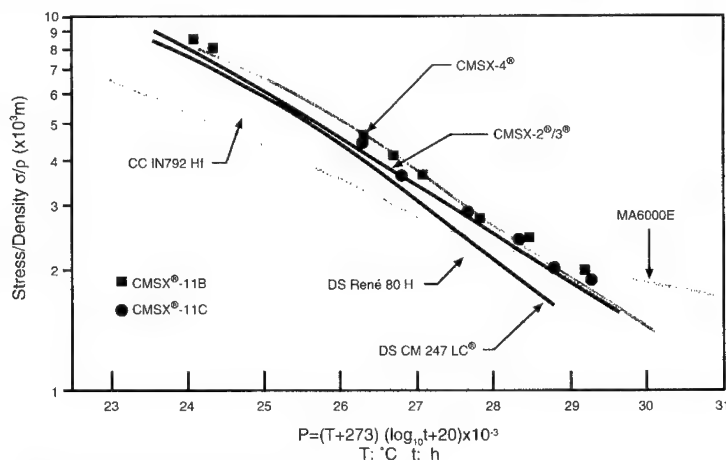


Figure 11 - Density corrected stress-rupture strength of several alloys.

Along this line, non-density-corrected log stress vs. log time rupture strength comparison of the IN 738 LC, DS CM 247 LC, CMSX-4 and CMSX-11B alloys at 982°C is shown in Figure 12. Interestingly, the non-Re containing CMSX-11B alloy is shown to exceed the CMSX-4 alloy's rupture strength for tests run to between 1500-2000 hours life. Although not shown, the CMSX-11B alloy 1% average creep strengths demonstrated in these tests were not quite as good as the averaged CMSX-4 capability, however, they did not lag significantly. Similarly, Figure 13 compares the log stress vs. log rupture life of CMSX-4 and CMSX-11B for tests performed at 1038°C (also without density correction), and illustrates a significant advantage occurring with CMSX-11B for a test run to about 3000 hours. As comparative CMSX-4 alloy creep data is not

available for the given test, future efforts will define the CMSX-4 alloy's creep-rupture characteristic, as well as expand the CMSX-11B data base in the 1038°C - 1100°C temperature regime.

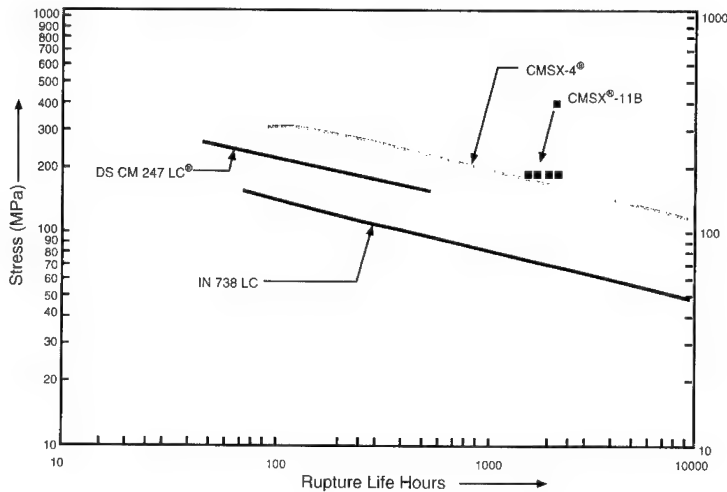


Figure 12 - 982°C stress-rupture strength of several alloys.

Figure 13 - 1038°C stress-rupture strength comparison of CMSX-11B and CMSX-4.

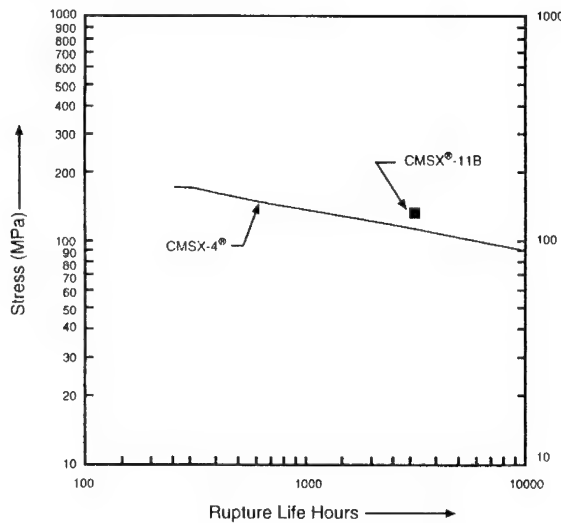


Figure 14 illustrates the CMSX-11B γ' structure for a specimen tested at 1010°C/103 MPa condition and which ruptured at 17,278.8 hours. Fracture and thread section views are presented, with both illustrating an absence of TCP phase. This absence of TCP is significant since Re-containing alloys generally form TCP under similar condition and exposure time. Interestingly, this individual rupture result is near the extrapolated life prediction which could be made for the CMSX-10 alloy tested at identical condition.

A review of superalloy 10,000 hour rupture strength capability, on the basis of alloy chromium content, is presented in Figure 15. While traditional superalloy experience suggests that higher alloy chromium levels are accompanied by lower alloy strength, the CMSX-11B and CMSX-11C materials are shown to exhibit uniquely high relative strengths for their 12.5 and 14.5% respective

Cr levels. Of particular significance is the positive strength comparison with the second generation, 3 wt. % Re containing superalloys such as PWA 1484 and CMSX-4. The data also illustrates that Re containing SX superalloys don't necessarily provide long-term rupture strength advantages since other non-Re containing SX alloys such as René N4, CMSX-2 and PWA 1480 apparently perform similarly for 10,000 hour rupture life at the 160 MPa stress level, as determined through 1000 to 3000 hour rupture data extrapolation undertaken by a collaborating gas turbine engine producer.

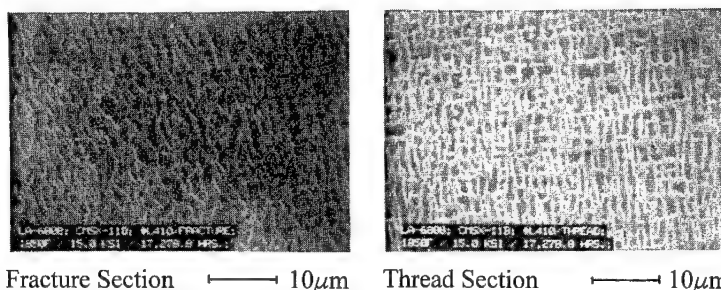


Figure 14 - Two post-test views of a CMSX-11B alloy specimen tested at 1010°C/103 MPa condition to rupture at 17,278.8 hrs.

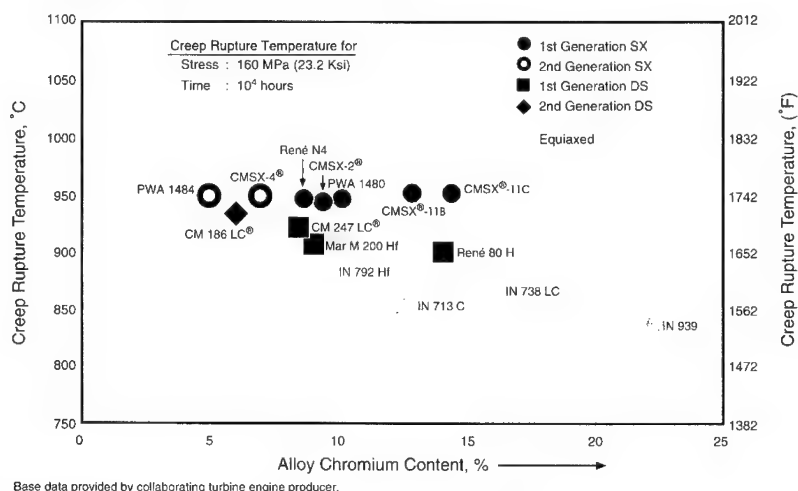


Figure 15 - 10,000 hour rupture strength of several alloys.

Environmental Properties

Environmental tests performed on superalloy materials often give rise to varied results, depending on methods employed and sources employed. In this investigation, four different turbine producers performed both hot corrosion and oxidation tests on the CMSX-11 alloy derivatives. The tests performed were undertaken by both burner rig and crucible evaluation methods, with the significance of the results comparing favorably between three of the four investigative sources, thereby lending credibility to the results achieved.

Figure 16 illustrates the derivative alloys' 500 hour hot corrosion characteristics determined in comparative crucible tests undertaken at 750°C, 850°C and 900°C. Similarly, Figures 17 and 18 present results of hot corrosion tests performed at 732°C and 899°C, with comparison to the IN

738 LC alloy capability. The results appear to confirm that the CMSX-11 materials behave similar to the IN 738 LC material with exposure at around 750°C, and that with long term exposure at about 900°C, the higher Cr containing derivative, CMSX-11C, exhibits an advantage vs. the CMSX-11B alloy, while continuing to perform as well as IN 738 LC to at least 2400 hours.

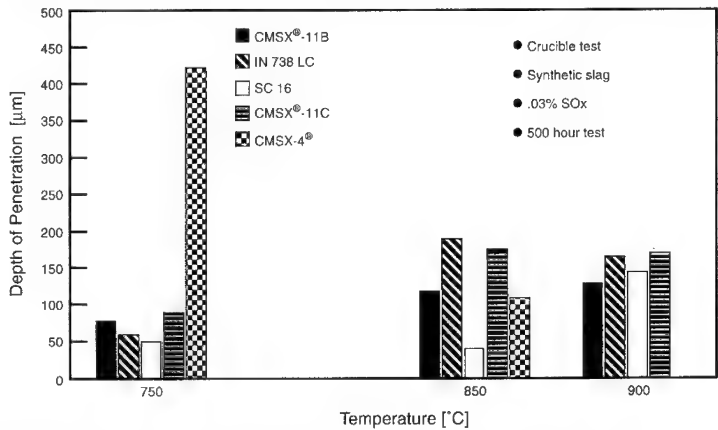


Figure 16 - Hot corrosion of various alloys at 750, 850 and 900°C.

Figure 17 -
732°C cyclic hot
corrosion of
several alloys.

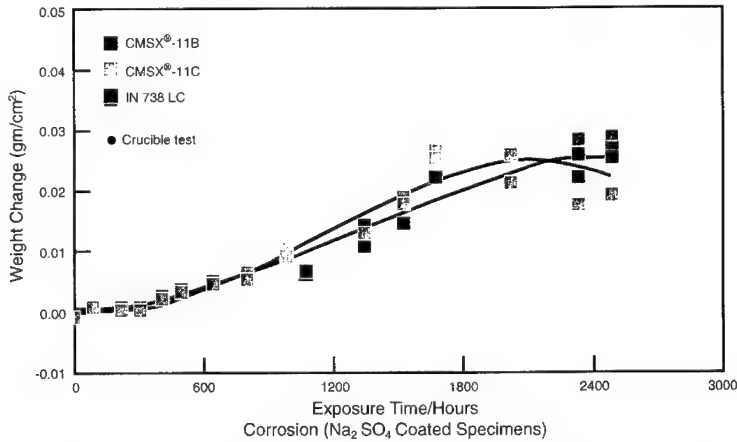
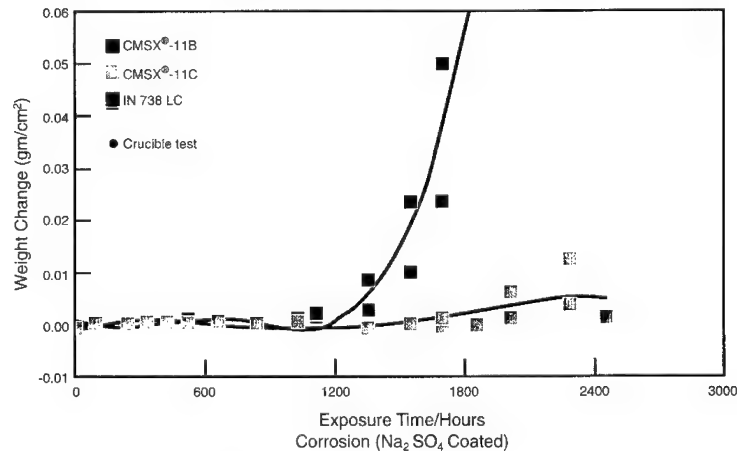
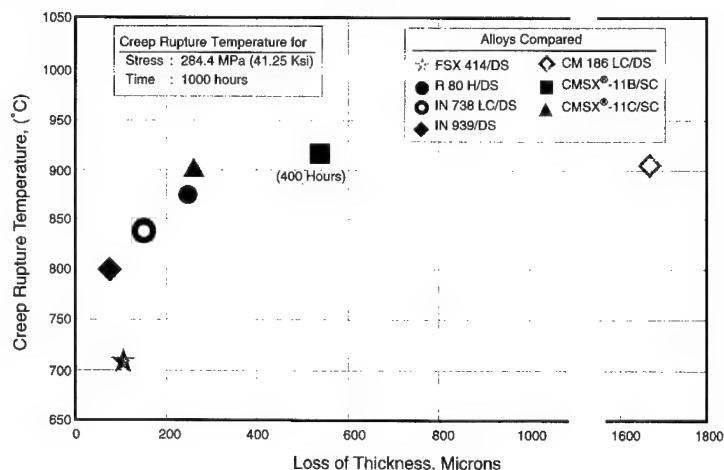


Figure 18 -
899°C cyclic hot
corrosion of
several alloys.



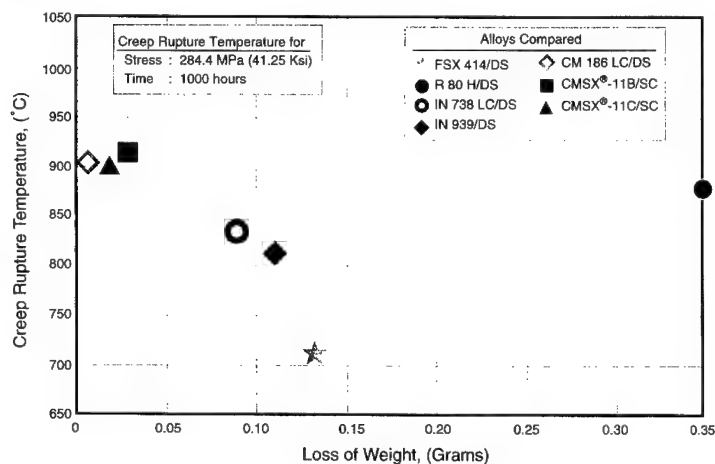
The results of extremely aggressive burner rig hot corrosion tests performed to 500 hour duration at 1050°C are shown in Figure 19. Hot corrosion results are presented through comparison to other widely used gas turbine alloys such as FSX-414, DS René 80 H, DS IN 738 LC, DS IN 939 and DS CM 186 LC. The actual corrosion results are presented in terms of test specimen thickness loss, while the respective material's strength capabilities are expressed on the figure's y-axis as creep-rupture temperature capabilities for 1000 hour lives with a testing stress of 284.4 MPa. For this testing, the figure illustrates that the CMSX-11C alloy develops DS René 80 - type hot corrosion resistance with an attendant 25°C strength advantage. The CMSX-11B alloy doesn't provide quite as good hot corrosion capability in the test, but is significantly better than the DS CM 186 LC alloy, a material also considered for some industrial turbine applications.

Figure 19 - Alloy strength and 1050°C/500 hour burner rig hot corrosion comparison of several alloys.



Burner rig oxidation test results are shown in Figure 20. The alloys compared (along with the result presentation methods employed) are identical to those presented in Figure 19. For this run at 1200°C and exposure of 500 hours, the CM 186 LC alloy is shown to exhibit the best alloy oxidation resistance, with the CMSX-11B and CMSX-11C materials behaving quite similarly; a unique capability for materials exhibiting IN 738/IN 792/ René 80 type corrosion resistance. To that point, Figure 20 also exhibits the reduced oxidation resistance of the René 80 and IN 738 LC alloys in comparison to CMSX-11.

Figure 20 - Alloy strength and 1200°C/500 hour burner rig oxidation comparison of several alloys.



Confirmation of the CMSX-11 oxidation characteristic is provided in Figure 21 where the results of a cyclic crucible test performed at 1000°C on the CMSX-11B, CMSX-11C and IN 738 LC alloys are presented. While the IN 738 LC alloy oxidation resistance is low, the two CMSX-11 alloy derivatives exhibit relatively good oxidation characteristic for the duration of the test, ie., 3000 hours. While not presented, the Figure 21 test data source has developed unpublished data at identical conditions for the PWA 1483 alloy which show it's capability appearing between the IN 738 LC and CMSX-11C test results. Similar oxidation testing undertaken at 1010°C at another turbine builder shows similar results for the CMSX-11 alloys, as illustrated in Figure 22.

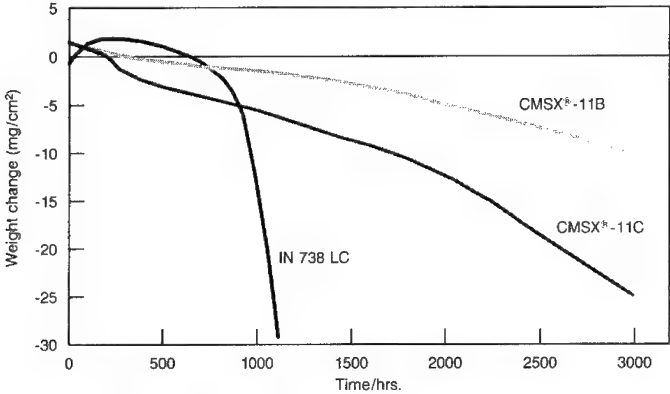


Figure 21 - 1000°C cyclic oxidation of three alloys.

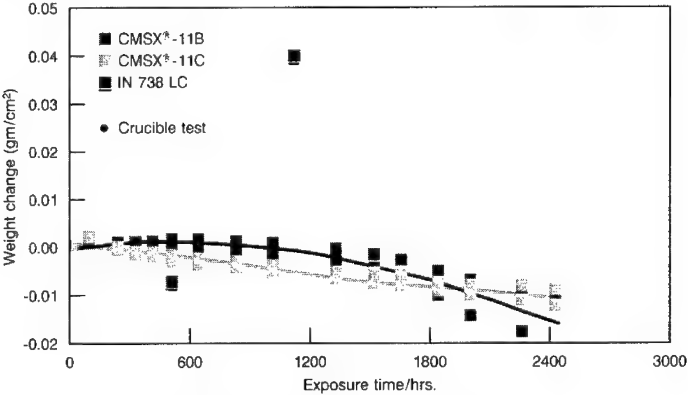


Figure 22 - 1010°C cyclic oxidation of three alloys.

The alloys, therefore, provide surprisingly good oxidation characteristics, as confirmed through both burner rig and crucible tests performed by multiple gas turbine engine manufacturers. At the same time, similar multiple source testing confirms both alloys exhibit very good hot corrosion capabilities (IN 738 LC/René 80/IN 792 level). The ability of the CMSX-11B and CMSX-11C alloys to provide good hot corrosion and oxidation characteristics, in tandem, is thought unique among available turbine materials.

Summary

Two unique single crystal casting superalloys have been developed for gas turbine engine blade and/or vane application where demanding strength and environmental issues prevail. The non-rhenium containing alloys, CMSX-11B and CMSX-11C, exhibit short-term creep rupture strengths which are as good or better than other lower chromium-containing, first generation SX superalloys. Moreover, both alloys develop long-term creep-rupture strengths which are as good or better than Re-containing second generation SX alloys at conditions pertinent to gas turbine blade and vane component operation. Furthermore, the CMSX-11B and CMSX-11C alloys also provide uniquely attractive blends of bare hot corrosion and oxidation resistance; a characteristic thought unique among superalloys commercially available.

Acknowledgment

The invaluable assistance of several turbine engine companies, who wish to remain unidentified at this point, is gratefully acknowledged.

References

1. "Turbine Market Forecast, 1994 to 2003", Turbomachinery International Handbook, pps. 31-34, 1994.
2. "G.E. Forecasts Worldwide Plant Orders of 925,000 MW Between now and 2001", Independent Power Report, p. 1, 3 July 1992.
3. "ABB's New Gas Turbine Decouple Efficiency and Temperature", Turbomachinery International, pps. 20-24, January/February 1994.
4. Robert Farmer, "First V84.3 to Met Ed for Joint 'B.O.T.' Demo Project", Gas Turbine World, pps. 24-33 July/August 1993.
5. Thomas Barker, "Siemens' New Generation", Turbomachinery International, pps. 20-22, January/February 1995.
6. Robert Farmer, "See 57% net efficiency combined cycles powered by 2400°F '3A' series turbines", Gas Turbine World, pps. 18-28, January/February 1995.
7. "Advanced Turbine Systems: Follow-up", World Power Systems Intelligence, pps. 6-7, Issue No. 179, 22 September 1993.
8. Irwin Stambler, "Technology base in place for next phase of ATS development program", Gas Turbine World, pps. 10-14, September/October 1995.
9. "Future Gas Turbines for Power Generation", Turbomachinery International, pps. 30-31, January/February 1994.
10. Chester T. Sims, private communications during technical meeting at Cannon-Muskegon, 1989.
11. M. Gell, D.N. Duhl and A.F. Giamei, "The Development of Single Crystal Turbine Blades" *Superalloys 1980* (Warrendale, PA: TMS 1980) pps. 205-214
12. C.S. Wukusick (Final Report NAVAIR/N62269-78-C-0315, 25 August 1980).
13. J.W. Holmes and K.S. O'Hara, *ASTM STP 942* (Philadelphia, PA: ASTM 1988), pps. 672-691.
14. M.J. Goulette, P.D. Spilling and R.P. Arthey, "Cost Effective Single Crystals" *Superalloys 1984* (Warrendale, PA: TMS, 1984) pps. 167-176.
15. D.A. Ford and R.P. Arthey, "Development of Single-Crystal Alloys for Specific Engine Application" *Superalloys 1984* (Warrendale, PA: TMS, 1984) pps. 115-124.

16. E. Bachelet and G. Lamanthe (Paper presented at the National Symposium on SX Superalloys, Viallard-de-Lans, France 26-28 February 1986).
17. T. Khan and M. Brun, *Symp. on SX Alloys* (Munich/Germany: MTU/SMCT, June 1989).
18. K. Harris and G.L. Erickson, Cannon-Muskegon Corporation, U.S. patent 4,582,548—CMSX-2 Alloy.
19. K. Harris and G.L. Erickson, Cannon-Muskegon Corporation, U.S. patent 4,721,540—CMSX-6 Alloy.
20. M. Doner and J.A. Heckler (Paper presented at the Aerospace Tech. Conf., Long Beach, CA, October 1985).
21. T. Khan and P. Caron, "Development of a New Single Crystal Superalloy for Industrial Gas Turbine Blades," *High Temperature Materials for Power Engineering 1990* (Kluwer Academic Publishers) pps. 1261-1270.
22. G.L. Erickson, Cannon-Muskegon Corporation, U.S. patent 5,489,346—CMSX-11B Alloy.
23. G.L. Erickson, Cannon-Muskegon Corporation, U.S. patent pending—CMSX-11C Alloy.
24. K. Harris and G.L. Erickson, Cannon-Muskegon Corporation, U.S. patent 4,643,782—CMSX-4 Alloy.
25. A.D. Cetel and D.N. Duhl, "Second Generation Nickel-Base Single Crystal Superalloy", *Superalloy 1988* (Warrendale, PA: TMS, 1988), pp. 235-244.
26. Garrett, U.S. patent 4,935,072—SC 180 Alloy.
27. P. Caron and T. Khan, "Development of a New Nickel Based Single Crystal Turbine Blade Alloy for Very High Temperatures," *Euromat '89* (1989), pps. 333-338.
28. C.S. Wukusick, L. Buchakjian, Jr., General Electric Company, U.K. patent application GB 2 235 697 A. Published March 13, 1991 "Improved Property-Balanced Nickel-Base Superalloy for Producing Single Crystal Articles."
29. G.L. Erickson, Cannon-Muskegon Corporation, U.S. patent 5,366,695—CMSX-10 Alloy.
30. W.S. Walston et al., General Electric Company, U.S. patent 5,455,120—René N6 Alloy.
31. G.L. Erickson, "Superalloy VIM and EBCHR Processes," *International Symposium on Liquid Metal Processing and Casting* (Santa Fe, New Mexico, 11-14 September 1994).
32. D.N. Duhl and M.L. Gell, United Technologies Corporation, G.B. patent 2112812A—PWA 1483 Alloy.
33. D. Goldschmidt, "Single Crystal Blades," *Materials for Advanced Power Engineering 1994* (Kluwer Academic Publishers), pps. 661-674.

THE AGING ALLOYS HAVE MATURED

Carl H. Lund

Lockheed Martin Corporation
Bethesda MD, 20817

Abstract

Now nearly 50 years old, the nickel-base superalloys have become a mature product in the marketplace. The guidelines for basic chemical composition have been strengthening mechanisms, microstructural stability, and failure mechanisms, always with a wary eye on corrosion/oxidation. The understanding of these principles has reached a high degree of sophistication. But compositions and formulae do not "fly"; one utilizes actual hardware. The true measure of maturation of superalloy technologies has been the processing developments necessary to bring these components to reality.

Introduction

The thermal demands of the gas turbine found a good match with the properties of superalloys, and this match has been the basis for a long lasting love affair. With no significant competitor emerging, the affair has been fueled by abundant funding from private and Government sources, and driven by never-ending demands for increased performance. It is perhaps unfortunate that much of the progress has been made by demands for military applications, but significant commercial derivatives permit people and products to be delivered anywhere in our world on an overnight basis.

The relationship could be said to have begun on a day in July 1944 when the Me-262, the world's first operational jet aircraft rose to intercept the onslaught of allied bombers over Europe. First flown in 1942, the Me-262 was a sleek, swept-wing(another first), twin engine aircraft capable of 565 miles per hour, about twice that of its major prey, the B-17, and about 150 miles per hour faster than any existing propeller driven aircraft. The Me-262 was powered by the JUMO 004 engine developed by Anselm Franz at Junkers. It was an in-line axial design with a single stage turbine rotor and cannular combustors (Fig.1)(1). The alloys used were almost totally devoid of strategic materials, and the components

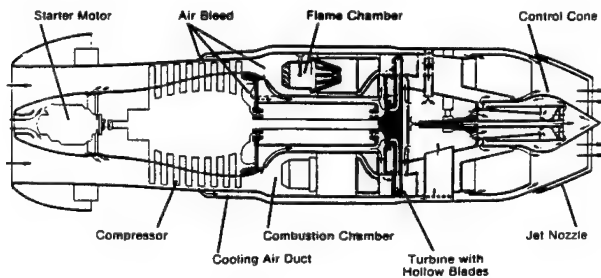


Figure 1. Jumo 004 Gas Turbine Engine

manufactured largely by conscripted labor at widely separated locations. For earlier models, the turbine blades were solid and made from Tinidur, an alloy containing 30% Ni, 12% Cr, and 2% Ti, but in later, operational models, the blade material was downgraded of strategic elements to Cromadur, at 18% Mn, 12% Cr, 0.7% V, 0.2% N, and were air cooled to accommodate lower allowable blade temperatures(2). The burner cans were 1010 carbon steel with an aluminum coating. All told, the final engine contained less than 5 pounds of strategic elements and no nickel. It had a turbine-enlet-temperature(TET) of 600C, a thrust-to-weight ratio of 1.1 to 1, and a compression ratio of 3 to 1.

From this start, current operational designs having TET of about 1500C, thrust-to-weight ratio of about 8 to 1, and compression ratios of 25 to 1 have been developed(3). The

designated operational parameters for very near future programs e.g. IHPTET, HSCT, EJ200 etc. require near stoichiometric temperatures of about 1750C as TET, thrust-to-weight of about 14 to 1, and compression ratios over 40 to 1. Many of the components for these designs are already running in bench demonstrators. Fig.2(4) symbolizes the historical rise in design complexity followed by the current return to design "simplicity (at least fewer parts)" attributable to the upgrading of temperature capability of producible components. While new revolutionary materials will be a major help in other parts of the engine, the turbine is expected to be forced to rely on derivatives of current nickel-base superalloys. With an incipient melting point limit of about 1320C, a maximum metal temperature limit of about 1200C is expected. Therefore, turbine materials will require cooling of up to 550C; today's cooling schemes operate regularly at up to about 225C.

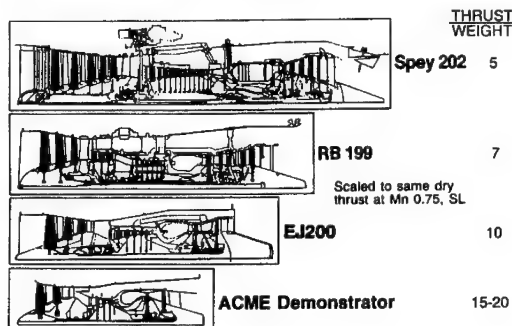


Figure 2. Trend in supersonic fighter engines

The increase in allowable turbine temperature has been a combination of alloy development and utilization of cooling designs. The former has been limited by the melting point of nickel, and the latter by manufacturing technologies to produce the increasingly more complex cooling schemes. Physical limitations of melting point limit metal temperatures to about the 1200C level, so cooling must take allowable gas temperatures the rest of the way. I would like to classify the chemical portion of alloy development as having reached a "sophisticated" level, whereas the true maturation of superalloys would be the development of the processing techniques to manufacture the parts.

Alloy Chemical Sophistication

Looking at the steps toward sophistication, a good starting point would be the Ni-Cr alloys existing in the 1930's. Small amounts of Al and Ti were routinely used for deoxidation, resulting in small but reproducible increases in microhardness and strength. Limitations on analytical equipment capability restricted identification of the

strengthening mechanisms but subsequent studies showed particles of Ni_3Al (gamma prime) and Ni_3Ti (eta) phases. Eta proved to be a line compound with no solubility for other elements and was largely by-passed. Gamma prime, however, had extensive alloying capability. It also proved to have variable solubility (increasing with temperature) in the gamma matrix, with the precipitation reaction being instantaneously reversible with temperature changes. Gamma prime and gamma are both FCC structures of nearly identical lattice parameter, with that of gamma prime slightly larger but coherent with the gamma. Much work led to identification of how alloy additions partitioned, and their effect on lattice parameter (5,6,7). Some e.g. Ti, Nb, V, preferred the gamma prime; others e.g. Cr, Mo, Co, preferred gamma; still others were non-discriminatory (W) or variable (Ta). Those elements within the host gamma matrix would also tend to partition to the dendritic or inter-dendritic areas depending on melting point. Each of the elements also had an effect on the corrosion resistance and carbide morphologies of the microstructure.

For alloys intended for use at temperatures up to about 800C, it was common practice to maintain high coherency stresses within the forced registry between gamma and gamma prime while simultaneously strengthening each of the phases. In most cases this was accomplished with additions of Ti to the gamma prime, and addition of Mo to the basic Ni-Cr matrix. Many of the early blade alloys were of this Ti-Mo combination which led to their use for disks as the disk rim temperature built-up to 760C. For applications when long term creep was preeminent, a low level of lattice parameter mismatch was desirable so as to have a low stress interface (8). Here W was a help, not only for its effect on diffusion rates at high temperatures, but also because it tended to partition equally between gamma and gamma prime. Such developments led to very high strength levels with low minimum creep rates at temperatures up to 1000C but ductility degenerated to almost zero, particularly at the intermediate temperature levels (760-800C) (9). At this point Hf was found to increase ductility without seriously sacrificing creep rate; the alloys were no stronger, they lasted longer with guaranteed tertiary creep (10).

About the same time, directional solidification (DS) became commercially available. One advantage was increased strength in the longitudinal direction (transverse properties remained equal to those of equi-axed), but the main advantage of DS was the much improved resistance to thermal fatigue of the leading and trailing edges of the airfoils; the improvement being due to the lowered modulus of the preferred orientation of the grains. Hafnium provided the grain boundary integrity that allowed the longitudinal grain boundaries to survive during cooling of the mold. DS did not raise the permissible metal blade temperature but it profoundly affected service life.

The next step in maturation of the processing technology permitted the removal of grain boundaries altogether. This did significantly raise the allowable blade metal temperatures as it eliminated the need for grain boundary

strengtheners(DS columnar still had transverse grain boundaries) such as C, B, Hf, Zr. This permits the alloys to be homogenized during solution heat treatment without incipient melting at the grain boundaries(11). Second and third generation alloys have also added higher melting point refractory elements, mainly rhenium for now, that have raised the allowable blade metal temperature about 100C. It also severely complicated the casting procedures by raising the melting point of the alloys to temperatures beyond the capability of conventional molds and cores, thereby requiring further maturation of processing technologies(and materials) in order to successfully produce components on a commercial basis.

It is at this point that sophistication in chemical composition of alloy development takes on a selective quality where the major large engine companies e.g. Pratt&Whitney Aircraft(PWA), General Electric(GE), Rolls Royce(RR), Societe Nationale D'Etude et de Construction de Moteurs D'Aviation(SNECMA), USSR each derived a variation for its own use based on "tailoring" the chemistry to match processing and coating considerations. Within the USSR, government restrictions based on availability of strategic elements put limitations on allowable compositions. The sole proprietorship position of the engine companies appears to be dissolving, given the economics involved and the governments approval for joint programs such as GE/PWA on engines for the Boeing 747-500/600 and the HSCT.

Tables 1 thru 7 show examples of commonly used alloys in the USA, Western Europe, and the USSR for combustors, disks, and turbine airfoils. The compositions are intended to show trends and examples of specific tailoring by the large engine companies. The earlier, but still widely used alloys such as Incoloy 901, Astroloy, Inco 718, Udimets 500 and 700, and the Nimonic series are not included for reasons of clarity.

Combustors

For many years the alloys used were unchanged, although coatings were employed as service times were extended. The HS 188, Hastalloy X. and HS 230 alloys are used throughout the USA and Europe. Nimonic 263 is used by RR and represents the first step upward in strength with higher Al+Ti content.

Table.I COMBUSTOR - COMPOSITIONS

	C	CR	CO	W	Mo	Al	Ti	Fe	La	Ni
HS 188	.10	22	bal	14	-	-	-	-	-	22
HAST X	.10	22	2	.6	9	-	-	19	-	Bal
HS 230	.10	22	-	14	2	.3	-	-	.02	Bal
NIMONIC 263	.06	20	20	-	6	.5	2.1	-	-	Bal
EI 868	.10	25	-	14	-	.5	.8	-	-	Bal
GTD 222	.10	23	19	2	-	1.2	2.3	1 Ta		Bal
							+	.7 Nb		
FLOAT WALL	.10	8	10	-	6	6.0	1.0	+4 Ta		Bal
(PWA 1455)								+1.3 Hf		

The USSR has used EI 868 for just about all combustor applications. For the higher temperatures of newer engines, GE(GTD 222)(12) increased the strength by increasing not only the Al+Ti but the Ta and Nb as well. PWA changed design and casts shingles from HP airfoil alloys like PWA 1455. The shingles fit together to make a coat-of-mail to accommodate thermal fatigue. The next class of materials will be based on stone/ceramic.

Disks

Only the newer compositions are listed and are basically all powder products(EI 698 is forged from ingot, and U 720 can be ingot or powder). All are sensitive to processing variables and can be consolidated by extrusion, HIP, isothermal forge, die forge or combinations thereof to achieve the desired microstructure. All emphasize fatigue and fracture toughness, with GE (88DT) actually incorporating DT(damage tolerance) in the designation. The USSR entry is the only high Al, low Cr, high refractory element blade airfoil type alloy. It also is the only one used in service in the as-HIP-only condition. PWA, SNECMA, and USSR have utilized Hf to help control carbide reactions.

Table II. DISK COMPOSITIONS

	C	Cr	Co	W	Mo	Cb	Hf	Al	Ti	B	Zr
U 720	.03	18	15	1.2	3	-	-	2.5	5.0	.03	.03
MERL 76	.03	13	18	-	3	1.4	.7	5.0	4.3	.02	.03
RENE 95	.03	13	8	3.5	3.5	3.5	-	3.5	2.5	.02	.03
EI 698	.06	14	-	-	2.7	2	-	1.4	2.4	-	-
88 DT	.03	16	13	4	4	.7	-	2.1	3.7	.02	.03
N 18	.02	11	16	-	6.5	-	.5	4.4	4.4	.02	.03
EP 741NP	.04	9	16	5.5	4	2.6	.3	5.1	1.8	-	-

DS Columnar

The first generation alloys(above the line)are basically Hf-containing modifications of previous equi-axed casting compositions. The GE alloy(Rene 80H) reflects their previous emphasis on corrosion resistance (high Cr and Ti), and the USSR(ZhS6FN) gain strength by use of V rather than Ta. For second generation alloys, all but the USSR(ZhS26) contain rhenium(Re) accommodated by the lowering of Cr. Because Re partitions primarily to the gamma phase, some other element already present must be removed in order to prevent the formation of unwanted intermetallic phases due to supersaturation of the gamma. Chromium is the obvious choice as it contributes least to the strengthening mechanisms. All of the alloys are now aluminide formers, having high Al, and low Ti and Cr. The selection of refractory elements

(W+Mo+Ta+Re) is a matter of personal choice, but the total Wt% is in a narrow range near 15%. Because second generation alloys contain Re, and with longitudinal grain boundaries present, heat treatment becomes very complex to affect solution treatment without losing ductility.

Table III. D.S. COLUMNAR - COMPOSITION

	C	Cr	Co	W	Mo	Re	Ta	Nb	Hf	Al	Ti	V
PWA 1422	.14	9	10	12.5	-	-	-	1	1.8	5.0	2.0	-
RENE 80H	.15	14	10	4	4	-	-	-	.8	3.0	5.0	-
MAR-M 247	.14	8	10	10	.6	-	3	-	1.4	5.5	1.0	-
CM247 LC	.09	8	9	9	.5	-	3	-	1.4	5.6	.7	-
MM 002	.14	9	10	10	-	-	3	-	1.4	5.5	1.5	-
ZhS6FN	.11	6	9	12	1	-	-	2.6	.9	5.3	1.0	.9
PWA 1426	.10	6.5	10	6.5	2	3	4	-	1.5	6.0	-	-
RENE 142	.12	6.8	12	5	1.5	3	6.4	-	1.5	6.0	-	-
CM 186	.07	6.0	9	8	.5	3	3	-	1.5	5.7	1.3	-
ZhS26	.13	4.4	4	12	1.1	-	-	1.7	-	6.0	1.0	.9

Single Crystals

The compositions are grouped by general classification of first, second, and third generation. With the exception of GE(N4+,N5,N6) all of the alloys have had the grain boundary elements removed, except for minor additions of carbon for melt cleanliness. GE intentionally adds C,Hf,B to all of their alloys(13). In general, first generation has no Re, second generation has 3%, and third has about 6%; only two third generation alloys are considered to be commercial, GE(N6) and Cannon Muskegon CMSX 10(14). As the Re increases, the Cr must decrease for reasons of microstructural stability. Also the Ti goes from some to little to none. The second and third generations have settled on refractory elements at about 8Ta, 1.5Mo, 7W, and Re to add up to about 18-20W/0%.

Industrial-Land Based

Table V reflects the nearly universal use of all developed by International Nickel Company(INCO) for those nickel-base alloys in cast airfoil applications. These were designed to be used in at moderate gas temperatures(up to about 975C) and sulfur-containing fuels so Cr levels were kept high. As co-generation units come on-line to provide higher efficiencies by use of high gas temperatures and natural gas fuels, sulphidation is a much lessened problem thereby permitting the use of aircraft propulsion type compositions(16). It would be advantageous to utilize DS and single crystals as well, but the very much larger airfoil size has required considerable scale-up for the casting industry; currently components up to 24 inches in length are being made.

Table IV SINGLE CRYSTAL - COMPOSITIONS												
	C	Cr	Co	W	Mo	Re	Ta	Nb	Hf	Al	Ti	OTHER
PWA1480	.02	10	5	4	-	-	12	-	-	5.0	1.5	
N4+	.05	6.5	8	6	1.5	-	5	.5	.15	4.2	3.5	.004B
CMSX 3	-	8	5	8	.6	-	6	-	.10	5.6	1.0	
RR 2060	-	10	10	3.3	1.6	-	1.6	.8	-	5.8	2.5	.8 V
SRR 99	.02	8.5	5	9.5	-	-	3	-	-	5.5	2.2	
AM-1	-	8	6.5	6	2	-	8	-	-	5.2	1.0	
AM-3	-	8	5.5	5	2.3	-	3.5	-	-	5.2	1.0	
PWA1484	.02	5	10	6	2	3	8.7	-	.10	5.6	-	
N5	.05	7	7.5	5	1.5	3	6.5	-	.15	6.2	-	.004B
CMSX 4	-	6.5	10	6	.6	3	6	-	.10	5.6	1.0	
SC 180	-	5	10	5	1.7	3	8.5	-	.15	5.5	.7	
MC-2	-	8	5	8	2.0	-	8	-	-	5.0	1.5	
ZhS 36	.005	4.5	10	12	1.5	2	-	1	-	6.0	1.0	
ZhS 40	.005	6.5	.5	7	4.0	-	7	.2	-	5.3	-	
N 6	.05	4.5	12	6	1.2	5.4	7.5	-.15	5.8	-	.004B	
CMSX10	-	2.0	3	5	.4	6	8	.1	.03	5.7	.2	

Table V. INDUSTRIAL-LAND BASE												
	C	Cr	Co	Mo	W	Ta	Nb	Al	Ti	Hf	B	Zr
IN 738	.10	16	8.4	1.7	8.4	1.7	.7	3.6	3.4	-	.015	.05
IN 939	.15	22	19	-	2	1.4	1	1.9	3.7	-	"	.08
IN 792	.10	13	9	2	4	4	-	3.2	4.2	-	"	.05
IN 792+Hf	.08	12	9	2	4	4	-	3.5	4.0	1	"	.03
D.S. COLUMNAR												
MAR-M 247	.13	8	10	.6	10	3	-	5.5	1.0	1.4	"	.04
CM 247LC	.08	8	9	.5	9.5	3	-	5.6	.7	1.4	"	.02
GTD 111	.10	14	9.4	1.5	3.7	3	-	3.0	5.0	.2	"	.02
SINGLE CRYSTAL												
SC 16	-	16	-	3	-	3.5	-	3.5	3.5	-	-	-

Low Density Alloys

This class of alloys is essentially IN-100 and its derivatives. Although used as a casting, IN-100 represents the final stage in loading as much Al+Ti as possible into the gamma prime phase with offsetting Mo additions to gamma. The very high Al+Ti level gives an alloy of relatively low density, some 7% lower than the higher refractory element superalloys, and thus lower stresses at similar rotational speeds, but the lack of refractory elements restricted the temperature capability. DS gave no strength improvement; single crystals were developed by RR(17) and Cannon Muskegon to use in derivative engines where IN-100 had previously been employed.

Table VI. LOW DENSITY ALLOYS

EQUI-AXED							D.S.	EXCL			
USA			IN-100				-	CMSX 6			
WESTERN EUROPE			IN-100				-	RR 2000			
EASTERN EUROPE			VZhL12E				-	-			
	C	Cr	Co	W	Mo	Ta	Cb	Hf	AL	Ti	V
IN-100	.16	10	15	-	3	-	-	-	5.5	4.8	1
VZhL12E	.12	10	9	1.2	3	-	.7	-	5.1	4.4	.7
CMSX 6	-	10	5	-	3	2	-	.10	5.0	4.8	-
RR 2000	-	10	15	-	3	-	-	-	5.5	4.0	1

Specialty Alloys

A few alloys have been developed for use at only very high temperatures, above where the gamma prime/gamma reactions dominate. These are for static components, and only the mechanically-alloyed(MA) MA 754 has been used regularly for an airfoil application; that by GE in the F404 and F110 engines. This is a good example of the maturation of superalloy processing techniques, from the initial cold crushing to amalgamate elemental powders, followed by extrusion, and directional recrystallization to a billet having high aspect ratio elongated grains. The solid billet is machined by electrical discharge machining(EDM) to a specified outer contour with internal compartments into which tubes are placed for impingement cooling of the inside surfaces. Holes are then drilled through the walls to provide boundary-layer cooling of the outer surfaces. The finished airfoil is then attached to inner and outer platforms made from an equi-axed casting. Figure 3(18) shows an exploded view of the unassembled pieces; it is truly a work of art and science.

Table VII. SPECIALTY ALLOYS

	C	Cr	Co	W	Mo	Cb	Al	Ti	
MA 754	.05	20	-	-	-	-	.3	.5	Y203= 0.6
TD-Ni	Ni plus THO2 = 2.0 %								
TD-NiCr	Ni + 20% Cr plus ThO2 = 2.0 %								
VDU-2	NI plus HfO2 = 2.0 %								

Maturation-Processing

As the chemistry portion of the alloy development programs raised its level of sophistication, the limiting

factor became one of actually producing the parts. For reasons of grain size and defect control, most of the early airfoils were made as wrought product. However, this was a self defeating policy by definition, the intent being to produce alloys resistant to deformation at high temperatures, and then manufacture them by the process of hot deformation.

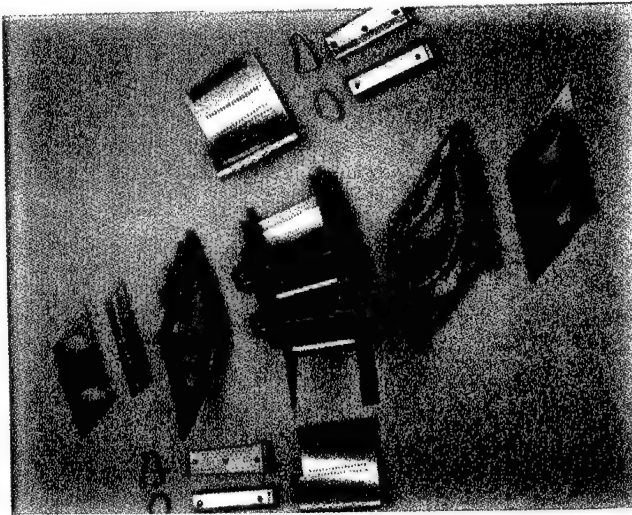


Figure 3. Exploded view MA 754 vane

None-the-less, nearly all blades and certainly all disks were produced by forging until the mid-1960's. At this point the engine dictated higher temperature capability blades and a new era of quality control entered the casting industry. The results were astounding. Soon after, the newly established casting capability allowed the production of the sought-after internal cooling designs that were impossible to produce by forging, although RR did successfully produce air-cooled wrought airfoils of relatively simple radial hole design(19). What follows are the progressively more complex internal cooling schemes produced in DS and single crystals. For a short while, two piece split blades were produced by DS casting of matched longitudinal airfoil halves which were then diffusion bonded after inspection of what ultimately would be the internal cooling channels.

Bi-Casting. Bi-casting involves the placement of previously cast articles into another mold and a second casting is poured around those articles. Such a procedure allows that single crystals can be incorporated into smaller gas turbines, where the first stage stationary airfoils are often produced as a singular entity. In this case, previously cast single crystal airfoils are assembled into a circular mold, and the inner and outer platforms are cast around the peripheries of the single crystal airfoils(20). One end of the airfoils is locked in place by the cast ring while the other end is unattached to permit expansion, through a slot

in the circumferential ring, to eliminate restraint as a result of thermal expansion during operation.

The maturation of the wrought processing has been equal in quality to that of casting. As direct forging became more difficult, the wrought producers turned to powder metallurgy in order to obtain uniform properties throughout an article the size of a turbine disk. Various means were developed to achieve small particles, each particle being of the complete intended composition, which were free of impurities. Several methods are used including vacuum atomization, hydrogen saturation, rotating electrode, and inert gas. The powder can then be compacted by canning followed by extrusion, HIP, direct forge, iso-thermal forge, or combinations thereof. Consolidation parameters and heat-treatment are combined to give any desired set of properties. Usually a combination of extrusion-isothermal forge, or HIP plus forge are used although the USSR regularly flies commercial and military disks in the as-HIP only condition.

Dual Wheels. It must be remembered that with all the emphasis on airfoil properties, the airfoils must be attached in some fashion to a disk, drum, or hub. For large engines, this is usually accomplished by a machined fir-tree configuration on the airfoil root, with a matching contour machined on the edge of the rim. As temperatures in this area reach 760-800C with very high loadings, intermediate temperature properties are as important as minimum creep rate. For smaller engines, where it is impractical to use inserted individual blades, two practices are generally used. For engines of moderate TET the entire wheel (blades plus disk) is cast as one piece from one alloy. With multiple temperature and stress loadings, alloy selection is critical. Castability is a must as a single defect can reject an entire large casting; nickel-base alloys are very difficult to repair weld. These are termed integral wheels.

The alternative procedure is to join a wrought alloy disk with a ring of cast blades. The joint is just below the rim area and can be done by inertia welding (the ring held firmly in place and the disk rotated to appropriate speed and then forced against the stationary blade ring) or by solid state diffusion bonding.

Coating

As good as the nickel-base superalloys are in basic oxidation/corrosion resistance, virtually all high pressure turbine components are coated for additional protection. Many types of coating are utilized including straight aluminide, duplex aluminide, boundary layer (MCrAlY), and thermal barrier-type (stabilized zirconia). The thermal barrier coatings are usually used over a previously applied layer of MCrAlY which provides a complaint zone to minimize differences in coefficient-of-thermal-expansion (CTE). The various coatings can be applied by vacuum pack, dipping, low or high pressure plasma, or chemical vapor deposition. Many blades have the internal passages as well as the external surfaces coated, most often with different types of coating. In some cases the internal and external surfaces can be

coated simultaneously with different types of coatings. Coatings are of such importance to successful performance that it is not uncommon to have alloy selection and composition to be strongly influenced by coating compatibility.

Prototypes and Bench Testing

A quick look at current blade developments are shown in Fig.4 and Fig.5. Fig.4 shows some detail on the Lamilloy process by Allison Gas Turbine where thin sheets of MA alloy are photo-etched to form channels of a desired cooling scheme, and then diffusion bonded to form a blade providing continuous interconnecting channels(21). Differential pressure control through progressive channels provide transpiration cooling at the surface. This is a well developed process that has been running successfully on high temperature bench rigs for sometime; the engines are asking for it now. Fig.5(22) shows a standard single crystal blade having complex internal passages vented to the outer surface. The second configuration has a Lamilloy internal structural core which is covered by an envelope of a thin single crystal sheet having multiple small diameter holes cast-in. When viewed against the light, the sheet looks like porch screening. The trailing edge is then diffusion bonded to form the complete composite blade. A section of the thin, cast single crystal perforated envelope is shown in the illustration at the lower left. The last diagram shows a late development, new to the test rigs for advanced programs. This is done by the CASTCOOL process, also by Single Crystal Airfoils of Allison, where a complete blade is cast into a transpiration-cooled configuration; all at one time, all in one piece, and all a single crystal. A close-up view is shown in Fig. 6(23).

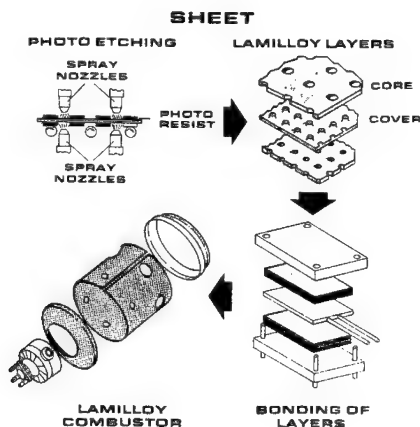


Figure 4. Lamilloy

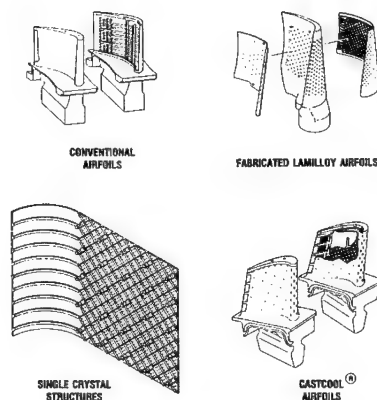


Figure 5. Cooling Methods

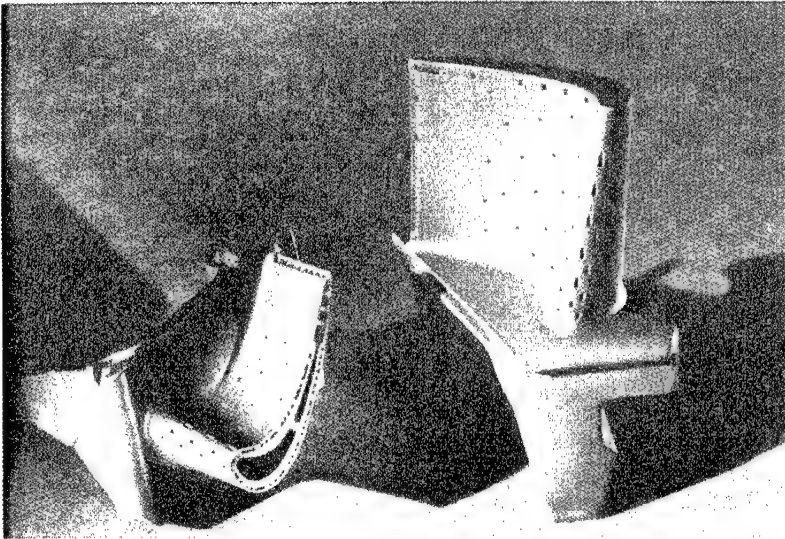


Figure 6. CASTCOOL product

Newest But Still Proprietary

Three areas of future interest but not yet in the public domain would be:

a. alloy development- a new patent assigned to GE(24) describes the discovery of new insight into "reverse partitioning" of refractory elements at high temperatures which profoundly affect possible problems of supersaturation particularly at coating interfaces.

b. chemical vapor deposition- workers at the Alliance Corp(25), a joint effort by PWA and Paton Institute in Kiev, are pioneering production of cooled airfoils by chemical vapor deposition rather than conventional melting techniques.

c. NiAl (Beta)- Recent work by GE has produced a set of airfoils for engine test made from alloyed NiAl(26). This compound has always tantalized the industry because of high melting point, excellent oxidation resistance, and high thermal conductivity, but also has low strength and minimal ductility at low to intermediate temperatures. Suitable attachment is difficult. Components have been produced and early engine tests have been completed.

References

1. Walter Boyne, Messerschmitt ME 262, Washington D.C., Smithsonian Press, 1980, 184 pps.
2. Walter Boyne, Donald Lopez, The Jet Age, Washington City, Smithsonian Press, 1979, 72
3. Powerful Potential, Flight International, 15-21 July 1992, pp 25-29

4. Rolls Royce Brochure, Farnborough Air Show, 1988
5. O. Kriege, J. Baris, Chemical Partitioning of Elements In Gamma Prime Separated From Precipitation Hardened High Temperature Nickel-Base Alloys, Trans. ASM, Vol. 62, 1969, 195-200.
6. R. Dreshfield, J. Wallace, Gamma-Gamma Prime Region of Ni-Al-Cr-Ti-W-Mo System at 850C, Met Trans, Vol. 5, Jan 1974, 71-78
7. R. Ricks et al, Growth of Gamma Prime Precipitate In Nickel-Base Superalloys, Acta Metall, Vol. 31, 1983, 43-53
8. R. Decker, Strengthening Mechanisms In Nickel-Base Superalloys, Symposium On Steel Strengthening Mechanisms, May 1969, Zurich Switzerland.
9. C. Sims, N. Stoloff, W. Hagel, eds., Superalloys II, New York, Wiley & Sons, 1987
10. US Patent No. 3,677,747, C. Lund, J. Hockin, M. Woulds, Martin Marietta Corp.
11. J. Jackson et al Effect of Volume Percent of Fine Gamma Prime On Creep of DS MAR-M 200 +Hf, Met Trans A, Vol. 8a, Oct. 77, 1615-1620.
12. P. Schilke et al, Advanced Materials For Land Base Turbines, Advanced Materials and Processes, Apr. 92, 22-30.
13. US Patent No. 5,399,313, E. Ross, C. Wukusick, R. King, General Electric.
14. G. Erickson, A New Third Generation Single Crystal Casting Superalloy, JOM, Vol. 47, Apr. 95, 36-39.
15. Private Communication, G. Erickson, Cannon Muskegon, May 96
16. T. Gibbons, Materials For Combined Cycle Gas Turbines, Processing and Design Issues in High Temperature Materials, Engineering Foundation Symposium, Davos, Switz., 1996.
17. D. Ford, R. Arthey, Development of Single Crystal Alloys For Specific Engine Applications, Fifth International Symposium on Superalloys, TMS-ASM, Superalloys 1984, 115-124.
18. Total Capability, Product Brochure, Johnson Technology, Muskegon, MI.
19. Forged Nimonic Blades, Flight, Vol. 10, Sept. 1954, 421
20. US Patent No. 4,728,258, Blazek et al, TRW
21. Lamilloy, Technical Brochure, Allison Engine Co., Sept 1988

22. Single Crystal Airfoils, Brochure of Single Crystal Operations, Allison Engine Co.

23. Ibid

24. US Patent No. 5,482,789, O'Hara,Walston,Ross,Darolia, GE

25. Aviation Week&Space Technology, May 10, 1993, 53

26. R. Darolia, NiAl For Turbine Airfoil Application, Structural Intermetallics, First International Symposium On Structural Intermetallics, TMS, R.Darolia et al eds. 1993,495

DEVELOPMENT OF ADVANCED STEELS FOR STEAM TURBINE APPLICATIONS

R.B. Scarlin

ABB Power Generation Ltd.
Baden, Switzerland

Abstract

There is a considerable advantage to be gained from increasing the operating efficiency of power generation equipment. A major improvement can be made by increasing the inlet temperature of a steam turbine from the current conventional value of about 560°C to a value, for example, of 600°C or more. Typically such an increase in operating temperature will improve efficiency by about 4%. In order to accomplish this, improved steels have been required. This paper describes a co-operative development programme which has resulted in the identification, testing and qualification of advanced 9 - 12 % Cr steels with improved creep strength.

Introduction

Currently high-temperature components of steam turbines, such as rotors, blades, casings and steam pipes are manufactured from 12 % Cr steels. Although the use of austenitic steels would permit temperatures to be increased, such materials are expensive, so that the cost of electricity might rise. They also suffer from the disadvantage of high coefficients of thermal expansion and low thermal conductivity, so that rapid temperature changes would lead to unacceptable thermal stresses. As a results turbine start-up and operational flexibility would be limited. Hence there was a need for ferritic steels with improved properties, appropriate for the fabrication of these critical components.

Major activities have been initiated in Japan [1], the USA [2] and Europe [3-5] (Fig.1).

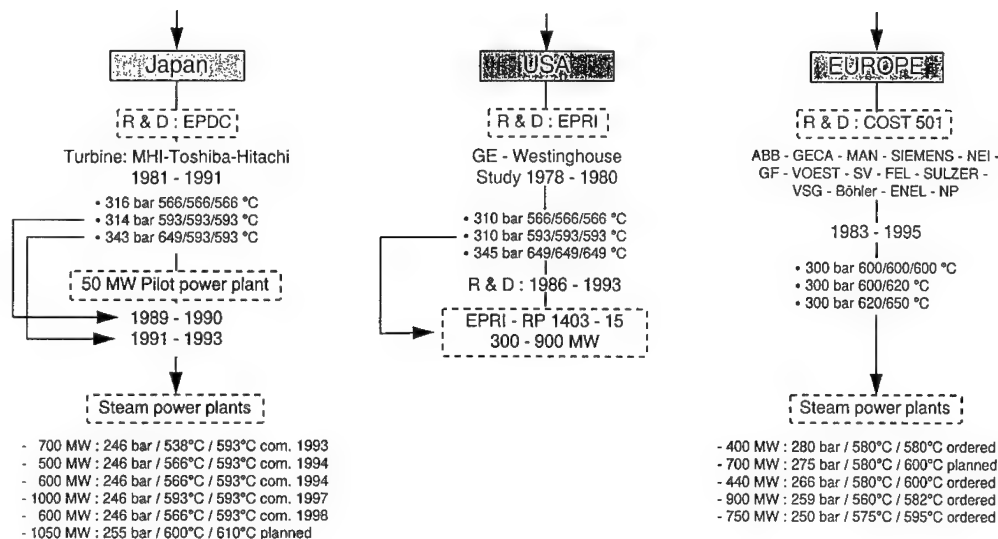


Fig.1: International Development Programmes on Advanced Steam Cycles

Development activities of this kind are frequently carried out through co-operation between a number of organisations, since it is possible in this way to share the costs and benefits. In addition it is possible to produce a much broader database of information, on the basis of which standardisation and general acceptance can more easily be achieved. In particular the European COST Programme (CO-operation in Science and Technology) has been successful in developing and validating such steels, some of which are now in service. Participants in the COST programme have been the major European turbine and boiler manufacturers, producers of forgings, castings and pipes, electric power utilities and testing institutes.

Issues limiting development and use of materials

The use of a material at elevated temperatures is generally limited by its creep strength and resistance to degradation, generally in the form of embrittlement or softening. This in turn is related to the microstructural stability. The specific requirements for the present application are the following:

- high creep strength at a temperature of about 600°C
- high toughness and resistance to embrittlement during long-term use at high temperature
- resistance to steam oxidation and in the case of boiler components also fireside corrosion
- ease of fabrication for large forged and cast components, including weldability where appropriate

For example, for rotor forgings the following targets were set in the COST programme:

- uniformity of mechanical properties in forgings of up to 1200 mm in diameter
- yield strength above 600 or 700 MPa
- a creep strength at 600°C and 100'000 hours of 100 MPa
- toughness and low cycle fatigue properties better than current materials

The general approach began with an evaluation of the properties of presently available materials and a study of the development work currently being performed. Particular attention was paid to the understanding of the mechanisms of strengthening of steels in the 9 to 12% Cr class, since a good combination of creep strength and oxidation resistance can be expected. Metallographic investigations have been extensive [6]. Specifically optical microscopy has been used to determine grain structure and uniformity in large components, quantitative transmission electron microscopy to correlate stability of microstructural features with mechanical properties and field ion microscopy, with which all elements present in the alloys can be precisely located and quantitatively analysed. Microstructural observations of the type, size and distribution of precipitates, along with their evolution at high temperature as a function of time and applied stress, have permitted models to be developed to describe and predict the volume fractions of precipitates both after heat treatment and also extended periods of service. This will lead to the development of further generations of improved alloys.

Alloy development and metallurgy of 9 to 12 % Cr steels

Steels with a content of 9 to 12 % Cr provide a good combination of creep strength and oxidation resistance in steam. The best possible combination of mechanical properties can be achieved through quenching to produce a practically fully martensitic microstructure and then tempering the steel to precipitate carbides, thereby increasing toughness to the required level. At the same time it is desirable to employ a tempering temperature which is as high as possible, and preferably at least 100°C higher than the anticipated service temperature. i.e. at least 700°C for a subsequent temperature of operation of 600°C. This criterion serves to ensure that service of the component, typically for 200'000 hours at the service temperature of 600°C, will have little further tempering effect after the original heat treatment of typically 12 hours at $\geq 700^{\circ}\text{C}$. Nevertheless the microstructures of these steels are not fully stable and further precipitation reactions occur, some of which are beneficial and some deleterious to the mechanical properties.

Alloying of steels is complex. Some elements are added specifically on account of the beneficial effects they have whereas others, such as sulphur, phosphorus, silicon and the other tramp elements (Sn, Sb, As, etc.), are kept to the minimum level which can be economically achieved on account of their negative effects, generally on toughness. Beneficial effects are provided by the following:

Chromium at a level between 9 and 12 % provides a good combination of creep strength and oxidation resistance. Higher Cr levels cause the appearance of δ -ferrite.

Carbon at a level of 0.1 to 0.2 % is added to form carbides (mostly of chromium) which provide strength after heat treatment. Higher C levels may cause cracking during welding.

Nickel is added at a level below 1 % to delay transformation during cooling so that a 100% martensitic microstructure can be obtained even in components with large dimensions and hence slow cooling rates. Higher Ni contents lower the temperature of transformation to austenite to a value close to the heat treatment temperature so that microstructural instability results.

Molybdenum additions serve to form stable carbides and also contribute to solid-solution strengthening. Levels of 0.5 to 1.5 % are generally used.

Tungsten also makes a major contribution to solid-solution strengthening, but levels above 1 % can lead to the rapid formation of a coarse Laves phase, which can be detrimental to overall strengthening.

Niobium at a level of about 0.06 % forms a small volume fraction of carbides which are extremely stable at the austenitising temperature and hence prevent grain growth and consequent loss of toughness.

Vanadium is added at a level of about 0.20 to 0.25 % and forms nitrides with the nitrogen dissolved in the alloy. These vanadium nitride particles (also referred to as MX precipitates) are extremely stable at the intended service temperatures and have a major creep strengthening effect.

Boron has long been known to improve the creep strength of austenitic steels, even when added in very small quantities. However the mechanism of this beneficial effect has not been satisfactorily explained.

As mentioned above, the presence of nickel improves through hardening and hence the uniformity of mechanical properties in large components, but at the same time it can reduce long-term microstructural stability. For this reason attempts have been made to reduce Ni to a low level but ensure a fully martensitic microstructure through the addition of manganese and/or cobalt. Mn contents of up to 1 % and Co contents of 2 % or more have been used on a trial basis.

If particular importance is placed on the resistance to steam oxidation or to fireside corrosion in the boiler then chromium content should preferably be about 11 to 12 %. In this case δ -ferrite may be observed with a corresponding loss in toughness. This may again be prevented by the addition of nickel (or preferably of cobalt and/or manganese). Alternatively copper may be added to discourage the formation of δ -ferrite in thick walled components. A consideration of this kind, which led to the development of the pipework steel HCM12A is shown in Fig.2 [7].

An improvement in long-term creep strength can be achieved by increasing the Mo-equivalent ($\text{Mo \%} + 0.5\text{W \%}$) from 1.0 to 1.5 %. Fig.3 shows the creep strength for a temperature of 600°C and a duration of 30'000 hours for a number of 9 to 12 % Cr steels with different contents of W, Mo and B. The compositions of a number of steels investigated in the COST programme are also shown.

Qualitative observations have revealed that in such steels heat treatment leads to the generation of a tempered fully martensitic microstructure in which martensite lath boundaries are pinned by M_{23}C_6 particles. These precipitates also serve to stabilise the high dislocation density maintaining high strength. In addition fine MX particles, which are predominantly VN, may also be observed. W and Mo are primarily in solid solution and should contribute to mechanical strengthening.

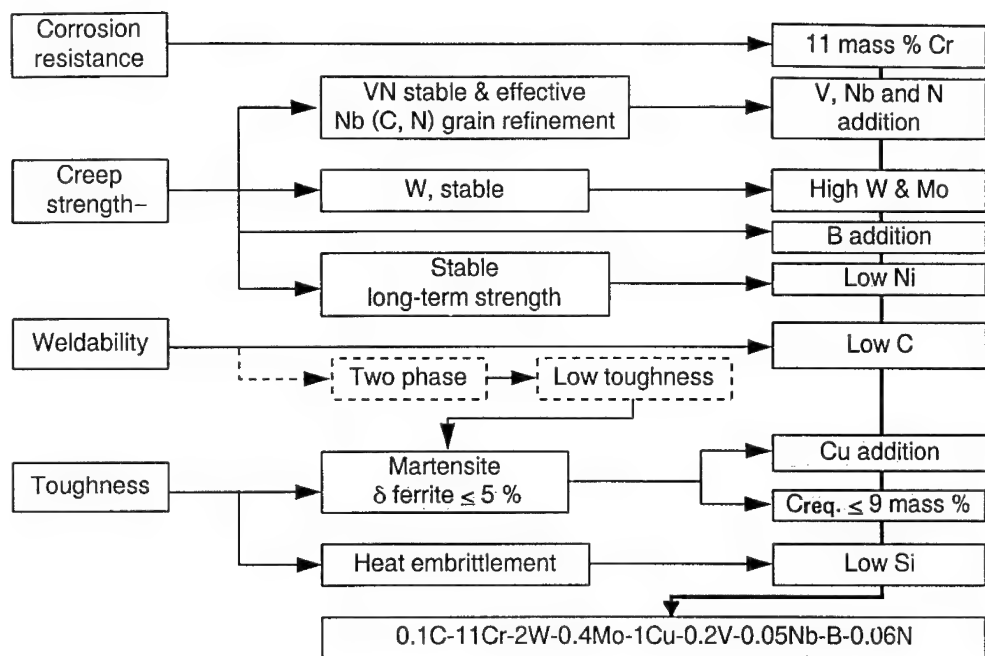


Fig.2: Philosophy for the Development of 0.1C-11Cr-2W-0.4Mo-1Cu large Diameter and Thick-walled Pipe (HCM12A)

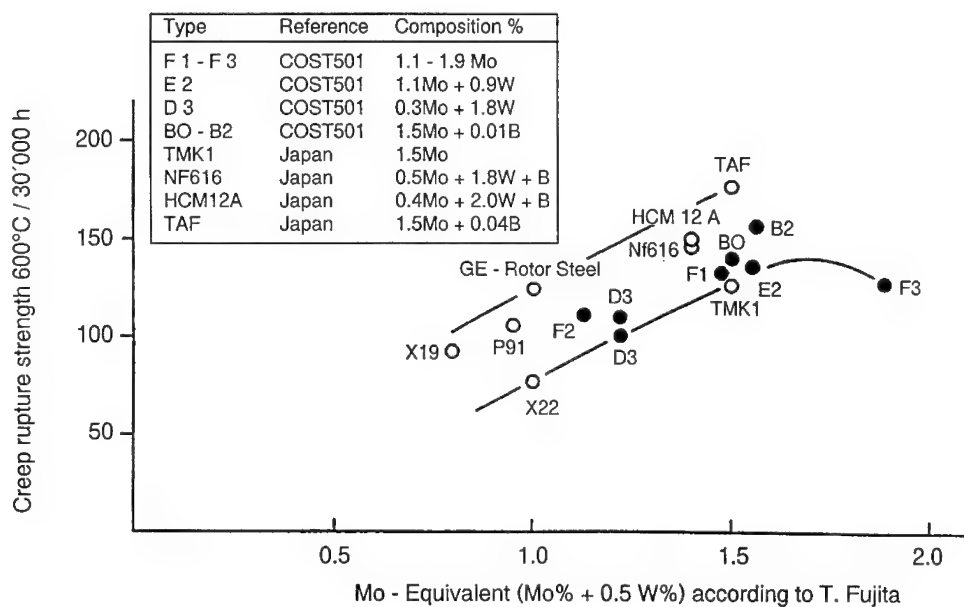


Fig.3: 30'000 hour Creep Rupture Strength of 9 to 12 % Cr steels as a function of Mo-Equivalent

Development Concept

The approach adopted in the COST programme has been the following:

- Potential alloys for forgings and castings were identified after a critical review of the existing grades and steelmaking developments in Europe and elsewhere
- Small trial melts (typically about 200 kg) were manufactured, heat treated and subjected to a standard mechanical testing programme, including measurements of strength, toughness, creep properties and resistance to long-term thermal instability
- Trial components were manufactured from the steels showing the best combination of mechanical properties and were tested nondestructively and destructively with particular emphasis on uniformity of mechanical properties in large components and long-term creep and exposure testing
- Components have now been manufactured and are successfully in service in power plant.

Pre-Evaluation Programme for Forgings

The steel grades showing the best properties are:

Steel Group B: Boron Grades. An earlier COST programme already identified the potential of steels containing about 100 ppm of B. Creep strength is improved and impact energy is not reduced at this level of boron.

Steel Group D: Tungsten Grades. Work in Japan has indicated that additions of tungsten, in partial replacement of molybdenum, at a level approaching 2 % leads to a significant increase in creep strength. A total of 3 test melts was made, for which Mo-equivalent was about 1.2 %.

Steel Group E: Tungsten/Molybdenum Grades. Three melts were selected with lower tungsten contents of 0.5 to 1.0 %, while Mo level was retained at about 1 %.

Steel Group F: Molybdenum Grades. Test melts were selected with molybdenum level of about 1.5 %, but no additions of W or B.

The standard investigation programme for the trial melts comprises:

- microstructural investigation
- tensile testing at ambient and elevated temperature
- impact testing at ambient temperature and transition temperature determination
- isothermal creep rupture tests using plain and notched samples
- isostress rupture tests at 100 MPa.

Material was also aged for durations of 10'000 hours followed by determination of tensile and impact properties. Long-term ageing had no significant effect at 480°C but ageing at 600 or 650°C led to an increase of about 25°C in the value of the Fracture Appearance Transition Temperature (FATT). Creep strength data for the steels with the lower yield strength value in the range 600-650 MPa, plotted on the basis of the Larson-Miller parameter is shown in Fig.4. Creep testing times exceed 60'000 hours. The results show that the target creep strength values can be met. They lie considerably above those for the currently employed steel, standardised in the DIN standard SEW555. The lowest values are for steels of the Group D containing about 2 % of tungsten. Subsequent metallographic investigation of these steels showed the rapid nucleation and growth of tungsten-containing Laves Phase, with a simultaneous loss of the strengthening effect of tungsten in solid solution.

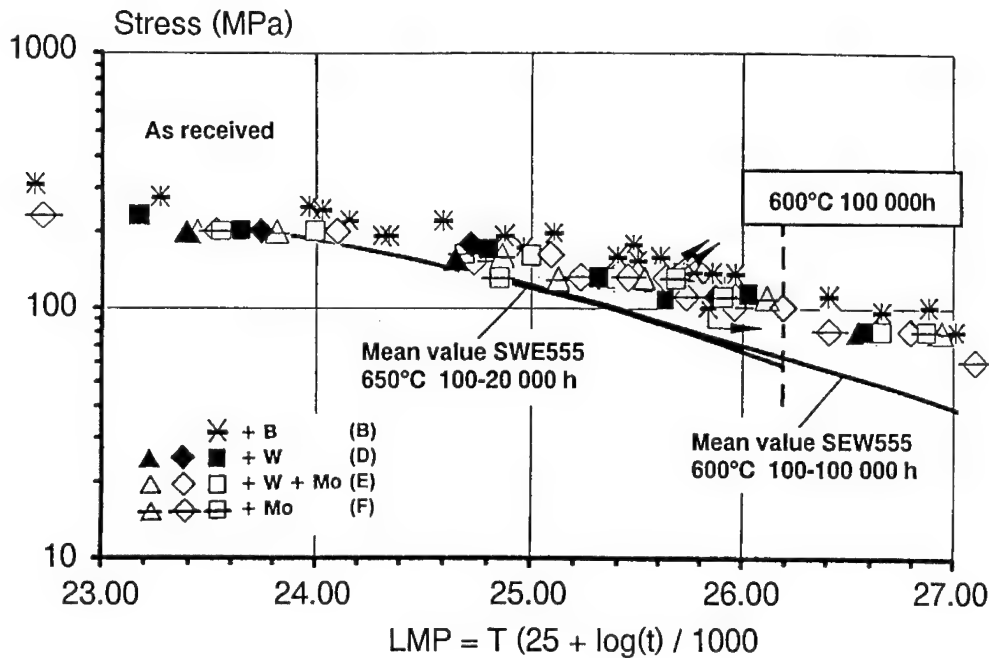


Fig.4: Creep Behaviour of Steels with Yield Strength of 600 to 650 MPa.

Manufacture of Full-Scale Forgings

Analysis of all results permitted the identification of those steels and heat treatments most promising for the production of full-scale rotor forgings. Where the forging diameter was below the diameter of 1200 mm a slower cooling rate from the austenitising treatment was selected in order to simulate the full-sized component.

Fig.5 shows the sampling plan for one of the rotors (Rotor E). Using the following procedure it was possible to investigate both strength levels on a single rotor:

- Rotor was forged to shape and austenitised and provided with the first tempering treatment at 570°C
- Second tempering was performed at the lower temperature intended to produce a yield strength of > 700 MPa
- A radial trepanned core was removed from the rotor body to permit investigation of this strength level at any radial location in the rotor body
- The alternative second tempering treatment at the higher temperature was performed on the remaining part of the rotor body in order to attain a yield strength of > 600 MPa.

Results of the mechanical property tests for the lower yield strength condition of trial rotor E are shown in Fig.5. Values are very uniform, showing little difference between rim and centre locations of the rotors. In addition in all rotors the amount of δ -ferrite is << 1 % and no significant segregation could be observed. Mechanical testing of samples from different locations in the rotors is being performed, including Low Cycle Fatigue (LCF) lifetime, fracture toughness and resistance to subcritical crack propagation.

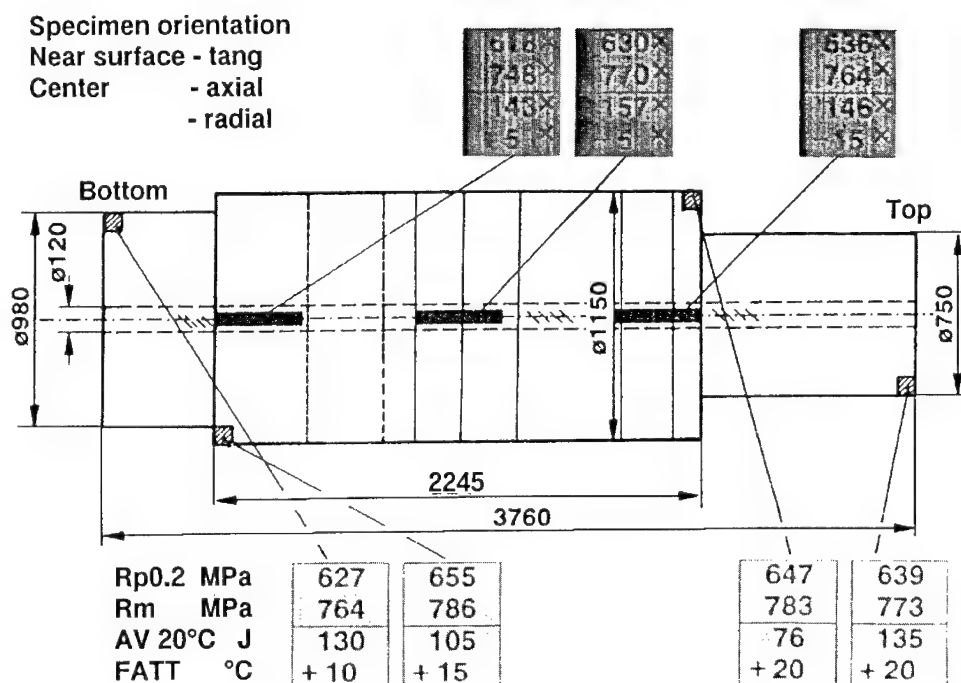


Fig.5: Mechanical Properties at different Locations in Trial Rotor E (Yield Strength > 600 MPa).

Pre-Evaluation Programme for Castings

A similar approach was employed in the development of cast steels for higher steam inlet temperatures of up to 600°C. Based on the results of earlier testing and the evaluation of published information an attempt was made to identify compositions which would provide a further improvement in creep strength. On the basis of a cast version of the steel P91, an improvement was sought through modification of the heat treatment and through further alloying additions.

Accordingly melts No. 4 and 5 (without and with 1 % tungsten, respectively) were manufactured in the pre-evaluation programme. In each case the chromium content had been increased in comparison with P91 in order to improve the solubility of nitrogen, thereby reducing the probability of surface porosity and increasing the potential for precipitation of MX (VN) which is believed to be a potent creep strengthening mechanism. Plates of size 800 x 400 x 100 mm were cast and heat treated and subjected to a testing programme similar to that for the forged materials. In addition welding of cast steels is a requirement both for the repair of any minor cracks which may result during the casting process (manufacturing welds) and also for the joining of cast parts, such as valve bodies or turbine casings, to other components, such as steam pipes (design welds).

The minimum prescribed values of tensile and impact properties were exceeded for all alloys and heat treatment conditions, whereby the tungsten-free material has higher notch impact energy values than the tungsten-containing material. Nevertheless after long-term ageing for 10'000 hours at 480, 600 and 650°C the reduction in impact energy is greater for the tungsten-free material, so that the values are rather similar in the aged condition. Impact energy values are still acceptable in the long-term exposed condition.

The longest creep tests of base material at 600 and 650°C are now approaching a duration of 50'000 hours. Fig.6 shows a Larson-Miller representation of the creep rupture strength of tungsten-free and tungsten-containing material. The tungsten-containing version shows a slight superiority over the entire range of times and temperatures and lies even a little above the pipe steel P91 (shown by the curve "mod. 9 Cr 1 Mo / ORNL") for all heat treatment conditions.

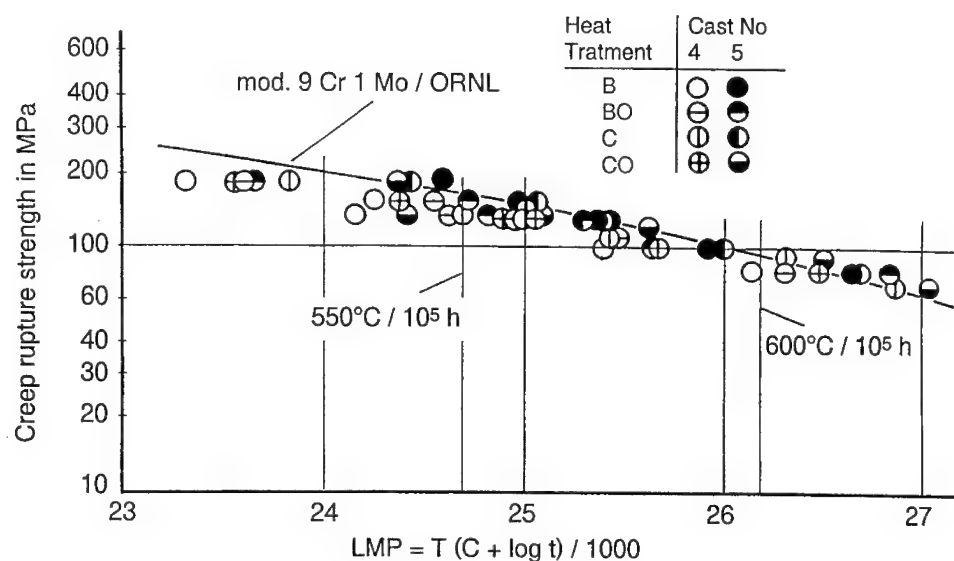


Fig.6: Creep Rupture Strength of 10 % CrMoVNbN and 10 % CrMoWVNbN Cast Steels (Casts 4 and 5)

Manufacture of Cast Component

The excellent behaviour of the tungsten-containing steel resulted in this composition being chosen for the component programme, in which plates of 100 mm in thickness and also a pilot valve chest of about 6 tons in weight were manufactured. Manufacture was not accompanied by any difficulties. The number and size of flaws observed by non-destructive testing were similar to those found in low-alloy cast steels conventionally used for the manufacture of such components. Mechanical testing was carried out on one rim and two core positions from the valve body and two manufacturing weld locations. Tensile and impact values from the base material are uniform and satisfactory. The impact energy of $\geq 30\text{J}$ is considered sufficient (currently used steels have similar values). Tensile strength of the weld metal is higher than for the base material and impact energy satisfies the requirements.

Short-term tests have been completed and confirm the good results obtained from the pre-evaluation programme. Creep testing results have now exceeded 40'000 hours and confirm the results from the pre-evaluation programme. Long-term exposure tests have exceeded 30'000 hours. Cross-weld creep specimens show the normal reduction in creep strength with failures occurring in the weld metal or heat affected zone (Type IV cracking).

In conclusion it can be stated that both cast and forged steels have been identified with a creep strength improvement of about 40°C in comparison with those previously employed. Representative forged and cast components have been manufactured and exhibit uniform properties. Components of these steels have now entered service in commercial steam power plant.

Metallographic Analysis

The metallurgy of this class of steels is complex, the long-term strength being dependent on the precipitate distribution generated by heat treatment and its stability in the long term, along with further precipitation reactions which occur successively during extended periods at elevated temperatures. These reactions can be accelerated by simultaneous plastic deformation. An "ideal" microstructure in this class of steels could be considered to comprise a tempered martensite with a small lath size and a high density of dislocations stabilised by a large number of finely distributed hard particles. Elements added to provide solid-solution strengthening should remain uniformly distributed in the matrix. This microstructure should remain essentially unchanged during prolonged high-temperature service.

Qualitatively it is known that during long-term thermal exposure the following effects can be observed:

- Laves phase containing a high proportion of W and Mo is inhomogeneously nucleated and coarsens rather rapidly, reducing the extent of solid-solution strengthening
- $M_{23}C_6$ particles are coarsened so that their effect in maintaining the high dislocation density and hence the high creep strength is partially lost
- MX particles remain essentially stable.

Metallurgical understanding of the processes controlling microstructural stability can be obtained by quantitative analysis and modelling of the diffusion-controlled processes.

Computer software packages, such as Thermocalc [8], have recently become available for the prediction of the phases which will be present at a certain temperature in steels such as those presently under discussion. The programme is able to predict from the chemical composition of the steel alone the amount and composition of phases such as δ -ferrite, $M_{23}C_6$, Laves Phase and MX under equilibrium conditions. Fig.7 shows a typical example for the steel Nf616 containing about 2 % W [9]. Metallographic investigations have shown that the programme is able to predict transformation temperatures, the presence of specific phases and their chemical compositions reasonably well. Each of these phases has been identified in the steels under consideration.

However kinetic processes of nucleation and growth of the precipitates will be of major importance and long times may be required before equilibrium conditions are reached.

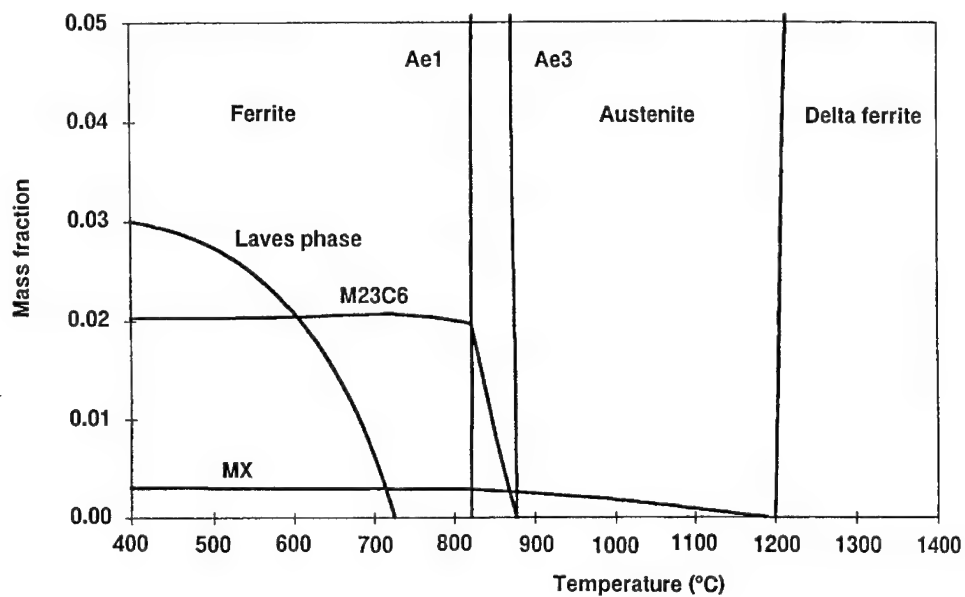


Fig.7: Equilibrium Phases in the Steel Nf616 (calculated by Thermocalc)

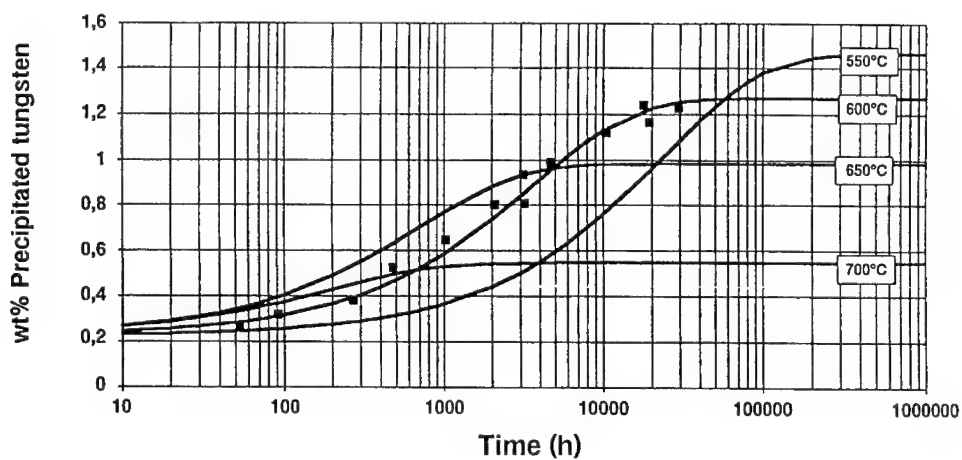


Fig.8: Calculated amount of Tungsten precipitated in Nf616. Points represent measured Values used to calibrate the Model.

Precipitation of Laves Phase

The process of precipitation of Laves phase in the steel Nf616 is shown in Fig.8 [9]. Isothermal ageing of the heat treated alloy at different temperatures shows a progressive loss of tungsten in the matrix, in accordance with the progressive precipitation of Laves phase. The total amount of tungsten in the alloy is 1.8 %. As shown in the diagram, a higher temperature of exposure leads to a more rapid precipitation of tungsten and a more rapid attainment of the equilibrium condition, but the total amount precipitated in the equilibrium condition is correspondingly lower. At a typical service temperature of 600°C the equilibrium condition may only be reached at about 20'000 hours. However half of the available tungsten is already present in the form of Laves phase after only 4'000 hours at this temperature. Accordingly Fig.9 indicates the measured and calculated amounts of Laves phase present in the steel as a function of time and temperature of exposure. At temperatures above 700°C the phase is thermodynamically unstable and at temperatures below 600°C the thermally activated processes of precipitate nucleation and growth require longer times. Nevertheless the loss of tungsten from the matrix progresses rapidly at the anticipated service temperature of the steel. It is then essential to know to what extent the strengthening effect of the tungsten in solid solution is lost and to what extent this can be compensated by a precipitation hardening effect of the Laves phase.

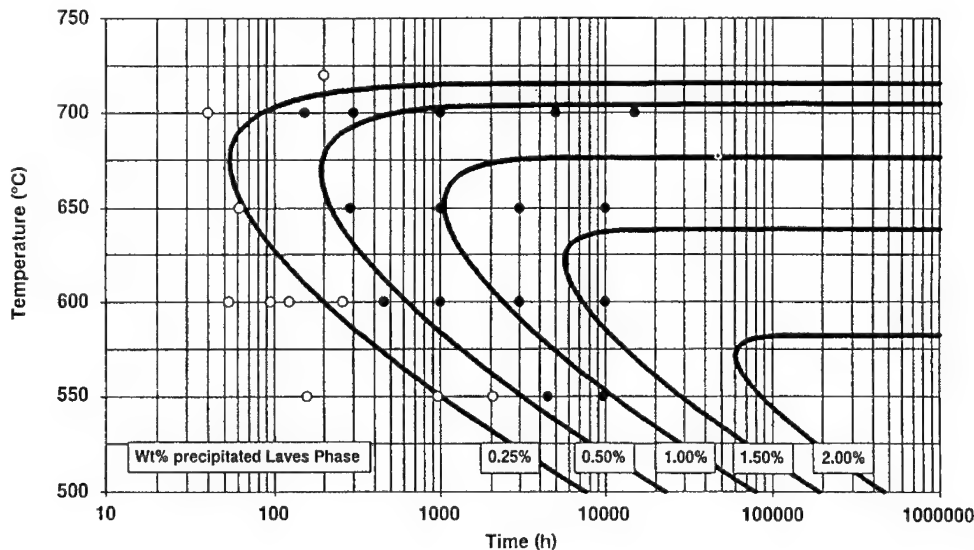


Fig.9: Calculated Time-Temperature-Precipitation Diagram for Laves Phase in Nf616 (Open Circles = No Laves Phase / Full Circles = Laves Phase measured by Nippon Steel)

In order to address this question Hald [9] performed different heat treatments of the material followed by isostress rupture testing. In particular specimens were given heat treatments of 200 hours at 720°C (during which no Laves phase is precipitated) or 10'000 hours at 650°C (during which the equilibrium amount of Laves phase is precipitated). Both treatments have the same Larson-Miller value and similar amounts of $M_{23}C_6$ and MX are present. However they show different behaviour in subsequent isostress tests, as shown in Fig. 10, along with tests of normally heat treated material. The observation that material heat treated at 720°C has a much higher creep strength than that aged at 650°C and that the material heat treated at 720°C approaches the creep strength of normally heat treated material at longer testing times indicates that precipitation of Laves phase during the creep test is an important strengthening factor. It is not known to what extent this process could be dependent on strain rate. A strain-rate dependency would imply that data for design against creep failure should be obtained at very low strain rates, i.e. through long-term testing.

The similarity of the rupture times for short term tests of material in which tungsten was either "fully" precipitated (10'000 hours at 650°C) or "fully" in solid solution (200 hours at 720°C), and in which little further precipitation of Laves phase is possible during the test, indicates that the solid solution strengthening effect of tungsten at this temperature is minor.

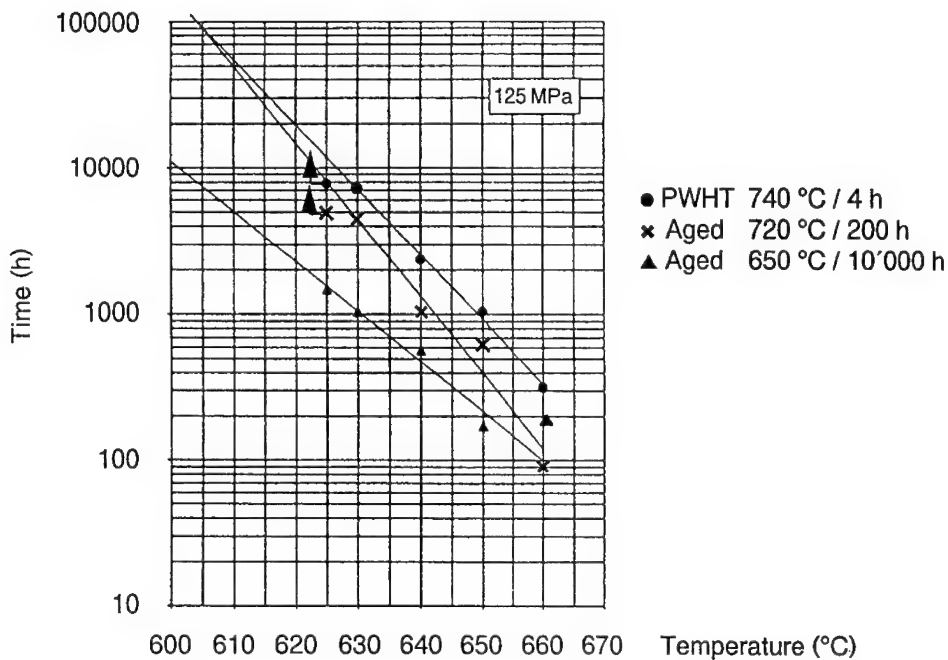


Fig.10: Isostress Tests on Nf616 in different Heat Treatment Conditions

Stability of $M_{23}C_6$ and MX Precipitates

The steels developed in the COST programme have been subjected to extensive qualitative and quantitative analysis by means of electron microscopy [6]. Specimens of selected steels were examined both in the as heat treated condition and after long-term exposure at elevated temperatures, either with or without superimposed creep stress. One specific observation concerns the apparent effect of boron.

In the steel B it is seen that there is a larger number of the $M_{23}C_6$ precipitates and their coarsening rate appears to be lower than in boron-free steels. At the same time the steel is more resistant to dislocation re-ordering than the other steels. However transmission electron microscopy (TEM) was not able to reveal the mechanism by which boron was producing this beneficial effect.

Lundin [10] used the technique of atom probe field ion microscopy (APFIM) to examine these materials on the atomic scale. Using this technique, samples of the materials under investigation are prepared as fine tips with radius less than 100 nm. These can first be examined in the TEM to identify whether precipitates of the desired type are present. If this is the case APFIM is carried out. Applying a high voltage to the tip in a chamber containing a low concentration of a noble gas results in ionisation of the atoms of the gas. They are projected on a screen to provide imaging of the specimen surface on an atomic scale. The incorporation of an aperture to limit imaging to only one point on the surface of the specimen and of a mass spectrometer then permits chemical identification of the individual atoms. The technique has provided the following results for the steels B, E and a variant of E containing additionally about 20 ppm of boron:

$M_{23}C_6$

- Nucleation of $M_{23}C_6$ precipitates is faster and their coarsening rates may be slower than in the absence of boron
- In the as-tempered condition about half of the boron is present within these carbides
- A change in composition of the $M_{23}C_6$ is seen during creep - the composition tends from the equilibrium value at the tempering temperature towards the equilibrium value appropriate to the creep testing temperature. The process is limited by the corresponding diffusion rates.

MX

- No boron has been observed within the MX particles, but in the presence of boron their morphology changes from discs to needles.

The possibility of a "latent" creep strengthening effect as a result of precipitation of MX particles on dislocations is proposed. This may be a type of dynamic regenerative precipitation, since the precipitates are believed to redissolve when the dislocations are pulled away as a result of plastic deformation. Further precipitation of MX on the dislocations is then possible. This mechanism would account for the higher dislocation densities observed in boron-containing materials as well as the improvement in creep strength, despite the comparatively low observed number of MX particles.

An analysis of the creep properties of a number of 9 to 12 % Cr steels has been published recently [11], along with a recommendation as to how the creep strength could be optimised. The nitrogen content in solid solution is considered to be critical in determining the precipitation of MX, the major creep-strengthening phase. The nitrogen content is maximised by reducing the levels of aluminium and niobium, which otherwise form nitrides which are coarse and hence ineffective from the point of view of creep strengthening.

Further development and future concepts

Steels which have so far been manufactured and tested in the COST programme have properties which permit their use in steam power plant at temperatures up to 600°C. However there is a considerable driving force to increase temperatures of operation even further in order to obtain further improvements in operating efficiency [12]. A net operating efficiency of about 50 % can be attained with steam inlet temperatures of about 620°C. Based on the development activities initiated in the present phase of the COST programme it is anticipated that such plant could be constructed and commissioned by the year 2005. For this purpose use is being made of the information and understanding gained concerning microstructural stability at elevated temperatures along with modelling activities which describe not only the equilibrium phases, but also the kinetic processes governing microstructural evolution. This constitutes a complex process of continuous nucleation, growth, coarsening and redissolution of different phases.

A further major step could then be made through the use of nickel based alloys for the high-temperature components in the steam cycle. In order to justify the use of these considerably more expensive materials a large improvement in operating efficiency will be required, and for this reason inlet temperatures are expected to rise to 700°C or more [12]. A concept for the realisation of such a high-efficiency steam power plant is under development [13]. In this design major large components such as rotors, blades, casings and main steam pipes will be exposed to temperatures of up to 720°C. Use can be made of experience obtained from the design of gas turbines, for which temperatures may be even higher. However the components will be of larger size and particular emphasis must be placed on the question of up-scaling. For construction of plant with generating capacities up to 1000 MW, rotors will be required with diameters of typically one meter and weights in excess of 20 tons. Castings will have large outer diameters (about two meters). There is as yet no experience with the manufacture of such large parts in nickel-based alloys. Attention will have to be paid to the subjects of segregation in large cast blocks, forging capability of available presses, uniformity of mechanical properties in large components and non-destructive testing capability.

Alternatively it may be appropriate to employ manufacturing techniques, such as powder metallurgy, in order to avoid segregation problems, or welding, as a means of building up large components from smaller forgings.

Conclusions

The research and development activities described here have resulted in the validation and application of a number of 9 to 12 % Cr steels with considerably improved high-temperature properties. They are appropriate for use at temperatures up to 600°C. Detailed microscopic investigations have led to an improved understanding of the mechanisms of creep strengthening and microstructural stability, on the basis of which further efforts are being made to raise the upper limiting temperature for a further range of steels. These are currently being manufactured and tested.

A further major increase in operating temperature of steam turbines to 700°C or more will only be possible through the use of nickel-based alloys. Whereas advantage can be taken of experience from the gas turbine field, larger component sizes will pose new questions.

Acknowledgements

The author is grateful to his colleagues and partners in the COST programme for their contributions to some parts of the work reported here and for many helpful discussions during the course of the work. Thanks are also extended to the COST Management Committee for their guidance of the programme and to the national funding bodies for their financial support of the individual projects.

References

- [1] Y.Nakabayashi et al., "Japanese Development in High Temperature Steam Cycles", COST Conference on High Temperature Materials for Power Engineering 1990, Liège, Belgium, Sept. 24 - 27, 1990
- [2] G.L.Toughton, "EPRI Improved Coal-Fired Power Plant Project", First International Conference on Coal-Fired Power Plants, November 21, 1986, Palo Alto, USA
- [3] C.Berger, R.B.Scarlin, K.H.Mayer, D.V.Thornton and S.M.Beech, "Steam Turbine Materials: Forgings", COST Conference on High Temperature Materials for Power Engineering 1994, Liège, Belgium, Oct. 3 - 6 1994, p.47
- [4] R.B.Scarlin, C.Berger, K.H.Mayer, D.V.Thornton and S.M.Beech, "Steam Turbine Materials: Castings", *ibid*, p.73
- [5] C.J.Franklin and C.Henry, "Material Developments and Requirements for Advanced Boilers", *ibid*, p.89
- [6] R.W.Vanstone, "Microstructure and Creep Mechanisms in Advanced 9-12 % Cr Creep Resisting Steels - A Collaborative Investigation in COST 501/3 WP11", *ibid*, p.465
- [7] Y.Sawaragi, A.Iseda, K.Ogawa and F.Masuyama, "Development of a High-Strength 12 Cr Steel (HCM12A)", *ibid*, p.309
- [8] B.Sundman, B.Jansson and J.O.Andersson, *Calphad*, 9, 2, 1985, 153 - 190
- [9] J.Hald, "Materials Comparisons between Nf616, HCM12A and TB12M - III: Microstructural Stability and Ageing", EPRI / National Power Conference, 11th May 1995, London, p.152
- [10] L.Lundin and H.O.Andren, "Atom Probe Investigation of a Creep-Resistant 12 % Chromium Steel", in *Surface Science* 266 (1992) p.397
- [11] V.Foldyna and Z.Kubon, "Optimised Composition of Chromium Steel for Rotor Forgings with respect to Maximum Precipitate Strengthening", Conference on Materials Engineering in Turbines and Compressors, 25-27 April 1995, Newcastle upon Tyne, UK, p.353
- [12] S.Kjaer, "Anforderungen an das Kraftwerk 2000/2015", Conference on Coal-Fired Power Plant in 2000/2015, 30th and 31st March 1995, Dresden, Germany, p.41
- [13] C.Berger, R.B.Scarlin, K.H.Mayer, "Werkstofftechnische Entwicklungsaufgaben für Dampfturbinen mit Eintrittstemperaturen von max. 700°C", *ibid*, p. 239

Materials for Advanced Power Plant

Dr. Thomas B. Gibbons

ABB Power Plant Laboratories

Combustion Engineering, Inc.

2000 Day Hill Road

Windsor, CT 06095

USA

Phone: (860) 285-3593 Fax: (860) 285-2513

The widespread availability of natural gas and the drive to operate with increased efficiencies to preserve resources and minimize CO₂ emissions has led to the increase in the application of gas turbine combined cycle technology for generation of power. However, a strong demand for coal-fired plant remains and efforts are being made to improve the efficiency and reduce the costs of this type of equipment.

These developments present a significant challenge to the materials engineering fraternity because materials availability and performance lie at the heart of the effort to improve power generation technologies. In this paper, some of the materials requirements for advanced power plants are described and recent developments outlined.

Introduction

Since natural gas has become available in large quantities in many countries of the world, gas turbine combined cycle units have dominated the market for power generation. The advantages of this type of system compared to the more conventional pulverized coal (PC) units that had been dominant hitherto are well known, viz:

- lower capital cost
- reduced construction time
- higher efficiency
- low emission levels

While availability remains a critical requirement for all types of power plant, improved efficiency has been a requirement in many parts of the world because of anxieties about global warming and the need to reduce emission of CO_2 . Fig. 1 shows recently published information giving the trend in average temperatures since the middle of the last century, and clearly there has been a significant increase since 1980.

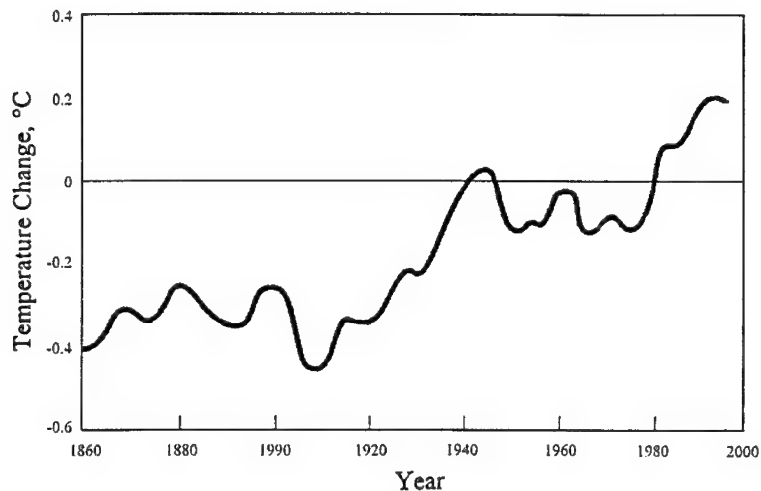


Fig. 1: Rise in average global temperature

Despite the emphasis on combined cycle plant, there remains a significant demand for PC fired units, particularly from countries in Asia where there are large supplies of coal and also in parts of Europe where natural gas is not available or supplies are unreliable. For this type of plant, the drive has been to reduce capital costs, lower construction intervals and improve efficiency to compete more effectively with combined cycle plant. Other types of power generation systems involving the use of coal such as pressurized fluidized bed combustion (pfbc) and coal gasification remain in the advanced development or demonstration stage but cost competitiveness may slow the introduction of these technologies. A comparison of costs and efficiencies of the various types of power generation system are shown in Table I. A recent innovation has been the decision to develop a power generation system based on ammonia-

steam as the working fluid, i.e., the so-called Kalina cycle, which will give benefits in increased efficiency and reduced plant costs (see Table I).

Table I: Typical values of efficiency and installed costs for modern power generation systems.

SYSTEM	TYPICAL EFFICIENCY %	INSTALLED COST \$/k W
Gas Turbine Simple Cycle	35	175
Gas Turbine Combined Cycle	55	450
Subcritical PC	38	1000
Supercritical PC	43	1150
Kalina System	45	1000
PFBC*	44	1300
IGCC*	45	1300
Nuclear	32	2000

Note: "Efficiency" refers to net plant efficiencies on a LHV basis

In this paper, the implications for the materials community will be considered in terms of the critical requirements for these competing systems. The emphasis will be on PC boilers and on gas turbine combined cycle systems where some of the most challenging materials problems have to be overcome.

Materials For Advanced PC Plant

General Considerations

In order to achieve higher efficiencies in units of this type, it is necessary to increase the steam temperatures beyond those currently in operation, and this necessarily involves an increase in steam pressure. Thus, the requirement is for materials with improved load-carrying capacity at temperatures beyond 565°C (1050°F) which is the current maximum steam temperature. A plan for the phased introduction of a higher efficiency plant has been established in Europe, driven by the demands of the Danish utilities where a decision has been made to develop ultra supercritical (USC) plant for base load power demands and the proposed development program is summarized in Table II. In order to implement this strategy, it will be necessary to improve the performance of ferritic steels currently used in boiler and steam turbine applications, but for temperatures above 650°C higher strength materials such as superalloys may be required.

Boilers

The allowable stresses as defined by the ASME Code for ferritic alloys that are currently approved for critical components in boilers are shown in Fig. 2, and it is clear that the steels based on 9-12% Cr with additions of tungsten (e.g. Gr122) provide an advantage of about 30% in strength compared with the best materials used hitherto.

Table II: Development plan for once-through supercritical power plant in Europe.

YEAR	STEAM CONDITIONS	MATERIALS		EFFICIENCY (%)
1990s	560 - 600°C	Boiler	P91 347 HFG T12, T22	45 - 47
	275 - 290 bar	Turbine	Steel F*	
2000	590 - 600°C	Boiler	P92 347 HFG T 23	47 - 48.5
	300 - 310 bar	Turbine	Steel F*	
2005	600 - 630°C	Boiler	P93 347 HFG T 23	50
	310 - 330 bar	Turbine	Steel E*	
2015	700 - 750°C	Boiler	Superalloys Austenitics T122	52 - 53
	350 - 400 bar	Turbine	Superalloys	

* Steels being developed in European Project COST 501

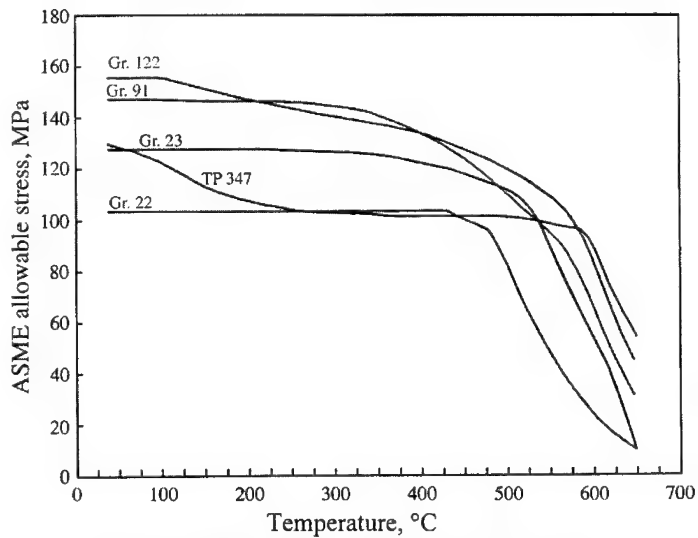


Fig. 2: ASME allowable stresses for boiler steels

Thus, materials are available for critical components such as headers, superheater sections, and main steam pipes which will be operated with metal temperatures up to about 620°C. Further

developments are in progress with the aim of enabling ferritic steels to be used at temperatures up to 650°C. These steels, which feature an addition of about 3% Co to the basic 9-12% Cr composition will show some performance improvement⁽¹⁾ and a 100,000h rupture stress of about 120 MPa at 650°C is being claimed on the basis of extrapolation from tests of up to 10,000h duration, Fig. 3.

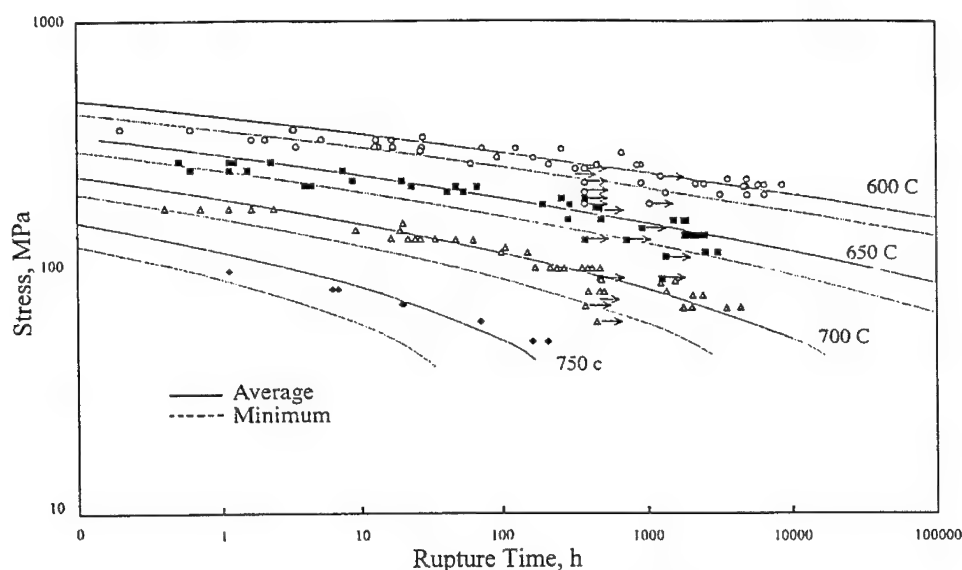


Fig. 3: Stress-rupture properties of NF 12

This evidence that further development potential exists for the 9-12% Cr steels is encouraging and raises the general question of the limit that can be reached with these steels which are strengthened mainly by carbide particles but where Laves phase is also believed to have an influence in contributing to the available strength.⁽²⁾ However, in order to achieve efficiencies of around 45%, it will be necessary to operate with higher steam temperatures, i.e., 700-750°C. The implications for materials selection of a requirement to generate steam at these temperatures has recently been considered⁽³⁾ and, based on an ASME code approach, superalloy materials, e.g. IN617, would enable these conditions to be achieved, Fig. 4. However, any advance on this requirement, e.g. to temperatures appropriate to efficiencies around 50%, with a Rankine Cycle, would require the use of stronger materials, e.g. ODS alloys.

Steam Turbine Rotors

Since any modern power plant must be capable of cyclic operation, some effort has been devoted to the development of high strength ferritic steels for this application. The lower coefficient of thermal expansion and greater thermal conductivity of these materials will result in a reduced thermal fatigue susceptibility compared with austenitic materials so that the operational flexibility of the plant will be enhanced.

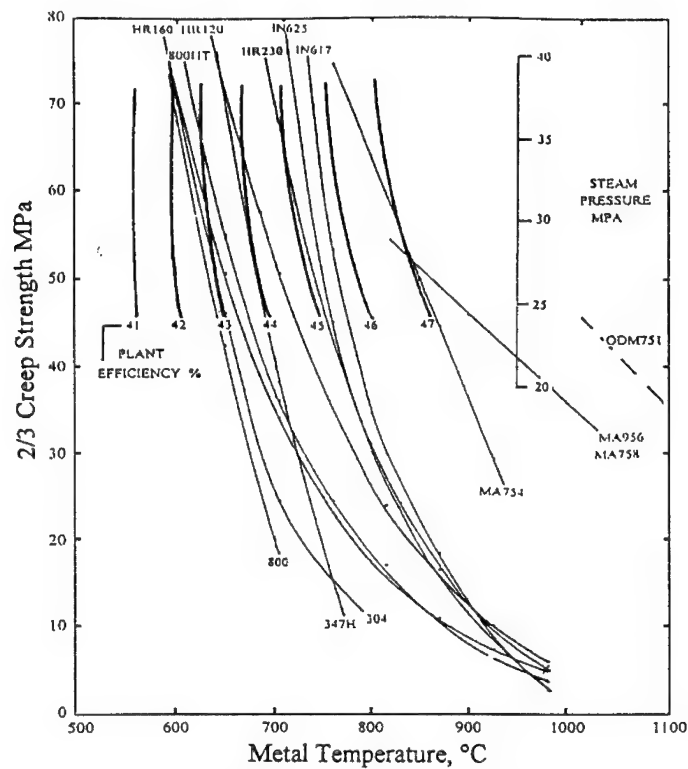


Fig. 4: ASME allowable stresses for rupture in 10^3 h. with data on efficiency and steam pressure

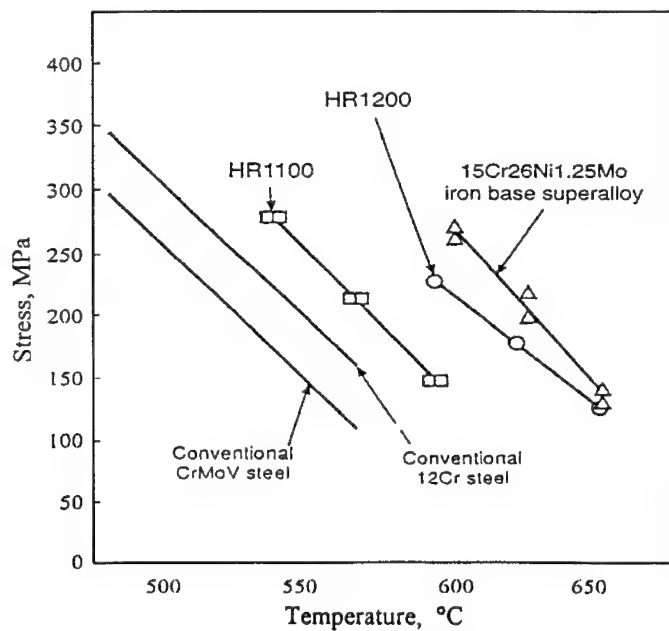


Fig. 5: Stress rupture properties of rotor steels

Activities in Europe and Japan have been focused on the development of ferritic steels with good strength at temperatures up to 650°C. Typical data on stress-rupture performance are shown in Fig. 5 where the stress for rupture in 100,000 h is shown as a function of temperature for several high strength alloys. The steel designated HR1200 clearly has rupture properties similar to those of the iron-base superalloy A286 which has been used as a turbine material in demonstrator USC plant.

The important conclusion is that in this case also, developments in ferritic steels are bridging the gap between alloy steels and superalloys and eliminating the need to consider austenitics.

Materials For Combined Cycle Gas Turbines

General Considerations

In order to achieve efficiencies of 55% or better in a gas-turbine combined cycle power plant it is necessary to increase firing temperatures substantially compared to those that were common a few years ago when lower grade fuels were burned. The impurity levels in natural gas are similar to those in aviation fuel so that the technology and operating conditions of large combined-cycle gas turbines are nowadays more akin to those of aero engines. The implications for materials for hot gas path parts have been significant and there has been a tendency to introduce materials for blades and vanes with higher strength at temperatures up to 1000°C and good oxidation resistance but reduced corrosion resistance. Also there has been increased emphasis on improved cooling technology and the application of thermal barrier coatings to allow the rotor inlet temperature (RIT) to be increased for the highest efficiency levels. Some published information on RIT values for state-of-the-art gas turbines is given in Table III and the novel combustion system in the ABB unit enables high efficiencies to be achieved for a relatively low value of RIT.

Table III: Data on rotor inlet temperatures and efficiencies of modern engines

Engine	RIT, °C	Predicted Efficiency %
Westinghouse 501G	1426	58
Siemens V84/3a	1310	57
ABB GT24/26	1240	57
GE 7FA	1290	55

In order to foster the continued development of gas turbines for combined cycle operation, the Department of Energy in the USA has initiated a major development program, the Advanced Turbine System (ATS) Program, with funding of more than \$400 million with the aim of demonstrating advanced technology capable of giving combined cycle efficiencies in excess of 60%.

Alloys for Blade and Vanes

The properties of the materials used in the hot section of the gas turbine have a critical influence on overall engine performance because the temperature capability of the alloy will determine the amount of cooling air necessary in the component which in turn has a direct influence on

efficiency. In order to operate with higher RIT the major engine manufacturers have introduced improved superalloy materials for blades and vanes with the following characteristics:

- Cr contents between 6.5 and 10% by weight
- γ' volume fraction of 50% or more
- Increased amounts of Al for strength and oxidation resistance.

However, the most important development has been the widespread introduction of directionally solidified (DS) and single crystal castings for large (300mm) components. Thus, for high pressure turbine components, technology similar to that of the aero gas turbine has been developed but for very much larger parts.

The critical factor as far as single crystal components is concerned is that grain boundary strengthening additions such as boron and zirconium can be eliminated and this allows the solution treatment temperature to be increased so that the volume fraction of γ' produced during the subsequent aging treatment can be maximized. In the casting of large components there is a greater risk of the occurrence of defects and, for example, some alloy manufacturers have retained a small amount of grain boundary strengthening addition (eg, 0.1% Hf) to avoid a serious deterioration in properties as a result of low angle boundaries. It is claimed⁽⁴⁾ that the most recently developed single crystal alloys give a temperature advantage of about 110°C compared to IN738LC in the conventionally cast form.

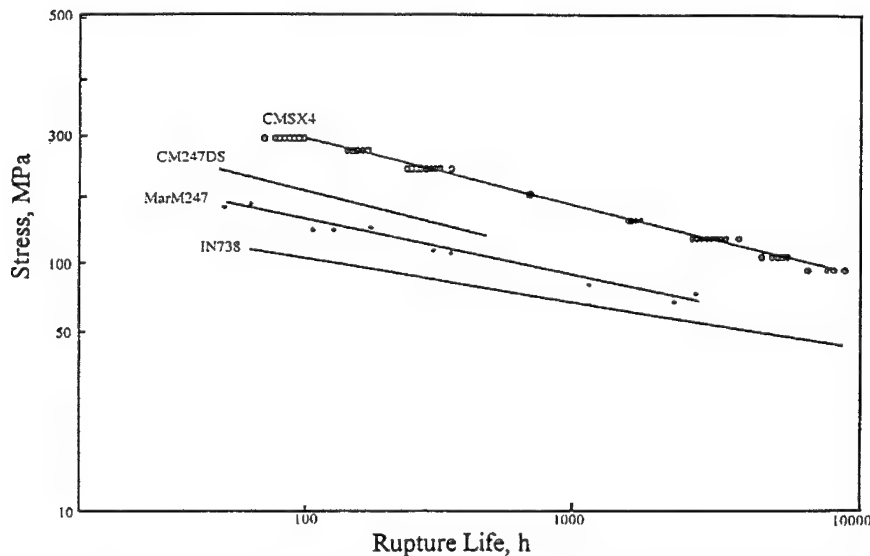


Fig. 6: Stress rupture properties at 982°C of advanced alloys for blades and vanes with data for IN738 for comparison

Compositions of some typical alloys used for directionally solidified and single crystal components are shown in Table IV. The feature to note is the absence of grain boundary strengthening additions such as B, Zr, C and Hf in the single crystal compositions and the addition of the element rhenium in some of the more recently developed alloys of this type.

Also, with the exception of alloy SC 16, the Cr level in the single crystal compositions is less than 10%. Stress rupture properties at 982°C (1800°F) are compared in Fig. 6 where data for CM247 in directionally solidified and conventionally cast form and for the single crystal alloy developed from this composition CMSX4 have been plotted together with results for the well-established alloy IN738LC.

Table IV: Compositions of directionally solidified and single crystal alloys in weight percent with the balance Ni in each case.

Alloy	Cr	Co	Mo	W	Al	Ti	Ta	B	Zr	C	Hf	Others	Density ρ (Mg/m ³)
Directionally Solidified													
CM247LC	8.1	9.2	.5	9.5	5.6	.7	3.2	.015	.015	.07	1.4	--	8.54
GTD111	14	9.4	1.5	3.7	3	5	3	.100	.010	.10	.15	--	8.3
IN792LC	12.5	9	1.85	4.1	3.4	3.8	4.1	.015	.020	.08	1	--	8.4
Alloy I	12	9	--	9	3.5	3	5	.012	.010	.07	--	--	--
Single Crystal													
CMSX-4	6.5	9	.6	6	5.6	1	6.5	--	--	--	.1	3.0 Re	8.7
PWA1484	5	10	2	6	5.6	--	9	--	--	--	.1	3.0 Re	8.95
Rene N4	9	8	2	6	3.7	4.2	4	--	--	--	--	.5 Nb	8.56
SC 16	16	--	3	--	3.5	3.5	3.5	--	--	--	--	--	8.21
MC2	8	5	2	8	5	1.5	6	--	--	--	--	--	8.63

The significant improvement in strength obtained with the lower Cr alloys is evident and can be attributed to the larger volume fraction of the γ' strengthening phase present in these materials. Also the effect of directionally solidified and single crystal structures in providing an enhancement in performance compared to the conventionally cast material is clearly demonstrated. By comparison with IN738, the load carrying capacity of the single crystal alloy is greater by a factor of about three. Some further improvement in the performance of single crystal materials can be expected and one approach has been to increase the amount of Re addition while lowering the Cr level to about 5% by weight.

Disc Alloys

With the higher temperatures in the high pressure turbine sections of modern engines, a replacement has had to be provided for the low alloy steels traditionally used hitherto for turbine discs. The alloy which has emerged as an appropriate material is IN706, which is a "lean" version of the well-established alloy IN718 widely used in aero applications. The difficulty that must be overcome is to develop processing methods which will allow large diameter discs to be produced with consistent properties throughout the section.⁽⁵⁾

Table V: Compositions of disc alloys in weight percent

Alloy	C	Mn	Si	Cr	Ni	Fe	Ti	Al	Mo	Nb+Ta
706	.03	.2	.2	16	41.5	40	1.8	0.2	--	2.9
718	.04	.2	.2	19	52.5	18.5	0.9	0.5	3	5.1

The composition of the alloy is shown in Table V together with that for IN718 and the development program for large turbine discs focused on four main requirements:

- freedom from segregation in larger sizes than those possible for IN718
- hot workability within the capabilities of existing forging facilities
- better machinability than IN718
- no increase in costs compared to IN718

In order to achieve these objectives, the chemistry was modified to improve fabricability, i.e., forging, machining and welding while maintaining strength and phase stability to ensure adequate toughness. The alloy is produced by a triple melting process involving vacuum induction melting (VIM) followed by electro-slag remelting (ESR) and vacuum arc remelting (VAR). The VIM stage provides the clean starting material with well controlled chemistry, further refining is carried out during ESR and the final VAR involves a shallow melt pool to minimize segregation. The result is an ingot free of macro-segregation which can be forged and heat-treated to optimize either tensile strength or creep resistance and typical tensile data are given in Fig. 7. The alloy is now used for large discs typically 1900 mm diameter, 300 mm thick in advanced gas turbines for power generation.

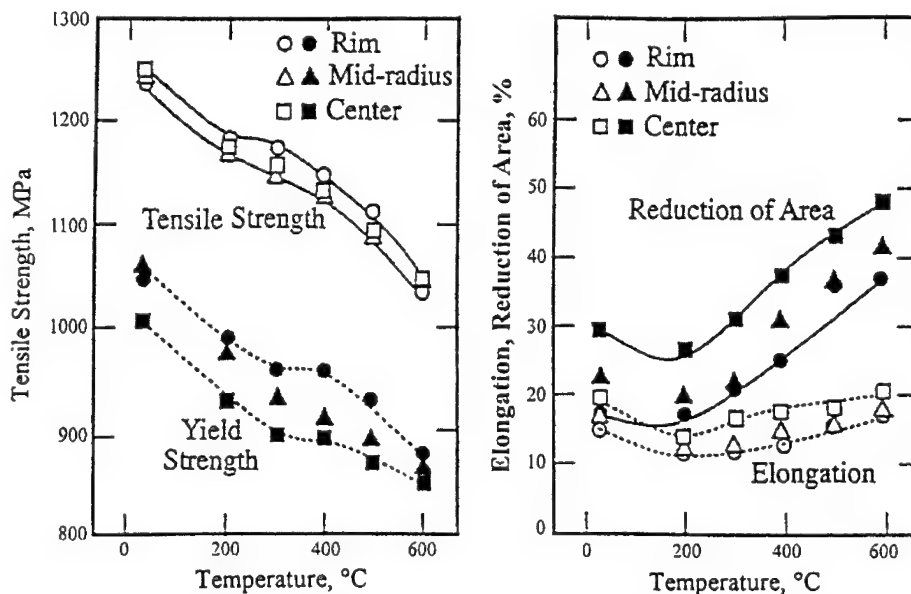


Fig. 7: Tensile properties for IN706 as a function of temperature

Future Advances

A key area of materials development is in the application of ceramics as thermal barrier coatings (TBCs) on gas turbine blades and vanes, and it is evident from Fig. 8 that the use of this type of coating in industrial engines is at a relatively early stage of development compared with military applications.

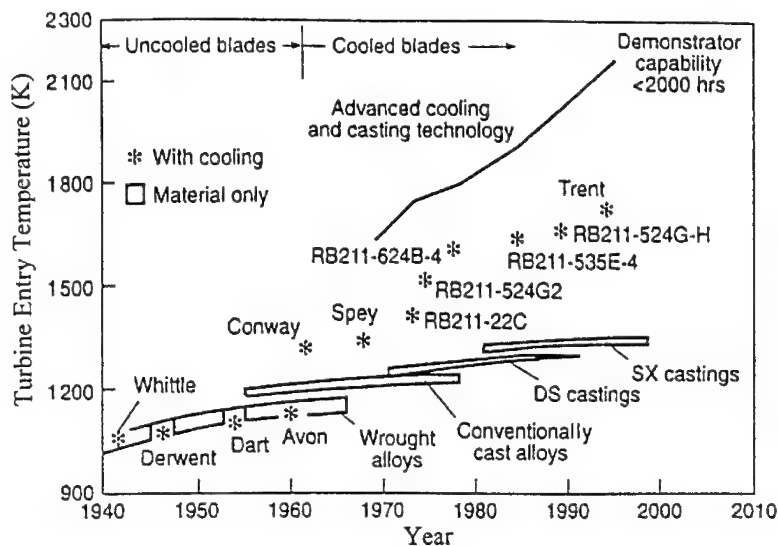


Fig. 8: Illustration of benefit in increased TET as a result of combined effects of thermal barriers and blade cooling

Hitherto, for large engines, TBCs have largely been applied to give an added margin of protection for a component where conditions were likely to be demanding. The aim of current development work is to apply coatings of this type in a "prime reliant" mode, i.e., where the design of the component assumes the presence of an effective thermal barrier to limit the metal temperature to provide the desired component lifetime. In order to achieve this objective, a coating system with the following characteristics is required:

- good adherence to substrate
- resistance to cracking in thermal cycling
- resistance to erosion

Current technology for large components involves a coating of zirconia stabilized with yttria and applied by an APS method which provides a fairly porous structure with a rough surface. An alternative method which is now widely used for aero-engine components involves vaporization of ceramic in an electron beam (EB) and deposition on the substrate. This technique of electron-beam physical vapor deposition (EB-PVD) gives a columnar grained structure tolerant to thermal stress, and with a smooth surface.

With an efficient blade cooling system and a suitable thickness of TBC, the metal temperature can be reduced by about 300°C thereby enhancing the life of the component and reducing the rate of degradation of the bond coat. For reliable coatings in a "prime reliant" application, the properties of the bond coat, which provides oxidation protection, an adherent surface and has a coefficient of thermal expansion intermediate between that of the ceramic and the metal substrate, are critical. Bond coats are typically M CrAlY type overlay coatings about 50 µm thick, with Al contents of about 25% for good oxidation resistance. Since the strains induced in the TBC by growth of the oxide layer on the bond coat are believed to be a major cause of spalling of the TBC, the oxidation rate of the bond coat is an important factor in the overall durability of the TBC.

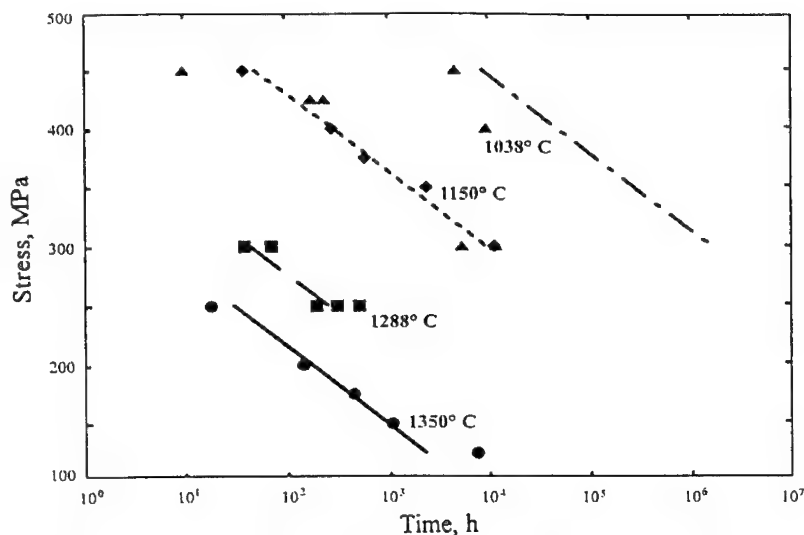


Fig. 9: Stress-rupture properties of silicon nitride: the lines were calculated on the basis of a Monkman-Grant model

Some effort continues, particularly in the USA and Japan, to develop monolithic ceramics for blade and vane applications in gas turbine engines. An important development in this regard has been the work within the ATS Project to develop a database for component design in silicon nitride and silicon carbide.⁽⁶⁾ A key factor has been the procurement of relatively long-term creep and stress-rupture data, in tension, for these ceramic materials and typical results are shown in Fig. 9. Since metal temperatures are currently around 1000°C with about 300°C of cooling, it is evident that ceramic parts will be required with good strength at temperatures of 1300°C and above. The availability of a suitable database on well-established materials will be an important step in assessing the extent to which monolithic ceramics will find future applications in gas turbines for power generation.

Conclusions

1. The introduction of higher steam temperatures in PC power plants will depend on the continued development of steels for critical components.
2. Materials such as superalloys and ODS alloys offer considerable potential provided costs can be reduced and consistency of properties assured.
3. Substantial progress has been made in introducing aero-engine technology in combined cycle gas turbines and efficiency gains have been substantial.
4. Further progress will depend on the development of prime reliant thermal barrier coating systems.

Acknowledgment

The author gratefully acknowledges the generous assistance of the following in providing some of the data presented in the paper: Dr. H. Naoi, Nippon Steel, Fig. 3; C. Lund, Martin Marietta (M247) and Dr. K. Harris, Canon Muskegan (CMSX4), Fig. 6; and Dr. K. Breder, Fig. 9.

References

1. H. Naoi, Nippon Steel Corporation, private communication, April 1996.
2. J. Hald, Proceedings, "New Steels for Advanced Plant up to 620°C", The Society of Chemical Industry, London, May 1995, ed. E. Metcalfe, 152.
3. N. Birks and C.A. Smith, Proceedings, "Materials Issues in Heat Exchangers and Boilers", The Institute of Materials, to be published.
4. R.L. Bannister et al, Mechanical Engineering, June 1994, 68
5. P.W. Schilke, J.J. Pepe, and R.C. Schwant, Proceedings, "Superalloys 718, 625, 706", ed. E.A. Loria, (TMS Publications, 1994), 1
6. K. Breder, unpublished work at Oak Ridge National Laboratory, Oak Ridge, Tennessee

INTERMETALLICS

DESIGN OF Ni₃Al ALLOYS FOR STRUCTURAL USE*

*C. T. Liu, E. P. George, V. K. Sikka and S. C. Deevi***

*Metals and Ceramics Division
Oak Ridge National Laboratory
Oak Ridge, TN 37831*

Abstract

This paper provides a brief review of recent advances in research and development of Ni₃Al-based alloys. Recent studies indicate that binary Ni₃Al is intrinsically quite ductile at room temperature, and its poor tensile ductility and brittle grain-boundary fracture are caused mainly by moisture-induced hydrogen embrittlement when the aluminide is tested in ambient air. Boron additions suppress environmental embrittlement and enhance grain-boundary cohesion, resulting in a dramatic increase of tensile ductility at room temperature. Both B-doped and B-free Ni₃Al alloys exhibit brittle intergranular fracture and low ductility at intermediate temperatures (300-850°C) because of oxygen-induced embrittlement in oxidizing environments. Chromium is found to be most effective in alleviating elevated-temperature embrittlement. Parallel efforts on alloy development using physical metallurgy principles have led to the development of several Ni₃Al alloys with promising mechanical and metallurgical properties for structural use.

*Research sponsored by the Division of Materials Sciences, U.S. Department of Energy, under contract number DE-AC05-96OR22464 with Oak Ridge National Laboratory, managed by Lockheed Martin Energy Research Corporation.

**Guest Scientist from Philip Morris Research and Development Center, Philip Morris, Richmond, VA 23234.

"The submitted manuscript has been authored by a contractor of the U.S. government under contract NO. DE-AC05-96OR22464. Accordingly, the U.S. Government retains a nonexclusive, royalty-free license to publish or reproduce the published form of this contribution, or allow others to do so, for U.S. Government purposes."

Processing and Design Issues
in High Temperature Materials
Edited by N.S. Stoloff and R.H. Jones
The Minerals, Metals & Materials Society, 1997

Introduction

For the past two decades, considerable efforts have been devoted to the study of brittle grain-boundary fracture and alloy design of the nickel aluminide, Ni_3Al , for structural use at elevated temperatures in hostile environments [1-4]. Ni_3Al is the most important strengthening constituent, referred to as the γ' phase, in commercial Ni-base superalloys which are used extensively as high-temperature structural materials for jet-engine and aerospace applications. It is responsible for the strength and creep resistance of the superalloys at elevated temperatures. In addition, Ni_3Al containing about 24 % Al has the ability to form protective aluminum oxide scales in oxidizing environments, resulting in excellent oxidation resistance.

Single crystals of Ni_3Al are highly ductile, whereas its polycrystals are brittle at ambient temperatures. The brittleness of Ni_3Al originates at its grain boundaries. Contrary to the common experience with conventional materials, Ni_3Al grain boundaries are usually clean and free of impurities, as evidenced by Auger analyses [5,6]. Similar results were observed in other L1_2 ordered intermetallics [1-4]. Because of both scientific and technical interest, substantial effort has been focused on the understanding of the intrinsic grain-boundary brittleness in Ni_3Al and other L1_2 intermetallics [7]. Only recently has it become clear that binary Ni_3Al is actually quite ductile at room temperature, and its brittle grain-boundary fracture and low ductility are caused mainly by moisture-induced hydrogen embrittlement when the aluminide is tested in ordinary laboratory air [8-13]. Similar environmental effect has been observed in many other intermetallic alloys with the L1_2 structure [14].

The structural use of polycrystalline Ni_3Al was hampered by its brittle grain-boundary fracture at ambient and elevated temperatures. In 1979, Aoki and Izumi [15] first reported that the tensile ductility of Ni_3Al polycrystals was substantially improved by doping with boron additions. Then, Liu et al. [5] found that boron has a strong tendency to segregate to Ni_3Al grain boundaries and that the best ductilizing effect can be achieved only in Ni_3Al with hypostoichiometric compositions (≤ 24 at. % Al). These results have stimulated the interest in the study of alloying effects and alloy design of ductile polycrystalline Ni_3Al alloys for structural applications. At present, several Ni_3Al -based alloys with promising mechanical and metallurgical properties have been developed, and they are now on the market for industrial use.

This paper provides a brief review of research and development of Ni_3Al alloys. Since several review papers on Ni_3Al alloys were published in conference proceedings [10,12,13], this paper will focus mainly on the recent progress, with emphasis on recent study of environmental embrittlement in Ni_3Al alloys. In addition to the introduction section, this paper contains five additional sections: (1) brittle grain-boundary fracture and ductility improvement at ambient temperatures, (2) oxygen-induced embrittlement and ductility improvement at intermediate temperatures, (3) alloy design of polycrystalline Ni_3Al , (4) materials processing and industrial use, and (5) concluding remarks.

Grain-boundary Fracture and Ductility Improvement at Ambient Temperatures

Ni_3Al , like many other L1_2 intermetallics, showed brittle grain-boundary fracture with limited tensile ductility at room temperature [5,15]. The brittle intergranular fracture is caused by two major factors: poor grain-boundary cohesion (intrinsic factor) and

environmental embrittlement (extrinsic factor) [8]. Previous studies suggested that the grain-boundaries in Ni₃Al were intrinsically brittle. This was based mainly on the Auger analyses which showed no appreciable segregation of impurities on fractured grain-boundary facets [5,6]. During the past several years, however, sufficient evidence has evolved to assert that moisture-induced hydrogen is a major cause of brittle grain-boundary fracture when Ni₃Al alloys are tested in ordinary laboratory air [8-13]. It should be noted that both the intrinsic and extrinsic factors are affected to a certain extent by other metallurgical parameters such as alloy stoichiometry, thermomechanical treatments, impurities, and alloy additions [5,12,16]

In 1991, Liu et al. [8,17] had made a first attempt to link brittle intergranular fracture with environmental embrittlement in binary Ni₃Si and Ni₃Al. Table 1 shows the tensile properties of recrystallized polycrystalline Ni₃Al (24% Al) produced by repeated cold forging and 1000°C-annealing of a cast ingot [8]. The binary aluminide showed only 2.6 % elongation in air but 7.2 % in dry oxygen, an increase in ductility by a factor of about 3. Later, George et al. [9] reported a larger environmental effect in polycrystalline Ni₃Al (23.4%) carefully prepared by recrystallization of cold-worked single-crystal material. This polycrystalline material also showed a tensile ductility of 3 % in air. However, as shown in Fig. 1, its tensile ductility increases steadily as the vacuum improves, and it reaches as high as 23 % in a ultra-vacuum of 10⁻⁸ Pa. Their work vividly demonstrated the dominant role of environmental effect on tensile ductility of Ni₃Al at room temperature [9,12].

Table 1. Effect of Boron Additions on Environmental Embrittlement of Ni₃Al (24%Al)
Tested at Room Temperature

Strain Rate (s ⁻¹)	Test Environment	Elongation (%)	Yield Strength (ksi)	Ultimate Tensile Strength (ksi)
<u>IC-2: Ni-24 at. % Al</u>				
3.3 x 10 ⁻³	Oxygen	7.2	40.5	63.7
3.3 x 10 ⁻³	Air	2.6	40.6	48.3
<u>IC-19: Ni-24%Al + 100 wt ppm B</u>				
3.3 x 10 ⁻³	Oxygen	39.5	31.4	189.3
3.3 x 10 ⁻³	Air	18.2	31.2	101.4
3.3 x 10 ⁻³	Water	12.6	30.1	75.2
<u>IC-15: Ni-24%Al + 500 wt ppm B</u>				
3.3 x 10 ⁻³	Oxygen	39.4	41.9	190.8
3.3 x 10 ⁻³	Air	41.2	42.1	182.9
3.3 x 10 ⁻⁵	Air	39.4	39.1	177.3
3.3 x 10 ⁻⁵	Water	38.7	41.8	174.0

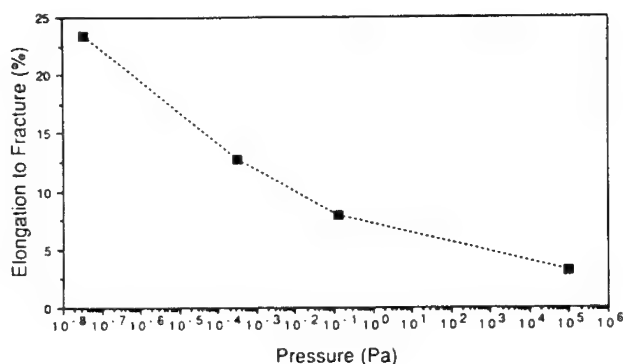


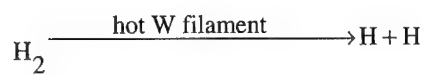
Figure 1. Room-temperature tensile ductility of polycrystalline Ni-23.4 at. % Al as a function of vacuum level [9].

The environment effect in Ni₃Al, as well as other aluminides, can be simply explained by a chemical reaction [18,19]:



In this case, aluminum atoms in Ni₃Al react with moisture in air during testing, resulting in the generation of atomic hydrogen that penetrates into crack tips and causes brittle grain-boundary crack propagation and premature failure. This embrittlement is similar to hydrogen embrittlement [20-22], except that here hydrogen is generated by dissociation of moisture in air, rather than hydrogen sources such as hydrogen gas or cathodically charged hydrogen. Consistent with the reaction in Eq. 1, a better ductility is generally obtained in a vacuum chamber when it is evacuated and back filled with dry oxygen, which suppresses hydrogen generation by direct formation of Al₂O₃. The degree of the embrittlement is affected by two major factors: dissociation kinetic and hydrogen diffusion at crack tips. The embrittlement can be reduced by increasing testing velocity, as observed experimentally [12].

Gleason et al.[23] first reported the possible release of hydrogen from water decomposition on surfaces of polycrystalline aluminides using a temperature-programmed-desorption technique. Recently, Chia and Chung [24] studied the reaction of D₂O molecules with single-crystal Ni₃(Al,Ti) and discovered that the reaction kinetics strongly depend on the crystallographic orientation of the surfaces. The thermal desorption spectra shown in Fig. 2 indicate that D₂O chemically adsorbed reacts with (100) planes and generates deuterium during heating of the specimens to 200°K and above. Their results clearly confirm the suggested reaction of moisture with aluminides at ambient temperatures. On the other hand, no D₂ was detected during thermal desorption from the (111) surfaces on which D₂O had been chemically adsorbed. This provides the evidence that the moisture reaction is highly dependent on atomic arrangement and chemical composition of crystallographic planes. Furthermore, Zhu et al. [25] successfully detected atomic hydrogen, produced by



Eq. 2

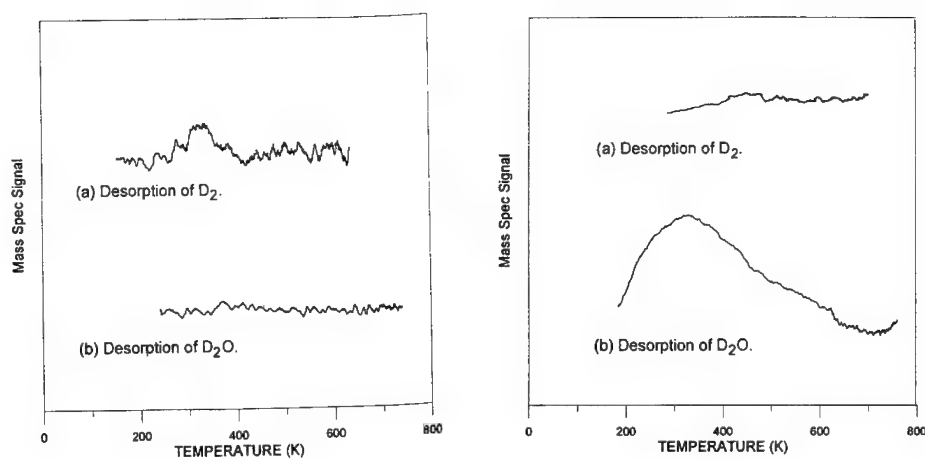


Figure 2. Thermal desorption spectra from Ni₃(Al,Ti) on (a) (100) surfaces and (b) (111) surfaces after exposure to D₂O at 200°K [24].

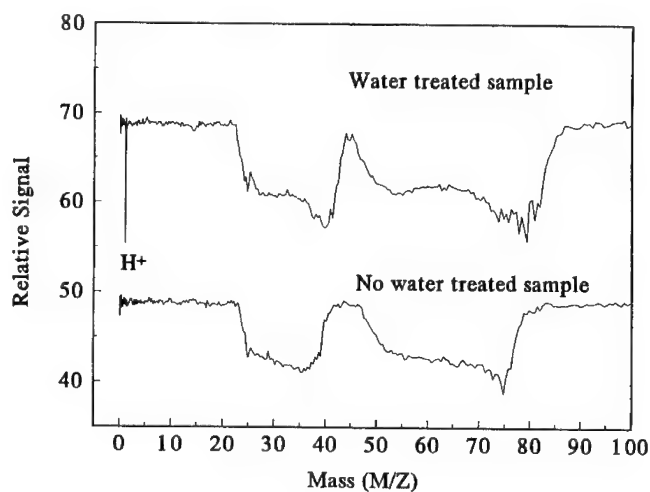


Figure 3. Measurement of H in vacuum-treated (no water) and water-treated FeAl samples using Laser Desorption Mass Spectrometer [25].

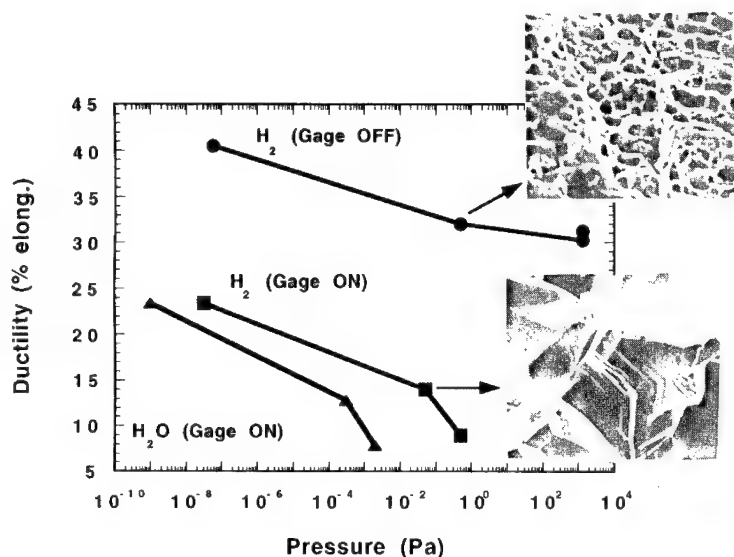


Figure 4. Effect of test environment (H_2O and H_2) and ion gage (hot filament) on room-temperature ductility of Ni_3Al (23.4 at. % Al) [26].

the reaction of moisture with an iron aluminide, using laser desorption mass spectrometry. As shown in Fig. 3, H was clearly detected in the FeAl specimens treated with water, while such H was not detected in FeAl specimens treated in vacuum. All these results provide a direct support of the proposed mechanism that moisture-induced hydrogen is the cause of severe embrittlement in aluminide alloys when tested in moisture-containing environments at ambient temperatures. Recently, Cohren et al. [26] compared the embrittlement effect of moisture with that of low-pressure H_2 gas in Ni_3Al . Their results are shown in Fig. 4. H_2 at low pressures ($<10^2$ Pa) does not severely embrittle polycrystalline Ni_3Al (23.4 % Al) with the ionization gage (used to measure the vacuum) off, suggesting that molecular H_2 does not dissociate very efficiently into atomic H on Ni_3Al surfaces. On the other hand, low-pressure H_2 is readily dissociated into atomic H by the hot tungsten filament (see Eq. 2) in an ionization gage, which in turn causes a severe embrittlement of Ni_3Al .

The tensile ductilities measured with the ionization gage on are about half to a quarter of those measured with the gage off. The decrease in the tensile ductilities is accompanied by a change in the fracture mode from ductile transgranular to brittle intergranular. Their results clearly indicate that it is atomic H which causes severe embrittlement, and that the degree of embrittlement is strongly influenced by the kinetics of dissociation processes from hydrogen-containing molecules into atomic H.

The tensile ductility of Ni_3Al can be improved by substitutional and interstitial alloying elements [10,27]. Among all the elements, boron is found to be most effective in eliminating brittle grain-boundary fracture and increasing tensile ductility of Ni_3Al with hypostoichiometric compositions (≤ 24 % Al) [5]. This is because B is able to enhance grain-boundary cohesion and suppress environmental embrittlement. The beneficial effect

of B is also shown in Table 1. Ni_3Al (24 % Al) doped with 100 wppm B showed a ductility as high as 40 % in dry oxygen at room temperature. The ductility, nevertheless, decreased to 18.2 % in air and 12.6 % in water, indicating that doping with 100 wppm B is sufficient to take care of the poor grain-boundary cohesion but insufficient to suppress the environmental embrittlement. The aluminide doped with 500 wppm B, on the other hand, showed a high ductility of 40 % and transgranular fracture, independent of test environments and strain rates. These results suggest that both grain-boundary cohesion and environmental embrittlement problems have been solved by doping with as much as 500 wppm B. Auger studies showed that B tends to segregate to Ni_3Al grain boundaries and that the amount of segregation depends on the bulk concentration of B [28]. Apparently, B at levels >100 ppm is required to suppress moisture-induced hydrogen embrittlement along the grain boundaries. Furthermore, it is found that even more B doping is necessary in order to ductilize Ni_3Al with near stoichiometric and hyperstoichiometric compositions.

The work by Wan et al. [29] demonstrated the boron doping reduces hydrogen diffusion along Ni_3Al grain boundaries. In their study, they charged hydrogen cathodically in Ni_3Al doped with 120 and 1000 wppm B. By measuring the depth of the grain-boundary fractured region and correlating it with the mean square penetration depth of hydrogen during cathodic charging, they estimated the grain-boundary diffusivity (D) of hydrogen in two B-doped materials:

$$\frac{D_{120 \text{ ppm B}}}{D_{1000 \text{ ppm B}}} = 17 \quad \text{Eq. 3}$$

This result suggests that boron doping slows down hydrogen diffusion along Ni_3Al grain boundaries and reduces the severity of moisture-induced embrittlement.

Oxygen-induced Embrittlement and Ductility Improvement at Intermediate Temperature

Test environment affects the ductility and fracture in polycrystalline Ni_3Al alloys at not only ambient temperatures but also elevated temperatures. As mentioned in the foregoing section, ambient-temperature embrittlement is associated mainly with hydrogen released from the reaction of moisture in air with aluminum atoms in Ni_3Al . The embrittling agent at elevated temperatures is oxygen that penetrates along grain boundaries and causes brittle intergranular fracture [30-33]. Single crystals of Ni_3Al also show a ductility minimum at intermediate temperatures [34], which may also be related to environmental embrittlement.

Recently, George et al. [11] studied the tensile properties as functions of test temperature and environment for polycrystalline binary Ni_3Al (23.4 % Al) produced by careful recrystallization of cold worked single-crystal material. Figure 5 is a plot of tensile ductility as a function of test temperature for different test environments. The air-tested curve shows two ductility drops located at around room temperature and 500°C. The low-temperature drop is caused by moisture-induced hydrogen embrittlement, while the higher temperature one is due to oxygen-induced embrittlement. These embrittlements can be readily understood by comparing the ductility in vacuum with that in air or oxygen. At elevated temperatures, tests in O_2 yield the same low ductilities as those in air, demonstrating that the elevated-temperature embrittlement is due to O_2 . Early studies showed that B-doped Ni_3Al alloys exhibited this elevated-temperature ductility trough [30-32] (see Fig. 6), indicating that B is not able to suppress O_2 -induced embrittlement.

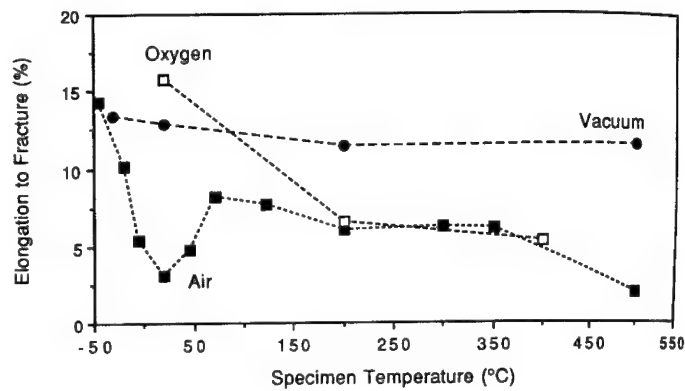


Figure 5. Effect of temperature on tensile ductility of polycrystalline B-free Ni_3Al (23.4%Al) in air, vacuum, and oxygen [11].

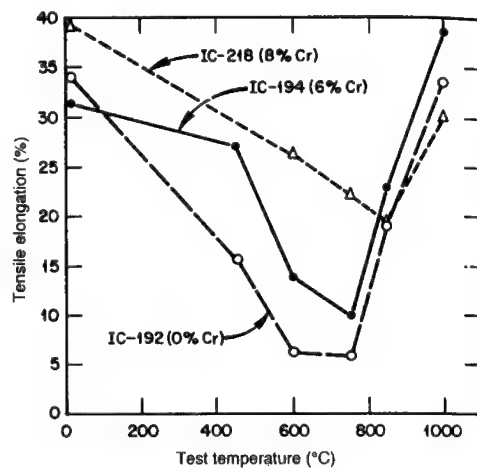


Figure 6. Effect of Cr additions on the tensile elongation of Ni_3Al alloys tested at room temperature to 1000°C [31].

The environment affects not only the tensile properties but also the fatigue behavior. Stoloff et al. reported that the fatigue life of Ni_3Al (24 % Al) prepared by powder metallurgy [35] showed a sharp drop in fatigue life above 500°C in a vacuum of 10^{-3} Pa. This result suggests that a conventional vacuum is not good enough to suppress the embrittlement in alloys containing 24 % Al. The drop in the fatigue life was accompanied with a change in fracture mode from transgranular to intergranular.

The embrittlement at elevated temperatures is mainly due to a dynamic effect involving simultaneously gaseous oxygen, elevated temperature, and localized stress concentration [32]. Such a dynamic effect involves repeatedly weakening and cracking the grain boundaries as a result of oxygen absorption and penetration at crack tips. The reduction in the ductility of Ni_3Al alloys is always accompanied by a change in fracture mode from ductile transgranular to brittle intergranular. Hipsley and Devan [36] proposed a model to explain the multi-sequential steps required for such an embrittlement.

Environmental embrittlement by oxygen is dependent on its penetration along grain boundaries at crack tips. Takeyama and Liu [37] found that the grain size in Ni_3Al plays an important role in the formation of protective oxide films that affect oxygen penetration along grain boundaries. In their study, Ni_3Al specimens with various grain sizes (17-200 μm) were preoxidized at 1000°C for 10 min and then tensile tested at 600 and 760°C in vacuum. The results are compared with those from bare specimens tested in vacuum [38] in Figure 7. The preoxidation causes no embrittlement in the fine-grained, boron-doped Ni_3Al ; however, the ductility of the preoxidized specimens decreases with increasing grain size, despite the fact that the ductility of bare specimens is nearly insensitive to the grain size. A severe embrittlement occurs at 760°C for the largest-grained material, with a change in fracture mode from ductile grain boundary fracture for the bare specimen to completely brittle grain boundary fracture for the preoxidized specimen. The loss of ductility is attributed to oxygen penetration along the grain boundary during the preoxidation treatment. Auger analyses revealed a large amount of oxygen on the grain boundaries in the preoxidized, large-grained specimen but little oxygen in the bare specimen. The analyses also revealed an oxygen gradient from surface to specimen center, indicating a diffusion of oxygen along the grain boundaries in the preoxidized specimen.

The interesting result with the Ni_3Al preoxidation is the finding of no oxygen at grain boundaries by Auger analyses of preoxidized, fine-grained specimens. Such grain-size dependence of oxygen penetration is related to the difference in formation of surface oxide films in the fine-grained and large-grained specimens: a continuous, thin, aluminum-rich oxide layer on the specimen surfaces of the fine-grained materials, and a predominantly nickel-rich oxides on the large-grained samples. The former layer effectively blocks oxygen penetration into the alloy and prevents any loss of ductility, whereas the latter allows oxygen to penetrate along the grain boundary and causes severe embrittlement. Formation of aluminum-rich oxide in the fine-grained specimen is a result of short-circuit-path diffusion of aluminum atoms from interior to surface along the grain boundaries.

Oxygen-induced embrittlement is the main cause of the low ductility and brittle fracture in Ni_3Al at elevated temperatures. This problem can be alleviated or reduced by (i) control of surface conditions, (ii) control of grain shape, and (iii) alloy additions. Control of surface conditions is a simple way to alleviate environmental embrittlement resulting from surface reactions. In several cases, preoxidation to form protective oxide scales was proven to be beneficial in reducing oxygen embrittlement at elevated temperatures [32]. Unfortunately, the oxide films are cracked after a couple of percent strain during tensile testing, and their protective effect disappears. Surface coating with ductile materials should be useful in protecting underlying materials; however, this effect has not yet been well demonstrated. Columnar-grained structures produced by directional solidification has been shown to be effective in reducing environmental embrittlement in Ni_3Al at elevated temperatures [39].

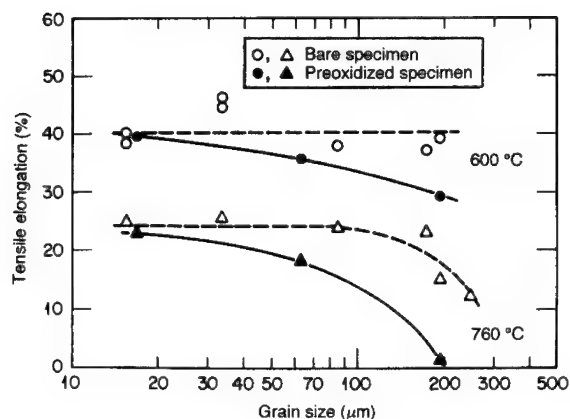


Figure 7. Change in ductility with grain size of bare and preoxidized Ni_3Al with boron ($\text{Ni-23Al-0.5Hf-0.5B}$, at. %) tested at 600 and 760°C in vacuum.

Liu and Sikka [31] found that chromium is effective in alleviating elevated-temperature embrittlement in oxidizing environments. Figure 6 shows that alloying Ni_3Al with 8 at. % Cr substantially reduced the environmental embrittlement at 600-800°C in air. The chromium containing alloys, however, exhibit better ductility in vacuum than in air, indicating that this embrittlement is not completely eliminated by chromium additions. The beneficial effect of chromium is considered to be associated with self-healing films of chromium oxides that reduce the penetration of oxygen into grain boundaries. The chromium effect is sensitive to alloy composition, with the best result from alloys containing 10-15 vol. % of the disordered γ phase. We found that no other elements have a beneficial effect on oxygen-induced embrittlement in Ni_3Al alloys.

Alloy Design of Polycrystalline Ni_3Al Alloys

The mechanical and metallurgical properties of polycrystalline Ni_3Al can be improved by alloying additions. Through alloy design efforts in past years, several Ni_3Al -based alloys with improved properties were developed for structural use [31,40,41]. The composition of these alloys are listed in Table 2.

In these aluminide alloys, chromium at a level of 7 to 9 at. % is added for reducing environmental embrittlement in oxidizing environments at elevated temperatures. Zirconium or hafnium additions are most effective in improving the high-temperature strength via solid-solution hardening effects. Molybdenum additions are used for improving strength at ambient and elevated temperatures. Microalloying with boron reduces moisture-induced hydrogen embrittlement and enhances grain-boundary cohesive strength, sharply increasing the ductility at ambient temperatures. Carbides and borides are added to the alloys for additional strengthening effects. In some cases, moderate amounts of cobalt and iron are added to replace Ni, and Al and Ni, respectively, in order to gain further hardness and corrosion resistance. The alloys with optimum properties usually contain 5-15 vol% of the disordered γ phase which has the beneficial effect of reducing environmental embrittlement in oxidizing atmospheres.

Table 2. Compositions of Ni₃Al-base Alloys Available Commercially

Alloy No.	Composition (wt %)		Remarks
IC-50	Ni-11.3Al	-0.6Zr-0.2 B	Fabricable
IC-218	Ni -8.7Al-8.1Cr	-0.2Zr-0.02 B	Fabricable
IC-221M	Ni -8.0Al-7.7Cr-1.4Mo-1.7Zr-0.008B		Cast
MX-246*	Ni -8.5Al-7.8Cr-0.9Ti -1.7Zr-0.10B-0.5Mn-0.1C		Fabricable

* From ref. 41.

Cast aluminide alloys usually possess a coarse grain structure which lowers the yield strength at ambient temperatures. The strength can be increased by alloying with molybdenum via solid-solution hardening [40]. Figure 8 compares the tensile properties of a cast Ni₃Al alloy (IC-221M) with commercial alloys, such as the cast superalloy IN-713C that is commonly used at high temperatures by industry. The strength of the advanced aluminide alloy is comparable to that of IN-713C at room temperature, but it is higher at elevated temperatures because of the significant increase in yield strength with temperature. The aluminide alloys prepared by investment casting showed excellent fatigue resistance. As indicated in Figure 9, the 650°C high-cycle fatigue life of IC-221M is higher than that of IN-713C by more than two orders of magnitude [42]. The cast aluminide alloys usually have tensile elongations of 10-30% at room and elevated temperatures.

The wrought aluminide alloys such as IC-218 could be fabricated by cold rolling or hot extrusion. These alloys are not easy to fabricate by hot rolling. The wrought alloys with fine grain structures have excellent strengths at ambient temperatures ($\sigma_y > 600$ MPa), but lower creep resistance because of grain-boundary sliding [43] above 700°C. The alloys generally showed good fatigue crack growth resistance [44]. The fatigue and crack growth behaviors of Ni₃Al alloys are sensitive to the test environment; nevertheless, the aluminide alloys containing Cr show fatigue-crack resistance better than Cr-free alloys when tested in air at elevated temperatures.

Because of high Al concentrations combined with 8 % Cr, the Ni₃Al alloys in both cast and wrought conditions have excellent oxidation and carburization resistances. The superior oxidation resistance of the aluminide alloys is shown in Fig. 10 for oxidizing in air with 5 % water vapor at 1100°C [45]. No appreciable weight change was observed in the aluminide alloys even when oxidized with a 250-d exposure, whereas Alloy 800 lost over 150 mg/cm² over a 40-d exposure [45]. The aluminide alloys offer excellent carburization resistance as compared to many of the furnace fixture materials such as HU, HK, and Alloy 800 alloys (Fig. 11). The excellent oxidation and carburization resistances allow the use of Ni₃Al-base alloys at high temperatures for furnace fixtures such as heat-treating trays, posts, and guide rolls [45].

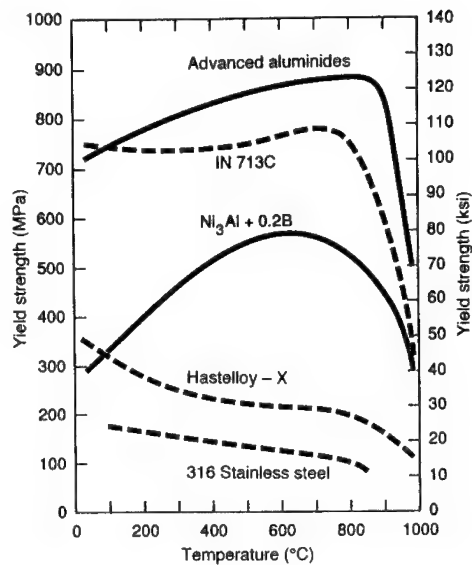


Figure 8. Comparison of the yield strength of Ni₃Al alloys with that of commercial alloys (IN 713C, Hastelloy X, and 316 stainless steel) [38].

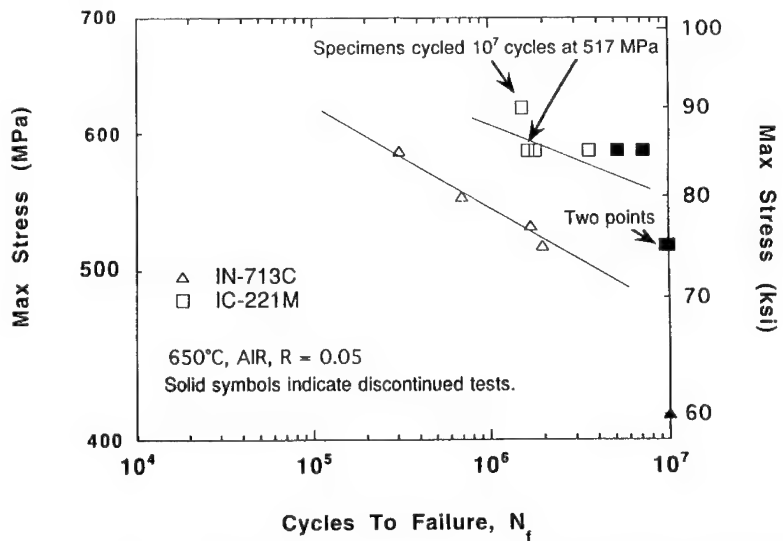


Figure 9. Comparison of cyclic fatigue life of Ni₃Al-based alloy IC-211M with IN 713C superalloy [42].

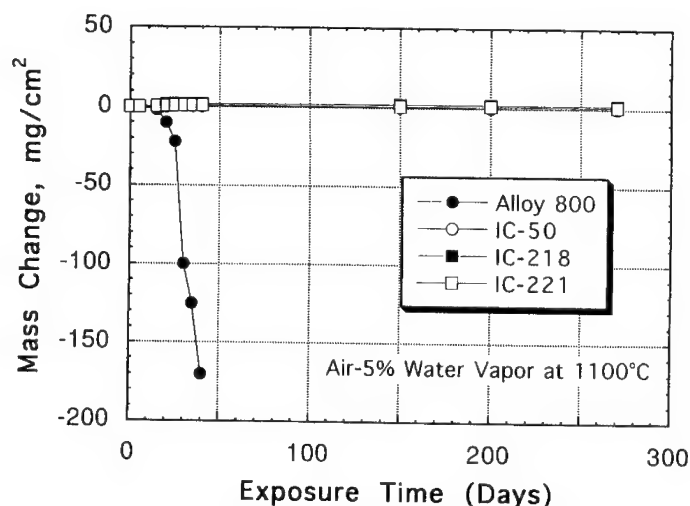


Figure 10. Comparison of oxidation resistance (in air with 5% water vapor at 1100°C) of Ni₃Al-based alloys with commercial Alloy 800 [45].

Material Processing and Structural Use

Melting remains the primary processing technique to obtain a variety of cast, wrought products, and the melting technique will determine whether an aluminide alloy can be obtained economically with good control of the composition, and with a minimal of defects and porosity in the cast structure[45].

Substantial heat will be released when elements are combined to form intermetallic alloys during melting. To implement the combustion-synthesis principles in the melting of nickel aluminides, a modification of the conventional melting process in which aluminum melt stock is added to the molten nickel bath, is a necessity. This is because the addition of aluminum to the molten nickel melt stock initiates a violent exothermic reaction instantaneously [46]. A peak temperature of 2300°C was noted within 1 min, and the crucible was at a temperature of 2100°C for several minutes. The temperatures attained were above the melting temperatures of the commonly used crucibles such as alumina, zirconia, mullite, etc. Also, a high-temperature vapor cloud escaped from the crucible as a result of the oxidation of aluminum and zirconium.

To address the safety issues associated with the melting, casting, and processing of Ni₃Al and other intermetallic alloys for the commercial utilization of intermetallics a new process called the "Exo-Melt™ process" was recently developed by Deevi and Sikka [46]. The Exo-Melt™ process consists of dividing the melt stock into several parts in a furnace-loading sequence such that a very exothermic reaction with a high-adiabatic combustion temperature is favored initially, leading to a molten product.

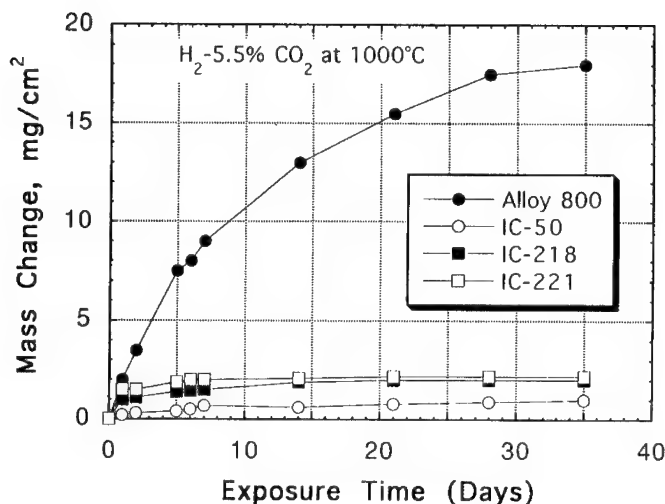


Figure 11. Comparison of carburization resistance (in H₂-5.5%CO₂) of Ni₃Al-based alloys with commercial Alloy 800 [45].

The furnace-loading sequence used in the Exo-Melt™ process is shown schematically in Fig. 12 for melting of nickel aluminide alloys. It is important to note that aluminum melt stock is vertically placed inside the wall of the zirconia crucible so that molten aluminum will react with part of the nickel melt stock in a controlled manner. All of the alloying elements of a particular melt stock are loaded between the top and bottom layers of nickel. The remaining nickel melt stock is loaded at the bottom. Temperature measurements and a video recording of the melting confirmed the occurrence of exothermic reaction in the top layer. Exothermic reaction continued until the reaction between the molten aluminum and the heated nickel melt stock was complete [46].

In the Exo-Melt™ process, the power required to melt a batch of IC-221M is 47% lower (2.9 kWh) than with the conventional process (5.5 kWh). This is due to the fact that exothermic reactions are initiated just after the melting of aluminum in the Exo-Melt™ process, whereas the melting of nickel melt stock is required in the conventional process. The time required to melt and pour the intermetallic by the Exo-Melt™ process is also reduced by 50% as opposed to a conventional process. All of these resulted in substantial savings in energy and a reduction in processing cost. While yield and ultimate tensile strengths did not differ significantly between the Exo-Melt™ process and the conventional process, the tensile elongations of conventionally melted alloy IC-221M are significantly lower than for the alloy processed by the Exo-Melt™ process.

The target composition of an alloy was reached easily and safely with the Exo-Melt™ process as compared to the conventional process. The high levels of aluminum present in the nickel aluminides promote rapid formation of a continuous Al₂O₃ film on top of the molten metal. Very low levels of oxygen and nitrogen elements in air induction melting (AIM) suggests that the oxide film is impervious to the penetration of oxygen and nitrogen. Typical oxygen and nitrogen values in nickel and iron aluminides are <40 ppm by weight. These values are similar to oxygen levels of <20 ppm by weight possible in aluminum-deoxidized steels.

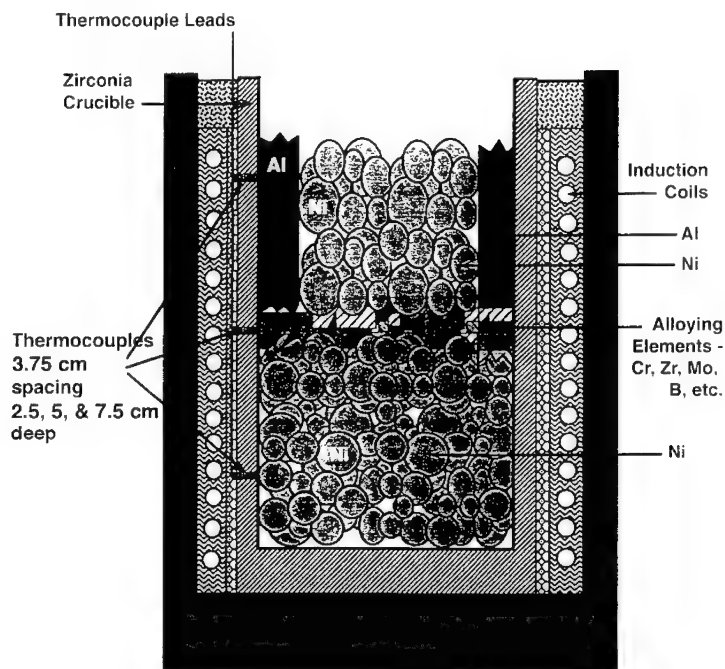


Figure 12. A schematic representation of furnace loading employed in the Exo-Melt™ process [45].

Components of nickel aluminides can be obtained by sand, investment and centrifugal casting, directional solidification, and innovative near-net-shaping techniques. The castability responses of the aluminides are related to the process as well as the product. The process-related castability concerns deal with the steps involved in the casting process, whereas the product-related issues deal with the porosity and microstructural features of the cast components.

The full potential of nickel aluminide alloys can only be reached with further advances in welding and innovations in alloy design and processing. There are two issues in the welding of aluminides: the first deals with cosmetic repair of casting defects, and the second deals with the structural welds needed for the assembly of components. To make either one of these welds, the welding-wire composition and welding procedures need identification. A composition identified as IC-221LA (in weight percent, consisting of 16% Cr, 4.5% Al, 1.5% Mo, 1.5% Zr, and balance Ni) is used for weld repairs and low-stress or less demanding structural welds. The composition identified as IC-221W (Ni-8Al-7.7Cr-1.5Mo-3Zr-0.003B) is used for normal structural welds. The currently used wire of both IC-221LA and IC-221W compositions is prepared by incorporating a powder composition in a nickel sheath (powdered-core wire). The prealloyed powder composition is adjusted for the extra nickel content that comes from the sheathing. The powdered-core wire is acceptable for welding by gas tungsten arc (GTA) and machine inert gas (MIG) methods.

The GTA method has been used most commonly for welding nickel aluminides. Section thicknesses up to 2.5 cm prepared by air melting using the Exo-Melt™ process have been successfully welded. For consistently good-quality welds, C, S, Si, B, and Zr need to be closely controlled. These elements are easy to control but need to be recognized at the time of melting. The tensile and creep properties of the weldments meet or exceed those of the base metal. The IC-221LA and IC-221W wires have also been successfully used in depositing Ni₃Al-based alloy on carbon, chromium-molybdenum, and stainless steel.

Industrial interest in Ni₃Al-based alloys is high at the present time [45-47]. For instance, during the past year, a total of 15,000 kg of melt stock were melted by industry for casting a variety of components using the Exo-Melt™ process. The interest arises from the fact that the aluminide alloys possess a unique combination of properties including (a) excellent corrosion resistance in oxidizing and carburizing environments, (b) good strength at room and elevated temperatures (up to 1100°C), (c) good fatigue and wear resistance, (d) relatively low cost for material preparation (because of exothermic melting and capability of air casting), and (e) relatively low material density as compared to Ni-base superalloys. A brief description of the industrial interest in the aluminide alloys is given below [45,47].

1. Transfer rolls to operate at or above 900°C in steel plants (see Fig. 13). Transfer rolls have shown no degradation due to thermal and mechanical loading during a 1-year period in a continuous operation, and tests are progressing. In this application, the Ni₃Al-based alloy competes with an HU or modified HU steel roll and provides better performance through its higher strength and better oxidation resistance with resultant oxide of uniform thickness and nonabrasive properties.
2. Heat-treating trays and posts for operation in carburizing furnaces. In this application, the Ni₃Al-based alloy competes with the most commonly used HU alloy. The Ni₃Al-based alloy performs better because it resists carburization and corresponding embrittlement. It also provides longer life because of its higher tensile and creep strengths and resistance to thermal fatigue resulting from frequent quenching in oil.
3. Rails for walking-beam furnaces. The walking-beam furnaces are used for heating bars of steel prior to their hot forging into shapes. The rails provide a means of moving (walking) the workpiece being heated from the loading end to the exit end after reaching the desired temperature in the range of 1100 to 1200°C. In this application, the Ni₃Al-based alloy provides the advantage of high-temperature strength and oxidation resistance.
4. Centrifugally cast tubes and static sand-cast return bends for radiant-burner-tube applications in gas-fired heating application. Once again, the alloy being replaced is HU steel, and advantage is taken of higher tensile and creep strengths, oxidation, and carburization resistances of Ni₃Al-based alloys. For some furnaces operating at temperatures approaching 800 to 900°C, the FeAl alloy tubes offer the benefit of significantly lower density and resistance to sulfidation and molten-salt corrosion.

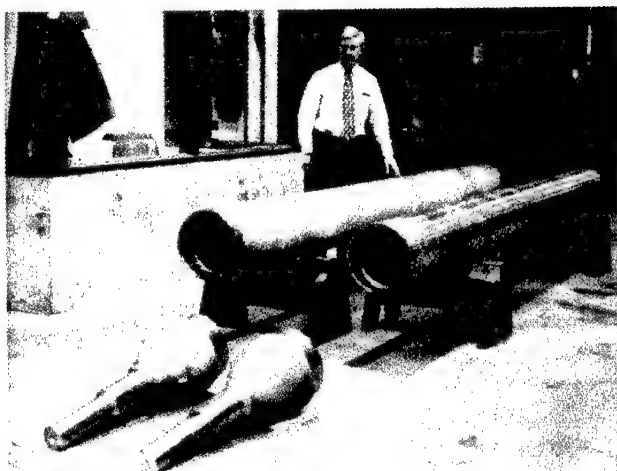


Figure 13. Fabricated transfer-roll assembly for operational trials in heat-treating furnaces.

5. Grate bars of IC-221M. These bars are used for calcination of ores at high temperatures. The Ni_3Al -based alloy IC-221M provides the advantage of its superior strength (resistance to sag under loading condition) and resistance to carburization and oxidation from the calcination environment. Several grate bars are currently in a production test.
6. Die blocks for closed-die for hot forging. In this application, advantage is taken of the higher wear resistance from the oxide scale that builds up on the steel bars heated in air prior to forging. Advantage is also taken of the higher strength at die-skin temperatures which approach 800 to 900°C and resistance to thermal fatigue.
7. A paddle for mixing ceramic slurries and a high-temperature guide roller for furnaces. In these applications, advantage is taken of superior wear resistance at high temperatures.
8. Corrosion-resistant tool bits for the pump and paper industry based on Ni_3Al as a binder phase in WC- Ni_3Al composites. The Ni_3Al -based tungsten carbide replaces cobalt, the conventional binder, which is both expensive and more toxic.
9. Hydroturbines. Nickel aluminides, which offer excellent vibration cavitation resistance in water, are being considered for either repair of current hydroturbine rotors or even replacement of the entire units with these alloys.

Apart from the above, the aluminide alloys offer potential as piping and tubing in chemical and petrochemical industries, high-temperature shields, exhaust manifolds, and catalytic-converter substrates.

Concluding Remarks

For the past fifteen years, considerable effort has been devoted to the study of Ni_3Al , a model material for ordered intermetallics. As a result, a great deal of knowledge has been gained in understanding the physical metallurgy and mechanical behavior of Ni_3Al alloys, especially the flow and fracture properties. Brittle failure and poor fracture resistance are the major concerns for structural use of the aluminide. Recent studies have led to identifying both intrinsic and extrinsic factors governing the fracture behavior of Ni_3Al alloys [3,8]. Several promising Ni_3Al -base alloys have been developed, and industrial interest in these alloys with improved mechanical and metallurgical properties is high. Examples of industrial involvement in processing and utilization of these alloys are briefly mentioned.

In spite of the concentrated effort on Ni_3Al and its alloys, there are areas needing additional research. For structural applications, there is room for further improvement. Suggested future research and development of Ni_3Al alloys include:

(i) mechanisms governing the solid-solution hardening behavior at ambient and elevated temperatures, (ii) effect of alloy stoichiometry on moisture-induced hydrogen embrittlement and grain-boundary cohesion, (iii) environmental embrittlement in single-crystal Ni_3Al alloys at elevated temperatures in oxidizing environments, (iv) grain-boundary sliding and superplastic forming, (v) effects of minor additions on creep resistance and hot ductility and fabricability, (vi) improvement in hot cracking and weldability of B-doped Ni_3Al alloys, (vii) near-net-shape processing via reaction synthesis, (viii) understanding of solidification processing and cavity formation in cast Ni_3Al alloys, (ix) development of strong single-crystal and directionally solidified Ni_3Al alloys for aerospace applications.

At present, there is world-wide interest in research and development of ordered intermetallic alloys for structural use at elevated temperatures in hostile environments. The knowledge and experience gained from the Ni_3Al studies have been extended to other aluminides, silicides and other intermetallics. A prominent example is the improvement in ductility of Ni_3Al alloys by boron additions [5,15], which have a similar beneficial effect in iron aluminides and other intermetallics [7,48].

References

1. MRS Proceedings, "High-Temperature Ordered Intermetallic Alloys," Vol. 39, 81, 133, 213, 288, and 364, MRS Publications, Pittsburgh, PA, 1985 to 1995.
2. S. H. Whang, C. T. Liu, D. P. Pope, and J. O. Stiegler, ed. "High Temperature Aluminides and Intermetallics," Proc. TMS/ASM Symp. (TMS, Warrendale, PA, 1990).
3. S. H. Whang, C. T. Liu, D. P. Pope, and J. O. Stiegler, ed. "High-Temperature Aluminides Intermetallics," *Mater. Sci. Eng.* **A152/A153** (1992).
4. D. P. Pope, C. T. Liu, and S. H. Whang, "High-Temperature Intermetallics," *Mater. Sci. Eng.* **A192/193** (1995).
5. C. T. Liu, C. L. White, and J. A. Horton, *Acta Metall.* **33**, 213 (1985).
6. T. Takasugi, E. P. George, D. P. Pope, and O. Izumi, *Scr. Metall.* **19**, 551 (1985).
7. C. T. Liu, ed. "Intergranular Fracture and Boron Effects in Ni_3Al and Other Intermetallics, a Viewpoint Set in *Scr. Metall.* **25**, 1231-1288 (1991).
8. C. T. Liu, *Scr. Metall.* **27**, 25 (1992).
9. E. P. George, C. T. Liu, and D. P. Pope, *Scr. Metall.* **28**, 857 (1993).
10. C. T. Liu, "Structural Intermetallics," ed. Darolia et al., TMS publications, Pittsburgh, 365-79 (1993).

11. E. P. George, C. T. Liu, and D. P. Pope, *Acta Metall.* **44**, 1757-63 (1996).
12. E. P. George, C. T. Liu, H. Lin, D. P. Pope, *Mater. Sci. Eng.* **A192/193**, 1757-63 (1996).
13. E. P. George and C. T. Liu, MRS Proc. **304**, "High Temperature Ordered Intermetallics," ed. Horton et al., MRS publications, Pittsburgh, 1131-47 (1995).
14. N. S. Stoloff and C. T. Liu, *Intermetallics* **2**, 75-87 (1994).
15. K. Aoki and O. Izumi, *Nippon Kinzoku Gakkaishi* **43**, 1190 (1979).
16. H. Lin and D. P. Pope, *Acta Metall.* **41**, 553, (1993).
17. C. T. Liu and W. C. Oliver, *Scr. Metall.* **25**, 1993 (1991).
18. C. T. Liu, E. H. Lee, and C. G. McKamey, *Scr. Metall.* **23**, 875 (1989).
19. C. T. Liu, C. G. McKamey, and E. H. Lee, *Scr. Metall.* **24**, 385-90 (1990).
20. A. K. Kuruvilla and N. S. Stoloff, *Scr. Metall.* **19**, 83 (1985).
21. N. S. Stoloff, *J. Metals* **40**, 18 (1988).
22. T. Takasugi, N. Masahashi, and O. Izumi, *Scr. Metall.* **20**, 1317 (1986).
23. N. R. Gleason, C. A. Gerken, and D. R. Strongin, *Appl. Surf. Sci.* **72**, 215 (1993).
24. W. J. Chia and Y. W. Chung, *Intermetallics* **3**, 505 (1995).
25. Y. F. Zhu, C. T. Liu, and C. H. Chen, *Scr. Metall.* (in print) (1996).
26. J. W. Cohron, E. P. George, L. Heatherly, C. T. Liu, and R. H. Zee, *Intermetallics* **4**, (in print) (1996).
27. C. T. Liu and D. P. Pope, "Intermetallics Compounds: Principles and Practices," ed. Westbrook and Fleischer, John Wiley and Sons (1994).
28. A. Choudhury, "The Intergranular Segregation of Boron in Substoichiometric Ni_3Al ," ORNL/TM-10508, Oak Ridge National Laboratory, Oak Ridge, TN, 37831, Dec. 1987.
29. X. J. Wan, J. H. Zhu, K. L. Jing, and C. T. Liu, *Scr. Metall.* **31**, (1994).
30. C. T. Liu, C. L. White, and E. H. Lee, *Scr. Metall.* **19**, 1247-1250 (1985).
31. C. T. Liu and V. K. Sikka, *J. Metal* **38**, 19 (1986).
32. C. T. Liu and C. L. White, *Acta Metall.* **35**, 643 (1987).
33. A. I. Taub, K.-M. Chang, and C. T. Liu, *Scr. Metall.* **20**, 1613 (1986).
34. P. H. Thornton, R. G. Davies, and T. L. Johnston, *Metall. Trans.* **1**, 207 (1970).
35. N. S. Stoloff, G. E. Fuchs, A. K. Kuruvilla, and S. J. Choe, p. 247 in ref. 2 (1987).
36. C. A. Hippsley and J. H. DeVan, *Acta Metall.* **37**, 1485 (1989).
37. M. Takeyama and C. T. Liu, *Acta Metall.* **37**, 2681 (1989).
38. M. Takeyama and C. T. Liu, *Acta Metall.* **36**, 1241 (1988).
39. C. T. Liu and B. F. Oliver, *J. Mater. Res.* **4**, 294 (1989).
40. C. T. Liu, U.S. Patent **5**, 108,700 (1992).
41. Feng Di, Ye Nujun, Han Guangwei, and Luo Heli, *Acta Metall. Sinica* **8**, 503 (1995).
42. B. G. Gieseke and V. K. Sikka, unpublished results, Oak Ridge National Laboratory, Oak Ridge, TN 37831 (1992).
43. V. K. Sikka, *Mater. Manuf. Proc.* **4**, 1-24, (1989).
44. W. Matuszyk, G. Camus, D. J. Duquette, and N. S. Stoloff, *Metall. Trans.* **21A**, 2967 (1990).
45. S. C. Deevi and V. K. Sikka, *Intermetallics* **4**, 357 (1996).
46. S. C. Deevi and V. K. Sikka, *Intermetallics* **4** (in press) (1996).
47. V. K. Sikka, J. T. Mavity, and K. Anderson, *Mat. Sci. Eng.* **A153**, 712 (1992).
48. C. T. Liu and E. P. George, *Scr. Metall.* **24**, 1285-90 (1990).

PROCESSING, MICROSTRUCTURAL DESIGN AND PROPERTIES OF γ -TITANIUM ALUMINIDES FOR INDUSTRIAL APPLICATIONS

M. Nazmy¹⁾, C. Nosedà¹⁾, M. Staubli¹⁾, and B. Phillipsen²⁾

¹⁾ ABB Power Generation Ltd., 5401 Baden, Switzerland

²⁾ ABB Turbo Systems Ltd., 5401 Baden, Switzerland

Abstract

A γ -TiAl base intermetallic alloy has been developed and evaluated with respect to the tensile and creep properties. A microstructural evaluation has been carried out, using transmission electron microscopy, to characterize the different microstructural features and their effect on the mechanical properties of this material. This alloy has been successfully applied to a turbocharger mixed flow turbine. It has been demonstrated that the casting route is the most economical way to produce components such as turbocharger turbines. Other components such as automotive exhaust valves and aero engine parts can be also produced by the precision casting technique. With the suitable heat treatment, it was possible to achieve the most favourable microstructure and thus the best combination of mechanical properties for a certain application. It was also shown that one can improve the strength and ductility of γ -TiAl by isothermal forging.

Introduction

Two phase γ -titanium aluminides are considered as a new class of light weight high temperature materials with the potential to substitute for conventional titanium and nickel or iron based alloys in gas turbine¹ and in automotive engine applications^{2,3}. Amongst the various processing technologies, which include forging and powder metallurgy routes, investment casting is regarded as the most economic processing technology for γ -TiAl with the possibility to generate a vast variety of microstructures by different heat treatments⁴. Turbocharger wheels and exhaust valves for automotive engines as well as blades and vanes for usage in aero engines can be precision cast such that they are free from pores and flaws after adequate hot isostatic pressing⁴. Since the binary alloy Ti-48Al does not possess the adequate properties, major efforts have been made in alloy modifications⁵⁻⁹. Appropriate modifications of the alloy chemistry have been shown to lead to improved properties, i.e. tensile, creep, fatigue strength, fracture and impact toughness, oxidation and corrosion resistance⁵⁻¹⁰. It has also been shown that forging and hot extrusion of γ -TiAl alloys can lead to improved strength and ductility⁴⁻¹¹. Hence, one can apply such processes to the specific parts in the component where such combination of strength and ductility are required¹². In the present study, the development and application of γ -TiAl to turbocharger turbines will be described.

Material Development, Microstructure And Mechanical Properties

The conventional turbine wheels of turbocharger rotors are made of nickel-base superalloys with a density of 8 g/cm³. Advanced ceramics like Si₃N₄, with the density of 3.2 g/cm³, have recently been applied to turbocharger rotors¹³. The reason for such application is the weight reduction, associated with ceramics, which will result in an improvement in the turbocharger response and thus the engine response to load changes. Nevertheless, the ceramics are brittle and hence designers are forced to design components specifically for the use of ceramics.

In addition, the large difference in the thermal expansion coefficients of ceramics and metal casing can lead to a wide tip clearance at the operating temperatures, which will consequently lead to a sacrifice in the turbine efficiency. Moreover, the brittle behavior of ceramics raises the concern about their reliability with respect to foreign object damage.

The attractive combination of high strength and low density of γ -TiAl, i.e. $\rho=4.12$ g/cm³, has drawn the attention of investigations to apply such material to small turbocharger wheels. The expected advantages of such

intermetallic turbines, with approximately 130 mm in diameter, over nickel-base superalloy IN738LC have been reported².

At ABB, a proprietary γ -TiAl intermetallic based on Ti-47Al-2W-0.5Si with the designation ABB-IMN2, has been developed and patented⁹. The impetus for such activity is to reduce the reaction or response time of the turbine for the applications where such characteristic is crucial. Hence, the goal of this activity was to develop, manufacture and engine test a γ -TiAl turbine rotor of the mixed flow type, with a size of approximately 130 mm in diameter.

Several heats have been manufactured by VAR casting and HIP'ing in the form of bars with a diameter of approximately 15 mm. The HIP conditions were 1260°C / 4 h / 172 MPa. These bars were heat treated as follows: 1300°C / 20 h / GFC + 900°C / 4 h / GFC. This heat treatment was designated A2. Several tensile and creep specimens were prepared and tested. Figures 1 to 4 give the results on tensile and creep tests from three heats with the chemical compositions given in table I. The scatter of the results was quite reasonable.

For the sake of comparison, a cylindrical mass was forged at 1100°C and $\epsilon=10^{-3}\text{s}^{-1}$ to a true strain of approx. 1.3. Then, it was heat treated at 1300°C for 1 hour, cooled to 900°C and kept there for 6 hours. The corresponding tensile results are also indicated on the same figures. One can observe the improved strength and ductility exhibited by this forged specimen.

Table I Chemical composition of the produced heats, in weight percent

Heat No.	Al	W	Si	Fe	Cu	O (ppm)	H (ppm)	N (ppm)	Ti
7	30.34	9.8	0.31	0.09	<0.01	808	11	63	Bal.
10	30.11	9.47	0.37	0.1	<0.01	741	12	79	Bal.
11	30.93	9.28	0.36	0.06	0.01	567	13	48	Bal.
N-7	30.96	9.19	0.3	0.061	<0.01	807	5	51	Bal.

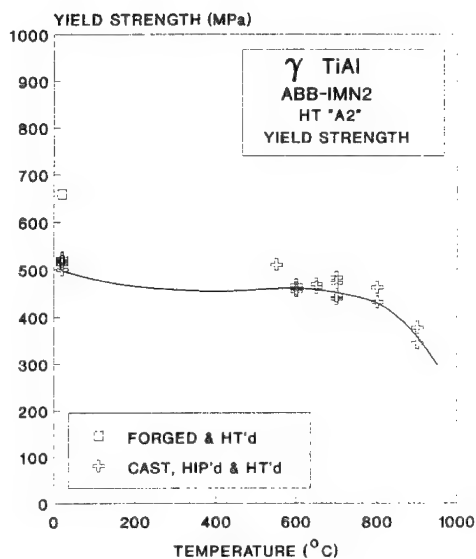


Figure 1

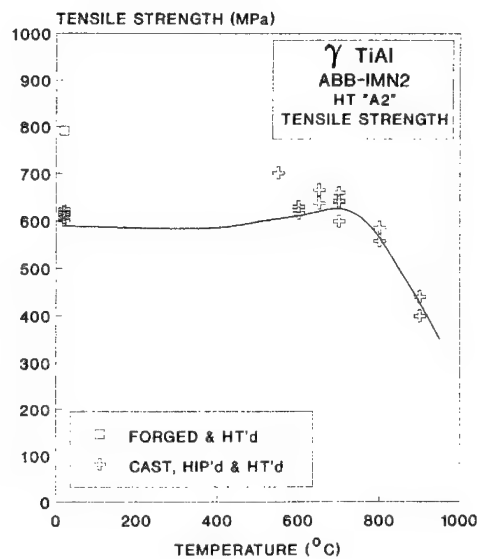


Figure 2

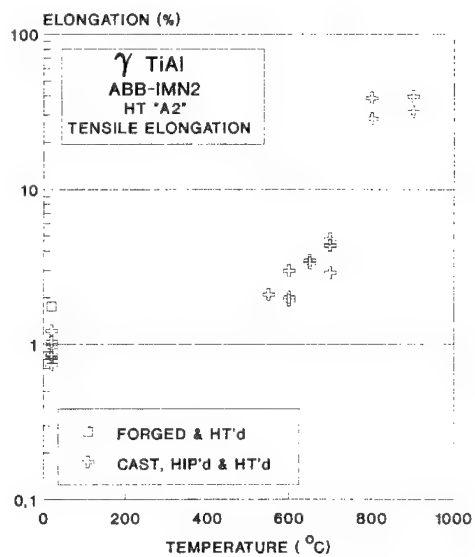


Figure 3

Figures 1, 2 & 3 - Yield strength, ultimate tensile strength and elongation of γ -TiAl as a function of the test temperature.

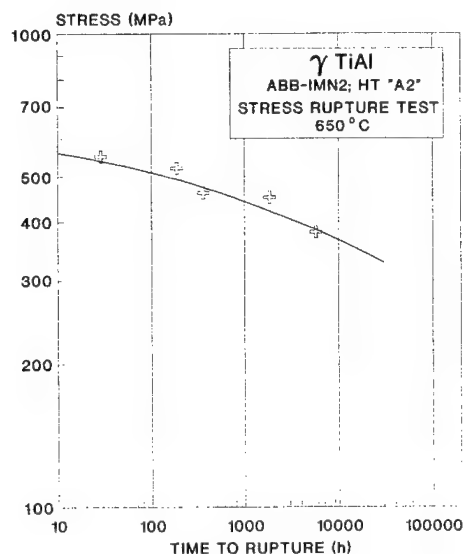


Figure 4 - Creep rupture curve of γ -TiAl at 650°C.

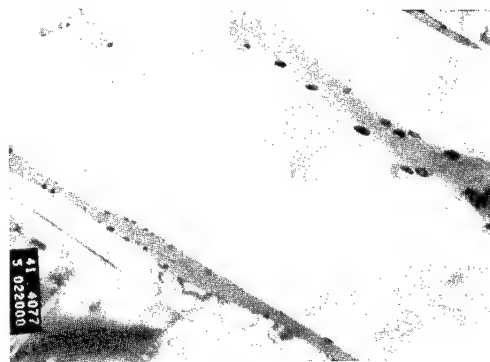
The general feature observed in the microstructure of the cast, HIP'd and heat treated material is the duplex type of the γ grains with lamellar colonies.

General transmission electron microscopic observations supported by EDX analysis indicated the presence of two types of second phase particles. The first type is rich in both Si and W and exists as discontinuous phase, see Figure 5. The second type is Si-rich and precipitated at the interfaces of the discontinuous phase as well as in the lamellar γ as shown in Figures 6 and 7, respectively.



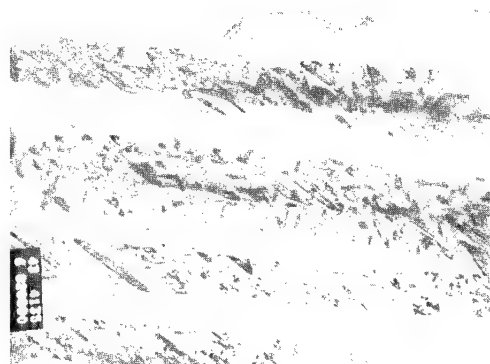
10 μ m

Figure 5 - TEM micrograph showing fine lamellar structure (upper right), discontinuous phase particles rich in Si and W (bottom) and coarse γ (upper center).



1 μm

Figure 6 - TEM micrograph showing fine second phase precipitates rich in Si, at the interface of the discontinuous phase.



1 μm

Figure 7 - TEM micrograph showing second phase particles, rich in Si, in the fine lamellar γ .

The microstructure of the forged specimen is characterized by a fine grain size and the existence of a fine lamellar structure, coarse γ grains with discontinuous phase plus the other phase, which is rich in Si. These general features are shown in Figure 8.



Figure 8 - TEM micrograph showing fine lamellar structure (upper right), coarse γ (upper left) and coarse discontinuous second phase (center and left).

It is suggested that the existence of these two types of second phases is the reason for the relatively high tensile and creep strengths of this alloy, specially at high temperatures. In addition, it is proposed that the enhanced ductility and yield strength at room temperature of the thermo-mechanically treated, i.e. forged specimen, is due to the fine grain size as well as the fine lamellar spacing of the γ/α_2 structure.

Several turbines of the ABB RR151 turbocharger were precision cast from ABB IMN-2, i.e. the patented alloy. They were then hot isostatically pressed, heat treated and non destructively tested by liquid penetrant and x-ray techniques. These turbines were joined to the low alloy steel shafts by a patented friction welding process¹⁴.

Figure 9 shows a photograph of the complete turbocharger turbine rotor.

The steady-state and the transient load response of the ABB RR151 turbocharger fitted with a γ -TiAl turbine were measured twice on engine testing with different load steps. The measurements have shown 20% reduction in the recovery time, as compared with that of the nickel-base superalloy turbine under the chosen operating conditions with generator brake. It is noteworthy to point out that the reduction in recovery time depends highly on the chosen operating conditions. When the engine control system makes full use of the low inertia of the turbocharger, a reduction of up to 50% in the recovery time can be achieved.

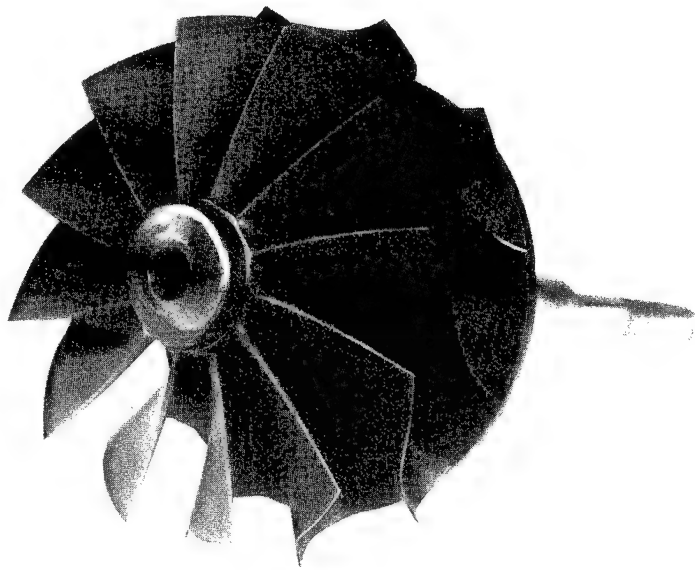


Figure 9 - A general view of the complete RR151 turbocharger rotor fitted with the developed γ -TiAl turbine.

Conclusions

- 1) The γ -TiAl base intermetallics are finding important industrial applications in the automotive and aircraft engines as well as in turbochargers.
- 2) The investment casting, HIP and heat treatment of γ -TiAl is considered the most economical route for producing several industrial parts such as aero engines blades, turbocharger turbines and exhaust valves.
- 3) The developed γ -TiAl intermetallic, i.e. ABB IMN-2 exhibited improved tensile properties as well as creep rupture strength combined with good castability.
- 4) The advantage of applying cast γ -TiAl to turbocharger turbines has been demonstrated.
- 5) Forging, followed by heat treatment, can be used to enhance the strength and ductility of the γ -TiAl intermetallic.

References

1. C.M. Austin and T.J. Kelly, Structural Intermetallics, Eds. R. Darolia et al., TMS, 1994, p. 143-150.
2. M. Nazmy, M. Staubli and M. Unverricht, Turbocharging and Turbochargers, Mech. Eng. Publications Ltd., 1994, p. 39-43.
3. M. Yamaguchi, Private Communication, Kyoto Univ., Japan, 1996
4. B. London and T.J. Kelly, Microstructure/Property Relationship in Titanium Aluminides & Alloys, Eds. Y.-W. Kim and R. Boyer, TMS, 1991, p. 285-295.
5. Y.-W. Kim, J. of Metals, 41(7), 1989, p. 24-30.
6. T. Tsujimoto and K. Hashimoto, High Temperature Ordered Intermetallic Alloys III, Eds. C.T. Liu et al., MRS, 133, 1989, p. 391-396.
7. Y.-W. Kim and D.M. Dimiduk, J. of Metals, 43(8), 1991, p. 40-47.
8. S.C. Huang and E. Hall, High Temperature Ordered Intermetallic Alloys III, Eds. C.T. Liu et al., MRS, 133, 1989, p. 373-383.
9. U.S. Pat. # 5,207,982 and European Pat. # 455 005 B1.
10. M. Nazmy and M. Staubli, Scripta Met. et Mat., 31(7), 1994, p. 829-833.
11. M. Nazmy, M. Staubli and D. Anton, Scripta Met. et Mat., 26, 1992, p. 105-108.
12. U.S. Pat. # 5,299,353 and European Pat. # 513 407 B1.
13. Y. Nishigama et al., High Temperature Aluminides & Intermetallics, Eds. S.H. Whang, C.T. Liu, D. Pope and J.O. Stiegler, TMS, 1989, p. 557-584.
14. U.S. Pat. # 5,431,752 and European Pat. # 590 197 B1.

PROCESSING AND DESIGN ISSUES IN HIGH TEMPERATURE MATERIALS -

SOME ISSUES IN TiAl-BASED ALLOYS

M H Loretto

IRC in Materials for High Performance Applications,
The University of Birmingham, Edgbaston B15 2TT, UK

Abstract

The research and development programme on TiAl-based materials which is underway in the IRC is briefly reviewed. The areas of the programme which are covered are melting, grain size control, fracture of hard grains and phase transformations in rapidly cooled samples. Control of melting conditions is shown to be necessary in the ingots produced by plasma melting if significant fluctuations in the Al content are to be avoided; the generation of fine grained structures is shown to be desirable but is not always able to arrest premature failure; the nature of the massive transformation, which occurs in welded samples, is shown to lead to an understanding of the role of high temperature extrusion in the refinement of the lamellar spacing.

§ 1. Introduction

The development of TiAl-based alloys for use in applications where low density and good high temperature properties, including oxidation resistance are paramount, is reaching the stage where demonstrator projects have been successfully undertaken. It is clear that at last the enormous effort that has been put into these materials will begin to pay off. This situation is in no small way due to the recognition by many workers that alloy development and process development must go hand in hand.

In this review paper some of the issues that have been focused on in the group at the IRC in Birmingham and Swansea UK will be discussed, with the aim of identifying those areas where further developments appear still to be required. The TiAl programme in the IRC covers melting of new alloys, forging, forging modelling and extrusion of the ingots, property and microstructure assessment as well as the manufacture of demonstrator components; most of these topics will be covered, albeit briefly, in this short review article which draws on the work of a large number of colleagues. The areas where the work in the IRC is relevant to the topic of this symposium are:

- (i) Compositional homogeneity of ingots - melting practice.
- (ii) Grain size control.
- (iii) Grain orientations with respect to the stress axis and with respect to adjacent grains.
- (iv) Phase transformations in rapidly cooled alloys

These topics will be dealt with in turn.

§ 2. Observations and Discussion.

- (i) Compositional homogeneity of ingots - melting practice.

The TiAl-based alloys manufactured in the IRC are made using a twin torch plasma melter where each torch is rated at 150kW (see figure 1).

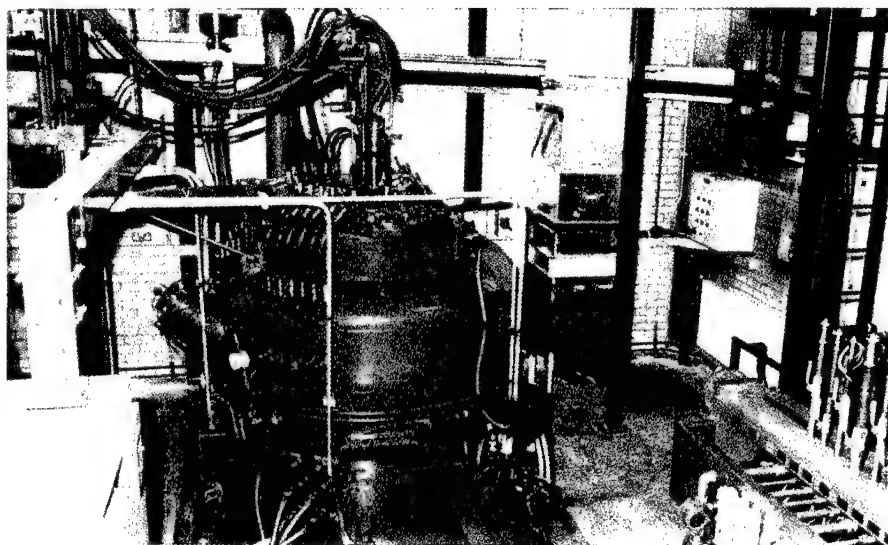


Figure 1. The photograph of the plasma melter shows the feed mechanism in the foreground and the furnace and two torches in the background. The control console is just visible on the left hand side of the picture. The main furnace body is about 1.5m high.

The melter is capable of producing alloys up to 150mm in diameter and 1.5m in length from compacted feed stock, which is made up into blended Ti sponge with appropriate alloy additions either as small pieces of master alloy or elemental additions. The feedstock is melted into a water-cooled copper hearth where a "skull" is formed which prevents the molten alloy interacting with the hearth. The two torches are computer-controlled to melt the feedstock, to sweep molten alloy over the lip of the copper hearth and to hot-top the ingot which is formed in a water-copper collar in which the molten alloy is solidified and withdrawn using a dovetail fitting which initially is flush with the bottom of the collar. The typical casting rate which is used is about 1kg per minute and production of a 100kg ingot therefore takes of the order of two hours.

The furnace is illustrated in figure 1 where the feed system is in the foreground and the furnace with its two torches is behind this. The control console is just visible on the left of the figure. Figure 2 shows a close up of the hearth and the two torches and the 10cm diameter crucible into which the molten metal is cast. The pre-blended alloy is fed through the hole visible at the rear of this photograph.

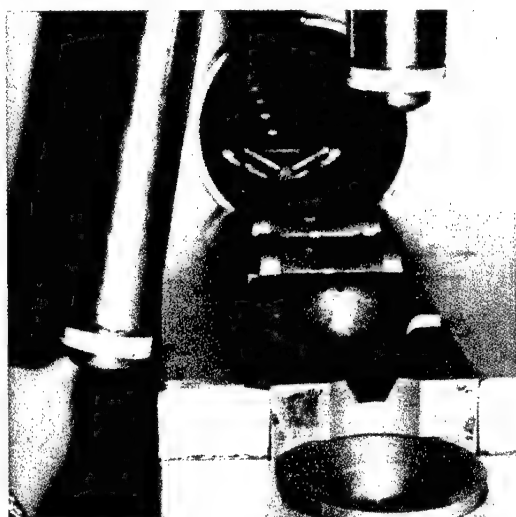


Figure 2. Close up of the two torches and the hearth in the plasma melter. The 10cm diameter crucible into which the molten metal is cast is visible in the foreground.

Since early work showed that compositional variations in ingots were associated with transients during melting a data collection/control system is being developed with the aim of allowing totally steady-state conditions to be maintained shortly after start-up. Both longitudinal and cross section samples from single-melted, double-melted and triple-melted ingots have been analysed using a glow discharge facility which allows analyses to be carried out at a spatial resolution of about 4mm. From the early results, variations of Al contents of up to $\pm 2\text{at}\%$ were commonly observed across the section and along the length of the ingots which were clearly on a scale associated with macrosegregation (rather than simply coring) which would not be removed during subsequent thermomechanical processing. As would be expected the magnitude of these changes was found to be smeared out using techniques used industrially such as X-ray fluorescence where the spatial resolution is about 20mm. Double-melted ingots are now being produced where the maximum variation in Al content is $\pm 0.5\text{at}\%$, i.e. within the accuracy of most techniques used for checking control of melting conditions. (1)

Consideration of the segregation patterns which have been observed suggests that they are due to complex interactions between the various factors that lead to macrosegregation; the extent of this type of segregation would be expected to be worse with larger diameter ingots. Such segregation cannot be removed during subsequent processing, although the microstructural differences associated with them may not always be obvious. Local differences in the response to processing of areas with large differences in composition is very likely to lead to major differences in structure and hence to the response to imposed stress. If scatter in properties is found to be associated with this segregation in large casts it is clear that spray-forming or powder route materials may have to be used for applications where this is significant.

(ii) Grain size control.

The development of alloys with additions of about 0.8at%B has allowed cast and forged TiAl-based alloys to be developed which have much finer grain sizes than the first generation alloys (2). This in turn has led to improved properties in cast products and to easier thermomechanical processing in wrought components. Problems arise when B is added to alloys containing W or Ta since large clusters of borides tend to be formed under most melting conditions and it may be that such alloys cannot be refined using B(3). Other methods are being developed involving, for example, heat treating in a high temperature alpha/beta phase field when the beta grains can be used to pin alpha grain boundaries.

(iii) Grain orientations with respect to the stress axis and with respect to adjacent grains.

One of the factors that lead to failure of TiAl-based alloys is the weakness of lamellae interfaces and in coarse grained material such failure could lead to early fracture. In fine grained material the failure across an interlamellar region oriented unfavourably with respect to the stress axis will in general not lead to catastrophic fracture since other more favourably oriented grains will arrest the crack. Nevertheless it is clear that the grains which are oriented unfavourably with respect to the stress axis may well fracture before slip or twinning can occur and observations have shown that a significant number of grains in this orientation do indeed fail between lamellae at very low strains both in compression and tension (3). The significance of this type of failure under service conditions has not been assessed but it is likely that these alloys will have to be used at stresses well below that which leads to such failures.

A series of measurements of crack growth rates during fatigue has shown that even with fine grained material samples can fail under fatigue after far fewer cycles than would be expected. Observation of the fracture surface in such samples shows that there are clusters of fine grains which allow interlamellar failure because of the small local misorientations between these grains. (4) It is not obvious that such clusters of similarly oriented grains can be avoided in fine grained alloys and it will be necessary either to use these alloys at lower stresses than would otherwise be the case or to find ways of strengthening the lamellar interfaces.

(iv) Phase transformations in rapidly cooled alloys

The control of the distribution of the phases in TiAl-based alloys is central to the development of alloys with an appropriate balance of properties and work aimed at understanding the way in which these alloys transform during heat treatment or during cooling is an important part of a broadly-based research programme. In this final section of this paper some detailed microstructural observations which provide an understanding of the nature of the massive transformation will be presented. This transformation is seen in TiAl (and in a wide range of other alloys) when samples are cooled reasonably rapidly as in phase transformation studies and in the case of welding.

Low magnification optical micrographs of a sample which had been welded using an electron beam and the region which was heated to a high temperature and cooled rapidly through conduction show light regions of retained alpha and the dark regions massively transformed gamma, i.e. gamma which had formed via a massive transformation from the high temperature alpha phase (5).

The microstructure of the massively transformed region is very complex and has been shown to contain a very high density of crystal defects. Many of these defects show contrast in the transmission electron microscope characteristic contrast of antiphase domain boundaries (i.e. they show fringe contrast which is symmetrical in bright and dark field and is complementary in dark and bright field when imaged with a superlattice reflection). However extra diffraction maxima are associated with these regions and detailed analysis of the patterns and of the image contrast showed that associated with the APDB there was a thin region where the [001] direction was orthogonal to the [001] in the domains either side of the APDB (6,7,8). Micrographs taken using a high resolution transmission electron microscope have confirmed this structure. The origin of this complex boundary has been discussed in detail elsewhere and will not be elaborated upon here.

The welded samples have been valuable in throwing light upon the detailed nature of the massive transformation as illustrated in figure 3. In this figure a region near a prior alpha/alpha grain boundary is shown (arrowed at the bottom of the micrograph) and it can be seen in the grain on the left (which is imaged in dark field with a gamma reflection) that some gamma lamellae have been formed which show up brightly in this micrograph. Also illuminated in this image (and therefore having the gamma structure) is a region which is growing from these lamellae across the boundary into the original alpha grain on the right hand side of this micrograph. The diffraction pattern of this grain shows that there is no orientation relationship between the gamma and the alpha original alpha grain. Thus by nucleating on a preexisting gamma region the gamma growing into the right hand grain has an incoherent (and therefore mobile) interface. This therefore propagates rapidly and the massive transformation is able to dominate the kinetics of the transformation during rapid cooling

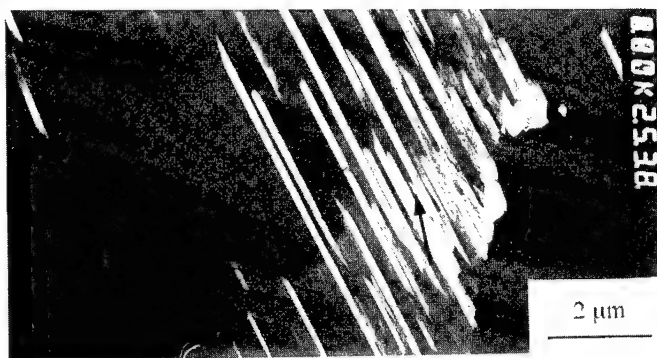


Figure 3. A dark field transmission electron micrograph taken using a gamma superlattice reflection of a rapidly cooled region in a welded sample of Ti 48Al 2Mn 2Nb containing an original alpha/alpha grain boundary. The lamellae (arrowed) in the left hand grain are illuminated in this micrograph and are therefore gamma, as is the small region propagating into the grain on the right hand side. For full explanation see text. (After ref 5).

The observations shown in figure 3 taken together with many other observations on rapidly cooled samples have shown that the dominant method of forming the gamma lamellae in two phase TiAl-based alloys, is through the propagation of appropriate partial dislocations from grain boundaries which then provide the nuclei for the ultimate formation of tetragonal lamellae from the hexagonal parent phase; the number of stacking faults formed or pre-existing in the grain centres is negligible. This observation suggests that if samples could be deformed during transformation (and thus provide more partial dislocations) the interlamellae spacing could be reduced below that found in samples simply cooled from the alpha phase field. Experiments carried out in the IRC and the earlier work on extruding powder route samples (9) have indeed shown that the properties are enhanced and the interlamellae spacing reduced if samples are extruded at the appropriate high temperature during cooling(10).

§ 3. Conclusions

The brief review of the problems which still face the application of TiAl-based alloys shows that despite the enormous progress that has been made over the last few years that there are further developments required before they can be used with confidence in critical parts.

Acknowledgements

I would like to thank the many past and present members of the IRC whose results I have freely quoted. Financial support from EPSRC through the main IRC grant and from a wide range of industrial sponsors is gratefully acknowledged.

References

- 1 B Godfrey-Macha (unpublished research, IRC The University of Birmingham)
- 2 D E Larsen. Titanium 92. Science and Technology TMS Warrendale Pa. 1033.
- 3 A Godfrey (PhD thesis the University of Birmingham)
- 4 A James and P Bowen Mat Sci and Eng A153 486,
- 5 X D Zhang, S Godfrey, M Weaver, M Strangwood, P Threadgill, M J Kaufman and M H Loretto. Accepted for publication in Acta Met and Mat.
- 6 X D Zhang Y G Li, M J Kaufman and M H Loretto. Accepted for publication in Acta Met and Mat.
- 7 Y G Li and M H Loretto. Acta Met and Mat, 41, 3413,1993
- 8 X D Zhang and M H Loretto. Phil Mag Letters 68, 289, 1993
- 9 C T Liu, P J Maziasz, D R Clemens, J H Schneibel, V K Sikka, T G Nieh, J Wright and L R Walker. Gamma Titanium Alumindes. TMS (Eds Y W Kim, R Wagner and M Yamaguchi) 679, 1995
- 10 A Godfrey and D Hu (unpublished research, IRC, The University of Birmingham)

INTERMETALLICS RESEARCH IN JAPAN - WITH PARTICULAR EMPHASIS ON TiAl

Masaharu Yamaguchi and David R. Johnson

Department of Materials Science and Engineering
Kyoto University
Sakyo-ku, Kyoto 606-01, Japan

Abstract

An eight-year national program aiming at the development of high-temperature intermetallics was started by The Agency of Industrial Science and Technology of The Ministry of International Trade and Industry (AIST-MITI) in 1989. In 1992, The Ministry of Education, Science, Sports and Culture (MESSC) assigned "high-temperature intermetallics" one of the research areas to be studied intensively and started a three-year basic research program called "Intermetallic Compounds as New High Temperature Structural Materials." In parallel to these national programs, considerable research effort has been made for structural applications of TiAl alloys in automotive, iron & steel and heavy machinery industries which are not involved in the AIST-MITI program. Such R&D activities on gamma titanium aluminide alloys and the two national programs with emphasis on basic aspects of the properties and processing of high-temperature intermetallics have been giving a considerable impetus to intermetallics research in Japan. This is an overview of the current research and development activities in Japan concerning intermetallic compounds, in particular TiAl alloys recognized as new light weight high temperature structural materials.

Introduction

Intermetallic compounds, in particular aluminides and silicides with high melting points, have immense potential as new high-temperature structural materials since they often possess not only attractive high-temperature mechanical properties but also excellent oxidation resistance. In recent years there has been an enormous increase in the research and development activity on such intermetallic compounds for high temperature structural applications. This is because the requirements for the strength and stiffness and the oxidation and corrosion resistance at high temperatures are becoming increasingly severe in the field of high temperature technologies such as gas turbines.

Intermetallics research activities in Japan are closely associated with two national programs on high-temperature intermetallic compounds by The Ministry Education, Science, Sports and Culture (MESSC) and The Agency of Industrial Science and Technology of The Ministry of International Trade and Industry (AIST-MITI). These two national programs together with R&D efforts for industrial applications of TiAl in automotive, iron & steel and heavy machinery industries which are not involved in the AIST-MITI program have been playing a decisively important role in accelerating the pace of intermetallics research in Japan. The AIST-MITI program was started in 1989 and will continue until the end of March 1997. The purpose of the program is to develop new structural materials based on intermetallic compounds, TiAl and Nb₃Al and to establish the basic technologies related to such new materials. Results of the program have been published in proceedings of the "Symposium on High-Performance Materials for Severe Environments" which has been held once a year since 1991. A detailed explanation of the AIST-MITI program and its steering system is presented in reviews by one of the authors [1] and by Maruo and Tomita [2] of R&D Institute of Metals and Composites for Future Industries (RIMCOF) which has been in charge of the administrative aspects of the program.

The MESSC research program "Intermetallic Compounds as New High Temperature Structural Materials" was started in 1992 as one of the priority areas of scientific research and was ended in 1994. In the program, the following fundamental topics on high-temperature intermetallic compounds, in particular aluminides and silicides, were studied: (i) crystal structure and phase stability, (ii) deformation and fracture mechanisms, (iii) design and control of microstructure, and (iv) environmental embrittlement and other environmental effects. A total of 67 research teams from more than 15 universities were involved in the program. Of the research teams, 31 teams participated in the program for the whole three years, 13 teams for two years and 23 teams for only one year. The steering committee of the program organized an international symposium "Intermetallic Compounds for High-Temperature Structural Applications" in conjunction with the Third Japan International SAMPE Symposium held in Makuhari, Chiba on December 7 - 9, 1993 [3]. The research teams have published numerous papers in the proceedings and various other conference proceedings and journals. These are listed in the report submitted to MESSC [4]. Recent papers and some selected reviews by 27 research teams will be published in a special issue of *Intermetallics* [5] sponsored by MESSC. Recently, superplasticity was assigned to be one of such priority research areas and a three-year project "Innovation in Superplasticity" was started in April 1996. Superplastic deformation of metallic materials including intermetallic compounds and various ceramics materials will be studied intensively in the project. In this paper, an overview on the trend and status of recent intermetallics research, in particular that on TiAl in Japan is presented focusing attention mainly on the results of the two national programs.

AIST-MITI Program

Alloy Development

The research objectives of the TiAl program are as follows: (1) to develop TiAl alloys with a specific strength of 100 MPa/g/cm³ (around 380 MPa) at 1100°C and 3% tensile elongation at room temperature, and (2) to establish basic technologies for rolling such alloys into the sheet form and subsequent superplastic forming of sheets. The so-called TiAl alloys possess a two-

phase microstructure consisting of the TiAl phase and a small volume fraction of the Ti₃Al phase. The strength of polycrystalline two-phase TiAl alloys with such a two-phase microstructure strongly depends on the microstructure which is usually in the lamellar or the duplex form. Tensile properties are generally good in the duplex form while the fracture and high-temperature properties are so in the lamellar form. The mechanical properties of each microstructural class depend also on its microstructural constituents such as grain size and volume fraction of lamellar grains in the duplex microstructure. Thus, in order to achieve the research objectives both the class of microstructure as well as the microstructural constituents must properly be chosen and optimized. By wrought processing followed by heat treatment and/or ternary alloying additions such control over the microstructure is possible.

In recent years, considerable research resource and effort were invested to improve the mechanical properties of gamma alloys in duplex forms through microstructure control and alloying. Transition metals such as Cr, Nb, V, Mo, Ta and W were common alloying elements examined in these studies. Attempts to interpret alloying effects in terms of variations of intrinsic properties of the gamma phase such as lattice tetragonality, unit cell volume, site occupancy and twinning activity were inconclusive. Currently, we believe that the alloying effects resulting from adding transition metals can be attributed to changes in microstructure and to solution hardening of constituent phases. However, further understanding the phase equilibria in the Ti-Al-X systems (X: transition metals) is required to optimize the effects of alloying, hot-working and subsequent heat treatment on the mechanical properties of Ti-Al-X ternary alloys. Thus, phase relationships in the Ti-Al-X systems have been intensively studied by the use of rapid quenching, diffusion couple, differential thermal analysis and high-temperature X-ray diffraction methods. In parallel to these experimental approaches, calculations of the phase equilibria in Ti-Al-X systems have been done using computer programs [6]. The computer programs are constructed in such a way that they can bundle thermodynamic data for relevant systems in an optimizer module to arrive at numerical values for adjustable parameters defining thermodynamic functions. The adjustable parameters for Ti-Al-X systems have been considerably refined using the data of thermophysical measurements made in the research on TiAl alloys. The phase equilibria in Ti-Al-Nb and Ti-Al-Cr systems can be calculated at any composition and temperature, and the results of calculations are in good agreement with the relevant experimental results. The predictive ability of programs has recently been considerably improved for Ti-Al-W and Ti-Al-Mo systems. The results of such studies of phase diagrams of Ti-Al-X systems have been published in [7,8].

Strength of TiAl alloys at high temperatures is significantly increased by adding refractory metal elements such as W, Nb and Ta. Figure 1 shows tensile strength values of ternary TiAl alloys containing Nb at 1000°C and 1100°C as a function of Nb content [8]. Ingots of ternary alloys were prepared by plasma arc melting and HIPped at 1300°C and 1500 atm for 2 hours. These ingots were then isothermally forged at 1100 - 1300°C and subsequently heat treated at 1000°C - 1300°C for 5 - 120 hours depending on alloy composition to produce a fine and homogeneous duplex structure [8]. Tensile strength of ternary alloys containing Nb increases with increasing Nb content regardless of Al content up to 6 at% Al. When Nb is added more than 8 at%, tensile strength of ternary alloys decreases with increasing Nb content. This is probably because Nb is soluble in the gamma and alpha-2 phases up to about 7 and 5 at%. Adding more than 5 at% Nb results in the occurrence of beta phase whose high-temperature strength is low and whose volume fraction increases with increasing Nb content. This is the reason for the decrease in tensile strength for the range of Nb content higher than 8 at%. Of the three refractory metals, W, Nb and Ta, W is the most effective in increasing the high temperature strength of TiAl alloys [8]. In addition, dispersion of alumina particles in the stabilized lamellar matrix of as-cast alloys results in a strength greater than 300 MPa at 1100°C. However, this is still lower than the targeted strength to be achieved at 1100°C. Thus, another approach, producing composites by incorporating particles of hard carbides such as TiC, NbC and ZrC into the TiAl matrix is being investigated.

In the research on TiAl alloys of the AIST-MITI program, such composites are produced by a rheocasting method, where the solidifying alloy in the liquid-solid state is vigorously agitated by a stirring rod rotating at speeds of 900 - 4200 rpm and is poured to fill the mold when the viscosity is still low [9,10]. Vigorous agitation during solidification results in breaking off

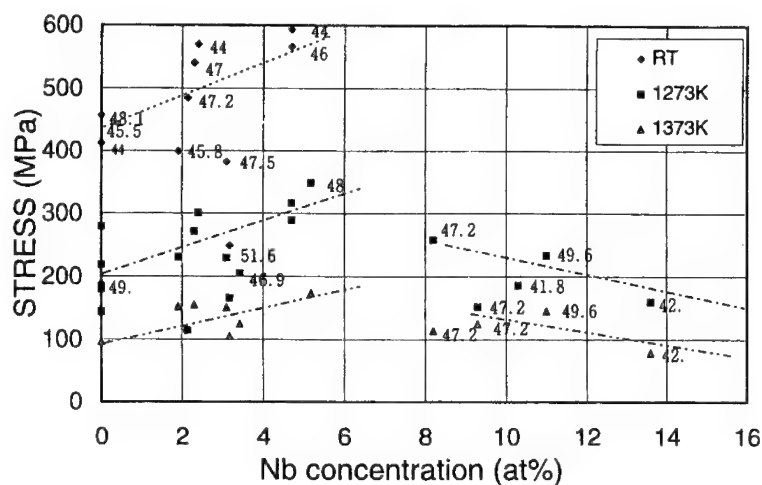


Figure 1 - Effects of Nb content on tensile strength of TiAl-base alloys at room temperature, 1000°C and 1100°C [8]. Numbers in the figure indicate Al contents of alloys.

dendrite fragments and forming a fine grained microstructure. When Ti-44 at%Al alloys are rheocast, no lamellar structure has been observed, but a refined microstructure with a grain size of 2µm has been observed. The characterization of the fine grained microstructure is in progress. They are generally superior to conventionally cast alloys with the same composition in terms of both room-temperature ductility and high-temperature strength. Table 1 shows the values of tensile strength and elongation of conventionally cast and rheocast alloys at four different temperatures.

Table 1. Tensile properties of conventionally cast and rheocast Ti-44 at% Al [10]

Casting Condition	Temperature(°C)	Tensile Strength (MPa)	Elongation (%)
Conventionally Cast	Room	245	2.0
	800	320	2.5
	900	363	1.7
	1000	389	4.3
Rheocast (900rpm)	Room	359	2.7
	800	475	3.3
	900	309	1.7
	1000	323	20.7
Rheocast (4200rpm)	Room	468	3.3
	800	406	2.3
	900	538	5.2
	1000	439	4.2

Rheocasting principles such as rheological behavior and structure of the partially solidified and agitated matrix are beneficial to the fabrication of metal-matrix composites containing nonmetallic hard particles. A Ti-44 at% Al matrix composite containing 10 vol% ZrC has been reported to exhibit 4% room-temperature elongation and a tensile strength at 1100°C as high as 280 MPa [10]. The fabrication of composites with the matrix consisting of ternary TiAl alloys containing

Nb and W is currently in progress. Their strength at 1100°C is expected to be close to the target strength at 1100°C since the high-temperature strength of these ternary alloys is much higher than that of binary TiAl alloys [7,8].

Rolling and Superplastic Forming

Structural materials for aerospace industries are one of the most important fields to which the application of new structural materials developed in the AIST-MITI program should be extended. We may use TiAl alloys as a material to construct the body of future aerospace planes, taking advantage of their low weight and high strength at elevated temperatures. In this case, TiAl alloys in the sheet form should be available and they should be able to be formed to structure parts with various shapes. From such a point of view, considerable research effort has been invested to develop basic technologies for the isothermal rolling and superplastic forming of TiAl alloys.

Isothermal rolling of TiAl alloys was performed using an isothermal mill which was designed and constructed for the AIST-MITI program. To determine the pass schedule to produce TiAl alloy sheets with a fine grained and homogeneous microstructure, numerous multi-step compression tests and microstructure examinations of compressed specimens were performed [11-13]. A typical example of rolled sheet of Ti-46 at%Al is shown in [11]. The sheet exhibits a deformed as-cast lamellar microstructure including a small volume fraction of equiaxed gamma grains. However, recent progress in understanding changes in microstructure during isothermal rolling makes it possible to convert such as-cast lamellar structure into an equiaxed duplex structure during isothermal rolling. Recently, this has been reported to be the case even for Ti-46 at% Al - 4 at% Nb which exhibits the highest strength among the Ti-Al-Nb alloys investigated. The microstructure of Ti-46 at% Al - 4 at% Nb alloy isothermally rolled at 1100°C with a reduction rate of $1 \times 10^{-3}/s$ - $3 \times 10^{-2}/s$ was shown in [13].

The superplastic flow properties have been examined for various alloys that have been isothermally rolled and subsequently heat treated in the temperature range 900 - 1250°C. The following conclusions have been drawn from these intensive investigations[14,15]: (i) Ti-46 at% Al with a uniform and fine grained structure exhibit the best Superplastic formability among the binary alloys investigated, (ii) the addition of Cr is beneficial to the superplastic formability of 46 at% Al base alloys only when more than 2 at% Cr is added, (iii) 46 at% Al base alloys containing more than 2 at% Cr exhibit a considerably low flow stress and a high strain rate sensitivity exponent (m) in comparison to those for the binary Ti-46 at% Al alloy, (iv) the highest m value is obtained for sheets heat treated at 900°C after isothermal rolling, however, such sheets tend to be non-uniformly deformed during superplastic forming because of the non-uniformity of their microstructure, (v) the best superplastic formability is obtained for sheets heat treated at 1250°C after isothermal rolling because their microstructure becomes entirely equiaxed and fine grained with a large amount of beta phase and without any remnants of lamellar structure which causes non-uniform deformation, (vi) Ti-46Al-3Cr (at%) alloy heat treated at 1250°C after isothermal rolling exhibits the best superplastic formability among the alloys investigated so far and the m value of 0.52 observed for the alloy is comparable to that for a typical superplastic 7475 aluminum alloy, (vii) sheets of Ti-46Al-3Cr (at%) alloy produced by isothermal rolling and subsequent heat treatment at 1250°C were subjected to superplastic half-sphere bulge forming tests and their excellent Superplastic formability was verified. Figs. 2 and 3 respectively show the flow stress and m value and the change of grain size and cavity formation during 150 % tensile deformation for Ti-46Al-3Cr (at%) sheets as a function of heat treatment temperature.

Heat Treatment after Superplastic Forming

Superplastically formed TiAl alloys exhibit microstructures in the fine grained duplex form often with a volume fraction of beta phase and therefore very low high-temperature strength. In order to restore their strength at high temperatures, they have to be heat treated at a temperature near the $\alpha/(\alpha+\gamma)$ phase boundary to convert their microstructure into the lamellar form. However, if a fully lamellar microstructure with a large lamellar colony size such as that observed in as-cast ingots is restored, the material would exhibit a high strength at high

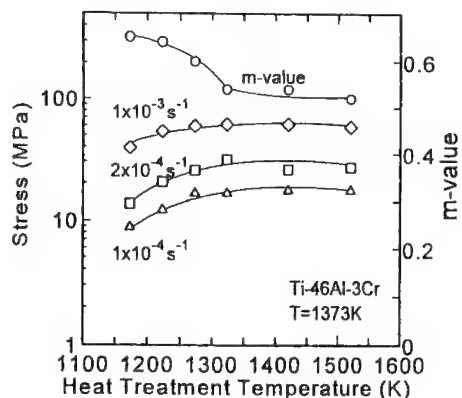


Fig.2

Figure 2 - Flow stress and m-value of isothermally rolled Ti-46Al-3Cr (at%) alloy at 1100°C as a function of heat treatment temperature [15].

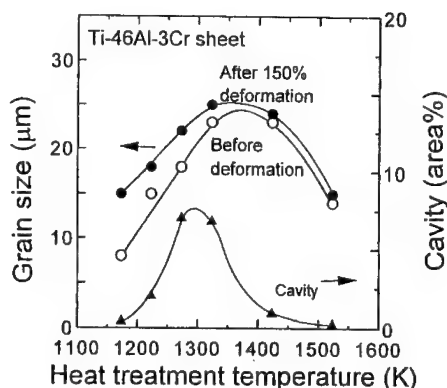


Fig.3

Figure 3 - Grain size and cavity formation in isothermally rolled sheet of Ti-46Al-3Cr (at%) alloy before and after 150% tensile deformation at 1100°C [15]

temperatures, but would exhibit a very poor ductility at low temperatures. Thus, the heat treatment at temperature near the $\alpha/(\alpha+\gamma)$ phase boundary should be performed so that a good combination of high-temperature strength and low-temperature ductility is achieved. Intensive investigations of microstructure/mechanical properties relationships for isothermally rolled and subsequently heat treated sheets have resulted in finding that such a good combination of strength and ductility can be achieved by forming a microstructure consisting of lamellar grains with a lamellar colony size in the range of 100 - 200 μm and equiaxed γ grains surrounding lamellar grains like a necklace. This microstructure is called the "partial lamellar structure [15]". In the case of Ti-46Al-3Cr (at%) alloy, such a microstructure is formed by heat treating superplastically formed sheets, for example, at 1312°C for 2 hr (single-step heat treatment) or at 1325°C for 15 min - 3 hr and subsequently at 1200°C for 1 hr (two-step heat treatment) [15]. The strength at 1000°C for a Ti-46Al-3Cr (at%) alloy in the partially lamellarized form can be as high as 250 MPa with about 2 % tensile elongation at room temperature.

MESSC Program

Intensive studies on the crystal structure, phase stability, deformation and fracture mechanisms, microstructures, oxidation and environmental embrittlement of various intermetallic compounds have been carried out in the program. In particular, it should be noticed that basic properties such as phase equilibria, elastic constants, diffusion coefficients and thermal expansion coefficients have been measured for various new systems where these properties had not previously been available. Recent selected papers from research groups supported by the program will be published in a special issue of *Intermetallics*. In this paper, we pick up just one topic, i.e. directional solidification (DS) of TiAl alloys since studying the topic is believed to lead us to a new aspect of utilizing the lamellar structure of TiAl alloys.

DS Processing of TiAl Alloys

As previously shown [16-18], the mechanical properties of two-phase TiAl alloys greatly depend upon the orientation of the lamellar microstructure. The anisotropic nature of the lamellar microstructure plus the extremely large lamellar grain size that develops upon casting has resulted in materials with a poor combination of properties, such as ductility versus fracture toughness. However, it should be possible to take advantage of the anisotropic nature of the lamellar microstructure by producing material containing only one lamellar orientation via

directional solidification. If the lamellar orientation can be aligned parallel to the growth direction (parallel orientation), then the combination of strength and toughness would be optimized in the resulting composite microstructure [19,20].

Unfortunately, when two-phase TiAl alloys with nearly equiatomic compositions are unidirectionally solidified, the resulting microstructure typically consists of columnar grains with the lamellar microstructure whose lamellae are perpendicular to the growth direction (perpendicular orientation). Such a microstructure results in almost zero tensile ductility even at 1000°C as long as the lamellar microstructure is maintained [21]. However, since these DS ingots have only one lamellar orientation, it may be possible to change the lamellar alignment with the appropriate processing technique. The main difficulty in microstructural control by directional solidification is that the lamellar microstructure is not formed from the liquid but from the solid state. Thus the solidification path in addition to the solid state reactions must be known for each TiAl-based alloy considered.

For directional solidification, the final lamellar orientation will depend upon the initial ingot composition. Small changes in the alloy composition can change the primary solidification phase and thus alter the final microstructure. One method to prevent the formation of lamellar grains with the perpendicular orientation is to adjust the alloy composition such that the ingot solidifies as the beta phase first. Assuming a $\langle 100 \rangle$ growth direction for the beta phase, the alpha phase will nucleate on the close packed planes of the beta phase with an orientation relationship of $(0001)\alpha // (110)\beta$. As the temperature is decreased, the gamma phase will nucleate upon (0001) of the alpha phase producing the lamellar microstructure with an orientation relationship of $(111)\gamma // (0001)\alpha$. Thus the final DS microstructure will consist of lamellar grains with orientations parallel and 45 degrees to the growth direction.

However, if the aluminum content is increased such that the ingot composition lies within the $L + \beta = \alpha$ peritectic region, then a banded microstructure would result [22]. Initially, the ingot would grow as beta, but once the solid-liquid interface temperature drops below the peritectic temperature, the alpha phase would quickly cover the beta phase effectively stopping the reaction. However, when the peritectic composition is greater than the ingot composition, steady-state growth conditions cannot be maintained for the alpha phase. Thus an unstable situation exists and the beta phase would eventually renucleate at the growth front. For this case, the lamellar orientation would vary along the length of the ingot as the growth front changes between the beta and alpha phases. A more promising microstructure would result as the aluminum content of the ingot is increased above the peritectic composition. Again, the beta phase will nucleate first and alpha will nucleate next via the peritectic reaction. However for this composition, a steady-state alpha growth front can be maintained after the alpha phase has nucleated. Therefore, the remaining ingot can solidify as alpha if a planar solid-liquid interface is maintained. Hence, the beta phase can act as a seed for the alpha phase. For example, if a single alpha crystal is nucleated, then a polysynthetically twinned (PST) crystal [16-18] is grown. However, if a planar solid-liquid interface is not maintained, then under dendritic growth the alpha phase may grow with the preferred $[0001]$ orientation resulting in lamellar grains with the perpendicular orientation as is typical in cast gamma alloys.

Lastly, if the aluminum content is increased so that the alpha phase is nucleated first, then casting an ingot with a single lamellar orientation is possible. Since alpha-phase dendrites have a preferred $[0001]$ growth direction, the final microstructure will consist of columnar grains all having a lamellar microstructure with perpendicular orientation. However, the ability to produce an ingot having only one lamellar orientation suggests that microstructural control may be achievable by using a seed material. The basic idea is to control the orientation of the alpha phase upon nucleation from the liquid. Since the lamellar microstructure forms with the $(111)\gamma // (0001)\alpha$ orientation relationship, once the orientation of the alpha phase is determined then the orientation of the lamellar microstructure is also determined. In addition, previous work on PST crystals has shown that when the lamellar microstructure is heated above the $\alpha = \alpha_2 + \gamma$ eutectoid temperature into the $\alpha + \gamma$ two phase region, the lamellar microstructure is stable and the α_2 phase simply disorders to alpha. Furthermore, upon further heating, the volume fraction of alpha increases by the thickening of alpha lamellae

and not by nucleation of new alpha grains. And finally, upon cooling, the processes is reversed and the original orientation of the lamellar microstructure is restored [23]. Hence, if such a process is followed and if recrystallization can be avoided, then it is should be possible to align the lamellar microstructure using a seed material.

Therefore, alignment of the lamellar microstructure in gamma alloys of near equiatomic compositions may be accomplished by DS techniques using an appropriately oriented seed crystal. The problem encountered in this approach is that the alpha phase is not stable up to the melting temperature in the Ti-Al binary system. For example, a composition where alpha is the primary solidification phase would pass through the gamma single phase region upon heating or cooling causing recrystallization to occur. Thus, the composition of the seed must come from a ternary system where the alpha phase is stable until melting. Suitable alloying additions for the seed material are ones that shift the primary alpha region towards lower aluminum content, thus missing the gamma single phase region upon cooling. For example, silicon has such an effect [20]. Thus, alignment of the TiAl/Ti₃Al lamellar microstructure parallel to the growth direction should be possible by using an appropriately oriented seed from the TiAl-Si system. We have directionally solidified 15 different alloys whose compositions are varied in TiAl-Si, TiAl-Nb-Si, and Ti-Al binary systems using seed crystals whose composition was kept constant at Ti-43Al-3Si (at.%). Table 2 show the results of DS processing of these alloys. The alloys whose lamellar microstructure is aligned parallel to the growth direction are indicated by "yes". It is found that the lamellar

Table 2. Compositions of directionally solidified ingots and the results of the seeding experiment using Ti-43Al-3Si seed with the parallel orientation and a growth rate of 5 mm/h

Alloy Composition (at.%)	Aligned (parallel orientation) Lamellar Microstructure
(TiAl-Si)	
Ti-43Al-3Si	Yes
Ti-45Al-2Si	Yes
Ti-45.5Al-1.5Si	Yes
Ti-46Al-1.0Si	Yes
Ti-46.5Al-0.5Si	Yes
Ti-47Al-0.5Si	No
Ti-48.5Al-0.5Si	No
Ti-49Al-0.3Si	No
(Binary TiAl)	
Ti-50Al	No
Ti-49.5Al	No
Ti-48Al	No
Ti-47Al	Yes
TiAl-Nb-Si)	
Ti-49Al-3Nb-0.5Si	No
Ti-48Al-3Nb-0.5Si	No
Ti-46.5Al-3Nb-0.5Si	Yes

microstructure can be aligned for alloys containing approximately 47at.% Al in each of these systems. For the composition of seed material, Ti-43Al-3Si, where alpha is the primary solidification phase, the original orientation of the lamellar microstructure is maintained after heating to and cooling from single phase alpha region making seeding of the alpha-phase possible. When this silicon containing seed is used, the nucleation of the primary beta-phase in master alloys of Ti-(47-x)Al-xSi (x=0 to 1 at%) could be suppressed resulting in the nucleation and growth of only the alpha-phase with an orientation determined by the seed crystal. For master alloys with compositions of Ti-(47-x)Al-xSi (x=0 to 1 at%), the silicide phase which is

present in the seed material can be eliminated in the final directionally solidified material greatly increasing the tensile ductility. These results will be reported in more detail elsewhere [24].

Closing Remarks

Extensive progress and improvements have been made in the science and technology of gamma titanium aluminide alloys within the last decade. In particular, our understanding of their microstructural characteristics and property/microstructure relationships has been substantially deepened. Based on these achievements, various engineering two-phase gamma alloys have been developed and their mechanical and chemical properties have been assessed. Aircraft and automotive industries are pursuing their introduction for various structural components. Very recently, a major automotive company of Japan disclosed its development activities and future production plan of TiAl exhaust valves in a major daily news paper. This is a very encouraging news on industrial applications of TiAl and we hope it will continue. Industrial success in structural applications of TiAl is soon coming.

Acknowledgments

This work was supported by Grand-in Aid for Scientific Research on the Priority Area 'Intermetallic Compounds as New High Temperature Structural Materials' from the Ministry of Education, Science, Sports and Culture, Japan, and in part by the NEDO International Research Grant for the Intermetallic Team and the research grant from the Research and Development Institute of Metals and Composites for Future Industries. DRJ would like to thank the Japan Society for the Promotion of Science (JSPS) and the National Science Foundation (NSF) for a research fellowship.

References

1. M. Yamaguchi, Mater. Sci. Tech, 8(April) (1992) 299-307.
2. T. Maruo and M. Tomita, Critical Issues in the Development of High Temperature Structural Materials, ed. N. S. Stoloff, D. J. Duquette and A. F. Giamei, TMS, 1993, pp.477-490.
3. Proc. Intermetallic Compounds for High Temperature Structural Applications, 3rd Japan International SAMPE Symposium (Dec. 7-9, 1993), ed. M. Yamaguchi and H. Fukutomi.
4. Research Report for Grant-in-Aid for Scientific Research on the Priority Area "Intermetallic Compounds as new High Temperature Structural Materials" from The Ministry of Education, Science, Sports and Culture, 1992-1994.
5. A special issue of *Intermetallics* to be published in August, 1996.
6. B. Sundman, B. Jansson and J. O. Anderson, CALPHAD, 9 (1985) 153.
7. K. Hashimoto, T. Hanamura and Y. Mizuhara, Proceedings of the 5th Symposium on High-Performance Materials for Severe Environments, R&D Institute of Metals and Composites for Future Industries (RIMCOF), 1994, pp.57-65.
8. K. Hashimoto, T. Hanamura and Y. Mizuhara, Proceedings of the 6th Symposium on High-Performance Materials for Severe Environments, R&D Institute of Metals and Composites for Future Industries (RIMCOF), 1995, pp.67-75.
9. K. Ichikawa, Proceedings of the 5th Symposium on High-Performance Materials for Severe Environments, R&D Institute of Metals and Composites for Future Industries (RIMCOF), 1994, pp.47-55.
10. K. Ichikawa and Y. Kinoshita, Proceedings of the 6th Symposium on High-Performance Materials for Severe Environments, R&D Institute of Metals and Composites for Future Industries (RIMCOF), 1995, pp.57-66.
11. N. Fujitsuna, Y. Miyamoto and Y. Ashida, Structural Intermetallics, ed. R. Darolia, J. J. Lewandowski, C. T. Liu, P. L. Martin, D. B. Miracle and M. V. Nathal, TMS, 1993, pp.187-194.
12. J. Miyamoto and N. Fujituna, Proceedings of the 5th Symposium on High-Performance Materials for Severe Environments, R&D Institute of Metals and Composites for Future Industries (RIMCOF), 1994, pp.67-76.

13. N. Fujituna, K. Sakamoto, J. Miyamoto and Y. Seki, Proceedings of the 6th Symposium on High-Performance Materials for Severe Environments, R&D Institute of Metals and Composites for Future Industries (RIMCOF), 1995, pp.77-85.
14. H. Sato and T. Tuzuku, Proceedings of the 5th Symposium on High-Performance Materials for Severe Environments, R&D Institute of Metals and Composites for Future Industries (RIMCOF), 1994, pp.77-85.
15. T. Tsuzuku, H. Sato and T. Yamada, Proceedings of the 6th Symposium on High-Performance Materials for Severe Environments, R&D Institute of Metals and Composites for Future Industries (RIMCOF), 1995, pp.87-97.
16. T. Fujiwara, A. Nakamura, M. Hosomi, S. R. Nishitani, Y. Shirai and M. Yamaguchi, *Phil. Mag. A*, 61(4) (1990) 591-606.
17. H. Inui, M. H. Oh, A. Nakamura and M. Yamaguchi, *Acta, metall. mater.*, 40(11) (1992) 3095-3104.
18. S. Yokoshima and M. Yamaguchi, *Acta mater.*, 44(3) (1996) 873-883.
19. K. Kishida, D. R. Johnson, Y. Shimada, H. Inui, Y. Shirai and M. Yamaguchi, *Gamma Titanium Aluminides*, ed. Young-Won Kim, Richard Wagner and M. Yamaguchi, TMS, 1995, pp.219-229.
20. D.R. Johnson, H. Inui, and M. Yamaguchi, *Acta Mater.*, 44(6) (1996) 2523-2535.
21. H. Inui, K. Kishida, M. Misaki, M. Kobayashi, Y. Shirai and M. Yamaguchi, *Phil. Mag. A*, 72 (6) (1995) 1609-1631.
22. W.J. Boettinger, *Met Trans.* 5 (1974) 2023.
23. H. Inui, Y. Toda, Y. Shira, and M. Yamaguchi, *J. Japan Inst. Metals*, 59(5) (1995) 588-589.
24. D. R. Johnson, Y. Masuda, H. Inui and M. Yamaguchi, to be published.

CHALLENGES IN THE DEVELOPMENT AND APPLICATION OF β -NiAl AS A
STRUCTURAL MATERIAL

V.I. Levit, J. Hu, I.A. Bul, J.S. Winton and M.J. Kaufman

Dept. of Materials Science and Engineering
University of Florida
Gainesville, Florida 32611

Abstract

High purity single crystals of stoichiometric NiAl have been deformed in tension over a range of temperatures and strain rates. Elongations approaching 35% are possible at room temperature when the sample geometry is controlled properly whereas elongations as high as 200% have been achieved at intermediate temperatures (e.g., 600K). Subsequent analysis of the dislocation substructure, the macroscopic shape change and the nature of the fracture indicate that deformation in the soft-oriented crystals is dominated by slip of $\langle 001 \rangle$ dislocations and that the material remains brittle even when the elongations are as high as 200%. Finally, the implications of these results on the applicability of NiAl as a structural material are discussed in some detail.

Introduction

In the past decade, there has been a resurgence of interest in developing β -NiAl as a structural material. This is largely a consequence of its high melting temperature, reasonably low density and excellent oxidation resistance. As with many other intermetallics, however, NiAl has low toughness at low temperatures and low strength at all temperatures. Clearly, the challenge has been to enhance both the strength and toughness of this compound although most studies have tended to address one deficiency while largely ignoring the other.

There have been several excellent reviews on the subject of NiAl (1, 2). Based on these reviews as well as more recent publications, a number of things that influence the mechanical properties of NiAl have been identified as summarized below:

- a. deviations from stoichiometry;
- b. concentration of thermal vacancies as influenced by heat treatment (3, 4);
- c. substitutional and interstitial impurities (4, 5, 6, 7, 8);
- d. surface condition (9);
- e. orientation (single crystals) (10, 11);
- f. texture (polycrystals) (12); and
- g. prestraining to produce mobile dislocations (13, 14, 15);

The purpose of this paper is to discuss some of these issues along with some new experimental data that will allow us to make some definitive statements concerning the viability of NiAl as a potential engineering material.

Low Temperature Properties

It is well established that the critical resolved shear stress (CRSS) for $\langle 100 \rangle$ slip in NiAl is quite low although there is considerable controversy as to the actual values, slip planes, etc. Clearly, the various published data mentioned above indicate that the CRSS is strongly dependent on such parameters as purity, thermal history, deviations from stoichiometry, prestrain, etc. It is also widely accepted that the number of active slip systems in NiAl is insufficient to allow for the "general" deformation of a random polycrystalline body according to the von Mises criterion. What has not been addressed adequately in our view is the rather low tensile ductility in single crystals oriented in soft (non- $\langle 100 \rangle$) directions. Specifically, the question of why high purity NiAl, which has a very low CRSS (~ 60 MPa) when oriented for single (e.g., tensile axis (TA) parallel to $\langle 112 \rangle$) or double (e.g., TA parallel to $\langle 011 \rangle$) slip, fractures after elongations typically below 5% remains unanswered. In addition, it is also unclear why NiAl single crystals microalloyed with Fe, Mo and Ga displayed higher elongations when tested parallel to $\langle 110 \rangle$ (double slip) than the single slip orientations in the study by Darolia, et al. (16).

In this study, the initial tensile specimens were cut with an EDM to have rectangular (nominally 1.6×2.4 mm prior to electropolishing) cross sections, 10-15 mm gage lengths and 25-30 mm total lengths instead of the cylindrical button-head geometry (produced by centerless grinding) used in the majority of the previous studies to date. In the preliminary tests with $[\bar{2}13]$ tensile specimens, elongations above 25% were achieved at room temperature. Furthermore, it became clear that the elongation was strongly dependent on the orientation of the slip plane and direction relative to the face and side of the specimen; i.e., the highest elongations were obtained

with the slip plane orthogonal to the 2.4 mm “face” of the specimen (see Fig. 1). Furthermore, it was noted that (1) the change in the geometry and dimensions of the gage cross section, (2) the rotation of the tensile axis during the deformation, and (3) the measured work hardening rate were all consistent with the deformation occurring mostly by single slip on the $[001](\bar{1}10)$ system and that the slip plane is not $\{hk0\}$ where $h \neq k$ as was suggested as a possibility by Takasugi, et al. (11). TEM analysis of these samples after different elongations revealed the presence of pile-ups of edge dislocations with $\mathbf{b}=[001]$ on $(\bar{1}10)$ planes. These were spaced approximately 1 μm apart depending on the deformation level. No pure screw dislocations were observed consistent with their elastic instability as pointed out by Loretto (17).

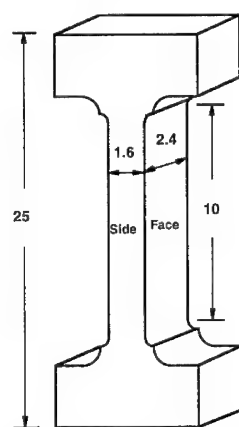


Figure 1 - Geometry of tensile specimens used in the current study. All dimensions in mm.

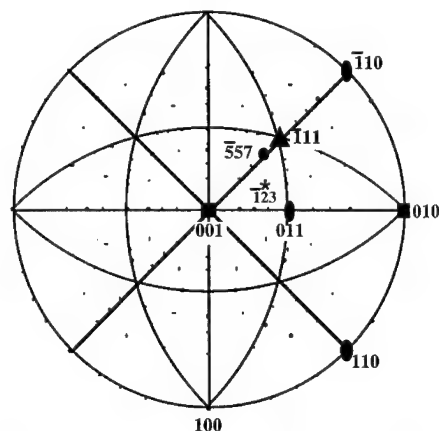


Figure 2 - Stereographic projection with the relevant directions indicated.

In order to examine this phenomenon more thoroughly, tensile specimens were intentionally oriented for single slip with their TA parallel to either $[557]$ or $[\bar{1}11]$ (Schmid factors of 0.5 and 0.47, respectively) (see Fig. 2). For these orientations, the specimen rotation due to slip on the $[001](\bar{1}10)$ system is about the orthogonal $[110]$ axis. Thus, the specimens were cut with either the (110) plane parallel to the face or side in Fig. 1 in order to provide insight into the specimen constraint and geometry issue. The results of these tests are summarized in Table 1 where it is apparent that (1) the strengths are indicative of high purity material and (2) the samples with their faces cut approximately parallel to (110) exhibit considerably larger elongations (9-34%) compared with the samples cut with their sides parallel to (110) (2.5-15%). In all cases, the ensuing fracture was brittle cleavage in spite of the single slip nature of the deformation which usually does not lead to brittle fracture. Finally, the measured work hardening rates were also consistent with single slip being approximately 5×10^{-4} times the shear modulus, μ , in the $[001]$ direction where $\mu_{001} = 112.1$ GPa according to Wasilewski (18). In order to determine what factors led to the higher elongations in the “Face (110) ” specimens, such things as specimen cross section, constraints in the grips, and gage length were varied systematically. The results indicate clearly that constraints in the grip are important at low plastic strains and become less important at the higher elongations (above $\sim 3\%$). This appears to be the reason that the cylindrical, button-head specimens exhibit higher elongations when tested parallel to $\langle 110 \rangle$ as it is this orientation in which there is no rotation as described above. However, for the purer crystals that undergo higher elongations, it appears that it is the

specimen geometry (the aspect ratio) which is more important for achieving the higher strains. In fact, when single slip causes the cross section to change from rectangular to square, the elongations are typically greater than those where the aspect ratio deviates further from square. This clearly had a greater effect than changes in the gage length or whether the face or side was parallel to the slip direction. Typical shear stress - shear strain curves depicting this behavior are shown in Fig. 3. These variations and their effects on properties will be covered in greater detail in a separate paper. TEM analysis of the deformation substructure in these specimens revealed again that the dislocations present after deformation were similar to those observed in the $[1\bar{2}3]$ specimens (19).

Sample Description	$\sigma_{0.2}$ MPa	Elong. %	σ_r MPa
Side (110)	140	6.2	205
15 mm gage	132	4.5	184
	127	10.3	196
	137	15.0	239
	134	12.6	221
	141	2.5	183
Face (110)	101	16.6	196
15 mm gage	98	9.4	158
	100	22.0	195
	97	12.1	215
	94	26.0	203
	105	13.9	188
Face (110)	115	17.9	218
10 mm gage	114	33.9	266
	109	16.2	190

Table 1 Mechanical properties of NiAl crystals tested parallel to $\langle 557 \rangle$ at room temperature.

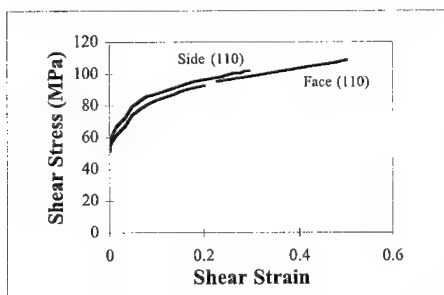


Figure 3 - Shear stress vs. shear strain for $[557]$ crystals tested at room temperature illustrating the importance of the specimen geometry on elongation.

As mentioned above, specimens oriented for double slip with their TA along $[011]$ were also investigated. Unlike the single slip samples, however, this orientation is stable with respect to rotation during straining due to the offsetting nature of the two active slip systems, namely $[001](010)$ and $[010](001)$ which are at right angles to each other. The results of this comparison indicated that (1) this orientation is indeed stable with respect to rotation, (2) the tensile elongations are lower than in the single slip samples, (3) the CRSS for slip of $b=\langle 001 \rangle$ dislocations on cube planes is similar to that on $\{011\}$ planes, and (4) the work hardening rate is about an order of magnitude higher than for the single slip case. For the comparison of CRSS values, specimens taken from the same crystals indicate that, indeed, the CRSS values are similar (60 ± 5 MPa).

The dislocations observed in the samples tested in this orientation were also primarily edge in nature and again were distributed as pile-ups parallel to the cube slip planes. As anticipated, there were approximately equal amounts of dislocations corresponding to the two slip. The unusual geometry of double slip in NiAl and the manner in which dislocation intersections might occur is quite interesting and will be addressed further in a subsequent paper.

In light of these high tensile elongations at room temperature, it is of interest to reconsider the issue of low elongation in

single crystals of compounds that have fewer than five independent slip systems yet where the Von-Mises criterion is only applicable to polycrystalline deformation or to complex loading of single crystals. This work suggests that multiple systems are required for uniaxial tensile deformation of single crystals oriented for easy glide if the sample is constrained whereas the removal of the constraints allows the sample to deform to larger strains before the stress at some sort of stress concentration(s) reaches the fracture stress. In other words, materials such as NiAl that have low CRSS values are still likely to be brittle in single crystal form when the other slip systems have much higher CRSS values. Such behavior has been observed in certain oxides such as MgO which is also both soft and brittle. In both materials, the stress concentrations that develop during deformation can not be relieved by activating other slip systems.

Influence of Temperature on Deformation Behavior

Based on the realization of the importance of specimen geometry on tensile elongation, similar samples of binary NiAl were tested over a range of temperatures. The results for $[\bar{1}11]$ crystals (Fig. 4) clearly indicate that the CRSS is a strong function of temperature as is characteristic of BCC and HCP metals and alloys. Significantly, finite elongations were also measurable at sub-ambient temperatures (Fig. 5).

As the testing temperature is increased above room temperature, the tensile elongation increases to high values (above 200% in some cases) at intermediate temperatures (e.g., 600K) and then decreases again much like in the reports of Takasugi, et al. (20) and Lahrman, et al. (21) (Fig. 5). It is also clear that the present specimen geometries were superior for achieving higher elongations at all temperatures and that the temperature range of the high elongations in the UF specimens was considerably larger than in the previous investigations.

Typical load-elongation curves for the samples undergoing the highest elongations are shown in Fig. 6a where it is clear that the load decreases after yielding before increasing again. This drop in load is quite gradual and is not characteristic of typical Lüders behavior where the drop is much more rapid. In an effort to analyze this behavior more completely, the crosshead was stopped at different points on the stress-strain curve, the sample was then cooled to room temperature and the specimen photographed. This examination allowed us to note that the sample begins to neck immediately after yielding; this neck continues to localize and then stops as the work hardening increases the flow stress locally. Based on these intermediate observations, it is possible to draw approximate shear stress-shear strain curves; the results (Fig. 6b) imply that the shear stress doesn't drop and that the work hardening rate is quite low except at the localized region of the neck. It should be mentioned that similar results have been observed in Cu-In single crystals (22) and Mg crystals (23).

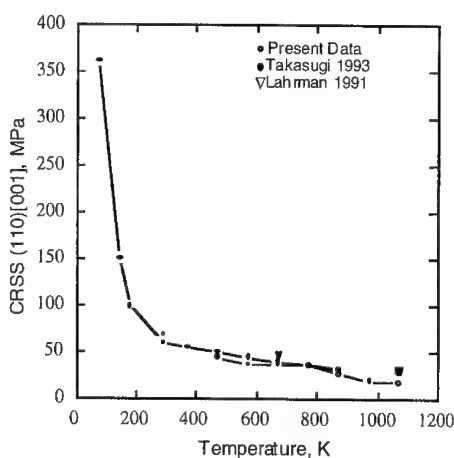


Figure 4 - CRSS vs. temperature for the $[001](\bar{1}10)$ slip system taken from tests on $[\bar{1}11]$ specimens.

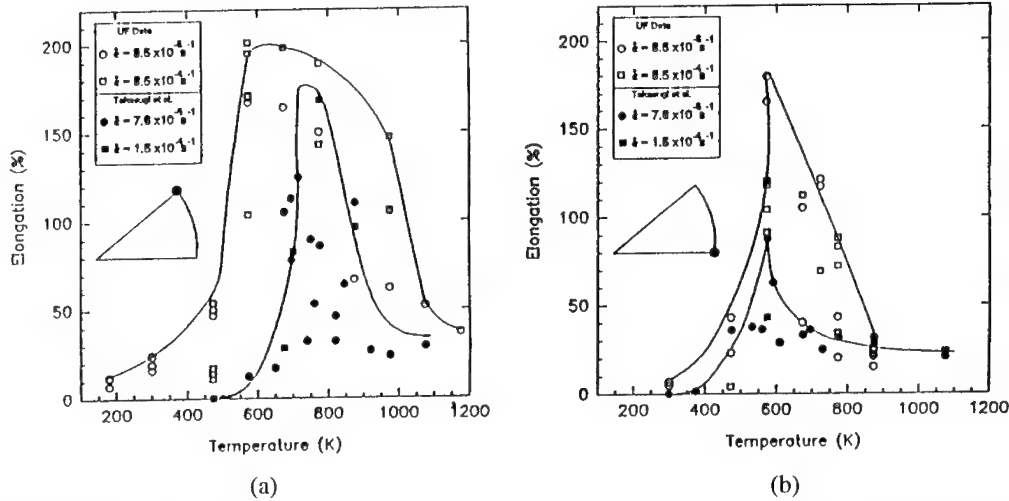


Figure 5 - Tensile elongation vs. temperature for (a) $\langle 111 \rangle$ and (b) $\langle 110 \rangle$ samples comparing the present data with that of Takasugi, et al. (20) and Lahrman, et al. (21).

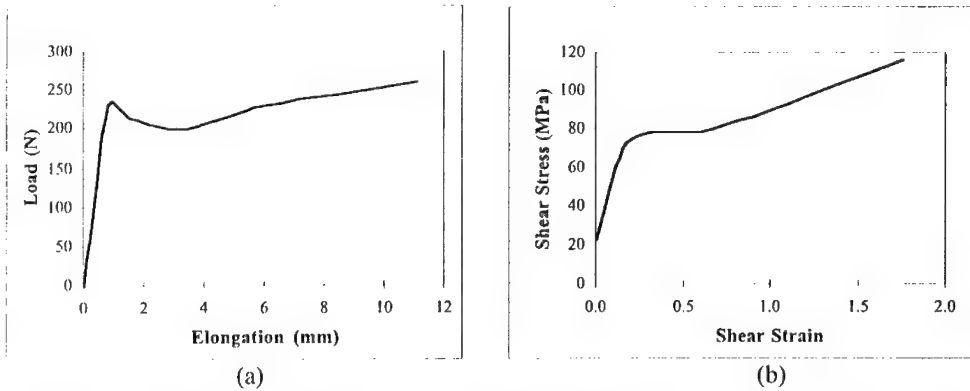


Figure 6 - (a) Load vs. elongation for $\langle 111 \rangle$ crystal tested at 573K. (b) Shear stress vs. shear strain of same taking into account both Lüders band propagation (actual area) and specimen rotation during elongation. Strain rate = 10^{-3} s^{-1} .

Comparable results were also obtained on the $[011]$ specimens although the range of temperatures over which the high elongations were observed was considerably narrower.

After the Lüders band propagates along the total length of the specimen, the material then begins to demonstrate a fairly typical work hardening response as is clear in Fig. 6. During this deformation, the material is relatively resistant to necking and tends to undergo extensive elongations. These observations are consistent with the recent theoretical work by Hahner (24, 25) who used a dynamic dislocation model to predict the behavior of Lüders bands in both single crystals and polycrystals. In spite of these large elongations, the ensuing fracture is still brittle in appearance.

The drop-off in the elongation at elevated temperatures (Fig. 6a) can be correlated with an increased tendency for the material to neck prior to fracture (Fig. 7). When the strain rate sensitivity and work hardening rates were examined as a function of temperature, it became obvious that the strain rate sensitivity increases with increasing temperature whereas the work



hardening rate drops off presumably due to dynamic recovery effects. However, the drop in work hardening rate outweighs the increase in SRS resulting in the increased tendency for the necks to localize the deformation and lead to fracture at shorter total elongations.

Implications of Deformation Behavior

Taken collectively, the present results indicate that high elongations are achievable in high purity NiAl when both orientation and specimen geometry are controlled properly. As expected for "unconstrained" deformation, the highest elongations are observed in the samples oriented for single slip due to the lower work hardening rates associated with Stage I deformation. Even though the CRSS for slip on {011} and {001} planes is similar, a direct comparison of the deformation response is difficult since slip on cube planes is always duplex whereas slip on the {011} planes is rarely duplex (e.g., for $[\bar{u}v\bar{v}]$ between $[\bar{1}11]$ and $[\bar{1}22]$). This behavior is rather unique for metals and intermetallics and is of academic interest for this reason.

Figure 7 - Scanning electron micrographs of $[\bar{1}11]$ samples tested at (a) 573K (strain rate = 10^{-3} s^{-1}) and (b) 873K (strain rate = 10^{-4} s^{-1}) showing the greater necking at the higher temperatures.

It should be mentioned that the behavior after some plastic deformation may change from single to multiple slip depending on the initial orientation and the amount of strain.

In spite of the high elongations at both room and elevated temperature, it is clear from the present results that the possibility of producing tough, damage tolerant, monolithic NiAl is low. As already stated, this is due to the lack of a sufficient number of operative deformation mechanisms which, in turn, is related to the disparity between the CRSS values of dislocations with $\mathbf{b}=\langle 001 \rangle$ vs. those with $\mathbf{b}=\langle 011 \rangle$ and $\mathbf{b}=\langle 111 \rangle$. This realization combined with the fact that the fracture of NiAl is brittle even after large 100-200% elongations implies that the transition from negligible to high elongation cannot be correlated directly with the BDTT. In fact, it appears that the true BDTT must actually occur at temperatures above that where the highest elongations are observed, since the latter still exhibit brittle cleavage fracture. This indicates that the correlation of the BDTT with high tensile elongation may be nebulous in intermetallic compounds of this type. Likewise, this may explain why investigators have moved away from using Chevron-notch specimens to more traditional impact experiments.

Based on these results, it is important to reconsider the mechanism of the high elongations in greater detail. This issue has been somewhat controversial with some groups promoting the idea that climb of $\langle 001 \rangle$ edge dislocations (1) is responsible for the transition to high elongations while others suggest that it is related to the operation of secondary slip systems (26). It would appear from the present results that the former mechanism is more likely due to both the nature of the dislocation substructures as well as the macroscopic shape changes that occur at the high strains. In fact, the latter can only be accounted for by the operation of $\langle 001 \rangle$ edge dislocations. Significantly, Takasugi found that the high elongations observed at intermediate temperatures displayed a strong strain rate dependence consistent with the climb mechanism. Thus, it appears that the high elongations are possible whenever the stresses at stress concentrations can be relieved by the combination of glide and climb of the cube dislocations. Clearly, such factors as interstitial and substitutional solute content, deviations from stoichiometry, vacancy concentration, strain rate, dislocation density (prestraining effects), etc., are important and need to be considered when studying the behavior of this compound.

Summary and Conclusions

The present results indicate that it is possible to achieve fairly high elongations in NiAl at temperatures well below the so-called BDTT by careful control of the sample geometry and purity. Unfortunately, high elongations do not necessarily equate to high toughness and ductility. Based on these results, it is possible to draw the following conclusions:

1. High elongations (approaching 35% at room temperature) are possible in single crystals of NiAl at both sub-ambient and ambient temperatures when the specimen geometry and purity are controlled.
2. At intermediate temperatures, the elongations frequently exceed 200%. This has been correlated with lower initial flow stress, decreasing work hardening rates and increasing strain rate sensitivities with increasing temperature. The fracture surfaces after such high elongations are still brittle in nature.
3. Above the temperature of maximum elongation, localized necking occurs due to the decreased work hardening rate. Even so, the fractures are still brittle except for the samples that neck to a chisel point.
4. The soft, brittle nature of NiAl appears to be reasonably well understood at this point. Unfortunately, it is our belief that it will not be possible to enhance both the strength and toughness of monolithic NiAl due to the fact that the toughness of the high purity NiAl is negligible and that elements added to enhance the strength will reduce the toughness.

Acknowledgements

This work was sponsored by the Air Force Office of Scientific Research (URI Grant F49620-93-0309) under the direction of Dr. Charles H. Ward.

References

1. R. D. Noebe, R. R. Bowman, M. V. Nathal, in *Physical Metallurgy and Processing of Intermetallic Compounds, Chapter 9* N. S. Stoloff, V. K. Sikka, Eds. New York, NY, 1994).
2. D. B. Miracle, *Acta. metall. mater.* **41**, 649-684 (1993).
3. J. E. Hack, J. M. Brzeski, R. Darolia, *Scripta Met. et Mat.* **27**, 1259-1263 (1992).
4. M. L. Weaver, R. D. Noebe, J. J. Lewandowski, B. F. Oliver, M. J. Kaufman, *Mats. Sci. & Engr.* **A192**, 179-185 (1995).
5. E. P. George, C. T. Liu, *J. Mater. Res.* **5**, 754-762 (1990).
6. D. Goldberg, G. Sauthoff, *Intermetallics* **4**, 143-158 (1995).
7. J. M. Brzeski, J. E. Hack, R. Darolia, R. D. Field, *Mats. Sci. & Engr.* **A170**, 11-18 (1993).
8. J. M. Brzeski, J. E. Hack, R. Darolia, *Mat. Res. Soc. Symp. Proc.* **364**, 419 (1995).
9. J. H. Schneibel, S. R. Agnew, C. A. Carmichael, *Met. Trans. A* **24A**, 2593-2596 (1993).
10. D. F. Lahrman, R. D. Field, R. Darolia, *Mats. Res. Soc. Symp. Proc.* **288**, 679 (1993).
11. T. Takasugi, S. Watanabe, S. Hanada, *Mats. Sci. & Engr.* **A149**, 183-193 (1992).
12. T. R. Bieler, R. D. Noebe, M. Hebsur, R. Saminathan, The effects of extrusion parameters on recrystallization kinetics, texture, and corresponding fracture toughness of NiAl, J. J. Jonas, T. R. Bieler, K. J. Bowmans, Eds., *Advances in Hot Deformation Textures and Microstructures*; The Minerals, Metals & Materials Society 1994),
13. R. W. Margevicius, J. J. Lewandowski, *Metall. and Mat. Trans. A* **25A**, 1457-1470 (1994).
14. Margevicius, Lewandowski, Locci, *Scripta Metallurgica et Materialia* **26**, 1733-1736 (1992).
15. M. A. Morris, J.-F. Perez, R. Darolia, *Phil. Mag. A* **69**, 507-526 (1993).
16. R. Darolia, D. F. Lahrman, R. D. Field, A. J. Freeman, in *High Temperature Ordered Intermetallic Alloys III* . C. T. Liu, A. I. Taub, N. S. Stoloff, C. C. Koch, Eds. (Materials Research Society, Boston, 1989),
17. M. H. Loretto, R. J. Wasilewski, *Phil. Mag.* **23**, 1311-1328 (1971).
18. R. J. Wasilewski, *Trans. Metall. Soc. AIME* **36**, 455-457 (1966).

-
19. V.I. Levit, I.A. Bul, J. Hu and M.J. Kaufman, *Scripta Mater.* **34**, 1925-1930 (1996).
 20. T. Takasugi, J. Kishino, S. Hanada, *Acta. metall. mater.* **41**, 1009-1020 (1993).
 21. D. F. Lahrman, R. D. Field, R. Darolia, The Effect of Strain Rate on the Mechanical Properties of Single Crystal NiAl, L. A. Johnson, D. P. Pope, J. O. Stieglers, Eds., High-Temperature Ordered Intermetallic Alloys IV (Materials Research Society, Boston, Mass., 1991), vol. 213, pp. 603-607.
 22. B. J. Brindley, D. J. Corderoy, R. W. K. Honeycombe, *Acta Met.* **10**, 1043 (1962).
 23. R. E. Reed-Hill, *Physical Metallurgy Principles*. (D. Van Nostrand Company, New York, 1973).
 24. P. Hahner, *Appl. Phys. A* **58**, 41-48 (1994).
 25. P. Hahner, *Appl. Phys. A* **58**, 49-58 (1994).
 26. R. D. Field, D. F. Lahrman, R. Darolia, *Acta Metall. Mater.* **39**, 2951-2959 (1991).

FATIGUE AND FRACTURE OF HIGH TEMPERATURE INTERMETALLICS

N. S. Stoloff

Materials Science and Engineering Department
Rensselaer Polytechnic Institute
Troy, New York 12180-3590

Abstract

Two issues dealing with the fatigue and fracture behavior of several high temperature aluminide and silicide intermetallics, as well as some of their composites, are reviewed. Specifically, environmental effects and the role of toughening phases on brittleness of several intermetallic systems is discussed. The effects of processing on microstructure and properties, as well as the roles of temperature, strain rate and test environment will be discussed. It will be shown that crack growth behavior in several intermetallic systems is adversely affected by moist atmospheres at low temperatures, and by oxygen at high temperatures. Various approaches to improving fatigue and fracture resistance are described.

Introduction

Although several intermetallic compounds have been identified that could conceivably equal or exceed the mechanical properties of currently utilized high temperature alloys, a recurring concern with the intermetallics is their relatively low fracture toughness, impact resistance and fatigue crack growth resistance. In most cases a brittle to ductile transition is seen; accordingly, emphasis in research and development activities has been placed upon identifying failure mechanisms and developing approaches to improved toughness. It is now known that some intermetallics, eg MoSi_2 , NiAl and Cr_2Nb , are intrinsically brittle, while others, such as Ni_3Al , Fe_3Al and FeAl are quite ductile when tested in dry environments. Similar behavior is manifested under cyclic loading conditions. For example, crack growth rate exponents are very high in some compounds, such as TiAl or Fe_3Al (when the latter is tested in moist air,) but much lower exponents are noted when toughening is achieved through composite formation or by the provision of a dry environment.

This paper will summarize recent developments in fracture and fatigue of the following classes of alloys: aluminides of nickel, titanium, iron and niobium, and silicides of chromium and molybdenum.

Nickel Aluminides

Ni_3Al

Recent work by George et.al.[1] has shown that high purity Ni_3Al , when tested in a dry environment, exhibits moderate ductility. The embrittling effects of moisture on this material were overlooked for many years in part because of the successes obtained with alloying with boron. Small boron additions suppress embrittlement so well that workers in the field tended to study only boron-doped material. The intrinsic ductility of Ni_3Al is still not very high, and there is a pronounced tendency towards intergranular fracture. Therefore, poor grain boundary strength also contributes to the perceived brittleness of this alloy system.

There has been little reported in the literature recently concerning the fatigue behavior of Ni_3Al alloys. However, Sikka[2] has shown that at 650°C the high cycle fatigue resistance of alloy IC-221M is superior to that of the nickel-base superalloy IN-713C.

NiAl

Surprisingly little has been reported on the fatigue resistance of NiAl , in spite of great interest in this compound for gas turbine applications. Several studies of low cycle, strain controlled, fatigue have been carried out,[3,4] but no crack growth data have been reported. Given the low ductility and extreme notch sensitivity of both single crystals and polycrystals of NiAl at low temperatures, it is to be expected that crack growth rates will be high. Several in-situ composites based upon NiAl have been prepared, and moderate levels of monotonic toughness have been observed, see Fig. 1[5]. Fatigue data have not been reported for these materials. Unfortunately, the toughest composites tend to have the lowest creep resistance at 1300°K .

Iron Aluminides

The iron aluminides Fe_3Al and FeAl are not high temperature materials in the same sense as other intermetallics discussed in this paper. Nevertheless, the combination of low density, low cost and excellent oxidation and corrosion resistance has led to extensive work on their mechanical properties at both room and elevated temperatures. Both alloys are extremely sensitive to moisture and to hydrogen, but exhibit modest ductility in dry environments[6]. Current research efforts are directed both at minimizing the effects of moisture and at improving creep resistance. One technique that shows considerable promise in the latter area is the incorporation of oxides into the microstructure[7]. However, this work is in early stages, so this paper will review only efforts to understand and reduce environmental embrittlement.

Fe_3Al

It is now well established that maximum ductility in air is obtained at

aluminum and chromium levels of 28 and 5a%, respectively[7]. Recent efforts at alloy development, carried out principally at the Oak Ridge National Laboratory and at Asea Brown Boveri in Switzerland, have included the use of small amounts of the carbide formers niobium or zirconium[8]. Tensile and fatigue crack growth experiments have been carried out by us on the alloys listed in Table 1[9,10]. Note that a simple Fe-28%Al-5%Cr alloy is included for base line data, as is a disordered Fe-16%Al alloy designated FAP-Y.

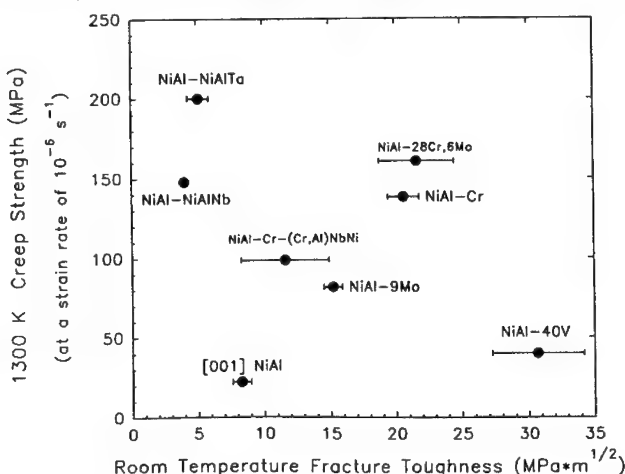


Fig. 1 Performance of NiAl-based directionally solidified eutectics compared to binary single crystal NiAl and a single crystal superalloy.[5]

TABLE 1
Composition of Iron Aluminide Alloys (Atomic %)

	FAP-Y	FA-129	Fe-35%Al	Ternary	1%ZrC	0.5%ZrC	0.5%Zr
Fe	77.07	66.17	65.0	67.0	65.95	66.45	66.5
Al	16.12	28.08	35.0	28.0	28.0	28.0	28.0
Cr	5.44	5.04	-	5.0	5.0	5.0	5.0
Zr	0.11	-	-	-	1.0	0.5	0.5
C	0.13	0.20	-	-	0.05	0.05	-
Mo	1.07	-	-	-	-	-	-
Nb	-	0.51	-	-	-	-	-
Y	0.06	-	-	-	-	-	-
Grain Size	42μm	*	385μm	180μm	*	*	*

* - partially recrystallized

Our research has focussed on the influence of composition, microstructure and strain rate on tensile behavior of Fe₃Al alloys. In addition, the influence of test frequency on fatigue crack growth rates has been studied.

Fig. 2 summarizes fatigue crack growth data for these alloys at room temperature in air. Alloys designated B2 possess partial B2 (FeAl) type order, while alloys designated DO₃ have been subjected to a heat treatment leading to nearly complete DO₃ order. Several studies of the influence of metallurgical variables as well as environment, temperature and test frequency have been published, showing how the constants C and m in the Paris-Erdogan equation:

$$da/dN = C\Delta K^m$$

vary. The highest crack growth rates by far are noted for the disordered FAP-Y alloy, while an alloy containing 0.5%Zr+carbon has the lowest growth rates, especially at high values of stress intensity range. When tested in an inert environment (oxygen or high vacuum) these alloys generally display much lower crack growth rates, with low crack growth exponents, except in the near-

threshold region, where there is little effect of the environment[10]. In this respect the iron aluminides differ from conventional alloys, which generally show a larger effect of an aggressive environment at low stress intensities. These studies have revealed that crack growth is slower for a given alloy in the B2 condition, and that there is little effect of the grain structure on growth rates. Further, Zr is the most effective element studied to date in reducing growth rates, whether or not carbon is present. Anomalous ductilizing effects of Zr also have been noted in Ni_3Al alloys;[1] no convincing explanation for the beneficial effects of Zr in these alloy systems has been proposed as yet, although Zr may affect film formation at high temperatures in iron aluminides[11].

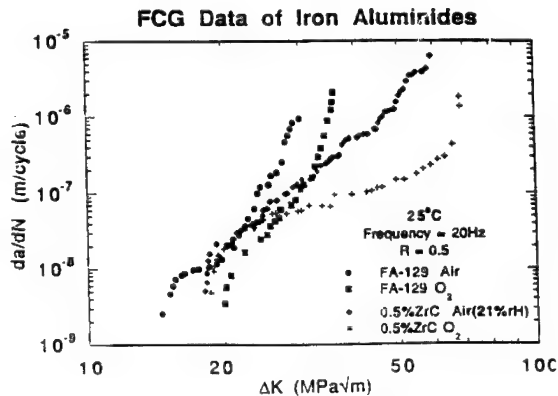


Fig. 2 Comparison of crack growth rates in various Fe-Al alloys.[9,10]

FeAl

FeAl alloys also are very susceptible to moisture and hydrogen, with most studies having been carried out under monotonic loading[12-14]. Under cyclic loading, Paris slopes for Fe-35%Al range from 16.9 in hydrogen gas to 4.7 in oxygen, but K_{IC} , the critical stress intensity for fracture in fatigue, is only increased by about 20% in hydrogen relative to oxygen[9]. Fatigue and fracture data for two phase FeAl alloys have not yet been reported.

Titanium aluminides

Significant changes in the fatigue crack growth resistance of titanium-aluminum alloys can be noted as aluminum content increases, see Fig. 3[15]. There is a general trend to higher thresholds as the structure changes from $\alpha+\beta$ to $\alpha_2+\beta$ to $\alpha_2+\gamma$ to γ , and as may be seen clearly, a very large increase in growth rates for single phase TiAl. These results are further affected by heat treatment to produce different microstructures. It is not possible in this paper to summarize the entire literature; therefore, only some very recent observations will be reviewed here.

Ti₃Al

Bowen et al[16] have reported the effects of microstructure and test environment on the FCG behavior of two Ti_3Al alloys at 20°C, Fig. 4. Note that crack growth rates are much higher in air at low ΔK , but that a crossover occurs at higher ΔK . A similar effect is noted at 600°C. The highest crack growth exponents, 27-28, were noted for the two alloys tested in vacuum at 20°C, while exponents of 1.6 and 1.9 were recorded in air at 600°C. As in the case of FeAl alloys described above, there is a wide range of rates and exponents observed, depending on experimental conditions, composition and microstructure. Similar results have recently been obtained by Fox et al[17] who showed that specimen orientation has a significant effect on fatigue parameters, especially in the basket weave structure, see Table 2, confirming a conclusion of Sadananda and Vasudevan[15]. Davidson and Campbell[18], on the other hand, report a large orientation effect in lamellar microstructures. Similarly, when precipitate particles or ductile reinforcements are present, anisotropic FCG behavior is to be expected. It is interesting to note that even though hydrogen is severely embrittling to Ti_3Al alloys at low temperatures,

in this case hydrogen did not appear to be detrimental at 732°C.

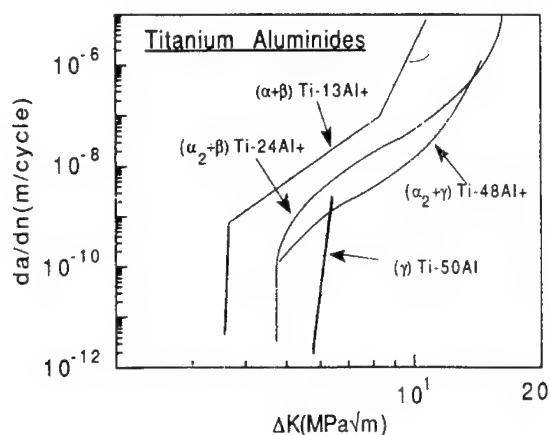


Fig. 3 Fatigue crack growth rates in various Ti-Al alloys, showing high threshold in γ Ti-50Al. [15]

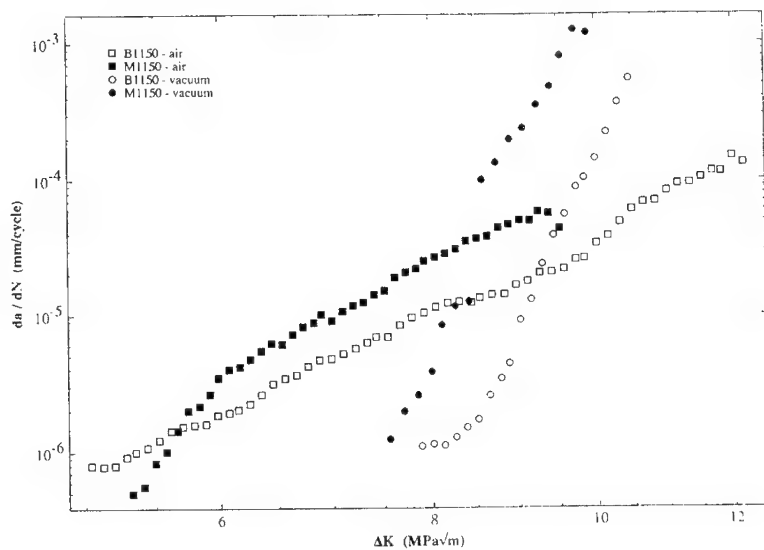


Fig. 4 Crack growth resistance curves, da/dN vs. ΔK , for two $\alpha_2+\beta$ alloys obtained in air and in vacuum at room temperature; B1150 is Ti-23 Al-11Nb-0.9Si and M1150 is Ti-23Al-9Nb-2Mo-0.5Si. [16]

TiAl

In recent years work on titanium aluminides has shifted to emphasis on gamma TiAl. Several studies have reported high crack growth exponents, m , in the range 20-56, the latter value being reported for a quaternary alloy tested at 700°C in air [16]. These values are comparable to those of ceramics and are far higher than are reported for conventional alloys. Efforts to improve crack growth resistance have included compositional and microstructural changes in monolithic TiAl, Fig. 5 [19] as well as the incorporation of particulate reinforcements in composites. The high cycle fatigue resistance of XD-TiAl containing 7v%TiB₂ is reported to be excellent, but the crack growth resistance is no higher than for the lamellar monolithic alloy shown in Fig. 5 [20].

Deformable particles such as Nb and TiNb improve toughness, but even these do not have a major positive effect on crack growth resistance, see Fig. 6[21]. Premature failure of the ductile particles occurs in fatigue, so that crack bridging is much less of a positive factor than under monotonic conditions. Further, platelet orientation is an important factor; best results are achieved for a crack orientation perpendicular to the faces of the plates. Plate thickness, on the other hand, has little effect on the results. The exponent, m , in Eq. 1 decreases with increasing volume fraction of TiNb. Another important factor is stress ratio, R ; crack growth rates increase sharply with R [22].

TABLE 2
Influence of Microstructure and Environment on
Crack Growth of Ti-24Al-11Nb.[17]

Atmos.	Temp.	Micro.	Micro. Size(μ m)	Orienta.	Freq(Hz)	ΔK range (MPa \sqrt{m})	m/cycle@ 10 MPa \sqrt{m}	Paris C	Paris n
Air	25°C	Equiaxed	6.6	TL	10,20	10 - 17	$\sim 1 \times 10^{-4}$	3.3×10^{-16}	7.30
				LT	5,10,20,30	12 - 32	$\sim 1 \times 10^{-4}$	3.6×10^{-13}	4.41
		Baktwve.	9.3x0.9	TL	10	7 - 11	5×10^{-7}	4.4×10^{-14}	7.16
				LT	10	6 - 8	$\sim 5 \times 10^{-7}$	1.1×10^{-14}	8.08
Argon	732°C	Equiaxed	6.6	TL	10	6 - 19	1×10^{-7}	7.5×10^{-11}	3.26
				LT	20	10 - 19	$4 \times 10^{-4} - 1 \times 10^{-7}$	1.3×10^{-12}	4.60
		Baktwve.	9.3x0.9	TL	10	9 - 11	$\sim 1 \times 10^{-7}$	1.2×10^{-4}	0.91
				LT	10	11 - 13	$< 4 \times 10^{-4}$	7.4×10^{-10}	1.87

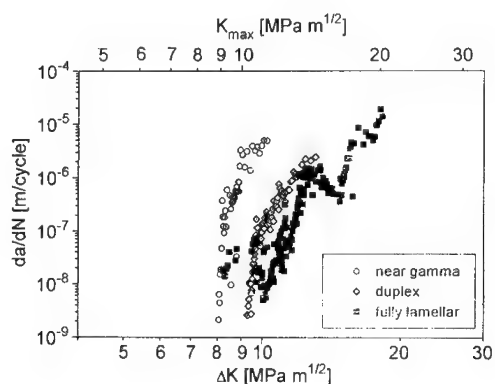


Fig. 5 Fatigue crack growth curves obtained from tests on near gamma, duplex, and fully lamellar specimens.[19]

Niobium aluminides

While most work on Nb₃Al has been directed at processing and the measurement of tensile properties, a small amount of data is now available on toughness and crack growth resistance of the monolithic alloy as well as composites based on this alloy. Davidson and Anton[23] reported FCG data for a Nb-18a%Al alloy with a microstructure consisting of a fine distribution of filamentary Nb within a Nb₃Al matrix. The data exhibited considerable scatter; a threshold value of less than 5 MPa \sqrt{m} was observed, and the slope of the crack growth curve was about 11. There was little effect of microstructure on these properties.

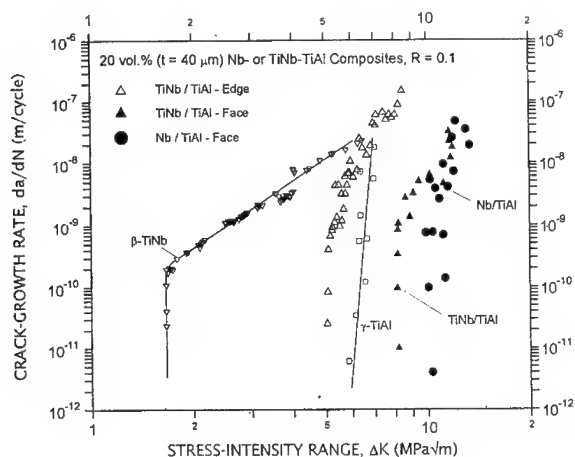


Fig. 6 Influence of ductile TiNb and Nb particles on crack growth of TiAl.[21]

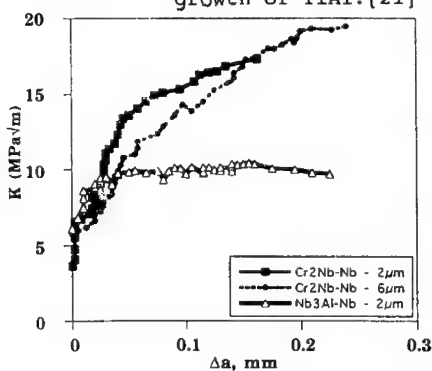


Fig. 7 Fracture resistance curves for Nb₃Al-Nb (2μm) and Cr₂Nb-Nb(Cr) (6μm) laminates.[24]

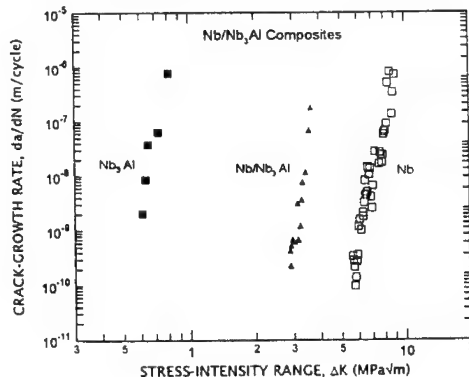


Fig. 8 Crack growth rates for Nb/Nb₃Al composites as well as Nb₃Al and Nb.[26]

Rowe, et al[24] have reported fracture resistance or R curves for Nb₃Al-Nb microlaminates, see Fig. 7. Note that there is a rapid increase in K with crack extension, but the maximum value is only 10 MPa^{1/2} after 0.05mm of crack propagation. Note the much higher maximum values for Cr₂Nb laminates, although all three samples showed an initiation toughness of about 5 MPa^{1/2}.

A different study, on an Nb/Nb₃Al in situ composite containing about 40v%Nb particles, showed a toughness of 7 MPa^{1/2}, compared to only 1 MPa^{1/2} for unreinforced Nb₃Al[25]. In this case, fatigue crack growth studies showed a similar effect, see Fig. 8[26]. Note that crack growth rates for the composite are much lower than for the unreinforced intermetallic, although not nearly as low as for pure Nb. Failure in the composites occurs by premature fracture of the ductile Nb ligaments, but is still delayed relative to the pure compound. The results of the two investigations support the view that toughening is very dependent upon reinforcement morphology as well as volume fraction. In this system, as well as in the MoSi₂/Nb composite, particles of a ductile phase are not nearly as effective as fibers or layers of reinforcement.

Dipasquale et al[27] have reported the toughness and fatigue threshold values for Nb-15%Al-10%Ti and Nb-15%Al-25%Ti alloys in which Nb₃Al precipitates of unknown volume fraction are dispersed in a B2 matrix. Toughnesses as high as 20 MPam^{1/2} were recorded for the latter alloy, but the fatigue crack threshold was only 3.0 MPam^{1/2} for the same material.

Niobium silicides

The binary Nb-Si system has been widely studied in an effort to develop tough, creep resistant composites. A wide two phase field consisting of Nb and Nb₃Si, is stable to 1660°C. Composites consisting of these two phases have been directionally solidified or consolidated from powders to provide specimens for which fracture toughness or R-curve data could be established. Bewlay et al[28] have reported toughness data on DS in-situ composites containing 10-25%Si. Highest K_Q values are obtained at 10at% Si, see Fig. 9. Rigney et al[29] have reported R curve behavior for Nb-10at%Si alloys prepared by vacuum arc casting and subsequent extrusion and heat treatment. The resulting Nb + Nb₃Si microstructure exhibited R curve behavior, with a maximum K_R value of 37 MPam^{1/2}, see Fig. 10[29]. The toughening of this material was due to the ductile niobium particles; however, exposure to air, hydrogen or oxygen embrittled the particles, thereby sharply reducing toughness of the composite. In fact, deleterious effects of oxygen and hydrogen may be expected whenever the refractory metals niobium, molybdenum, tungsten or tantalum are utilized as reinforcements.

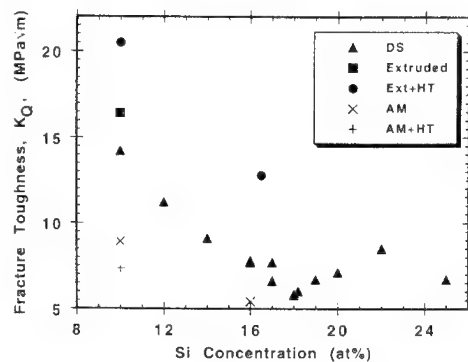


Fig. 9 Fracture toughness data of DS Nb-Si in situ composites of binary Ni-Si alloys with compositions from 10 to 25% in various conditions.[28]

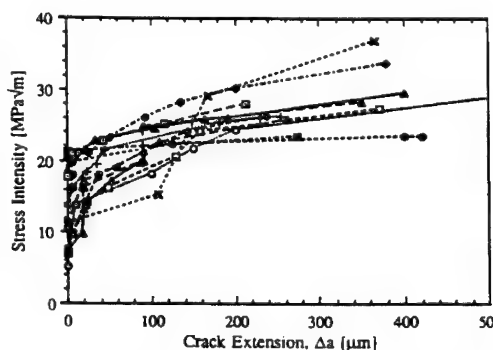


Fig. 10 R-curve behavior exhibited by Nb-10at.% Si composites. Data compiled from thirteen different samples.[29]

The effects of particle morphology on the fracture behavior of powder processed Nb/Nb₃Si composites also have been reported. Spherical particles always were bypassed during fracture and were unable to toughen, while acicular particles increased toughness from about 3 to 12 MPam^{1/2}[30]. Studies of crack growth behavior of this system, as well as of Cr₂Nb/Nb and Nb₃Al/Nb composites, shows that ductile phase toughening does not always result in improved fatigue crack growth resistance; the effects of crack bridging appear to be reduced during cyclic loading[31].

Chromium silicides

The cubic Al₅ compound Cr₃Si has an attractive combination of high melting point, low density and excellent oxidation resistance. However, as with all other refractory silicides, toughness and ductility are very low. For example, room temperature fracture toughness is about 2.5 MPam^{1/2}; higher values have been obtained for the Cr-Cr₃Si eutectic system[32]. Recent work in our laboratory has focussed upon powder processing of composites with a Cr₃Si, Mo matrix reinforced with Pt and Pt alloy fibers[33]. Unfortunately, the fibers are so weak that they are mechanically disrupted during hot pressing. Nevertheless, preliminary bend test results show some toughening by the fibers

at 800°C. Fracture surfaces reveal a mixed intergranular, transgranular crack path.

Molybdenum Disilicide

The most widely studied silicide for structural applications has been MoSi_2 , which is nearly a line compound. Several studies[34-36] have shown that the very low toughness of this compound can be improved by adding continuous fibers of niobium, while discontinuous fibers or particle of niobium were much less effective[35]. More recent work by Chen et al[37] and Badrinarayanan et al[25] have extended these observations to cyclic loading experiments. Chen et al[37] measured sub-critical crack growth in MoSi_2/Nb at ΔK as low as $1.7 \text{ MPa}\sqrt{\text{m}}$, with a Paris exponent of about 14. Wire mesh reinforcements of Nb are much more effective than Nb particles in toughening under both monotonic and cyclic loading conditions. The wire-reinforced material exhibited a more than 100% increase in toughness relative to unreinforced or particle-containing material. Fig. 11 shows a comparable effect on fatigue crack growth; both threshold and Paris regime behavior are markedly improved by the wire mesh. As in earlier work[34-36], the fracture mode of the niobium varied with its morphology and the consequent constraint of the surrounding matrix. The principal difference between monotonic and cyclic behavior is manifested in the diminished role of crack bridging in the latter experiments due to fatigue failure of the Nb.

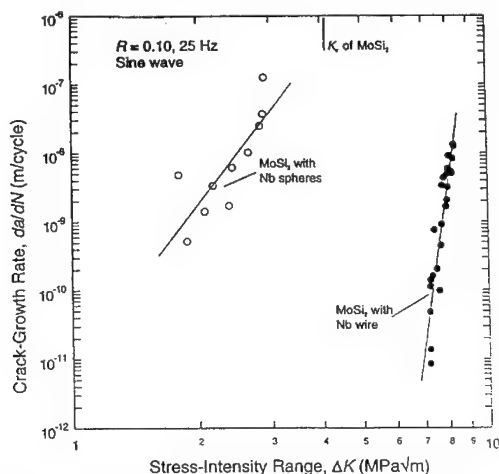


Fig. 11 Effect of Nb morphology on crack growth in MoSi_2 . [25]

Discussion

This paper has dealt with two significant factors, the use of ductile reinforcements and the avoidance of embrittling environments, that influence the fatigue and fracture properties of high temperature intermetallics. It seems clear that even when the environment is controlled so as to exclude water vapor or hydrogen at low temperatures or oxygen at high temperatures, many intermetallics lack sufficient toughness to be viable candidates for structural applications. It is in this context that one must look to means of improving the intrinsic properties of the compounds by control of the microstructure without exacerbating changes in the environmental sensitivity. In-situ composites have proven to be especially beneficial with respect to improved toughness, see Table 3. Unfortunately, the use of ductile phase reinforcements brings with it two distinct disadvantages: the likelihood of reduced creep strength and impaired oxidation resistance, as is especially clear with niobium or tantalum. For example, the cyclic oxidation resistance of MoSi_2 is sharply reduced by adding Nb as aligned or random short fibers, see Fig. 12.[39]. Rigney et al[29] have shown that the toughness of a $\text{Nb}_3\text{Si}_3\text{-Nb}$ composite is reduced from $38 \text{ MPa}\sqrt{\text{m}}$ to $19 \text{ MPa}\sqrt{\text{m}}$ by pre exposure to air at 600°C for 4 hrs. This was a consequence of an embrittled layer on the surface. Oxygen and hydrogen, both of which are known to embrittle Nb, also produced sharp drops in toughness of the Nb-Si composites.[29] Interstitial impurities in refractory metal reinforcements also can reduce toughness of the composite, as in the V-

V_3Si system, see Fig. 13[38]. Further, the reinforcements must have a high aspect ratio, either as continuous fibers, elongated platelets, or laminates, to be effective. In the case of fibers, large diameters are required, while recent work on laminates suggests that layer thickness must be large for maximum toughening to be realized. It has been pointed out by Bloyer, et al[40] that for similar interface properties and failure mechanisms, the volume of metal undergoing plastic deformation increases with thickness of the layers because of lower triaxial constraint. They suggest that optimal fracture resistance should occur when the layer thickness is equivalent to the maximum plastic zone size under plane stress conditions. These suggestions do not bode well for the usefulness of nanoscale microstructures in improving toughness. However, it is entirely possible that nanostructured alloys may exhibit diminished environmental susceptibility, thereby countering the reduced effectiveness of ductile phases in toughening.

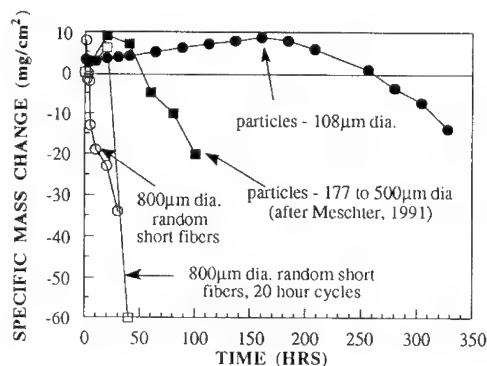


Fig. 12 Effect of Nb morphology on oxidation of $MoSi_2$. [39]

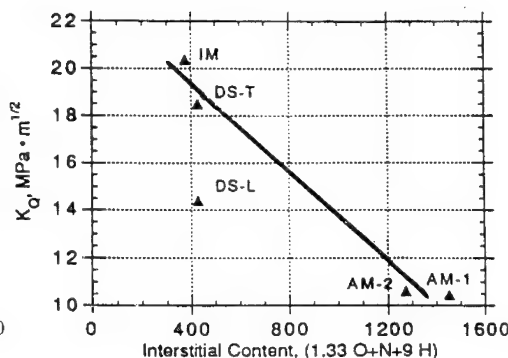


Fig. 13 Influence of total interstitial content on fracture toughness of $V-V_3Si$ in-situ composites. [38]

TABLE 3

Fracture of Directionally Solidified Intermetallic Composites

System	COMPOSITION at%	T °C	K_{Ic} or K_{Qc} MPa \sqrt{m}	REFERENCES
Nb-Nb ₃ Si	Nb-18.7%Si	20	6.0	[28]Bewlay et al
V-V ₃ Si	V-13%Si	20	6.8	[44]Bewlay et al
Cr-Cr ₃ Si	Cr-15%Si	20	7.3	[44]Bewlay et al
Nb-Nb ₃ Si	Nb-18.7%Si	400	5.8	[44]Bewlay et al
V-V ₃ Si	V-13%Si	400	16.5*	[44]Bewlay et al
V-V ₃ Si	V-7.3%Si	20	14.4-18.5	[38]Strum et al
Nb-(Nb,Ti) ₃ Si	Nb-33Ti-16Si	20	11.1	[28]Bewlay et al
Nb-(Nb,Ti) ₃ Si, Nb ₃ Si	Nb-32Ti-19Si	20	12.4	[41]Bewlay et al
Nb-Nb ₃ Si	Nb-10%Si	20	14.2	[28]Bewlay et al
Nb(Ti) ₃ -(Nb,Ti) ₃ Si	Nb-27Ti-16%Si	20	11.3	[28]Bewlay et al
NiAl-Cr	NiAl-34%Cr	20	20.4-21.8	[5]Johnson et al
NiAl-Cr,Mo	NiAl-31%Cr-3%Mo	20	19.8-21.3	[5]Johnson et al
NiAl-Cr,Mo	NiAl-28%Cr-6%Mo	20	19.6	[5]Johnson et al
NiAl-NiAlTa	NiAl-14.5%Ta	20	4.1-6.3*	[42]Johnson et al
NiAl-NiAlTa-(Mo,Ta)	Ni-42%Al-12.5Ta-7Mo	20	5.2	[43]Johnson et al
NiAl-(Cr,Al)NiTa-Cr	Ni-30.5%Al-6Ta-33Cr	20	13.6-15.9	[43]Johnson et al
Cr ₂ Nb-Cr	Cr-50%Nb	20	3.1	[28]Bewlay et al
Cr ₂ Nb-Nb	Cr-17%Nb	20	3.6	[28]Bewlay et al

* varies with orientation
- varies with heat treatment

Although considerable data on fatigue crack growth now have been published for intermetallics and some artificial composites, see Table 4, no data have been published on the recently developed in-situ composite systems. Further work in this area is clearly warranted, especially in view of the fact that threshold stress intensities in the systems listed in Table 4 are very low, and values of K_{max} are generally not much higher. These results show that cracks are readily initiated, and then propagate rapidly to failure.

TABLE 4

Threshold and Maximum Stress Intensities for Intermetallics and Intermetallic Composites

System	Type	V_f %	ΔK_{th} Mpa \sqrt{m}	K_{max} Mpa \sqrt{m}	References
Nb ₃ Al	hot press	-	0.6	1.1	[26] Muruges et al, 1993
Nb ₃ Al-Nb	hot press	40	3	1.5	[26] Muruges et al, 1993
MoSi ₂ -Nb	particles	20	<2	3	[25] Badrinarayanan et al, 1996
MoSi ₂ -Nb	wire mesh	20	7	8	[25] Badrinarayanan et al, 1996
MoSi ₂ -Nb	particles	20	2	3	[37] Chen et al, 1994
TiAl	duplex	-	6.5	7.5	[22] Venkateswara Rao et al, 1995
TiAl	lamellar	-	10	13	[22] Venkateswara Rao et al, 1995
48Al-2Cr	duplex	-	9	-	[19] Behr et al, 1995
TiAl-TiB ₂	XD	7	8	20	[20] Kumar and Bao, 1994
Nb ₃ Al	15Al-10Ti	-	4.5	-	[27] Dipasquale et al, 1995
Nb-Nb ₃ Al	15Al-25Ti	-	3.0	-	[27] Dipasquale et al, 1995
Nb-Nb ₃ Al	12.5 Al-41Ti	-	4.5	30	[27] Dipasquale et al, 1995
Nb ₃ Al-Nb	1.5 Mo cast, h.t. 18% Al	-	5.3	10.3	[23] Davidson and Anton, 1993

Acknowledgements

The author is grateful to ARPA and ONR for financial support under Grant No. N000-14-92-J-1779 and to ONR for financial support under Grant No. N000-14-94-1-0723

References

1. E.P. George, C.T. Liu and D.P. Pope, in High Temperature Ordered Intermetallic Alloys V, MRS, Pittsburgh, PA, 288 (1993) 941.
2. V.K. Sikka in Advances in High Temperature Structural Materials and Protective Coatings, Natl. Res. Council of Canada, (1994) 282.
3. R.D. Noebe, R.R. Bowman and M.V. Nathal, in Physical Metallurgy and Processing of Intermetallic Compounds, N.S. Stoloff and V.K. Sikka, Eds. Chapman and Hall, (1996) 212.
4. C.G. Kallingal, T.R. Smith, C. Nemec, N.S. Stoloff and K. Rajan, Mat. Sci. and Eng., A192/193 (1995) 502.
5. D.R. Johnson, X.F. Chen, B.F. Oliver, R.D. Noebe and J.D. Whittenberger, Intermetallics 3 (1995) 99.
6. N.S. Stoloff and D.J. Duquette, J. of Metals 45(12) (1993) 30.
7. M.N. Srinivasan and V.K. Sikka in Processing, Properties and Applications of Iron Aluminides, TMS, Warrendale, PA, (1994) 69.
8. V.K. Sikka in Processing, Properties and Applications of Iron Aluminides, TMS, Warrendale, PA (1994) 3.
9. A. Castagna and N.S. Stoloff, Mat. Sci. and Eng., A192/193 (1995) 399.
10. N.S. Stoloff and D.A. Alven, Acta Metall. Sinica (English Letters) 3(4-6) (1995) 375.
11. P. Tortorelli, Oak Ridge National Lab., private communication, 1995.

12. C.T. Liu, E.H. Lee and C.G. McKamey, Scripta Metall. 23 (1989) 875.
13. D.B. Kasul and L.A. Heldt, Scripta Metall. 25 (1991) 1047.
14. R.J. Lynch, K.A. Gee and L.A. Heldt, Scripta Metall. 30 (1994) 945.
15. K. Sadananda and A.K. Vasudevan, Mat. Sci. and Eng., A192/193 (1995) 490.
16. P. Bowen, R.A. Chave and A.W. James, Mat. Sci. and Eng., A192/193 (1995) 443.
17. T.R. Fox, D.B. Knorr and N.S. Stoloff, submitted to Fatigue and Fracture of Engineering Materials and Structures, (1996).
18. D.L. Davidson and J.B. Campbell, Metall Trans A 24 (1993) 1555.
19. R. Behr, A. Wanner, H. Clemens and D.W. Glatz, in High Temperature Ordered Intermetallic Alloys VI, MRS, Pittsburgh, PA, 364, part 2, (1995) 781.
20. K.S. Kumar and G. Bao in Composites Science and Technology, 52 (1994) 127.
21. K.T. Venkateswara Rao and R.O. Ritchie in Fatigue and Fracture of Ordered Intermetallic Materials I, W. Soboyejo, T.S. Srivatsan and D.L. Davidson, Eds., TMS, Warrendale, PA, (1994) 3.
22. K.T. Venkateswara Rao, G.R. Odette and R.O. Ritchie, Acta Metall., 42 (1994) 893.
23. D.L. Davidson and D. Anton, in High Temperature Ordered Intermetallic Alloys V, MRS, 288 (1993) 807.
24. R.G. Rowe, D.W. Skelley, M. Larsen, J. Heathcote, G. Lucas and G.R. Odette, in High Temperature Silicides and Refractory Alloys, MRS, Pittsburgh, PA, 322 (1995) 461.
25. K. Badrinarayanan, A.L. McKelvey, K.T. Venkateswara Rao and R.O. Ritchie, Report No. UCB/R/95/A1111, U. C. Berkeley, submitted to Metall Trans. A, 1996.
26. L. Muruges, K.T. Venkateswara Rao and R.O. Ritchie, Scripta Metall. 41 (1993) 1107.
27. J. Dipasquale, D. Gahutu, D. Konitzer and W. Soboyejo in High Temperature Ordered Intermetallic Alloys VI, MRS, Pittsburgh, PA, 364, part 2, (1995) 1347.
28. B.P. Bewlay, H.A. Lipsitt, M.R. Jackson, W.J. Reeder and J.A. Sutliff, Mat. Sci. and Eng. A192/193 (1995) 534.
29. J.D. Rigney, P.M. Singh and J.J. Lewandowski, in High Temperature Silicides and Refractory Alloys, MRS, Pittsburgh, PA, 322 (1995) 503.
30. D.M. Dimiduk, P.R. Subramanian and M.G. Mendiratta, Acta Metall. Science (English Letters) 8(4-6) (1995) 519, see also L.S. Apgar, Ph.D. Thesis, Univ. of Dayton, 1995.
31. D. L. Davidson and K.S. Chan, Final Report, AFOSR Contract #F49620-92-C-0022, April 1995.
32. J.W. Newkirk and J.Z. Sago, in Intermetallic Matrix Composites, MRS, Pittsburgh, PA, 194 (1990) 183.
33. S. Augustin, M. Nazmy and N.S. Stoloff, unpublished research.
34. M.L. Sastry, R. Suryanarayanan and K.L. Jerina, Mat. Sci. and Eng., A192/193 (1995) 881.
35. N.S. Stoloff and D. E. Alman, Ceramics Intl. 21 (1995) 289.

36. L. Shaw and R. Abbaschian, *Acta Metall.* 42 (1994) 213.
37. L.-C. Chen, N. Bahtishi, R. Lederich and W. Soboyejo, in *Intermetallic Matrix Composites III*, MRS, Pittsburgh, PA, 350 (1994) 183.
38. M.J. Strum, G.A. Henshall, B.P. Bewlay, J.A. Sutliff and M.R. Jackson, in *High Temperature Silicide and Refractory Alloys*, MRS, Pittsburgh, PA, 322 (1994) 511.
39. D.E. Alman and N.S. Stoloff in *High Temperature Silicides and Refractory Alloys*, MRS, Pittsburgh, PA, 322 (1994) 255.
40. D.R. Bloyer, K.T. Venkateswara Rao and R.O. Ritchie, submitted to *Mat. Sci. and Eng. A* (1996).
41. B.P. Bewlay, M.R. Jackson, W.J. Reeder and H.A. Lipsitt, in *High Temperature Ordered Intermetallic Alloys VI*, MRS, Pittsburgh, PA, 364 (part 2) (1995) 943.
42. D.R. Johnson, X.F. Chen, B.F. Oliver, R.D. Noebe and J.D. Whittenberger, *Intermetallics* 3, (1995) 141.
43. D.R. Johnson, B.F. Oliver, R.D. Noebe and J.D. Whittenberger, *Intermetallics* 3 (1995) 493.
44. B.P. Bewlay, K-M. Chang, J.A. Sutliff and M.R. Jackson in *Intermetallic Matrix Composites II*, MRS, Pittsburgh, PA, 273 (1992) 417.

**DAMAGE TOLERANCE IN INTERMETALLIC AND CERAMIC MATERIALS
AT AMBIENT AND ELEVATED TEMPERATURES: ROLE OF
EXTRINSIC VS. INTRINSIC MECHANISMS**

K. T. Venkateswara Rao, C. J. Gilbert and R. O. Ritchie

Department of Materials Science and Mineral Engineering and
Materials Sciences Division, Lawrence Berkeley National Laboratory
University of California at Berkeley, Berkeley, CA 94720-1760

Abstract

Recent experimental results on the fracture toughness and fatigue-crack growth behavior of intermetallics, ceramics and their composites are reviewed. In particular, the role of extrinsic crack-tip shielding on crack propagation under monotonic and cyclic loading is contrasted with intrinsic damage mechanisms, both at ambient and elevated temperatures. For example, the fracture and fatigue properties in a toughened SiC ceramic are almost exclusively controlled by extrinsic shielding; marked resistance-curve toughening is achieved under monotonic loading by grain bridging, which is severely diminished under cyclic loading through progressive wear at the sliding grain interfaces. Cyclic crack growth rates in ceramics, as a result, are extremely sensitive to K_{\max} and less dependent on ΔK at room temperature. At elevated temperatures, behavior in ceramics is influenced by extrinsic and intrinsic effects associated with deformation and damage of grain boundary amorphous films. Conversely, damage tolerance characteristics of intermetallics like TiAl, TiNb/TiAl and Nb/MoSi₂ are found to be a function of both intrinsic and extrinsic mechanisms, intermediate to behavior in metals and ceramics at all temperatures. Extrinsically, ductile-particle and shear-ligament bridging are dominant under monotonic loading and become less effective under cyclic loading; crack-propagation rates are moderately sensitive to both ΔK and K_{\max} . From an intrinsic stand point, fatigue properties of γ -TiAl intermetallic alloys are slightly degraded in the 600-650°C range, just below the ductile-to-brittle transition temperature for TiAl. The strong dependence of cyclic crack growth rates on the applied stress intensity (K_{\max} or ΔK) in advanced ceramics and intermetallics necessitates the use of design and life-prediction procedures based on crack initiation, small crack or fatigue-threshold philosophies.

Introduction

A majority of intermetallic and ceramic materials, currently under development for high-temperature structural use, have been designed on notions of toughening using crack-tip shielding to overcome their limitations of low toughness and ductility at room temperature [1-4]. The approach is rather distinct from intrinsic mechanisms, which enhance the inherent microstructural resistance of the material by phenomena that are generally active in the process zone ahead of the crack-tip (Fig. 1). Thermomechanical treatments aimed at variations in grain size, precipitate size and distribution in microstructures of metallic materials like steels, aluminum alloys and superalloys are good examples of intrinsic toughening. Extrinsic mechanisms, on the other hand, are primarily active behind the crack tip and retard crack advance by reducing the near-tip crack-driving force through closure tractions imposed in the wake. The tractions may be induced by *in situ* phase transformations, interlocking grains, or by incorporating fibers, whiskers or ductile reinforcements in the microstructure. These strategies have led to the development of advanced ceramics and intermetallics with significantly improved toughness at room temperature.

Concurrently however, the shielding approach to materials development also renders brittle materials, such as ceramics, to be susceptible to fatigue failure [4,5]. Although there appears to be no clear intrinsic mechanism for cyclic crack growth in these materials, particularly ceramics, the progressive degradation of *extrinsic* shielding *behind* the crack tip during cyclic loading is considered to be the principal cause for fatigue crack extension [4-6]. By contrast, fatigue in metallic materials is an *intrinsic* damage process occurring *ahead* of the crack tip involving crack growth by alternating blunting and resharpening of the crack or along alternating slip planes [7,8], clearly distinct from monotonic fracture mechanisms. The two systems, metals and ceramics, represent the extremes with respect to the role of intrinsic vs. extrinsic effects on fracture and fatigue behavior of materials, respectively; behavior in intermetallics lies in between the two. In this short review, examples of fracture and fatigue behavior in selected ceramic and intermetallic systems are presented with specific emphasis on the relative role of intrinsic and extrinsic mechanisms influencing crack growth under monotonic and cyclic loading. Influence of temperature on their fracture and fatigue properties and resultant implications to structural design and life prediction are also discussed.

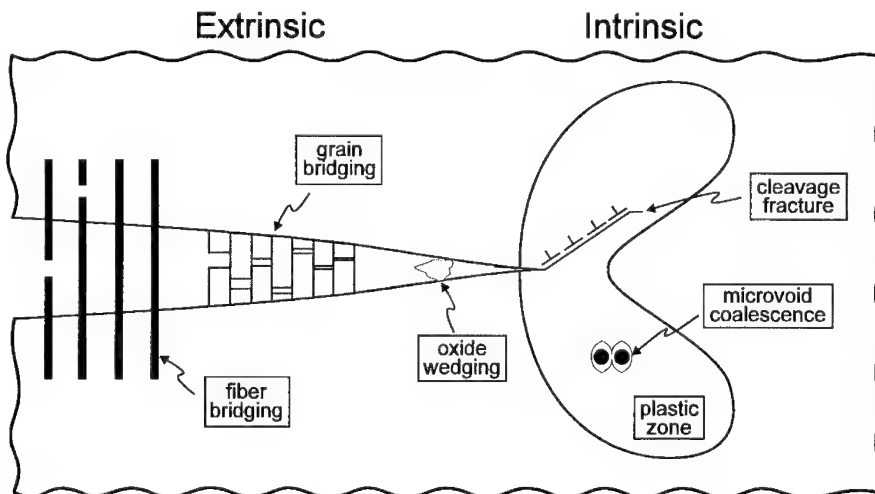


Figure 1- Schematic illustration of various toughening mechanisms in materials- *Intrinsic* mechanisms (transgranular cleavage and microvoid coalescence) that are active in the process zone *ahead* of the crack tip, and *Extrinsic* mechanisms (fiber bridging, grain bridging and oxide wedging) that are active in the wake *behind* the crack tip.

Ceramics

Various ceramics have been toughened at ambient temperature using the extrinsic approach; the principal mechanisms include transformation toughening (partially-stabilized zirconias), fiber bridging (LAS/SiC), ductile-phase toughening (Al/Al₂O₃) and grain bridging (SiC, Si₃N₄ and Al₂O₃). All these materials develop their toughness through a resistance curve (or R-curve), where the stress-intensity required for further crack advance increases with crack extension as tractions developed in the crack wake locally shield the crack tip. Such wake phenomena, however, may degrade under cyclic loading leading to fatigue crack advance by a mechanism essentially identical to that seen during monotonic loading, but at significantly reduced driving forces. An example of behavior in toughened SiC ceramics [9,10] at ambient and elevated temperatures is described below.

High Toughness Silicon Carbides

SiC ceramics generally exhibit excellent creep and oxidation resistance, high thermal conductivity and low thermal expansion properties compared to most other ceramic materials at high temperatures. The widespread use of monolithic SiC, however, has been limited by its low toughness ($K_{IC} \sim 2\text{--}3 \text{ MPa}\sqrt{\text{m}}$) at ambient temperature. Recent developments in hot-pressed SiC using Al, B, and C as sintering additives (referred to as ABC-SiC) have shown that microstructures consisting of elongated SiC platelets, following the $\beta(3C)$ to $\alpha(4H)$ phase transformation, exhibit toughnesses approaching nearly $10 \text{ MPa}\sqrt{\text{m}}$ [9,10], while retaining a high modulus of rupture ($\sim 660 \text{ MPa}$). Such improvements in the room temperature toughness and strength, however, lead to a susceptibility to fatigue failure, and can have a detrimental influence on mechanical properties at high temperatures. Results in ABC-SiC and underlying crack-growth mechanisms are discussed below.

Behavior at Room Temperature: Initiation of fracture in the ABC-SiC under monotonic loading is seen at an initial stress intensity, $K_I \sim 5.5 \text{ MPa}\sqrt{\text{m}}$ (Fig. 2a), and the crack-growth resistance increases over $\sim 600 \mu\text{m}$ to a maximum value of $K_{IC} \sim 9 \text{ MPa}\sqrt{\text{m}}$. This represents more than a threefold improvement in the fracture toughness compared to commercial SiC (Hexoloy SA), which shows no R-curve behavior and fails catastrophically at $K_{IC} \sim 2.5 \text{ MPa}\sqrt{\text{m}}$ (Fig. 2a). Analogous to behavior in Si₃N₄, the dramatic increase in fracture resistance of ABC-SiC can be ascribed to the heterogeneous, elongated plate-like grain structure. Crack paths and fracture-surfaces show clear evidence of extensive crack deflection along the α -grain boundaries, which in turn leads to intergranular cracking (Fig. 2b) and frictional grain bridging [10]. In contrast, Hexoloy exhibits transgranular cleavage cracking with no crack deflection or bridging consistent with the absence of an R-curve.

Under cyclic loading, crack-growth rates in ABC-SiC are significantly faster than corresponding crack velocities under quasi-static loading at equivalent stress-intensity levels [10], with a marked dependence on applied ΔK . The resulting fracture surfaces reveal the presence of a profuse amount of damage and debris (Fig. 2d) which is not observed on static fracture surfaces (Fig. 2b). The debris results from repetitive contact between the crack faces during cyclic loading - a characteristic of cyclic fatigue in grain bridging ceramics [5,6]. In comparison, Hexoloy SiC displayed no evidence of subcritical crack growth under cyclic loading, as indicated by the vertical line corresponding to its toughness (Fig. 2c). It is therefore clear that the very microstructure (elongated grains/platelets) that promotes toughening in SiC also enhances its susceptibility to fatigue at ambient temperature.

At higher load ratios ($R=K_{min}/K_{max}$), fatigue-crack growth rates, at a given ΔK , are accelerated and fatigue thresholds (ΔK_{TH}) reduced, as shown in Fig. 3a. Such load-ratio differences, however, are less apparent when the results are correlated in terms of the maximum stress intensity, K_{max} (Fig. 3b), demonstrating that fatigue-crack propagation in SiC, in direct contrast to behavior in metals [11], is mostly controlled by K_{max} rather than ΔK . The relative dependence can be quantified by expressing the data in terms of a modified Paris power-law relation to include the effect of both ΔK and K_{max} as follows:

$$da/dN = C (K_{max})^n (\Delta K)^p, \quad (1)$$

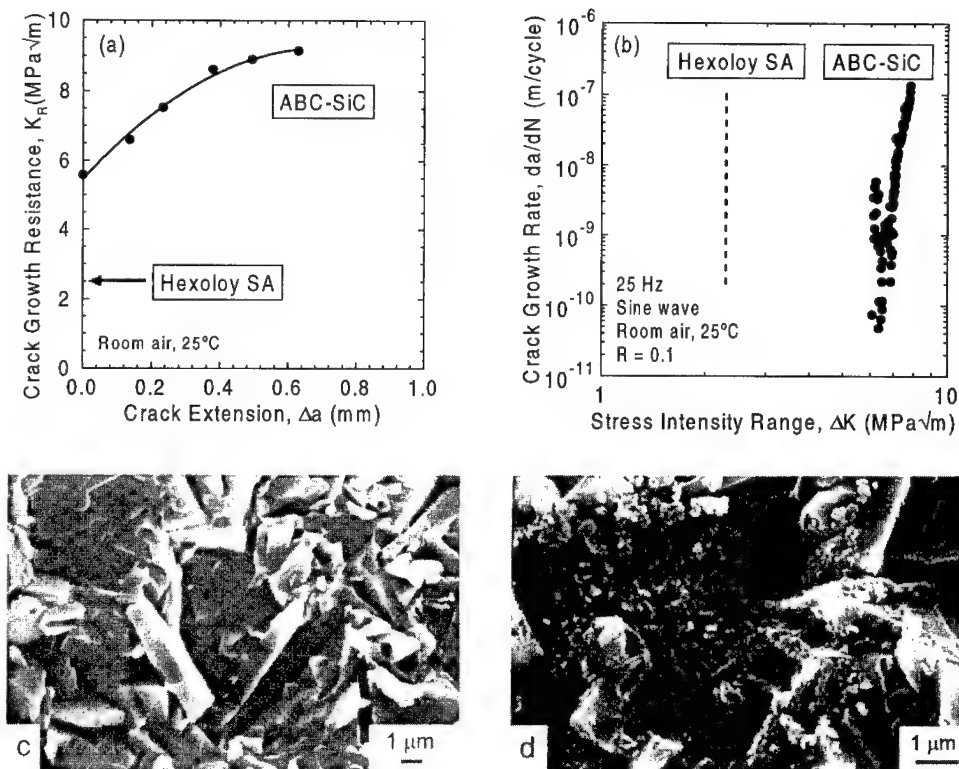


Figure 2- (a) Resistance curve and (b) fatigue-crack growth behavior in ABC-SiC in room temperature air ($R=0.1$, 25 Hz), compared to commercial SiC (Hexoloy SA), that shows no apparent R-curve or fatigue effects. (c) Clean and faceted intergranular failure observed under monotonic loading, and (d) wear debris on fatigue fracture surface from repetitive grain sliding under cyclic loading [8].

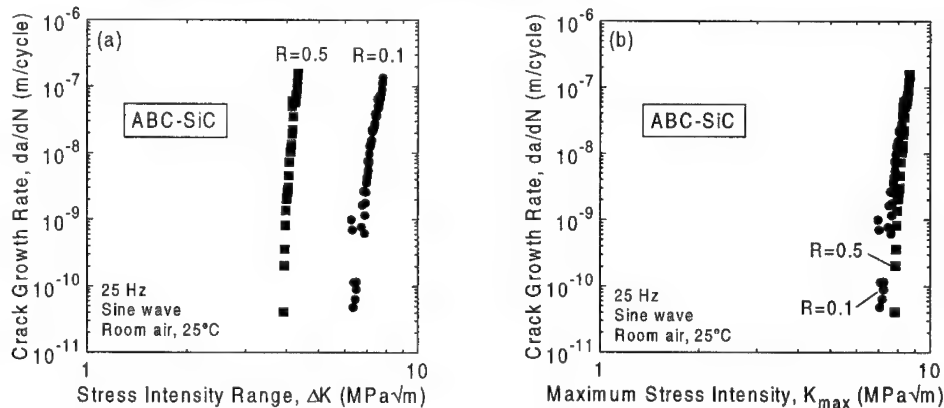


Figure 3- Variation in fatigue-crack propagation rates in ABC-SiC ceramic plotted as a function of (a) applied ΔK and (b) maximum stress intensity, K_{max} at different load ratios. The data are normalized when correlated to K_{max} , suggesting that the cyclic crack advance mechanism is identical to that seen under monotonic loading [8].

where C is a scaling constant (independent of K_{\max} , ΔK and R), and n and p are experimentally determined exponents. A regression fit to data in Fig. 3 yields $n \sim 36$, and $p \sim 1.9$ indicating the strong growth-rate dependence on K_{\max} , comparable to other ceramics (Table I). For results obtained at a given load ratio, Eq. (1) can be rewritten using: $K_{\max} = \Delta K/(1-R)$, to give the more familiar form of the Paris equation:

$$da/dN = C'(\Delta K)^m, \quad (2)$$

where $m = n + p$ and $C' = C/(1-R)$. Values of ΔK_{TH} , C' and m are listed in Table I; the exponents are characteristically higher than values of $m \sim 2-4$ typically reported for metals [11].

The high growth-rate exponents, and in particular, the marked dependence of growth rates on K_{\max} rather than ΔK , are characteristic of cyclic fatigue growth in many ceramic systems that is motivated by the cyclic suppression of crack-tip shielding in the wake [4-6,10,12,13]. Specifically, in grain-bridging ceramics such as Al_2O_3 , Si_3N_4 and the current ABC-SiC, the suppression/degradation process is dominated by progressive wear of the frictional grain bridges, which markedly reduces the toughening capacity and increases the near-tip driving force for crack extension. Similar mechanisms have also been reported in ceramic composites toughened from frictional bridging by partially bonded whiskers or fibers [14]. Conversely, the low-toughness Hexoloy SA is essentially immune to cyclic fatigue degradation because its transgranular crack morphology precludes the formation of any such shielding zones in the crack wake.

Table I: Power-Law Exponents in Fatigue-Crack Growth Relations for Selected Materials Systems

Material	Total Exponent m	ΔK Exponent p	K_{\max} Exponent n	Constant C^+
<i>Metals:</i>				
Ni-base superalloy	3.4	3.0	0.4	--
<i>Intermetallics</i>				
TiB ₂ /TiAl	15.9	10.3	5.6	2.85×10^{-23}
TiNb/TiAl	12.4	6.3	6.1	7.32×10^{-19}
Nb/MoSi ₂	20.7	7.5	13.2	6.31×10^{-29}
<i>Ceramics</i>				
SiC/ Al_2O_3	15	4.8	10.2	6.79×10^{-18}
SiC	37.9	1.9	36	4.8×10^{-43}
Al_2O_3	31.6	9.8	21.8	7.32×10^{-19}
Si_3N_4	30.3	1.3	29	3.71×10^{-28}

⁺ Units: m/cycle (MPa \sqrt{m})^{-m}

Behavior at High Temperature: R-curve toughening is also evident in ABC-SiC at elevated temperatures of 1200°C (Fig. 4a). Both, crack-initiation and maximum toughness values are roughly equivalent at ambient (~ 9 MPa \sqrt{m}) and 1200°C (~ 10 MPa \sqrt{m}), although the crack extends over larger dimensions (~ 2 mm) at the higher temperature before reaching a plateau. Such behavior is attributed to softening of grain boundary films, which not only reduce the magnitude of tractions but also extend the bridging zone length. Crack bridging by the glassy-phase ligaments were observed spanning the crack faces several millimeters behind the crack tip at 1200°C (Fig. 4c), compared to frictional interlocking between grains at ambient temperature (Fig. 4d).

Fatigue-crack growth rates at 1200°C in ABC-SiC are nearly an order of magnitude faster than at room temperature (Fig. 4b), and the fatigue threshold, ΔK_{TH} , is reduced from ~ 6.5 MPa \sqrt{m} to ~ 4 MPa \sqrt{m} . In addition, similar to recent results on hot-pressed Si_3N_4 [15], the growth rates exhibit a lower dependence on ΔK at high temperatures compared to room temperature (Fig. 4a); the exponent in the Paris equation given in Eq. (2), $m \sim 20$ at 1200°C versus ~ 37 at 25°C for a load ratio, $R = 0.1$. The acceleration of growth rates at high temperatures is likely due to enhanced creep deformation associated with cavitation and the softening of the glassy phase present at grain boundaries.

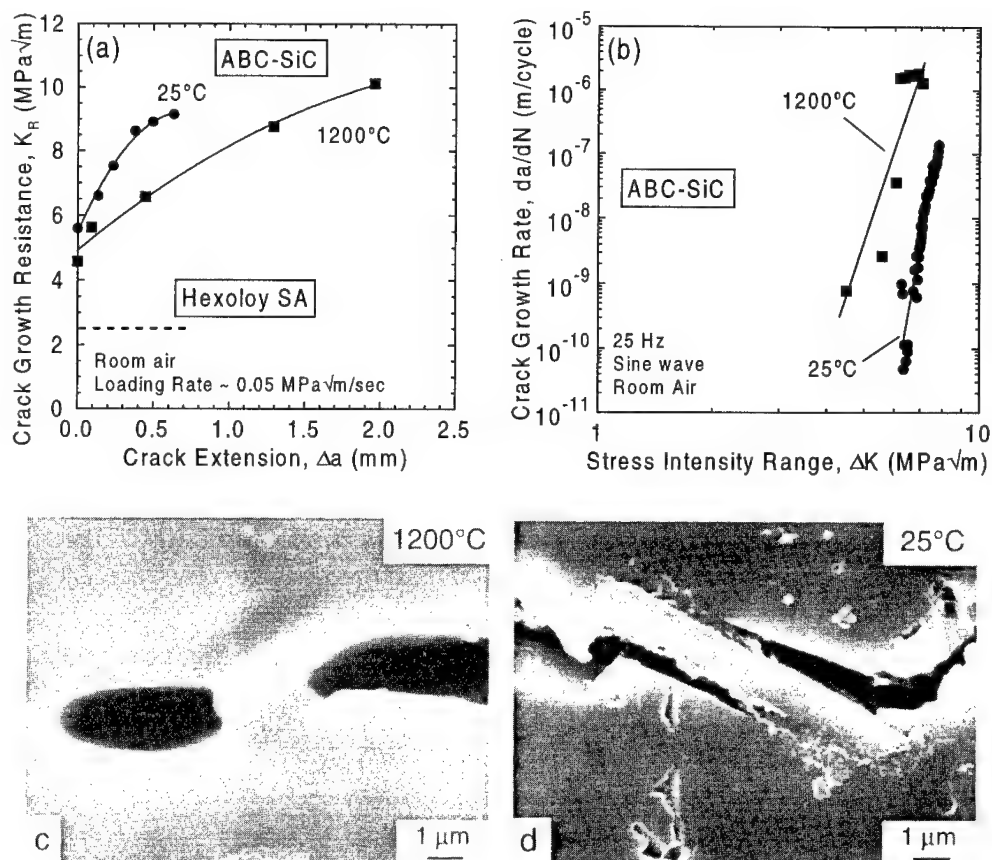


Figure 4- (a) R-curve and (b) fatigue-crack propagation behavior in ABC SiC at 1200°C in air ($R=0.1$, 25Hz). Note that the R-curve at 1200°C is due to (c) bridging from viscous films present at grain boundaries compared to (d) frictional grain bridging observed at room temperature.

Of greater importance for ceramics, however, is to ascertain whether cyclic fatigue or static creep crack growth is more damaging at elevated temperatures. At room temperature, it is now becoming increasingly clear [4-6,10,12,13] that cracks propagate much faster under cyclic loading than static loading in many toughened ceramics, including Al_2O_3 , zirconias, Si_3N_4 and SiC. The picture at high temperatures is not clear. Limited data exist, yet, there is no consensus on either the mechanisms of crack growth or the relationship between cyclic and static crack growth rates at high temperature. For example, two separate studies on hot-pressed Si_3N_4 concluded that cyclic crack growth rates are faster [15] or slower [16] to crack velocities measured under static loading. Such results are most likely the result of mutual competition between *intrinsic* creep damage ahead of the crack tip via cavitation and grain-boundary sliding, aided by the presence of amorphous films at grain boundaries (formed during processing), and *extrinsic* shielding from grain and viscous-film bridging. Depending on the relative potency of each of these mechanisms with respect to composition, environment, temperature and strain rate, cyclic fatigue may be more or less damaging than static creep at elevated temperatures.

Intermetallics and Intermetallic-Matrix Composites

Titanium Aluminide Composites

Behavior at Room Temperature: γ -TiAl based intermetallic alloys are currently of interest as low-density alternatives to conventional titanium alloys for use in high-performance gas-turbine engines; efforts are aimed at improving their tensile ductility and fracture toughness at room temperature. Both composite reinforcement and alloying techniques have been used to toughen TiAl with considerable success [17-23]. The composite approach incorporates small amounts of ductile TiNb, Nb or Ti-6Al-4V particles into the microstructure to arrest the crack and enhance toughness through extrinsic crack bridging mechanisms, as detailed below.

A substantial improvement in fracture resistance of TiAl can be achieved through reinforcement with ductile particles at room temperature [17,18]. As shown in Fig. 5a, adding ~20vol.% of TiNb particles to TiAl increases crack-initiation toughness to ~18 MPa \sqrt{m} , more than twice that of pure γ -TiAl (~8 MPa \sqrt{m}) due to crack trapping by TiNb particles and crack renucleation effects. Fracture resistance further increases with crack extension (R-curve) due to crack bridging associated with the formation of unbroken ductile TiNb ligaments in the crack wake (Fig. 5c). As these bridging zones under monotonic loading are fairly large, ~3-6 mm [18], results presented in Fig. 5a are undoubtedly influenced by large-scale bridging effects. The degree of toughening increases with volume fraction of reinforcements, and the stronger TiNb reinforcements yield higher toughness compared to Nb reinforcements, independent of particle orientation.

Under cyclic loading, both TiNb and Nb reinforcements result in a modest increase in fatigue-crack growth resistance of γ -TiAl *only* in the face (C-L) orientation (Fig. 5b), where faces of pan-cake shaped particles are oriented normal to the crack plane [18]. Conversely, in the edge (C-R) orientation, where particle edges are oriented perpendicular to the crack plane, ductile particles actually *degrade* the fatigue resistance of the composite relative to γ -TiAl. Such behavior is primarily due to the premature fatigue failure of ductile ligaments which restricts the development of a bridging zone and resultant shielding at the crack tip (Fig. 5d). In the face orientation, small shielding contributions from crack branching, matrix cracking and coplanar bridging within ~100-200 μ m behind the crack tip provide a moderate increase in fatigue resistance. Note that these dimensions are far below the bridging-length scales observed during monotonic loading, providing an indication of the extent of shielding degradation possible under cyclic loading. Moreover, in contrast to microstructural effects on fracture resistance, weakly-bonded Nb particles are more effective in preserving shielding from bridging compared to the strongly-bonded TiNb and therefore offer better fatigue-crack propagation resistance over TiNb particles.

Effect of load ratio on cyclic crack-growth rates, in the 20 vol.% TiNb/ γ -TiAl composite are compared in Fig. 6, in terms of ΔK and K_{max} . As noted previously, increasing R accelerates crack-growth rates for a given ΔK and lowers the fatigue threshold. Crack closure levels, K_{cl} , are ~0.4 K_{min} suggesting that shielding is important for $R < 0.4$ [18]; however, marked differences in behavior between $R = 0.5$ and 0.7 imply that other factors are relevant. The differences with respect to load-ratio are not normalized by K_{max} , as was the case for ceramics (Fig. 3) suggesting that cyclic crack growth in TiNb/TiAl composites is not completely governed by monotonic shielding mechanisms. Regression fits to crack-growth data in Fig. 6 yield equivalent values for the exponents n (6.3) and p (6.1), implying the role of intrinsic fatigue damage in the composite. Intrinsic effects may presumably be related to repeated blunting and resharpening of the crack in the TiAl and TiNb constituent phases, akin to mechanisms proposed in metallic materials. In addition, static cleavage fracture modes are prevalent in the TiAl regions, particularly at K_{max} levels approaching K_{Ic} of the γ -TiAl matrix.

High-Temperature Properties: Ductile TiNb particles also enhance the fracture resistance of TiAl at 650 and 800°C [19], although measured toughness is somewhat lower at 650°C (Fig. 7a). Crack bridging is still prominent at high temperatures during monotonic loading, although tractions imposed

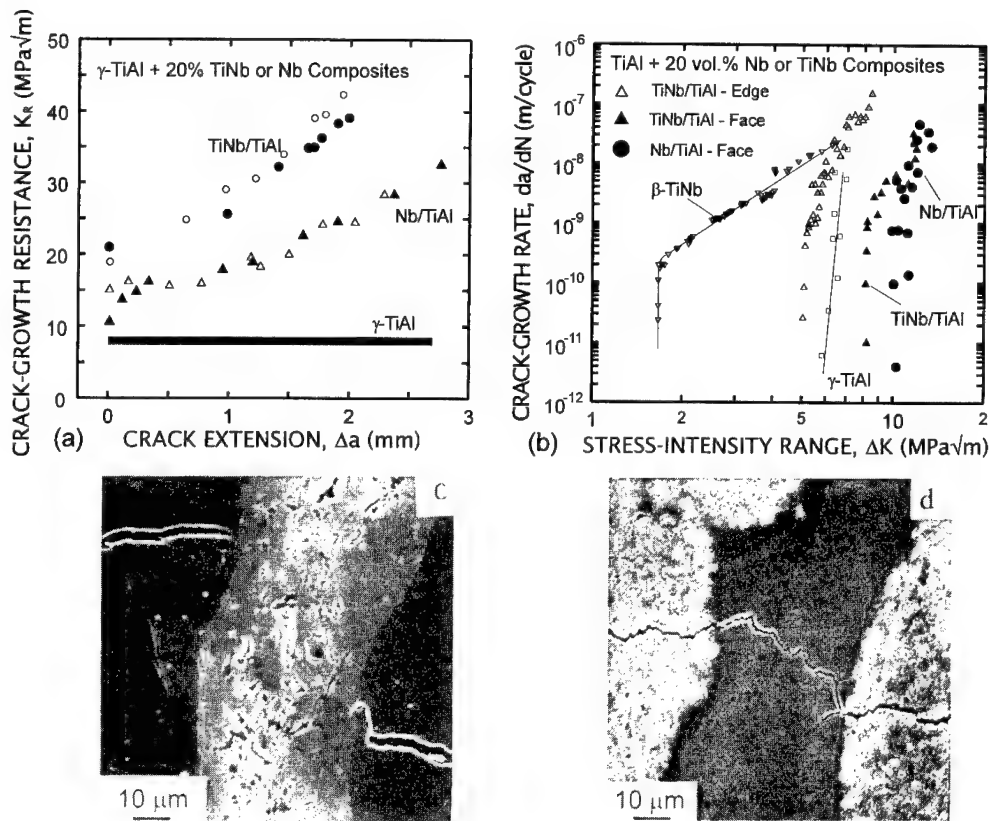


Figure 5- (a) Fracture toughness and (b) fatigue-crack growth behavior in a 20vol.% TiNb-reinforced TiAl composite at room temperature ($R=0.1$, 25 Hz), in the edge (open symbols) and face (closed symbols) orientations, compared to data in pure TiAl, TiNb and Nb/TiAl composites. Micrographs (c) and (d) illustrate the presence and absence of crack bridging under monotonic and cyclic loading, respectively [19].

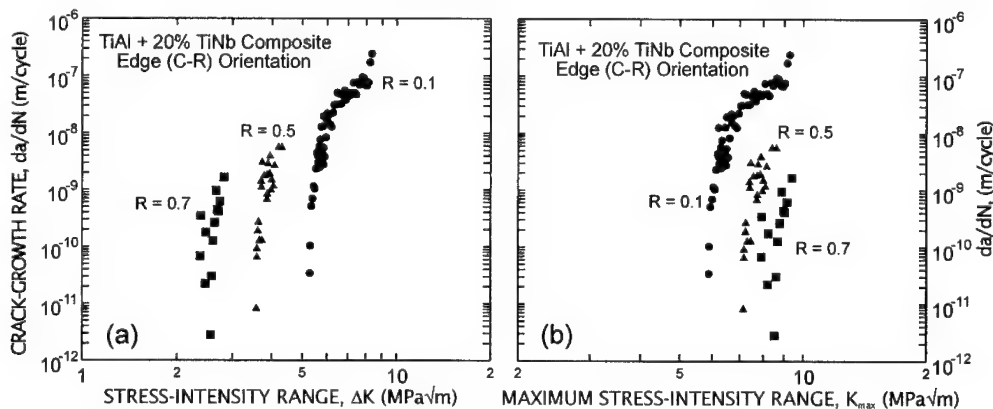


Figure 6- (a) Fatigue-crack propagation rates in the TiNb/TiAl composite at various load ratios correlated in terms of (a) applied ΔK and (b) maximum stress intensity, K_{max} . Note that unlike the SiC ceramic in Fig.4, K_{max} does not normalize the data suggesting intrinsic fatigue effects and greater dependence on ΔK in the intermetallic composite.

in the crack wake are lower due to a reduction in particle strength at elevated temperatures [19]. This decrease in extrinsic bridging efficiency is offset by an increase in intrinsic ductility and toughness of the TiAl matrix, especially above the ductile-to-brittle transition temperature (DBTT) of $\sim 700^\circ\text{C}$ for γ -TiAl [20]; the competing effects account for the lower composite toughness at 650°C . However, toughening from TiNb particles may not be realized over extended periods of time at high temperatures since TiNb is prone to environmental attack in unprotected atmospheres due to the poor oxidation resistance of Nb-bearing alloys. Suitable protective coatings are essential to minimize environmental degradation before these materials are contemplated for use in structural applications.

Subcritical fatigue crack growth at elevated temperatures is observed in the composite at ΔK levels between ~ 4 - $10 \text{ MPa}\sqrt{\text{m}}$, well below stress intensities of ~ 12 - $18 \text{ MPa}\sqrt{\text{m}}$ needed to initiate crack growth under monotonic loading (Fig. 7b). Growth rates are slightly faster at 650°C relative to behavior at 25 and 800°C , and their sensitivity to applied ΔK remains high at all temperatures with exponents (m) ranging between 7-10. Similar to behavior at room temperature, the ductile TiNb particles fail via transgranular shear in fatigue (Fig. 7d), distinct from microvoid coalescence failures observed under quasi-static loading (Fig. 7c), suggesting that suppression of crack-tip shielding from TiNb-ligament bridging under cyclic loading continues to be a principal factor influencing fatigue-crack growth at all temperatures. However, because of the reduced efficiency of bridging at high temperatures [19], shielding degradation from TiNb-particle failure does not significantly accelerate crack-growth rates in the composite relative to unreinforced TiAl, unlike behavior at room temperature; at 650°C , cyclic crack-growth rates between the monolithic alloy and composite are equivalent.

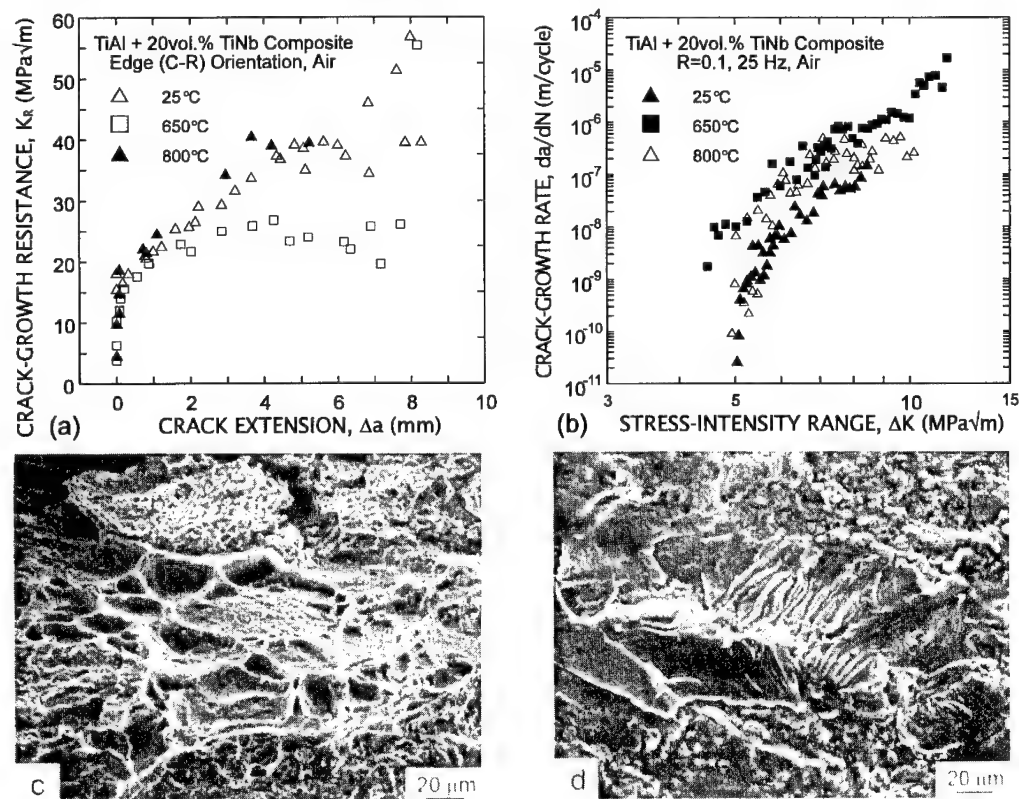


Figure 7- (a) Fracture toughness and (b) fatigue-crack growth behavior ($R=0.1$, 25 Hz) in the TiNb/TiAl composite at various temperatures, and fracture surfaces at 800°C under (c) monotonic and (d) cyclic loading. Note the clearly distinct (microvoid coalescence vs. transgranular shear) failure modes in the TiNb under monotonic and cyclic loading [20].

The notion of fatigue-crack advance by cycle-dependent degradation of bridging in the crack wake is similar to mechanisms described above for ceramics. There is one significant difference though for fatigue behavior in intermetallics. In TiNb/TiAl, fatigue-crack growth is seen at ΔK levels far below the crack-initiation toughness (K_i) on the R-curve, specifically $K_{\max, TH} \sim 0.25-0.4 K_i$. This implies that in addition to the *extrinsic* effects of limited shielding under cyclic loading, there are *intrinsic* damage mechanisms uniquely associated with fatigue failure in intermetallics (Figs. 7c,d). There is no apparent intrinsic fatigue damage mechanism in ceramics at room temperature; crack advance of the tip occurs by an identical under monotonic and cyclic loads. Accordingly, the maximum stress intensity at fatigue threshold in ceramics is comparable to the crack-initiation toughness (i.e., $K_{\max, TH} \sim K_i$).

Titanium Aluminide Alloys:

Microalloying TiAl intermetallics with small amounts of Cr, V, Mo and Nb followed by thermomechanical treatment yields two-phase microstructures comprising lamellar colonies of alternating γ and α_2 (Ti₃Al) layers [21-25]. Improved toughness, especially in coarse-lamellar structures, results from crack deflection and microcracking along interlamellar boundaries which generates a crack wake bridged by intact lath colonies undergoing shear deformation- a phenomenon referred to as shear-ligament bridging. These crack-tip shielding processes elevate crack-initiation toughness of TiAl alloys to $\sim 15-20 \text{ MPa}\sqrt{\text{m}}$; R-curve behavior is observed with maximum toughness values as high as $50-60 \text{ MPa}\sqrt{\text{m}}$, depending on the colony size and specimen dimensions.

Fatigue-crack growth characteristics in lamellar TiAl intermetallic alloys at ambient and elevated temperatures are quite similar to features noted in TiNb/TiAl composites [24-26]. First, cyclic crack growth rates in TiAl alloys show a greater sensitivity to applied ΔK compared to metals, yet lower relative to ceramics. Second, when behavior is partitioned in the form of Eq. 2, the dependence on K_{\max} and ΔK are comparable with a slightly higher dependence on ΔK . For example, in a nearly-lamellar XDTM processed 1 vol%TiB₂-reinforced Ti-47.7Al-2Nb-0.8Mn (at.%) alloy [25], exponents for ΔK and K_{\max} are $p=10.3$ and $n=5.6$, respectively, suggesting that both extrinsic and intrinsic mechanisms contribute to cyclic crack growth; in fact, cyclic degradation of shear-ligament bridges has been verified to be the extrinsic mechanism influencing fatigue crack advance. Finally, fatigue crack growth rates are fastest in the 600-650°C range, just below the DBTT of TiAl [26-28]; ongoing studies are aimed at examining this anomalous temperature dependence in more detail.

Molybdenum Disilicide Composites

Materials based on MoSi₂ intermetallic compound are attractive for structural use at temperatures above 1200°C [3], yet like other ceramics and intermetallics, they suffer from problems of low ductility and toughness at room temperature. Ductile-phase toughening using high-aspect ratio reinforcements [29,30] has been a successful approach to prevent catastrophic failure in MoSi₂ at K_{Ic} values $\leq 4 \text{ MPa}\sqrt{\text{m}}$. Using 20 vol.% Nb short fiber (wire) reinforcements, the onset of cracking in the composite is seen at $\sim 5 \text{ MPa}\sqrt{\text{m}}$ [30] and proceeds stably up to about $14 \text{ MPa}\sqrt{\text{m}}$ after extending $\sim 1.5 \text{ mm}$; crack deflection, renucleation and crack bridging by Nb particles are the principal mechanisms responsible for the higher toughness.

In fatigue, general features are similar to those seen in TiAl alloys and composites- (i) growth rate exponents are high ($m \sim 20$) compared to metals, (ii) load-ratio effects are not normalized by K_{\max} , and (iii) Nb bridges degrade in fatigue and suppress shielding. Two notable differences [30], however, are striking. First, fatigue response of the Nb/MoSi₂ composite is more ceramic-like, with crack-growth rates showing a slightly greater dependence on K_{\max} than ΔK , most likely due to the lack of plasticity in monolithic MoSi₂ at room temperature. Moreover, no fatigue effects have been reported in pure MoSi₂ [30], unlike TiAl where limited plastic deformation and intrinsic fatigue are apparent. And second, the Nb wires also yield remarkable improvements in fatigue-crack growth resistance of MoSi₂, despite the reduced effect of bridging under cyclic loading. This is principally associated with extensive crack deflection along the weak Nb/MoSi₂ interface (at angles of up to 70°) and interface debonding, which promote shielding in fatigue from premature contact and wedging between fracture surface asperities (termed roughness-induced crack closure [31]), akin to behavior many structural materials [2].

Design and Life Prediction

The marked sensitivity of fatigue crack growth rates to the applied stress intensity in intermetallics and ceramics, both at ambient and elevated temperatures, presents unique challenges to damage-tolerant design and life-prediction methods for structural components. In metallic structures for safety-critical applications, such procedures generally rely on the integration of the crack-growth rate (da/dN or crack velocity) vs. applied stress intensity (ΔK or K_{max}) to estimate the largest undetectable initial flaw (a_i) to propagate to a critical size (a_c), yielding an expression for life, N_f , of the form:

$$N_f = \frac{2}{(m-2)C' (Q \Delta\sigma)^m \pi^{m/2}} \left[a_o^{(2-m)/2} - a_c^{(2-m)/2} \right] \quad (3)$$

where $\Delta\sigma$ is the applied stress range, Q is the geometric factor; C' and m ($\neq 2$) are the scaling constant and exponent in the crack-growth relationship (Eq. 2). For the high-temperature materials discussed in this paper, this approach may be difficult to implement in practice due to the large values of m because projected life is proportional to the reciprocal of the applied stress raised to a large power. In other words, the life spent in crack propagation in these materials will be extremely limited (or infinitely large, depending on the stress level) due to the steepness of the da/dN - ΔK curves.

A better approach may be to design on the basis of the fatigue threshold, ΔK_{TH} , for no crack growth or fatigue-crack initiation (stress-life, or S-N) data obtained under appropriate service loading conditions. For example, using the ΔK_{TH} value, components may be designed to stress levels below those necessary to extend the largest undetectable flaw ($\Delta\sigma < \Delta K_{TH}/Q\sqrt{\pi a_i}$) in the material. Or alternatively, life-prediction procedures may use S-N data with appropriate safety factors to guarantee structural integrity during service. However, both methods may not be conservative due to small-crack effects, where in metallic materials, flaws of limited wake are known to propagate at ΔK levels far below the thresholds measured for long cracks. In extrinsically toughened intermetallics and ceramics, small crack effects may arise because shielding is activated only after some crack extension. A few studies have reported sub-threshold growth of small fatigue cracks in ceramics and intermetallics.

Concluding Remarks

Although significant progress has been made in the last ten to fifteen years in improving the room-temperature fracture resistance of ceramics and intermetallics using the extrinsic shielding approach to toughening, it is evident that cyclic loading can severely degrade such shielding and promote subcritical fatigue-crack growth. In ceramics, especially at room temperature, extrinsic shielding appears to be the primary mechanism governing toughness and cyclic fatigue. As a result, fatigue-crack growth rates are extremely sensitive to K_{max} (which governs shielding) than applied ΔK , in direct contrast to metal fatigue, which is primarily an intrinsic process more dependent on ΔK rather than K_{max} (at least in the intermediate and near-threshold regimes). Fatigue crack growth in intermetallics, conversely, depends on both intrinsic and extrinsic factors intermediate to behavior in ceramics and metals; crack-growth rates are equally dependent on K_{max} and ΔK .

Apart from shielding, intrinsic effects are important for ceramics and intermetallics, particularly at high temperatures. In intermetallics, fracture mode changes associated with DBTT and environmental interactions lead to a complex variation in properties with temperature; behavior in TiAl alloys is worst just below the DBTT. In ceramics like SiC, the mechanism is altered from one of frictional grain bridging at room temperature to viscous film bridging at elevated temperatures. Of greater concern for ceramics, however, is to ascertain whether cyclic fatigue or (static) creep is more damaging at high temperatures; both phenomena need further work to provide better understanding.

The marked sensitivity of growth rates to the applied stress-intensity in ceramics and intermetallics implies that projected lifetimes will be a very strong function of stress and crack size; this makes life prediction using damage-tolerant design extremely difficult. Accordingly, design approaches based on the fatigue threshold or a fatigue limit (in S-N data) must be contemplated, although even these may not be conservative due to the growth of small cracks. Clearly, this is an area that mandates increased attention if these materials are ever to find widespread structural use.

Acknowledgements

This work was supported by the U.S Air Force Office of Scientific Research under Grant Nos. F49620-93-1-0107 and 0289 (for studies on intermetallics) and Office of Basic Energy Sciences, Materials Sciences Division of the Department of Energy under Contract No. DE-AC03-76SF00098 (for studies on ceramics). Our thanks are due to Professors G. R. Odette (University of California, Santa Barbara) and L. C. DeJonghe (University of California, Berkeley) for their collaboration and helpful discussion.

References

1. A. G. Evans, *J. Am. Ceram. Soc.*, **74** (1991), 255.
2. R. O. Ritchie, *Mater. Sci. and Eng. A*, **A103** (1988) 15.
3. C. T. Liu, J. O. Stiegler and F. H. Froes, *Metals Handbook*, vol. 2 (Metals Park, OH: American Society for Metals International, 1991), 913.
4. R. O. Ritchie and R. H. Dauskardt, *J. Ceram. Soc. Japan*, **99** (1991), 1047.
5. R. H. Dauskardt, *Acta metall. mater.*, **41** (1993), 2765.
6. S. Lathabai, J. Rödel and B. Lawn, *J. Am. Ceram. Soc.*, **74** (1991), 1340.
7. C. Laird and G. C. Smith, *Phil. Mag.*, **7** (1962), 847.
8. R. M. N. Pelloux, *Eng. Fract. Mech.*, **1** (1970), 697.
9. J. J. Cao, W. J. MoberlyChan, L. C. DeJonghe, C. J. Gilbert and R. O. Ritchie, *J. Am. Ceram. Soc.*, **79** (1996), 461.
10. C. J. Gilbert, J. J. Cao, W. J. MoberlyChan, L. C. DeJonghe and R. O. Ritchie, *Acta mater.*, **44** (1996) in press.
11. R. H. VanStone, *Mater. Sci. Eng.*, **A103** (1988), 289.
12. H. Kishimoto, *ISME Intl. J.*, **34** (1991), 393.
13. D. S. Jacobs and I.-W. Chen, *J. Am. Ceram. Soc.*, **78** (1995), 513.
14. D. Rouby and P. Reynaud, *Compos. Sci. Technol.*, **48** (1993), 109.
15. U. Ramamurty, T. Hansson, and S. Suresh, *J. Am. Ceram. Soc.*, **77** (1994), 2985.
16. S.-Y. Liu, I.-W. Chen, and T.-Y. Tien, *J. Am. Ceram. Soc.*, **77** (1994), 137.
17. C. K. Elliott, G. R. Odette, G. E. Lucas and J. W. Sheckherd, in *High-Temperature/High-Performance Composites*, ed. F. D Lemkey et al. (Pittsburgh, PA: The Materials Research Society, 1988), 95.
18. K. T. Venkateswara Rao, G. R. Odette and R. O. Ritchie, *Acta Metall. Mater.*, **42** (1994), 893.
19. K. T. Venkateswara Rao and R. O. Ritchie, *Acta Mater.*, **44** (1996), in review.
20. H. A. Lipsitt, D. Schectman and R. E. Schafrik, *Metall. Trans. A*, **6A** (1975), 1991.
21. Y. W. Kim and D. M. Dimiduk, *J. Metals*, **43:8** (1991), 40.
22. H. E. Dève, A. G. Evans and D. S. Shih, *Acta Metall. Mater.*, **40** (1992) 1259.
23. K. S. Chan, *J. Metals*, **44:5** (1992), 30.
24. K. T. Venkateswara Rao, Y. W. Kim, C. L. Muhlstein and R. O. Ritchie, *Mater. Sci. and Eng. A*, **A192/193** (1995), 474.
25. J. P. Campbell, K. T. Venkateswara Rao and R. O. Ritchie, in *Fatigue '96*, ed. G. Lutjering and H. Nowack, (New York, NY: Pergamon Press, 1996), vol. III, 1779.
26. S. J. Balsone, J. M. Larsen, D. C. Maxwell and J. Wayne Jones, *Mater. Sci. Eng. A*, **A192/193** (1995), 457.
27. K. T. Venkateswara Rao, Y. W. Kim and R. O. Ritchie, *Scripta metall. mater.*, **33** (1995), 459.
28. A. L. McKelvey, J. P. Campbell, K. T. Venkateswara Rao and R. O. Ritchie, in *Fatigue '96*, ed. G. Lutjering and H. Nowack (New York, NY: Pergamon Press, 1996), vol. III, 1743.
29. S. M. Pickard and A. K. Ghosh, in *High-Temperature Ordered Intermetallic Alloys VI*, ed. J. Horton et al. (Pittsburgh, PA: The Materials Research Society, 1995), 905.
30. K. Badrinarayanan, A. L. McKelvey, K. T. Venkateswara Rao and R. O. Ritchie, *Metall. Trans. A*, **27A** (1996), in press.
31. S. Suresh and R. O. Ritchie, *Metall. Trans. A*, **13A** (1982), 1627.

DEVELOPMENT OF A NEW SERIES OF Nb ALUMINIDES FOR

ELEVATED TEMPERATURE APPLICATIONS

R. Wheeler , S.S. Yang, D.-H. Hou and H.L. Fraser

Department of Materials Science and Engineering
The Ohio State University
2041 College Road
Columbus, OH 43210, USA

Abstract

Some aspects of the materials science underlying the development of a new series of Nb aluminides are described. The study involves three alloys, with compositions given by Nb-15Al-xTi, where x=10, 25 and 40, having the B2 crystal structure. The ordering scheme of these compounds is described with the aid of the recently introduced concept of *ordering tie-lines* from which it is shown that while the crystal structures are the same (B2), the ordering scheme in these compounds differs quite significantly. The deformation mechanisms have been determined, and have been considered in the light of the tensile ductilities exhibited by the compounds. Finally, the oxidation behavior of these aluminides has been studied.

Introduction

Recently, a series of Nb aluminides containing various amounts of Ti and possessing the B2 crystal structure have been developed [1,2]. Three examples of these intermetallic compounds have compositions given by Nb-15Al-xTi, where x=10, 25 and 40 (all compositions in atomic % unless otherwise stated), as indicated in the ternary phase diagram (taken from [3]) shown in Fig. 1. These compounds with x=10, 25 and 40 will be referred to as 10Ti, 25Ti and 40Ti, respectively. The three compounds exhibit a series of attractive properties, particularly concerning application at temperatures $\approx 800^\circ\text{C}$. Various aspects of these compounds are considered here, including the ordered state of the compounds, the operative deformation mechanisms, and their oxidation response.

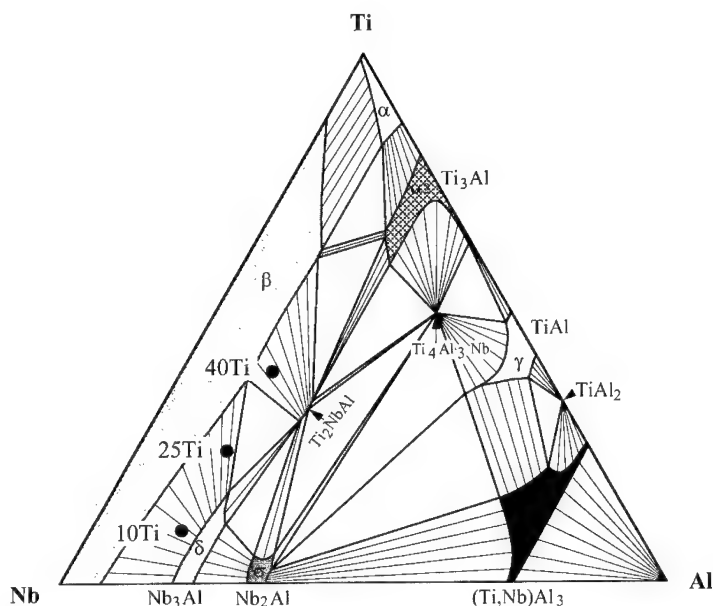


Fig. 1. - Section of a Nb-Al-Ti ternary phase diagram at 700°C , taken from Kattner and Boettinger [3] showing the three compositions of the Nb-15Al-10Ti, -25Ti and -40Ti alloys

Ordering Scheme

In view of the stoichiometry usually associated with the B2 structure, the compounds described here are extremely interesting. Thus, the compositions of the 10Ti, 25Ti, and 40Ti alloys do not correspond to an $\text{A}_{50}\text{B}_{50}$ stoichiometry, but nevertheless, they all exhibit the B2 crystal structure in the as-cast and heat-treated forms. Consequently, the site occupancy of these ternary B2 compounds will differ from that of stoichiometric B2 compounds, where each sublattice site is occupied essentially by one type of atom. Hence, it is of interest, and also important, to determine the site occupancies of these ternary B2 compounds.

In this paper, a new approach is applied to define a general "ordering scheme" of the B2 structure in a ternary alloy [4]. This new concept, the Ordering Tie Line (OTL), is used to describe this ordering scheme, from which the site occupancies or atomic configurations of the B2

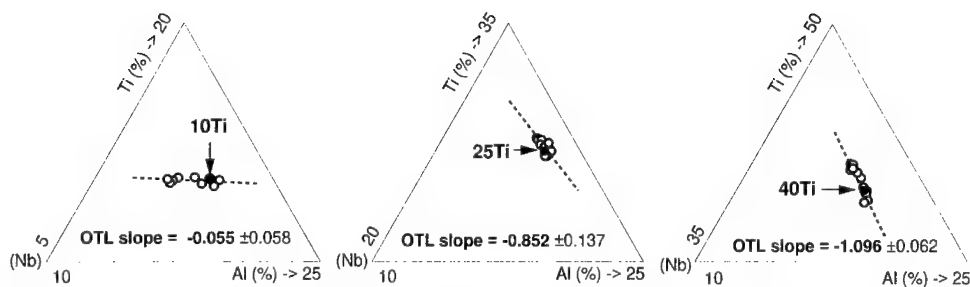


Fig. 2. - Results of Alchemi experiments (apparent compositions) for the three alloys shown (i.e. Nb-15Al-xTi, where x=10,25, or 40), plotted on Nb-Al-Ti composition diagrams.

alloys can be derived. Experimentally, it has also been shown [4] that the OTL can be determined by the ALCHEMI technique [5]. The ordering schemes of these three B2 alloys, as represented by their OTL's, have been determined, and these are discussed below. Details concerning the basis of the OTL method are available in reference [4].

Thin foils have been made from homogenized samples of the three alloys (i.e. 10Ti, 25Ti and 40Ti). ALCHEMI experiments have been performed, and the apparent compositions determined from these experiments have been plotted on the composition diagrams shown in Fig. 2. The trace of the OTL is then drawn as the best line fit through the measured apparent compositions. The resulting OTLs are plotted in the composition diagram shown in Fig. 3. The errors in the orientations ($\Delta C_{Ti}/\Delta C_{Al}$) of OTLs have been determined statistically, and these errors are represented by the shaded areas in Fig. 3. As a first approximation, the most ordered state for each of these compounds has been assumed, so that the OTLs have been stretched out until a boundary of the composition diagram has been reached (i.e. the Nb-Ti boundary in each of these cases). It should be noted that for the elements present in the samples which are the subjects of these experiments, the effects of delocalization [6,7] should be assessed. However, it has been shown in [8] that although the delocalization effect may alter the orientation of OTL, the actual correction is rather small. In fact, the correction modifies the actual values of the sublattice compositions more or less within their experimental error. For this reason, delocalization is not considered further here, although its importance in ALCHEMI experiments is recognized.

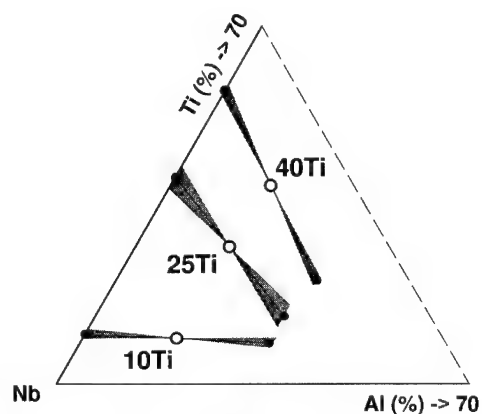


Fig. 3 - OTLs for the three alloys shown, deduced from the data shown in Fig. 2. The shading about each of the OTLs represents an estimate of the errors involved in the measurements.

As has been stated above, the orientation of an OTL is derived directly from an ALCHEMI experiment, whereas the location of the end-points of an OTL are best estimates. In the case of the OTLs presented in Fig. 3, the approximation used to determine the end-points has been based on the assumption that the compounds will be in their most ordered state. It is possible to make more quantitative assessments of the locations of the end-points. For example, in the case of CuAuPd compounds with the $L1_0$ structure, a combination of the intersecting Kikuchi line (IKL)

method and ALCHEMI have been used successfully to deduce sublattice compositions [9]. It has not been possible to apply this combination of techniques in the case of the present alloys, and a different approach has been adopted. Thus, for the case of the Nb-15Al-40Ti alloy the dynamical theory of electron diffraction (17 beams) has been used to calculate the estimated spread of measured apparent compositions as a function of long range order parameter (LROP, as defined using OTLs in [4]) which would be expected from ALCHEMI experiments. The results of these calculations are shown graphically in Fig. 4. Here, the theoretical spread in apparent compositions with negative deviations from Bragg have been used (the reason for this is discussed elsewhere [8]). As can be seen, in the case of the 40Ti alloy, this experimental spread is $\approx 2\%$, and as shown in Fig. 4, this corresponds to a LROP of ≈ 0.5 . Similar analyses (i.e. simulation using the dynamical theory) for the case of alloys containing 10Ti and 25Ti yield LROPs of 0.88 and 0.25, respectively. The corresponding OTLs are shown in Fig. 5. From these analyses, it appears that the 10Ti alloy is close to being in its most ordered state, while the other two alloys are not so fully ordered.

It should be noted that it is the orientation of the OTL which is the quantity measured with confidence in ALCHEMI. It represents the trend in B2 ordering, which is obtained without further assumptions. Therefore, it is most reliable to assess the ordering of the current B2 alloys by comparing the orientations of the OTL's. It is clearly seen that the OTL of the Nb-15Al-40Ti alloy runs in a different orientation from that of the 10Ti alloy. This suggests that the ordering scheme of the 40Ti alloy is different from that of the 10Ti alloy. The orientation of the OTL of the 25Ti alloy is in between those of the 10Ti and the 40Ti alloys indicating a gradual change of ordering scheme from the 10Ti, to 40Ti alloy. Interestingly, the LROP for this alloy was determined to be only 0.25, and this low value is consistent with a gradual change in the nature of ordering. Inspection of the OTLs for the three alloys studied, shown in Fig. 3 for the case assuming most ordering, reveals that the significant factor in achieving the most ordered state is that all Al atoms remain on the one sublattice. This requirement for the Al atoms implies that the partitioning of Al atoms between the two sublattice sites is a critical factor for B2 ordering in these ternary Nb-Al-Ti alloys. This suggestion can be further supported by the fact that the B2 phases have been found in some Nb-Al alloys [10] but not in the Nb-Ti binary systems.

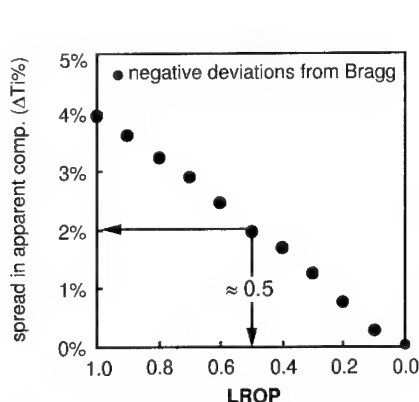


Fig. 4 - Spread in measured apparent composition (maximum of Ti% in -s channeling orientations - Ti% of the crystal) of the 40Ti alloys versus various LROP's calculated by dynamical theory of electron diffraction (17 beams)

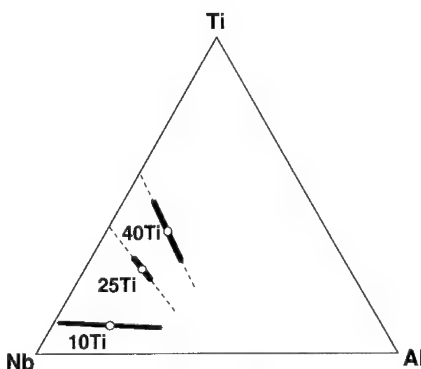


Fig. 5 - OTLs from the three alloys with end points estimated by dynamical calculations (Fig. 4). Thin lines represent OTL's measured from Alchemi experiments and thick lines represent the estimated OTL's.

Deformation Mechanisms

It is interesting to note the differences in mechanical response exhibited by these compounds. Thus, the compounds containing 10Ti and 25Ti exhibit essentially no tensile ductility, a fracture surface from a room temperature tension test being shown in Fig. 6(a), whereas that containing 40Ti can yield tensile ductilities up to $\approx 30\%$ at room temperature, a representative fractograph being shown in Fig. 6(b). This lack of ductility in compounds with higher Nb contents is one of the factors limiting the development of these compounds for applications regarding high strength, and it is of interest to determine the factors that influence these differences in mechanical response.

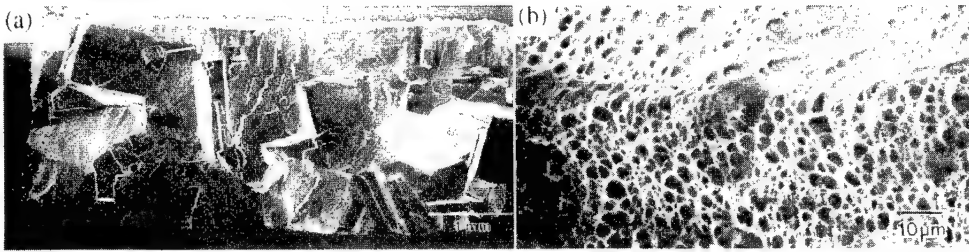


Fig. 6 - SEM fractographs showing the typical (a) brittle fracture surface of the 10Ti and 25Ti alloys and (b) ductile fracture surface of the 40Ti alloy. Specimens are tensile tested at room temperature at a strain rate of 10^{-4} sec^{-1} .

Dislocation Glide

Dislocation glide in the three compounds occurs by motion of coupled pairs of superpartial dislocations with Burgers vectors, \mathbf{b} , given by $\mathbf{b} = 1/2\langle 111 \rangle$ on planes such as $\{110\}$, $\{112\}$ and $\{123\}$ [11]. Slip is not homogeneously distributed, but dislocations tend to be restricted to a series of slip bands, an example of such dislocation substructure being shown in fig. 7. In addition to this behavior, the tensile behavior of the compounds tends to be of interest, as evidenced by features on stress-strain curves. Thus, as shown in Fig. 8, which is a stress/strain curve for a sample taken from a solution-treated 40Ti alloy (i.e. single phase with B2 structure) tested in tension, there is a marked yield point, followed by a gradual decrease in stress with increasing strain, indicating work softening. These various observations may well be the result of a very fine

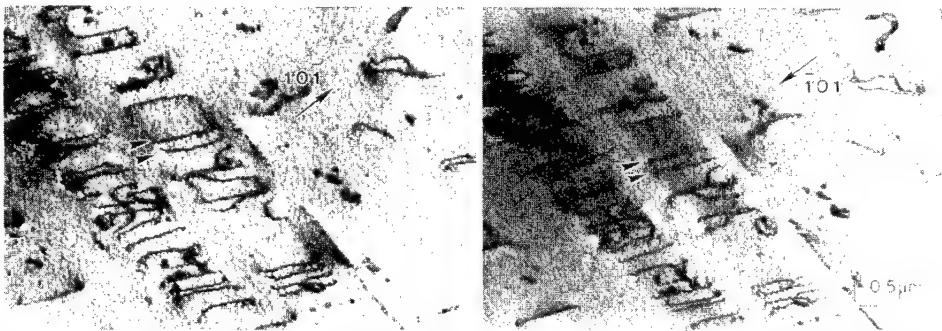


Fig. 7 - TEM bright-field micrographs of the 25Ti alloy showing inhomogeneous dislocation slip. Specimen has been solution treated to have single phase B2 structure and compression tested at room temperature at a strain rate of 10^{-4} sec^{-1} .

particle dispersion, as shown in Fig. 9. Diffuse intensity consistent with the presence of the ω phase are also observed in the 40Ti alloy. Hence, the slip bands could correspond to slip localization typically observed in alloys with short-range ordering, and the work softening would be caused by continued cutting of the ω phase particles, reducing their effectiveness as obstacles to dislocation motion. In alloys that are annealed to promote coarsening of any refined particle distribution, not only is a marked yield point observed, but also the continued deformation is characterized by serrated yielding. The role of the ω phase or similarly refined phase in deformation of these compounds is the subject of further work. It is unclear whether the differences in tensile ductilities exhibited by the three compounds may be attributed to the presence of a dispersion of a refined phase.

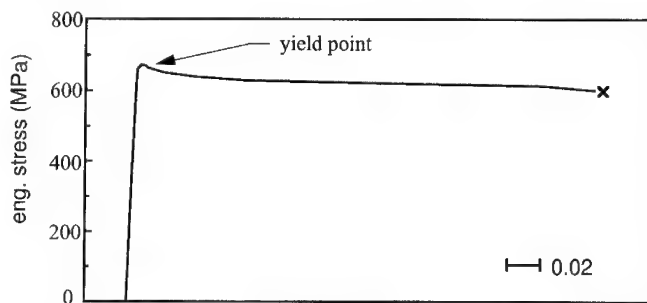


Fig. 8 - Stress-strain curve of the 40Ti alloy tensile tested at room temperature at a strain rate of 10^{-4} sec^{-1} . Specimen has been solution treated at 1100°C to obtain single phase B2 structure and then annealed at 400°C for 10 minutes followed by furnace cooling.

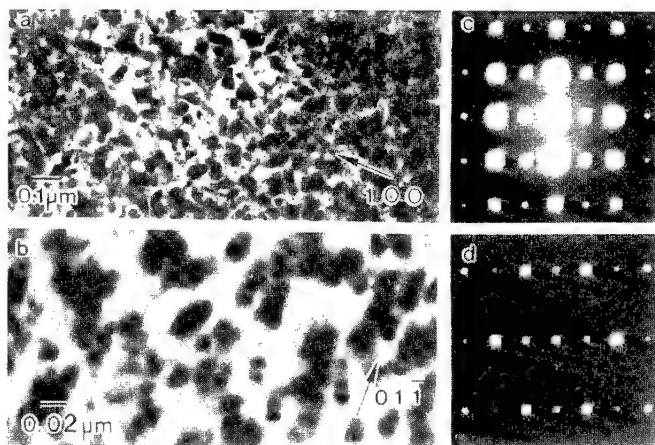


Fig. 9 - TEM (a) dark field and (b) bright-field images and (c,d) SADP's showing the ω -phase precipitates in the 10Ti alloy. Specimen is heat treated at 900°C for 10 minutes followed by furnace cooling.

Pseudo-twinning/Stress-Induced Martensite

In addition to dislocation glide, a “pseudo-twinning” deformation mechanism was also observed [12]. Since the matrix phase exhibits the B2 ordering structure, a new ordered phase with orthorhombic symmetry will form as a result of pseudo-twinning. The mechanism may also be referred to as a stress-induced martensite. *It should be noted that these defects are observed in the 10Ti and 25Ti, but never in samples of 40Ti.*

Observation and Mechanism The typical microstructure and SADP's of the pseudo twins formed during deformation in the 25Ti alloy is shown in Fig. 10. The extra reflections which arise from the pseudo twins has an apparent twin relationship with respect to the matrix spots (Fig. 10(b, f and i)). These pseudo twins can be made "invisible" by using appropriate diffraction vectors (\mathbf{g}), and when this is done the twinning direction (η_1) is determined as $[1\bar{1}\bar{1}]$. The twinning plane (K_1) is also determined by trace analysis to be $(1\bar{1}2)$. Thus, the twinning system is $\langle 111 \rangle \{112\}$ which is similar to the case of mechanical twinning in *bcc* metals. However, the resulting "twins" in the current B2 alloys exhibit a different crystal structure than the parent phase. This is evidenced by an extra reflection in the $[3\bar{1}1]$ zone axis SADP (Fig. 10(f)) which occurs at the midpoint between the transmitted and the "twinned" (011) matrix reflection. This indicates that the interplanar spacing (d) corresponding to this reflection is twice the largest d -spacing in the B2 crystal, i.e. d_{110} . Therefore, the resulting "twin" cannot be a "true" twin, but rather is a pseudo-twin.

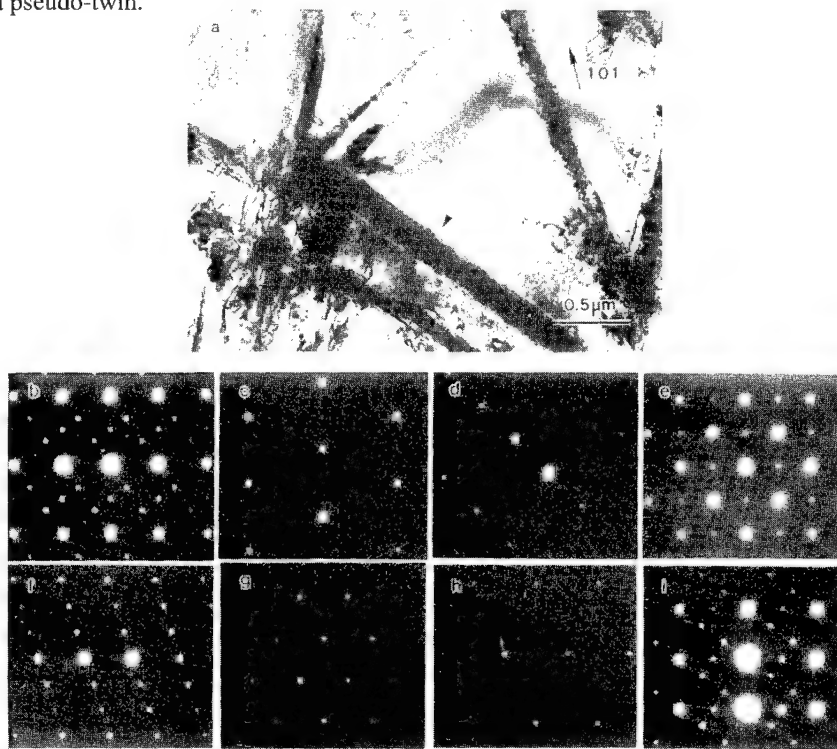


Fig. 10 - TEM micrographs of the deformed 25Ti alloy showing (a) the plate-like microstructural feature, (b) $[0\bar{1}1]$, (c) $[0\bar{1}2]$, (d) $[1\bar{1}3]$, (e) $[001]$, (f) $[3\bar{1}1]$, (g) $[1\bar{1}\bar{1}]$, (h) $[201]$, and (i) $[101]$ zone axis SADPs.

Similar pseudo twins have been reported and characterized in β Fe-Be alloys [13]. They suggested that the pseudo-twins are produced by the same twinning mechanism in *bcc* metals, i.e. by the passage of partial dislocations with $b=1/6\langle 111 \rangle$ on successive $\{112\}$ planes. As shown in Fig. 11(a), by applying the same mechanism to the B2 matrix, the product phase (i.e. the pseudo twin) will have a lattice exhibiting a twin relationship with the matrix but have a different ordering scheme. This ordering is evidenced by the extra reflections corresponding to the $1/2(011)$ matrix reflection mentioned above. The unit cell of the pseudo-twin, which has a structure of side centered orthorhombic, is shown in Fig. 11(b). Simulated SADP's based on this orthorhombic phase and orientation relationship are consistent with those recorded experimentally [14]. It is

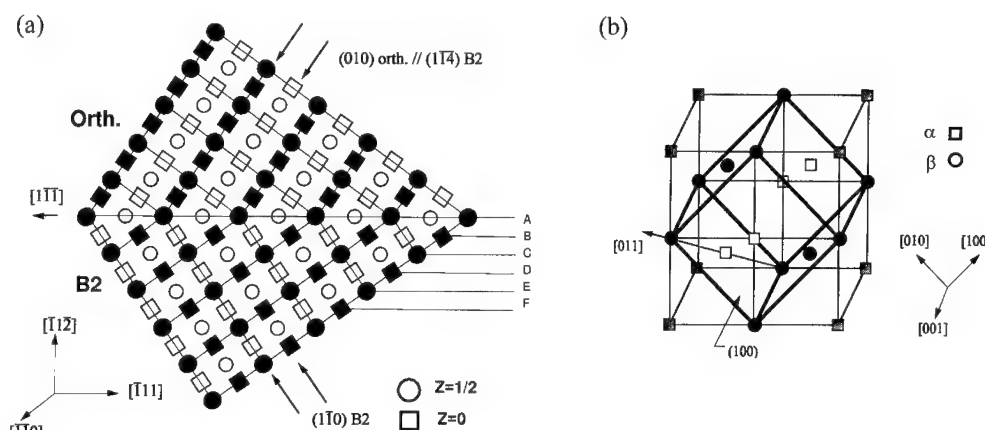


Fig. 11 - (a) Schematic diagram showing the atomic movements during $(\bar{1}\bar{1}2)[1\bar{1}1]$ twinning of a B2 crystal. Filled and open symbols represent different types of atom. (b) the ordered orthorhombic structure created by pseudo-twinning mechanism in a B2 crystal

noted that the pseudo-twins in current 25Ti and 10Ti alloys differ than those in the Fe-Be alloys in a way that they are formed in a monolithic B2 matrix, while the Fe-Be alloys have a modulated structure consisting of fine B2 domains in a primary *bcc* matrix [13].

Influence of pseudo twins on ductility It has been shown above that at room temperature both the 10Ti and 25Ti alloys exhibit essentially no ductility, whereas the 40Ti alloy can exhibit up to $\approx 30\%$ tensile elongation. The occurrence of pseudo-twins in both the 10Ti and 25Ti alloys, but not in the 40Ti alloy, may then provide some insight into the difference in ductilities exhibited by this alloy system. For example, the intersection of two pseudo-twins, may produce crack nucleation sites and then inhibit ductility. This hypothesis is supported by the following observations.

Firstly, pseudo twins are found to be formed in samples loaded at stress levels (520MPa) much lower than the macroscopic yield (710MPa). This establishes unequivocally that at the yield stress, samples will contain a significant density of pseudo-twins, which might serve as possible crack nucleation sites. Secondly, a large number of traces from intersecting pseudo-twins associated with the cracks (Fig. 12) are found on the outer surface of samples tested by three point bending. Surface relief resembling a possible crack nucleation site can be seen at the junction of two intersecting pseudo twins (Fig. 12(b)). Lastly, it can be shown that the lattice

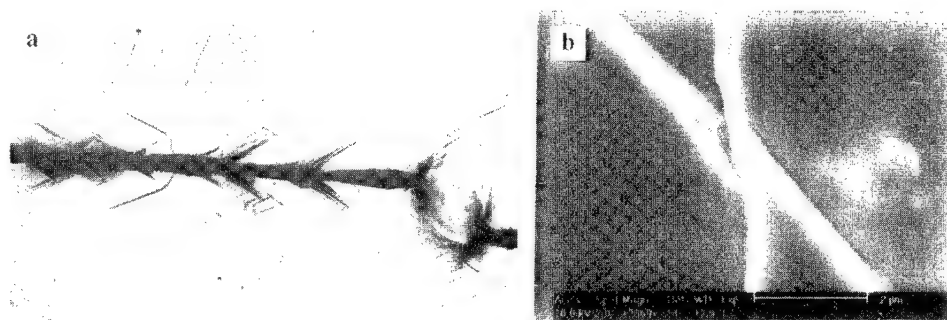


Fig. 12 - The (a) optical and (b) SEM micrographs taken from the surface crack region of the 25Ti alloy by three point bend-test.

displacement resulting from the combination of the two pseudo-twinning shears would be consistent with the initiation of cleavage (Yang 1995). TEM thin foils were produced from samples such as those shown in Fig. 12(a), i.e. from the surfaces of bend-test samples. The pseudo twins observed on both sides of a crack (Fig. 13) have been characterized. Based on common crystal coordinates, the shears are $1/6[\bar{1}\bar{1}1]$ on $(1\bar{2}\bar{1})$ and $1/6[1\bar{1}\bar{1}]$ on (211) for the pseudo twin shown in Fig. 13(a) and Fig. 13(b), respectively. The combination of these two shears is the displacement described by $1/3[0\bar{1}0]$, precisely the displacement which has been considered to be that which would act as a nucleus for cleavage cracks in *bcc* metals.

The above observations are consistent with the notion that pseudo twins are responsible for crack nucleation, and hence lack of tensile ductility in 25Ti and 10Ti alloys. However, it is not possible to claim unambiguously that intersection of pseudo twins are the cause of crack nucleation unless the process is monitored *in-situ* in these experiments.

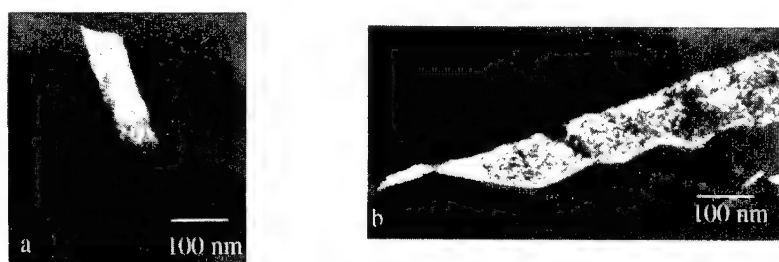


Fig. 13 - TEM dark-field micrographs showing the pseudo twins on both side of a crack in a bend test specimen.

Oxidation Behavior

Although, niobium alloys can exhibit excellent low temperature ductility coupled with good medium and high-temperature strength, they generally show poor high-temperature oxidation resistance [15]. This is the primary factor limiting their use in turbine engine applications. The high-temperature oxidation resistance of Nb-Ti-Al alloys containing low aluminum levels have also been investigated [16-18]. Here again, acceptable behavior in terms of ductility was offset by poor oxidation resistance. Here, the Nb-Ti-Al alloys with the slowest rates of high-temperature oxidation formed mixed oxide scales with either rutile-type (TiO_2) or Al_2O_3 - NbAlO_4 structures [16-18]. The Nb-40Ti-15Al alloy has shown excellent ductility and tensile strength at room temperature with good stiffness and flow stress at temperatures in excess of 700°C . However, little fundamental work exists on the oxidation of this or similar Nb-rich alloys which must be studied before practical application of these materials is possible.

Oxidation testing has been conducted on Nb-40Ti-15Al and similar quaternary alloys in the temperature range of 600°C to 1200°C . Isothermal and cyclic oxidation tests have been carried out on several alloys where analysis of the 40Ti compound shows rate behavior similar to that of pure Ti. A study to identify the fundamental mechanisms of oxidation in these materials is being approached by relating the measured oxidation properties to the microstructures which develop during high temperature oxidation. Detailed microstructural and phase analyses have been conducted using standard techniques as well as the relatively novel application of cross sectional transmission electron microscopy (TEM) to study the surface region following oxidation. This has been carried out using a Philips CM200 equipped with an ultra-thin window energy dispersive X-ray (EDX) detector.

Microstructural Observations The rate determining mechanism does not seem to change with temperature over short testing periods, hence, our microstructural analyses have concentrated on relatively coarse well-developed microstructures found in samples tested at 1100°C. Here, any microstructural features which might influence deformation and fracture behavior can be readily characterized. In Fig. 14(a), a BSE image taken in the SEM shows a cross section of the 40Ti alloy after oxidation for 24 hours. This image illustrates that the base metal, at the bottom of the figure, is separated from the surface oxide by a multicomponent case layer, indicated by C. Only a limited amount of the oxide scale which did not spall during initial cooling from 1100°C or break during specimen preparation is intact on the sample. Hence, the bulk of the oxide scale was no longer present. The case layer exhibits a microstructure composed of large colonies of wavy lamellae. More detailed analyses of the phases and morphologies seen here require higher magnification SEM and TEM characterization.

The backscatter electron image in Fig. 14(b) shows the near interface region between the case layer and the external oxide of the 40Ti alloy. This SEM image, showing the case/oxide interface, was recorded from a cross-sectional TEM specimen prepared from a cyclic oxidation specimen after 6 heating cycles of 1 hour each. At this magnification and contrast setting, the case layer appears more complex than in Fig. 14(a). Immediately below the oxide scale labeled "O", the case layer exhibits a medium gray intensity, shown labeled "C_i", along a band parallel to the scale/metal interface. Adjacent to this band and further away from the surface, the case

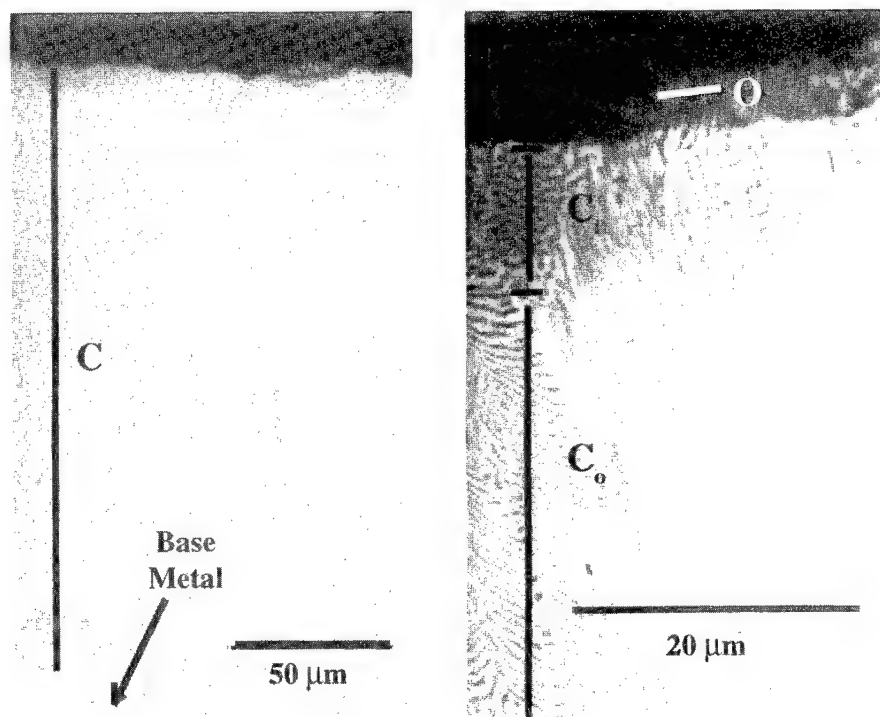


Fig. 14 - (a) SEM backscatter electron (BSE) image of cross section of Nb-40Ti-15Al alloy oxidized at 1100°C for 24 hours in air showing deep case layer "C". (b) SEM/BSE image showing enlargement of (a) where distinct regions in the case layer become clear. The layers show varying gray levels in accordance with their average oxygen content with the highest level of oxygen occurring at the top in the oxide, "O", followed by the internally oxidized region, "C_i", and the oxygen stabilized microstructure, "C_o".

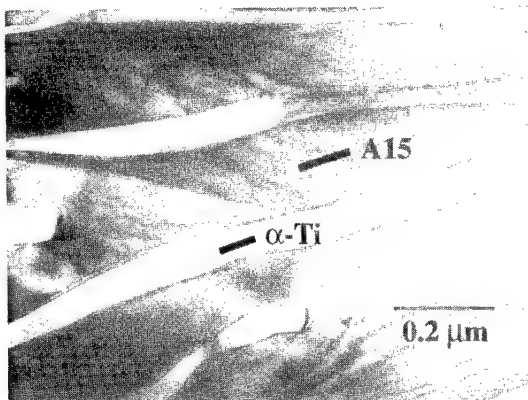


Fig. 15 -TEM bright field image of cross sectional sample from case layer region C_0 of Fig. 14(b). The two phase microstructure is composed of oxygen stabilized α -Ti and A15.

layer displays a lighter contrast indicated by " C_0 " in Fig. 14(c). Throughout the entire case layer, labeled " C ", the microstructure consists of two constituents, one light and one dark, with the morphology of wavy lamellae. Here, the dark component in the case is discontinuous and alternating with the lighter lamellae which compose a continuous matrix. Contrast in the BSE image results from composition variations within the microstructure where lighter intensity is associated with material composed of elements with a higher average atomic number, Z . Hence, the phase separation clearly evident in region C_0 is apparently followed by another subtle compositional change in region C_i before completely converting to the oxide compounds in the external scale. Ultimately, the compositional segregation initiated in region C_0 is transmitted through to the oxide as seen in the dark (low average Z) oxide scale microstructure, labeled O , which exhibits the same lamellar structure.

Closer examination of the deep case layer (" C_0 " in Fig. 14(b)) is shown in the bright field TEM image of Fig. 15. Energy dispersive x-ray (EDX) analyses of the two phases suggests the presence of an oxygen and/or nitrogen-stabilized Ti phase and a Nb-rich phase with a composition of approximately Nb-20Ti-20Al (in at%). Electron diffraction was used to identify the two constituents as the α -Ti and the A15 phases. Oxygen is known to stabilize the alpha phase in Ti, which suggests that oxygen dissolution near the sample surface during oxidation has led to the phase separation of α -Ti from the B2 matrix. The depletion of Ti from the surrounding B2 material results in the simultaneous stabilization of the brittle A15 phase[19]. The volume fraction of the α -Ti (Ti-15Nb-5Al) and A15 phases measured from Fig. 15 are 25% and 75% respectively. This is in good agreement with the phase equilibria predicted by the 1100°C isothermal section of the Nb-Ti-Al system. Within the band labeled C_i , an elevated level of oxygen was noted suggesting the presence of an internal oxidation product. This is also consistent with the change in contrast associated with the presence of a refined oxide leading to a lower average Z . It is important to note that both the α -Ti and the A15 phases making up the case layer are very brittle (the α -Ti contains significant levels of oxygen) and this layer will not be mechanically sound. Hence, one cause of poor oxidation behavior may be due to oxygen diffusion and phase destabilization, resulting in mechanical instabilities.

Acknowledgments

This work has been supported by the US Office of Naval Research, with Dr. George Yoder and Mr. Andrew Culbertson as Program Managers.

References

1. J. Shyue et al., in High Temperature Ordered Intermetallic Alloys V, edited by I. Baker, J.D. Whittenberger, R. Darolia, and M.H. Yoo, (Mater. Res. Soc. Proc., 288, Pittsburgh, PA, 1992), 243.

2. D.-H. Hou et al., in Alloy Modeling and Design, Eds. Stock and Turchi, Symposium on "Alloy Modeling and Design" (Pittsburgh, PA, 1993), 276.
3. U.R. Kattner and W.J. Boettinger, Mat. Sci. Eng., 152(1992), 9.
4. D.-H. Hou, I.P. Jones and H.L. Fraser, Philos. Mag. A, (1996), in press.
5. J.C.H. Spence and J. Taftø, J. Microscopy, 130(1983)147.
6. C. Rossouw and V.W. Maslen, Ultramicroscopy, 1(1987), 77.
7. S.J. Pennycook, Ultramicroscopy, 26(1988), 239.
8. D.-H. Hou and H.L. Fraser, submitted to Philos. Mag. A, (1996)
9. S. Matsumura, T. Morimura and K. Oki, Mat. Trans., JIM, 32(1991), 905
10. H. Kohmoto et al., Scripta Metall., 29(1993), 1271.
11. J. Shyue et al., J. Matls. Sci. and Eng., A170(1993), 1.
12. S.S. Yang et al., in High Temperature Ordered Intermetallic Alloys VI, Eds., J. A. Horton et al., MRS Proc. 364(II)(1994)1359.
13. M.L. Green, "Pseudotwinning and Pseudoeelasticity in β Fe-Be Alloys", Acta Metallurgica., 27(1979)1523.
14. S.S. Yang, Ph.D. Thesis, The Ohio State University, 1995
15. R.A. Perkins and G.H. Meier, JOM, 42 (8)(1990), 17.
16. G. Meier et al., in Proceedings of First International Conference on Structural Intermetallics, edited by R. Darolia, J.J. Lewandowski, C.T. Liu, P.L. Matrin, D.B. Miracle and M.V. Nathal (TMS, Warrendale, PA, 1993), p. 861.
17. M. Allouard et al., J. De Physique, IV 3(1993), 419.
18. C.M. Austin et al., "Rapidly Solidified Oxidation Resistant Niobium Base alloys", (Report: WL- TR-93-4059, 1992) p. 70.
19. J. Shyue et al., in Proceedings of First International Conference on Structural Intermetallics, edited by R. Darolia, J.J. Lewandowski, C.T. Liu, P.L. Matrin, D.B. Miracle and M.V. Nathal (TMS, Warrendale, PA, 1993), p. 631.

CERAMICS AND COMPOSITES

OXIDE FIBER/OXIDE MATRIX COMPOSITES

K. K. Chawla¹, H. Schneider², M. Schmücker², and Z. R. Xu¹

¹Department of Materials and Metallurgical Engineering, New Mexico Tech
Socorro, NM 87801, U.S.A.

²Materials Research Institute, German Aerospace Research Establishment (DLR),
D-51140, Köln, Germany

ABSTRACT

Oxide fiber/oxide matrix composites form an important and attractive subpart of ceramic matrix composites because of their inherent stability in oxidizing atmospheres at high temperatures. An important attribute of such composites, however, is that the interfacial bond between oxide matrix and oxide fiber is generally very strong, and consequently, the toughness and damage tolerance of such composites are low. One way to overcome this problem is to tailor the interface such that energy dissipating phenomena such as debonding and crack deflection at the fiber/matrix interface, followed by fiber pullout are brought into play. In this paper, we summarize the salient points regarding control of interface characteristics in oxide fiber/oxide matrix composites. Main emphasis will be on engineering the interface in alumina fibers in silica-based glass and mullite fibers in mullite matrix composites.

INTRODUCTION

Ceramic matrix composites (CMCs) capable of maintaining excellent strength and fracture toughness are required for high temperature structural applications. Many of these applications require exposure to an oxidizing environment, as such the thermodynamic stability and oxidation resistance of CMCs become important issues [1]. The thermodynamic stability and oxidation resistance of CMCs will depend on properties of the fiber, matrix, and interface. In particular, it is important to understand the characteristics of any interfacial reaction product(s). Nonoxides have relatively poor oxidation resistance, by which we mean that they show significant rates of oxidation at or below 1000 °C. Nonoxides such as C, TiC, B₄C, and BN would fall in this category, with carbon being the worst. On the other hand, nonoxides of Si, particularly SiC, Si₃N₄, and MoSi₂, can form an effective protective layer of SiO₂ when the oxygen partial pressure in the system is not too low, and no secondary reaction occurs as would happen in non-stoichiometric SiC.

A strong fiber/matrix interface and any reactions between the fiber and matrix may result when an oxide matrix is reinforced with an uncoated oxide fiber. Hence, the toughness of these composites is not much improved compared to the monolithic ceramics. As a consequence, a barrier layer needs to be introduced to prevent chemical interaction between fiber and matrix. In this paper, we describe some of the issues in the development of oxide fiber/oxide matrix composites, with a particular emphasis on interface tailoring to obtain a non-catastrophic failure.

OXIDE MATRIX MATERIALS

Among the crystalline oxide ceramics, the two most important ones are alumina and mullite. Aluminum oxide, Al₂O₃, with a melting point of 2000 °C, is chemically one of the most stable and mechanically one of the strongest of the refractory oxides, particularly at moderate temperatures. Alumina is stable in the presence of both oxidizing and highly reducing atmospheres and can be used in either type of atmosphere at temperatures up to about 1990 °C. Creep in alumina, however, at temperatures above 1200 °C can be a problem. Mullite, approximately 3Al₂O₃·2SiO₂, occurs in almost all aluminosilicate ceramics [2]. Mullite crystals produced by reaction sintering processes and by sol-gel route are small and often acicular, a circumstance which contributes to the formation of an interlocked refractory network to which aluminosilicate refractories owe much of their high temperature strength.

matrix. The functions of a such an engineered interphase or interface in oxide/oxide composites are to prevent any reaction between the matrix and the fiber during composite processing and in service, to allow interfacial debonding and fiber pullout to occur during fracture, and also to prevent fiber degradation. The following points must be kept in mind in order to achieve these objectives:

- chemical compatibility of the fiber and matrix at the interface at high temperatures.
- Stresses at the interface due to interfacial roughness and thermal mismatch between the components, at room temperature and at high temperatures.
- Possible improvements in the processing of composites.

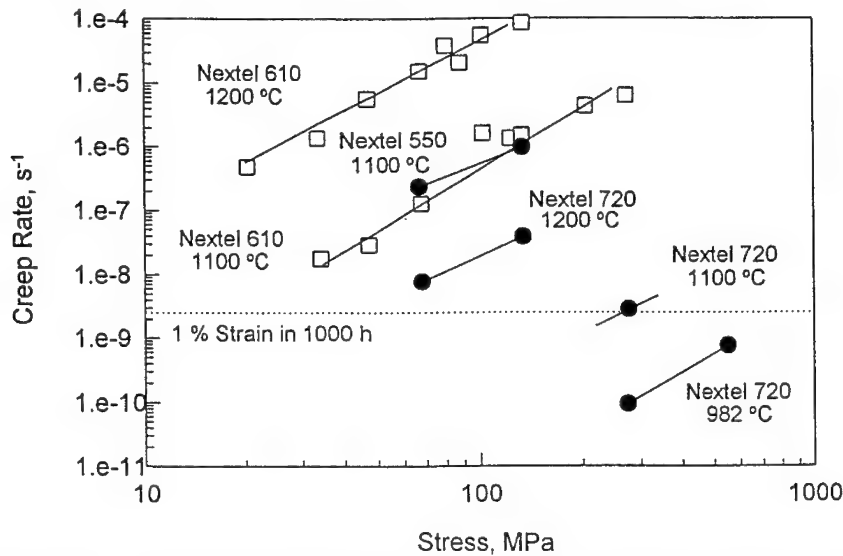


Fig. 1 A comparison of the creep behavior of three different Nextel fibers. Note the superior creep resistance of Nextel 720 fiber (courtesy of 3M Co.).

Chemical compatibility at high temperature

Ceramic matrix composites are generally fabricated and used at high temperatures where chemical reactions occur readily. Chemical interaction between matrix and fiber can result in strong interfacial bonding. This strong chemical bond can then lead to a brittle failure of CMC. Carbon has been used as an interphase in glass and glass-ceramic matrix composites. Because of its layer structure, graphitic carbon slips easily on basal planes and works fine as a weak interface for crack deflection. The oxidation, however, is a problem for carbon. It is readily oxidized at temperature above 400 °C in air. BN has a similar layer structure as graphitic carbon, but is more oxidation resistant than carbon. The chemical compatibility

of a given fiber/matrix system can in most cases be predicted by reference to the existing information in literature on the phase diagrams and by thermodynamic estimates based upon free energies of various reactions. For example, in the alumina/silica system, one would expect a strong chemical bond at the fiber/matrix interface. Thus, chemical stability would not be expected in any Al_2O_3 - SiO_2 -based system. A strong interfacial bond in such composites causes the failure mode to be similar to that of monolithic ceramics. In some systems of simple eutectic type, such as Al_2O_3 - SnO_2 with no solubility between Al_2O_3 and SnO_2 [4], and Al_2O_3 - ZrO_2 with very limited solubility between Al_2O_3 and ZrO_2 [5], the composites should be relatively stable. There are, however, only a small number of such simple eutectic type oxide systems.

Some ideas of chemical interaction between the components of a composite can be obtained from thermodynamic information. In a composite system, we need to consider the chemical interactions between the three components (fiber, coating, and matrix) as well as the reaction of composite components with the environment. For example, for an alumina fiber reinforced silica-based glass with BN coating, a variety of chemical reactions are possible, all leading to the formation of B_2O_3 . In all cases, the BN coating is degraded and, consequently, the mechanical properties of the composite are degraded. It is not unusual to have the BN coating disappear during high temperature fabrication of a composite. The reaction kinetics also play an important role in controlling the extent of those reactions. Therefore, a combined theoretical and experimental approach is required in most cases regarding the thermochemical compatibility of oxide/oxide composites. The important variables which influence chemical reactions are the composition of the fiber, coating, and matrix, plus temperature and environment.

Morgan and Marshall [6] have discussed the potentially useful interfacial coatings for alumina fiber/alumina matrix composites. Amphoteric alumina is phase compatible with a few simple oxides because it can react readily with either acidic or basic oxides. Only oxides of a few elements toward the center of the periodic table such as SnO_2 , ZrO_2 , HfO_2 , and TiO_2 are compatible with alumina. Morgan and Marshall investigated LaPO_4 -coated alumina fiber/alumina matrix composites and they found LaPO_4 can be an effective oxide coating in oxide/oxide composites. SnO_2 has been used as an interphase material in alumina fiber/glass matrix composites [7, 8]. Since there is no solubility of SnO_2 in Al_2O_3 , no chemical bonding is expected between the fiber and matrix. The introduction of a weak interface via SnO_2 coating changed the failure mode from brittle in sapphire/glass composite to a non-brittle one in sapphire/ SnO_2 /glass composite. Figure 2 shows the fiber pullout of Saphikon fibers

in a Saphikon/SnO₂/glass composite. It should be pointed out that SnO₂ is not stable in neutral or reducing environment. It reduces to SnO which has a melting point of 1125 °C while SnO₂ has a melting point of 1680 °C. An example of the damage tolerant behavior of ZrO₂ coated Saphikon fiber in a reaction bonded mullite matrix is shown in Fig. 3. Note that the cracks emanating from the indentations go around the coated fibers. Among other candidate coating materials, there are some mixed oxides, especially where an element from the acidic side and an element from the basic side form a fairly neutral mixed oxide, such as BaSO₄ and CaTiO₃.

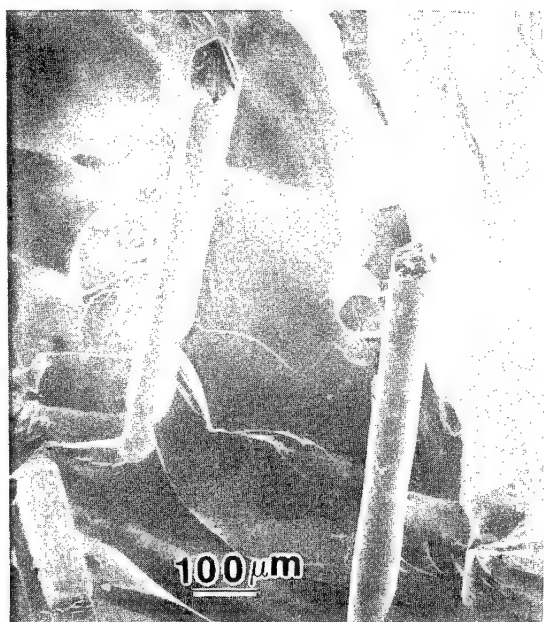


Fig 2 Fiber pullout in a Saphikon/SnO₂/glass composite.

Magnetoplumbites are yet another class of materials that may provide some suitable coatings (9-11). We know that a layered microstructure with weak bond between layers allows for easy cleavage. Common examples are, of course, pyrolytic carbon and hexagonal boron carbide. Compounds having β -alumina or magnetoplumbite structure have such an anisotropic layered oxide structure. These layered oxides can be regarded as structural analogs of C and BN. Potentially, such layered oxides, capable of easy cleavage along basal planes can be attractive as interfacial coating materials. A possible limitation of a β -alumina compound is its thermal stability at high temperatures due to any loss of alkali, e.g., loss of Na₂O during heat treatment of β -alumina is well known. Sambasivan et al. (11) have used large alkali atoms to stabilize the β -alumina. Rubidium stabilized β -alumina has been suggested as a potential interface coating for oxide/oxide CMCs. Sambasivan et al. observed

morphologically stable coating in a hot pressed Saphikon fiber/alumina matrix composite. indentation tests showed interface debonding but pushout tests did not show inter-

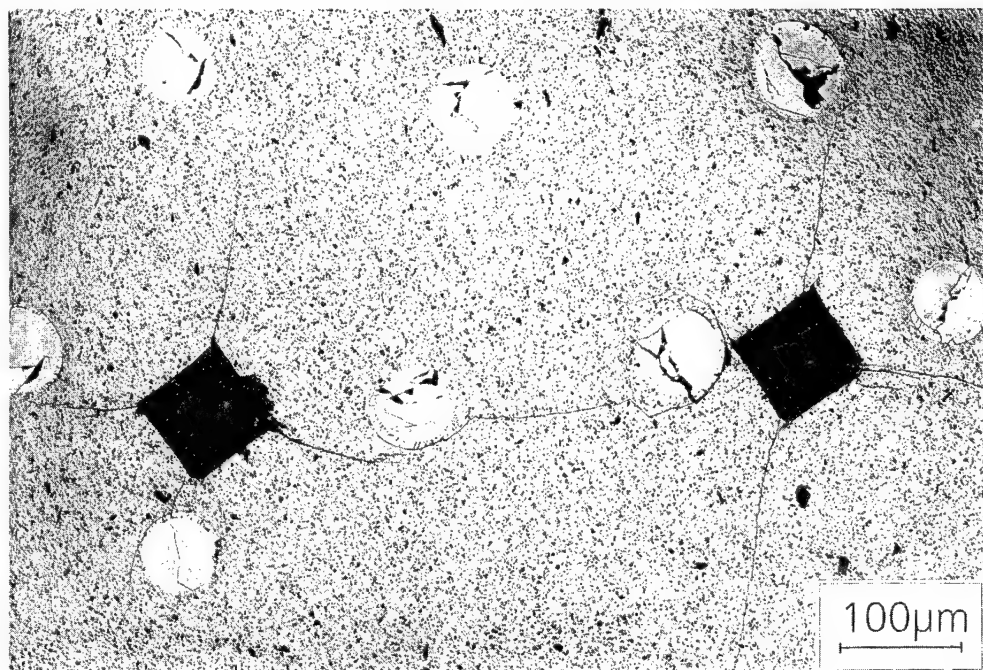


Fig. 3 An example of the damage tolerant behavior in a ZrO_2 coated Saphikon fiber/ reaction bonded mullite composite. Note the indentation cracks going around the coated fibers.

facial debonding. Another possible candidate is $\text{KCa}_2\text{Nb}_3\text{O}_{10}$, which shows easy fracture along basal planes. Indentations in bulk $\text{KCa}_2\text{Nb}_3\text{O}_{10}$ produced cracks parallel to the basal planes, see Fig.4. However, on making composites by hot pressing in a reducing atmosphere, they observed a loss of rubidium. Fiber coatings of phyllosilicates or micas have also been tried. They are, however, unstable above 700°C because the hydroxyl (OH^-) groups in their crystal lattice decompose. The thermal stability of phyllosilicates can be improved by eliminating the OH^- groups. A modification of phyllosilicates, called phyllosiloxides, having a mica like layered structure but without the OH^- groups has been suggested [12].

Stresses due to interfacial roughness and thermal mismatch

Mechanical keying of the matrix into the hills and valleys of the surface (due to roughness) of the reinforcement is an important aspect of the interface in all composites. Increasingly,

the importance of interface roughness-induced mechanical bonding is recognized in different composites - polymer, metal, and ceramic-based composites. In ceramic matrix composites, roughness-induced interfacial gripping, especially in the radial direction, will affect the interface debonding, the sliding friction of debonded fibers, and the fiber pullout length. We pointed out the desirability of having a purely mechanical bond at the fiber/matrix interface in a CMC rather than a strong chemical bond for the fiber pullout to

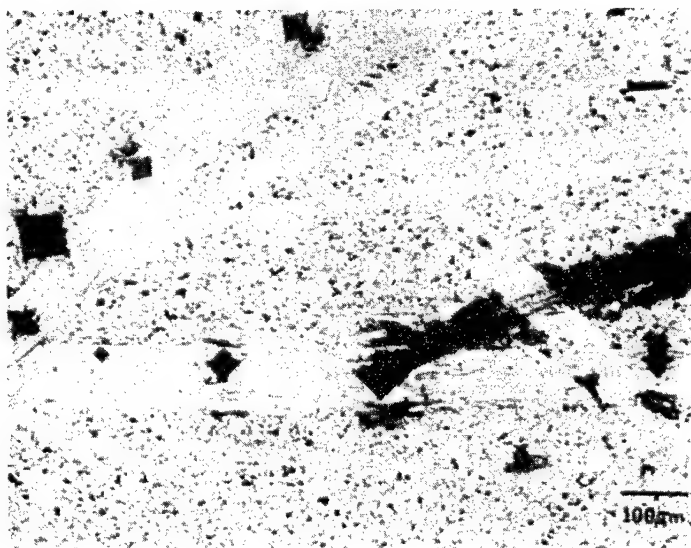


Fig. 4 Indentations in bulk $\text{KCa}_2\text{Nb}_3\text{O}_{10}$ produced cracks parallel to the basal planes (courtesy of S. Sambasivan).

occur. In this regard, the distribution of residual stresses due to the thermal mismatch between the components distribution after processing thermal is quite important. An important point here is that the effect of thermal mismatch will be present after cooling from the processing temperature to room temperature as well as during high temperature use beyond the processing temperature. It turns out that even when the coefficients of thermal expansion of the coating, fiber, and matrix are such that a radial tensile stress exists at the fiber/coating interface, fiber pullout may not occur because of a strong mechanical bonding due to a roughness induced clamping at the fiber/matrix [7]. This roughness induced clamping at the fiber/matrix in the radial direction needs to be considered together with the

thermal stresses. The sense of the two can be same or opposite. The fiber surface roughness leads to an increase in the interfacial normal pressure. The effective normal stress σ_n at the interface due to residual thermal stresses and roughness induced stresses can be written as [13]

$$\sigma_n = \sigma_t + \sigma_r$$

where σ_t and σ_r are thermal and roughness induced stresses, respectively. The thermal stress and roughness induced stress can be expressed as

$$\sigma_t = b (\Delta\alpha\Delta T)$$

$$\sigma_r = b (A/r)$$

where $\Delta\alpha$ is the difference in thermal expansion coefficients between matrix and fiber, ΔT is the temperature differential ($T_2 - T_1$), b is a term containing elastic constants, A is the amplitude of roughness, and r is the fiber radius. Thus, in composites with extremely rough interface, such as in the PRD-166/SnO₂/glass composite, the pullout was virtually nonexistent and they failed like monolithic materials. This is because in alumina (PRD-166)/SnO₂/glass composites the compressive stress due to interfacial roughness is more dominant than residual radial thermal stresses [7, 14]. When a smooth alumina fiber, Saphikon, was substituted for PRD-166 fiber, neat fiber pullout was observed as shown in Fig. 2.

Innovative processing

Conventional ceramic processing methods normally require high temperatures to provide adequate consolidation of a ceramic body. Under such conditions, fiber/matrix interactions are difficult to control. For example, in order to obtain a reasonable densification, conventional mullite powders must be processed (e.g., subjected to hot pressing) at temperatures above 1500 °C. Processing at such high temperatures can lead to fiber degradation by grain growth and/or deformation of the fibers and reactions at the interface. For making oxide fiber/mullite matrix composites, the processing temperature for mullite matrix can be reduced by using a sol-gel route to synthesize mullite powder. Mullite gels can be single phase or diphasic according to the scale of component mixing, depending on the nature of the alumina and silica precursors. Single phase gels are prepared from aluminum and silicon alkoxides or salts and have a molecular-scale mixing because of a polymerized-oxide network formed by hydrolytic condensation. Diphasic gels can be produced by mixing colloidal sols of boehmite and silica or by mixing one colloidal component with the alkoxide or salt of the other. The scale of the component mixing in diphasic gels is determined by size of the colloidal particles, typically in the range of 10-30 nm, which is larger than that of

the single phase gels. Because of the different scales of component mixing, the single phase and diphasic gels show different types of mullite crystallization behavior during heating. In single phase gels, chemical interdiffusion distance is very short because of the molecular scale mixing, and therefore, mullite crystallization occurs below 1000 °C. In diphasic gels, the diffusion distance is much longer, so mullite crystallization does not occur until above 1250 °C. The retarded mullite crystallization of the diphasic gels enhances the matrix densification through viscous phase sintering and can give above 95 % of the theoretical density by sintering between 1200 °C and 1300 °C for 1 h. Compared to this, in single phase gels, crystalline mullite formed at very low temperatures, making densification difficult because of the high degree of covalent bonding, so that the sintered densities obtained under the same temperature are much lower. In this case of mullite fiber/mullite matrix composite, we used two types of coatings, a thicker BN (1 μ m) to allow for a part of the coating to be sacrificed and a BN/SiC double coating. The SiC coating was to provide oxidation protection to BN during processing. In both cases, we got a non-catastrophic failure mode. Figure 5a shows an example of the BN coating in the as-made composite while Fig. 5b shows the fiber pullout observed in these composites [15-17]. Needless to say that no fiber pullout was observed in the uncoated mullite/mullite composites.

CONCLUSIONS

Chemical interactions between oxides occur frequently such that the selection of possible oxide fiber/oxide matrix composite system is limited. Therefore, an interface engineering to obtain a nonbrittle fracture in oxide/oxide composites is extremely important in the sense that chemical interactions in the composite system are prevented and to provide a *weak* interface to improve the toughness of the composites. A weak mechanical interface is usually required in ceramic matrix composites from a fracture toughness viewpoint. Even in the absence of chemical bonding, there may be present a strong mechanical bond component, originating in the radial compressive stress due to a thermal expansion mismatch and/or the surface roughness of the interface. In this context, the question whether this expansion mismatch produces a strong mechanical bonding at room temperature or at high temperature must be kept in mind in order to determine the temperature region of maximum toughness of the composite.

Processing procedures must be tailored in order to eliminate the processing-induced degradation of fibers. In addition, the problem of complex shape formation of such composite

has to be addressed by using thin layers of fiber preregs or fabrics.

Finally, creep resistance is enhanced by having a "strong" interface. An optimum interface tailoring therefore will involve a compromise taking into due considerations the requirements for use at high temperatures. Practical oxide/oxide composite systems are very much limited because of poor creep resistance of oxides. A key limitation in such system is the availability of reinforcements that have good high temperature capability. A good creep resistant oxide matrix is also a key limitation.

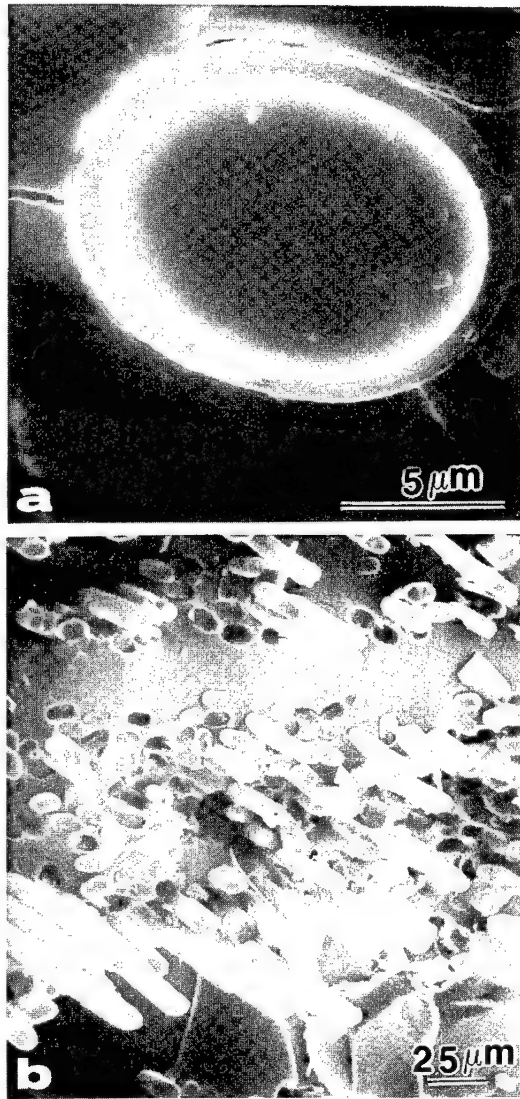


Fig. 5 (a) An example of crack propagation around the BN coated mullite fiber in a mullite matrix in the as-made state (b) Fiber pullout observed in the coated composites. No fiber pullout was observed in the uncoated mullite/mullite composites.

ACKNOWLEDGMENTS

The main support for this work came from The US Office of Naval Research, Contract No. N0014-89-J1459 and was monitored by Dr. S. G. Fishman. Additional support was obtained from: the US Dept. of Energy, Assistant Secretary for Energy Efficiency and Renewable Energy, Office of Transportation Technologies, as part of the High Temperature Materials Laboratory User Program HTML Faculty Fellowship Program under contract DE-AC05-84OR21400 managed by Martin Marietta Energy Systems, Inc.; The German Aerospace Research Establishment (DLR); and NATO.

REFERENCES

1. K.K. Chawla, *Ceramic Matrix Composites*, Chapman & Hall, London, 1993, chapter 3.
2. H. Schneider, K. Okada, J. Pask, *Mullite and Mullite Ceramics*, John Wiley & Sons, West Sussex, England, 1994.
3. K.K. Chawla, *Fibrous Materials*, Cambridge University Press, in press.
4. V. J. Bavczak, R. H. Insley, *J. Am. Ceram. Soc.* **45** (1962) 144.
5. A. M. Alper, G. H. Stewart, in *Science of Ceramics*, Academic Press, London, 1967, vol. 3.
6. P. E. D. Morgan, D. B. Marshall, *Mater. Sci. & Eng.*, **A162** (1993) 15.
7. K. K. Chawla, M. K. Ferber, Z. R. Xu, R. Venkatesh, *Mater. Sci. & Eng* **A162** (1993) 35.
8. K. K. Chawla, Z. R. Xu, R. Venkatesh, and J.-S. Ha, in *Proc.: 9th Intl. Conf. on Composite Materials*, ICCM/9, 1994.
9. M. K. Cinibulk, *Ceram. Eng. Sci. Proc.*, **15** (1994) 721.
10. R. S. Hay, *Ceram. Eng. Sci. Proc.* **14**(1993) 922.
11. S. Sambasivan, J.A. Morris, and W.T. Petuskey, *Ceram. Eng. Sci. Proc.* **17**(1996) in press.
12. P. Reig, G. Demaziou, and R. Naslain, *Eur. J. Solid State Inorg. Chem.*, **32** (1995) 439.
13. R. J. Kerans and T. A. Parthasarathy, *J. Am. Ceram. Soc.*, **74** (1991) 1585.
14. R. Venkatesh and K.K. Chawla, *J. Mater. Sci. Lett.* **11**(1992) 650.
15. J.-S. Ha and K.K. Chawla, *Ceram. International* **19** (1993) 299.
16. J.-S. Ha and K.K. Chawla, *J. Mater. Sci. Lett.* **12** (1993) 84.
17. J.-S. Ha, K.K. Chawla, and R. E. Engdahl, *Mater. Sci. & Eng.* **A161** (1993) 303.

DIRECTIONALLY SOLIDIFIED HIGH TEMPERATURE IN-SITU COMPOSITES

B.P. Bewlay¹, M.R. Jackson¹ and H.A. Lipsitt²

¹General Electric Company, Corporate Research and Development,
Schenectady, New York 12301.

² Department of Mechanical and Materials Engineering,
Wright State University, Dayton, Ohio 45435.

Abstract

This paper describes processing and properties of high temperature directionally solidified (DS) in-situ composites. Directional solidification is performed using cold crucible Czochralski crystal growth for alloys with melting temperatures up to 2250°C in order to generate aligned composite microstructures. This composite approach is being used to improve the low-temperature fracture toughness of intermetallic-based composites and thereby generate a material with a combination of attractive high-temperature properties and acceptable low-temperature properties. Microstructures, room temperature fracture toughness, and elevated temperature property data of DS in-situ composites generated from Nb-Si and Cr-Nb binary eutectics, and higher order systems will be presented. Fracture toughness values of $>20 \text{ MPa}\sqrt{\text{m}}$ have been measured in these composites. High-temperature tensile strength and creep behavior have also been examined in selected silicide-based composites and will be described; tensile strengths of $\sim 370 \text{ MPa}$ at 1200°C and creep rupture lives of >500 hours at 1100°C and 100 MPa have been measured.

Introduction

The present paper describes the microstructures and properties which have been generated in intermetallic-matrix composites based on the Laves phase, Cr_2Nb , and niobium silicides, such as Nb_3Si and Nb_5Si_3 . Particular emphasis is placed on the improvements in room temperature fracture properties and elevated temperature tensile strength (up to 1200°C), which can be effected by additions of Ti and Hf to directionally solidified (DS) in-situ composites based on Cr_2Nb and Nb_3Si . These composites are toughened by a Nb solid solution.

The Laves phase Cr_2Nb has been studied previously because it has a high melting temperature (1770°C), a lower density (7.7 g/cc) than nickel (8.9 g/cc), and promising oxidation resistance [1-7]. Although Cr_2Nb has attractive creep and tensile strengths [1, 2], it has very poor room temperature fracture toughness [4-6], a ubiquitous limitation of intermetallic-based systems. There have been previous attempts to improve the fracture toughness by generating two-phase composites with Nb and Cr [4-6], but these have met with limited success. However, composites consisting of other intermetallic materials with metallic second phases have recently been shown to possess sufficient toughness for component damage tolerance [8-11]. In this arena, Nb-Si in-situ composites, which consist of a Nb-based solid solution, (Nb), with Nb_3Si and/or Nb_5Si_3 silicides have displayed an attractive balance of high and low temperature mechanical properties [4, 6, 8-11]. From model binary Nb-Si alloys, whole families of ternary, quaternary and higher order alloys have been generated and studied [8-10]. These in-situ composite systems are beneficial because they possess long term morphological and chemical stability at elevated temperature.

In an attempt to improve the balance of high and low temperature properties of DS in-situ composites, Cr_2Nb and niobium-silicide alloys with Hf and Ti were prepared. Hf and Ti additions were considered for three reasons. First, Ti additions improve the ductility of (Nb) [12], and therefore, in a composite there is the possibility of the (Nb) providing greater composite toughness. However, Ti additions have the disadvantage of reducing the alloy melting temperature. Second, Hf is added because it is a strong solid solution strengthener for (Nb) [12, 13]. Third, Hf and Ti additions to Cr_2Nb , Nb_5Si_3 , and the Nb-based solid solution improve the oxidation resistance of both phases of the composites, as reported by Subramanian, et al. [9, 10] and Jackson, et al. [13]. Cr also improves the oxidation resistance of Nb [9]. All elements partition to varying degrees between the different phases of the composites [8, 13], and this was taken into consideration in designing the alloys from which the composites were directionally solidified. By appropriate alloy selection, composites with metal volume fractions from 30-50% were designed to allow the evaluation of toughening and strengthening.

The Cr-Nb phase diagram contains two eutectics between Cr_2Nb and the constituent individual refractory metals [14, 15]. The temperature and composition of the Cr_2Nb -Nb eutectic, which contains a volume fraction of Cr_2Nb of ~70%, are $1650 \pm 50^\circ\text{C}$ and ~50 %Nb, respectively. All compositions in the present paper are given in atom per cent. The Cr-Hf phase diagram is analogous, there are also two eutectics, Cr_2Hf -Hf and Cr_2Hf -Cr [14]. Cr_2Ti is also a Laves phase, but it forms from a bcc Cr-Ti solid solution rather than

on solidification, as is the case for Cr_2Nb and Cr_2Hf . Thus, Cr_2Hf and Cr_2Nb can be considered to be essentially isomorphous.

Three Laves phase based alloys were investigated, in addition to the binary Cr_2Nb -Nb eutectic, in order to generate in-situ composites by directional solidification; the three quaternary alloy compositions investigated are shown in Table I. The first of the quaternary alloys was based on the Cr_2Nb -Nb eutectic [14, 16], but it was modified with Hf and Ti substituted for Nb by using a composition of Nb-16.5Ti-52.5Cr-9.5Hf. Phase compositions are shown in Table II for the metallic and Laves phases of a similar Al-containing composite heat treated at 1200°C. The Hf and Ti modified $\text{Cr}_2(\text{Nb})$ -(Nb) eutectic was designed to possess ~70% by volume of the Laves phase, which is the approximate volume fraction of the Laves phase in the Cr_2Nb -Nb eutectic [3, 4]. The additional two quaternary compositions shown in Table I contain total volume fractions of Laves phase of ~60% and ~50%. This range of compositions was selected in order to investigate the effect of volume fraction of metallic phase on room temperature fracture toughness and high temperature strength. The Hf and Ti modified Laves phase is denoted by $\text{Cr}_2(\text{Nb})$ in the present paper because Hf and Ti generally substitute for Nb on the Nb sub-lattice (there may be some substitution on the Cr sub-lattice, but the defect level is unknown). There is some solid solubility of all alloying elements in the Nb-based metallic phase of all the composites described in the present paper, and the metallic phase is therefore described as (Nb).

Table I : Compositions of the quaternary $\text{Cr}_2(\text{Nb})$ -(Nb) composites, together with $\text{Cr}_2(\text{Nb})$ volume fractions, melting temperatures, and tensile properties.

Composition	Liquidus Temperature (°C)	Volume Fraction of Laves Phase	Tensile Stress (MPa) Temperature : YS : UTS	Elongation (%)
Nb-50Cr	1650	0.70	Tensile bars too brittle	--
Nb-16.5Ti-52.5Cr-9.2Hf	1550	0.76	Tensile bars too brittle	--
Nb-21.2Ti-44.5Cr-8.4Hf	1563	0.60	1200°C : 132 : --	0
Nb-26Ti-36.5Cr-7.5Hf	1514	0.53	1100°C : 210 : 265 1200°C : 120 : 153	52.2% 6%

The present paper also describes an analogous in-situ composite generated from a more complex Nb-Ti-Hf-Si-Al-Cr alloy based on the Nb_3Si -(Nb) eutectic. A range of complex Nb-silicide composites have been generated from multi-element Nb-based alloys, but only one of these composites is described in the present paper. The composition of the alloy that was directionally solidified to generate this composite was Nb-24.7Ti-8.2Hf-2.0Cr-1.9Al-16.0Si. Throughout the present paper this composite will be referred to as the metal and silicide composite (MASC). This composite was derived from the binary Nb-16Si composition [4, 11].

The basis for the niobium-silicide composite is the Nb-rich side of the Nb-Si phase diagram where there is a eutectic between Nb₃Si and (Nb) [4, 14]. This eutectic occurs at 1880°C and 18.2Si. There is also a eutectoid of the form Nb₃Si-->(Nb)+Nb₅Si₃, but this has little effect on the as-DS microstructures, because of slow decomposition kinetics. A range of Nb₃Si-(Nb) composites have been directionally solidified from binary Nb-Si alloys [4]. Analogous ternary Nb-Ti-Si alloy composites have also been investigated [8-10].

The aim of the present paper is to describe the microstructure and tensile properties of Hf and Ti-modified DS Cr₂(Nb)-(Nb) and Nb-silicide-based in-situ composites. The microstructures of DS composites containing 50-70% by volume of the Laves phase Cr₂(Nb) which was modified with Hf (7.5-9.2%) and Ti (16.5-26%) are described. Room temperature fracture toughness and tensile properties at 1100 and 1200°C are compared with those of the MASC. Stress rupture behavior of the MASC is also presented. The MASC displays a better balance of high and low temperature mechanical properties [8, 16] than do the Laves phase composites. The high temperature rupture properties are also compared with those of the most recent Ni-based superalloys.

Experimental

Directional Solidification

Alloys for directional solidification were prepared using a 50g charge of high purity (99.99%) elements. These elements were induction levitation melted in a segmented water-cooled copper crucible [17]. Each alloy was triple melted in order to ensure homogeneity prior to directional solidification. Directional solidification was performed by lowering a seed of the same alloy into the induction levitated melt and withdrawing the seed at a constant pre-selected rate in the range 0.5-5 mm/minute. This process has been described in further detail elsewhere [17]. Several samples were grown of each composition in order to generate enough bars for tensile testing. The melting temperatures of the alloys were measured using a two wavelength optical pyrometer which was calibrated against 99.9% pure Ti. Samples with a diameter of ~10 mm and a length of ~75 mm were directionally solidified using this method.

The melting and directional solidification operations were conducted sequentially in an atmosphere of ultra high purity argon. Before backfilling with argon, the chamber was evacuated to ~10⁻⁵ Torr. An atmosphere of ultra high purity argon was used in order to prevent contamination with interstitials. In this class of materials, the mechanical properties and phase equilibria are sensitive to interstitials, such as nitrogen, oxygen and hydrogen. Conventional microscopy and electron beam microprobe analysis were performed to characterize composite microstructures and phase chemistries.

Mechanical Properties

Fracture Toughness Measurements

Single edge notched bending specimens (SENB) were machined for room temperature fracture toughness measurements using electro-discharge machining (EDM). EDM was also used to machine a 50µm notch at the mid-point of each SENB. The samples were machined so that their longitudinal axis was parallel to the growth direction.

Fracture toughness measurements were performed using monotonic loading and four point bending. The procedures provided by the ASTM standard E-399 [18] were employed. The toughness values from the monotonic loading experiments are reported as K_Q . K_{IC} values were obtained from R-curve measurements which were performed on additional samples following the ASTM standard E-561-94 [19]. R-Curve measurements were also performed using four point bending in the displacement control mode. The crack opening displacement (COD) was monitored using a double cantilever beam type COD gage.

Tensile and Creep Rupture Testing

Tensile testing was performed in a vacuum of $\sim 10^{-4}$ Torr using an initial strain rate of $8 \times 10^{-4} \text{ s}^{-1}$. The button head samples used possessed a gauge diameter of 2 mm, and a length of 10.7 mm. The samples were machined first by EDM and then by centerless grinding to the final dimensions. The tensile specimens were machined so that the growth direction was parallel to the axis of the tensile bar. There was less breakage of the MASC samples than the $\text{Cr}_2(\text{Nb})$ based samples during centerless grinding. Creep rupture testing was performed using similar sample geometries in an argon atmosphere.

Results and Discussion

DS Composite Microstructures

$\text{Cr}_2(\text{Nb})$ -(Nb) Composites

Typical microstructures of the DS binary Cr_2Nb -Nb eutectic are shown in Figure 1. These micrographs were obtained using back scatter electron imaging (BSE); the Cr_2Nb is the dark phase and the Nb is the light phase. The microstructure consists of Nb rods and ribbons ($0.5 \pm 0.1 \mu\text{m}$) in the Cr_2Nb matrix. The aspect ratio of the Nb rods was typically ~ 10 and there was incomplete alignment with the growth direction under these directional solidification conditions. The Cr_2Nb had the C15 structure with the $[110]$ parallel to the growth direction [3].

Microstructures of the Nb-16.5Ti-52.5Cr-9.2Hf quaternary alloy which was based on the Cr_2Nb -Nb eutectic are shown in Figure 2. BSE imaging and energy dispersive spectrometry (EDS) indicated that the $\text{Cr}_2(\text{Nb})$ was the light phase and the (Nb) was the dark phase. The $\text{Cr}_2(\text{Nb})$ contained more Hf and less Ti than the darker (Nb), and as a result it provided brighter contrast than the (Nb), even though it contained more Cr and less Nb than the (Nb). It was difficult to obtain strong BSE contrast between the two phases in the quaternary alloys, because Hf is the heaviest element and it partitions to both phases in the approximate ratio of 2:1 for Laves phase to metal. In both the longitudinal and transverse sections, lighter regions were observed at the centers of the $\text{Cr}_2(\text{Nb})$ laths. This brighter contrast was probably due to Hf enrichment and/or Ti depletion at the centers of the laths.

The transverse section of the $\text{Cr}_2(\text{Nb})$ -30%(Nb) shown in Figure 2(b) indicates that the structure consisted of coarse laths, which appeared to be arranged in grains with a width of $\sim 300 \mu\text{m}$. The width of the (Nb) laths was $\sim 20 \mu\text{m}$ and the width of the $\text{Cr}_2(\text{Nb})$ laths was $\sim 60 \mu\text{m}$. The grains appeared to have an approximately hexagonal morphology; this type of grain morphology was not observed in the case of the binary eutectic. It is important to

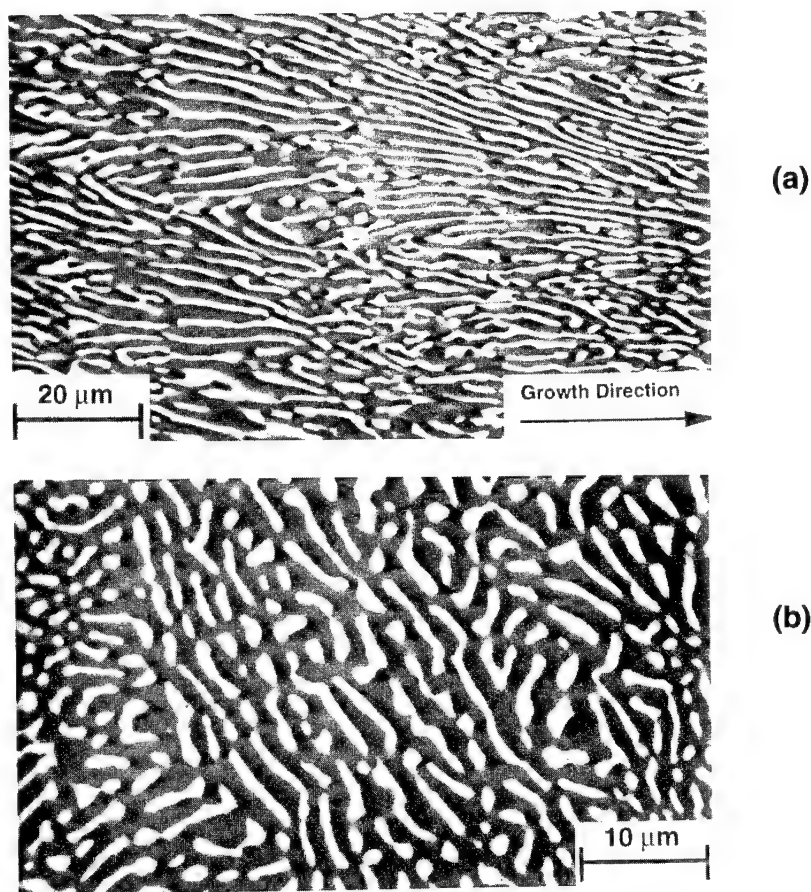


Figure 1 Longitudinal (a) and transverse (b) sections of the DS Cr_2Nb -Nb eutectic grown at 1 mm/min. (BSE images).

note that the microstructure had a much coarser scale than that of the binary eutectic. No primary dendrites were observed in the microstructure. In addition, the (Nb) did not exist as fibres, ribbons or lamellae, as was the case for the binary eutectic. Thus, the microstructure of the $\text{Cr}_2(\text{Nb})$ -(Nb) eutectic was quite different to that of the Cr_2Nb -Nb binary eutectic, even though there were similar volume fractions of metallic phase in each case. The measured volume fraction of (Nb) in the Nb-16.5Ti-52.5Cr-9.2Hf alloy was 0.24, which was smaller than that predicted. The longitudinal section in Figure 2(a) showed some alignment of the $\text{Cr}_2(\text{Nb})$ with the growth direction, but the (Nb) was not so well aligned and it did not possess a high degree of continuity.

Cr_2Hf is essentially isomorphous with Cr_2Nb , but it has a higher melting temperature (1825°C versus 1770°C), which is consistent with Hf enrichment being observed at the cores of the laths. The melting temperatures of the three quaternary alloys investigated are also included in Table I; these temperatures are relatively low, being in the range 1514-1563°C. X-ray diffraction data (XRD) indicated that the $\text{Cr}_2(\text{Nb})$ possessed the C15 crystal structure. Binary Cr_2Nb has the cubic C15 crystal structure at temperatures below 1585°C and a hexagonal C14 structure above 1585°C [4, 15]. Cr_2Hf also possesses low

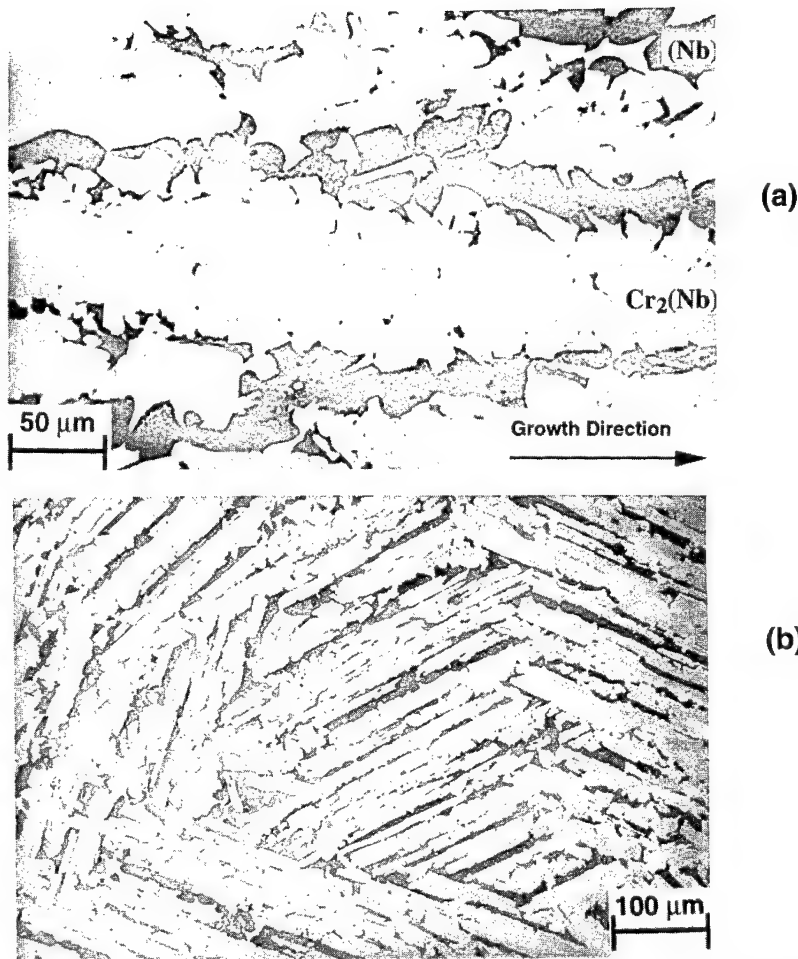


Figure 2 Typical scanning electron micrographs (BSE images) of, (a) the longitudinal, and (b) the transverse sections of DS $\text{Cr}_2(\text{Nb})$ -30%(Nb) (Nb-16.5Ti-52.5Cr-9.2Hf) composite.

temperature, C15, and high temperature, C14, crystal structures. The low temperature C15 phase is stable from room temperature to 1335°C, and the C14 phase is stable from 1335°C to the melting temperature. The XRD data indicate that the C15 $\text{Cr}_2(\text{Nb})$ was stabilized in the quaternary alloy Laves phase composites.

The lattice parameters of the Cr_2Nb of the three quaternary compositions were measured using XRD as 0.70932(5), 0.71015(5) and 0.70964(5) nm for the Nb-26.0Ti-36.5Cr-7.5Hf, Nb-21.2Ti-44.5Cr-8.4Hf and Nb-16.5Ti-52.5Cr-9.2Hf alloys, respectively. The numbers in parentheses represent the uncertainty in the last digit. In comparison with the lattice parameters in the binary Laves phases, these lattice parameters are all similar, indicating that the phase chemistry was similar for $\text{Cr}_2(\text{Nb})$ in the three alloys. These measurements suggest that the C15 crystal lattice is expanded as a result of the Hf additions; the lattice parameters of binary stoichiometric Cr_2Nb and Cr_2Ti are 0.6978 nm and 0.6940 nm, respectively, and the lattice parameter of binary stoichiometric Cr_2Hf is 0.7157 nm. The

lattice parameters of the binary Laves phases in the eutectics are modified according to the composition at the phase boundary [15], as is probably the case in the quaternary alloys. The lattice parameter measurements of the (Nb) were 0.32519 and 0.32490 nm for Nb-26.0Ti-36.5Cr-7.5Hf and Nb-21.2Ti-44.5Cr-8.4Hf alloys, respectively. Pure Nb has a lattice parameter of 0.33067 nm [15]. Binary alloys of Nb-Cr show lattice contraction, while Nb-Ti show no significant change, and Nb-Hf show expansion relative to the Nb lattice. These measurements indicate that there is some contraction of the Nb lattice as a result alloying with Cr and Ti, and this is greater than any expansion due to the Hf.

Electron microprobe data shown in Table II for similar arc-melted alloys containing Al, indicate that partitioning of Hf was approximately two times greater in the Laves phase than in the metal (~10% versus ~5%). The Cr concentration of the Laves phase was ~58%, while in the metal it was ~13% after heat treatment at 1200°C. Partitioning of Ti was stronger to the metal phase than to the Laves phase, and vice versa for Nb. Since the metallic phase strength and oxidation resistance is improved by Hf additions of 4-5% [12], the overall DS composite alloy chemistries were chosen in order to provide ~5%Hf in the metallic phase and ~10%Hf in the Laves phase.

Table II : Phase compositions for the metallic and Laves phases in Cr₂(Nb)-based composites heat treated at 1200°C for 50 hours in vacuum.

Phase	Temperature (°C)	Nb	Ti	Cr	Hf	Al
Cr ₂ (Nb)	1200°C	17.4	12.5	57.9	10.3	1.9
(Nb)	1200°C	38.9	38.7	13.0	4.6	4.8

The microstructure of the Nb-21.2Ti-44.5Cr-8.4Hf composition, which was used to generate the Cr₂(Nb)-40%(Nb) composite, was similar to that of the Cr₂(Nb)-30%(Nb) composite in both its scale and morphology, but there was a smaller volume fraction of Cr₂(Nb). The microstructure of the Cr₂(Nb)-50%(Nb) composite (Nb-26.0Ti-36.5Cr-7.5Hf) had a similar morphology to that of the quaternary Cr₂(Nb)-30%(Nb) eutectic-based composition, but it had a larger volume fraction of (Nb) and as a result the (Nb) "laths" had a greater degree of continuity. The hexagonal type grains observed in the Cr₂(Nb)-(Nb) eutectic were not observed in the 50%(Nb) composite. This was probably a result of the lower volume fraction of Cr₂(Nb), and the texture associated with it. The widths of the (Nb) and Cr₂(Nb) phases were 13±4 μm and 12±4 μm, respectively. The Cr₂(Nb) was finer than in the Cr₂(Nb)-30%(Nb) eutectic. No primary (Nb) dendrites were observed. The measured volume fraction of (Nb) in the nominal Cr₂(Nb)-50%(Nb) composite was 0.47, very close to that originally predicted for the selected alloy chemistry.

Niobium-Silicide Composite

A typical scanning electron micrograph (BSE imaging) of a longitudinal section of the MASC is shown in Figure 3. The composite contained both metallic and (Nb,Hf,Ti)₃Si intermetallic dendrites, a small amount of an (Nb,Hf,Ti)₅Si₃ intermetallic, and an interdendritic eutectic of (Nb,Hf,Ti)₃Si intermetallic and (Nb). Again, Hf partitioning leads to only small differences in the average atomic weight of the different phases, and this results in weak BSE contrast. The metallic and intermetallic dendrites of the MASC were aligned

with the growth direction. The MASC consisted of interpenetrating dendrites of the composite phases (20-40 μm). The volume fraction of the metallic phase was ~50%. The MASC is entirely analogous to hypoeutectic binary Nb-Si and ternary Nb-Ti-Si composites reported previously [4]. Typical microstructures of longitudinal and transverse sections of a Nb-33Ti-16Si ternary composite are shown in Figure 4, where the absence of Hf allows strong contrast between the phases. The $(\text{Nb,Hf,Ti})_3\text{Si}$ dendrites shown in Figure 4 possessed the distinctive faceted morphology that has been reported previously in the binary hypereutectic binary Nb-Si alloys and the ternary Nb-Ti-Si composites [4, 10].

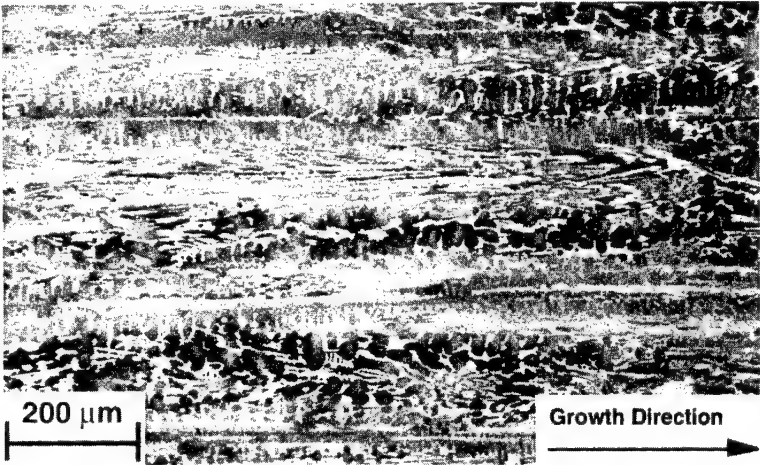


Figure 3 Micrograph (BSE image) of the longitudinal section of the DS Nb-24.7Ti-16Si-8.2Hf-2.0Cr-1.9Al composite (MASC).

The composition ranges observed in the three phases are shown in Table III. The Si concentrations of the $(\text{Nb,Hf,Ti})_3\text{Si}$ and $(\text{Nb,Hf,Ti})_5\text{Si}_3$ silicides were close to the stoichiometric values. Very low concentrations of Al and Cr were observed in both the $(\text{Nb,Hf,Ti})_3\text{Si}$ and $(\text{Nb,Hf,Ti})_5(\text{Si,Al})_3$ silicides. There was strong Hf partitioning between the phases : 5% Hf was observed in the metallic phase, 8% Hf in $(\text{Nb,Hf,Ti})_3\text{Si}$, and 12.5% Hf in $(\text{Nb,Hf,Ti})_5(\text{Si,Al})_3$; the bulk Hf composition was nominally 8.2%. The Nb:Ti:Hf ratio in the metallic phase was 12:6:1. The Nb:Ti:Hf:Si ratio in the $(\text{Nb,Hf,Ti})_3\text{Si}$ was 6:2:1:3. In the $(\text{Nb,Hf,Ti})_5(\text{Si,Al})_3$ the Nb:Ti:Hf:Si ratio was 2:2:1:3. In the overall MASC chemistry, the Nb:Ti:Hf:Si ratio was approximately 6:3:1:2.

Table III : Composition ranges for the silicide and metallic phase observed in the composite which was directionally solidified from the Nb-24.7Ti-8.2Hf-2.0Cr-1.9Al-16.0Si alloy.

	Nb	Ti	Hf	Si	Al	Cr
Metallic Phase	58-61	27.2-29.4	5.0-5.3	0.9-1.3	2.5-3.0	2.8-3.9
$(\text{Nb,Hf,Ti})_3\text{Si}$	48.3-49.0	18.2	7.8	24.7-25.4	0.1	0.13-0.16
$(\text{Nb,Hf,Ti})_5\text{Si}_3$	25.5-27.9	22.2-23.2	12.5-12.9	35.4-37.5	1.0-1.5	0.35-0.5

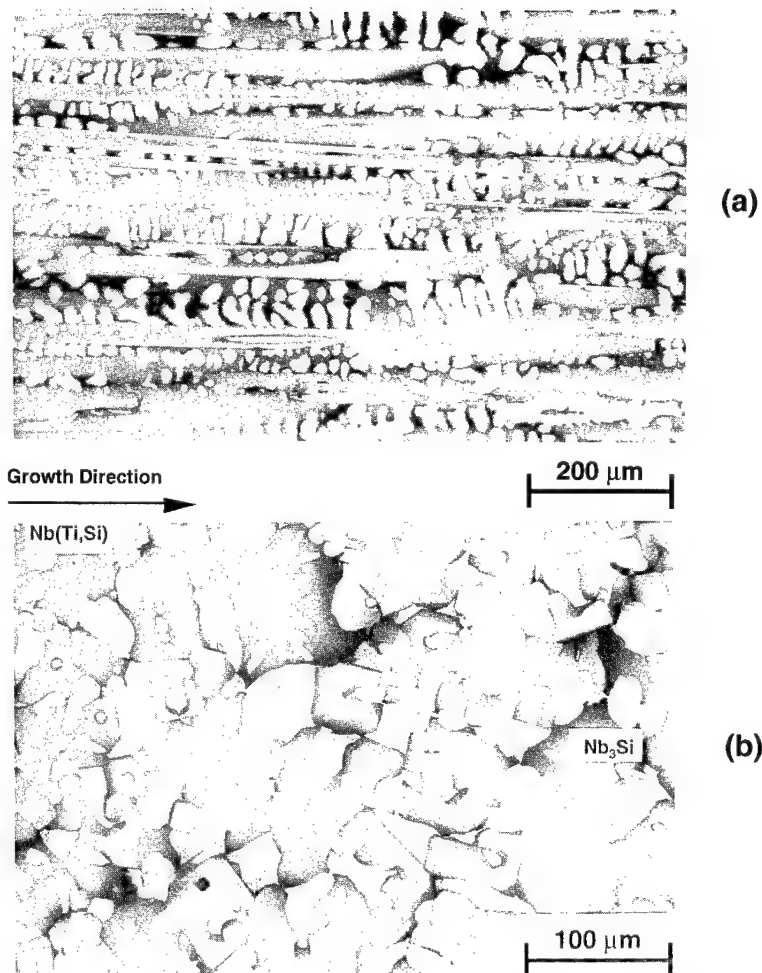


Figure 4 Scanning electron micrographs (BSE images) of (a) the longitudinal, and (b) the transverse sections of a DS Nb-33Ti-16Si composite. The structure consists of non-faceted Nb(Ti, Si) dendrites (white phase), together with large-scale ($\sim 50\mu\text{m}$) faceted $(\text{Nb,Ti})_3\text{Si}$ dendrites (grey phase).

Mechanical Properties

Room Temperature Fracture Toughness

Fracture toughness measurements of the composites from the quaternary alloys were not performed, but given the difficulty of preparing tensile specimens, as indicated in Table I, it can be assumed that the toughness was probably $<10 \text{ MPa}\sqrt{\text{m}}$. The room temperature fracture toughness of the binary stoichiometric Laves phase, Cr_2Nb has been reported by Davidson and Chan as $1.4 \text{ MPa}\sqrt{\text{m}}$ [6], and fracture toughness values of the $\text{Cr}_2\text{Nb-Nb}$ and $\text{Cr}_2\text{Nb-Cr}$ binary eutectics have been reported as $3.1 \text{ MPa}\sqrt{\text{m}}$, and $3.6 \text{ MPa}\sqrt{\text{m}}$ [4] respectively.

It was not possible to grind tensile bars from the binary and quaternary eutectics, which contained a volume fraction of Laves phase of $\sim 70\%$. Thus, the fracture toughness of the $\text{Cr}_2(\text{Nb})\text{-(Nb)}$ eutectic was probably similar to that of the binary eutectic, even though the

(Nb) phase width in the quaternary alloy was larger than the Nb rod width in the binary eutectic; previously it has been shown that increasing the scale of the toughening phase can lead to an increase in the toughness [4]. Given the poor machining performance of the 40% and 50% metal-containing composites, the fracture toughness values of these composites were probably $<10 \text{ MPa}\sqrt{\text{m}}$, and there was little improvement at higher (Nb) volume fractions.

Room temperature fracture toughness values, K_{Q} , of $18.2\text{--}23.3 \text{ MPa}\sqrt{\text{m}}$ were measured from monotonic loading experiments for the MASC. R-curve measurements are shown in Figure 5, and the K_{IC} values for the MASC were $19\text{--}22 \text{ MPa}\sqrt{\text{m}}$. Higher toughness values were obtained from the MASC than were estimated for the quaternary Laves phase composites. Toughness values greater than $15 \text{ MPa}\sqrt{\text{m}}$ have also been measured in ternary Nb-Ti-Si composites [8, 9]. The form of these R-curves is similar to those reported previously in binary Nb-10Si in-situ composites, which displayed K_{IC} values of $>20 \text{ MPa}\sqrt{\text{m}}$ in the extruded condition [9, 11].

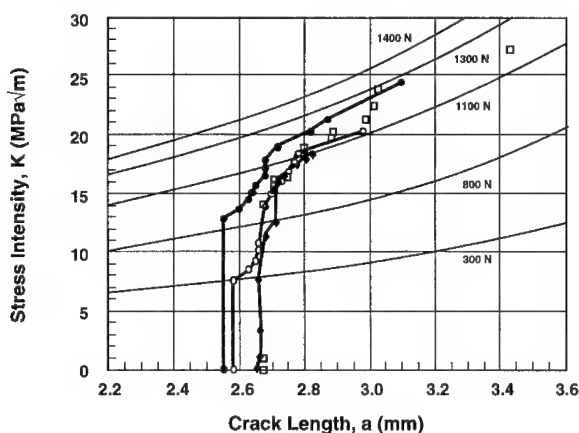


Figure 5 R-curve behavior of the DS MASC. Data points from four samples are shown.

Figure 6 shows fracture surfaces of the DS MASC. At lower magnification, the fracture surfaces were highly convoluted and suggested a high work of fracture. The (Nb) dendrites failed in a ductile manner, and were pulled out of the matrix. The fine-scale (Nb) between the silicide dendrites was also pulled to a chisel point, and microcracking of the silicide matrix was observed. All of the $(\text{Nb,Hf,Ti})_3\text{Si}$ and $(\text{Nb,Hf,Ti})_5\text{Si}_3$ intermetallic dendrites failed by cleavage. This suggests that the majority of the toughness was provided by the (Nb), although microcracking and interface debonding have made significant toughening contributions.

Elevated Temperature Strength

The tensile strengths of the Laves phase-based composites are shown in Table I and Figure 7. Compressive strengths at 1200°C for monolithic Cr_2Nb [2, 16] are also shown for comparison. The $\text{Cr}_2(\text{Nb})\text{--}40\%(\text{Nb})$ composite had a fracture stress of 132 MPa at 1200°C . The yield strength of the $\text{Cr}_2(\text{Nb})\text{--}50\%(\text{Nb})$ composite at 1200°C was 120 MPa . At

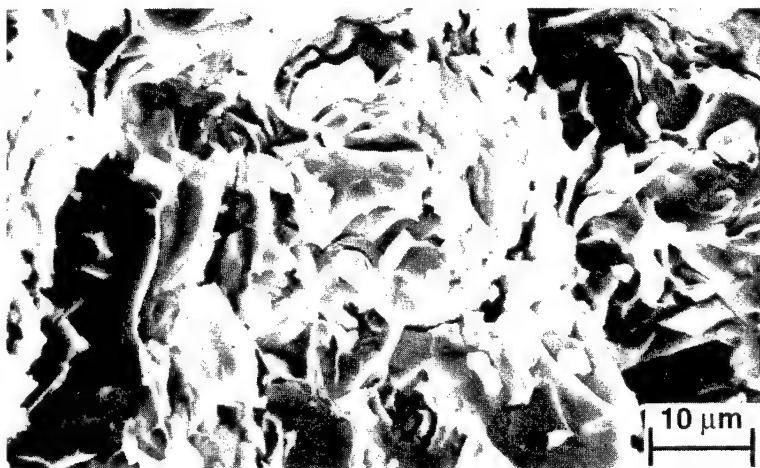


Figure 6 Fracture surface of the MASC, showing microvoid coalescence in the (Nb) and cleavage in the (Nb,Ti)₃Si.

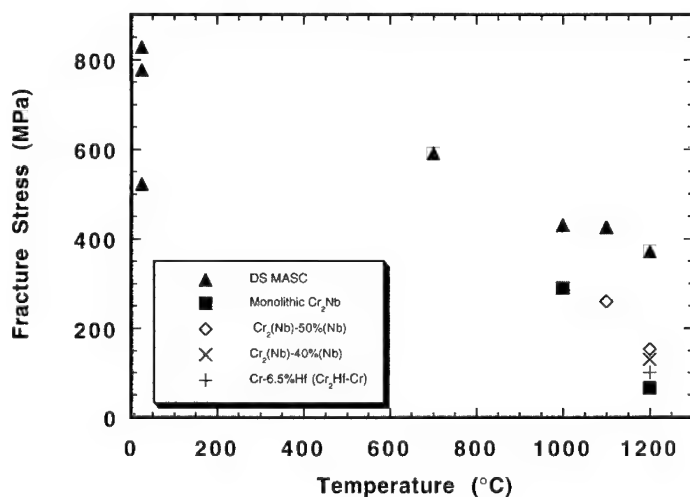


Figure 7 Tensile strengths of the MASC and the Laves phase-based composites as a function of temperature. The improvement of high temperature strength of the silicide composite over Laves phase-based composites with similar intermetallic volume fractions is apparent. Literature data for monolithic Cr₂Nb [2] and a Cr₂Hf-Cr [20] composite are included.

1200°C an ultimate tensile strength of 153 MPa and an elongation of 56% was measured for this composite. For comparison, a monolithic Nb-based alloy with a similar composition to that of the metallic phase in these composites (except for the addition of Al) had a yield strength in the range 55-70 MPa at 1200°C [12], indicating a factor of approximately two increase in the strength effected by the Laves phase. Kumar and Miracle [20] reported a compressive yield strength of two phase as-forged Cr-6.5Hf Cr₂Hf-Cr composite of ~100 MPa at 1200°C, which is less than that measured in tension for the

Cr₂(Nb)-(Nb) composites. This may be due in part to the lower volume fraction of Laves phase. Tensile testing of the Laves phase-based composites at room temperature was not performed because of the flaw sensitivity of these composites.

Examination of the Laves phase composite data indicates that there are two important points. First, the Cr₂(Nb)-(Nb) composites which contained Hf and Ti, had higher fracture strengths at 1200°C than either the monolithic Cr₂Nb, or the binary Cr₂Hf-Cr composite [20]. Second, the fracture strengths of the Cr₂(Nb)-(Nb) with 40% and 50% (Nb) were similar. Although compressive strengths of ~600 MPa at 1200°C have been reported for Cr₂Nb-Nb by Takasugi et al [7], these strength levels have yet to be demonstrated in tension.

The yield strengths of the MASC are also shown in Figure 7. The tensile fracture stress was ~750 MPa at room temperature and the yield stress was 370 MPa at 1200°C. At 1200°C the scatter in the yield stress was ~20 MPa. However, several hundred MPa scatter was observed in the room temperature fracture stress measurements; this was probably due to the flaw sensitivity of the fracture stress at room temperature, as in the case of ceramics. At 1200°C significant plastic deformation of both the metallic and silicide phases was observed, but below 1100°C only the (Nb) exhibited plastic deformation. Monolithic alloys of similar compositions to the metallic phase of the composite have yield strengths in the range 55-70 MPa at 1200°C [12]. It can clearly be seen that at temperatures up to 1200°C, the yield strengths of the silicide-based composites were approximately twice those of the Laves phase-based composites. Thus, for a given volume fraction of intermetallic, the silicide-based composites offer a more attractive balance of room temperature fracture toughness and high temperature strength. At room temperature, the metallic phase provides the MASC with improved toughness, whereas at elevated temperatures (>1000°C) the silicide phases serve to maintain its strength. The (Nb) and Cr₂(Nb) in the Laves phase composites are less effective in both of these capacities. The higher Cr concentration of the metal in equilibrium with the Laves phase, compared to the metal in equilibrium with the silicides, may lead to a smaller contribution to composite toughening in Laves phase composites.

Density-normalized bending strength-temperature data have been reported previously for Nb-42.5Ti-15Si, Nb-40Ti-15Si-5Al [9] and binary Nb-10Si composites [11]. The binary Nb-10Si composite showed bending strength levels at 1200°C of ~370MPa [11]. However, the reductions in the high temperature strength levels displayed in ternary Nb-Ti-Si and quaternary Nb-Ti-Si-Al are not experienced by the MASC. This suggests that Hf additions can have a powerful effect on the high temperature strength of the silicide and Laves phase composites, and that Hf is more effective in the former than in the latter.

Creep Rupture Behavior

Figure 8(a) compares the creep rupture behavior of the MASC with single crystal Ni-based superalloys, CMSX4 and CMSX10 [8] using a Larson-Miller plot. At 1100°C and 105 MPa the rupture life was greater than 500 hours. The density-normalized stress rupture behavior is shown in Figure 8(b) accounting for the reduced density of the composite in comparison with CMSX4 and CMSX10. Figure 8(b) illustrates that the stress rupture behavior of the MASC is similar to that of advanced single crystal Ni-based superalloys

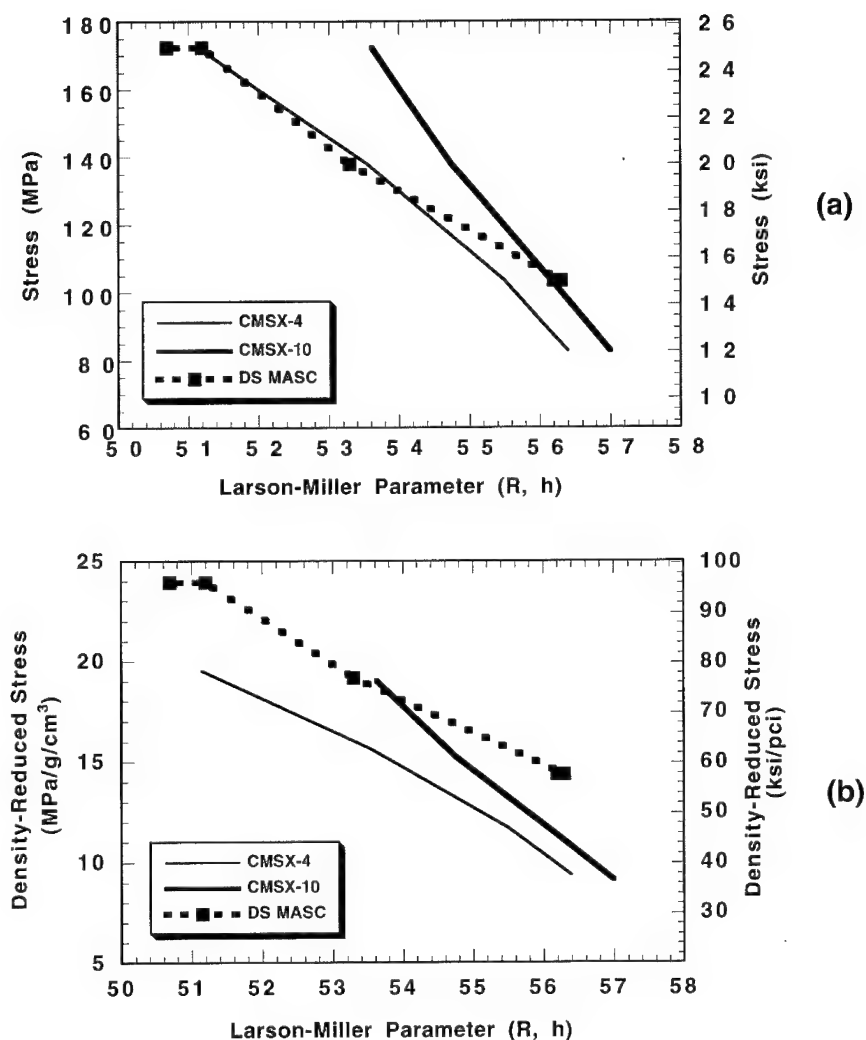


Figure 8 Stress rupture behavior of the DS MASC is compared to that of second- and third-generation single crystal Ni-based superalloys [8] in Larson-Miller plots ($C=20$) where the temperature-time parameter is plotted against (a) rupture stress or (b) rupture stress/material density. Stress rupture testing of MASC was performed in argon.

under similar test conditions but, after accounting for the lower density of the MASC, there is a significant improvement in the stress rupture behavior. The composite tensile creep rates have been reported separately [8], and are more than an order of magnitude lower than for commercial Nb alloys. The tensile yield strength of the best Laves phase composites at 1200°C is ~130MPa. Because the stress range that was used for creep rupture testing of the MASC was close to the yield strengths of the Laves phase composites, creep rupture testing of the latter was not performed.

Conclusions

Laves phase and niobium-silicide based composites with Hf and Ti alloying additions have been directionally solidified with intermetallic volume fractions in the range 70-50%. Complex microstructures and phase chemistries were observed in each family of composites. In the Laves phase composite, the Hf and Ti additions provided a coarser two-phase microstructure than was observed in the binary $\text{Cr}_2\text{Nb-Nb}$ composite. However, estimates of the room temperature fracture toughness values of the quaternary Laves phase composites were low ($<10 \text{ MPa}\sqrt{\text{m}}$). In the niobium silicide-based composite, the metallic phase provides more effective toughening, since toughness values of $> 20 \text{ MPa}\sqrt{\text{m}}$ have been measured.

Tensile strengths for the Hf and Ti containing $\text{Cr}_2(\text{Nb})\text{-(Nb)}$ composites of up to 153 MPa at 1200°C were measured. However, at 1200°C these strengths are only ~40% of that of a niobium silicide-based composite with a similar volume fraction of metallic phase. The MASC composite combines high-strength low-toughness silicides with a lower-strength high-toughness Nb-based metallic phase in order to generate a composite that has improved high temperature and low temperature mechanical properties. Room temperature fracture toughness values of $>20 \text{ MPa}\sqrt{\text{m}}$ were measured with a tensile strength of 370 MPa at 1200°C . The stress rupture behavior of the MASC is similar to that of advanced single crystal Ni-based superalloys under similar test conditions and thus, due to the lower density (~25%) of the MASC, there is an increase in the density-normalized stress rupture behavior of more than one Larson-Miller parameter.

Acknowledgments

The authors would like to acknowledge W.J. Reeder for the fracture toughness measurements, C. Canestraro for the tensile testing, and L.A. Peluso for the microprobe analyses. The authors would also like to thank D.J. Dalpe for the directional solidification experiments. This research was partially funded by AFOSR under contract #F49620-93-C-0007 with Capt. C.H. Ward as Program Manager.

References

- [1] D.L. Anton and D.M. Shah, *Mat. Sci. Eng.*, **A153** (1992), pp. 410-415.
- [2] D.L. Anton and D.M. Shah, *Mat. Res. Soc. Symp. Proc.* **213** (1991), pp. 733-738.
- [3] B.P. Bewlay, J.A. Sutliff, M.R. Jackson and H.A. Lipsitt, *Acta Metall. Mater.*, **42(8)** (1994), pp. 2869-2878.
- [4] B.P. Bewlay, H.A. Lipsitt, M.R. Jackson, W.J. Reeder and J.A. Sutliff, *Mat. Sci. Eng.*, **A192/193** (1995), pp. 534-543.
- [5] M. Takeyama and C.T. Liu, *Mat. Sci. Eng.*, **A132** (1991), pp. 61-66.
- [6] D.L Davidson and K.S. Chan, AFOSR Final Report, April 1995.
- [7] T. Takasugi, S. Hanada and K. Miyamoto, *J. Mater. Res.*, **8 (12)** (1993), pp. 3069-3077.

-
- [8] M.R. Jackson, B.P. Bewlay, R.G. Rowe, D.W. Skelly and H.A. Lipsitt, J. of Metals 48 (1) (1996), p. 39-44.
- [9] P.R. Subramanian, M.G. Mendiratta and D.M. Dimiduk, J. of Metals 48 (1), (1996), pp. 33-38.
- [10] P.R. Subramanian, M.G. Mendiratta and D.M. Dimiduk, Mat. Res. Soc. Symp. Proc. 322 (1994), pp. 491-502.
- [11] M.G. Mendiratta, J.J. Lewandowski and D.M. Dimiduk, Metall. Trans. 22A (1991), pp. 1573-1581.
- [12] M.R. Jackson and K.D. Jones, in Refractory Metals Extraction, Processing and Applications, Ed. K.C. Liddell, D.R. Sadoway and R.G. Bautista (TMS Publications, Warrendale, PA, 1991) pp. 310-320.
- [13] M.R. Jackson, R.G. Rowe and D.W. Skelly, Annual Report, *WRDC Contract # F33615-91-C-5613*, (1994).
- [14] T.B. Massalski, Binary Alloy Phase Diagrams, ASM Metals Park, Ohio (1991).
- [15] D.J. Thoma and J.H. Perepezko, Mat. Sci. Eng., **A156** (1992), pp. 97-108.
- [16] B.P. Bewlay and M.R. Jackson, Accepted for publication in J. Mater. Res., April 1996.
- [17] K-M. Chang, B.P. Bewlay, J. A. Sutliff and M.R. Jackson, J. of Metals 44 (6), (1992), p. 59-65.
- [18] "Standard Test Method for Plane-Strain Fracture Toughness of Metallic Materials", ASTM STP E-399, American Society for Testing and Materials, July 1983, pp. 488-512.
- [19] "Standard Practice for R-Curve Determination," ASTM STP E 561-94, American Society for Testing and Materials, Philadelphia, 1994.
- [20] K.S. Kumar and D.B. Miracle, Intermetallics 2 (1994), pp. 257-274.

Biasing Reaction Pathways in In-Situ Composites

S.G. Fishman
Office of Naval Research
800 N. Quincy St.
Arlington, VA 22217

Abstract

In-situ composites include materials in which desirable reinforcements, matrices or interphases, are formed during processing. One of the most attractive approaches to obtaining such materials involves biasing reactions to alter the sequence of phase formation such that desirable phases and morphologies can be obtained. Opportunities for this arise because of the multiplicity of diffusion pathways existing in systems which are of ternary order or higher. The paper discusses processing strategies which offer potential to produce stable, inexpensive composite designs.

Introduction

Although the advantages of advanced inorganic composites, as structures in aerospace and other demanding applications, have been well-documented by numerous applications analyses and hardware evaluations, they have found few applications outside the military arena. A primary detriment to the use of these materials in commercial applications is their high cost. Typically, processing of advanced composites involves embedding strong, stiff fibers, which can cost hundreds or thousands of dollars per pound, in whatever matrix is being used for the monolithic component by a series of cost-intensive steps. Since composites are, by definition, man-made materials, their constituents are rarely, if ever, thermodynamically compatible. Consequently, either during processing or extended high temperature operation, extensive reinforcement-matrix interaction can occur. The usual method for avoiding such reactions and providing required interfacial properties usually involves the application of one or more interfacial coatings. Such coatings add additional hundreds of dollars per pound (of coated fibers) to composite cost. Ideally, high temperature composite materials would be fabricated from inexpensive constituents with desirable reinforcements, interphases, and matrices formed by-reaction, in-situ, during processing.

In the hierarchy of structural materials, in-situ composites can be considered to be intermediate between monolithics and artificial composites. Monolithic materials, containing natural multiphases, are cheap, but have limited material property flexibility. Artificial composites, containing man-made reinforcements, are expensive, but offer great flexibility in terms of mechanical, electrical, thermal, etc., properties. In-situ composites take advantage of synthetic multiphases to achieve property flexibility, but are processed by reaction from cheap constituents, and thus should have costs similar to those of monolithics. Since the probability of forming desirable phases and morphologies for optimum composite performance is small, it is clear that effective processing strategies, based upon consideration of relevant phase diagrams and kinetic information such as interdiffusion path and rates, must be developed in order to fabricate stable, in-situ composite designs. In particular, it is necessary to predict and select reaction paths to achieve formation of desired phases and morphologies.

Issues involved in governing phase formation and microstructures in real composites include multicomponent phase equilibria, interdiffusion kinetics, phase sequencing, kinetic pathways, etc. Opportunities for

selecting reaction pathways arise because of the multiplicity of diffusion paths which exist in diffusion couples with three or more constituents. The diffusion path is a line on a ternary isotherm, representing the locus of average compositions in planes parallel to the original diffusion couple interface, within the reaction zone. Figure 1 shows two of the many possible diffusion paths possible for a hypothetical diffusion couple between a component A and a compound BC[1]. Although it is not possible to determine which of these pathways will be selected, by using some simple rules, one can obtain guidance on predicting which pathways can be ruled out. The first has to do with conservation of mass. Considering an infinite diffusion couple A/BC, the mean composition at any point within the reaction zone must lie on the locus of points connecting compositions A and BC on the isotherm. A direct consequence of this is that the diffusion path must cross the straight line joining these terminal compositions at least once[2]. Considering the two cases shown in Figure 1, it can be seen that case (a), (diffusion path A/A₂B/BC) lies all on one side of this line, violating the rule for conservation of mass, and thus being ruled out as a possible pathway. Case (b) (diffusion path A/A₂B/C/BC), on the other hand, crosses the connecting line, and obeys conservation of mass.

Further guidance in predicting reaction pathways can be obtained from thermodynamic considerations, taking into account the difficulty of a mobile species diffusing intrinsically against its own chemical potential or activity gradient[3]. Figure 2 shows activity diagrams, for case (b), in terms of diffusing species A and C. Species B is considered to be immobile. In order for reaction layers C and A₂B to grow, A atoms must diffuse through both layers to the A₂B/BC interface, and C atoms must diffuse from BC to the A₂B/C interface, respectively. The activity of A atoms decrease, as they diffuse along this path. However, it can be seen that the activity of C atoms, as they pass through A₂B to the A₂B/C interface increases, making the A/C/A₂B/BC pathway unlikely. If one considers a third pathway, A/A₂B/C/BC, both diffusing species show continuously decreasing activities and the pathway obeys conservation of mass, thus making it a possible diffusion path. In order to be able to design composites, one needs not only to predict, but must be able also to select optimum reaction pathways for desirable composite properties.

Strategy for Biasing Reaction Pathways

As mentioned above, it is the multiplicity of diffusion pathways which offers opportunities for altering phase formation. By controlling

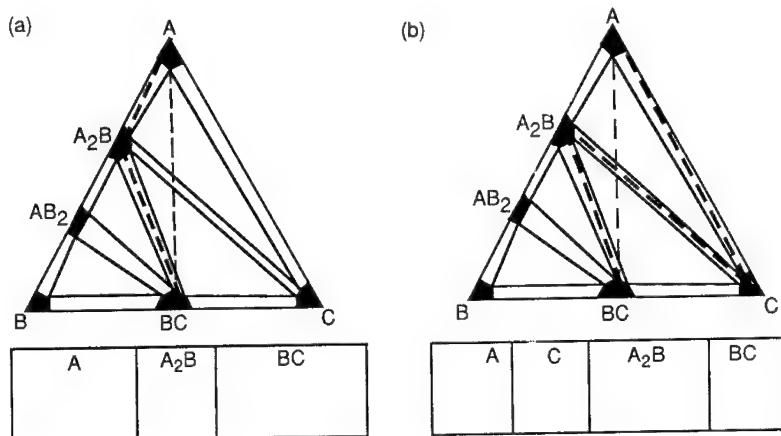


Figure 1 - Two of the possible diffusion pathways in hypothetical diffusion couple A/BC [15]

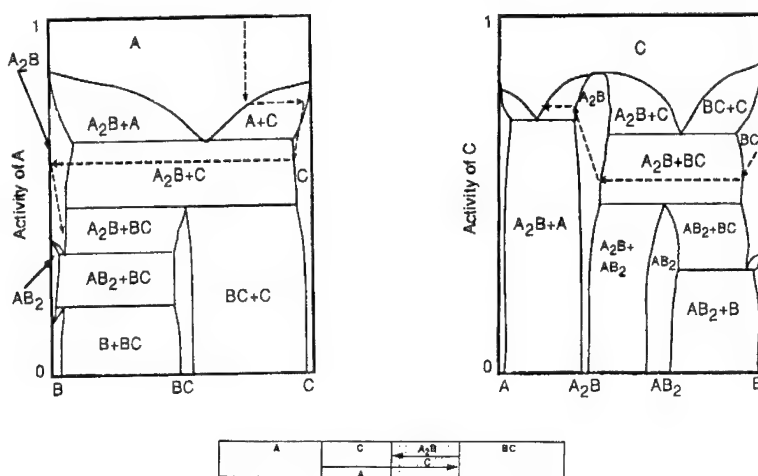


Figure 2 - Activity diagram for diffusion couple A/BC pathway shown in Figure 1 (b) [15]

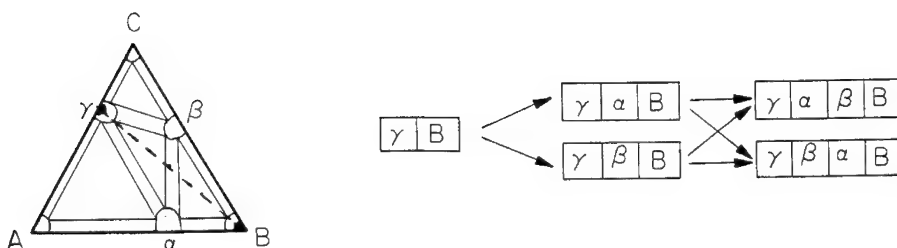


Figure 3 - Potential reaction layer formation in a γ/β diffusion couple involving stable pairings of phases [4]

the sequence of phase formation, it is possible to select the most desirable reaction pathway[4]. As described below, techniques for selecting or biasing reaction pathways involve introducing coatings of stable phases, taking advantage of limited reactant reservoirs and concentration gradients, use of transient phases, and matrix alloying.

Considering the hypothetical ternary phase diagram for a composite of matrix B reinforced with compound γ , presented in Figure 3, it can be seen that there are two reaction paths which obey conservation of mass, $\gamma/\alpha/\beta/B$ and $\gamma/\beta/\alpha/B$. If it is desirable to avoid contact between γ and α , a simple way to control first phase formation is by coating γ with β prior to reacting to preclude the $\gamma/\beta/\alpha/B$ sequence. Once the γ/α couple is formed, formation of β is inhibited, since the residual thermodynamic driving force for its nucleation is reduced.

The sequence of phases formed can be altered by the extent of the reservoir of reactant materials. This has been demonstrated in a comparison between reaction products formed within infinite and reactant-limited Fe/Si diffusion couples[5]. A diffusion couple, with a large reservoir of reactants, can be represented as an infinite couple. In such a system, it is expected that over a long enough period of time, and barring any nucleation difficulties, all phases existing under those conditions of temperature and pressure in the phase diagram will appear. However, when one of the reactant reservoirs is limited, the diffusion couple is represented by a semi-infinite couple, the latter being the usual case in real composite systems. Since, in the semi-infinite couple, there is a limited source of a reacting component, the final reaction sequence need not include all of the phases predicted from the phase diagram. For example, as shown in the schematic in Figure 4, comparing the infinite and limited reactant reservoir cases, the reaction sequence for the infinite Fe/Si couple was:



The observed reaction sequences for the Si- and Fe-limited Fe/Si couples were:



In a recent investigation on a model system of Al/Ni multilayers, it was demonstrated that first phase nucleation can be altered by controlling interfacial concentration gradients[6]. Phase evolution from annealed ion-beam-sputtered multilayers was studied using X-ray

diffraction and differential scanning calorimetry on samples with modulation wavelengths (i.e. one sequence of Al and Ni layers) varying between 10 nm and 440 nm. The sequence of phase formation depended upon the modulation wavelength and the average composition. At longer modulation wavelengths, independent of average composition, the first phase nucleated from annealed multilayers was metastable Al_9Ni_2 . At the shortest wavelengths, however, the first phase nucleated was the closest stable phase with the same average composition as the sample (i.e. AlNi from $\text{Al}_{0.40}\text{Ni}_{0.60}$ and Al_3Ni from $\text{Al}_{0.75}\text{Ni}_{0.25}$). DSC scans exhibited both sharp exothermic peaks, due to phase nucleation, and broad exotherms, interpreted as evidence of atomic mixing prior to nucleation. An explanation of these observations, in terms of the finite aspect of the multilayer samples and their ability to maintain a critical concentration gradient at a dissimilar material interface, has been presented, as shown in Figure 5. In multilayers with both long and short modulation lengths, initial composition gradients are the same. In the former case, the period of atomic intermixing prior to nucleation of a new phase results in compositional excursions (on the A-side of the interface) into the region a-a' of the free energy-composition diagram. Consequently, the expected first phase to nucleate is gamma. In the case of small modulation lengths and subsequent limited supply of reactant species, however, the period of atomic intermixing prior to nucleation of the new phase results in a decrease in the concentration gradient such that compositional excursions are in the range b-b'. The result being that gamma phase is by-passed and the first phase to nucleate is δ . In a separate study, kinetic aspects of the formation of Al_9Ni_2 phase, were determined[7]. A reaction temperature-time plot, indicating the time duration for completion of Al_9Ni_2 phase development, is shown in Figure 6. Such results suggest a strategy for kinetic control of phase selection during in-situ interfacial reactions in composite systems. That each possible intermediate phase will have different time-temperature-transformation behavior, allows different times and temperatures to be selected which will in turn allow for the selection of different phases during the in-situ processing of composites.

It is also possible to use transient phases to bias pathways. Recently, it was demonstrated that a transient layer of pure Ti, inserted between the α_2 Ti_3Al and TiSi_2 end members of a $\text{Ti}_3\text{Al}/\text{TiSi}_2$ diffusion couple, altered the reaction path[4]. Figure 7 (a) illustrates the calculated Ti-Al-Si ternary phase diagram and observed reaction path for the diffusion couple at 1000 °C without a Ti-biasing layer. Initially, it was supposed that, because of the excess of reactants used, Ti_5Si_3 , a high melting phase which exhibits equilibria with many of the Ti-Al binary phases would form. The observed phase sequence within the reaction

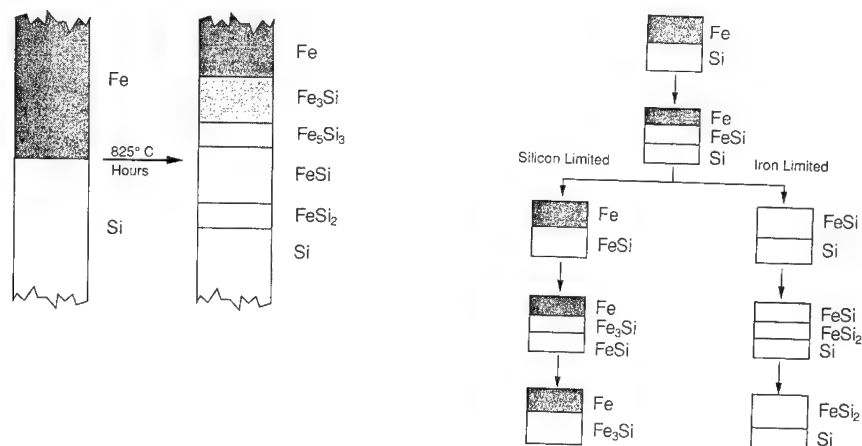


Figure 4 - Observed phase formation in infinite and semi-infinite Fe/Si diffusion couples [5]

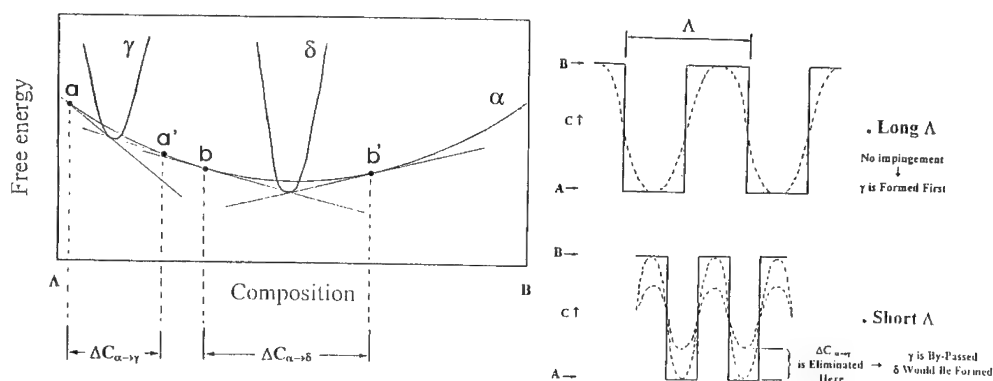


Figure 5 - Role of composition gradients in first phase nucleation [16]

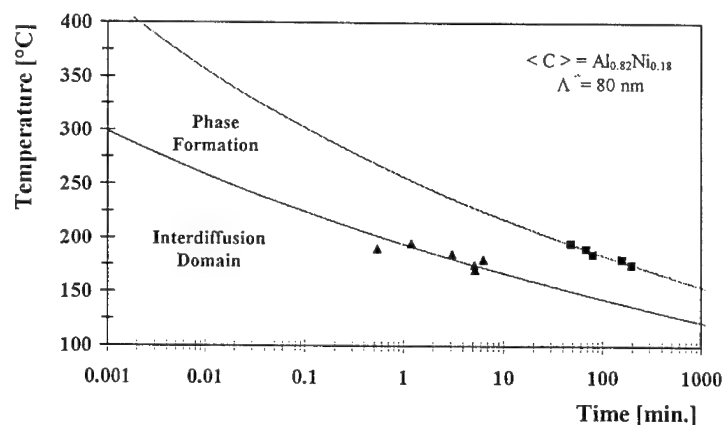


Figure 6 - Reaction temperature-time diagram for isothermal Al₉Ni₂ formation [7]

couple was:



From the diffusion path, it is apparent that a large flux of Ti develops from the Ti_3Al phase, resulting in the formation of TiAl and TiAl_2 . The addition of Ti as a biasing layer, locally converts the system to two binary diffusion couples $\text{Ti}_3\text{Al/Ti}$ and Ti/TiSi_2 , and, as shown in Figure 7 (b), alters the reaction path to:



With further reaction, the β -Ti layer would be consumed. The Ti layer, is thus transient, and can be used to alter the phase sequencing and then disappear. The use of wedge-shaped diffusion couple has been demonstrated as an efficient way to determine the optimum thickness bias layer to modify the phase sequence and be totally consumed[3].

Matrix alloying, in order to change terminal compositions in diffusion couples, can be an effective way to modify diffusion path trajectories in multicomponent systems. Such an approach can be effective in avoiding matrix/reinforcement interactions, either by reducing matrix activity and subsequent reactivity with reinforcing phases, or by altering diffusion trajectories to include an additional phase which can act as a diffusion barrier. An advantage of the latter approach, as compared with artificially applied diffusion barriers which often are perforated or break down promoting catastrophic failure, is that such reaction coatings are "self-healing".

Evidence of how even minor changes in matrix composition can be used to alter reaction paths was demonstrated in considerations of the Ni-Al-O system at 1400 °C[8, 9]. A schematic of the 1400 °C isotherm is presented in Figure 8. As shown, Ni is in equilibrium with Al_2O_3 , NiAl_2O_4 , and NiO. The enlargement of the Ni-rich corner of the isotherm illustrates how the diffusion path is determined by the terminal compositions of the diffusion couple. The diffusion path, in-turn, fixes which tie-lines are selected. For pure Ni in contact with Al_2O_3 (path 1), no reaction occurs. However, deviations in oxygen content of the Ni, even on the order of a few hundreds of parts-per-million, can result in altering the diffusion path and selection of another tie-line (path 2). In this example, one would expect a spinel interphase to form between the Ni and Al_2O_3 . Figure 9 compares the structures of Ni/ Al_2O_3 interfaces hot pressed at 1390 °C[10]. The upper photomicrograph, for an interface between oxygen-free Ni and Al_2O_3 , shows formation of a reaction layer- free interface. The

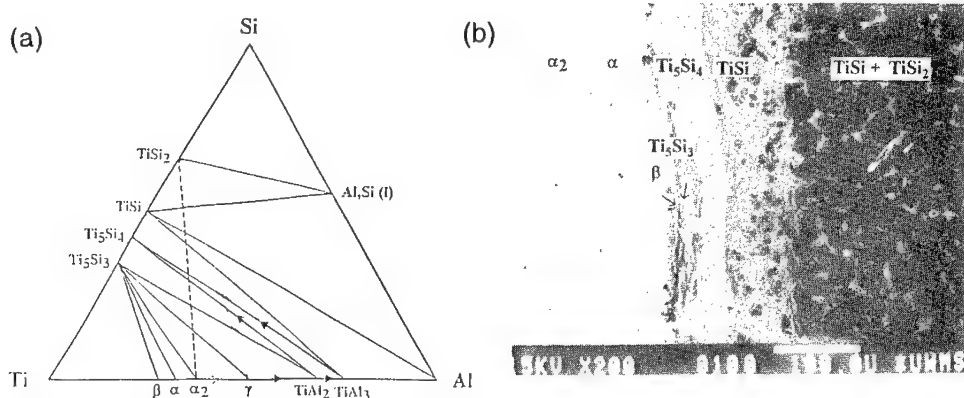


Figure 7 - (a) Calculated 100 °C Ti-Al-Si ternary equilibrium phase diagram with diffusion pathways indicated by arrows
(b) Cross section of α_2 /Ti/TiSi₂ diffusion couple [4]

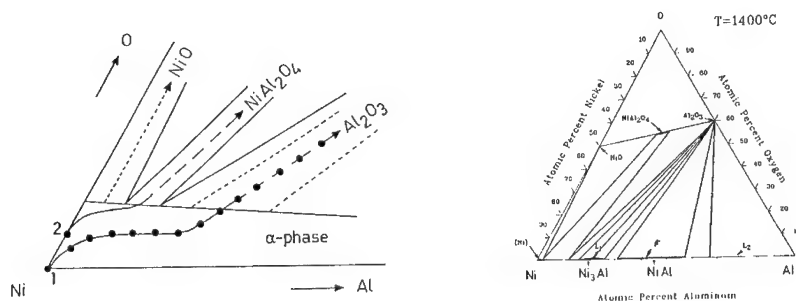


Figure 8 - Ternary isotherm for Ni-Al-Ti at 1400 °C [8]

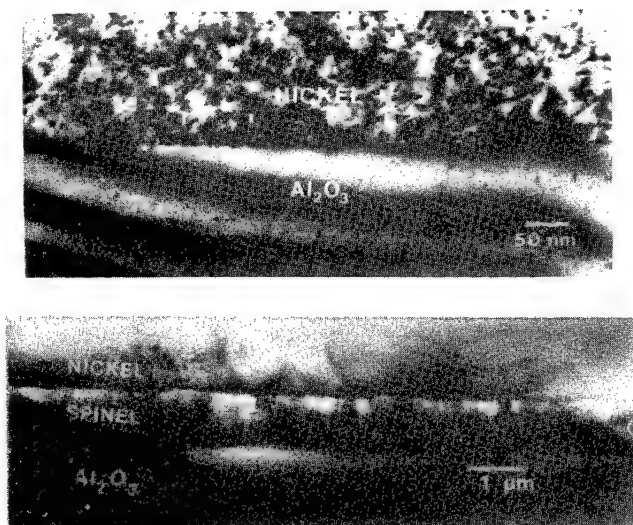


Figure 9 - Ni-Al₂O₃ interfaces formed at 1390 °C using oxygen-free Ni (top) and Ni containing 670 ppm oxygen (bottom) [10]

lower, in which the Ni contained 670 ppm oxygen, had a spinel reaction layer approximately 10^{-6} m thick.

Morphological Effects

The discussion above has not addressed reaction morphologies, which can be layered (either simple or periodic) or aggregate[11]. The nature of reaction morphology depends upon the growth or damping-out of interfacial protuberances, depending upon the relative direction of interface growth with respect to the slow diffusing atomic species[12]. For example, as shown in Figure 10, for a hypothetical A/BX diffusion couple, if A atoms diffusing to the AX/B interface are the slow diffusing species, interfacial irregularities are damped out, and the morphology is layered. On the other hand, if X atoms are the slow diffusing species, interfacial irregularities grow and an aggregate morphology is obtained. If one is interested in maintaining a reaction-grown diffusion barrier, the morphology of interest is obviously layered. However, one can exploit the aggregate structure to form in-situ reinforcements (e.g. AX-reinforced B). Thus, microstructures that are important for composite strength and toughness, and not easily achievable by other processing methods, can be obtained.

A SiC platelet-reinforced MoSi₂ composite processed by reacting a mixture of Si and Mo₂C powders is shown in Figure 11[13]. In this material, Si is the fastest diffusing species. The first phase to nucleate was the ternary Mo₅Si₃C phase which then reacted by a solid displacement reaction with Si to form MoSi₂. Metallographic observations coupled with the predictions of a one-dimensional reaction-controlled moving interface diffusion model indicated that C was rejected ahead of the MoSi₂/Mo₅Si₃C interface, and the SiC nucleated within the Mo₅Si₃C. As expected, the presence of SiC platelets enhanced the toughness of the MoSi₂ matrix by introducing crack-deflection at reinforcement-matrix interfaces. Mechanically, these inexpensive in-situ formed composites compared quite respectably to materials processed by blending and hot pressing expensive VLS-SiC whiskers and MoSi₂ powder. Effects of temperature on bend strength for the two types of SiC/MoSi₂ composites are presented in Figure 12.

Summary

Inorganic composites, long investigated for elevated temperature structural applications, have found few applications, primarily because of

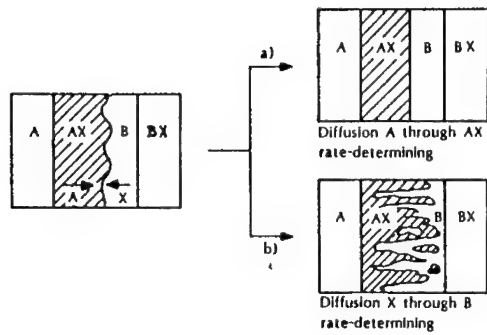


Figure 10 - Effect of the rate-determining diffusing species on morphology of reaction zone in hypothetical diffusion couple A/BX [12]

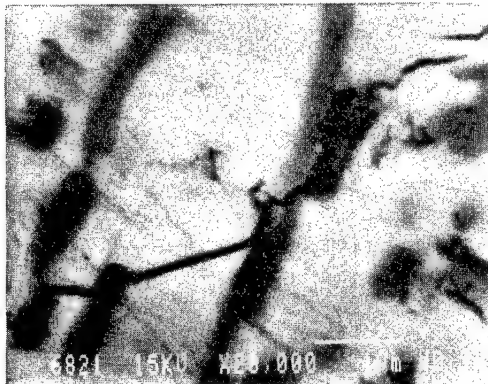


Figure 11 - SiC/MoSi₂ composite formed by solid state displacement reaction between Mo₂C and Si [13]

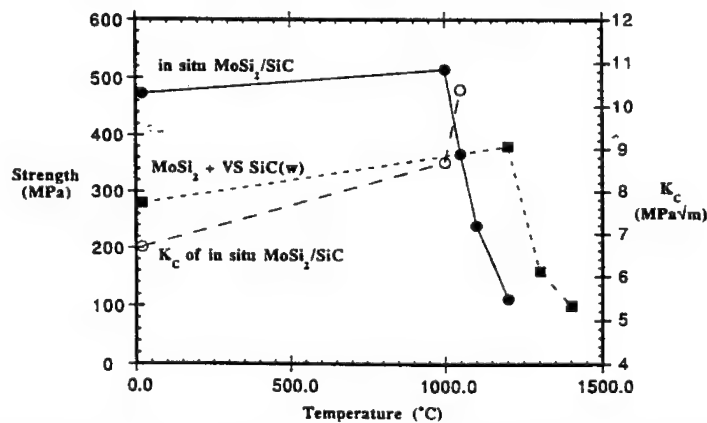


Figure 12- Bend strength and fracture toughness as a function of temperature for SiC/MoSi₂ composites (SiC (w) data from ref. 14) [13]

their great cost. Processing costs in such materials are dominated by the cost of reinforcements and interphase coatings necessary for insuring good mechanical behavior and preventing reactions between matrices and reinforcements. In the past, composites have been fabricated by embedding strong, stiff reinforcements in metallic or ceramic matrices, with little attention paid to constituent reactions, necessitating inclusion of expensive diffusion barrier coatings. By understanding thermodynamics and kinetics of reactions occurring at interfaces between dissimilar materials, and the development of approaches to selecting reaction pathways leading to the nucleation and growth of desirable phases and morphologies, it will be possible to design and process robust in-situ composites, which will not only have attractive engineering properties, but will cost little more than conventional monolithic materials.

References

- [1] Perepezko, J.H., *Compos. Interfaces*, 1, No. 6, 463 (1993).
- [2] Kirkaldy, J.S., Brown, L.C., *Can. Met. Quat.*, 2, 89 (1963).
- [3] van Loo, F.J.J., *Prog. Solid St. Chem.*, 20, 47 (1990).
- [4] Perepezko, J.H., da Silva Bassani, M.H., Park, J.S., Edelstein, A.S., and Everett, R.K., *Matls. Sci. & Eng.*, A195, 1 (1995).
- [5] Novet, T., and Johnson, D.C., *J. Am. Chem. Soc.*, 113, 3398 (1991).
- [6] Edelstein, A.H., Everett, R.K., Richardson, G.R., Qadri, S.B., Foley, J.C., and Perepezko, J.H., *Matls. Sci. & Eng.*, A195, 13 (1995).
- [7] da Silva Bassi, M.H., Perepezko, J.H., Edelstein, A.S., and Everett, R.H., *Matls. Sci. Forum*, *ISMANAM-95*, July 1995, Quebec, to be pub.
- [8] Backhaus-Ricoult, M., *Ber. Bunsenges. Phys. Chem.*, 90, 684 (1986).
- [9] Metselaar, R., and van Loo, F.J.J., *Mater. Sci. Forum*, 34-36, 413 (1988).
- [10] Trumble, K.P., and Ruhle, in M. Ruhle, A.G. Evans, M.F. Ashby, and J.P. Hirth (eds.), *Metal-Ceramic Interfaces*, Pergamon Press, Oxford, 144 (1990).

- [11] Osinski, K., Vriend, A.W., Bastin, G.R., and van Loo, F.J.J.,
Z. Metallkunde, 73, 258 (1982).
- [12] Yurek, G.J., Rapp, R.A., and Hirth, J.P., *Metall. Trans.*, 4, 1293 (1973).
- [13] Henager, C.H., Jr., Brimhall, J.L., and Brush, L.N., *Mats. Sci. & Eng.*,
A195, 65 (1995).
- [14] Carter, D.H., Gibbs, W. S., and Petrovic, J.J., in V.J. Tennery (ed.),
Ceramic Materials and Components for Engines, A. Cer. Soc.,
Westerville, OH, 977 (1989).
- [15] Chang, Y.A., Personal communication.
- [16] Perepezko, J.H., Personal communication.

Interfacial Structure and Properties for the Design of Fiber-Reinforced Metal Matrix Composites

D. B. Miracle, D. B. Gundel*, and S. Warrior[£]

Air Force Wright Laboratory/ Materials Directorate
2230 Tenth St Ste 1
Wright-Patterson AFB, OH 45433 USA

* Systran Corporation
4126 Linden Ave
Dayton, OH 45432 USA

[£] UES, Inc
4401 Dayton-Xenia Rd
Dayton, OH 45432 USA

Abstract

A perspective of the design and development of continuously-reinforced Ti-aluminide composites for gas turbine applications will be presented. While axial properties are generally adequate for anticipated design loads, current Ti-aluminide composites are not able to support the required off-axis loads. Approaches to improving the transverse composite properties emphasize improvements in the matrix response and increasing the ability of the fiber/matrix interface to support a normal load. In spite of the large effort to study interface properties in SiC/Ti-alloy composites, relatively little understanding of the transverse response of the complex interfacial region exists. Such an understanding is critical, so that a rational approach to improved interface properties can be undertaken.

Early studies have suggested that the interfaces typically employed in continuously-reinforced SiC/Ti-alloy composites have no ability to support a normal load beyond that supplied by the compressive radial residual stress. More recent results have shown that these interfaces do indeed possess a significant chemical component to bonding. The experimental and numerical studies which have led to this conclusion will be presented. The ability of typical fiber/matrix interface combinations to support an off-axis load will be quantified, and the sequence of failure for each of the interfacial systems studied will be discussed. The temperature dependence and volume dependence of interface properties will be presented. Comments concerning the structure of C-coatings on the observed properties will be made.

Design Considerations

The current cycle of research and development activity on fiber-reinforced Ti-alloy metal matrix composites (MMC's) was initiated in support of programs to design aerospace vehicles which would travel at many times the speed of sound. These materials were considered candidates for skins and primary structural components by virtue of the high specific strength and stiffness possessed by fiber-reinforced composites in uniaxial form. However, skins require isotropic properties within the plane of the sheet. The cross-ply composite architectures which produce this isotropy negate the beneficial specific strength and stiffness originally offered by the uniaxially-reinforced composites (1). The relatively complex geometry of many of the primary structural components (beams, stiffeners, etc.) provides a barrier to reliable manufacturing, and the payoff for implementing this class of materials in these applications is marginal.

Applications which are subjected to highly directional loading are best able to take full advantage of the properties provided by fiber-reinforced MMC's. Candidate component applications should have a relatively simple geometry to simplify fabrication and design, and should have a high payoff to provide sufficient incentive for the high cost and risk associated with the development and implementation of a new materials technology. Compressor ring rotors in advanced gas turbine engines satisfy these requirements. The loading is principally along the circumferential direction of the compressor rings, with small but significant loads along the radial direction of the rings (normal to the fiber axes). The hoop shape is relatively simple, providing several options for manufacturing. The payoff for the implementation of fiber-reinforced MMC compressor ring rotors is quite significant.

The axial mechanical properties of uniaxially-reinforced MMC's are generally adequate for the ring rotor application. However, the response of these same materials loaded transverse to the fiber axes are very poor- much poorer in fact than the unreinforced matrix alloy (1). Thus, efforts to develop these materials for compressor ring rotor applications must address the behavior of the matrix and interface, since these constituents dominate the transverse response of axially-reinforced composites. A reasonably clear understanding of the influence of matrix properties on the transverse properties of MMC's is available, and current efforts are now focusing on developing matrix alloys with an appropriate balance of physical and mechanical properties for this application. However, a rather poor understanding of the transverse properties of the interfacial region, and the features that control this response, has slowed progress. The purpose of this manuscript is to describe recent efforts to understand and characterize the interfacial region in SiC-reinforced Ti-alloy composites for compressor ring rotor applications. The mechanical response of model composites will be presented, along with a determination of the properties of the interfacial region and a description of the modes of failure. The features which influence the properties of the interfacial region will be presented and discussed.

Introduction

The interfacial region in SiC/Ti-alloy composites is complex, and may consist of several different interfaces and interphases. Three typical interfacial regions are illustrated in Figure 1; that of an uncoated SiC fiber in a Ti-alloy matrix, a C-coated SiC monofilament, and a SiC fiber with a graded C+SiC coating (such as SCS-6). The carbide phase is typically a non-stoichiometric titanium carbide (TiC_{1-x}), and the silicide phase is a complex ternary or quaternary phase based on the Ti_5Si_3 ordered binary compound (2). The detailed nature of the different interfaces themselves, such as the atomic structure, local chemistry, and the nature of bonding, are not known at all; only simplified model interfaces are thus far capable of being studied via computational or high-resolution electron microscopy techniques. The composition and structure of C-based fiber coatings has been studied in detail only for the SCS-6 fiber coating (3,4).

To measure the interface properties, full account of the residual stresses developed upon cooling from the processing temperature must be made. While a large compressive radial residual stress exists throughout the composite, the magnitude of this stress decreases near the free surface, and becomes a large tensile stress at the free surface (5). Although direct observation of interface failure resulting from this stress singularity has not been reported, it is likely that some form of damage does occur. Upon loading, physical separation of the fiber/matrix interface at the free surface has been observed by several techniques (6-9), and typically occurs at an applied far-field stress below 200 MPa. Further, this separation stress is the same for each of the interfacial

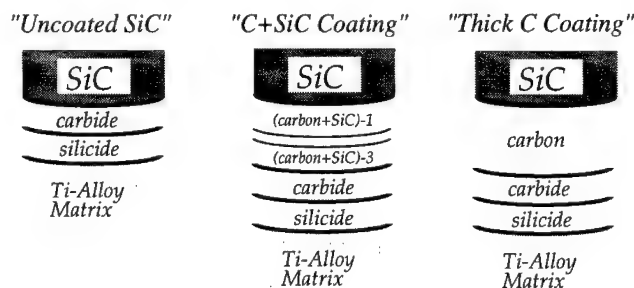


Figure 1 Schematic representation of the complex interfacial region in three characteristic SiC/Ti-alloy composites. The simplest of these, the uncoated SiC, has three distinct interfaces and two interphases. Other systems are more complex.

systems shown in Figure 1, and so this technique does not distinguish between interfaces with dramatically different shear properties. Finally, stable growth of the damage at the free surface has been determined in wide SiC/Ti-6242 samples (25 mm). Five strain gages were placed across the sample width. Non-linearity (interface separation) was measured at ~150 MPa at the edges, at about 200 MPa midway to the center, and the central strain gage registered a linear response (no interface separation) up to 350 MPa, the highest stress applied. Non-destructive investigation of similar single-fiber samples has corroborated this result by showing a progressive debond at the interface which grows inward from the free edge in response to increasing applied stress. It is thus concluded that transverse response in the straight-sided samples is dominated by the stress singularity at the free surface. Tests using narrow samples (≤ 20 mm), or tests which monitor sample strain by clamping at the edge of the composite panel are most susceptible to this effect.

Test Methodology

A cruciform sample has recently been employed to apply a transverse mechanical load without applying a mechanical stress at the free surface. The relevant features of the sample are shown in Figure 2. A detailed description of the sample preparation, test methodology, and stress analysis appears elsewhere (10-12). This manuscript will describe the results for nine different interfacial systems. Single-fiber cruciform samples of each of the nine fibers listed in Table I were produced as reported elsewhere (10-12). In all cases, the matrix alloy was Ti-6Al-4V (wt %). Duplicate tests were typically performed- where an error is specified in Table I, as many as 15 data points were collected. Tensile tests were performed at room temperature, and a limited number of tests were performed at elevated temperature.

Results

Stress/Strain Response

Typical stress/strain responses for three single-fiber cruciform samples, representing the three classes of interfacial regions in Figure 1, are shown in Figure 3. Each of the three systems remain linear to ~200 MPa and display a similar modulus. Just above 200 MPa, some C-coated fibers (Sigma 1140+ and 1240, and Trimarc) as well as a Y-coated SiC fiber display a smooth transition to non-linear behavior. The AC1 C-coating, as well as the graded C+SiC interfaces (the double-pass SCS-6 and the single-pass graded C+SiC coating, SCS-6 SP) remain linear to above 320 MPa, after which two distinct unstable events are observed. The stress at which these unstable events occur was repeatable, and varied for the different interfaces. Acoustic emission (AE) signals are detected at each of these events. After the second event, a non-linear response is observed. Uncoated SiC fibers (SCS-0, ACMF) display a linear response to ≥ 450 MPa, followed by a smooth transition to a non-linear curve. A single large instability is typically observed above 550 MPa, followed by a linear response with a significantly reduced stiffness. The stresses at which the non-linearity and the instability initiate are reproducible, and are different for the two systems. The data are presented in Table I.

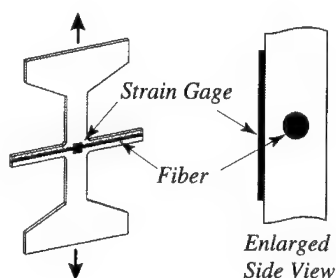


Figure 2 Schematic drawing of the cruciform sample used in the present studies.

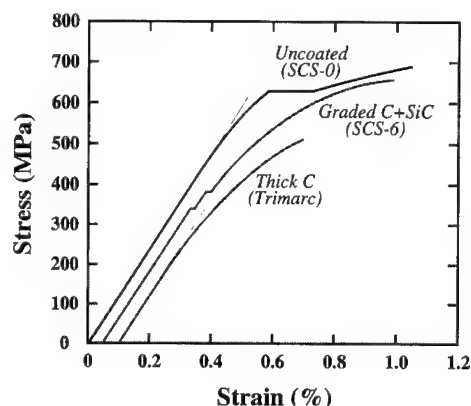


Figure 3 Typical stress/strain plots for samples which represent a weak interface bond (Trimarc), an intermediate interface bond (SCS-6), and a strong interface bond (SCS-0). The plots are offset along the strain axis for clarity.

Table I Summary of Interface Characteristics and Mechanical Properties

	Interface Coating	Non-Linear Stress (MPa)	Instability Stress (MPa)	Max Normal Stress (MPa)	Max Shear Stress (MPa)	Torsion Shear Strength (MPa)
TEXTRON						
SCS-0	None	520±47	635	>380	>310	>80
SCS-0 + Y	Y (0.5 µm)	205	N/A	~0	125	
SCS-6	Graded C+SiC (~4µm)	322±14	322±14	120	190	50
SCS-6 SP	Graded C+SiC (2µm)	398	398	220	240	
AMERCOM						
ACMF	None	450	550	>290	>270	
ACI	'Hard' C (~2 µm)	362	362	170	220	40
Trimarc	'H-S-H' C* (~3µm)	232±21	N/A	~0	140	
DRA/SIGMA						
I140+	C (3-5µm)	205±20	N/A	~0	125	
I240	C-TiB ₂ (~3 µm)	220±23	N/A	~0	130	

* 'H-S-H' is a three-layer coating of 'hard'-'soft'-'hard' carbon

Failure Site

Only two failure sites were observed for all of the interfacial regions containing a carbonaceous coating; at the C/TiC_{1-x} interface (Figure 4 (a)), or within the C-coating (Figure 4 (b)). None of the other interfaces or interphases showed any signs of damage. Well-consolidated samples often displayed failure at both locations (Figure 4 (b)). Failure within the C layer is typically poorly defined and difficult to detect. Samples that were incompletely consolidated always showed failure only at the C/TiC_{1-x} interface. Interface separation at a free surface is also observed only at the C/TiC_{1-x} interface, and so it is concluded that this location is favored when a stress concentration exists at the interface. Three failure sites are seen for uncoated SiC (Figure 4 (c)); at the SiC/TiC_{1-x} interface, within the SiC fiber, and radial cracking within the TiC_{1-x}.

Mechanical Properties of the Interfacial Region

The residual stress at the interfacial region in the center of the cruciform is comprised of a compressive radial residual stress that is about -300 MPa (11). This stress is uniform around the periphery of the fiber. There are no significant residual shear stresses (axial or tangential) (11). The applied mechanical stress is superposed over the residual stress, and introduces tangential shear and radial stresses that vary around the fiber periphery. The maximum tensile stress occurs where the interface normal is parallel to the applied stress ($\theta=0^\circ$), and the maximum tangential shear stress occurs where the interface normal is inclined at about 45° to the tensile axis. A detailed numerical analysis of the local stresses appears elsewhere (13). However, the interface stress (σ_{int}) at these two locations is well-represented by the following equation:

$$\sigma_{\text{int}} = k(\sigma_{\text{appl}}) + \sigma_{\text{res}} \quad (1)$$

where σ_{appl} is the applied mechanical stress, σ_{res} is the residual stress, and k is a stress concentration factor. For the radial interface stress at $\theta=0^\circ$, $\sigma_{\text{res}} = -300$ MPa and $k \approx 1.3$. The tangential shear stress at $\theta=45^\circ$ is given by $k \approx 0.6$ and $\sigma_{\text{res}} = 0$.

The local maximum shear and normal stresses supported by the interfacial regions studied (Table I) were determined with the equation above, where σ_{appl} is the non-linearity stress. Several C-coated systems (Trimarc, 1140+, and 1240) and the Y-coated fiber become non-linear as soon as the radial stress becomes tensile ($\sigma_{\text{int}} = 0$). However, significant tensile radial stresses are supported by the AC1 interface, by the C+SiC graded interfaces (SCS-6 and SCS-6 SP), and by uncoated SiC interfacial regions (ACMF and SCS-0). The C-based coatings can support tensile stresses from 120 MPa to 220 MPa.

At $\theta=0^\circ$ and 90° , there are no mechanical or residual shear stresses, so the stress state is well-represented by a simple radial stress. However, mixed-mode loading occurs elsewhere around the fiber periphery. At $\theta=45^\circ$, the stress is dominated by a tangential shear stress resulting from the applied stress. Therefore, an independent means of determining the response of the interfacial region under tangential shear is required to help distinguish between shear and normal failure. Single-fiber composites have been tested in torsion, and this test applies a tangential shear stress but no significant radial stresses (14). The tangential shear strength of selected interfacial regions determined from these torsion tests are summarized in Table I, and will be discussed later.

Temperature and Volume Dependence of Interfacial Properties

Studies of a statistically significant number of SCS-6/Ti-6Al-4V interfaces has recently been completed (12). The data are plotted on a single-parameter Weibull plot (Figure 5). When data from only well-consolidated samples (containing no processing defects) are considered, a Weibull modulus of about 27 is obtained. This rather large value suggests that the measured interface values are less sensitive to volume effects than many ceramic materials, including the SiC fiber itself. The results of limited testing at elevated temperature show a decrease in σ_{appl} required for debonding (Figure 6). This decrease is accounted for by the reduced magnitude of the radial residual stress at the test temperature. However, the chemical component of the bond in the interfacial region remains essentially constant. This is not surprising, since the two failure sites in the interfacial region, the C-coating itself and the C/TiC_{1-x} interface, are ceramic constituents, and the chemical bond is not expected to change significantly at this low homologous temperature and over a limited temperature interval.

Discussion

Sequence of Failure in the Interfacial Region

The results from torsional testing suggest that the C-based coatings fail at an applied tangential shear stress of about 50 MPa. The graphite in the SCS-6 coating has been determined to have a preferred orientation, with the basal planes normal to the radial direction of the fiber (3,4). Therefore, the tangential shear properties of this coating may be similar in magnitude to the axial shear properties. While other C-based coatings have not been analyzed in detail, similarities in the deposition process suggest that some degree of alignment may exist in these systems as well. Axial interfacial shear strengths for composites with the SCS-6 fibers have been determined from the fiber pushout technique, which range from 100-150 MPa (15,16). Torsional test values should not be directly comparable to values obtained by other techniques, since large-scale

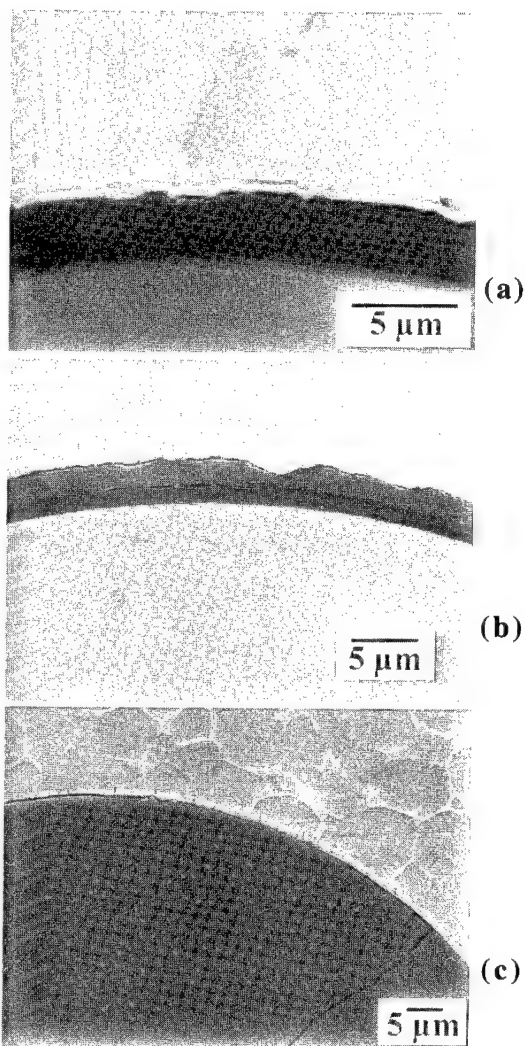


Figure 4 Interfacial failure (a) at the C/TiC_{1-x} interface in an SCS-6 fiber; (b) within the C-coating and at the C/TiC_{1-x} interface of a Trimarc fiber; and (c) within the SiC fiber and the TiC_{1-x} reaction zone, and at the SiC/TiC_{1-x} interface of a typical SCS-0 interfacial region.

sliding occurs in fiber push-out tests, but the sliding distance is very small in torsional testing; also, other techniques impose different degrees of normal interface stresses in addition to the shear stresses. Even so, the values obtained from torsional testing are quite small.

In spite of the uncertainty in the magnitude of the tangential shear strength of C-based coatings, it can be concluded that some C-based coatings (the graded C+SiC and AC1) fail first by tangential shear, since the local shear stress at the interfacial region for these systems is larger than measured shear strength values. The critical failure event for the remaining C-coatings (Trimarc,

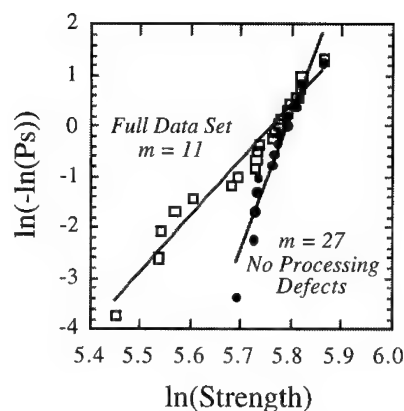


Figure 5 Weibull plot of the interface strength for the full data set, and for a reduced data set where samples with processing defects were removed.

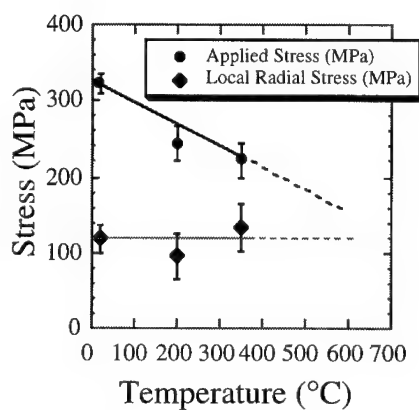


Figure 6 Temperature dependence of the applied stress required for interface debonding, and the resulting local interface radial stress, or interfacial tensile strength.

1140+, and 1240) and the Y-coating is uncertain, and depends upon the exact value of the tangential shear strength of the interfacial region. A lower shear strength, as suggested by the torsion testing or by the lower range of values obtained from fiber push-out, would suggest that shear failure occurs first in these systems, and is followed by separation of the interface later in the test.

Thus, the sequence of failure in the interfacial region can be discussed. Starting with "weak" interfacial regions (SCS-0+Y, Trimarc, 1140+, and 1240), normal separation of the interfacial region occurs as soon as the radial stress at $\theta=0^\circ$ becomes tensile. This is true whether or not the interface fails first in shear at $\theta=45^\circ$. The radial stress becomes tensile at an applied stress of about 230 MPa. At this critical stress, the local radial stress for $\theta>0^\circ$ is still compressive, and so the Mode I crack at $\theta=0^\circ$ will grow in a stable fashion, and the periphery of the interface will be pulled apart gradually with increasing σ_{appl} . This behavior will lead to a smooth transition from linear response to non-linearity of the stress/strain curve, as observed experimentally. Failure occurs within the C-coating itself, or at the C/TiC_{1-x} interface. Recent FEM studies have shown that if tangential shear failure precedes tensile failure of the fiber/matrix interface, then the stresses are redistributed around the periphery of the fiber, so that a tensile stress is achieved at $\theta=0^\circ$ at a lower σ_{appl} (17).

C-based interface coatings with an intermediate strength (SCS-6, SCS-6 SP, and AC1) are likely to fail first by tangential shear at $\theta=45^\circ$, as discussed above. This Mode II crack grows stably with increasing σ_{appl} , since the shear stress decreases away from $\theta=45^\circ$ and the radial stresses are still compressive. A large unsheared ligament remains, and this supports a tensile stress at $\theta=0^\circ$ after σ_{appl} exceeds 230 MPa. Eventually the unsheared ligament fails- either by exceeding the ability of the interfacial region to support a tensile stress, or by superposing a Mode I tensile force at the tip of the existing Mode II crack. In either case, the remaining ligament will fail in an unstable fashion. Since a net local tensile stress exists, the interface will physically separate immediately after this failure event, and a discontinuous increase in strain is expected to occur. This is experimentally observed. Two unstable events are typically observed for each sample, and so sufficient load transfer must occur due to the unsheared ligament around $\theta=90^\circ$ (the shear stress is zero and the radial stresses remain compressive throughout the test at this point).

The two weakest components of the interfacial regions described above (the C layer and the C/TiC_{1-x} interface) are absent in the uncoated SiC fiber systems (SCS-0 and ACMF), and so interfacial failure is observed at a much higher σ_{appl} . The mechanisms responsible for the observed behavior are different than for the preceding interfacial systems. The stable transition to a non-linear response above 450 MPa is not due to tensile failure of the interface, since post-test metallography of interrupted tests shows no separation. Numerical stress analysis shows that the local effective matrix stresses are below the yield point, and so matrix plasticity is not anticipated. Post-test metallography has shown radial cracking of the TiC_{1-x} reaction layer, and AE signals during the test suggest that this cracking occurs at 400 MPa. While the exact sequence of events is uncertain, the following is proposed. These radial reaction zone cracks induce a stress concentration in the matrix, and at the SiC/TiC_{1-x} interface. Localized slip occurs in the matrix; such slip at radial reaction zone cracks has been reported by others (7,18). This localized plasticity produces the observed inelastic response above 450 MPa. As slip progresses, the stress concentration at the other tip of the radial crack (at the SiC/TiC_{1-x} interface) increases until fracture of the SiC fiber occurs, producing the AE signal and the large instability. The role of failure at the SiC/TiC_{1-x} interface is not yet understood. Additional FEM studies and interrupted transverse tests are now underway to investigate this proposed sequence of events.

While tangential shear failure is expected to occur in several systems, it is important to point out that the resulting shear displacements are very small (19,20), and are not detected in the current studies. In fact, these displacements are sufficiently small (less than 1 μm) so that most techniques will not detect the occurrence of this mode of damage. The principle impact of this damage is to redistribute stresses around the fiber periphery, and to hasten the onset of tensile interface failure. The larger displacements associated with the normal separation of the interface, and the attendant matrix plasticity, are easily detected with the surface-mounted strain gage, and by other techniques typically employed in transverse tensile testing.

Influence of the Structure of C-Coatings

The C-based coatings studied in the present work show a broad range of mechanical properties. Subtle differences in the composition or structure of the C-based fiber coatings may influence the atomic bonding, and hence the mechanical properties, of the C/TiC_{1-x} interface. However, a rational discussion of this possibility is beyond our current ability to understand and model bonding at such a complex interface.

The atomic bonding in the C (graphite) crystal lattice consists of very strong sp^2 hybrid bonds within the basal plane, and weak π bonds normal to the basal planes. Thus, the physical and mechanical properties of graphite are highly anisotropic- it is very strong and stiff within the basal plane, and is weak and compliant along the c-axis. Significant variations in the microstructure of C-based materials, such as the turbostratic C used to coat SiC fiber, can be achieved, and these variations have a profound influence on the properties of the coating. Microstructural parameters which can influence the mechanical properties include the crystallite size of the basic structural units (BSU's) which comprise the C-coating, the degree of alignment of the BSU's, and the degree of cross-linking.

Only the SCS-6 coating has been studied in any detail, and it has been shown that the c-axes of the BSU's are reasonably well-aligned with the radial direction of the SiC fiber (3,4). This suggests that shear within the plane normal to the radial direction should be relatively easy. As stated earlier, while other C-based coatings may also possess some degree of preferred alignment, thus providing broad similarities in mechanical response to the SCS-6 system, differences in the degree of alignment from one system to another can have a strong influence on the magnitude of the interfacial properties. Within the 2-4 μm thick SCS-6 coating, there are as many as five distinct layers, and these layers themselves have been shown to possess different degrees of crystal alignment (3).

The extent of cross-linking, or the formation of strong bonds between basal planes, can be influenced by the deposition parameters used to produce fiber coatings. A higher proportion of crystal defects, or the presence of impurities such as oxygen, can increase the number of such bonds significantly. Variations in the proportion of cross-linked bonds is expected to have a very strong influence on the shear and tensile properties of the C coating. Product literature for several of the C-based coatings claim that the C is 'soft' (that is, fully graphitizable), or 'hard' (that is, cannot be fully graphitized due, in part, to the number of strong bonds between basal planes). However, this parameter has not been probed for any of the C-based coatings of current interest, and such terminology must be considered with care. Even within the studies reported here, it is difficult to consider the influence of such claims on the measured interfacial properties, since differences in the structure of the coating may have an important influence on the bonding at the C/TiC_{1-x} interface. Careful study of the structure of such coatings, coupled with measurements of the interfacial response, is required to understand more fully the possible influence of coating structure on the mechanical response of the interfacial region in SiC/Ti-alloy composites.

Implications for the Design of Fiber Coatings

The balance of interface properties required to produce an MMC with adequate off-axis properties and crack-bridging response is not yet known. The work presented here has taken the view of understanding the interface response when subjected to transverse loading, with the intent of improving this response. However, an increase in the transverse strength of the interface may result in a decrease in other properties influenced by the interface, such as crack deflection and crack bridging. In this regard, it is significant that the current studies have found that some interfaces already possess a significant intrinsic ability to support off-axis loads, and that earlier reports to the contrary are the result of sample geometry. Thus, several existing interfaces (such as SCS-6) may already possess adequate off-axis properties, and earlier studies have shown these interfaces to provide adequate crack-bridging response. Composites containing a high volume fraction of reinforcements are currently being tested in transverse tension and creep to determine if existing interfaces possess adequate transverse creep response in the cruciform geometry.

Concluding Remarks

It has been shown that the interfacial region in SiC/Ti-alloy composites possess a range of mechanical responses. Some C-based coatings are not able to support any tensile mechanical stress. It is not yet clear whether failure of these interfacial regions initiates from tangential shear stresses which are induced during transverse testing, or from tensile radial stresses. Several C-based coatings can sustain significant tensile stresses- up to 220 MPa. In these latter systems, failure in the interfacial region initiates via tangential shear, but this damage does not lead directly to the failure of the composite. The principle effect of shear failure is to redistribute the interfacial stresses, accelerating the tensile overload of the interface. The locus of failure in well-consolidated samples is either within the C-coating, or at the C/TiC_{1-x} interface, or at both of these locations. Uncoated SiC fibers bond strongly to the Ti-alloy matrix. Failure of the interfacial region is proposed to initiate with radial cracking of the TiC_{1-x} reaction layer, followed by localized slip in the matrix and fracture of the SiC fiber. A small volume dependence has been measured for fully consolidated samples. There is no significant effect of test temperature on the magnitude of the chemical bond in SCS-6/Ti-6Al-4V composites up to 350°C.

Further studies are suggested to establish the competition between shear failure and tensile failure in the interfacial region. Similarly, the competition between failure of the C-coating itself, and failure of the C/TiC_{1-x} interface need to be resolved. Tests are proposed to establish the sequence of damage and failure for uncoated SiC systems. Careful characterization of the various C-based fiber coatings, including the degree of alignment of the basic structural units and the degree of cross-linking present, is required to firmly establish the influence of the properties of the C coatings on the properties and response of the interfacial region.

Acknowledgements

The authors would like to thank B. Majumdar (UES, Inc.) for many stimulating discussions concerning the information presented in this manuscript. We would also like to acknowledge C. Boehlert (UES, Inc.) for assistance with some of the testing performed. Finally, we would like to extend our gratitude to Textron Specialty Materials, Atlantic Research Corp., and DRA/Sigma for supplying fiber for evaluation.

References

1. J.M. Larsen, S.M. Russ, and J.W. Jones; "An Evaluation of Fiber-Reinforced Titanium Matrix Composites for Advanced High Temperature Aerospace Applications", *Metall. Trans. A*, Submitted for publication
2. C.G. Rhodes; "Characterization of Fiber/Matrix Interfaces by Transmission Electron Microscopy in Titanium Aluminide/SiC Composites", in *Intermetallic Matrix Composites II*, (eds. D.B. Miracle, D.L. Anton, and J.A. Graves), MRS Symp. Proc., 273, 17 (1992)
3. X.J. Ning and P. Pirouz; "The Microstructure of SCS-6 SiC Fiber", *J. Mater. Res.*, **6**, 2234 (1991)
4. E.L. Hall and A.M. Ritter; "Structure and Behavior of Metal/Ceramic Interfaces in Ti Alloy/SiC Metal Matrix Composites", *J. Mater. Res.*, **8**, 1158 (1993)
5. R.D. Kurtz and N.J. Pagano; "Analysis of the Deformation of a Symmetrically-Loaded Fiber Embedded in a Matrix Material", *Compos. Eng.*, **1**, 13 (1991)
6. W.S. Johnson, S.J. Lubowinski, and A.L. Highsmith; "Mechanical Characterization of Unnotched SCS-6/Ti-15-3 Metal Matrix Composites at Room Temperature", in *Thermal and Mechanical Behavior of Metal Matrix and Ceramic Matrix Composites*, ASTM STP 1080, (eds. J.M. Kennedy, H.H. Moeller, and W.S. Johnson), ASTM, Philadelphia, 193 (1990)

7. B.S. Majumdar and G.M. Newaz; "Inelastic Deformation of Metal Matrix Composite: Plasticity and Damage Mechanisms", *Phil. Mag. A*, **66**, 187 (1992)
8. D.B. Marshall, W.L. Morris, B.N. Cox, J. Graves, J.R. Porter, D. Kouris, and R.K. Everett; "Transverse Strengths and Failure Mechanisms in Ti_3Al Matrix Composites", *Acta Metall. Mater.*, **42**, 2657 (1993)
9. L.L. Shaw and D.B. Miracle; "Effects of Fiber Distribution on the Transverse Tensile Ductility of Unidirectional SiC/Ti-6Al-4V Composites", *Scripta Mater.*, Submitted for publication
10. D.B. Gundel, B.S. Majumdar, and D.B. Miracle; "Evaluation of the Transverse Response of Fiber-Reinforced Composites Using a Cross-Shaped Sample Geometry", *Scripta Metall. Mater.*, **33**, 2057 (1995)
11. S.G. Warrier, D.B. Gundel, B.S. Majumdar, and D.B. Miracle; "Stress Distribution in a Transversely Loaded Cross-Shaped Single Fiber SCS-6/Ti-6Al-4V Composite", *Scripta Mater.*, **34**, 293 (1996)
12. D.B. Gundel, S.G. Warrier, and D.B. Miracle; "The Interface Debond Stress in Single and Multiple SiC Fiber/Ti-6Al-4V Composites Under Transverse Tension", *Acta Mater.*, Accepted for publication
13. S.G. Warrier, D.B. Gundel, B.S. Majumdar, and D.B. Miracle; "Interface Effects of the Micromechanical Response of a Transversely Loaded Single Fiber SCS-6/Ti-6Al-4V Composite", *Metall. and Mater. Trans. A*, In Press
14. S.G. Warrier, B.S. Majumdar, and D.B. Miracle; "Determination of the Interface Failure Mechanism During Transverse Loading of Single Fiber SiC/Ti-6Al-4V Composites from Torsion Tests", *Acta Mater.*, In Press
15. J.I. Eldridge; "Fiber Push-out Testing of Intermetallic Matrix Composites", in *Intermetallic Matrix Composites II*, (eds. D.B. Miracle, D.L. Anton, and J.A. Graves), MRS Symp. Proc., 273, 325 (1992)
16. C.J. Yang, S.M. Jeng, and J.-M. Yang; "Interfacial Property Measurement for SiC Fiber-Reinforced Titanium Alloy Composites", *Scripta Metall. Mater.*, **24**, 469 (1990)
17. S.G. Warrier, B.S. Majumdar, D.B. Gundel, and D.B. Miracle; "Implication of Tangential Shear Stress Induced Failure During Transverse Loading of SiC/Ti-6Al-4V Composites", *Acta Mater.*, Submitted for publication
18. S. Jansson, H.E. Deve, and A.G. Evans; "The Anisotropic Mechanical Properties of a Ti-Matrix Composite Reinforced with SiC Fibers", *Metall. Trans. A*, **22**, 2975 (1991)
19. P.D. Jero and R.J. Kerans; "The Contribution of Interfacial Roughness to Sliding Friction of Ceramic Fibers in a Glass Matrix", *Scripta Metall.*, **24**, 2315 1990
20. R.J. Kerans; "The Role of Coating Compliance and Fiber/Matrix Interfacial Topography on Debonding in Ceramic Composites", *Scripta Metall.*, **32**, 505 1995

HIGH FREQUENCY FATIGUE OF CONTINUOUS FIBER REINFORCED

CERAMIC MATRIX COMPOSITES*

N. Chawla[#] and J.W. Holmes⁺

Ceramic Composites Research Laboratory
University of Michigan
Ann Arbor, MI 48109

Abstract

A brief review of the high frequency fatigue behavior of continuous fiber ceramic composites (CFCCs) is presented. The fatigue of unidirectional and woven composites tested at frequencies of up to 350 Hz is described. It is shown that the reinforcing architecture and the nature of the fiber/matrix interface play key roles in determining the high frequency fatigue behavior of ceramic composites. Models were developed that correlated the interfacial shear stress at the fiber/matrix interface with the amount of heat generated by a specimen due to frictional sliding of debonded fibers. Damage mechanisms in unidirectional and woven composites subjected to high frequency fatigue are also presented and discussed.

* Research supported by the Air Force Office of Scientific Research (AFOSR) and the National Science Foundation (NSF).

[#]Graduate research assistant, Department of Materials Science and Engineering

⁺Associate Professor, Department of Mechanical Engineering and Applied Mechanics

Introduction

In many potential applications such as turbine engines and gas heat exchangers, continuous fiber ceramic composites (CFCCs) will encounter cyclic loading at high frequencies (75 Hz or higher) [1-3]. While most of the work in the area of fatigue of CFCCs has concentrated on low frequency behavior [4-6], it has been shown that fatigue at high frequencies can exacerbate the accumulation of microstructural damage and significantly decrease fatigue life [1-3].

This paper provides a brief review of the high frequency fatigue behavior of CFCCs. We begin with the simplest of systems, a unidirectional Nicalon fiber-reinforced calcium aluminosilicate (CAS) matrix composite, and then progress to composites with more complex fiber architectures. These include an eight-harness satin Nicalon fabric reinforced Si-C-O-N matrix composite (made by polymer infiltration and pyrolysis) and a plain weave Nicalon fabric-reinforced SiC with a carbon interface (made by chemical vapor infiltration). It will be shown that the reinforcing architecture and the nature of the fiber/matrix interface play key roles in determining the high frequency fatigue behavior of ceramic composites.

High Frequency fatigue in Unidirectional CFCCs

Nicalon/CAS

In the earliest high frequency experiments with CFCCs, Holmes et al. [1-2] investigated the effect of high frequencies on the internal heating and fatigue life of Nicalon/CAS composites. In their experiments, 0° composites were subjected to loading frequencies from 10 to 350 Hz. Due to the frictional sliding of fibers during cyclic loading, a significant amount of energy was dissipated, resulting in a substantial increase in the surface temperature of the composite. At a frequency of 350 Hz and maximum stress of 240 MPa, surface temperatures on the order of 160 K were observed (at the fiber/matrix interface, it is estimated that the temperature increase would be higher).

The temperature rise due to frictional heating can substantially affect the mechanical behavior of a composite. Differences in the coefficients of expansion between fiber, matrix, and fiber coating can cause residual clamping stresses on the fiber from the matrix, directly affecting the shear stresses at the interface. Wear of asperities along debonded interfaces, which is expected to change with sliding velocity, clamping pressure and temperature, can also cause changes in the interfacial shear stress, τ . Thus, the interfacial shear stress, one of the most critical parameters that influences toughness, damage tolerance, and strength in CFCCs is inherently frequency dependent.

The fatigue life of Nicalon/CAS was also significantly dependent on loading frequency [2]. With increasing frequency a significant decrease in fatigue life was observed, Fig. 1. It is believed that more accelerated wear of the fiber/matrix interface takes place at higher frequencies, making the reinforcing fibers susceptible to stress concentrators that induce failure in the composite.

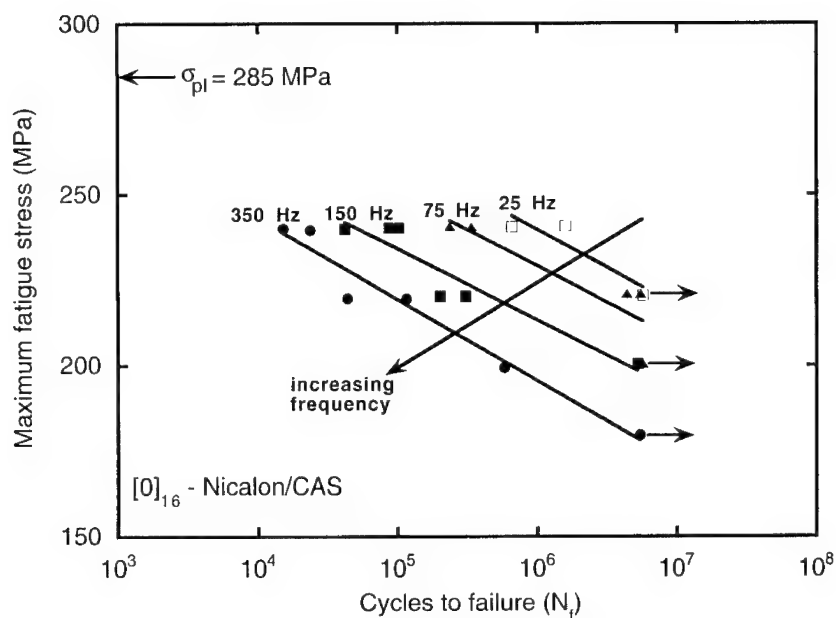


Figure 1. Effect of loading frequency on the fatigue life of unidirectional Nicalon/CAS [2]. Note significant decrease in fatigue life with increasing frequency.

In order to improve the fatigue life of the composite, the characteristics of the fiber/matrix interface would have to be changed to reduce the rate of wear during fatigue. One way of achieving this would be to "lubricate" the interface, so that during fatigue the rate of interface wear and fiber damage would be decreased. In an attempt to directly lubricate the interface in Nicalon/CAS, Sorensen and Holmes [3] statically produced an array of matrix cracks and gradually infiltrated oil into a specimen. A comparison of the temperature rise in dry and lubricated Nicalon/CAS specimens is shown in Fig. 2. The temperature of the dry specimen exhibited a steady increase until a maximum was reached, and then the temperature decreased until failure. The damage evolution in the dry Nicalon/CAS can be explained as follows. During the initial stages of fatigue, matrix cracking was followed by localized debonding of the fibers at the interface. With increasing slip, more energy was dissipated and the specimen temperature increased. Gradually, the fiber debond lengths became quite large, and significant sliding and wear at the fiber/matrix interface began to take place. After the specimen temperature reached a maximum, it began to decrease until failure of the composite. The decrease in temperature, which mirrors a slight recovery in modulus of the composite in this stage of fatigue, was postulated to be caused by an increase in the frictional shear stress at the interface. Such an increase in τ could be caused by accumulation of debris or the trapping of asperities at the fiber/matrix interface. With the addition of the lubricating layer of oil, less abrasion and wear at the interface seemed to be taking place, thus increasing the fatigue life of the composite.

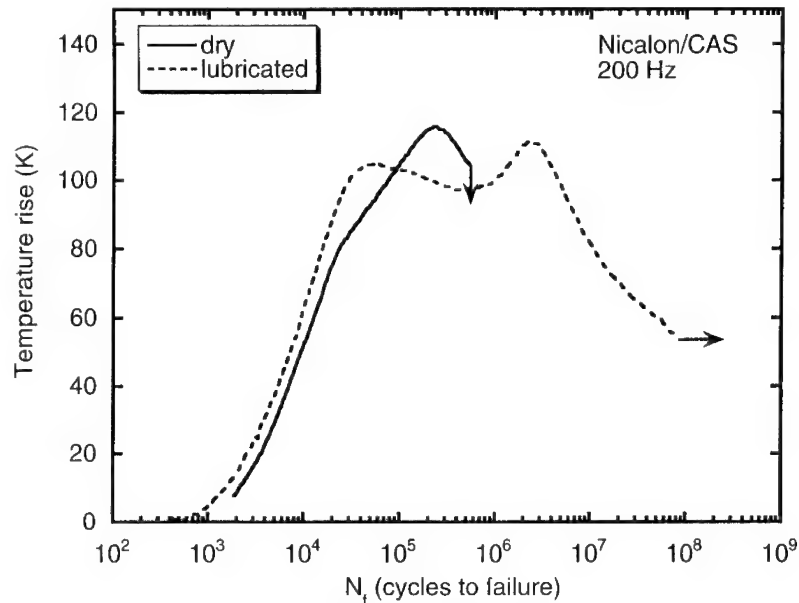


Figure 2. Comparison of temperature rise in dry and "lubricated" unidirectional Nicalon/CAS [3]. The lubricated specimen had a significantly longer life than the dry specimen.

High Frequency Fatigue in Woven CFCCs

The mechanisms of damage during fatigue of woven CFCCs are much more complex than those in unidirectional materials [7,8,10]. Because of the woven nature of the fabric, most of the damage takes place at crossover points in the weave where stress concentrations exist. Furthermore, due to the laminated nature of these materials and the inherent residual porosity from processing, linkage of cracks usually results in interlaminar shear failures.

Eight-harness satin Nicalon/Si-C-O-N

Chawla et al. [7] studied the fatigue behavior of an eight-harness satin weave Nicalon fabric reinforced Si-C-O-N matrix composite made by polymer infiltration and pyrolysis (PIP). The fibers were coated with a proprietary B-containing coating, which created a relatively strong bond between the fiber and the matrix. From fiber pushout tests, the debond initiation stress was about 900 MPa and the interfacial shear stress about 35 MPa [9]. During and after the fatigue test, through-cracks in the transverse bundles were not observed, although cracking was present in the vicinity of crossover points. This lack of transverse bundle damage was attributed to the matrix being soft and compliant. Thus, since debonding and interfacial sliding were not predominant, the lack of fiber sliding resulted in substantially less frictional heating than that observed in weakly bonded composites.

Most of the stiffness reduction in Nicalon/Si-C-O-N occurred in the first fatigue cycle. The major driving force for fatigue failure appeared to be the localized debonding of transverse and longitudinal plies at the crossover points in the fabric, which, when linked, promoted interlaminar damage and failure in the composite, Fig. 3. At stresses at which the composite did not fail, debonding at the crossover sites

resulted in alignment of the weave. This effect of reducing the stress concentrations at the debonded sites, may have been responsible for higher post-fatigue strength than that of the virgin material. This observation is similar to that of Shuler et al. who witnessed the same behavior in a plain weave C/SiC system [10]. Figure 4 shows a schematic of the weave-alignment processes that are thought to be operating during fatigue of woven composites. Microstructural observations of the matrix damage at crossover points of longitudinal and transverse fiber bundles is shown in Fig. 5.

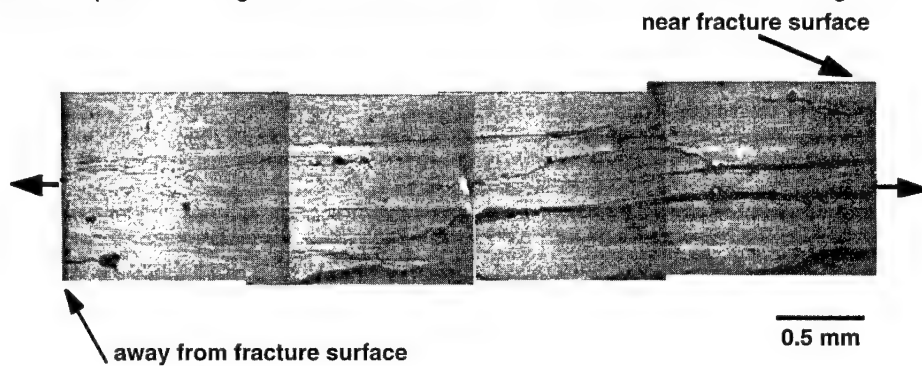


Figure 3. Interlaminar damage observed in the gage section of a failed woven Nicalon/Si-C-O-N composite [7]. Linkage of localized debonding cracks at crossover points in the fiber fabric promoted interlaminar damage and failure in the composite.

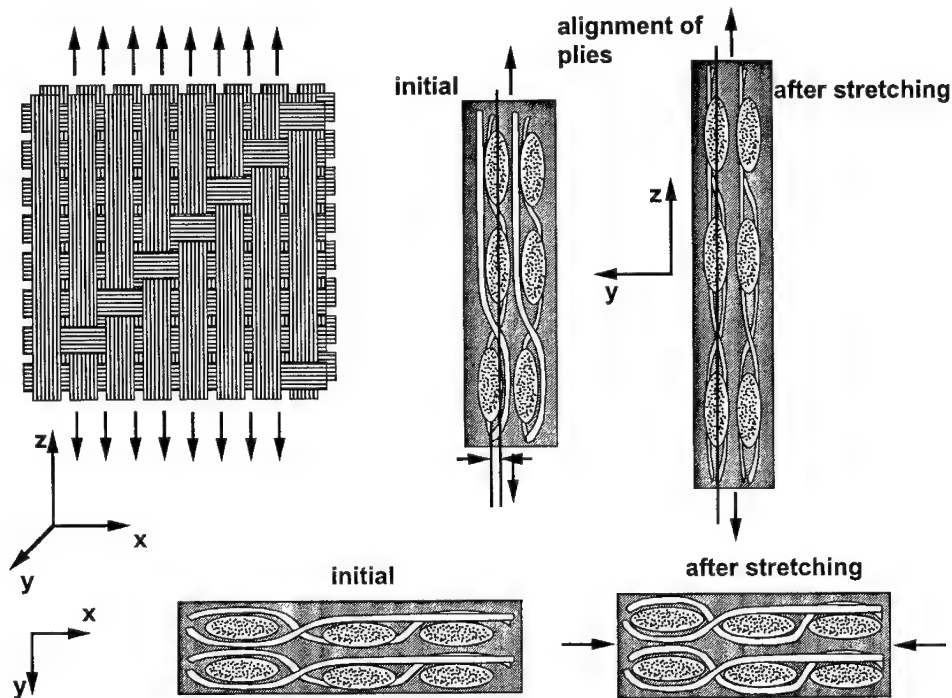


Figure 4. Weave-alignment processes that are believed to occur during the fatigue of woven fiber reinforced ceramic matrix composites [7].

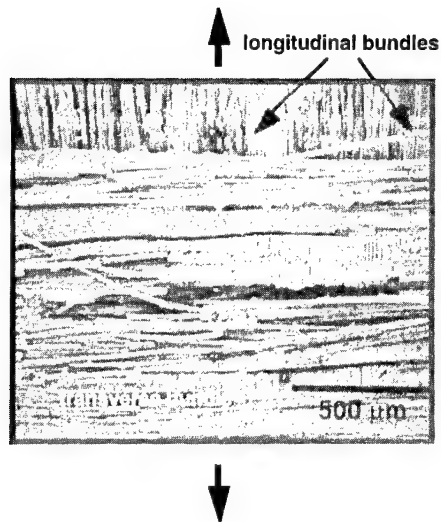


Figure 5. Matrix damage at the crossover points in the fiber fabric weave, where stress concentrations exist [7].

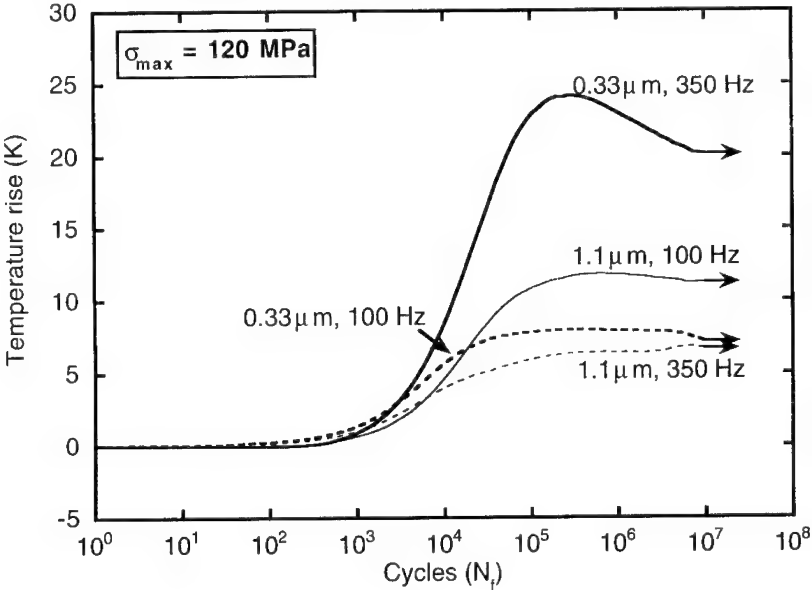
As noted above, due to the rather strong bonding at the interface of this composite, it is believed that fiber/matrix and fiber/fiber sliding were not significant. Thus, the interfacial wear and associated fiber fracture that were the likely mechanisms responsible for failure in Nicalon/CAS were not significant in fatigue of woven Nicalon/Si-C-O-N. This is corroborated by the fact that plots of stress versus cycles at 1 Hz [11] and 100 Hz are almost identical, i.e., unlike Nicalon/CAS where there was a dramatic effect of frequency on fatigue life, there was no real effect of frequency on the fatigue life of Nicalon/Si-C-O-N.

Plain-weave Nicalon/C/SiC with Variable Interfacial Coating Thickness

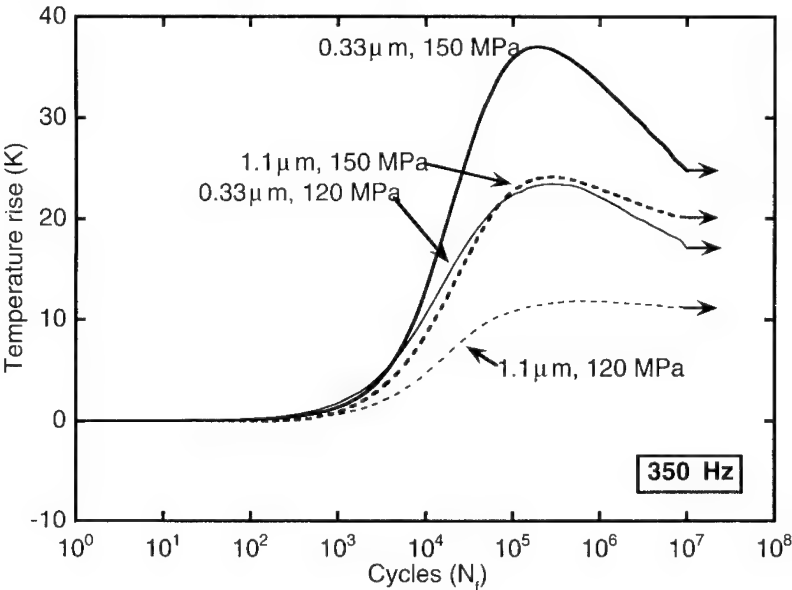
Following the observation by Sorensen and Holmes [4] that a lubricating layer may be beneficial in improving fatigue life of CFCCs, Chawla and Holmes [8] studied the role of the fiber/matrix interface on the frictional heating and fatigue behavior of a chemical vapor infiltrated (CVI) Nicalon/C/SiC composite. Specimens were fabricated with 0.33 μm and 1.1 μm carbon coating interfaces in order to investigate the effect of interfacial coating thickness. The fatigue tests were conducted at frequencies of 100 and 350 Hz. It was found that the thicker coating, which would be expected to provide further protection to the fiber against abrasion damage, resulted in less frictional heating due to less wear of the fibers during fatigue. Figure 6(a) shows the effect of frequency on the temperature rise of both composites. At higher frequencies, more heating was observed since the energy dissipated per unit time also increased. At both 100 Hz and 350 Hz, however, the composite with the thinner coating exhibited much higher frictional heating.

It is interesting to note that a decrease in temperature was observed after 10^5 cycles, Fig. 6(a). As was the case in Nicalon/CAS, the decrease in temperature was paralleled by a recovery in modulus. Thus, it is believed that the geometric aligning and stiffening of the weave caused the increase in modulus and increased

resistance to sliding. In both composites, higher stresses caused more significant heating, Fig. 6(b). A similar trend was reported by Koch and Grathwohl [12] in 100 Hz fatigue of Tyranno/C/SiC composites, although much higher temperatures were observed in the latter study. A comparison of the temperature rise versus applied stress for a variety of systems studied to date is shown in Fig. 7.



(a)



(b)

Figure 6. Temperature rise in Nicalon/C/SiC with variable interfacial coating thickness: (a) effect of loading frequency (constant stress) and (b) effect of applied stress (constant frequency) [8]. The composite with the thicker interfacial coating exhibits much lower frictional heating.

Substantial damage in terms of modulus was observed in fatigue of Nicalon/C/SiC. Once again, most of the damage occurred during the first cycle, Fig. 8(a). At a constant stress, the level of damage was not significantly dependent on frequency. At a given frequency, however, higher stresses induced more damage in both composites, Fig. 8(b). As mentioned above, the recovery in moduli of these woven composites is due to stretching and alignment of the plain-weave fabric during fatigue, creating a stiffer reinforcing architecture. These weave stretching and aligning mechanisms are believed to be similar to those observed in woven Nicalon/Si-C-O-N. Failure in Nicalon/C/SiC composites appeared to be similar to that of woven C/SiC and woven Nicalon/Si-C-O-N with localized matrix damage at the points where adjacent lamina were bonded to each other, Fig. 9.

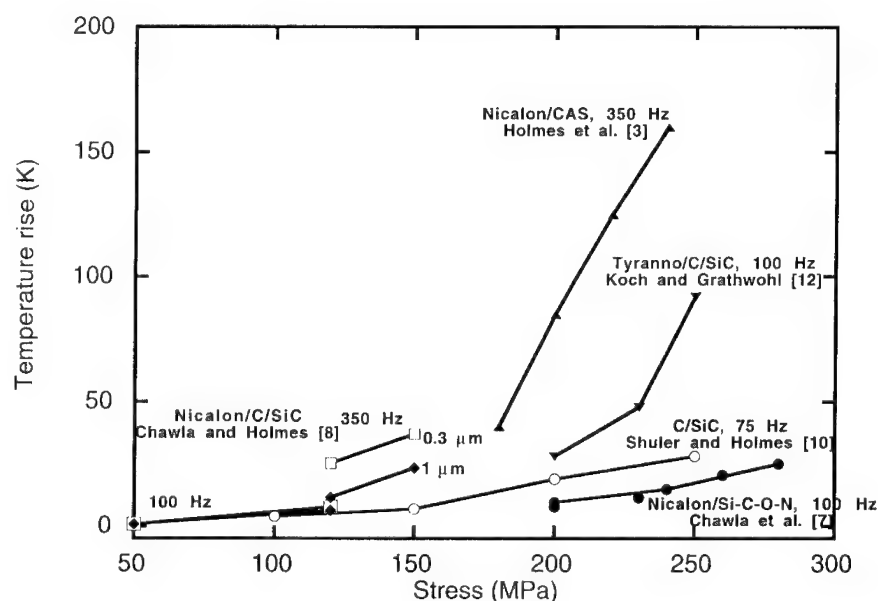


Figure 7. Comparison of temperature rise versus applied stress for a variety of CMC systems studied to date [2, 7, 8, 10, 12].

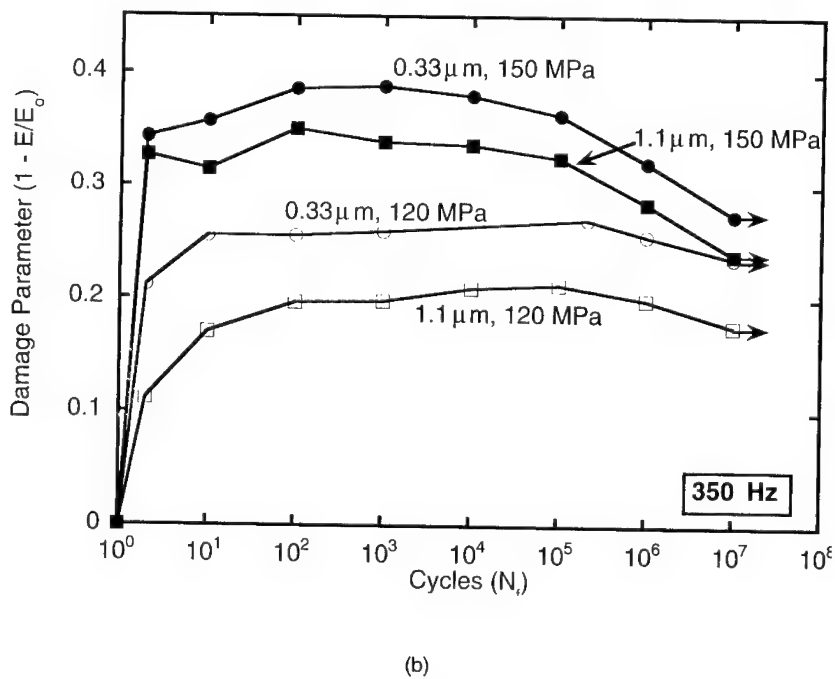
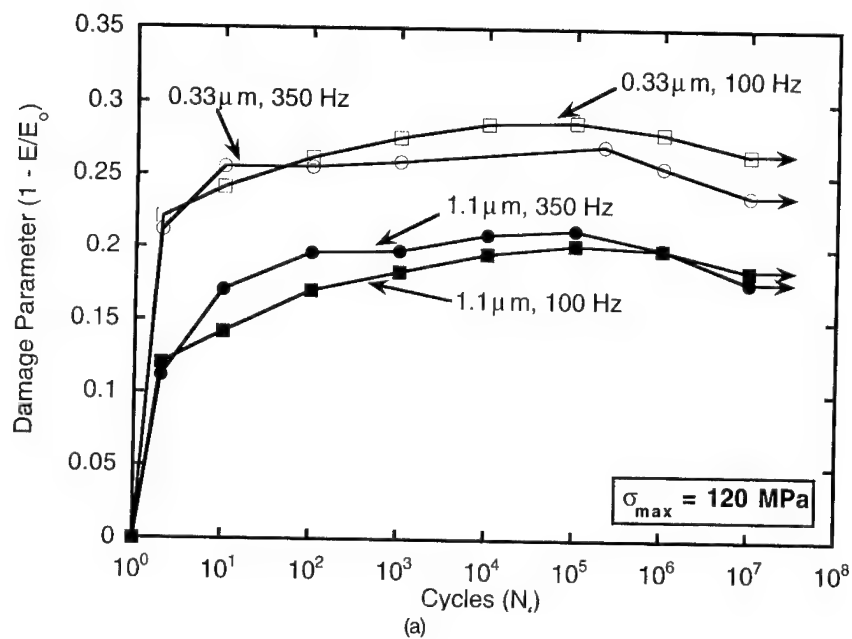


Figure 8. Damage in elastic modulus in Nicalon/C/SiC with variable interfacial coating thickness: (a) effect of frequency (constant applied stress) and (b) effect of applied stress (constant frequency) [8].

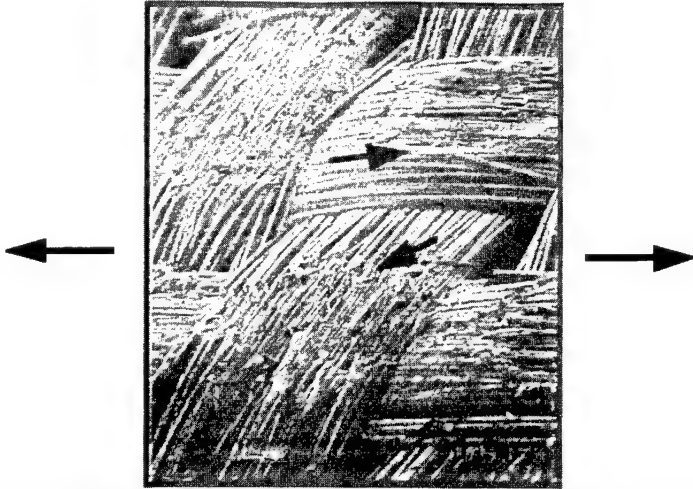


Figure 9. Localized matrix damage in Nicalon/C/SiC, at points where adjacent laminar were bonded together [8]. The arrows indicate the loading direction.

Modeling of high frequency fatigue behavior

Kotil et al. [13] and Cho et al. [14] have modeled some aspects of the frictional heating behavior in CFCCs. Kotil et al. [14] showed the dependence of fatigue behavior on the interfacial shear strength in the composite, by modeling microstructural damage in a series of "fatigue-damaged zones" surrounded by undamaged zones. A unidirectional composite was assumed, which was divided into cells containing a single fiber surrounded by the matrix. The compliance of each cell was modeled by a series of springs, while sliding blocks were used to represent frictional sliding of fibers in each cell. The cumulative damage during fatigue was modeled by random debonding and fracture of fibers on a cycle-by-cycle basis. For a fiber of diameter d_f , the frictional force acting on the embedded length of the fiber, L_d , was related to the interfacial shear stress, τ , by the following equation:

$$F_{\text{fric}} = \pi \tau L_d d_f \quad (1)$$

The model showed that the energy dissipated during fatigue, which can be measured by the temperature rise or the area of stress-strain hysteresis loops taken during a test was a maximum at intermediate values of τ , and was a minimum at very low or high levels of the frictional interfacial shear stress. This "bell shape" can be explained by examining equation 1. At low levels of interfacial frictional shear the fibers could slide freely within the matrix. For this case, no energy was dissipated (i.e., τ is small and L_d is large). At high values of shear, the slip of fibers was restricted (the debonded length decreases) and the fibers were not allowed to slide within the matrix (i.e., τ is large and L_d is small). In both these cases, the frictional force was small. At intermediate values of τ , a balance exists between τ and the debond length, L_d , so a maximum in energy dissipation was obtained.

Cho et al. [14] considered the work performed during frictional sliding of fibers in the matrix, during cyclic loading and unloading. Models were developed for both partial and full slip of the fibers, assuming that the fibers remained unfractured. The surface area over which sliding occurred was dependent on loading direction (loading or unloading) and the magnitude of the applied load. Therefore, the slip length during a given fatigue cycle was always changing. By equating the work performed during frictional slip of the fibers to the amount of heat generated during a

test, interfacial shear stresses were correlated to temperature rise, or some measure of the energy being dissipated in the composite. For partial slip along a debonded interface, the rate of work performed during fatigue was given in terms of the loading frequency, f , the applied stress amplitude, $\Delta\sigma$, and the matrix crack spacing, l :

$$\frac{dw_{\text{fric}}}{dt} = \frac{fd_f\Delta\sigma^3}{24E_f l\tau_d} \left[\frac{(1-V_f)E_m}{V_f E_c} \right] \quad (2)$$

where d_f is the fiber diameter, V_f is the volume fraction of fibers, and the elastic moduli of the fiber, matrix, and composite are E_f , E_m , and E_c , respectively.

The heat loss in the specimen, dq/dt , was estimated from the convective, radiative, and conductive heat loss per unit volume. dq/dt was related to the specimen surface temperature, T_s , and the ambient temperature, T_a , in the following expression:

$$\frac{dq}{dt} = \left[h(T_s - T_a) + \epsilon k(T_s^4 - T_a^4) \right] \frac{A_{\text{surf}}}{V} + \frac{2\beta A_{\text{cond}}}{V} \left[\frac{\Delta T}{\Delta z} \right]_{\text{axial}} \quad (3)$$

where $[\Delta T/\Delta z]_{\text{axial}}$ is the axial temperature gradient at the end of the gage-section, h is the heat transfer coefficient, ϵ is the emissivity, k is the thermal conductivity of the composite parallel to the direction of the fibers, β is the Boltzmann's constant, and V is the volume of the specimen gage section. Convective and radiative heat losses occurred through the surface area of the gage section, A_{surf} , and conduction heat losses took place through the cross-sectional area of the gage section, A_{cond} . Assuming steady-state conditions and ignoring any other means for the specimen to dissipate energy, dw_{fric}/dt was equated to the heat loss to the surroundings, dq/dt . Thus the temperature rise was used to estimate the evolution of interfacial shear stresses during the fatigue test. Figure 10 shows the temperature rise and the accompanying evolution of interfacial shear stress, calculated using the model by Cho et al. [14], in a Nicalon/CAS composite.

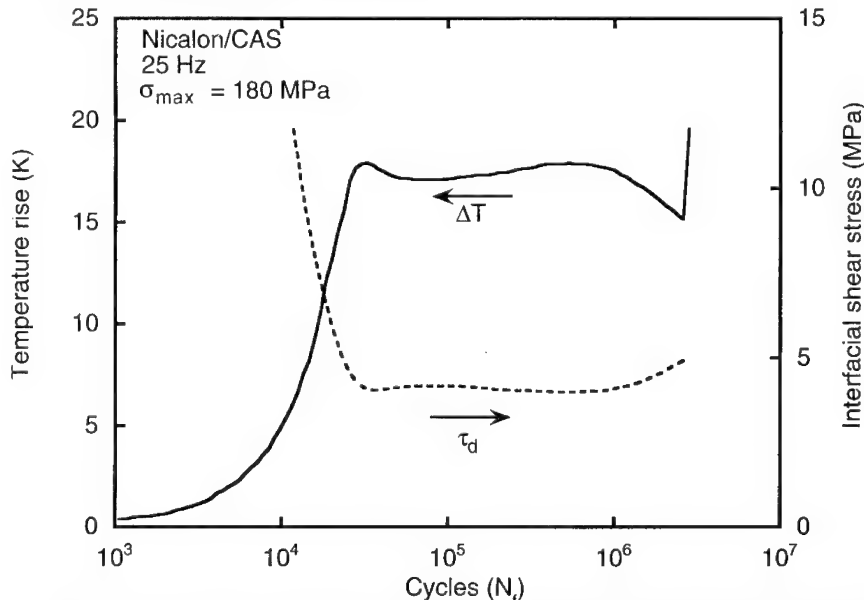


Figure 10. Temperature rise in unidirectional Nicalon/CAS and accompanying evolution of interfacial shear stress, calculated by the model of Cho et al. [14].

Conclusions

Several conclusions can be drawn about the high frequency fatigue behavior of continuous fiber reinforced ceramic matrix composites:

- In unidirectional composites, significant heating was observed due to fiber/matrix interface wear during high frequency fatigue loading. Lubrication was used to decrease the interfacial sliding stress and promote easy sliding for fibers during fatigue.
- With a strong fiber/matrix interface, such as that in Nicalon/Si-C-O-N, frictional heating was inhibited. Less sliding lengths and high interfacial shear strengths contained fiber/matrix sliding.
- In Nicalon/C/SiC, a thicker coating was more effective in providing a means to suppress frictional heating by protecting the fibers from wear damage. Less frictional heating and less damage in elastic modulus were observed with fibers with thicker coatings.
- Modeling of the frictional heating behavior showed that intermediate values of τ (and the debond length) resulted in the maximum amount of frictional heating and energy dissipation.
- By equating the work done by the specimen to the heat being lost during a test (measured and calculated using the temperature increase in the specimen), the evolution in interfacial shear stresses in the composite was obtained.

References

1. J.W. Holmes and C. Cho, "Experimental Observations of Frictional Heating in Fiber-Reinforced Ceramics," *J. Am. Ceram. Soc.*, **75** [4] 929 (1992).
2. J.W. Holmes, X. Wu, and B.F. Sorensen, "Frequency Dependence of Fatigue Life and Internal Heating of a Fiber-Reinforced/Ceramic-Matrix Composite," *J. Am. Ceram. Soc.*, **77** 3284 (1994).
3. B.F. Sorensen and J.W. Holmes, "Improvement in the Fatigue Life of Fiber-Reinforced Ceramic by use of Interfacial Lubrication," *Scripta Met. et. Mater.*, **32** 1393 (1995).
4. D. Rouby and P. Reynaud, "Fatigue Behaviour Related to Interface Modification During Cycling in Ceramic-matrix Fibre Composites," *Comp. Sci. & Tech.*, **48** 109 (1993).
5. D. Yao and J.-K. Shang, "Anomalous Temperature Dependence of Cyclic Fatigue-Crack Growth in a Silicon Carbide Matrix Composite," *J. Am. Ceram. Soc.*, **77** 2911 (1994).
6. N. Chawla, P.K. Liaw, E. Lara-Curzio, R.A. Lowden, and M.K. Ferber, "Effect of Fiber Fabric Orientation on the Mechanical Behavior of Continuous Fiber Ceramic Composites," p. 291 in *High Performance Composites - Commonality of Phenomena*, Proceedings of The Minerals, Metals, and Materials Society (Rosemont, IL, October 1994). Edited by K.K. Chawla, P.K. Liaw, and S.G. Fishman, TMS, Warrendale, PA, 1994.

7. N. Chawla, Y.K. Tur, J.W. Holmes, J.R. Barber, and A. Szweda, "The High Frequency Fatigue Behavior of Polymer-Derived Fiber Fabric Reinforced Ceramic Matrix Composites," submitted to *J. Am. Ceram. Soc.* (May 1996).
8. N. Chawla, J.W. Holmes, and R.A. Lowden "The Effect of Interfacial Coating Thickness on the Fatigue Behavior of Nicalon/C/SiC Composites," submitted to *Scripta Mater.* (June 1996).
9. E. Lara-Curzio, private communication.
10. S.F. Shuler, J.W. Holmes, X. Wu, and D. Roach, "Influence of Loading Frequency of the Room-Temperature Fatigue of a Carbon-Fiber/SiC-Matrix Composite," *J. Am. Ceram. Soc.*, **76** 2327 (1993).
11. E. Lara-Curzio, M.K. Ferber, R. Boisvert, and A. Szweda, "The High Temperature Tensile Fatigue Behavior of a Polymer-Derived Ceramic Matrix Composite," *Ceram. Eng. Sci. Proc.*, **16** 341 (1995).
12. D. Koch and G. Grathwohl, "Tensile Fatigue Testing of SiC-SiC Composites," p. 217 in *Composites Testing and Standardization ECCM-CTS*, EACM, Bordeaux, France, 1992.
13. T. Kotil, J.W. Holmes, and M. Comninou, "Origin of Hysteresis Observed During Fatigue of Ceramic-Matrix Composites," *J. Am. Ceram. Soc.*, **73** 1879 (1990).
14. C. Cho, J.W. Holmes, and J.R. Barber, "Estimation of Interfacial Shear in Ceramic Composites from Frictional Heating Measurements," *J. Am. Ceram. Soc.*, **74** (1991) 2802.

THE EFFECT OF TEMPERATURE, IN THE RANGE 750°C - 1500° C,
ON THE FLOW STRESS OF POLYCRYSTALLINE DIAMOND

E J Brookes, T Harris, R L Wallis and A Al-Watban

Department of Engineering Design and Manufacture
The University of Hull, Hull, East Yorkshire, HU6 7RX
United Kingdom.

Abstract

Earlier work has shown that the soft impressor method can be used to measure the flow stress of single crystal diamond as a function of temperature providing results which very clearly distinguish between the various types of diamond and the effect of nitrogen impurities. High dislocation mobility, multiple intersecting slip and impression creep all occur above a specific (Brittle-Ductile) transition temperature for a given type of diamond - e.g. 750° and 900° C for synthetic type Ib and natural type Ia respectively.

In this paper, the same method has been applied to investigate the effect of temperature on the initial flow stress of polycrystalline diamond. The microstructure of the specimens consists of primary diamond particles (about 2-20 µm in diameter) dispersed in a silicon carbide matrix. The results confirm that the high temperature behaviour of this material is directly comparable in nature to that of single crystal diamond with a Brittle:Ductile transition temperature of 770°C and similar rates of impression creep. It is also shown that the relevant flow stresses are higher in polycrystalline diamond than in single crystal diamond.

Introduction

The soft impressor technique was first described by Brookes and Green (1) and subsequently developed to estimate the critical resolved shear stress of diamond crystals and to investigate impression creep in diamond, at temperatures up to 1500°C (2, 3). This work has shown that the soft impressor method can be used to measure the flow stress of single crystal diamond as a function of temperature, providing results which very clearly distinguish between the various types of diamond and the effect of nitrogen impurities. The tensile stresses associated with conventional indentations in ceramics often initiate ring cracks, in the case of a spherical indenter, or radial cracks as in the case of sharp pyramidal indenters. In this technique, selection of a suitable mean contact pressure means that the tensile stresses which result in brittle failure or cracking can be avoided whilst the resolved shear stresses to cause dislocation initiation and multiplication can be realised. High dislocation mobility, multiple intersecting slip and impression creep all occur above a specific (Brittle-Ductile) transition temperature for a given type of diamond - e.g. 750° and 900°C for synthetic type Ib and natural type Ia respectively. Here, the method has been applied to investigate the effect of temperature on the initial flow stress of polycrystalline material, where the microstructure consists of primary diamond particles (about 2-10 µm in diameter) dispersed in a silicon carbide matrix.

Principles and Modelling

In essence, the method uses a cone, made from a material which is significantly softer than the specimen and initially having an included angle of 120°, but which then plastically deforms under an applied normal load to make a blunt circular contact. The resultant mean contact pressure is largely determined and controlled by the choice of suitable materials for the blunted cone or impressor. Furthermore, the range of available contact pressures can be extended by exploiting the creep properties of the cone material. When the material used for the soft impressor creeps under the applied load, the area of contact increases and the contact pressure decreases. Whilst the mean contact pressure is sufficient to exceed the flow stress of the specimen, the depth of the impression continues to increase. However, when it falls just below a critical value, plastic deformation of the specimen stops and new impressions are not formed using that blunted impressor. In this way, the minimum contact pressure to initiate plastic deformation, as revealed by a dislocation etchant, visible slip line formation and/or change in surface topography, is used to estimate the critical resolved shear stress on the basis of a suitable mathematical model.

A model based on the elastic stress field below a normally loaded circular contact, first analysed by Love (4), was proposed by Brookes *et al* (5) to identify the threshold pressure above which dislocation movement is initiated in single crystal diamond. Using the measurements of minimum or threshold mean pressure to produce dislocations on mechanically polished (001) surfaces of synthetic diamond, in conjunction with this model, the critical resolved shear stress was estimated for type Ib diamond. These results are reproduced in Figure 1 in the form of a schematic diagram of temperature vs threshold mean contact pressure (2).

At room temperature and in the elastic regime (I), there is no discernible dislocation movement and Hertzian fracture occurs, just outside the contact area on the {111} cleavage planes, at a sufficiently high contact pressure. In single crystal diamond, the tensile stress responsible for this type of fracture is about 3 GPa, approximately 20% of the lowest mean contact pressure required to initiate a crack (5). In the plastic regime (II), dislocation movement is observed on all {111} <110> slip systems and the minimum mean flow pressure

is less than that required to produce {111} ring cracks. If cracks are formed in this regime, they tend to lie on {110} planes and are considered to be initiated by dislocation reactions. The flow stress falls rapidly over this temperature regime but, ultimately, becomes relatively temperature insensitive in the third regime (III). The I:II transition or B-D-T temperature is dependent on the type of diamond, i.e. it is significantly lower for synthetic type Ib (750°C) than for natural type Ia diamonds (900°C) and the magnitude of the minimum flow stress for plastic flow at a given temperature in regime II varies similarly. Also, the onset of impression creep coincides with this transition temperature (2).

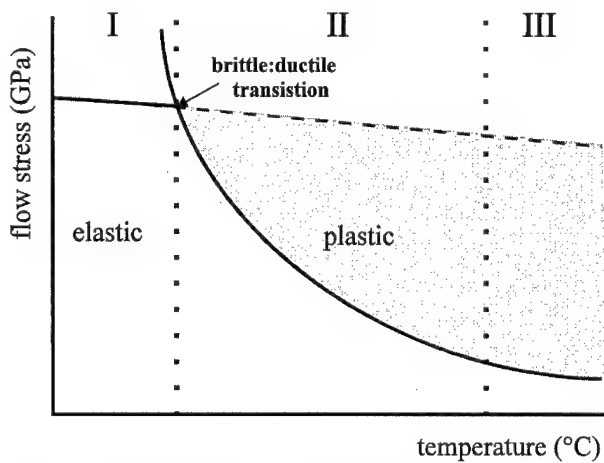


Figure 1. Schematic diagram of the flow stress vs temperature.

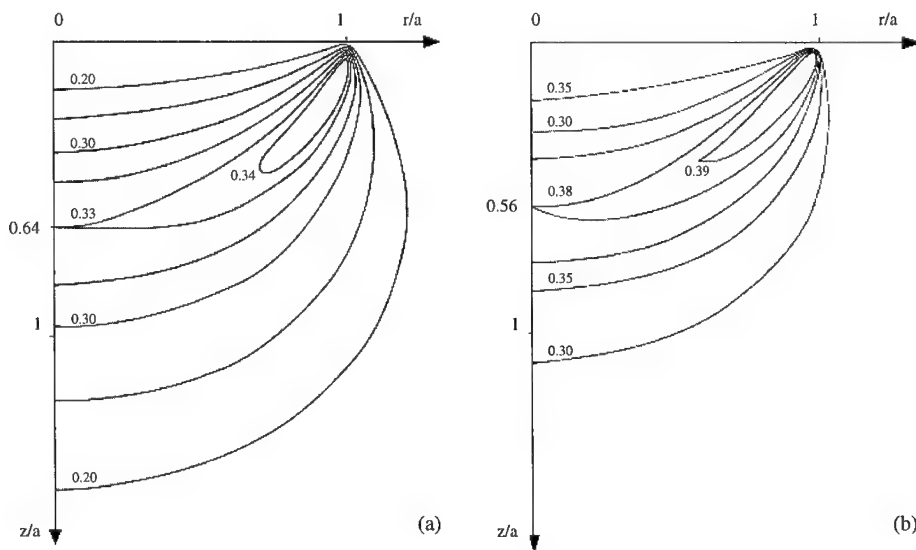


Figure 2. Contours of maximum shear stress beneath a circular contact on (a) polycrystalline copper (b) polycrystalline diamond.

In this work the technique has been extended to determine the flow stress of a diamond polycrystalline aggregate material as a function of temperature and a mathematical model has been proposed on that basis to estimate the flow stress in isotropic polycrystalline materials. Love (4) calculated the stresses in a semi-infinite elastic isotropic solid due to uniform pressure over a circular contact on a plane surface. Using the Love model, on the contact surface the highest value of maximum shear stress, S_{\max} / P , was found to occur close to the periphery of the contact area ($r/a = 1$) and was determined to be $(1-2\nu)/2$. Values of maximum shear stress beneath the contact area were also calculated and are plotted as contours in Figure 2 for copper and polycrystalline diamond. The applicability of this model was verified by correlating the yield strength of polycrystalline copper, measured in tension, with the determination of the minimum mean contact pressure to plastically deform copper ($H_K = 1.20$ GPa) using an aluminium impressor ($H_K = 1.0$ GPa) (7). The contour map of equal maximum shear stress for copper, reproduced in Figure 2a, shows that the peak stress occurs beneath the contact surface, close to the edge of the contact area and is toroidal in form. According to this analysis, the first evidence of plastic deformation should be observed at the contact periphery.

Figure 3(a) shows an impression made in polycrystalline copper using an aluminium impressor, which developed a mean contact pressure of 1.1 GPa. Gross plastic deformation can be seen as a very deep impression together with many slip lines outside the contact area. However, when the mean contact pressure was reduced to a value of 0.78 GPa, as a result of extensive creep of the aluminium impressor, an extremely shallow impression was formed, with evidence of just a few slip lines at the periphery of the contact area. This impression is shown in Figure 3(b). The value of maximum shear stress obtained by this method of soft impression and model, $S_{\max} = P((1-2\nu)/2) = 0.15$ GPa, compares well with the value of maximum shear stress obtained from a standard tensile test, $S_{\max} = 0.13$ GPa (7).

Experimental Procedure

The soft impressors were ground from polycrystalline cubic boron nitride in the shape of a standard stylus with an included angle of 120° . Polycrystalline cubic boron nitride is an aggregate material produced by sintering crystals of cubic boron nitride with an aluminium binder ($H_K = 31.5$ GPa), under conditions of high temperature and high pressure. The ceramic secondary phase is a mixture of aluminium nitride and aluminium diboride which is continuous leaving no voids or cavities.

The polycrystalline diamond cutting tool material used in this work was a proprietary material produced by sintering densely packed synthetic diamond particles with silicon powder as a binder. During the sintering process most of the silicon powder reacts with graphitised diamond to form the hard, abrasive and chemically stable β -SiC. The final product is a dense polycrystalline material containing approximately 16.5 - 18.9 vol. % β -SiC, with high strength and thermal stability up to 1200°C in a reducing atmosphere.

The micrograph in Figure 4 shows diamond particles, average diameter $15\text{ }\mu\text{m}$, partially surrounded by the ceramic secondary phase. Whilst there is significant contact between diamond particles, intergrowth between contacting grains is minimal with no clear orientation relationship between the grains. On the other hand, the β -SiC appears to form a continuous network. The inherent hardness is $H_K = 50$ GPa at room temperature and 12.7 GPa at 1100°C . Impressions were made on highly polished surfaces prepared using standard diamond polishing techniques.

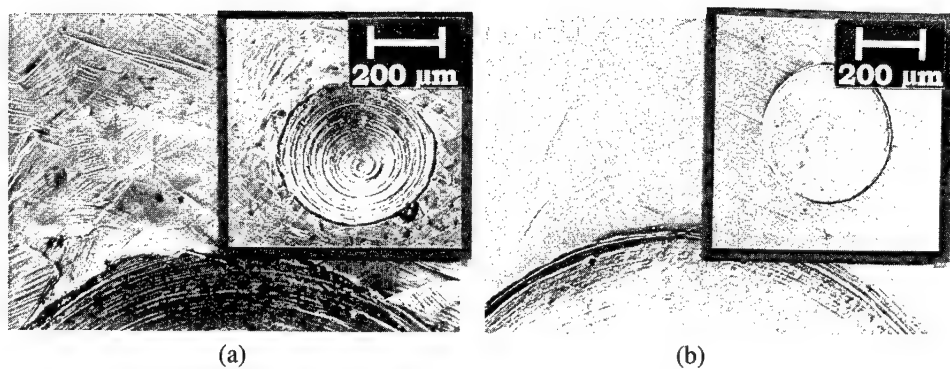


Figure 3. Impressions in polycrystalline copper: (a) $P_m = 1.1$ GPa (b) $P_m = 0.78$ GPa.

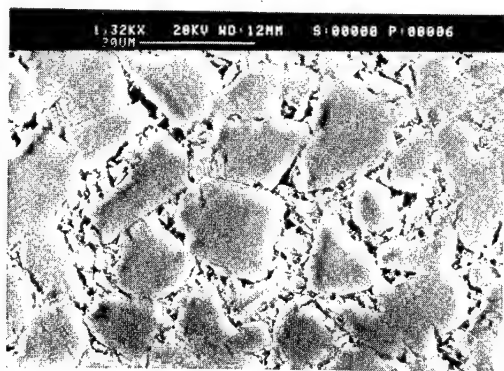


Figure 4. SEM micrograph of the polycrystalline diamond.

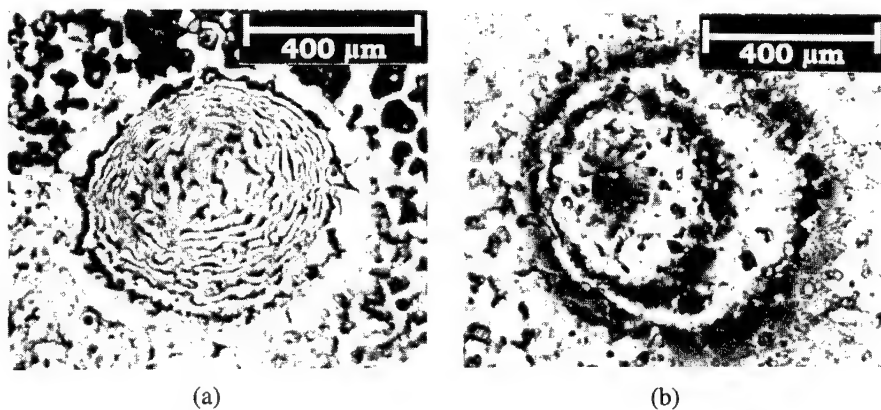


Figure 5. Interferograms of impressions in polycrystalline diamond at 1200°C : (a) 7.1 GPa (b) 4.1 GPa.

The experiments were all carried out in the vacuum apparatus described by Brookes (2). The range of experimental temperature was achieved using a radio frequency induction coil on a 50 kW, 450 kHz generator and the experiments were carried out in a vacuum of 10^{-5} bar.

A sharp impressor was used at each experimental temperature. Initially the impressor was loaded against the surface of the specimen for 600s at a load of 100N. The load was removed, a new site selected and the load re-applied for a further 600s. This procedure was repeated until the contact area of the impressor was such that no measurable plastic deformation was observed. The mean contact pressure for the onset of plastic deformation was taken as that pressure which produced very limited visible plastic deformation. Measurements of the mean contact area and the depth of impression formed in the polycrystalline diamond were made using a standard metallographic microscope and a direct phase detecting interferometer.

Results

Interferograms of impressions made in polycrystalline diamond at 1200°C are shown in Figure 5. The impression shown in Figure 5(a) was produced by a mean contact pressure of 7.1 GPa and is of the order of 4 μm in depth. The impression shown in Figure 5(b) was produced by a mean contact pressure of 4.1 GPa and is only 770 nm in depth. A mean contact pressure of less than 4.1 GPa produced no visible impression in the polycrystalline diamond and therefore this value was taken as the minimum mean contact pressure to cause plastic deformation at this experimental temperature.

The estimates of threshold mean contact pressures to produce minimal plastic deformation in polycrystalline diamond in the temperature range 700° to 1300°C are plotted in Figure 6 and enumerated in Table I. Results are plotted as the minimum contact pressure to initiate plastic deformation vs temperature for polycrystalline diamond and for synthetic type Ib diamond for purposes of comparison.

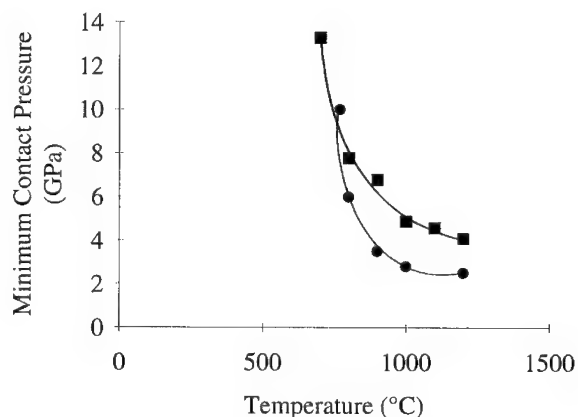


Figure 6. The minimum mean contact pressure vs temperature:
 ■ polycrystalline diamond
 ● synthetic type Ib single crystal diamond (2)

The values of maximum shear stress were evaluated from the expression $S_{\max} = P \frac{(1-2\nu)}{2} = 0.414 P_m$, taking Poisson's Ratio for polycrystalline diamond as $\nu = 0.086$ and the flow stress was calculated as $\sigma_{\text{flow}} = \frac{S_{\max}}{0.5}$.

Table I. The threshold mean contact pressure to produce plastic deformation and the estimate of the flow stress of polycrystalline diamond.

Temperature (°C)	Threshold Mean Contact Pressure (GPa)	Flow Stress (GPa)
700	13.3	11.01
800	7.8	6.46
900	6.9	5.63
1000	4.9	4.05
1100	4.6	3.80
1200	4.1	3.39

Discussion

In Regime I, room temperature - 750°C, deformation of single crystal diamond and polycrystalline diamond was purely elastic at low mean contact pressures but with fracture delineating the contact area at sufficiently high mean contact pressures. At these pressures cone cracks were formed on {111} cleavage planes in single crystal diamond (2) and similar ring cracks, transgranular and intergranular in form, were observed in polycrystalline diamond. In this work the mean contact pressures were lower than the fracture stress and the transition from elastic to plastic behaviour without fracture was observed.

The elastic:plastic or brittle:ductile transition occurred in the same temperature range for single crystal diamond and for the polycrystalline form and this transition marked the advent of impression creep (continued plastic deformation with increased dwell time of the impressor). Dislocations become mobile in single crystal diamond at relatively low homologous temperatures ($0.3 T_m$) and the critical resolved shear stress for synthetic type Ib diamond has been estimated as 3.5 GPa at 770°C (2). Under similar experimental conditions, plasticity is also the dominant mechanism in polycrystalline diamond but the mean contact pressure necessary to induce plasticity is higher and the flow stress is correspondingly greater, at 11 GPa.

In Regime II, the impressions in polycrystalline diamond were fully plastic and both the diamond network and the β -SiC network deformed plastically. The higher flow stress in polycrystalline diamond could be attributed to several mechanisms. An investigation of the deformation of single crystal diamond using the soft impressor technique has shown that the critical resolved shear stress is higher for type IIa diamond which contains significant numbers of dislocations (2). Furthermore, it has been shown that high levels of strain are introduced during processing of polycrystalline diamond, where the high temperature-high pressure conditions are sufficient to initiate both slip and twinning (8). A highly strained type Ib diamond network would require higher deformation pressures than strain free type Ib diamond and this would be reflected in an increased flow stress for the polycrystalline form. The role of both the silicon carbide network and possible grain boundary effects needs further investigation.

In Regime III, the flow stress of polycrystalline diamond and the critical resolved shear stress of single crystal diamond both become relatively temperature independent and the rate of impression creep increases. However, at temperatures above 1300°C polycrystalline diamond becomes thermally unstable.

Conclusions

This work has shown that the high temperature behaviour of polycrystalline diamond is directly comparable in nature to that of single crystal diamond, with a brittle:ductile transition temperature of 750°C. The flow stress is temperature dependent over a narrow temperature range and becomes temperature independent at temperatures approaching half the melting point or the point of thermal instability.

The polycrystalline diamond had a microstructure which consisted of primary synthetic diamond particles, of about 20 micrometers in diameter, dispersed in a matrix phase of cubic (β) silicon carbide with both diamond and silicon carbide forming a continuous network. The effect of temperature on the plasticity of this material was comparable with the schematic given here for single crystal diamond. The I:II transition temperature occurred at about 750°C and impression creep was observed at and above this temperature. Furthermore, the minimum contact pressures to plastically deform the polycrystalline diamond were significantly higher pressures than those required to plastically deform type Ib diamond - the primary constituent of this material.

Engineering applications of polycrystalline diamond normally involve the impression or sliding of a soft counterface on a harder one, e.g. the use of polycrystalline diamond as a cutting tool. The approach described in this paper is particularly suitable for the study of mechanisms of deformation in ceramics as it closely simulates service conditions. This soft impressor technique has been shown to be a reliable method for the determination of the elastic:plastic transition temperature and new results for the estimation of the flow stress of polycrystalline diamond in the temperature range typical of that developed in metal cutting applications, are presented.

Acknowledgments

The authors wish to acknowledge the continued financial support from De Beers Industrial diamond Distributors Ltd through the provision of a research studentship to T Harris and a grant to the laboratory. We also wish to thank the Government of Saudi Arabia for support for A Al Watban. We express our gratitude to Professor C A Brookes for guidance and discussions and the staff of EDM for technical assistance, in particular C Ingleby and G Robinson.

References

1. C. A. Brookes, and P. Green, "Deformation of Magnesium Oxide Crystals by Softer Indenters and Sliders" Nature, 246 (1973) 119 - 122.
2. E. J. Brookes, "The Plasticity of Diamond" (PhD thesis, University of Hull) (1992).
3. E. J. Brookes and C. A. Brookes, "Impression Plasticity and Creep in Hard Crystals" (Paper presented at "The Plasticity of Ceramics", Snowbird, Utah, 1994) 131 - 147.

4. A. E. H. Love, "The Stress Produced in a Semi-Infinite Solid by Pressure on Part of the Boundary" Proc. Roy. Soc. (London), A228 (1929) 377 - 4520.
5. C. A. Brookes et al., "A Comparison of the Plastic Deformation and Creep of Types I, Type II and Synthetic Diamonds at 1100°C Under Conditions of Point Loading" J. Hard Mater., 1 (1990) 3 -23.
6. G. Xing, "The Deformation of Diamond Under Conditions of Sliding Friction" (PhD thesis, University of Hull 1995).
7. A. S. Al Watban, "Mechanical Properties of Ultrahard Tool Materials" (PhD thesis, University of Hull, in preparation).
8. J. C. Walmsley, "The Microstructure of Ultrahard Material Compacts Studied by Transmission Electron Microscopy" Mater. Sci. Eng., A105/106 (1988) 549 - 553.

STRENGTH OF PARTICULATE COMPOSITES WITH A HIGH

CONTENT OF HIGH- MELTING POINT FILLER

L.L. Mishnaevsky Jr and S. Schmauder

University of Stuttgart
Staatliche Materialprüfungsanstalt (MPA)
Pfaffenwaldring 32, D-70569 Stuttgart (Vaihingen), Germany

Abstract

Interrelations between microstructural parameters of particulate composites with a high content of high melting point filler and the strength and damage initiation in the composite are studied using methods based on the fractal theory. Effects of the presence of a skeleton from filler grains in the composite, size of filler grains and structure of filler/matrix interface on damage initiation in a loaded composite are investigated theoretically. Conditions at which the skeleton is formed during sintering and optimal duration of the sintering process are determined on the basis of a probabilistic sintering model. A mathematical model for the formation of fractal interfaces in liquid-phase sintering of composites is developed and the influence of interface fractality on damage initiation in matrix is investigated.

Introduction

Liquid-phase sintered particulate composites are widely used in industry. For example, drilling and cutting tools are made from hard alloys and cermets; such materials are used in production of high- pressure apparatus, etc.

The strength of the composites influence the efficiency and service properties of tools made from these materials to a large extent. This paper seeks to study theoretically factors influencing the strength of composites, and to analyze ways to improve the composite strength by varying parameters of composite microstructure.

As shown in [1-3], a skeleton from filler grains is formed in sintering particulate composites with a high content of high-strength filler. This skeleton determines the strength of the composite at initial stages of loading (in particular, the load at which irreversible deformation begins) [2,3].

The destruction of a loaded composite with a high content of filler grains proceeds as follows: when the material contains a skeleton from filler grains, just the skeleton is deformed firstly; microcracks are formed in the skeleton and this process leads to the failure of the skeleton; thereafter, the irreversible deformation of the composite (with destroyed skeleton) begins; microcracks are formed both in the matrix and in the filler grains; the formation of microcracks in the matrix occurs mainly in the vicinity of filler grains or at interfaces, and the greater the stress concentration caused by the grains, the lower the critical stress at which microcracks are formed in matrix [4,5]; growth and coalescence of microcracks lead to the formation of initial cracks, which grow and propagate as well [6] and that determine failure of a loaded body, when the energy of loading is large enough. This short description of the mechanism of composite destruction is based on the results obtained and presented in [1,3,4].

Here, we consider mainly the influence of some parameters of composite structure (grain size, structure of interface) and condition of sintering (time of sintering, mass transfer, etc.) on the damage initiation in composites. It is rather evident that the more intensive is damage initiation at early stage of composite deformation, the less the strength of composite and time to failure (the greater is the microcracks density, the more the probability of crack formation and rate of crack growth [6]). Thus, when studying the interrelation between structure and strength of composite, one can consider firstly the influence of composite structure on the initiation of microcracks.

To model the formation of composite structure in sintering, one uses the methods of fractal theory and theory of fractal growth. These methods allow to take into account the complex nature of the formation of filler skeleton and filler/matrix interface as well as to describe the structure of as-formed objects on the basis of modelling their growth.

In [2], a mathematical model of formation of the skeleton, its destruction and its influence on the composite strength is developed on the basis of the reliability theory. Here, this model is used in order to determine the optimal duration of sintering (at which all workpiece contains a skeleton from joined filler grains) and the influence of the size of filler grains on the strength of composite. These parameters determine conditions of beginning of irreversible deformation in a loaded composite with high content of filler grains.

Influence of filler grain size on the strength of a composite

It is known that the size of filler grains has a great impact on the strength of particulate composites. The influence of this parameter on the composite strength is determined by the following physical mechanisms: strengthening of the soft matrix of the composite by hard inclusions, which present a barrier for dislocations movement; availability of skeleton from joined filler grains, which determine the hardness of material at initial stages of loading [2,3]; size effect: usually, the greater are filler grains, the less their strength and the greater the probability of their failure; etc. One can see that the influence of filler grain size on the composite strength is rather complex and depends on a number of contradictory tendencies. Here we consider only the influence of grain size on the compressive strength of composites with skeleton.

As was shown in [2], the compressive strength of particulate composites with a hard skeleton from filler grains is proportional to the square root of the contiguity of the skeleton:

$$P \propto \sqrt{S} \quad (1)$$

where P - compressive strength of a composite with the skeleton from filler grains, S - contiguity of the skeleton. The contiguity of the skeleton (which is defined as the grain/grain interface area divided by the total surface of particles per unit volume of the material [1]) depends on the conditions of sintering, and can be calculated by the formula from [2]:

$$S = \frac{1}{\pi d^2} \left(\frac{c_0 w}{2 + w} \right) t_c^{2/w+1} - c_0 \exp \left[\frac{nd(1 + vt_c)}{L} \right] \left(\frac{ndv}{L} \right)^{-2w-1} \Gamma_t(2/w + 1) \quad (2)$$

where S - contiguity of the skeleton, $c_0 = \pi\phi^2/4$, Γ_t - incomplete gamma-function, v - the rate of sample shrinkage in sintering, w and ϕ are constants of the filler material, which enter into the equation of diffusion-controlled growth of necks between filler grains in sintering [7] (i.e. the diameter of a neck is proportional to $\phi t^{1/w}$, where t - time [1]), d - diameter of grains, n - the amount of filler grains per unit volume of sample, t_c - time of sintering, L - average distance between grains.

Using eq. (2), one can analyze an influence of grain size on the compressive strength of composites. If one supposes that the main mechanism of neck growth during sintering is volume self-diffusion, the coefficients w and ϕ are equal to 5.0, and $(D_d G_2 d^2 \nu / k_b T)^{1/w}$, respectively, where T - temperature, G_2 is a free energy of solid/liquid interface, ν - volume of vacancies, D_d - diffusion coefficient, k_b - Boltzmann constant.

Fig. 1 shows the compressive strength of composite (which is normalized by the coefficient proportionality between P and \sqrt{S}) plotted versus size of grains. In the calculation, the following input data were used:

$$DG_2 \nu w t_c^{2/w+1} / 4k_b T (w + 2) \simeq 1;$$

$$n(1 + vt_c) / L \simeq 0.01;$$

$$DG_2 \nu \Gamma_t(2/w + 1) (nv/L)^{2/w+1} / 4k_b T \simeq 1.$$

It can be seen that the compressive strength is a decreasing function of the size of filler grains.

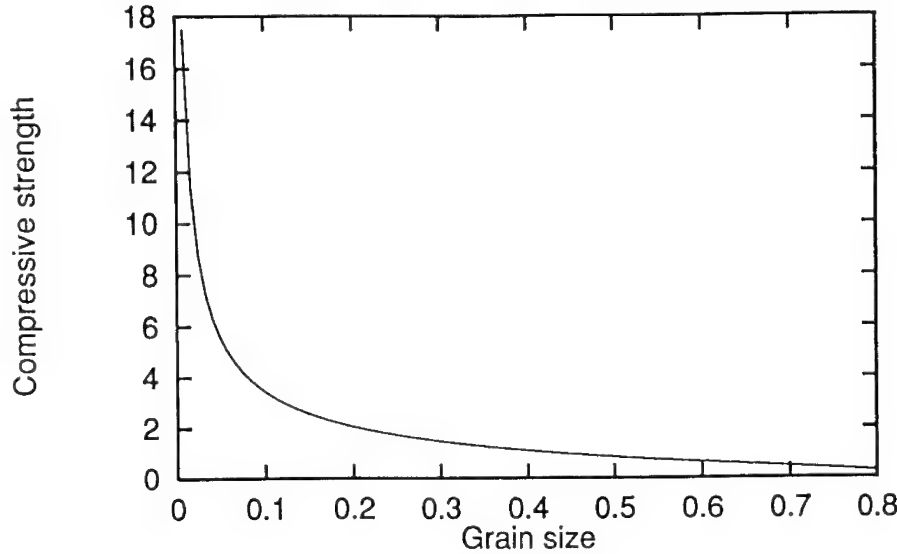


Figure 1: Compressive strength of composite with skeleton plotted versus grain size

Condition of skeleton formation in sintered composites

The availability of skeleton from filler grains increases the strength of composites, especially, at initial stages of loading [2,3]. The process of skeleton formation in sintering depends on the shrinkage rate, physical properties of the filler material, duration of sintering, etc. In the following, we consider conditions at which the skeleton is formed during sintering. The processes of joining small grains and formation of aggregates (skeleton) from them can be considered as being similar to the formation of fractal clusters from small particles (aggregation) [1,7]. The aggregation of small particles proceeds as follows: filler grains form relatively small aggregates, and thereupon the aggregates grow and coalesce. One can write the following equation of skeleton formation in sintering:

$$dM/dt = mp_t \Delta M \quad (3)$$

where M - number of filler grains which have integrated into the skeleton in a given time, ΔM - the average number of grains by which the value M increases due to joining other aggregate of filler grains, p_t - the probability of joining two particles per unit time, $m = F/\pi d^2$, F - exterior area of the aggregate of grains, m - the number of grains on exterior surface of the aggregate. If the process of cluster growth is isotropic, one can write: $F = 12.7L^2$, where L - linear size of an aggregate from filler grains. The relation between the number of elements in a fractal cluster and its linear size looks as follows [8]: $M = (L/d)^{D_f}$, where D_f - fractal dimension of the skeleton. This value characterizes a density of particles in the skeleton. Since the volume content of the filler in the composite is constant, the fractal dimension of skeleton characterizes the amount of particles which are interconnected in relation to the total amount of filler particles.

The probability of joining two aggregates from filler grains (or two filler grains) per unit time can be determined by the approximate formula from [2]:

$$p_t = \frac{vd(1-p_0)}{3l}(1-vt)^{2/3} \quad (4)$$

where $l = 1.24(n/\Delta M)^{-1/3}$, ΔM is taken to be equal to the average number of grains in the aggregates, p_0 - connectivity of skeleton (i.e., the ratio between the number of joints between filler grains and the number of particles [2]), v - shrinkage rate in sintering.

Substituting eq. (4) into eq. (3), one can find the time of sintering which is necessary for the formation of a skeleton from filler grains in a workpiece with linear size L_m :

$$t_c = 0.25(D_f d^2/p_t) \ln L_m, \quad (5)$$

Correlating eqs. (4) and (5) one can conclude that the time needed for the formation of a skeleton depends on the rate of shrinkage, size of filler grains and their density in the workpiece. One can note as well that the time of skeleton formation does not depend strongly on the workpiece size.

Eq.(5) allows us to determine the duration of sintering which is enough for formation of skeleton from interconnected filler grains in all sintered body. The availability of this skeleton contribute to the strength of composite, especially at initial stages of loading.

Redistribution of grain sizes during sintering and interface structure

In previous sections, the conditions of skeleton formation from filler grains and its maximal strength were considered. Yet, the strength of a composite is determined by the micro- and macrocracking not only in the filler grains, but in the matrix as well, especially, after failure of the skeleton. The initiation of microcracks in a particulate composite which does not contain a skeleton (or after the failure of skeleton) proceeds mainly at the filler/matrix interface, sites of high stress concentration in the matrix [4]. The stress concentration in the matrix depends on shape of filler grains, which is determined in turn by conditions of the liquid-phase sintering. Surface layers, and, consequently, shapes of filler particles are formed by the dissolution/precipitation of filler material in liquid phase. These processes cause redistribution of sizes of filler grains as well: the small filler grains dissolve in the liquid phase and then the dissolved material diffuses through the liquid phase and is deposited on the large filler grains [1, 7]. This is caused by the well-known dependence of the solubility of material on the radius of surface of a body which dissolves [9]. Such redistribution of the filler material leads to the increase in the average size of the filler grains. One can write the following equation for the growth of filler grains during sintering: $da/dt = F(a)$, where $F(a)$ is an increasing function of a , a is the average size of the filler grains, t - time. Suppose that the function $F(a)$ can be presented as a power function $F(a) = ma^n$, where m and n are some constants which characterize the intensity of grain growth. Consider mainly a group of relatively large filler grains (which grow during the mass transfer in sintering) since just large filler grains make higher stress concentrations in the matrix when the composite is loaded. If one accepts that a fractal object is formed due to the precipitation of dissolved filler material on the filler grains, one can

determine the fractal dimension of new formed surfaces as well. The following relation between the linear size of a grain and the number of particles which have aggregated and formed the grain can be written: $da/dN = \psi(a, N)$, where N - the number of particles which have formed the cluster by the mechanism of the random joining of particles, ψ - some function. Having determined the function ψ and integrating the equation of grains growth, one can find the fractal dimension D of the cluster as a index power in the formula: $N \propto a^D$ (this method of determination of the fractal dimension of growing objects was developed by Turkevich and Scher [10, 11]). The value $\nu = dN/dt$ is the content of the dissolved filler material in the liquid phase. Here, the value ν is supposed to be constant. After some rearrangements, one derives: $da/dN \propto (1/\nu)a^n$. By definition of the fractal dimension of a cluster, one deduces: $N \propto a^{n+1}$, and $D = n + 1$.

These relations mean that the greater is the rate of diffusion controlled mass transfer in the liquid-phase sintering, the greater the fractal dimension of large grain surfaces (grain/filler interfaces) in the as-formed composite. It is of interest to compare this conclusion with the results by Tanaka [12], which investigated interrelations between conditions of cold work in pure iron and the fractal dimension of grain boundaries.

Damage initiation in matrix in the vicinity of filler grains

Fracture of particulate composites begins with the initiation and coalescence of microcracks in the matrix. Let us consider now conditions of microcracks initiation in the matrix in the vicinity of filler grains. The local stress in any point of the composite can be determined by the formula like: $\sigma = K\sigma_0$, where σ_0 is the applied stress, and K is the stress concentration factor in point. If the grain is elliptically shaped, the stress concentration factor K is a linear function of $\sqrt{a/\rho}$, where a is the linear size of the grain, ρ is a radius of the hill on the grain surface [11]. Consider also the more realistic case when the grain (inclusion) has a surface like shown in Fig. 2. The following symbols were used: α - angle between two radii from the grain centre to the ends of a conditional hill on the grain surface, ΔR - the distance between the ends of the hill, a - the size of a grain).

In this case, any "hill" on this random surface concentrates stresses and a microcrack can be initiated at any site in which the stress concentration factor exceeds some critical value. The linear relation between K and $\sqrt{a/\rho}$ is appropriate for this case as well, but the values ρ and a depend on the random characteristics of the grain surface. Consider the dependence of these characteristics of the geometry of grain (a and ρ) on the grain surface structure. If the surface of filler grain is formed during liquid-phase sintering, and determined by the solution/ diffusion/deposition of the filler material, it means that the grains are fractal clusters [8] and the surface of the grains is fractal. Suppose that the deposition of the filler material and the grains growth proceed isotropically. Then, the relation between the length of its surface S and the distance between its ends ΔR for some "hills" looks as follows: $S \propto \Delta R^D$, where D - the fractal dimension of the surface of grain. If one approximates this hill by a semicircle, one can obtain $a/\rho = 1 - \cos(\alpha/2)$, where $S/\Delta R = (\pi/180)\alpha/\sin(\alpha/2)$, α is the angle shown in Fig.2. After some rearrangements one can derive a following approximate relation:

$$a/\rho \propto \Delta R^{D-1} \quad (6)$$

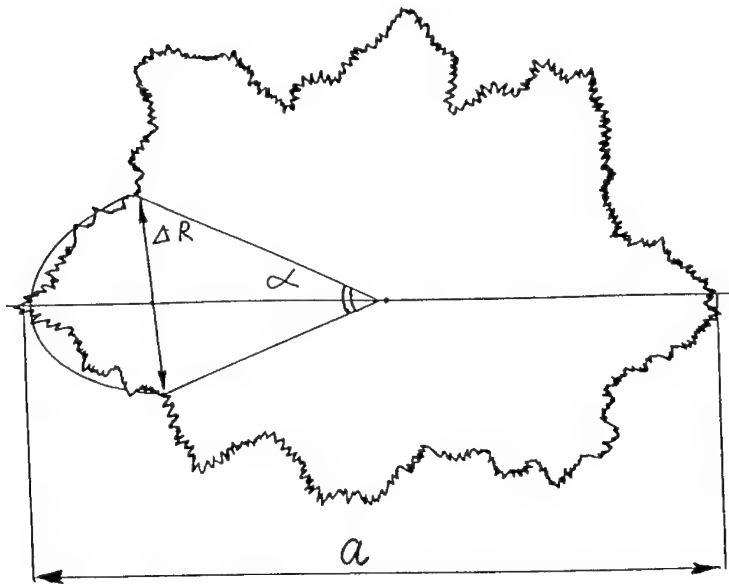


Figure 2: Filler grain with fractal surface

From the definition of the stress concentration factor and eq. (6), one can see that the stress concentration factor and the value $[g(a_1 + a)/N_h]^{(D-1)/2}$ are related. Here a_1 and a are the sizes of the elliptical grain, N_h is the number of "hills" on the grain surface and g is a characteristic of the ellipsoidal shape of the grain.

Thus, the fractal dimension of the filler/matrix interface and the stress concentration factor in the matrix of the composite are related: the greater the fractal dimension of the filler grains surface, the greater the stress concentration in the matrix of the composite. It is clear that the more the stress concentration in the matrix of composite, the greater the damage in the composite, and, consequently, the less its strength [6]. Thus, it can be concluded that the greater is the fractal dimension of the filler/matrix interface in particulate composites, the less the strength of the composites.

Conclusions

The influence of sintering conditions on the structure and damage formation in liquid phase sintered particulate composites is investigated theoretically on the basis of the methods of fractal theory. Conditions of formation of skeleton from filler grains in sintered composites are determined.

It is shown that the conditions of the diffusion mass transfer in liquid phase sintering influence the interface structure and strength of composites: the greater is the rate of mass transfer of filler material in sintering, the greater the fractal dimension of filler/matrix interface and the more intensive the damage initiation in composite matrix under loading.

Acknowledgement

The author (L.L.M.) is grateful to the Alexander von Humboldt Foundation for the possibility to carry out the research project at the University of Stuttgart, MPA (Germany).

References

1. P.S. Kisly et al, Physical and chemical foundations of production of high-melting superhard materials, (Naukova Dumka, Kiev, 1986), 53-173
2. L. Mishnaevsky Jr, "A New Approach to the Analysis of Strength of Matrix Composites with High Content of Hard Filler", J. of Appl. Comp. Matls, Vol.1, pp.317-324, 1995
3. S.B. Luyckx, "Contiguity and the fracture process of WC-Co alloys, in: Advances in Fracture Research", Proc. Int. Conf. Fracture-5, ed. D.Francois, (Pergamon Press, 1981) Vol.2
4. T.J. Chuang et al, "Creep rupture of metal-ceramic particulate composites", Proc.Int. Conf. Fracture - 7, eds. S. Salama et al (Pergamon Press, 1989) Vol.4, pp.2965- 2975
5. S. Schmauder, Die Modellierung zähigkeitbestimmender Prozesse in Mikrogefügen mit Hilfe der Finite-Elemente-Methode, VDI, Reihe 5, Nr. 146, (VDI-Verlag, Düsseldorf, 1988)
6. L.L. Mishnaevsky Jr., "Damage evolution in brittle materials", Materials Ageing and Component Life Extension, ed. V.Bicego et al (EMAS, London, 1995) Vol.2, pp.1135-1143
7. W.D. Kingery, Introduction into Ceramics, (Wiley, NY, 1960)
8. B.M. Smirnov, Physics of Fractal Aggregates (Nauka, Moscow, 1991)
9. R.A. Swalin, Thermodynamics of Solids, (John Wiley and Sons, 1968)
10. L. Turkevich and H. Scher, Fractals in Physics, eds. L. Pietronero and E. Tosatti, (North-Holland, NY, 1986)
11. L.L. Mishnaevsky Jr, "Structure of Interface in Sintered Composites and its Influence on the Strength of Composites", Proceeding EUROMAT-95 (4th European Conference on Advanced Materials and Processes, Venice/ Padua, 1995) (AIG, 1995)
12. M. Tanaka, "Effects of Cold Work on the Fractal Dimension of Grain Boundaries in Pure Iron", Z. f. Metallk., 87, No.4, (1996), pp.310-314

HYDROGEN EFFECTS AND MICROSTRUCTURE IN TITANIUM ALUMINIDE ALLOYS

Anthony W. Thompson
Lawrence Berkeley National Laboratory
Materials Sciences Division, MS 62-203, Berkeley, CA 94720

Abstract

Microstructure effects are becoming recognized as decisive in the kind and magnitude of hydrogen effects in titanium aluminide alloys, as they are in other structural materials. Metallurgical knowledge of microstructure development in titanium aluminide alloys based on both the α_2 and γ phases is now fairly extensive. Moreover, broadened knowledge of hydrogen effects makes possible a more complete description, though not yet entirely realistic modeling, of fracture phenomena.

Hydrides can form in these alloys at rather high hydrogen contents, but of more interest for possible applications are effects at much lower hydrogen contents. Then, the primary microstructural effect in the α_2 phase (when the alloy is based on α_2) is precipitation of orthorhombic or O phase which is stabilized by hydrogen. In TiAl-based alloys, typical microstructures are a mixture of α_2 and γ phases, and hydrides having either of two crystal structures, FCC or tetragonal can form. In α_2 alloys which contain either β or B2 phase, no hydride precipitation has been reported in the β or B2, but O phase can form. Accordingly, hydrogen fracture behavior for all these alloys must be interpreted by a combination of effects due to hydrogen in solution and to the presence of O phase, and when present, hydrides as well.

Introduction

The effects of hydrogen on titanium aluminide alloys, whether based on the Ti_3Al phase α_2 or on the TiAl phase γ , are becoming understood in more detail, including effects of microstructure which are the focus of this paper. In the following sections, discussion is largely limited to the α_2 alloys Ti-24-11 (Ti-24 Al-11 Nb, given as at. pct.) and Ti-25-10-3-1 (Ti-25 Al-10 Nb-3 V-1 Mo), and the γ alloy Ti-48-2-2 (Ti-48 Al-2 Nb-2 Cr). None of these alloys is normally prepared in a single-phase condition. The α_2 alloys usually contain retained β phase (ordered B2 in the case of Ti-25-10-3-1), and the microstructures of Ti-48-2-2 are normally mixtures of α_2 and γ phases; the α_2 phase in Ti-48-2-2 is richer than 25 at. pct. Al, often reaching 34 pct. Al or more (consistent with the Ti-Al binary phase diagram at elevated temperatures).

A wide range of microstructures can be prepared in these alloys, as has been discussed in detail in a number of papers [1-8]. The α_2 alloys have microstructures which are reminiscent of α - β titanium alloys, although there are also important differences from those alloys. Examples for Ti-25-10-3-1 are given [9] in Fig. 1. It should be emphasized that the dark "background" in these structures is partly retained B2 and partly very fine, transformed β , i.e. very fine plates of the α_2 phase. As is evident in Fig. 1, changes of cooling rate strongly affect final microstructures, as α_2 plates increase in size and in degree of parallelism (i.e. a tendency first to "packet" and then to "colony" structures rather than Widmanstätten structures of individual plates) with decreasing cooling rate or on cooling from lower starting temperatures [9,10].

The usual starting point in discussing hydrogen effects in these alloys is the titanium-hydrogen phase diagram [11], in part because there have been a number of reports of the prevalent hydride in that diagram, the FCC δ phase, nominally TiH_2 , in aluminides. As reviewed elsewhere [12-15], however, this now seems incorrect for most circumstances in α_2 alloys. Those alloys seem to respond predominantly to hydrogen with formation of orthorhombic or O phase [7,16,17], as discussed in more detail below. The relevance to γ alloys is also discussed below. Further consideration of the Ti-H phase diagram as a basis for interpreting behavior of titanium aluminides appears inappropriate; it is now evident that the occurrence of additional phases [18,19] makes the relative simplicity of the Ti-H diagram misleading.

The O Phase in α_2 Aluminides

Several reports now exist of the formation and stabilization of the O phase by hydrogen [12,20,21]. This was observed some time ago during thin-foil preparation by Banerjee, *et al.* [22] and more recently by Allen [23]. It also occurs in bulk specimens, as shown in some detail [12-15,24,25]; in the works cited, hydrides were sought at hydrogen contents up to 6000 ppm by wt., and none were found: only O phase. A number of detailed observations were made in these studies, and conclusions drawn from them. To summarize, the following points can be made:

- Hydrogen stabilizes and stimulates formation of O phase in α_2 alloys.
- For low hydrogen charging content, up to perhaps 300 wppm, O phase does not form by charging, but can occur when thin foils are electropolished (O phase is absent in ion-thinned foils and in X-rays of bulk material).

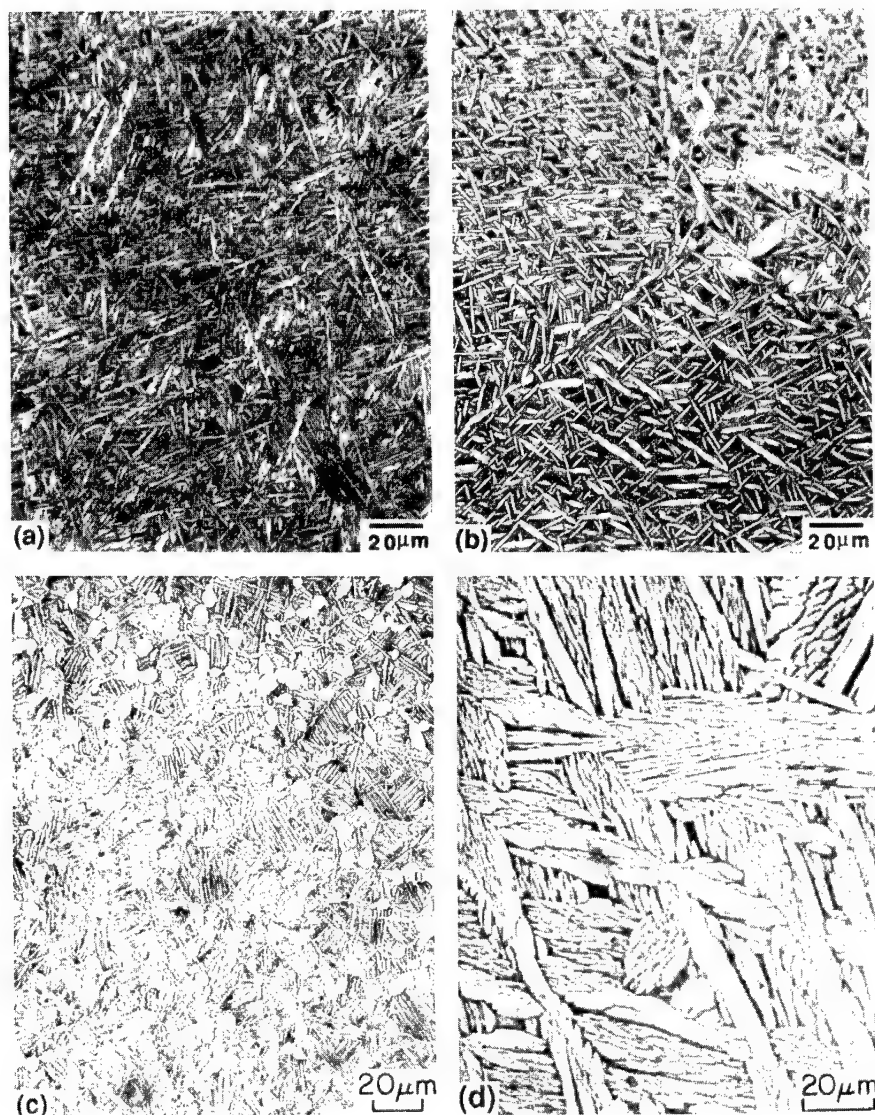


Figure 1. Development of microstructure in aluminide alloys based on the α_2 phase. (a) Widmanstätten or basketweave morphology of α_2 plates, formed in Ti-25-10-3-1 on cooling from the β field at 0.5 K/s. (b) Coarser basketweave structure formed by cooling at the same rate as in (a) but from high in the $\alpha_2 + \beta$ field. (c) Primary α_2 (white phase) in matrix of packet α_2 plates formed on cooling from the $\alpha_2 + \beta$ field. (d) Colonies of large plates cooled from low in the $\alpha_2 + \beta$ field at 5 K/s. From ref. 9.

- For larger amounts of charged hydrogen, above 1000 wppm, considerable amounts of O phase form at the expense of the α_2 phase, and the amount of O phase increases with increasing amounts of charged hydrogen.
- Hydrogen outgassing does slowly remove O phase formed by charging, although the time taken for removal is considerably longer than the time needed for outgassing.
- Hydrides of any structure have not been detected for hydrogen contents up to 6000 wppm H.

These observations are consistent with the phase diagram determined for hydrogen in the α_2 phase by Chu, *et al.* [26]. In the original work [26], it was thought that the precipitated phase in the two-phase region of this diagram was hydride, but it is now clear from considerable additional evidence that this diagram is really the α_2 -O diagram [27]. It is so shown below as Fig. 2. It should be emphasized that hydrogen charging and degassing was found to fully reversible [26], with the microbalance weight as well as the mechanical properties of the specimens restored on degassing.

As summarized above, it was shown that as charged hydrogen content increases, so does the volume fraction of the O phase. The O typically precipitates as thin, parallel plates [12,16]. Subdivision of the interior of α_2 laths in this manner would be expected to interfere with slip and thereby to produce substantial strengthening; but in fact the strengthening produced is modest [12], as Fig. 3 shows. Larger hydrogen content tends to result in formation of lenticular O phase particles and entire grains of O phase [18], which can be single-phase or can contain domain configurations which maintain stress-free inter-

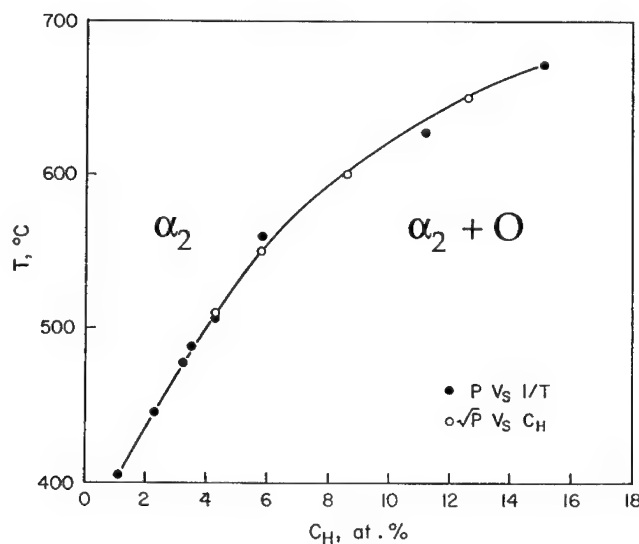


Figure 2. Phase diagram for Ti-24-11, showing terminal solubility of hydrogen in the α_2 phase in equilibrium with the O phase, i.e. solvus for O in α_2 . Measurements by two methods, P vs. $1/T$ and \sqrt{P} vs. C_H [26]. Figure from ref. 26; see also ref. 27.

faces [25]. This lack of internal stress accompanying O precipitation likely contributes to the lack of strengthening observed with hydrogen charging.

Hydrides in TiAl Alloys

Hydride precipitation in gamma alloys has not been extensively studied. However, recent work by Li [30] and her colleagues [19,31-33] has clarified a number of issues. The experiments were conducted largely in Ti-48-2-2, in microstructures containing large amounts of both γ and α_2 phases. Importantly, they have clearly shown a new hydride phase called θ , which has a tetragonal structure with a large c dimension, 2.808 nm. This in turn means that lattice fringes are readily obtained for {002} planes in this structure. They also found the usual Ti-H FCC hydride phase, δ , in a number of instances. Thus the gamma alloys appear to differ significantly from what was summarized above about α_2 alloys. However, it remains unclear [19] what is the relationship among these two hydride phases or with the local structure and composition of their parent phase(s).

Mechanical property data are very limited for these alloys containing hydrogen. An example of a set of stress-strain curves [32] is shown in Fig. 4. These make it clear that significant increases in yield strength accompany charging with hydrogen (amounts ranging from 1000 to 3000 wppm), but that work-hardening appears similar, as does the response to strain-rate changes.

Summarizing the findings on the TiAl alloys, both those just discussed and others in the published record [19,30-32], it has been found that:

- A new ternary hydride phase, θ , has been found, with approximate stoichiometry $Ti_{1.7}AlH_x$ and with a tetragonal structure.
- The θ phase forms predominantly in α_2 phase, less commonly in γ .

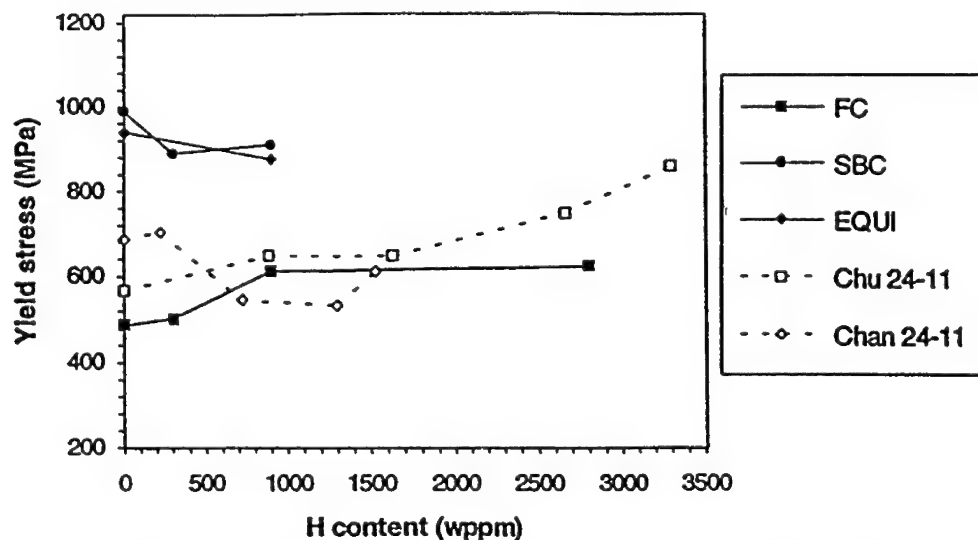


Figure 3. Dependence of yield strength in α_2 alloys on hydrogen content, for three microstructures of Ti-25-10-3-1 [12] and two similar microstructures in Ti-24-11 [28,29]. From ref. 12.

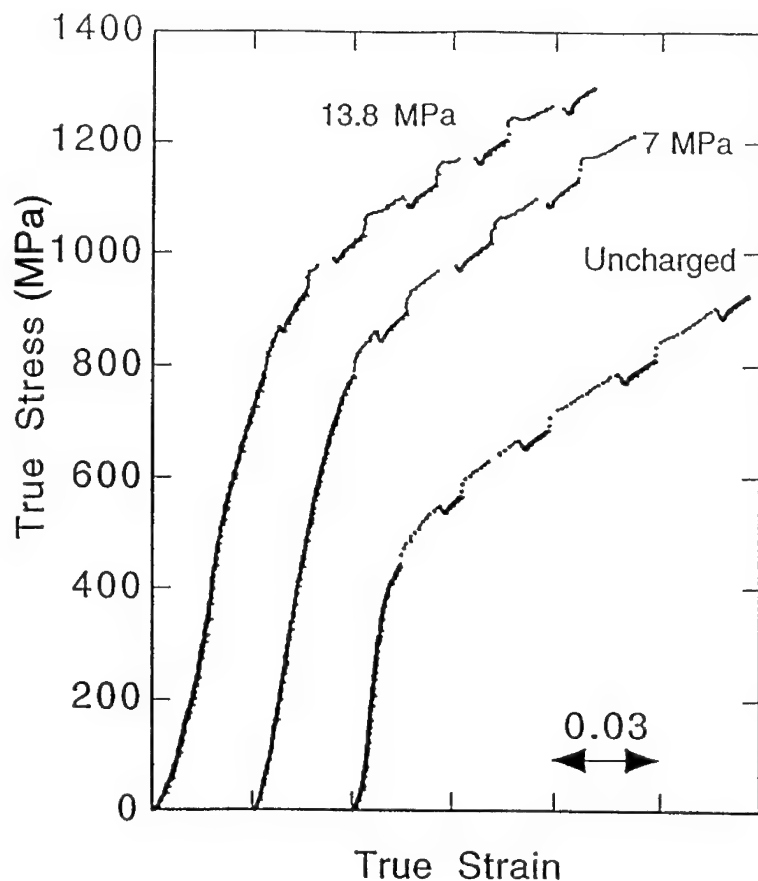


Figure 4. Stress-strain curves, showing results of strain-rate change experiments (base strain rate of 2×10^{-4} /s was increased two orders of magnitude) for uncharged and two charged conditions of cast Ti-48-2-2. Hydrogen content for 7 MPa charging was about 1800 wppm, and for 13.8 MPa was about 2300 wppm. From ref. 32.

- A second hydride found is FCC δ , TiH_2 isomorphous; forms in both α_2 and γ .
- At 0.1 MPa, θ and δ hydrides form in near-surface regions only (in 48-2-2).
- At 7 and 13.8 MPa, hydride(s) formed may be δ only (in lamellar 48-2-2), or both θ and δ (in duplex 48-2-2), or mostly δ , little θ (in single-phase Ti-52 Al).

Fracture Behavior

Fracture studies of several kinds have been carried out on these alloys. Most work has been concerned with the α_2 alloys, less systematic work being available for γ alloys. Much of the work on the α_2 alloys has been summarized elsewhere [4,12,24,28,34,35], so only a brief overview is given here.

Many studies of the titanium aluminides have reported only tensile ductility as a measure of fracture resistance. A comparison on this basis provides limited information about toughness, but does permit comparison of the work of several investigators. An

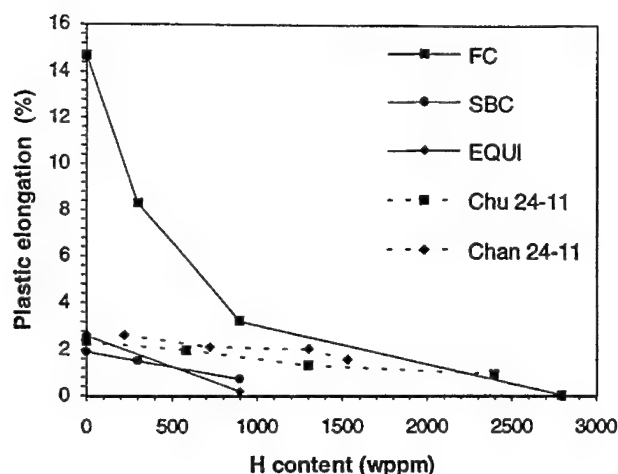


Figure 5. Comparison of ductilities of different microstructures of α_2 alloys, as a function of H content. Microstructures are described in the referenced papers [12,28,29].

example for α_2 alloys is shown as Fig. 5. Here it can be seen that not only the absolute level of the ductility, but also the rate of decrease of ductility with increasing hydrogen content, depends on microstructure. There are a number of detailed discussions of this point and its implications for alloy design [12-15,24,29,34,35]. In a few cases, toughness data have been reported, and an example is repeated here as Fig. 6.

Established procedures [28,35,37,38] have been used to estimate the effective surface energy, γ_{eff} , for fracture of Ti-24-11 [28], assuming Griffith-like fracture behavior [39]. The value obtained was 27 J/m^2 , about an order of magnitude greater than the expected value of the true lattice surface energy, γ_s , about 0.9 J/m^2 for Ti_3Al [28]. Such an "effective" energy value is broadly consistent with results on iron [39], where measured values of γ_{eff} are also about an order of magnitude larger than γ_s . It should be emphasized that this γ_{eff} corresponds to crack propagation [39] and thus is not directly related to the total fracture energy $\gamma = 2\gamma_s + \gamma_p$ (γ_p = plastic work), which in Ti-24-11 has a value [28] of about 3000 J/m^2 because of the large amount of precursor work associated with plastic zone development, typical of metallic alloys with toughnesses of $10 \text{ MPa}\sqrt{\text{m}}$ or more [28,39].

The fracture calculation just described effectively relies on a cleavage-like model for the failure [28,35,39]. But in light of fractographic indications (discussed below) that true cleavage probably does not occur in this alloy, a somewhat different approach might be preferred. Among the alternatives is an approach suggested by Ritchie, Knott and Rice [38], in the form of a "critical distance" model. This approach uses the measured ratio of σ_F to the yield strength YS to determine the distance l^* ahead of the crack tip at which that stress ratio must be maintained to propagate fracture [40]. For Ti-24-11 [28], $\sigma_F / \text{YS} = 2.37$, and the calculation [28] then yields a value for l^* of about $16 \mu\text{m}$. This estimated l^* value, equalling about three α_2 lath widths, is broadly consistent with the microstructural dimensions found in other determinations [38,40] of l^* .

Fractography has been an important issue in interpreting behavior of these alloys, because of its implications for identification of micromechanisms. Certainly all investigators agree that fracture surfaces are brittle in appearance for both α_2 and γ alloys, and in general a faceted type of appearance is noted, although the facets are not regular or well-

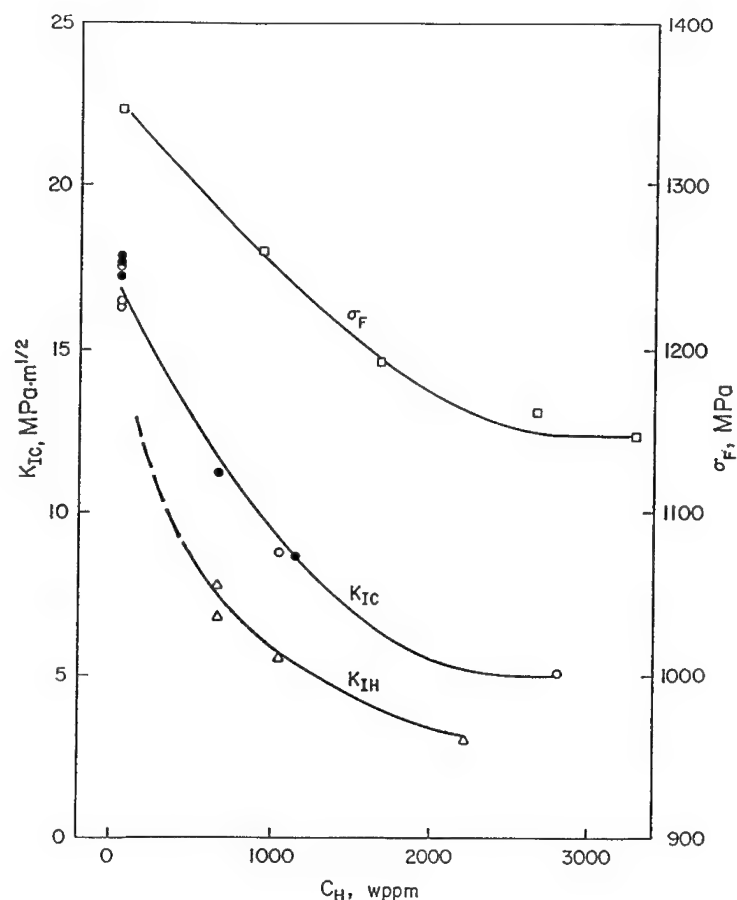


Fig. 6. The dependence of toughness on hydrogen content for a microstructure of Ti-24-11. The values of true local fracture stress, σ_F , were measured in notched bend bars; K_{IH} refers to the threshold value observed for sustained-load cracking in hydrogen-charged specimens. From ref. 36.

formed in appearance. An example for an α_2 alloy is shown as Figure 7; another example is Fig. 8 for a γ alloy. Facets in both these figures are poorly defined and examples can be found in both figures of curved or conchoidal shapes of these facets, which tends to rule out the possibility that they are on low-index crystallographic planes. The latter point is of interest because it is among the criteria for classical cleavage fracture [34,35]. Thus although it is commonplace for aluminide fracture facets to be described as "cleavage" features, their lack of flatness alone tends to contradict such a description. Moreover, other locally ductile features such as dimples and tear ridges are also visible [41]. Nor is this the end of the complications; even more complex, mixed-mode fractures can be observed, as Fig. 9 shows, and clearly no single mode adequately describes such fractures.

Among the needs in this area are modeling efforts. Since it appears unlikely that true cleavage is present, other brittle, transgranular fracture modes such as quasi-cleavage or QC [34,41] need exploration. Quantitative models of QC fracture do not exist, and it

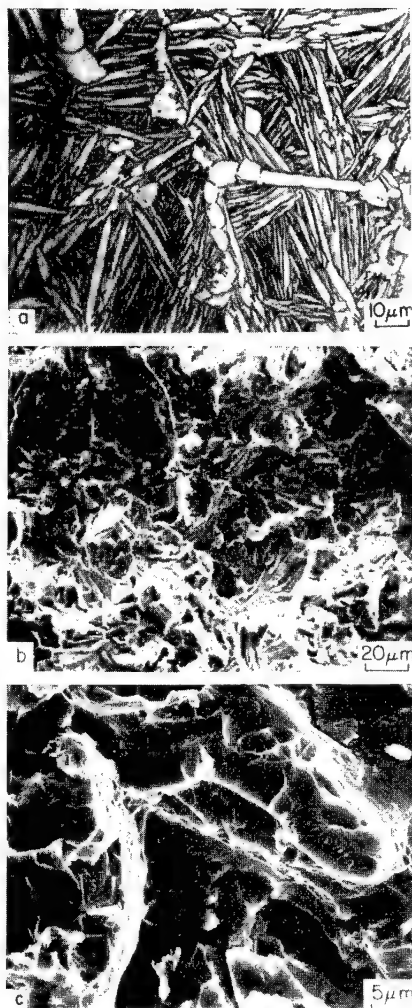


Fig. 7 (above). Fracture surface appearance in a microstructure of Ti-25-10-3-1 having a matrix structure of α_2 laths. (a) Microstructural appearance, light microscopy. (b) General view of fracture surface, SEM (scanning electron microscopy); note curved facets. (c) Detail view by SEM, showing mixture of dimpled areas, tear ridges, and quasi-cleavage. From ref. 41.



Fig. 8. Fracture surface appearance in a single-phase γ alloy (Ti-50 Al), SEM. Note large curved "facets" as parts of a generally brittle overall appearance. From ref. 42.

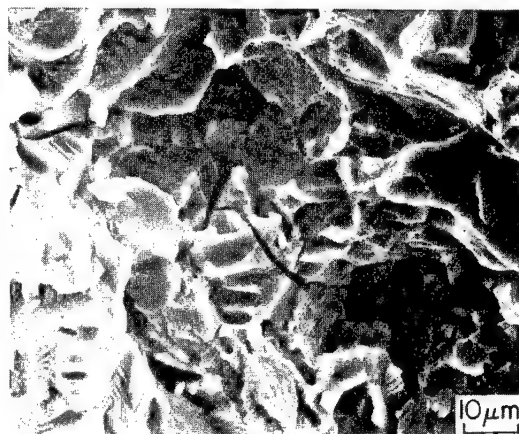


Fig. 9. Fracture appearance in an α_2 alloy, with coarse primary α_2 particles and an equiaxed matrix of B2 phase. Note both flat and curved facets, locally ductile areas, tear ridges, secondary cracking, and "fluted" appearance [12]. From ref. 35.

remains to be determined whether they will resemble those for true cleavage or not. Mechanical modeling to determine the interrelation among fracture properties is also needed, given the rather primitive tools of this kind now available [24,28,29,35,39]. Without such modeling developments, it is difficult to be more than semi-quantitative about the effects of microstructure on hydrogen embrittlement in titanium aluminide alloys.

Summary

For α_2 alloys, the main points about hydrogen effects are as follows:

- Hydrogen is readily absorbed at 500-650°C, below 1 atm pressure, and is equally readily removed by outgassing: absorption is fully *reversible*.
- The second phase precipitated on hydrogen charging is the orthorhombic phase; no hydrides have been detected up to 6000 wppm hydrogen content.
- Increases in yield strength with hydrogen charging are modest.
- Ductility and toughness decrease gradually with increasing hydrogen content; extent and rate of this decrease depend on microstructure.
- Fracture processes are complex in these alloys, and brittle fracture modeling is needed to understand micromechanisms.

For γ alloys, the main points are:

- Little hydrogen is absorbed near 1 atm pressure; large uptakes are possible but require pressures of several MPa and temperatures *ca.* 800-900°C.
- Hydrogen absorption is not readily reversible (must degas at 900-1100°C).
- Two hydrides, θ and δ , are formed; solubility limit(s) unknown.
- Considerable strengthening accompanies hydrogen charging.
- Fracture is brittle and complex, and would benefit from the same modeling efforts as mentioned for α_2 alloys.

Acknowledgements

I appreciate helpful discussions with R.O. Ritchie. This work was supported by the U.S. Air Force Office of Scientific Research under Grants F49620-93-1-0140 and F49620-96-1-0233, and by the David Jackson Fund for Scholarly Endeavors.

References

1. H.A. Lipsitt, in *Ordered Intermetallic Alloys*, MRS Symp. Vol. 39, ed. C.C. Koch, C.T. Liu and N.S. Stoloff (Pittsburgh, PA: Mater. Res. Soc., 1985), pp. 351-364.
2. R. Strychor, J.C. Williams and W.A. Soffa, *Metall. Trans. A*, 19A (1988), 225-234.
3. Y.-W. Kim and F.H. Froes, in *High Temperature Aluminides and Intermetallics*, ed. S.H. Whang, C.T. Liu, D.P. Pope and J.O. Stiegler (Warrendale, PA: TMS-AIME, 1990), pp. 465-492.
4. J.M. Larsen, K.A. Williams, S.J. Balsone and M.A. Stucke, *ibid.*, pp. 521-556.
5. Y.-W. Kim, in *Microstructure/Property Relationships in Titanium Aluminides and Alloys*, ed. Y.-W. Kim and R.R. Boyer (Warrendale, PA: TMS, 1991), pp. 91-103.
6. G. Proske, G. Lütjering, J. Albrecht, D. Helm and M. Daeubler, *Mater. Sci. Eng.*, A152

- (1992), 310-316.
7. D. Banerjee, A.K. Gogia, T.K. Nandy, K. Muraleedharan and R.S. Mishra, in *Structural Intermetallics*, ed. R. Darolia, J.J. Lewandowski, C.T. Liu, P.L. Martin, D.B. Miracle and M.V. Nathal (Warrendale, PA: TMS, 1993), pp. 19-33.
 8. M. Yamaguchi and H. Inui, *ibid.*, pp. 127-142.
 9. A.W. Thompson and T.M. Pollock, *ISIJ Int. J.*, 31 (1991), 1138-1145.
 10. F.-C. Dary and A.W. Thompson, in *Titanium '92 Science and Technology* (Proc. 7th Int. Conf. on Titanium), ed. F.H. Froes and I.L. Caplan (Warrendale, PA: TMS, 1993), Vol. I, pp. 375-382.
 11. A. San-Martin and F.D. Manchester, in *Phase Diagrams of Binary Titanium Alloys*, ed. J.L. Murray (Metals Park, OH: ASM, 1987), pp. 123-135.
 12. X. Pierron and A.W. Thompson, in *Fatigue and Fracture of Ordered Intermetallic Materials*, ed. W.O. Soboyejo, T.S. Srivatsan and D.L. Davidson (Warrendale, PA: TMS, 1994), pp. 355-368.
 13. A.W. Thompson, X. Pierron and D.B. Allen, in *Strength of Materials* (Proc. ICSMA-10), ed. H. Oikawa, K. Maruyama, S. Takeuchi and M. Yamaguchi (Sendai: Japan Inst. Metals, 1994) pp. 423-426.
 14. X. Pierron and A.W. Thompson, in *Hydrogen Embrittlement of Materials*, ed. A.W. Thompson and N.R. Moody (Warrendale, PA: TMS, 1996), pp. 765-774.
 15. D.B. Allen, A.W. Thompson and M. De Graef, *ibid.*, pp. 830-840.
 16. D. Banerjee, A.K. Gogia, T.K. Nandy and V.A. Joshi, *Acta Metall.*, 36 (1988), 871-882.
 17. R.G. Rowe, in *High Temperature Aluminides and Intermetallics*, ed. S.H. Whang, C.T. Liu, P.L. Martin, D.B. Miracle and M.V. Nathal (Warrendale, PA: TMS-AIME, 1990), pp. 375-401.
 18. M. De Graef, D.B. Allen, X. Pierron, T.M. Pollock and A.W. Thompson, in *Electron Microscopy 1994* (Proc. ICEM-13), Vol. 2A, ed. J.P. Chevalier, F. Glas and P.W. Hawkes (Paris: Les Editions de Physique, 1994), 665-666.
 19. K. Li, M. De Graef, T.M. Pollock, D.B. Allen and A.W. Thompson, in *Hydrogen Effects in Materials*, ed. A.W. Thompson and N.R. Moody (Warrendale, PA: TMS, 1996), pp. 809-818.
 20. D. Banerjee, T.K. Nandy, A.K. Gogia and K. Muraleedharan, in *Proc. 6th World Conf. on Titanium*, Vol. 2, ed. P. Lacombe, R. Tricot and G. Beranger (Paris: Les Editions de Physique, 1989), pp. 1091-1096.
 21. M. Saquib, L.S. Apgar, D. Eylon and I. Weiss, in *Titanium '92 Science and Technology* (Proc. 7th Conf. on Ti), ed. F.H. Froes and I.L. Caplan (Warrendale, PA: TMS, 1993), pp. 845-852.
 22. K. Muraleedharan, S.V.N. Naidu, D. Banerjee, *Scripta Metall. Mater.*, 24 (1990), 27-32.

23. D.B. Allen and A.W. Thompson, in *Second Workshop on Hydrogen Effects on Materials in Propulsion Systems* (NASA Conf. Publ. 3182), ed. B.N. Bhat, R.L. Dreshfield and E.J. Vesely (Washington, DC: NASA, 1992), pp. 243-250.
24. X. Pierron and A.W. Thompson, in *Fatigue and Fracture of Ordered Intermetallic Materials II*, ed. W.O. Soboyejo, T.S. Srivatsan and R.O. Ritchie (Warrendale, PA: TMS, 1995), pp. 31-38.
25. X. Pierron, M. De Graef, T.M. Pollock and A.W. Thompson, in *Proc. Microscopy and Microanalysis 1995*, ed. G.W. Bailey, M.H. Ellisman, R.A. Hennigar and N.J. Zaluzec (New York: Jones and Begell, 1995), pp. 520-521.
26. W.-Y. Chu, A.W. Thompson and J.C. Williams, *Acta Metall. Mater.*, 40 (1992) 455-462.
27. A.W. Thompson, W.-Y. Chu and J.C. Williams, *Scripta Mater.*, in press.
28. W.-Y. Chu and A.W. Thompson, *Metall. Trans. A*, 23A (1992), 1299-1312.
29. K.S. Chan, *Metall. Trans. A*, 24A (1993), 1095-1105.
30. K. Li, Ph.D. thesis, Carnegie Mellon University, Pittsburgh, 1996.
31. K. Li, T.M. Pollock, A.W. Thompson and M. De Graef, *Scripta Metall. Mater.*, 32 (1995), 1009-1014.
32. U. Habel, T.M. Pollock and A.W. Thompson, in *Hydrogen Effects in Materials*, ed. A.W. Thompson and N.R. Moody (Warrendale, PA : TMS, 1996) pp. 787-796.
33. U. Habel, K. Li, A.W. Thompson and T.M. Pollock, "Gas Phase Hydrogen Charging of γ -based Titanium Aluminides," to be published.
34. A.W. Thompson, in *Fatigue and Fracture of Ordered Intermetallic Materials*, ed. W.O. Soboyejo, T.S. Srivatsan, D.L. Davidson (Warrendale, PA: TMS, 1994), pp. 293-306.
35. A.W. Thompson, in *Micromechanics of Advanced Materials*, ed. S.N.G. Chu, P.K. Liaw, R.J. Arsenault, K. Sadananda, K.S. Chan, W.W. Gerberich, C.C. Chau and T.M. Kung (Warrendale, PA : TMS, 1995) pp. 393-400.
36. A.W. Thompson and W.-Y. Chu, in *Summary Proceedings of the 4th Workshop on Hydrogen-Material Interaction*, NASP Joint Program Office Workshop Pub. 1013, ed. H.G. Nelson (Hampton, VA : NASA-Langley, Feb. 1993) pp. 83-93.
37. J.R. Griffiths and D.R.J. Owen, *J. Mech. Phys. Solids*, 19 (1971), 419-431.
38. R.O. Ritchie, J.F. Knott and J.R. Rice, *J. Mech. Phys. Solids*, 21 (1973), 395-410.
39. A.W. Thompson and J.F. Knott, *Metall. Trans. A*, 24A (1993), 523-534.
40. R.O. Ritchie and A.W. Thompson, *Metall. Trans. A*, 16A (1985), 232-248.
41. A.W. Thompson, "Fractography and its Role in Fracture Interpretation," *Fatigue Fract. Eng. Mater. Struct.*, in press.
42. W.-Y. Chu and A.W. Thompson, *Scripta Metall. Mater.*, 25 (1991) 2133-2138.

Hydrogen and Oxygen Effects on Composites

Containing a Continuous Carbon Phase

Andrew J. Eckel* and James D. Cawley⁺

*National Aeronautics and Space Administration
Lewis Research Center
Cleveland, OH 44135

⁺Case Western Reserve University
Cleveland, OH 44106

Abstract

Carbon is frequently present in advanced materials in the form of fibers or an interphase layer on other materials/fibers. A great deal of work has been performed in recent years on the oxidation of these emerging materials, however, there is currently little in the open literature on the effects of high temperature gaseous hydrogen exposures. The differences and similarities between carbon reacting with oxygen and hydrogen are presented. The focus of the presentation is on the analytical solutions of gas phase diffusion controlled kinetics. Reaction rate, reaction sequence, oxidant partial pressure, total system pressure, pore/crack dimensions, and temperature are analyzed with respect to the influence of each on an overall linear-parabolic rate relationship. The analytical solutions are compared to the literature and experimental results for carbon-containing composites.

Introduction

The oxidation of bulk carbon, in its many varied forms, has been widely studied [1-3]. In all cases, the rates are rapid -- in the range of 10^{-4} to 10^{-1} g cm⁻² s⁻¹ (which corresponds to recession rates on the order of mm/hr to mm/min) for 1 atm oxygen at 1000°C. Similar recession rates have been reported for thin carbon interphases sandwiched between non-carbon matrices [4-10]. However, there is significantly less information available on the kinetics of carbon reacting with hydrogen in the bulk form [11] and no information where it is present as an interphase/fiber.

Based on thermodynamic calculations [12] the most probable reactions for carbon with oxygen are



and carbon with hydrogen are



In all cases, the product formed at the receding substrate interface is a gaseous phase. The general expression relating the recession distance, x , and the oxidation time, t , is the sequential linear-parabolic relationship [13]

$$x^2/k_p + x/k_l = t \quad (5).$$

In this equation k_p is termed the parabolic rate constant (m²/s) and k_l the linear rate constant (m/s). Specific situations are often well characterized by the limiting cases of Eqn (5). For example, if the overall rate is controlled by the rate of reaction then Eqn (5) can be reduced to

$$x/k_l = t \quad (6).$$

On the other hand, in situations where the rate is controlled by the supply, or flux, of oxygen or hydrogen, then the reaction rate is assumed to be infinitely fast and Eqn (5) can be expressed as

$$x^2/k_p = t \quad (7).$$

In the analysis that follows, attention is focused on the latter limiting case, where the overall kinetics are controlled by the mass transport of the oxygen or hydrogen to the solid substrate. The analysis for the linear limiting case is not addressed here. Surface reaction rates vary greatly for different carbons as they are known to be dependent on a variety of factors such as chemical composition, density, porosity and presence of surface defects, crystallinity and crystallographic orientation [1,2]. Thus, the linear rate constant can only be determined empirically.

In the following, the results of comprehensive analytical model is presented using reaction rate formalism and kinetic theory of gases. Only the results of the analysis are presented as the rigorous derivation, for the oxidation case, was previously published by the authors [4]. The analysis focuses on obtaining an expression for the carbon recession rate. In all cases, it is assumed that the dense and homogeneous carbon initially occupies a well defined volume which is finite in the two directions which are perpendicular to the recession direction and infinite in the direction parallel to the recession direction, as shown schematically in Fig. 1. The model assumes no reaction of the reactant gas with the pore walls. This is not necessarily true for many applications [6-9], particularly at higher temperatures. However, the objective here is to compare and contrast the differences between oxygen and hydrogen attack of a continuous carbon constituent, irrespective of the matrix in which it is contained. The results of the model are equally applicable to the recession of a carbon fiber (e.g., a carbon fiber reinforced

ceramic matrix composite) and a carbon coating (for example, the fiber/matrix interface coating in a silicon carbide fiber reinforced composite).

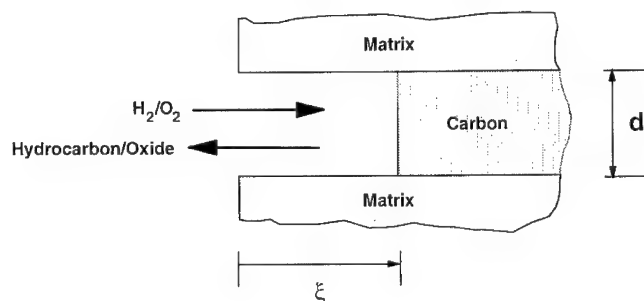


Figure 1 - Schematic of carbon recession during reaction with hydrogen or oxygen, in a nonreactive matrix.

Results of Analytical Model

Vapor phase diffusion can be classically divided into two regimes: molecular and Knudsen. In molecular, or convective diffusion, gas molecules interact more frequently with other gas molecules than with the pore walls. The condition to be met for this is when the mean free path of the gas, λ is much smaller than the pore diameter, d . In contrast, Knudsen diffusion is defined when $\lambda \gg d$. That is, in the Knudsen regime, a diffusing molecule is much more likely to interact with the pore walls than another diffusing molecule. There is a great deal of overlap between molecular and Knudsen regimes and this overlap is often termed the transition regime. This regime can and has been appropriately treated as a general case involving molecular and Knudsen diffusion (i.e., they are simply limiting cases of the general solution). The two regimes are treated separately here, to delineate the differences between each of the reactions listed above. The general solution is then applied to Rxn (1) to illustrate the functional dependence on temperature, partial pressure, total system pressure and pore size on all of the possible reactions.

In diffusion controlled kinetics the reaction at the carbon interface is assumed to be infinitely fast, but the above listed reaction sequences still affect mass transport. For the molecular regime, the gas concentration profiles in a crack/pore for each of the four reaction sequence cases are shown in Fig. 2 (a), (b), (c) and (d). All four will be considered here. It should be noted that although only one reaction sequence can be the correct description for a particular situation, it is plausible that different sequences will occur under different conditions.

Conservation of the reactant gas proves to be the most convenient frame of reference for most of the discussion. It is assumed that the concentration of the reactant gas at the surface, $x=0$, is fixed by the composition of the atmosphere to be χc_T , where χ is the fraction defining the partial pressure, and the concentration at the interface, $x=\xi$, is fixed by the appropriate phase equilibria (Eqn. (1) through (4)) to be c_ξ . It is further assumed that the quasisteady state exists, i.e., the flux density of hydrogen, j_{H_2} of oxygen, j_{O_2} , is not a function of position at any time, t . The flux density of hydrogen or oxygen over the domain $0 < x < \xi$ may be, in general written [14]

$$j_{H_2} = -D \frac{\partial c_{H_2}}{\partial x} + v^* c_{H_2} \quad (8)$$

or

$$j_{O_2} = -D \frac{\partial c_{O_2}}{\partial x} + v^* c_{O_2} \quad (9)$$

where v^* is the molar average velocity, which may be defined using

$$v^* = (\sum c_i v_i) / (\sum c_i) \quad (10)$$

where v_i is the velocity of the i th species with respect to a stationary coordinate system. By definition

$$j_i = c_i v_i \quad (11)$$

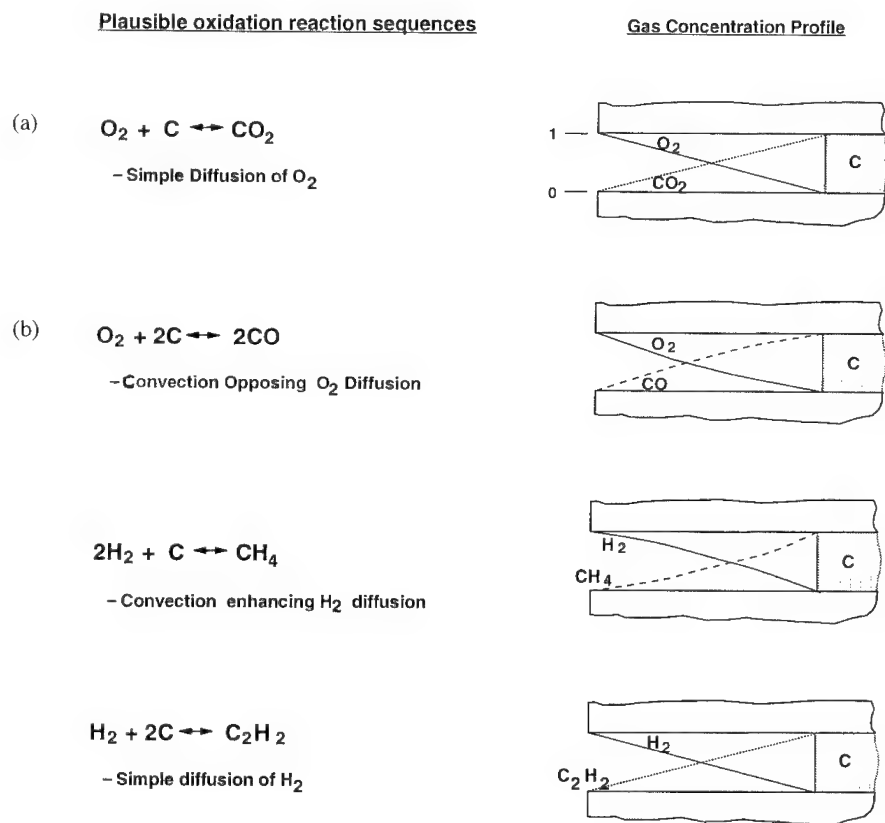


Figure 2 - Plausible reaction sequences. (a) O_2 diffusion in and CO_2 diffusion out, (b) O_2 diffusion in and CO diffusion out, (c) H_2 diffusion in and CH_4 diffusion out, and (d) H_2 diffusion in and C_2H_2 diffusion out.

Eqn. (10) can be rewritten, in the general form, as

$$v^* = \Sigma (j_i)/c_T \quad (12)$$

where c_T is the total concentration of gas molecules, which is a constant. For the cases considered here, c_T is simply the sum of the concentrations of reactant and product gases. For reactions (1) through (4), respectively, Eqn. (12) becomes

$$v^* = (j_{O_2} + j_{CO_2})/c_T \quad (13)$$

$$v^* = (j_{O_2} + j_{CO})/c_T \quad (14)$$

$$v^* = (j_{H_2} + j_{CH_4})/c_T \quad (15)$$

$$v^* = (j_{H_2} + j_{C_2H_2})/c_T \quad (16).$$

Conservation of mass for each of the respective reactions requires

$$j_{CO_2} = -j_{O_2} \quad (17)$$

$$j_{CO} = -2j_{O_2} \quad (18)$$

$$j_{CH_4} = -1/2j_{H_2} \quad (19)$$

$$j_{C_2H_2} = -j_{H_2} \quad (20)$$

and therefore, upon substitution, $v^*=0$ in Eqns. (13) and (16). For these cases, Eqn. (8) and (9) simplify to Fick's first law

$$j_i = -D \partial c_i / \partial x \quad (22).$$

Assuming quasisteady state yields a linear concentration gradient, which, upon substitution and integration gives

$$j_i \approx -D (c_i(\xi) - c_i(0)) / \xi \quad (23).$$

The recession rate, $d\xi/dt$, is given by mass balance. That is, the thickness removed is equal to the negative of the quantity of carbon away from the interface divided by the molar density of carbon, N , (mol/m^3). Substitution of the recession rate and integration yields an expression which can be written in a standard form for parabolic kinetics

$$\xi = k_p^{1/2} t^{1/2} \quad (24)$$

which is just a restatement of Eqn. (7).

In contrast to Rxns (1) and (4), Rxn (2) produces two mols of gaseous product, CO, for every mol of gaseous reactant, O_2 , consumed. And Rxn (3) produces one mol of gaseous product, CH_4 , for two mols of H_2 consumed. In both of these cases the convection term in Eqn. (8) or (9) is nonzero and the subsequent integration does not yield a linear concentration gradient. Perhaps the most straightforward means of comparing the kinetics for the different reactions is to compare the functional form of the parabolic rate constants, k_p . Table I lists the parabolic rate constants for all four reaction sequences where $c_i(0) \approx \chi c_T$ and $c_i(\xi) \approx 0$. Furthermore, if one takes the mole fraction of hydrogen or oxygen to be unity, $\chi = 1$, then the relationships can be simplified to those listed in Table II. Both Table I and II both also list the functional relationship for k_p for the Knudsen regime. Again, the details of the derivations for the Knudsen regime follow the paths taken in [4].

Examination of the parabolic rate constants in Table II, show two main differences. First is the magnitude of the numerical constants which precede the common Dc_T/N factor. Second it the value of diffusivity, D or D_K , for the specific cases. Each is treated in turn by comparing the differences within a regime and then between regimes.

It is interesting to compare the magnitudes of the Dc_T/N prefactors and reflect on their physical interpretation. In the Knudsen regime, where no convection terms are present, the hydrogen reaction to form methane produces the smallest prefactor. This is a result of the fact that it takes two mols of reactant gas to remove one mole of carbon. Next, by a factor of two, is O_2 diffusion in and CO_2 diffusion out. In this case, one mol of oxygen consumes one mol of carbon. For the remaining two cases, the prefactor is again increased by a factor of two over the CO_2 case, since one mol of reactant gas removes two moles of carbon.

The differences between the Knudsen and molecular cases are due to the convection terms in Eqns (8) and (9). For the cases where one mol of reactant gas produces one mol of product gas, no convection exists and the prefactors are equal in the molecular and Knudsen regimes. In contrast, O_2 diffusion in and CO diffusion out predicts kinetics which are twice as fast as the formation of CO_2 for the Knudsen regime, but only 39 percent faster in the molecular regime. The net increase is lower because the convection caused by the outward flow of 2 mols of CO for every mol of O_2 opposes diffusion of the oxygen. In a similar fashion, convection *enhances* the diffusion of hydrogen in the methane case, by 39 percent compared to the Knudsen regime, since only one mol of the CH_4 is produced for every 2 mols of H_2 .

Table I Functional form of parabolic rate constants for molecular and Knudsen regimes

Reaction Sequence	Molecular Regime	Knudsen Regime
$C + O_2 \rightarrow CO_2$	$k_p = 2 \chi \left(\frac{Dc_T}{N} \right)$	$k_p = 2 \chi \left(\frac{D_K c_T}{N} \right)$
$2C + O_2 \rightarrow 2CO$	$k_p = 4 \ln(1 + \chi) \left(\frac{Dc_T}{N} \right)$	$k_p = 4 \chi \left(\frac{D_K c_T}{N} \right)$
$2C + H_2 \rightarrow C_2H_2$	$k_p = 4 \chi \left(\frac{Dc_T}{N} \right)$	$k_p = 4 \chi \left(\frac{D_K c_T}{N} \right)$
$C + 2H_2 \rightarrow CH_4$	$k_p = 2 \ln \left(\frac{2}{2 - \chi} \right) \left(\frac{Dc_T}{N} \right)$	$k_p = \chi \left(\frac{D_K c_T}{N} \right)$

Table II Functional form of parabolic rate constants for molecular and Knudsen regimes with $\chi = 1$

Reaction Sequence	Molecular Regime	Knudsen Regime
$C + O_2 \rightarrow CO_2$	$k_p = 2 \left(\frac{Dc_T}{N} \right)$	$k_p = 2 \left(\frac{D_K c_T}{N} \right)$
$2C + O_2 \rightarrow 2CO$	$k_p = 2.77 \left(\frac{Dc_T}{N} \right)$	$k_p = 4 \left(\frac{D_K c_T}{N} \right)$
$2C + H_2 \rightarrow C_2H_2$	$k_p = 4 \left(\frac{Dc_T}{N} \right)$	$k_p = 4 \left(\frac{D_K c_T}{N} \right)$
$C + 2H_2 \rightarrow CH_4$	$k_p = 1.39 \left(\frac{Dc_T}{N} \right)$	$k_p = \left(\frac{D_K c_T}{N} \right)$

Values for diffusivities, D_{AB} and D are listed in Table III. Molecular gas phase diffusion coefficients, D_{AB} were predicted using Chapman-Enskog theory. The expression for the diffusion coefficient of gas A, in a stationary atmosphere of B, is [15]

$$D_{AB} = 5.9543 \times 10^{-24} [(1/M_A) + (1/M_B)]^{1/2} T^{3/2} / (P \sigma_{AB}^2 \Omega_{AB}) \quad (25)$$

where D is the diffusivity (m^2/s), T is the absolute temperature (K), M is the molecular weight (kg/mol), P is the total pressure (Pa), σ is the collision diameter (m), and Ω is a tabulated integral which is a function of the energy of molecular interaction parameter, ϵ (typically tabulated as a ratio to Boltzmann's constant, k). The relevant parameters for the systems of interest and the calculated gas phase diffusion coefficients are given in Table I. It should be noted that D_{AB} is equivalent to D_{BA} .

The Knudsen diffusion coefficients of gas A were calculated using [15]

$$D_{KA} = 1.534 \times 10^{-2} \cdot d \cdot (T/M_A)^{1/2} \quad (26)$$

with $d = 10^{-8}$ m. The values for d depend only on whether the diffusing species is O_2 or H_2 , since interactions between molecules are negligible.

It may be of greater interest to examine the practical significance of the differences in prefactors and diffusivities. A binary mixture of $CO-O_2$ was assumed and a family of three curves were generated using Eqns (25), (26), the values of Table III, and

$$\chi = 1 \text{ (1 atm pure } O_2 \text{)}$$

$$c_T = P/(RT) = 1.203 \times 10^{-1} \cdot (P/T) \quad (\text{mol}/m^3)$$

$$N = 1.5 \times 10^5 \quad (\text{mol}/m^3)$$

$$D = 1.593 \times 10^{-4} \cdot (T^{3/2}/P) \quad (m^2/s)$$

$$D_K = 8.575 \cdot T^{1/2} \cdot d \quad (m^2/s)$$

Table III. Parameters used in calculation of and gas phase diffusion coefficients calculated using Chapman - Enskog Theory. The values for Ω are interpolated from tabulated values [15].

Gas	M (kg/mol)	σ (m)	Mixture	Ω_{AB} (@ 1073 K)	D (m ² /s)	D _k (m ² /s)
O ₂	32x10 ⁻³	3.467x10 ⁻¹⁰	O ₂	-	-	3.06x10 ⁻⁴
CO	28x10 ⁻³	3.690x10 ⁻¹⁰	O ₂ /CO	0.737	1.95x10 ⁻⁴	-
CO ₂	44x10 ⁻³	3.941x10 ⁻¹⁰	O ₂ /CO ₂	0.784	1.41x10 ⁻⁴	-
H ₂	2x10 ⁻³	2.827x10 ⁻¹⁰	H ₂	-	-	1.22x10 ⁻⁴
CH ₄	16x10 ⁻³	3.758x10 ⁻¹⁰	H ₂ /CH ₄	0.732	8.72x10 ⁻⁴	-
C ₂ H ₂	26x10 ⁻³	4.033x10 ⁻¹⁰	H ₂ /C ₂ H ₂	0.754	5.40x10 ⁻⁴	-

The three curves are shown in Fig. 3. Two variables are explored; temperature and pressure. It is evident that temperature only weakly affects the magnitude and shape of the curve. In the molecular (large d) regime, D is proportional to $T^{3/2}$ and c_T is inversely proportional to temperature, so k_p is directly proportional to the square root of temperature. At 1 atm pressure, the limiting values in the molecular regime are calculated to be 1.42×10^{-8} and 1.55×10^{-8} m²/s, for 800 and 1000°C respectively, i.e., the difference is less than 10 percent. These values for k_p predict recession of one centimeter in roughly two hours; 7,030 and 6,460 s, respectively. The temperature effect in the Knudsen regime is also modest, but, interestingly, it is of opposite sign because D_k has a weaker temperature dependence, $T^{1/2}$, than D. In this regime, k_p is inversely proportional to the square root of temperature; at higher temperatures, k_p is smaller.

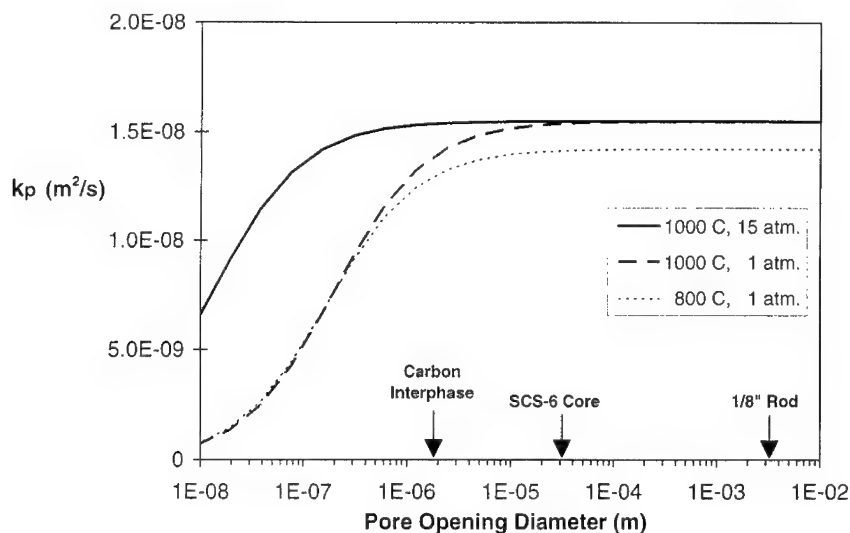


Figure 3 - Effect of variations in temperature and pressure on the parabolic rate constant, k_p , (assuming $O_2 + 2C \rightarrow 2CO$) [from [4].

Secondly, a reduction in the pore opening diameter, d , to ten microns is predicted to produce almost no effect for any of the three cases considered. More importantly, the magnitude of Knudsen effects are always small; at 1000°C and 1 atm pure O_2 , when ' d ' is 1 μm , k_p' is eighty percent $k_p'(\infty)$ and when ' d ' is 0.1 μm (which is the thickness often quoted as the minimum permissible for desirable mechanical properties in composites [16]) $k_p'(0.1)/k_p'(\infty)$ is 1/3. Finally, increasing pressure does not change the value of k_p' in the molecular regime because the direct proportionality of c_T is nullified by the inverse proportionality of D . However, at higher pressures the already modest Knudsen effects are further suppressed (at 15 atm and $d=0.1 \mu m$, k_p' and $k_p'(\infty)$ differ by less than two percent).

The same relative observations can be made for the other reactions. None of the different values for D , D_k or the prefactors changes the functional dependence on temperature or pressure. They will alter the magnitude and breadth of the transition regime, but will not change the relative irrelevance of the Knudsen regime for most applications. The practical importance of the analysis is that the parabolic rate constant is nearly identical for all reactions considered here. That value is on the order of $10^{-8} m^2/s$. This corresponds to a recession rate on the order of 0.5 cm/hr.

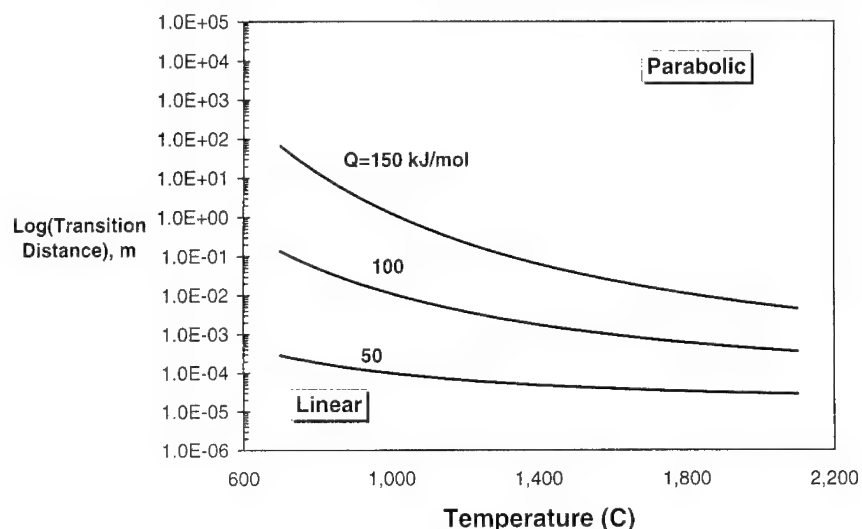
These calculated recession rates are indeed rapid. And, for the oxidation of carbon, rates of this magnitude have been observed [2,4]. However, in many cases, observed recession rates are significantly less than that predicted by the analysis above. In these cases, the recession rate is controlled not by the diffusion of the reactant gases, but by the reaction rate at the surface of the carbon. The reaction rate is controlled, in large part, by the activation energy for the reaction of interest. In a review paper, Shemet et al [2] tabulated oxidation activation energies reported for various carbons, in bulk form. The values ranged from 8 to 184 kJ/mol. Similarly, Chi and Landahl [11], performed a search of activation energies for hydrogen/carbon reactions and reported activation energies from 96 to 950 kJ/mol.

The net effect of different activation energies, or reaction rates, on the overall recession kinetics is to change the recession distance at which Eqn. (5) is dominated by linear or parabolic kinetics. Although it is recognized that the transition is broad (i.e., occurring over a wide range in time), it is possible to define the transition as the recession distance, or equivalently the reaction time, at which the two terms on the left-hand side of Eqn. (5) are equal. Fig. 4 shows a plot of this transition distance as a function of temperature for various activation energies. The specific reaction used is that for the production of methane from 1 atm of pure hydrogen and an appropriate pre-exponential value was assumed, for illustration purposes. However, similar plots can be constructed for all of the reactions. Fig. 4 illustrates that the transition from linear (reaction rate controlled) to parabolic (diffusion controlled) kinetics is strongly dependent, via the activation energy, on the nature of the particular carbon reacting. For example, at 1000 C and 50, 100 and 150 kJ/mol, the reaction is predominantly reaction rate controlled for depths of about 0.1 mm, 1 cm and 1m, respectively.

SUMMARY AND CONCLUSIONS

The results of the analysis can be summarized as follows. The parabolic constant, k_p , can be predicted using the kinetic theory of gases whereas k_l must be determined by fitting experimental data. The value for k_p is approximately $10^{-8} m^2/s$ for both hydrogen and oxygen reacting with carbon. The consequences of this work for conditions of engineering interest ($800^\circ C < T < 1200^\circ C$ and recession distances $\leq 1mm$) and experimental studies are many. Whether CO , CO_2 , CH_4 , or C_2H_2 is formed is an unimportant consideration for most applications. When the recession distance, ξ , is small, such that $\xi \ll \xi_{trans}$, the recession rate will be linear, inversely proportional to pressure, exponentially dependent on temperature, and the type of carbon will affect the recession rate. In the other limiting case, $\xi \gg \xi_{trans}$, recession will be parabolic, independent of the type of carbon, and weakly dependent on temperature and the nature of the gas phase reaction sequence. Lastly, the parabolic recession rate will be independent of pressure in the molecular regime, but directly proportional to pressure in the Knudsen regime. Knudsen effects are predicted to be very modest, i.e., carbon recession will be rapid even when the effective gas phase diffusion coefficient is D_k . Finally, carbon is exposed to hydrogen or oxygen,

Figure 4 - Recession distance for transition from linear to parabolic kinetics ($2\text{H}_2 + \text{C} \rightarrow \text{CH}_4$)



via pores or matrix cracks, attack of the carbon will proceed at a rapid rate, nearly independent of the magnitude of the pore/crack opening, the partial pressure of oxygen, or the total system pressure. The single, overriding, variable of consequence in moderating the kinetics is controlling the rate of chemical reaction at the receding carbon interface.

References

1. J. M. Thomas, Chemistry and Physics of Carbon, P.L. Walker, Jr. ed., Vol. 1 (Marcel Dekker, Inc., New York, 1965) 135-168.
2. V. Z. Shemet, A. P. Pomytkin, and V. S. Neshpor, "High Temperature Oxidation Behavior of Carbon Materials in Air", Carbon, 31 (81) (1993) 1-6.
3. D. W. McKee, "Borate Treatment of Carbon Fibers and Carbon/Carbon Composites for Improved Oxidation Resistance", Carbon, 24 (6) (1986) 737-741.
4. A. J. Eckel, J. D. Cawley and T.A. Parthasarathy, "Oxidation Kinetics of a Continuous Carbon Phase in a Non-Reactive Matrix" J. Am. Ceram. Soc. 78 (4) (1995) 972-980.
5. S. Drawin et al, "Oxidation Model for Carbon-Carbon Composites", (AIAA Paper 92-5016, Fourth International Aerospace Planes Conference, Orlando, FL) (7) (1992) 1112-1122.
6. F. Lamouroux, G. Camus, and J. Thebault, "Kinetics and Mechanisms of Oxidation of 2D Woven C/SiC Composites: I, Experimental Approach," J. Am. Ceram. Soc., 77 (8) (1994) 2049-2057.
7. F. Lamouroux, R. Naslain, and J.-M. Jouin, "Kinetics and Mechanisms of Oxidation of 2D Woven C/SiC Composites: II, Theoretical Approach," J. Am. Ceram. Soc., 77 (8) (1994) 2058-2068.
8. L. Filipuzzi, G. Camus, R. Naslain, and J. Thebault, "Oxidation Mechanisms and Kinetics of 1D-SiC/C/SiC Composite Materials: I, An Experimental Approach," J. Am. Ceram. Soc., 77 (2) (1994) 459-466.
9. L. Filipuzzi and R. Naslain, "Oxidation Mechanisms and Kinetics of 1D-SiC/C/SiC Composite Materials: II, Modeling," J. Am. Ceram. Soc., 77 (2) (1994) 467-480.
10. J. Bernstein and T. B. Koger, "Carbon Film Oxidation-Undercut Kinetics", J. Electrochem. Soc., 135 (8)

(1988) 2086-2090.

11. J. W. Chi and C. E. Landahl, "Hydrogen Reactions with Graphite Materials at High Temperatures and Pressures", Nuclear Applications, 4 (1968) 159-169.

12. A. K. Misra, "Thermodynamic Analysis of Chemical Stability of Ceramic Materials in Hydrogen-Containing Atmospheres at High Temperatures", (NASA Contractor Report 4271, 1990).

13. B. E. Deal and A. S. Grove, "General Relationship for the Thermal Oxidation of Silicon", J. Appl. Phys., 36 (12) (1965) 3370-3378.

14. R. B. Bird, W. E. Stewart, and E. N. Lightfoot, Transport Phenomena, (John Wiley and Sons, New York, NY, 1960) 496-501.

15. W. Geankoplis, Mass Transport Phenomena, (Ohio State University Bookstores, 1978) 27-28, 151-153.

16. P.F. Tortorelli et al., "Influence of Fiber Coatings on the Oxidation of Fiber-Reinforced SiC Composites", Ceram. Engr. and Sci. Proc., (1993) 358-366.

ENVIRONMENTAL EFFECTS ON THE HIGH TEMPERATURE

CRACK GROWTH OF SiC/SiC COMPOSITES

R. H. Jones, C. H. Henager, Jr., C. F. Windisch, Jr. and C. A. Lewinsohn

**Pacific Northwest National Laboratory
Richland, Washington 99352**

Abstract

The performance of SiC/SiC continuous-fiber ceramic composites (CFCCs) will depend on the service environment. Reaction between the environment and the fiber/matrix interphase is of primary concern because this will affect the structural properties of these composites. The effects of Ar+O₂ and Ar+H₂ environments on the weight loss and crack growth rates of SiC/SiC CFCCs have been determined and a model that correlates the time-dependent debonding resulting from the environmental reactions and the crack growth rates is presented. Boron nitride (BN) interphases were shown to be more stable than carbon (C) in Ar+O₂ environment for concentrations up to 10% of air as observed by a factor of 10 slower crack velocity at 1373 K for a CFCC with a BN-interphase as compared to a C-interphase. A factor of 10 lower weight loss was found for a CFCC with a C-interphase in Ar+H₂ environments of 100 and 1000 Pa H₂ as compared to an Ar+10 Pa O₂ environment. Interactions with the environment will introduce a number of design issues for the application of SiC/SiC CFCCs including: 1) time-dependent elastic properties, 2) reduced matrix cracking stress, 3) accelerated creep rates, 4) reduced fatigue strength, 5) increased subcritical crack growth rates and 6) reduced hermetic properties. The novel properties of these materials can be used beneficially by the designer but will also provide a challenge in their application while environmental interactions will increase the challenge in their use.

Introduction

Continuous fiber ceramic matrix composites (CFCCs) with a chemically-vapor infiltrated (CVI) SiC matrix and polymer-derived SiC fibers, so-called SiC/SiC materials, are being developed and evaluated for utilization in a wide variety of high-temperature applications. These applications can be divided into two categories: 1) high-temperature (>1273 K) in oxidizing environments and 2) moderate temperatures (1073-1273 K), inert chemical environments, and neutron environments. The first category includes applications such as combustors, liners, turbocompressors, glow plugs, valves, piston rings, heads, vanes, nozzles and turbine rotors for stationary, high-temperature gas turbine engines, tubes, support internals for air preheaters and recuperators for heat recovery systems, burners and combustors, waste incineration systems, separation, and filtration systems and chemical process equipment. The second category includes advanced fusion energy systems and fission reactors.

The primary environmental concern for category 1 is the high-temperature, oxidizing environment, while for category 2 the primary challenge is the neutron environment. High-temperature, oxidizing environments present a challenge to SiC/SiC CFCCs because of the chemical reaction between the fiber/matrix interphase material and oxygen. Carbon and boron nitride are two interphase materials that provide excellent combination of fiber/matrix bonding with sufficiently low fracture strengths to give fiber pull-out; however, both of these materials are oxidized in combustion environments [1-4]. Loss of the interphase material by oxidation results in a loss of fracture strength and increased crack growth rates [1] and is therefore a serious concern for the application of these materials. The high-temperature environment is also a factor for the microstructural stability and creep strength of the currently available SiC fibers.

Neutron environments pose different problems in contrast to oxidation of the interphase material; however, the results are similar. The response of SiC/SiC CFCCs to neutron irradiation was reported by Hollenberg et al. [5] where they demonstrated a loss of strength from fiber shrinkage and the accompanying loss of fiber/matrix bonding. Applications of SiC/SiC CFCCs for fusion energy and advanced fission reactors involves temperatures in the 1073 to 1273 K range and inert environments so the effects of fiber stability and strength and reaction of the interphase with the chemical environment are substantially less than for the category 1 applications. However, the neutron environment presents several new challenges including: 1) fiber shrinkage, 2) loss of strength, 3) loss of thermal conductivity, and 4) dimensional stability. A summary of the issues associated with the application of SiC/SiC CFCCs for fusion energy systems has been presented by Jones et al. [6-8].

The primary focus of this paper is to present data on the effects of an oxidizing environment on the mechanical properties of SiC/SiC CFCCs and the resulting design implications. Potential design implications of environmental interactions include: 1) time-dependent changes in the elastic properties, 2) a reduced matrix cracking stress, 3) accelerated creep rates, 4) subcritical crack growth rates leading to component failure, and 5) changes in the hermetic properties. These issues stem primarily from environmental reactions with the fiber/matrix interphase and their impact on the design life of the component.

Experimental Material

SiC/SiC CFCC materials fabricated by Refractory Composites Inc. with Nicalon[®]-CG and C- and BN-interphase (CG-C and CG-BN) and by DuPont with Hi-Nicalon[®] fibers and a C-interphase (Hi-C) were evaluated by thermal gravimetric analysis (TGA) and high-temperature mechanical testing. All material was made with eight plies of 0/90 fiber cloth and the composite plates were 4 mm thick.

Thermal Gravimetric Analysis (TGA)

Samples with dimensions of about 0.4 cm x 0.4 cm x 0.8 cm were tested at 1373 K with techniques similar to those reported by Jones et al. [9]. All of the sample faces, except for one resulting from a machine cut, retained the seal-coating (approximately 5 μm -thick) that had been applied during the last phase of composite fabrication. Since the single uncoated (0.4 cm x 0.8 cm) face of each sample was the only surface found to have reacted in our experiments, all rates were normalized with respect to this uncoated surface.

TGA studies at 3.1×10^2 Pa O_2 and above were performed using a Netzsch STA409 thermogravimetric analyzer. Gas flow was maintained at about 7.9×10^{-6} m^3/s through the instrument furnace, and composition was controlled using an MKS 147 multi-gas controller with O_2 content displayed on a Thermox meter. For experiments under 3.1×10^2 Pa O_2 , accuracy greater than 1 mg was required since, in some cases, the total mass loss during a 24 h period was on the order of a few milligrams. For these tests, a TA Instruments Simultaneous Differential Techniques 2960 module was used. Premixed gases were used and gas flows were maintained at 1.67×10^{-6} m^3/s for testing and pretest purging. The rest of the experimental conditions were similar to those used for the Netzsch system. Balance sensitivity was 0.1 micrograms with an accuracy of $\pm 1\%$.

Subcritical Crack Growth

The subcritical crack growth (SCG) studies were performed using constant-load tests for times up to 1×10^5 s, giving long-term crack velocity data, and using stepped load tests with load-holding times of 1000 s carried out at 1373 K in Ar and Ar plus varying O_2 levels. Single-edge-notched bend bar (SENB) specimens with dimensions of 4 mm x 5.5 mm x 50 mm were tested. The SENB specimens were tested in four point bending using a fully articulated SiC bend fixture. The specimens were typically loaded at an applied stress intensity of 7 to 8 $\text{MPa}\cdot\text{m}^{1/2}$ to begin the test. The test continued until a load drop was observed. Specimens that were tested in Ar plus O_2 were brought up to temperature in pure Ar.

The displacement-time curves for the 1000 s exposures at constant load in Ar indicate that the specimen displacement (and thus the crack-opening displacement) undergoes a transient period of displacement that is logarithmic in time over the 1000 s hold time. The slope of the displacement-curve over the final 600 s of the load step was taken as proportional to the crack velocity for each 1000 s period. The longer term hold displacement-time data were fit to polynomial functions and differentiated to give $\partial\delta/\partial t$.

Writing $\delta = PC(\alpha)$, where d is the displacement, P is the load, C is the specimen midpoint compliance, and α is equal to a/W (normalized crack length), gives

$$\frac{\partial d}{\partial t} = \frac{\partial}{\partial t}[PC(a)] = P \frac{\partial C}{\partial a} \frac{\partial a}{\partial t} = \frac{P}{W} \frac{\partial C}{\partial a} \frac{da}{dt} \quad (1)$$

which is used to derive an expression for da/dt ($= V_c$):

$$\frac{da}{dt} = V_c = \frac{(\partial\delta/\partial t)W}{PC'(\alpha)} \quad (2)$$

where V_c is the crack velocity and W is the specimen thickness. An expression for the mid-point compliance of an SENB specimen in four-point bending was used to calculate crack length and $C'(\alpha)$ [10]. The slope of the displacement-time curve at a given load is $\partial\delta/\partial t$.

The instantaneous specimen compliance at any point along the corrected load-deflection curve was calculated as the slope of the line from the origin to any point on the load-deflection curve. Bridging zone contributions to the specimen compliance were not included; i.e. the cracks, for the purposes of the compliance calculations, were idealized as unbridged elastic cracks obeying linear-elastic fracture mechanics. It is recognized that this assumption is not true and causes errors in crack length calculations [11]. However, visual observations of crack length during the test were not possible and, without detailed knowledge of the bridging zone, the specimen compliance cannot be corrected for bridging fiber contributions. Therefore, all references to crack length, velocity, and stress intensity are made with the understanding that the reference is to an effective elastic crack [11]. Data comparing calculated and measured crack lengths revealed the crack lengths are overpredicted by about 35%.

Experimental Results

Interphase Oxidation Kinetics

Effects of Oxygen and Temperature at Moderate Oxygen Concentrations. Mass losses from C-interphase oxidation measured by TGA were generally linear as a function of time for the composite materials between 3.1×10^2 Pa to 2.5×10^3 Pa O_2 , Figure 1, and between 1073 K and 1373 K, Figure 2. The data at 2.16×10^4 Pa O_2 were not reliable because the entire inventory of C oxidized within a very short period of time. Microscopic examination of the C-interphases in cross-sectioned SiC/SiC samples that had been exposed to oxidizing conditions revealed a remarkable uniformity in the recession distance from the unsealed surfaces exposed to O_2 . Recession rates (RR) calculated from these measured recession depths were compared to those calculated from TGA data assuming all the mass losses were due to C oxidation. The recession rates calculated from the two approaches were in acceptable agreement considering the experimental uncertainties. The order of the oxidation with respect to O_2 -partial pressure was found to be between 0.5 and 1.0, Figure 3; and the activation energy was about 50 kJ/mol.

Effects of Oxygen and Temperature at Low Oxygen Concentrations. Mass losses measured by TGA were linear-parabolic with time between 1.3×10^1 Pa and 1.9×10^2 Pa O_2 , Figure 4, and between 1073 K and 1373 K. The linear and parabolic terms in equations fitted to the data varied with O_2 -partial pressure. At 1373 K, the variation gave "orders" close to 1 and 1/2 for the linear and parabolic rate components, respectively. This suggests the linear term arises from the C-oxidation step, while the parabolic term is due to a mass transport (diffusion) step. The latter becomes more important at lower O_2 -partial pressures and higher temperatures.

Comparison of CG-Grade Nicalon and Hi-Nicalon Fiber Composites. The Hi-Nicalon-containing composites showed linear-parabolic behavior in mass loss vs. time similar to CG-Nicalon material at 2.5×10^2 Pa O_2 concentration and below. However, the Hi-Nicalon composites also showed an apparently higher mass loss rate than CG-Nicalon materials. The differences between oxidation rates of the CG and Hi-Nicalon materials is misleading because C-interphase oxidation occurred under the SiC-seal coat for the Hi-Nicalon material unlike the CG material where oxidation only occurred at the unsealed surface. The Hi-Nicalon material appears more reactive since the mass losses for both materials were normalized using only the unsealed surface area.

Subcritical Crack Growth Behavior. Fast-fracture experiments were conducted to investigate the mechanical response of the composites. The load-displacement behavior of SENB specimens of the three materials is compared in Figure 5. The Hi-C material was tested at 1473 K, whereas the CG materials were tested at 1373 K. The specimen dimensions were similar in all cases, permitting qualitative comparison. The values of fracture toughness shown in the figure were calculated from the peak load. Obvious differences can be seen in the mechanical behavior

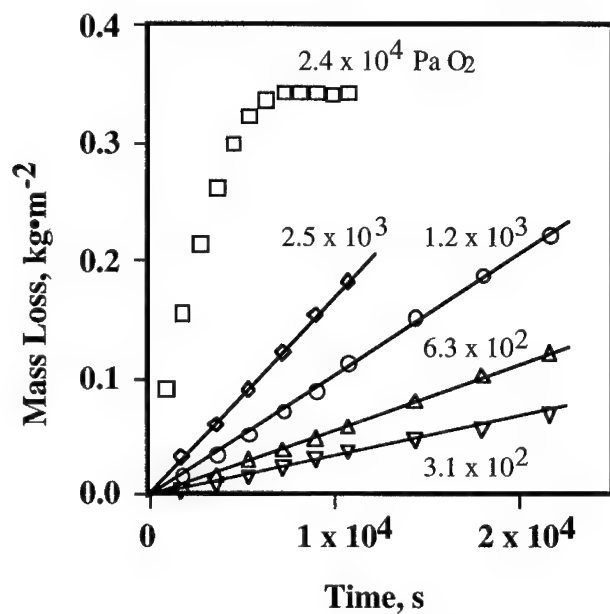


Figure 1. TGA mass loss as a function of time for SiC/SiC CFCC material (CG-C) exposed to various oxygen partial pressures at 1373 K.

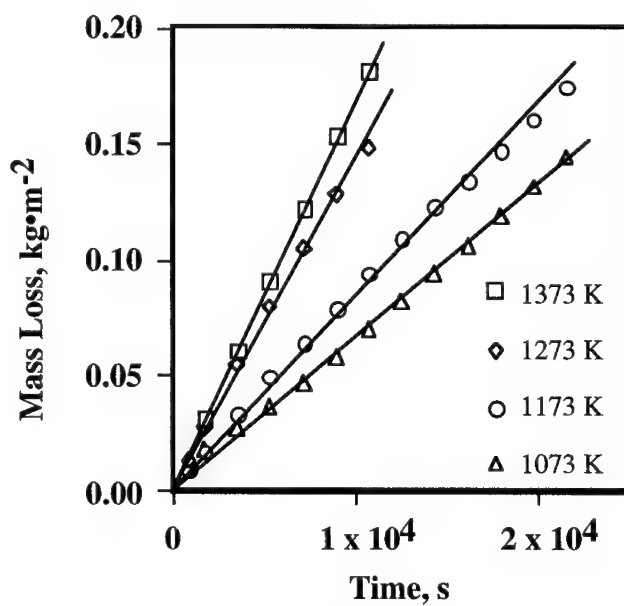


Figure 2. TGA mass loss as a function of time for SiC/SiC CFCC material (CG-C) exposed to $2.5 \times 10^3 \text{ Pa O}_2$ at various temperatures.

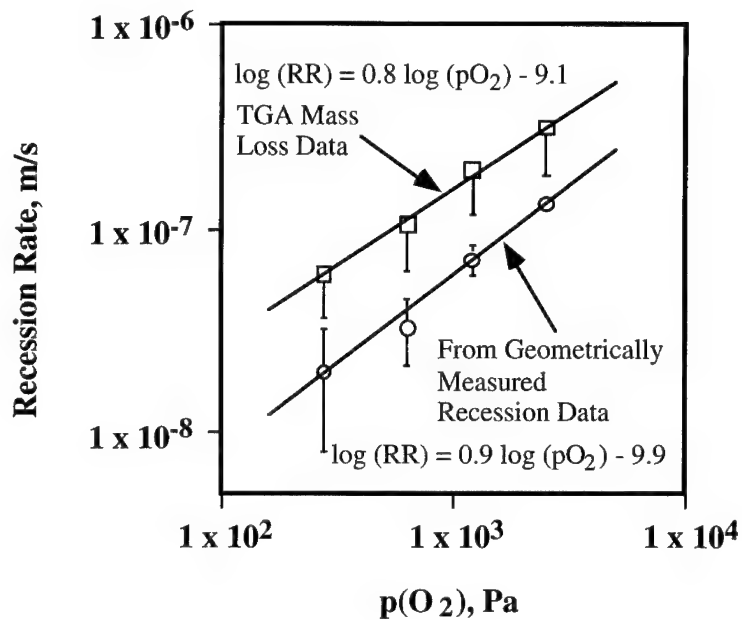


Figure 3. Comparison of geometrically measured and TGA-derived recession rates (RR) for CG-C material as a function of oxygen partial pressure at 1373 K.

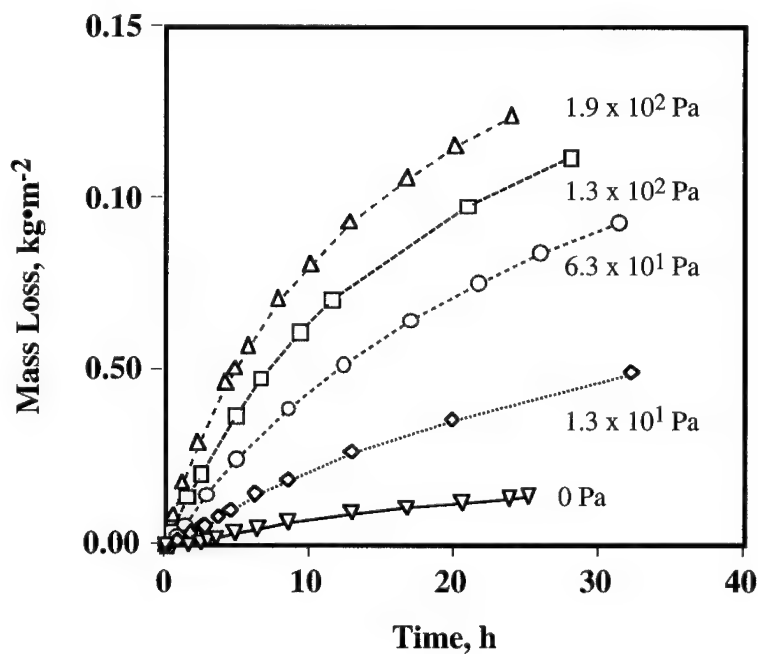


Figure 4. Mass loss as a function of time for long times at 1373 K (TGA mass loss data) for CG-C material at the various oxygen partial pressures indicated.

of the composites reinforced with CG and Hi-Nicalon fibers. All the materials exhibit an initial elastic loading followed by a non-linear loading. The materials reinforced with CG fibers exhibit a lower maximum stress compared to the material reinforced with Hi-Nicalon. In addition, the materials reinforced with CG fibers continue to carry loads after the maximum load is reached whereas the material reinforced with Hi-Nicalon fails nearly catastrophically at this load.

Typical slow-crack-growth data at 1473 K for Hi-C are shown in Figure 6. The elastic displacement of the samples is not shown, nor are the hysteresis-loops. Two curves are shown in Figure 6; one corresponds to a specimen tested in gettered argon and the other to a specimen tested in 3.1×10^2 Pa O_2 (balance argon). Previous studies [9, 12] have shown that the effect of oxygen is to remove the C-interphase via oxidation and thus decrease the stress on the fibers. Reducing the bridging stresses increases the crack-tip stress intensity and enhances crack propagation. The shape of the displacement versus time curve for the specimen tested in gettered argon is similar to those of the previously tested CG-C and CG-BN materials that exhibited slow-crack-growth controlled by time-dependent relaxation of the fiber-bridging stresses due to fiber creep. The results suggest that time-dependent bridging due to fiber creep occurs in the Hi-C materials tests in gettered argon, whereas in 3.1×10^2 Pa O_2 , the interphase is removed and the subsequent decrease of fiber-bridging causes more rapid crack propagation.

The displacement of the specimens was corrected for the compliance of the test apparatus, and the specimen compliance was converted to a crack length using a procedure described previously [12] based on experimentally measured crack length versus compliance data. The effective stress intensity factor at the crack tip was determined from the standard formula for a single edge notched beam (SENB) in four-point loading [13] using the calculated crack length. Previous results [12] have shown that, although this procedure under-predicts actual crack lengths, the effects of multiple cracks emanating from the notch increases the specimen compliance such that the effective crack velocities accurately reflect the true crack velocities in the damage zone.

The crack velocity as a function of stress intensity is shown in Figure 7 for the Hi-C and CG-C materials. In addition, data for a sintered alpha-silicon carbide material that was tested at 1173 K are also shown [14]. The sintered alpha-silicon carbide exhibited both stage-II and stage-III behavior under the conditions studied. The sintered alpha-silicon carbide material exhibited slow-crack-growth due to viscous sliding of the grain boundaries, and crack growth in this material was much faster than the silicon carbide composites studied, even at a lower temperature. The crack velocity at 1373 K of the Hi-C composite was slower than that of the CG-C composite, indicating that the Hi-Nicalon fibers had a lower creep rate than the CG fibers under the same conditions. This is indeed the case, as shown by Morscher [15], and is the basis for studying the Hi-C materials at higher temperatures than the CG-C and CG-BN materials. It has been shown previously that the crack velocity of the CG-C material can be predicted from a 2-dimensional micromechanical model that calculates the stress intensity at the crack tip due to time-dependent bridging stresses controlled by fiber creep. Therefore, under the conditions studied, the results indicate that slow-crack-growth controls the deformation behavior of the materials, although macroscopic creep of the composite and other time-dependent phenomena may occur.

The data for the C-interphase materials, when plotted as crack velocity as a function of applied stress intensity (V-K curves), reveal a stage-II region where the crack velocity is essentially independent of the applied stress intensity (Figure 8), followed by a stage-III, or power-law, crack growth region. The power-law region exhibits a strong dependence, but the stage-II region exhibits a weak dependence on the applied stress intensity. The data reveal a measurable increase in stage-II crack velocity because of O_2 in the gas. The crack velocity increases with increasing O_2 content for the C-interphase material (Figure 8). Also, the stress intensity required for the onset of stage III is shifted to a lower value of the applied stress intensity.

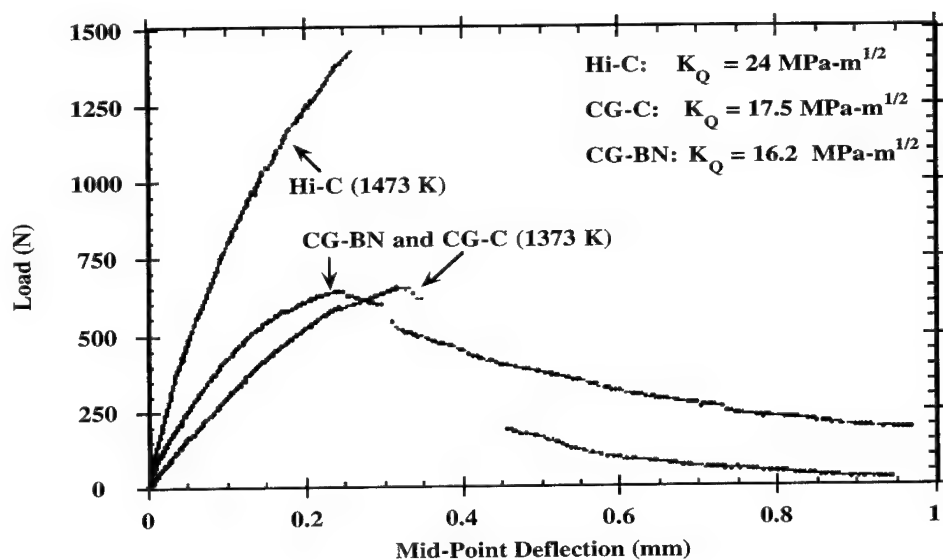


Figure 5. Fast-fracture behavior of indicated SiC/SiC CFCC materials. The CG-materials were tested at 1373 K and the Hi-C material was tested at 1473 K.

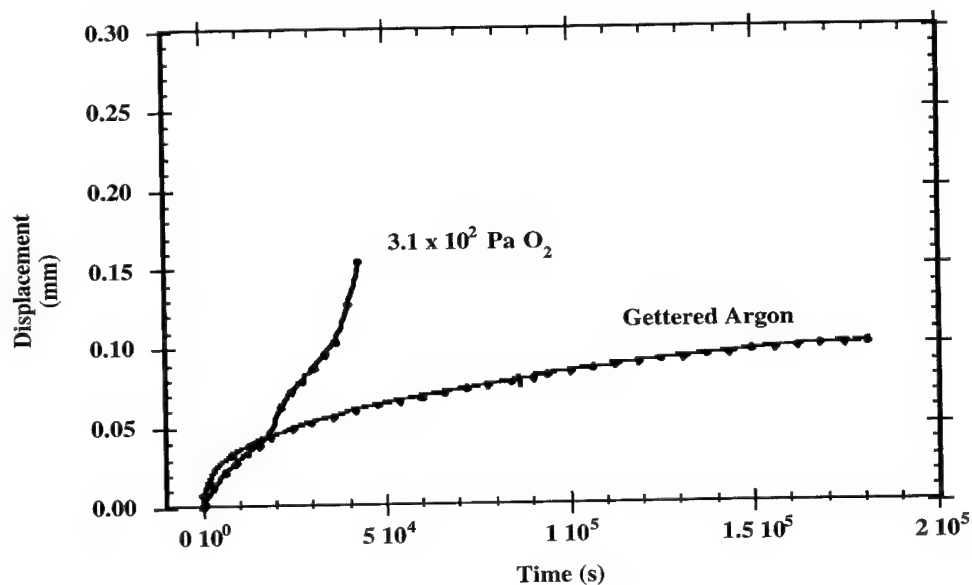


Figure 6. Specimen mid-point displacement during slow-crack growth experiments on Hi-C material at 1473 K in the indicated environment.

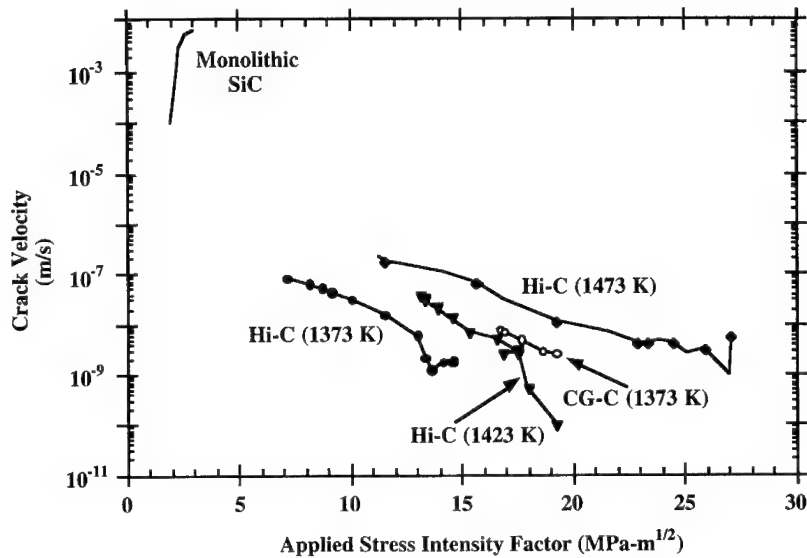


Figure 7. Comparison of the dependency of crack (damage zone) velocity on temperature and applied stress intensity among Hi-C, CG-C, and monolithic alpha-silicon carbide.

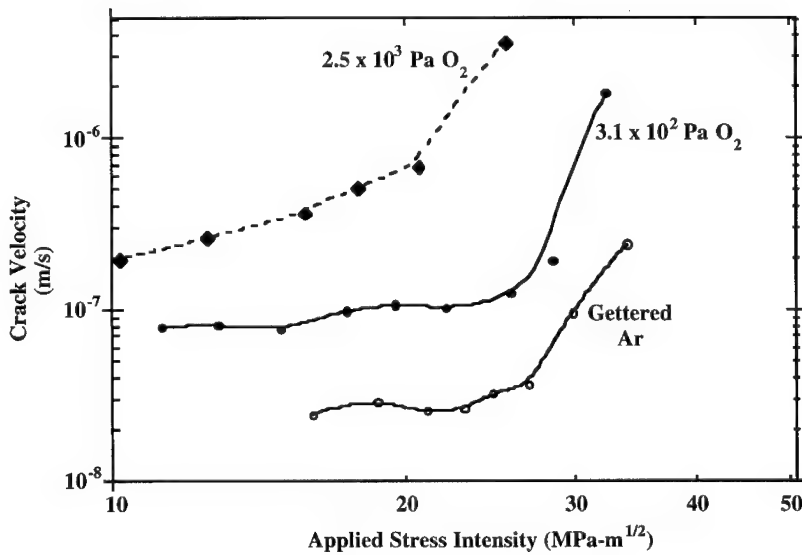


Figure 8. Crack velocity as a function of applied stress intensity for gettered argon and two oxygen levels for CG-C materials at 1373 K.

Discussion

Interphase Oxidation Kinetics

Effects of Oxygen and Temperature at Moderate Oxygen Concentrations. The activation energy for the C-interphase oxidation (about 50 kJ/mol) is within the range of values reported [16] for the oxidation of bulk carbon in the literature, although it is somewhat on the low side of this range. Two explanations for the low values are possible, which are indistinguishable with this data. First, the process may be reaction-rate-limited with an activation energy much lower than the typical value for bulk carbon. The typical activation energy for oxidation is over 200 kJ/mol. However, it is well known that the type of C, impurities and surface morphology strongly influence the measured activation parameters. A reaction-rate-limited process would be consistent with the linear reaction kinetics observed in this work.

Eckel et al. [17] also showed linear kinetics for C-cored SiC fibers under conditions of 1.01×10^5 Pa O_2 and 1073 K. They concluded the oxidation was reaction-rate-limited for their materials and conditions and determined a recession rate of 2.5×10^{-6} m/s. We obtained a similar recession rate (4.5×10^{-6} m/s) when our data was extrapolated to these conditions. The correlation lends support to the possibility that the oxidation is under reaction control.

Other considerations, however, indicate that the process is (at least partly) diffusion-rate-limited. Most studies have reported that the oxidation of C above 1073 K is under diffusion control and diffusion may play a role in our study as well. Since the recession and TGA mass loss data are linear, however, the rate-limiting diffusion step cannot be within the channels created by the oxidation of the C-interphase. If this were the case, then the data would depend nonlinearly on time because the diffusion distance would be increasing with time as the channels deepened. More likely, the rate-limiting diffusion step is through a boundary layer on the outside of the carbon composite. This layer has been proposed for C and C-containing composites [18] and helps explain oxidation rates in both static and dynamic systems. The thickness of the layer can vary from about 1×10^{-4} m to 5×10^{-2} m, depending on the flow conditions. If diffusion through the boundary layer is rate-controlling, then the kinetics should appear linear as long as the boundary layer thickness does not change and the extent of oxidation of the C-interphases is not enough to make diffusion through the channels rate-controlling. In other words, the thickness of the boundary layer must be significantly larger than the depth of the C-depleted region in the sample. In order for the latter condition to hold, the boundary layer in our study must have been quite large since the total recession depth of the interphases was several millimeters in some cases. Given the low flow rates used in our apparatus, a thick boundary layer may be reasonable.

In conclusion, the linear kinetics cannot distinguish between reaction or diffusion control. The dependence of the recession rates on the partial pressure of O_2 is also somewhat ambiguous since the order of the dependence falls between 0.5 and 1.0, although it is closer to unity. This suggests the process may be controlled by a mixture reaction and diffusion. If the process were under pure diffusion control, the order should have been 0.5. Under reaction control, the order can vary.

Modeling Oxygen Effects On Crack Growth. A comprehensive model of subcritical crack growth in CFCC materials should take into account all possible time-dependent behaviors in the crack-wake bridging zone. These include fiber creep, interphase creep, visco-elastic effects in the interphase, and time-dependent interphase removal due to oxidation. Any time-dependent deformation in the crack-wake region relaxes the crack closure forces. Fiber creep, which has been experimentally measured with Nicalon and Hi-Nicalon fibers from 1173 K to 1473 K [19], undoubtedly plays a role since the bridging fibers are highly stressed in the crack-wake region and are being held at those loads for long times. Interphase removal must also be important based on the TGA data, optical microscopy results, and the accelerated crack velocities in oxygen.

Activation energies for crack growth in Ar plus oxygen exhibited a much lower activation energy (50 kJ/mol) in oxygen than in argon alone, consistent with oxidation of C. Data from TGA experiments of C-interphase materials undergoing oxidation at 1373 K indicate that activation energy for weight loss as a function of time is about 50 kJ/mol [9]. The weight change of Nicalon-fiber-reinforced SiC composites depends on fiber and matrix composition, thickness, temperature, and oxygen pressure [2-4]. The use of an activation energy to describe these processes must be done with care, and a given reaction process may be valid only over a limited range of time-temperature-oxygen pressure phase space. However, the data presented in this study make it clear that a distinct and different process controls damage-zone growth in the presence of oxygen. Based on these results, the rate controlling step for crack growth in oxygen-containing environments is carbon oxidation which results in mechanical de-coupling of the fiber from the matrix due to fiber/matrix interphase removal.

Scanning electron micrographs of polished cross-sections of cracked specimens exposed to O₂ plus Ar revealed that oxidation at 1373 K partially removed the C-interphase where the crack intersects the bridging fibers [20,21]. The removal of this interphase material reduces the ability of the matrix to transfer load to the fibers, and, in turn, reduces the bridging-zone forces. Therefore, in addition to relaxation of bridging zone stresses by fiber creep, the strength of the fiber-matrix mechanical coupling will fall in time-dependent fashion as the interphase is removed. The result will be an increase in crack velocity and, since the bridging zone is less effective in screening the crack-tip from the applied stress intensity, a leftward shift in the stage-II-to-III transition.

The process envisioned for de-coupling the bridging-fibers from the matrix is shown schematically in Figure 9. In principle, the time-dependence of the fiber-bridging stress can be related to the rate of interphase removal by oxidation [9] through the implied time-dependence of the debonded region, λ , and fiber-matrix shear strength, τ . The interphase removal process (oxidation process) occurs at all fibers that intersect the crack and at the composite surface. Fiber-interphase material ahead of the crack is not subject to oxidation until the crack intersects the fiber and provides an oxygen transport path. Interphases that are oxidized to gaseous compounds, such as C-interphase going to CO and CO₂, will likely behave differently than those that are oxidized to viscous solids.

The nature of the agreement of the model with experiment when fiber creep is simulated is encouraging (Figure 10). The model not only predicts the absolute magnitude of the crack velocity, but it rationalizes the observed time-dependence of V_c . The model contains no adjustable parameters, and typical values for material constants were assumed. This work suggests that a more creep-resistant fiber will improve SCG-resistance in CFCC materials. The model developed here predicts results qualitatively similar to those obtained by Thouless [22], Nair et al. [23], and Jakus et al. [24]. Crack advance is controlled by the time-dependent behavior of the crack-bridging ligaments, whether the relaxation is due to visco-elasticity or thermal creep. The crack-opening displacement and, therefore, the crack-tip stress intensity, obey similar time-dependent relationships.

Implications of Environmental Interactions on the Performance of SiC/SiC Composites. Continuous fiber ceramic matrix composites are relatively new materials with little design experience. Continuous fiber polymer matrix composites have gained wide use such that designers have become familiar with their unique properties. However, CFCCs offer a new set of unique properties, including: 1) fracture resistance, 2) a subcritical crack growth regime that is independent of stress-intensity, 3) notch insensitivity, 4) an insensitivity to matrix cracking when the cracks are fully bridged, 5) fiber/matrix interfacial damage during cyclic loading, 6) environmental reactions, and 7) their anisotropic but engineerable properties. These characteristics have been described elsewhere so further detail will not be given. [8, 10, 12, 9].

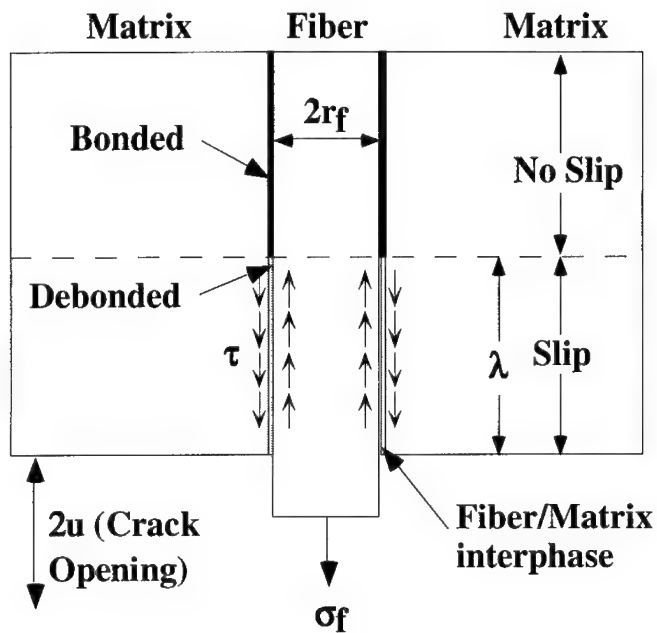


Figure 9. Schematic diagram of fiber debond model showing λ , τ , u , and σ_f . Oxygen ingress occurs along fiber/matrix interphase and increases λ . Thus, λ and τ become time-dependent.

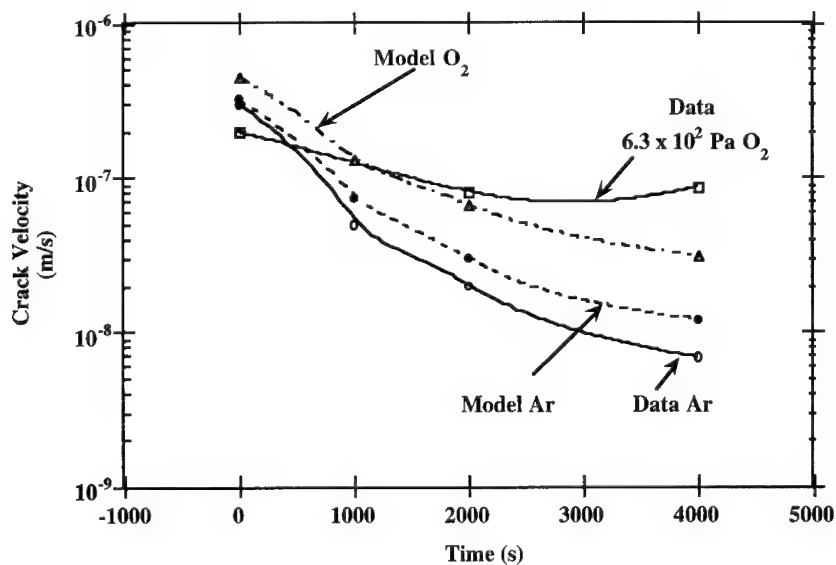


Figure 10. Calculated crack velocities for gettered Ar (fiber creep only) and in an oxygen pressure of 6.3×10^2 Pa. Model predicts fiber creep velocity and predicts increase in velocity when interphase removal is included for oxygen-containing environments.

Interactions between the environment and the fiber/matrix interphase are critical to the performance of high-temperature CFCCs. This effect for oxidation of the C- and BN-interphase materials is shown in Figure 11 where the crack velocity increases 10^3 times from about 10^{-9} m/s in high-purity Ar to about 10^{-6} m/s for the C-interphase and about 10^{-7} m/s for a BN-interphase in an environment of Ar + 2.5×10^3 Pa O_2 . This concentration of O_2 is 10% that of air so faster crack velocities are expected in an air or combustion environments. With the development of more stable interphases, such as porous SiC or layered SiC/C/SiC, reactions between the environment and the fiber could become an issue as well. Hi-Nicalon has excess C which could react with O_2 and result in a loss of fiber strength, for example. Environmental reactions with the more stable crystalline fibers would not be expected to be as severe.

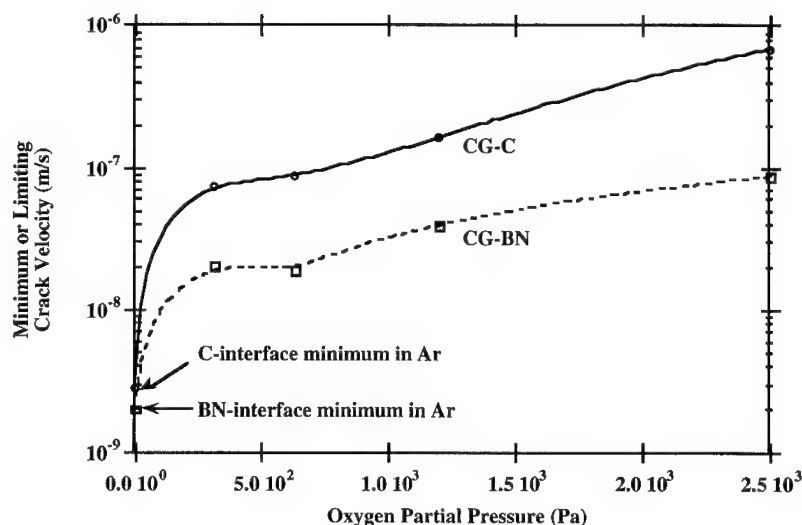


Figure 11. Minimum or limiting crack velocity for CG-C and CG-BN materials as a function of oxygen partial pressure at 1373 K.

Several mechanical properties of CFCCs will be affected by reaction of the fiber/matrix interphase with the environment. Accelerated crack growth rates, clearly demonstrated in Figures 6, 8, and 11, will result in a reduced design life. A crack velocity of 10^{-6} m/s will result in a crack length of over 10 m per year which is clearly intolerable for most applications. It is also likely that loss of the interphase will result in accelerated "creep rates" although this will be a pseudo-creep because it will result from matrix cracking as the fibers elastically unload. Other design considerations that would result from an environment reaction with the fiber/matrix interphase are: 1) a time-dependent elastic modulus, 2) reduced matrix cracking strength, 3) reduced fatigue life and 4) reduced hermetic properties. Each of these effects results from the loss of bonding between the fiber and matrix although these effects have not been demonstrated. A time-dependent change in the elastic properties will likely require the designer to select the minimum modulus expected with time. A linear-elastic design will also be affected by a time-dependent reduction in the matrix microcracking stress since this stress defines the limits of elastic behavior. Environmental interactions with the fiber/matrix interphase will also reduce the fatigue threshold or fatigue life of CFCCs. A designer would likely accommodate this time-dependent phenomenon in a manner similar to high-temperature creep or subcritical crack growth.

Summary

Continuous fiber ceramic matrix composites exhibit novel behaviors that can be used beneficially but also provide a challenge to designers. Some of these properties include their fracture resistance, a crack velocity regime that is stress-intensity independent, notch insensitivity, matrix crack insensitivity, and anisotropic and engineerable properties. Interactions between the environment and the fiber/matrix interphase alters their behavior and introduces design implications, such as time-dependent changes in: 1) elastic modulus, 2) matrix micro-cracking stress, 3) creep rates, 4) subcritical crack growth rates, 5) fatigue strength and 6) reduced hermetic properties. The high-temperature properties of CFCCs are controlled by fiber creep properties and interphase removal accelerates the crack growth rates through time-dependent debonding. Newer, creep-resistant fibers decrease crack velocities at a given temperature or increase the potential use temperatures of these materials; however, improved environmental resistance is required. This improvement could result from more stable fiber/matrix interphase materials such as porous SiC, use of glass formers in the matrix to seal the matrix microcracks, and use of coatings. The use of porous SiC-interphase material is the most appealing because additions of glass formers to the matrix affects composite properties while high-temperature, oxidation resistant coatings will crack as a result of thermal cycling and creep of the composite.

Acknowledgments

This research was supported by the Office of Basic Energy Sciences of the U.S. Department of Energy (DOE) under contract DE-AC06-76RLO 1830 with Pacific Northwest National Laboratory which is operated for DOE by Battelle Memorial Institute.

References

1. R. H. Jones, C. H. Henager, Jr. and P. F. Tortorelli, *JOM*, **45** [12] (1993) 26-29.
2. P. F. Tortorelli, S. Nijhawan, L. Riester, and R. A. Lowden, *Ceram. Engr. and Sci. Proc.*, **14** [7-8] (1993) 358-366.
3. L. Filipuzzi, G. Camus, R. Naslain and J. Thebault, *J. Am. Ceram. Soc.*, **77** [2] (1994) 459-466.
4. L. Filipuzzi, G. Camus, R. Naslain, and J. Thebault, *J. Am. Ceram. Soc.*, **77** [2] (1994) 467-480.
5. G. W. Hollenberg, C. H. Henager, Jr., G. E. Youngblood, D. J. Trimble, S. A. Simonson, G. A. Newsome and E. Lewis, *J. Nucl. Mater.*, **219** (1995) 70-86.
6. R. H. Jones, C. H. Henager, Jr. and G. W. Hollenberg, *J. Nucl. Mater.*, **191-194** (1992) 75.
7. R. H. Jones and C. H. Henager, Jr., *J. Nucl. Mater.*, **219** (1995) 55.
8. R. H. Jones and C. H. Henager, Jr., *J. Nucl. Mater.*, **212-215** (1994) 830-83.
9. C. H. Henager, Jr., and R. H. Jones, *J. Am. Ceram. Soc.*, **77** [9] (1994) 2381-94.
10. C. H. Henager, Jr. and R. H. Jones, *Mater. Sci. and Engr.*, **A166** (1993) 211-220.
11. A. Bornhauser, K. Kromp and R. F. Pabst, *J. Mater. Sci.*, **20** (1985) 2586.

12. R. H. Jones, C. H. Henager, Jr., and C. F. Windisch, Jr., *Mater. Sci. and Engr.*, **A198** (1995) 103-112.
13. ASTM E-399-90, American Society for Testing and Materials, Philadelphia, PA (1990).
14. K. D. McHenry, and R. E. Tressler, *J. Am. Ceram. Soc.*, **63** [3-4] (1980) 152-56.
15. G. N. Morscher, and J. A. DiCarlo, HITEMP Review 1993, *NASA Conf. Pub.* 19117, **Vol. III** (1993) 88-1 to 88-11.
16. J. M. Thomas, Vol. 1, P. L. Walker Jr., ed., *Marcel-Dekker*, New York, 1965, pp.135-68.
17. A. J. Eckel, J. D. Cawley and T. A. Parthasarathy, *J. Am. Ceram. Soc.*, **78** [4] (1995)972-80.
18. K. L. Luthra, *Carbon*, **26** [2] (1988) 217-24.
19. J. A. DiCarlo, *Compos. Sci. and Technol.*, **51** (1994) 213-222.
20. C. H. Henager, Jr. and R. H. Jones, Ceramic Transactions, **Vol. 38**, The American Ceramics Society, Westerville, OH, 1994, pp.317-328.
21. C. H. Henager, Jr., R. H. Jones, C. F. Windisch, Jr., M. M. Stackpoole, and R. Bordia, *Metall. et. Mater. Trans. A*, **27A** (1995) 839-849.
22. M. D. Thouless, *J. Am. Ceram. Soc.*, **71** [6] (1988) 408-413.
23. S. V. Nair and T. -J. Gwo, *J. Engr. Mater. Technol.*, **115** (1993) 273-280.
24. K. Jakus, J. E. Ritter, and R. H. Schwillinski, *J. Am. Ceram. Soc.*, **76** [1] (1993) 33-38.

LIMITATIONS AND BENEFITS TO THE USE OF STRUCTURAL SILICIDES UNDER COMBUSTION CONDITIONS

Peter Lipetzky and William B. Hillig

Materials Science and Engineering Department
Rensselaer Polytechnic Institute
Troy, New York, USA 12180-3590

Abstract

Silicides are candidate materials for combustion driven heat engines in which combustion gases may reach pressures up to 20 atmospheres and temperatures up to 1650°C. The oxidation resistance of most promising silicides depends on the formation of a protective silica diffusion barrier layer. The formation of this layer and its durability are affected by the gas environment. Water vapor accelerates the rate of formation of such layers, and affects their structure, but also promotes their loss by evaporation. The gas environment affects the damage processes in a SiC/SiC composite differently depending on the level of the mechanical stress. Experimental studies are presented that show these effects.

Introduction

The main driving force for the development of new high performance structural materials is to provide lighter, more durable and higher temperature materials for use in applications such as combustion driven heat engines. Silicides, such as given in Table I, either in the form of monolithics or composites are candidate materials, although they do not yet offer the strength, toughness, damage tolerance or forming capabilities of advanced superalloys that are now in service (*dissociation temperature). Hence, use of silicides as turbine blades and vanes is likely to be deferred in favor of other high-payoff, but less critical applications such as combustors, seals, and heat exchangers. In the NASA High-speed Civil Transport program, aimed at an advanced supersonic aircraft, the combustion for the turbine engines is expected to generate both oxidizing and reducing conditions to reduce low NO_x emissions [1]. The proposed strategy is to separate the combustion products into "rich" (oxygen deficient) and "lean" (oxidizing) regions. Therefore, the combustors must be capable of enclosing aggressive environments in which gas temperatures may exceed 1400°C and in some cases may reach 1650°C [2,3]. In either aircraft or power turbines, the combustion gases include CO, CO₂, H₂O, NO_x and residual air at total pressures in the range of 10 to 20 atmospheres.

Oxidation Resistant Silicides

Material	m.p. °C	density g/cm ³	Thermal Expansivity x10 ⁶ /°C	wt.change mg/cm ² /4hrs	
				1200°C	1500°C
SiC	[2500]*	3.2	5	0.3	0.4
Si ₃ N ₄	[1900]*	3.4	3	0.03	0.2
WSi ₂	2160	9.3	8	-17	-23
MoSi ₂	2030	6.3	8.3	0.3	1.3
V ₃ Si	[2060]*	4.7	12.0	-	-
TiSi ₂	1500	4.0	10.6	22	-
Cr ₄₀ Mo ₃₀ Si ₃₀	1700	7.2	11	0.3	-

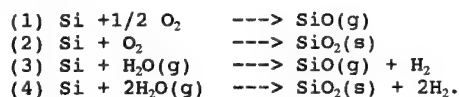
The oxidation resistance of silicides as a class results from forming a siliceous oxidation product that impedes the influx of aggressive chemical species. An exception is Cr₃Si in which the barrier layer is more complex [4], forming a Cr₂O₃ layer below 1000°C and mixed Cr₂O₃ + SiO₂ films above. We will treat SiC as a representative silicide because it contains significant Si and forms a protective SiO₂ layer in oxidizing conditions. However, the details of oxide formation kinetics and the properties of the oxide can vary among the different silicides [2]. Certain silicides, notably SiC, Si₃N₄ and MoSi₂, oxidize to form pure amorphous SiO₂ which has exceptionally low oxygen permeability, but is about ten-fold more permeable to water. The formation kinetics of the protective silica layer and its durability are affected by the environment. Hence, factors that enhance the diffusivity of oxygen in the film or attack the integrity of the film clearly affect the applicability of such silicides in thin shell structures such as combustors. In the case of a composite such as SiC/SiC rapid oxidation may assist in impeding environmental entry by sealing the surface cracks with silica. In MoSi₂ a thicker, less protective silica layer forms in air than in oxygen [5]. In addition stress has been shown [6] to affect oxide formation kinetics in MoSi₂. Oxidation products can also act as crack-face bridges and improve [7] the damage tolerance of silicide-based composites.

This paper first reviews the reactions and kinetics relating to the silica barrier layer; later we report on experimental studies of how gas environments, particularly water vapor, affect the integrity and performance of structural silicides at high temperature. The issues of particular concern are: (1) the long term durability of the protective oxide; (2) the effect of the gas environment, including water vapor, on mechanical properties; and (3) loss of the oxide layer by volatilization. It will be shown that water vapor has marked

effects on factors relevant to the use of silicides in combustion-related application.

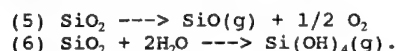
Reaction With The Environment

Consider first the possible reactions of elemental Si with an oxidizing gas environment:



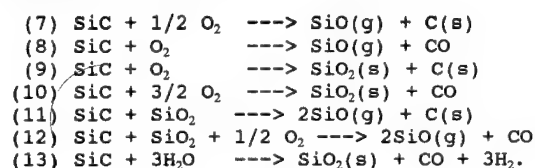
Reactions 3 and 4 show that water can act as an oxidizing agent. At low partial pressures of oxygen or water, relatively rapid active oxidation can occur because of the volatility of SiO which forms in reactions 1 and 3. The overall rate of oxidation is affected by the reaction kinetics at the free surface and by the inward and outward diffusion of the reactant and product species through the near-surface gas layer. In a flowing gas environment the rate of oxide removal varies with gas velocity and position in the gas stream. At higher oxidant concentrations passive oxidation occurs, reactions 2 and 4, which leads to the formation of a "protective" silica film on the surface. The oxidation in this case occurs at the Si/SiO₂ interface by transport of oxygen through the SiO₂. The observed growth kinetics can be analyzed to determine whether the oxidation rate is controlled by a chemical barrier at the Si/SiO₂ interface or by solid state diffusion of the oxygen through the oxide.

Once formed, volatilization loss of the protective SiO₂ layer can occur through the following reactions:



Reaction 5 occurs only under sufficiently reducing conditions. Reaction 6 shows that evaporation of the film is possible in the presence of water vapor through the formation of a volatile hydroxide species as will be discussed below.

The following additional reactions between SiC and either oxygen or water vapor are theoretically possible:



Reactions 7 and 8 show that, like Si, active oxidation of SiC can occur when the environment has a very low oxygen activity. Whether reaction 8 or 9 occurs depends on the stability of SiO and CO relative to the formation of SiO₂ and C under the particular conditions of temperature and pressure. The formation of a protective oxide layer requires a higher oxygen activity as written in reaction 10. For SiC and Si₃N₄, the formation of the oxide layer is accompanied by the production of volatile species. One mechanism involves oxygen diffusion through the silica layer as O₂, and subsequent formation of additional SiO₂ and CO upon arrival at the SiC/SiO₂ interface. Therefore, the CO must either be removed by outward diffusion or will build up in pressure (activity) at the growth interface and slow subsequent SiO₂ formation. Reactions 11 and 12 occur directly between the solid SiO₂ and SiC species. Reaction 13 also shows that water vapor can act as an oxidizing agent with the formation of volatile species at the SiC/SiO₂ interface. Clearly there is a complex interaction between these possible products, the kinetics of the oxide formation and the possible degradation of the oxide. In context of the current work, it has been observed that the passive oxidation kinetics of SiC in pure oxygen (reaction 9 or 10) are slower than for Si (reaction 2). Luthra [8] analyzed these reactions and concluded that diffusion kinetics of both products and reactants

limited the reaction rate at all stages of the oxidation process. Based on these results, he concluded that the implementation of SiC will be limited by the formation of CO gas bubbles in the silica film at 1550°C.

Many studies have shown that the presence of water vapor and other constituents in the atmosphere increases the complexity of the oxidation process as recently reviewed by Opila [9]. Water vapor additions to air can result in an increase in the oxidation rate of SiC up to 20-fold. Furthermore, oxidation in an Ar/H₂O mixture occurs about as fast as in an O₂/H₂O mixture [10] for a given partial pressure of water vapor. Therefore, under these conditions H₂O is a more effective SiC oxidant than O₂ because of the approximately ten-fold greater permeability through silica. Contaminants [9] in the oxide, such as sodium, further accelerate the oxidation kinetics and catalyze the conversion of the initially amorphous SiO₂ into cristobalite. Such contamination is practically unavoidable in combustion environments. Cristobalite undergoes a polymorphic transformation at 250°C with a large volumetric decrease on cooling that can lead to spalling. Other additions, such as Al₂O₃ or B, also cause enhanced oxidation rates by enhancing the rate of oxygen transport through the oxidation layer.

Volatility Of The Protective Oxide.

Under reducing conditions the loss of the protective oxide layer occurs by the reaction of solid SiO₂ to the volatile SiO. Conversely, the oxidizing ambient of water vapor can also cause evaporation of silica. Initially there were reports in the 1960's of weight loss when silica was exposed to high pressure steam. For example, Cheng and Cutler [11] reported a weight loss of crystalline SiO₂ in a steam partial pressure of 0.84 atm with a gas velocity near 1 cm/sec. They attributed this to volatilization via the formation of Si(OH)₄, with the rate of evaporation proportional to the square of the partial pressure of water vapor. The weight change they observed was proportional to time and increased with temperature up to a maximum of 1350°C, where the rate of loss was 1.2 µg/hr/cm²; this corresponds to a recession rate of 0.05mm per 10⁴ hours. If evaporative processes are controlling, the rate at which the surface recedes is determined by the gas velocity, the temperature, transport mechanisms, composition and other parameters. Jacobson estimated that the maximum recession rate allowable for a combustor application was 0.25mm per 10⁴ hours. Therefore, the total partial pressures of the siliceous vapor species must be less than 1 x 10⁻⁶ atm [2]. In a related work, Hashimoto measured the amount of Ca, Al, and Si contained in wet oxygen under a range of conditions, and was able to extract the enthalpies and entropies of formation of the volatile hydroxide species [12]. The equilibrium constant which he determined for reaction 6 can be used to calculate that at 1350°C, with a steam pressure of 1 atm, the vapor pressure of Si(OH)₄ is 6 x 10⁻⁶ atm. The actual partial pressure is likely a function of temperature for cases ranging from fuel-rich to fuel-lean combustion. The worst situation is the fuel-rich case, for which the maximum vapor pressure of 1 x 10⁻⁶ atm is reached at 1500°C. However, the estimation of 1500°C does not consider the water vapor transport mechanism.

Water vapor effects of SiC have all been studied. Opila and Hann [13] determined the weight changes of pure SiC exposed to a 50:50 water vapor/oxygen mixture as a function of time at 1200 and 1400°C. They observed passive oxidation in which the weight initially increased according to a parabolic growth law, as expected for a solid diffusion limited growth process. However, long term exposure showed a weight loss that was linear with time. Oxide thickness was observed to approach a fixed value, which is expected to occur when the rate of oxide formation equals the rate of its loss by volatilization. The volatile species following their experiments was also believed to be Si(OH)₄. In the range between 1200 and 1400°C the rates of recession showed no distinct temperature dependence but appeared to depend on the path by which the silica was produced. These loss rates exceeded the previously estimated limits for 10⁴ hours, but should be adequate for 10³ hours in a high pressure turbine combustor environment.

Effect of Water Vapor on Mechanical Properties of SiC/SiC

The reactions listed above can also affect the mechanical properties and the failure mechanisms of the composite. If the environment has access into the interior of the sample, it can attack the fiber-matrix interface as well as the load-bearing fiber reinforcements. The details of these attacks have

received considerable study in such composite systems as $\text{Si}_3\text{N}_4/\text{SiC}$ [14] and SiC/SiC [15,17]. Transverse cracks allow ingress of the gas environment. The onset of such cracks is detected by a pronounced change in the slope of strain versus stress, which defines the location of the proportional limit.

In our current investigation a SiC/SiC composite was used to study the effects of water vapor exposure on strength and stiffness. The air/water mixture was chosen to approximate the water content in a combustion environment; the water partial pressure was roughly 0.7 atm. The vapor was supplied by continuously bubbling air through 90°C water. Two different types of experiments were performed: The first involved loading a specimen beyond the proportional limit and subsequently exposing to the control environment at 1000°C (stress-free). The other involved applying stress and temperature simultaneously in the control environment. For such tensile tests, a jacket was fashioned that confined the vapor to the hot-zone region of the sample. In both cases, temperature was monitored directly at the specimen surface in the gauge sections.

The representative material chosen here was a SiC fiber-reinforced SiC composite manufactured by DuPont Lanxide Corporation. Each ply, composed of continuous, woven Nicalon(TM) fiber tows, is chemical-vapor coated prior to lay-up and consolidation. Approximately ten such plies in a 0/90 orientation were used to form composite plates, which were cut into tensile coupons along the 0° direction. A final SiC infiltration/coating treatment was applied after the cutting. Overall fiber volume fraction is near 30%, residual porosity is roughly 10% and as-received Young's modulus is consistently near 120 GPa. We consider decrease of specimen stiffness to be a direct measure of material damage and of the remaining lifetime [18,19].

Behavior in As-Received Condition

The mechanical behavior of the as-received composite tested in air serves as a reference baseline. Figure 1 shows that matrix failure fracture is not catastrophic because of the load transfer from matrix to fiber in locally cracked regions. The loss of linearity in the stress-strain behavior is often considered to indicate the onset of matrix cracking. The proportional limit occurs at about 75 MPa. Matrix cracking can also be detected by measuring electrical resistance of the sample, because matrix cracks are discontinuities in the electrical path. Figure 1 also shows the normalized electrical resistance as a function of stress up to 120 MPa, which is nearly 60% of the ultimate strength. Notice that the resistance of the composite remains constant until the stress level reaches approximately one half of the proportional limit, indicating that microcracking begins at a stress lower than can be detected mechanically. When the sample is unloaded the mechanical strain is shown to return to zero along the dotted line, whereas the resistance remains approximately 6% higher than in the original condition. This implies that the matrix cracks are mechanically closing, but are not reestablishing electrical contact.

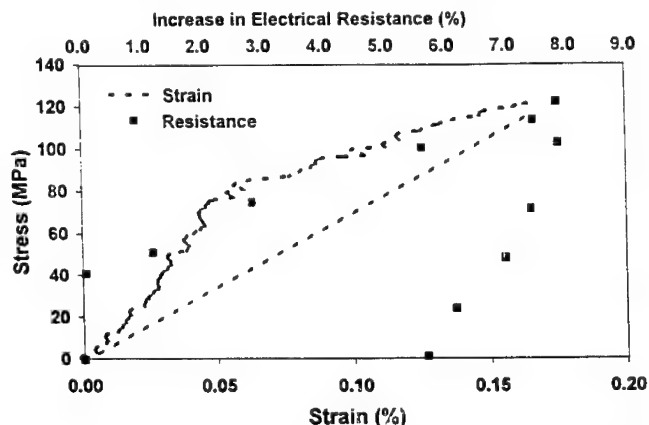


Fig. 1 Room temperature stress-strain and electrical resistance behavior of SiC/SiC composite.

Environmental Effect on Mechanical Behavior

As plotted on Figure 1, the samples were damaged to some degree by loading to 120 MPa, which is well above the proportional limit. This was followed by stress-free exposures to moist air as well as to argon and laboratory air at 1000°C. Subsequent stiffnesses normalized to original values are plotted as a function of time in Figure 2. Notice that modulus recovery occurs to some degree in all cases, including the argon-soak treatment, within the first 10 hours of exposure but not thereafter. In moist air the recovery processes increase the modulus from 50% to almost 100% of original stiffness, while in air and argon the recovery is limited to 85% and 70%, respectively. The composite does not lose any of its original ultimate strength even on 40 hours exposure to any environment. The water vapor exposure appears to be beneficial under these conditions in that it restores the elastic modulus to its original value without reducing the ultimate strength.

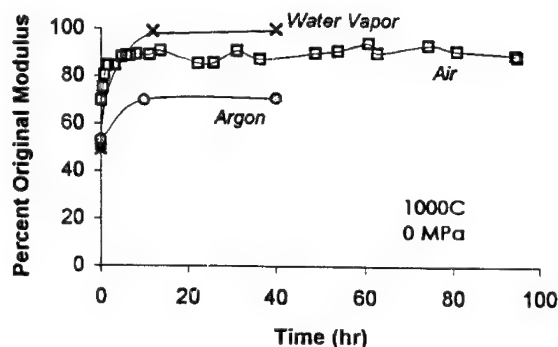


Fig. 2 Change in Young's modulus with time in dry air, argon, and water vapor environments at 1000°C.

A more application-relevant experiment consisted of subjecting the samples to combined stress, temperature and environment to explore the static fatigue effect. The damage state of each sample was monitored by measuring stiffness at various times. The stress level 80 MPa was chosen because it was slightly above the proportional limit and corresponded to the cyclic endurance limit in air at 1000°C [18]. Figure 3 shows a marked difference between the modulus evolution of samples held in air and in water vapor. After roughly 22 hours exposure in air, the modulus had dropped to half of its original level and the sample failed. Conversely, in water vapor the modulus did not drop from its as-received value and the sample remained intact. The modulus recovery mechanisms seen in Figure 2 (stress-free) are apparently also effective at 80 MPa. However, the recovery of the modulus upon exposure to water vapor cannot be primarily due to surface oxide formation. This was shown by removing the surface oxide film by etching with hydrofluoric acid. This treatment left the measured elastic modulus unaffected.

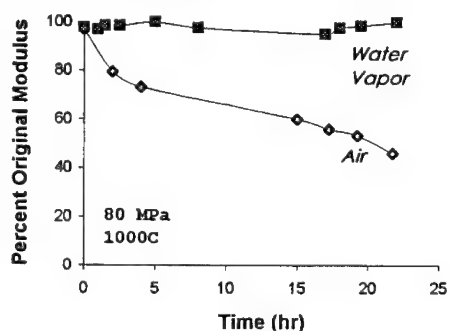


Fig. 3 Change in Young's modulus with time in dry air and water vapor environments at 1000°C under 80 MPa tensile stress.

However, when the stress was raised to roughly 1.8 times the proportional limit, exposure to water vapor failed to produce a recovery of the elastic modulus. In fact the static fatigue life was reduced to less than 40% of that for an identical sample exposed to dry air. Other stress levels were also examined [18].

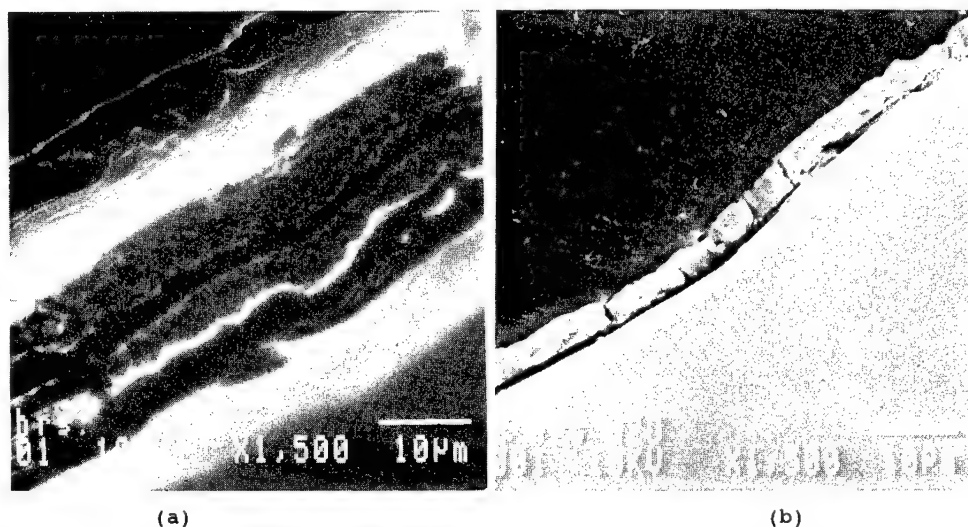


Fig. 4 Silica layer that forms on CVD SiC following 1200°C exposure for 150 hours: a) in dry air b) in water vapor.

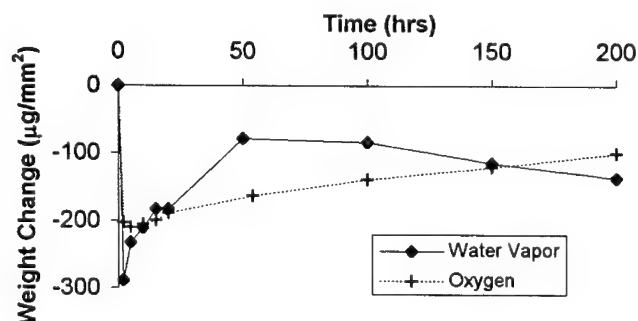


Fig. 5 Weight change per unit uncoated area of a SiC/SiC composite when exposed to dry oxygen and to water vapor at 1200°C.

Effect of Water Vapor on the Protective Silica layer in a SiC/SiC Composite

The morphology of the silica layer that formed on the CVD SiC coatings following exposure to dry air at 1200°C differed markedly from that exposed to water vapor as shown in Figures 4a and 4b. In dry air the oxide appears to form as a multi-layered lamellar structure, whereas in the moist environment the oxide forms as a dense coherent layer. This is consistent with the observations that water vapor produces a greater degree of modulus recovery and modulus retention, Figures 2 and 3. Weight changes in the SiC/SiC composite were measured as a function of exposure time up to 200 hours at 1200°C in oxygen and in water vapor. The composite specimens were cut from a block of coated material so that 4 of the total 6 faces remain coated with SiC. The results plotted in Figure 5 show that for very short exposure times in both environments the specimens lost weight. This is probably attributable to the

burning of the CVD carbon layer applied to the SiC fibers. Once this transient process slows, the specimens gain weight as the SiC oxidizes throughout the specimens. At long times in dry oxygen the composite continues to gain weight; in water vapor the composite loses weight over the same time span. The long-term loss is apparently due to the volatilization of the protective oxide as Si(OH)_4 , as discussed above.

Conclusion and Summary

It has now been established that the presence of water vapor in the environment can have a strong effect on the formation kinetics and durability of the silica layer and thus on the lifetimes of silicide materials in general. Specifically, water increases the rate of silica formation and simultaneously promotes its loss. Silica evaporation results from a reaction between water and the oxide to form the volatile species Si(OH)_4 . Although the loss process has been known for some time, the mechanism has only recently been confirmed. This volatilization process may ultimately define the use envelope for SiC and other silicides with respect to time, temperature, and environment.

Water vapor was also found to have both beneficial and detrimental effects on the mechanical properties of a SiC/SiC composite. Specifically, the reduction of Young's modulus that was caused by matrix cracking was later reversed to some extent by the formation of silica believed to bridge across the crack faces. If held stress-free at elevated temperature in a dry gas environment the modulus partially recovered; in a moist environment the recovery was essentially complete. In the absence of moisture, either not all cracks were bridged, or more likely, the bridging oxide was weaker. Under sustained load of 80 MPa at 1000°C in water vapor the modulus recovery mechanisms, combined with the formation of a protective surface film, essentially eliminated the static fatigue effect. Conversely, in air the static fatigue damage developed rapidly. The weight loss measurements confirm that water vapor is a more aggressive oxidant than even pure oxygen. Subsequently, when the stress level was further increased failure occurred much sooner for the sample in water vapor than in air. Apparently, the oxide formation even in the highly oxidative water vapor was not fast enough to bridge or seal the matrix cracks.

Acknowledgement

This work was made possible by support from an ARPA/ONR contract grant, N0001492J1779. The oxidation and volatilization behavior of the SiC/SiC composite was investigated by Ms. Mara Liebllich.

References

1. R.J. Shaw, S. Gilkey, and R. Hines, "Engine Technology Challenges for a 21st Century High-speed Civil Transport," NASA Technical Memorandum 106216, (1993).
2. N.S. Jacobson, "Corrosion of Silicon-Based Ceramics in Combustion Environments," J. Am. Ceram. Soc., 76 (1993) 3.
3. B.A. Wilcox and M.A. Rigdon, "High Temperature Materials: Processing and Applications," in Critical Issues in the Development of High Temperature Structural Materials, ed. N.S. Stoloff, D.J. Duquette, and A.F. Giamei, TMS, Warrendale, PA 15086, (1993) 1.
4. S.V. Raj, "An Evaluation of the Properties of Cr_3Si Alloyed with Mo," Mater. Sci. Eng., A201 (1995) 229.
5. D. Berztiss, R. Cerchiana, E. Gulbransen, F. Petit and G. Meier, "Oxidation of MoSi_2 and comparison with other silicide materials," Mat. Sci. Engr., A155 (1992) 165.
6. J. Mattuck, "Enhanced oxidation of MoSi_2 under tensile stress", Met. Trans., 1 (1970) 479.
7. S. Baskaran and J. Halloran, "Fibrous monolithic ceramics: III, Mechanical properties and oxidation behavior of SiC/BN systems," J. Amer. Ceram. Soc., 77 (1994) 1249.

8. K.L. Luthra, "Some New Perspectives on Oxidation of Silicon Carbide and Silicon Nitride," J. Am. Ceram. Soc., 76 (1991) 1095.
9. E.J. Opila, "Oxidation Kinetics of Chemically Vapor-deposited Silicon Carbide in Wet Oxygen," J. Am. Ceram. Soc., 77 (1994) 730.
10. B.E. Deal and A.S. Grove, "General Relationships for the Thermal Oxidation of Silicon," J. Appl. Phys., 36 (1965) 3770.
11. M-C. Cheng and I.B. Cutler, "Vaporization of Silica in Steam Atmosphere," J. Am. Ceram. Soc., 62 (1979) 593.
12. A. Hashimoto, "The Effect of H₂O Gas on Volatilities of Planet-forming Major Elements: I. Experimental Determination of Thermo-dynamic Properties of Ca-, Al-, and Si-hydroxide Gas Molecules and Its Application to the Solar Nebula," Geochim. Cosmochim. Acta, 56 (1992) 511.
13. E.J. Opila and R.E. Hann, Jr., "Paralinear Oxidation of CVD SiC in Water Vapor," submitted to J. Am. Ceram. Soc. (1996).
14. R.T. Bhatt, "Oxidation Effects on the Mechanical Properties of a SiC-Fiber-Reinforced Reaction-Bonded Si₃N₄ Matrix Composite," J. Am. Ceram. Soc., 75, (1992) 406.
15. P.F. Tortorelli, S. Nijhawan, L. Riester, and R.A. Lowden, "Influence of Fiber Coatings on the Oxidation of Fiber-Reinforced SiC Composites," Ceram. Eng. & Sci. Proc. 14, (1993) 358.
16. L. Filipuzzi, G. Camus, and R. Naslain, "Oxidation Mechanisms and Kinetics of 1D-SiC/C/SiC Composite Materials: I. An Experimental Approach," J. Am. Ceram. Soc., 77 (1994) 459.
17. L. Filipuzzi and R. Naslain, "Oxidation Mechanisms and Kinetics of 1D-SiC/C/SiC Composite Materials: II. Modeling," *ibid.*, 77 (1994) 467.
18. P. Lipetzky, N.S. Stoloff and G. Dvorak, "Effects of processing and environment on the properties of a SiC/SiC composite", in this proceedings.
19. P. Lipetzky, G. Dvorak and N.S. Stoloff, "Tensile properties of a SiC/SiC composite," in press, Mat. Sci. Engr., 1996.

EFFECTS OF PROCESSING AND ENVIRONMENT ON PROPERTIES OF SiC/SiC COMPOSITES

P. Lipetzky¹, N.S. Stoloff² and G.J. Dvorak¹

¹Department of Mechanical Engineering

²Department of Materials Science and Engineering
Rensselaer Polytechnic Institute
Troy, New York, USA 12180-3590

Abstract

In order to evaluate the suitability of a SiC-based composite for combustion-related applications, the mechanical properties of a continuous fiber-reinforced material have been evaluated at high temperature in both air and water vapor. Results of short-term tests show that stiffness, proportional limit and ultimate strength are neither temperature nor atmosphere dependent up to 1000°C. Isothermal fatigue experiments at 1000°C reveal that the endurance limit of fully-coated samples corresponds closely to the proportional limit. Removing one fourth of the protective SiC surface coating decreases the endurance limit by nearly 40%. Damaged, fully-coated samples under stress-free exposure to high-temperature air or water vapor show significant modulus recovery due to silica crack bridging. The recovery mechanism in water vapor is sufficiently robust so that static fatigue damage evolution is virtually eliminated even if stress equal to the endurance limit is applied; no similar behavior is seen in air. If the SiC surface coating is only 75% intact, recovery mechanisms are not active and static fatigue life decreases by a factor of five.

Introduction

The type of material used in many applications is ultimately governed by the chemical and mechanical stability requirements over the lifetime of the component. For high-temperature, load-bearing components such as in combined cycle power generation equipment, lifetime stability is critical due to prolonged exposure to corrosive and erosive conditions [1]. The overall goal for these types of materials has been reduced weight and increased durability at high temperatures. As an extreme case, flame temperatures for gas turbines will eventually exceed 1400°C and may reach as high as 1650°C, which is well beyond the capability of conventional superalloys [2-5].

Developmental materials in the area of combustion are based on both intermetallic and ceramic, aluminide and silicide systems [6,7]. The current work focuses on the behavior of a SiC-SiC composite, which is a candidate combustor material. Evaluating SiC for either this or a similar application involves not only strength and oxidation tests, but also the determination of static and cyclic fatigue life in various atmospheres. Based on these results, limiting stresses and temperatures can be established for future component design.

Material

The material used in this investigation is a continuous SiC fiber-reinforced SiC composite manufactured by DuPont Lanxide Composites. Tows of roughly 500 carbon-coated Nicalon fibers are woven into a 0°/90° plain weave fabric, which is subsequently chemical-vapor coated with 30-50 μm of crystalline SiC. Approximately 10 such plies, all in the 0°/90° orientation, are consolidated into the final plate. Tensile coupons are machined from these plates in the 0° direction. To investigate the effect of surface coating and environment on mechanical properties, the following two types of samples are noted: First, certain samples are cut from the plates as described and then completely coated with an additional SiC layer; these samples are "coated". Another group of samples is prepared by cutting prismatic coupons from the plate, coating uniformly with SiC, and finally grinding the edges to form a reduced section. This group has approximately 75% of the gauge section surface area coated; the designation here is "edge-ground". A micrograph of the material which has been sectioned transverse to the loading axis and diamond polished is shown in Fig. 1. The plain weave of the fibers is apparent, as is the SiC coating which has been applied to each layer (bright phase surrounding the fiber tows). Roughly 10% void space remains overall, but voids are not distributed uniformly. Fiber volume fraction is near 30%. Specimen density is approximately 2.3 g/cc.

Experimental Procedure

Experimental investigation of the mechanical properties involves both static and cyclic tensile testing performed at room- and elevated temperatures. Thermocouples were used to measure the surface temperature of the specimen in the induction furnace hot-zone. Samples were ramped to the test temperature in ten minutes and held for five minutes to allow temperature equilibration in the sample and the extensometer. Tensile coupons were gripped at room temperature using face-loaded blocks, rather than wedge blocks. For cyclic tests a loading frequency of 10 Hz was used with a constant load ratio, $R=0.1$. Following run-out at 1 million cycles, the stress maximum was increased and cycling continued. Additional details can be found elsewhere [8].

Atmospheric control under stress was maintained by supplying a steady, preheated flow of the desired ambient into a jacket around the gauge section of the sample. Stress-free atmospheric exposure was performed in a sealed horizontal tube furnace with a flowing ambient (~ 0.1 liter/min at RTP). Relevant ambient compositions included high-purity argon, air and water vapor, in progressive order of oxidizing strength. Water vapor has been shown to be a stronger oxidant than both air and oxygen for attack of SiC and SiO_2 [9,10]. Water vapor was supplied by bubbling 0.1 liter/min air through a reservoir of 90°C tap water. This amount of water in the gas phase, 0.7 atm., is comparable to the amount present in a gas turbine or combustion application. Additional details of the environmental apparatus and results are given elsewhere [10].

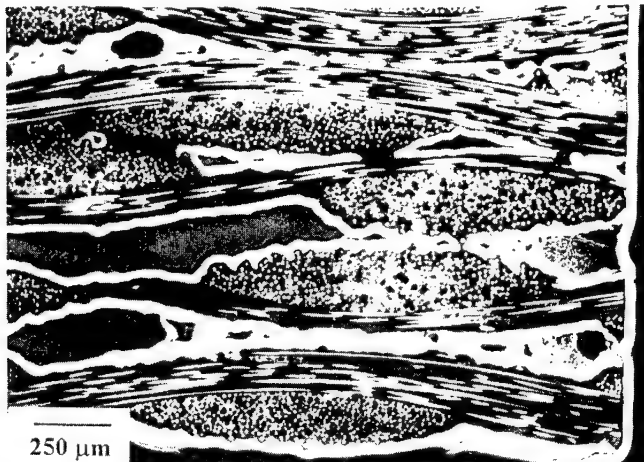


Fig. 1 Polished cross-section of the as-received SiC/SiC composite. Direction normal to the image is parallel to the load axis.

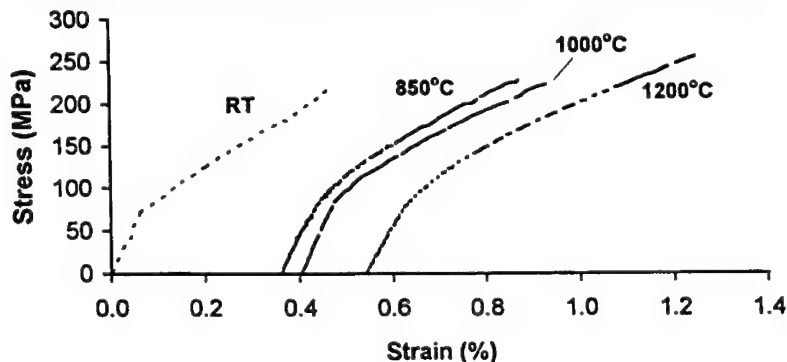


Fig. 2a Stress-strain behavior over a range of temperatures for as-received specimens tested in air.

Results and Discussion

The experimentally measured tensile properties for the composite are shown in Fig. 2a. Proportional limit and Young's modulus were roughly 75 MPa and 120 GPa, respectively, at all temperatures. Ultimate strength was near 210 MPa up to 1000°C, but increased to 275 MPa at 1200°C. Data shown are for coated samples; no difference was observed for edge-ground samples in either air or water vapor. Apparently, no significant environmental interaction or material degradation has occurred over these few minutes. Figure 2b shows that the stiffness decreased when the sample was loaded to progressively increasing stress maxima. The Young's modulus of the sample is an indication of the damage state of the material. Figure 2b also shows that almost no residual strain (0.01%) was measured during repeated loading. This implies that cracks are generally closed upon unloading.

Figure 3 shows that microstructural damage manifested itself largely as matrix cracks transverse to the loading axis. These were not observed for specimens loaded to stresses below the proportional limit. Fiber breakage, as indicated by missing or partial fibers, was not observed in samples loaded to any stress level. Fractographic examination showed that for temperatures up to 1200°C the material components were not degraded in short-term tests. At 1200°C less individual fiber pull-out is seen than at lower temperatures. The higher strength measured at 1200°C is a result of tows fracturing more uniformly and thus acting as macro-fibers [8].

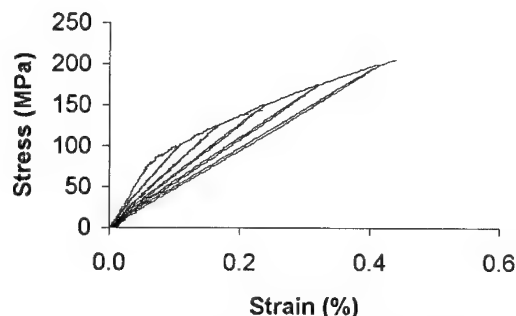


Fig. 2b Negligible hysteresis upon repeated unloading of an as-received sample tested in air at room temperature.

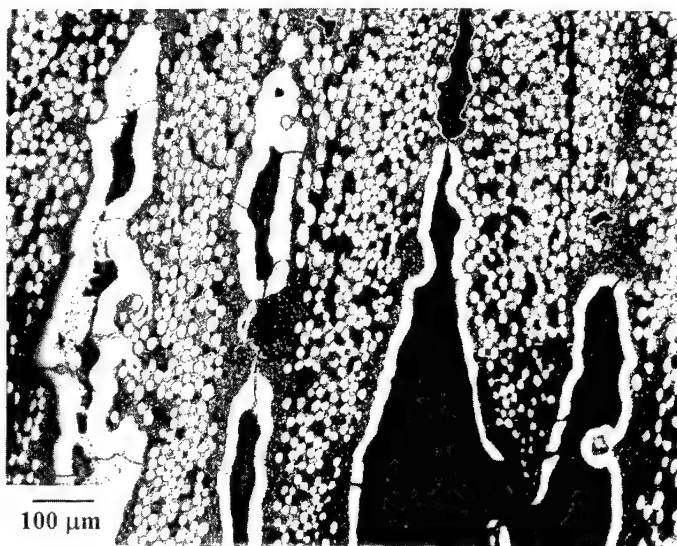


Fig. 3 The prominent damage features for samples loaded above the proportional limit are transverse matrix cracks.

With these data established as a baseline for further investigation, attention is now turned to the cyclic endurance limits in both air and water vapor. Data in Fig. 4a show stress maxima plotted as a function of the total number of cycles at 1000°C in air. Arrows show that the load-cycle history was increased stepwise; all samples were cycled to failure in this way. Run-out for coated samples was reached for stress maxima below approximately 75-80 MPa in air. Above 80 MPa samples did not consistently reach run-out. Notice that this endurance limit corresponds closely to the proportional limit. The endurance limit was near 50-55 MPa for edge-ground samples tested in air. This is expected considering the long-term nature of these tests and that a protective coating was absent on 25% of the sample surface.

Damage evolution during cycling was monitored by periodically measuring Young's modulus as plotted in Fig. 4b. Generally, stiffness decreases as damage increases prior to failure. For coated samples tested in water vapor, run-out was consistently reached at 80 MPa and no decrease in modulus was observed. At stress maxima of 85 MPa and higher, coated samples showed no atmosphere dependence and modulus decreased to near 70% of the original value before rupture. Apparently, the stress of 80 MPa is a threshold value because it corresponds to the onset of matrix cracking, see Fig. 3. Edge-ground samples exhibited no difference in air or water vapor at any stress.

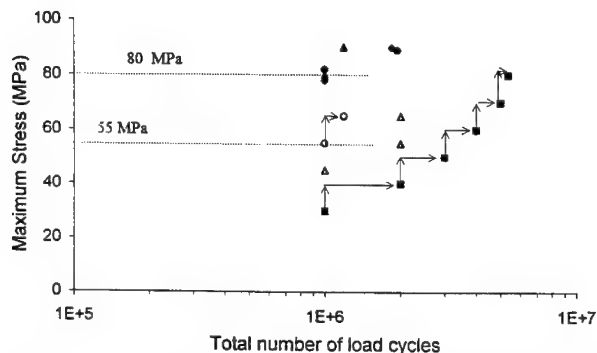


Fig. 4a Endurance limits for coated (solid) and edge-ground specimens (open) in air at 1000°C. ($R = 0.1$)

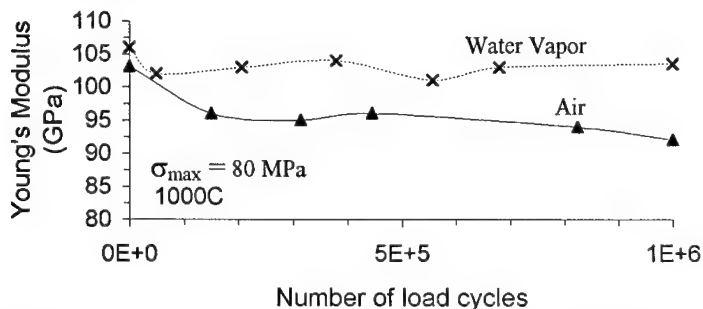


Fig. 4b Modulus evolution of coated samples during cyclic fatigue in air and water vapor at 1000°C. ($R=0.1$)

The stable modulus during cyclic fatigue in water vapor indicates that a recovery mechanism is active which offsets the damage caused by cycling. To further investigate this phenomenon, samples were damaged at room temperature by loading to 120 MPa and then given stress-free exposure to ambients of water vapor, air and argon at 1000°C. Modulus was measured periodically during exposure by ramping stress from 0 MPa to near 20 MPa and back. Figure 5 shows that the pre-exposure damage was reversed to some degree within the first 10 hours. The oxidation of SiC in both water vapor and air caused SiO_2 to form on crack faces throughout the damaged sample [10]. Microcrack bridging by SiO_2 is the apparent mechanism of modulus recovery. The finite modulus recovery in argon indicated that some reactive components remained in the samples after consolidation. Following the damage and soaking histories detailed in Fig. 5, samples were loaded to failure at 1000°C. It was found that none of the original strength was lost in any of the three ambients, since UTS is dominated by fiber properties, see Fig. 2.

To examine the range of conditions under which damage recovery occurs, experiments were conducted with finite applied stress. Young's modulus versus time data are plotted in Fig. 6 for specimens held at 80 MPa and 1000°C. A stress level of 80 MPa corresponds to the 1000°C endurance limit. For coated samples a distinct difference was observed between air and water vapor exposure. In air, samples showed a rapid decrease in modulus during the first 3 hours, followed by a slower, steady decrease until failure at roughly 22 hours. Samples exposed to water vapor did not lose modulus and did not fail after the same exposure time. Conversely, edge-ground samples suffered severe loss of modulus and failed independent of ambient after roughly 4 hours. Figure 7 shows the modulus versus time data for samples exposed to water vapor at higher stresses. A stress of 85 MPa caused an initial drop in modulus, although following approximately 20 minutes the modulus stabilized at a value near 97 GPa. The shorter transient modulus behavior in water vapor, 20 minutes versus 3 hours in air also indicates that water is a more powerful oxidant than air. Creep behavior must also be affected. Following exposure to 85 MPa and

the determination of the steady-state modulus value, stress was increased to 90 MPa. The modulus dropped initially when the higher load was applied, as in Fig. 2b, and proceeded to slowly decrease. Without any rapid decrease in modulus or unusually high strain rate, the sample failed after a total of only 4.5 hours exposure. Figure 6 shows that the final modulus prior to failure is as low as 45% to 50% of the initial value; thereby, modulus is a good indicator of remaining life. Conversely, the recovery action in water vapor alters the modulus-life correlation.

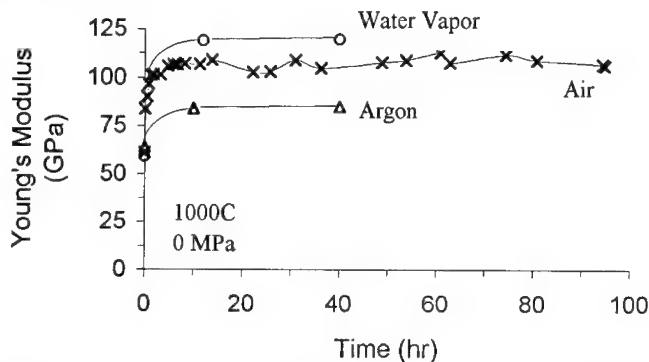


Fig. 5 Modulus evolution in damaged samples under stress-free exposure to argon, air and water vapor at 1000°C.

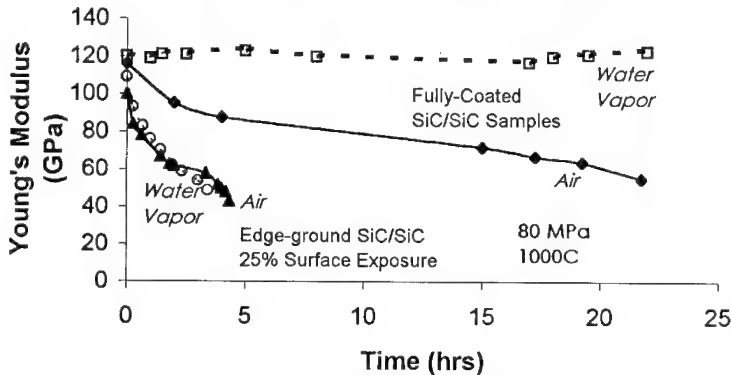


Fig. 6 Modulus retention at 80 MPa and 1000°C. Coated samples in water vapor show no loss. Edge-ground samples fail much sooner than coated samples in either ambient.

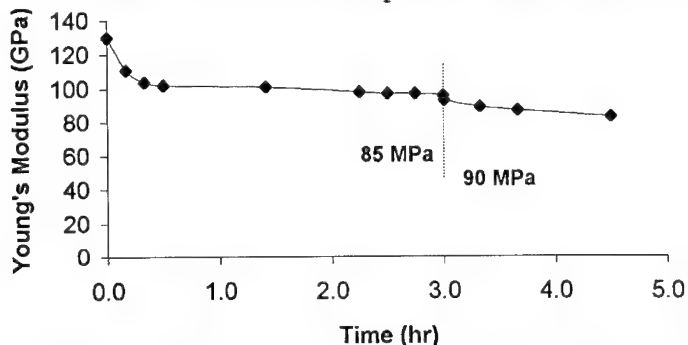


Fig. 7 Modulus retention for coated samples at 1000°C in water vapor. First 3 hours at 85 MPa, followed by 90 MPa.

Summary and Conclusion

This work has shown that environment and specimen preparation conditions can either improve or degrade the mechanical properties and lifetime of a SiC composite. A complete exterior SiC coating increased static fatigue survival time fivefold and roughly doubled the endurance limit compared to samples with only 75% of the surface area coated. In this case environmental ingress is minimized by the coating, and sample integrity is maintained. Rapid oxidation can also be beneficial because a coherent silica surface film retards oxidant penetration. Furthermore, the oxide can mechanically bridge cracks and improve modulus retention as well as affect modulus recovery. Modulus retention for coated samples occurs under stresses as high as the proportional limit during cyclic and static fatigue in water vapor, but not in air. Stress-free exposure to 1000°C water vapor caused damaged samples to regain 100% of their original stiffness and proportional limit without losing any fracture strength. Stress-free exposure of damaged samples to air and argon also produced some degree of recovery. No difference in properties was observed for edge-ground samples tested in either water vapor or air because the formation of a protective silica layer was far from complete.

Acknowledgements

This work was supported by a grant from ARPA/ONR under contract number N0001492J1779. The authors are grateful to Drs. W. Coblenz and S. Fishman, contract monitors, for their oversight of this program. We also thank Ms. Mara Lieblich for assistance with controlled atmosphere work.

References

1. M. Valenti, Mech. Engr., Feb. 1995, pg 68.
2. B.A. Wilcox and M.A. Rigdon, in Critical Issues in the Development of High Temperature Structural Materials, Ed. by N.S. Stoloff, D.J. Duquette, and A.F. Giamei, TMS, Warrendale, PA, (1993) 1.
3. R.J. Shaw, S. Gilkey, and R. Hines, "Engine Technology Challenges for a 21st Century High-speed Civil Transport," NASA Technical Memorandum 106216, 1993.
4. N.S. Jacobson, J. Am. Ceram. Soc., 78 (1993) 3.
5. Superalloys II, Ed. by C.T. Sims, N.S. Stoloff and W.C. Hagel, J. Wiley, New York, 1987.
6. D. Carruthers and L. Lindberg, pp 1258-72 in "Third International Symposium on Ceramic Components and Materials for Engines," Ed. by V. Tennery, Am. Ceram. Soc., Westerville, OH 1988.
7. D. Lewis, M. Singh and S. Fishman, Adv. Mat. Proc., 148 1 (1995) 29.
8. P. Lipetzky, G.J. Dvorak and N.S. Stoloff, Mat. Sci. Engr. in press, 1996.
9. K.L. Luthra, J. Am. Ceram. Soc., 76 (1991) 1095.
10. P. Lipetzky and W. Hillig, this proceedings.

PROCESSING AND DESIGN

Processing Issues Related to Environmental Effects in Superalloys, Composites
and Intermetallics

F.S. Pettit and G.H. Meier

Materials Science and Engineering Department
University of Pittsburgh
Pittsburgh, PA 15261

Abstract

Processing issues related to environmental effects in superalloys, composites and intermetallics are examined by considering impurity levels, retention of small concentrations of certain elements, alloy structure, and alloy homogeneity. Each case is discussed on the mechanistic level.

In the case of impurity levels it is shown that very small concentrations of certain elements can have a profound effect on oxidation resistance. An excellent example is sulfur in superalloys, where sulfur concentrations in excess of 1 ppm by weight, decrease the oxidation resistance of alloys due to spalling of protective scales of alumina. Other examples are presented to illustrate various aspects of the adverse effects produced by certain impurities on the environmental resistance of materials. This will include the effect of oxygen interstitials on the ductility of titanium matrix composites, the influence of nondiamond species on the behavior of diamond films at elevated temperatures, and impurities introduced into Si_3N_4 and SiC composites during sintering.

In some alloys it is necessary to retain elements at low concentrations because the beneficial effect of the element on environmental resistance exists only over a small range of concentrations. For example small amounts of yttrium, or misch metal, about 0.1 wt%, are used to improve the oxidation resistance of alloys by improving oxide scale adherence. However high concentrations of these materials produce adverse effects due to preferential oxidation and intermetallic compound formation.

The importance of microstructural control during processing is illustrated by examining the oxidation resistance of alloys containing two phases, one of which has poor oxidation resistance. Structural effects are also described by considering the intermetallic TiAl and the effects of surface condition on oxidation behavior.

All other factors being constant it is shown that homogeneous alloys usually are more resistant to environmental effects than those which are inhomogeneous. A good example is an alloy containing yttrium at levels where an intermetallic compound is formed in the alloy during processing.

Processing and Design Issues
in High Temperature Materials
Edited by N.S. Stoloff and R.H. Jones
The Minerals, Metals & Materials Society, 1997

Introduction

In discussing processing issues related to environmental effects, there are two different viewpoints. One relates processing to its influence on end product environmental properties, whereas the other relates environmental effects on processing itself. In this paper more emphasis will be placed on the former viewpoint. When considering processing - environmental interactions related to intermetallics, superalloys and composites, it is useful to categorize in a way that crosses over specific processes. In other words processing - environmental interactions that occur because of a specific condition. One such condition is the impurity level. Another is the retention of small concentrations of certain elements. Finally, alloy structure and homogeneity are also conditions that affect processing - environment interactions. In the following each of these conditions is discussed and illustrated by using various examples.

Impurity Levels

In processing of materials impurities are always present and the questions are at what levels can they be accepted and what are the costs to remove them. Sulfur is an impurity which can have a profound effect on the oxidation resistance of nickel base superalloys and coatings that rely upon the formation of external, continuous scales of α - Al_2O_3 for oxidation resistance. It is now well documented that the α -alumina spalls from such alloys when the sulfur concentration exceeds about 1 ppm⁽¹⁻³⁾.

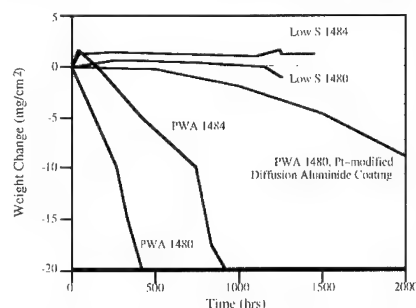
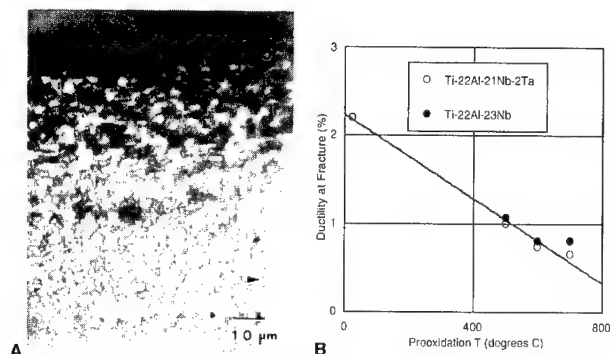


Figure 1. Cyclic oxidation data for superalloys (PWA 1480, 1484) with normal fabrication levels of sulfur (~ 5-8 ppm) and for these same superalloys with < 1 ppm sulfur. Data for PWA 1480 with a diffusion aluminide coating is also included.

Some typical results are presented in Figure 1 where the cyclic oxidation resistance of some superalloys are compared. The superalloys with sulfur concentrations less than 1 ppm have better oxidation resistance than these same alloys with diffusion aluminide coatings. Extensive research is now in progress to prepare alloys and coatings with small concentrations of sulfur. One method to control sulfur effects on α - Al_2O_3 adherence is to use reactive elements such as yttrium to getter the sulfur. However, such elements cannot be present in most alloys at high concentrations (e.g. ~ 1%) since intermetallic phases can be formed that produce adverse effects on mechanical properties and oxidation behavior. The retention of reactive elements at

low concentration levels will be discussed in a subsequent section of this paper.

The mechanical properties of some alloys such as titanium-base alloys can be adversely affected by interstitial elements such as oxygen. The concentration of interstitial oxygen can reach unacceptable levels in casting and rolling processes. In Figure 2a the microstructural features of the interstitial zone near the surface of a Ti-Al-Nb composite is shown and in Figure 2b the ductility of this alloy after 100 hours of exposure in air at different temperatures is presented. The ductility of this alloy decreases as the thickness of the zone of interstitials increases.



Diamond films can now be fabricated by a variety of techniques involving chemical and physical vapor deposition. While these films are predominantly diamond there are some nondiamond species present such as graphite and amorphous carbon. The perfection of the diamond films as indicated by the amount of

Figure 2. Interstitial affected zone formed on Ti-22Al-23Nb (at %) after 100 hrs. in air at 700°C, (a), and ductility of this alloy and Ni-22Al-21Nb-2Ta as a function of preoxidation at various temperatures for 100 hrs.

nondiamond species therefore determines properties of these films. In Figure 3a Raman spectra obtained with an ultraviolet microscope are presented where it is evident that nondiamond species are concentrated at the boundaries between grains in the film. Figure 3b shows that excessive oxidation occurs at sites at which these nondiamond species are concentrated. Control of the nondiamond species in diamond films by using in-situ Raman spectroscopy during deposition is being investigated⁽⁴⁾.

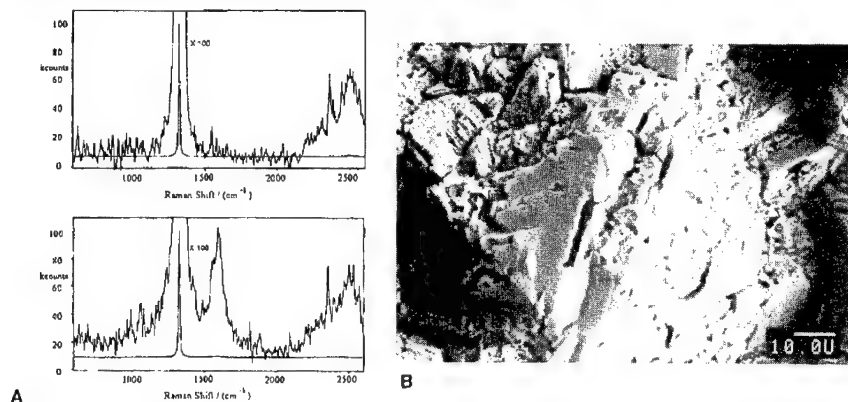


Figure 3. (a) Raman spectra of diamond at a crystal facet (upper spectra) and at an interstice between two facets (lower spectra), where it is evident that nondiamond species are present at the interstice as indicated by the peak at 1584 cm⁻¹. (b) Photograph of a diamond film after exposure to oxidizing conditions (24 hrs at 700°C in argon with 10⁻⁴ atm oxygen) where it is evident that oxidation has occurred at localized points and interstices between diamond facets.

When additives are used to improve the sintering of silicon nitride, these additives can affect the oxidation resistance of the sintered end products⁽⁵⁻⁸⁾. In Figure 4 parabolic rate constants for the oxidation of silicon nitride prepared by chemical vapor deposition and sintering are compared. The silicon nitride prepared by chemical vapor deposition (CVDSN) is pure but the sintered silicon nitride (SN) and the silicon nitride reinforced with SiC (SNSC) contains the sintering agents Al₂O₃ and Y₂O₃. These agents enter the SiO₂ scale during oxidation, Figure 5, and cause the SiO₂ to be less protective. The parabolic rate constants for oxidation of sintered Si₃N₄ can be two to three orders of magnitude greater than that for pure Si₃N₄.

Retention of Reactive Elements In Alloys at Low Concentrations

An effective method to negate the adverse effects of sulfur on the adherence of $\alpha\text{-Al}_2\text{O}_3$ is to add small concentrations of elements such as yttrium, cerium, or lanthanum to alloys. Such elements have a large affinity for sulfur and it is well documented that these elements significantly improve the adherence of $\alpha\text{-Al}_2\text{O}_3$ scales^(9,10). The concentrations of these

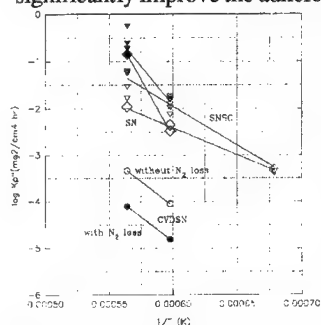


Figure 4. Temperature dependence of parabolic rate constants for oxidation of Si_3N_4 prepared by chemical vapor deposition and by sintering. (The rate constants for CVD Si_3N_4 were calculated using oxide scale thickness measurements).

elements in alloys must be high enough to reduce sulfur to levels less than 1 ppm. It is also possible that these elements affect $\alpha\text{-Al}_2\text{O}_3$ adherence by other effects in addition to gettering sulfur⁽¹¹⁾. When elements such as yttrium, cerium, or lanthanum are present in alloys at high concentrations, intermetallic phases are usually formed, and these phases are prone to preferential oxidation, Figure 6, moreover such intermetallics can adversely affect the mechanical properties of alloys. The effective use of reactive elements therefore requires control of these elements at concentrations in the range between about 0.05 to 0.3 weight percent⁽¹²⁾. These elements, in addition to possessing a large affinity for sulfur, also have an even greater affinity for oxygen. Reaction with mold materials as well as dissolved oxygen must be minimized. Processing of large quantities of alloy with control of reactive element concentrations in the 0.05 - 0.3 wt% range therefore is difficult and it is not uncommon to find some heats with insufficient concentrations of reactive elements.

Alloy Structure

Processing-environmental interactions involving alloy structural effects are numerous and only a few examples will be presented in this paper to illustrate the salient features. Molybdenum disilicide is an intermetallic compound which has been extensively used for high temperature applications, particularly furnace heating elements. The oxides of Mo (MoO_2 , MoO_3) are much less stable than SiO_2 so that silica should be the stable oxide for any but the most dilute Mo-Si alloys⁽¹³⁾. In fact, the nature of the external scale formed is a strong function of temperature. At temperatures above 600°C a protective film of SiO_2 develops on MoSi_2 . However, in the temperature range 300 to 550°C a protective silica film does not form. This leads to the phenomenon of "accelerated oxidation"^(13,14) which involves the formation of scales containing crystalline oxides of Mo and vitreous silica and rates which are orders of magnitude faster than those extrapolated from higher temperatures. Accelerated oxidation is a

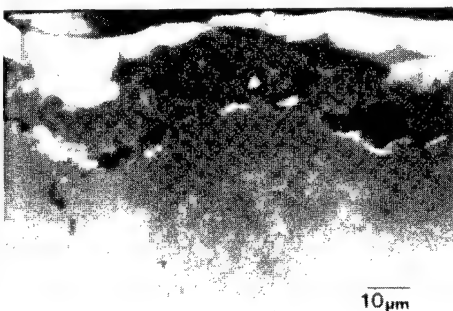


Figure 5. Scanning micrograph of oxidation products formed on sintered Si_3N_4 . The SiO_2 scale is permeated with silicates containing the sintering agents which have adversely affected its protective-ness.



Figure 6. Photomicrograph showing preferential oxidation of yttrides in a Ni-15Cr-6Al-3Y (wt %) alloy.

material property of MoSi_2 , including single crystals. It has been proposed that the transition to protective silica formation is associated with the increase in volatility of the Mo-oxides as temperature increases^(13,14). This is shown schematically in Figure 7. At high temperatures the transient Mo-oxides evaporate and allow the silica regions to grow laterally into a continuous layer. At low temperatures the reduced volatility of the Mo oxides and slower growth of the silica prevent the development of a continuous silica layer. The rapid inward growth of MoO_3 produces an intermixed layer of MoO_3 and SiO_2 .

If the MoSi_2 contains processing defects, such as microcracks or pores, the occurrence of accelerated oxidation within these defects can result in crack propagation and fragmentation of the MoSi_2 . This is seen in the macrophotographs in Figure 8. Fitzer⁽¹⁵⁾ first de-

scribed the phenomenon and named it "pest" in 1955. Since that time, many researchers have attempted to describe pesting of MoSi_2 and determine under what circumstances it occurs. Berkowitz-Mattuck et al.^(16,17) studied zone-refined material of less than 75% theoretical density and found that pesting occurs in oxygen, but not in nitrogen, carbon dioxide, carbon monoxide or argon, and that the rate of oxidation is very sensitive to the partial pressure of oxygen. Furthermore, as there is little or no lattice parameter change when MoSi_2 is equilibrated in oxygen, the solubility of oxygen in MoSi_2 is assumed to be very low. They concluded that, as a result of the high residual stresses introduced on cooling of the anisotropic material from the melt, a stress-enhanced oxidation could occur at the tips of Griffith flaws, eventually leading to brittle fracture. The disappearance of pesting at $T > 600^\circ\text{C}$ was explained as the result of plastic deformation of the matrix near the flaw accommodating the stresses. The cracks were found to be mostly transcrystalline. Westbrook and Wood⁽¹⁸⁾ proposed that the catastrophic nature of the "pest" mechanism was the result of preferential intergranular diffusion of a gaseous element (most likely oxygen or nitrogen), coupled with a temperature dependent hardening reaction. Fitzer et al.^(15,19,20) and Schlichting⁽²¹⁾ describe pesting of MoSi_2 as intercrystalline attack whereby each individual grain is enveloped by reaction product. They note that most oxidation occurs in pores or internally along pore canals, and failure occurs as

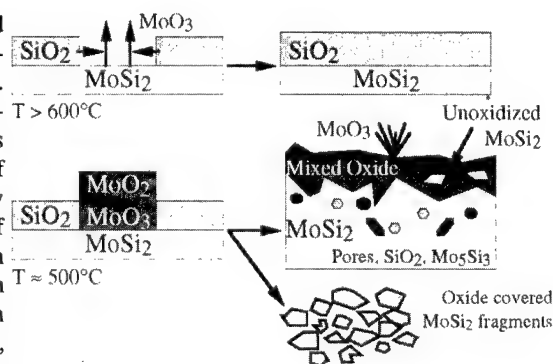


Figure 7. Schematic illustrating the formation of protective and nonprotective oxides during the oxidation of MoSi_2 , and the fragmenting of MoSi_2 that leads to pesting.

the result of a wedging effect from oxide growth in the defect. Fitzer and Schlichting give no evidence that this attack is intergranular and may only assume so, as pores tend to form predominantly along grain boundaries. This is inconsistent with Berkowitz-Mattuck et.al. who found fracture from pesting to be predominantly transcrystalline. Recent work⁽¹³⁾ has shown that, while accelerated oxidation is generic to all forms of MoSi₂, grain boundaries alone do not result in pesting since dense HIPed MoSi₂ did not pest even though it was polycrystalline. Only cast material, which contained

pre-existing microcracks, was observed to undergo pesting. It was concluded that pesting was the result of the occurrence of accelerated oxidation within the microcracks. There is a large change in volume going from Mo to MoO₃ (340%), along with the volume change of forming SiO₂ from Si (180%). These processes enhance the widening of the pre-existing cracks leading to pesting (i.e. turning to powder). These phenomena are illustrated schematically in Figure 7. This mechanism is supported by the observation of oxidation-induced growth of cracks formed in HIPed MoSi₂ by a microhardness indenter which ultimately resulted in pesting of a material which did not undergo pesting in simple oxidation exposures⁽²²⁾. McKamey et.al.⁽²³⁾ have also concluded that pesting occurs as the result of oxidation in preexisting cracks and pores.

Choudhury et al., in a classic paper,⁽²⁴⁾ studied the oxidation of TiAl (50 at% Al) in O₂ and air over the temperature range 800 - 1200°C. In O₂ cast TiAl which was abraded through 120 grit SiC formed alumina and exhibited k_p values 10^{-9} g²cm⁻⁴hr⁻¹ at 950°C but polished specimens formed TiO₂-rich scales and exhibited k_p values of about 10^{-5} to 10^{-6} g²cm⁻⁴hr⁻¹. Extruded TiAl formed alumina scales regardless of surface preparation. Choudhury et al. explained the

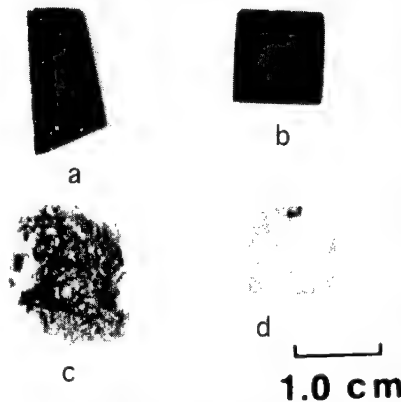
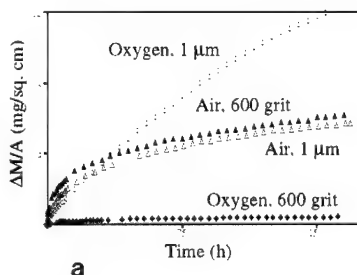


Figure 8. Photographs showing pesting of MoSi₂: (a) Cast material (b) HIPed material (30 Ksi for 5 hrs. at 1540°C) (c) Cast material after 82 hrs. of oxidation in air at 500°C, pesting has occurred (d) HIPed material after 168 hours in air at 500°C, accelerated oxidation has occurred.



a

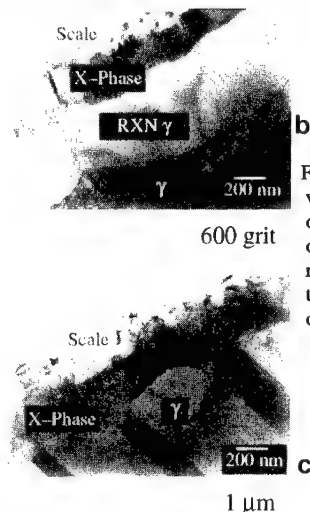


Figure 9. Weight change versus time data for the oxidation of TiAl in air and oxygen at 900°C, and microphotographs showing the microstructures after oxidation in oxygen.

effects of extrusion in terms of the absence of macroinhomogeneities which existed in the cast structure. The "surface finish effect", observed for the cast material, was presumed to result from coarse grinding homogenizing the alloy at the surface. A Ti_3Al layer was reported to form between the oxide and the alloy for all the exposures. Oxidation behavior in air at 950°C was independent of specimen preparation or fabrication method with titania-forming kinetics (k_p about 10^{-5} – 10^{-6} $\text{g}^2\text{cm}^{-4}\text{hr}^{-1}$) observed in all cases. The scales were similar to those formed on polished specimens in O_2 at 950°C . Experiments to determine the species

responsible for the difference between exposures in O_2 and air indicated that CO , CO_2 and H_2O impurities were not responsible nor was the difference in $p\text{O}_2$. It was, therefore, concluded that the increased rate of oxidation in air was a "nitrogen effect" although no N_2 -containing phases were identified in the scale or substrate.

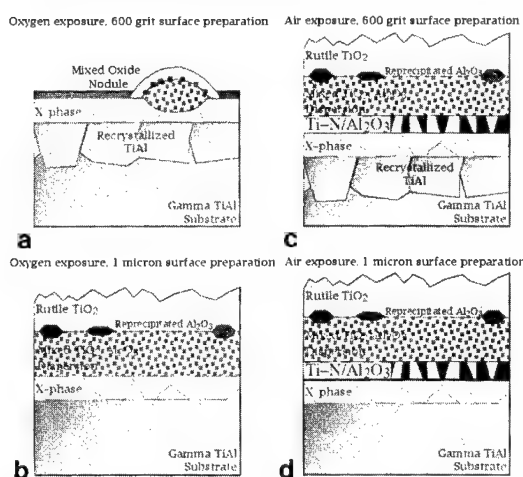
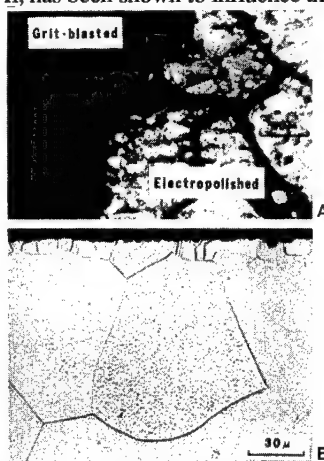


Figure 10. Schematic illustrating the effect of surface condition on the oxidation of TiAl in oxygen and in air.

The "surface finish effect" for oxidation temperatures below 1000°C is illustrated in the mass gain vs. time plot in Figure 9a for Ti-50at%Al oxidized at 900°C . The ground (600 grit) surface results in very slow kinetics in O_2 as the result of continuous alumina formation as shown schematically in Figure 10a. The $1\mu\text{m}$ diamond polished surface results in greatly accelerated kinetics due to the formation of a continuous layer of a mixed oxide, Figures 9a and 10b. Part of the beneficial effect of grinding may be in homogenizing the surface, as proposed originally by Choudhury et. al. (24). Indeed, the distribution of the minor α_2 phase, generally present in TiAl, has been shown to influence the composition of the external scale (25,26). However, an additional important effect is the recrystallization of the ground surface as illustrated in the transmission electron micrographs in Figure 9(26). The deformed layer, produced by grinding, recrystallizes during the initial oxidation exposure to produce gamma grains with a grain size on the order of $1\mu\text{m}$ (Figure 9b) from a starting gamma grain size on the order of $100\mu\text{m}$. No recrystallized layer forms on the polished surface (Figure 9c). It has been suggested (26) that enhanced Al diffusion in the fine-grained layer promotes the formation of continuous alumina.

The "nitrogen effect" prevents the formation of continuous alumina (27) so there is little effect of surface preparation on the oxidation rates of TiAl when the ex-

Figure 11. Photomicrograph of surface of Ni-10Cr (wt%) alloy after oxidation at 900°C in a CO-CO_2 gas mixture ($\text{CO/CO}_2 = 0.07$). A continuous layer of Cr_2O_3 has formed over that portion of the specimen surface that was grit blasted, (a). The microstructure of the grit blasted surface contains a zone of recrystallized grains, (b).



posures are carried out in air, Fig. 9a. The morphologies developed in air are presented schematically in Figures 10c and d. The micrographs in Figure 9 reveal an intermediate layer between the oxide and the gamma phase termed the X phase. This zone is depleted in Al and was originally thought to be α_2 ⁽²⁴⁾. However, an important observation was made by Dowling and Donlon in 1992⁽²⁸⁾ when they identified a cubic phase with a lattice parameter

of 0.69 nm and a Ti/Al ratio of approximately 2/1. These observations were confirmed⁽²⁹⁾ and the cubic phase was found to have 432 point group symmetry⁽³⁰⁾. Extensive TEM investigation of this phase using convergent beam electron diffraction (CBED)⁽³¹⁾ showed it to belong to one of two space groups, P4₃2 or P4₂32, and EDS analysis indicated an approximate composition of 57 at%Ti-33at%Al-10at%O⁽³²⁾. Increased exposure times and/or higher oxidation temperatures result in the Al-depleted zone becoming two-phase as the result of nucleation of α_2 at the interface between the cubic phase and the parent gamma⁽³³⁾. This observation confirms earlier suggestions of a two-phase depletion layer based on WDS measurements⁽³²⁾, Auger electron spectroscopy⁽³³⁾, and x-ray diffraction⁽³⁴⁾. The influence of the depleted zone on the oxidation behavior of gamma alloys is not yet clear, however, it is crucial to the mechanical properties.

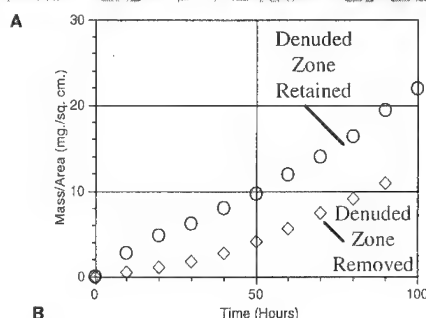
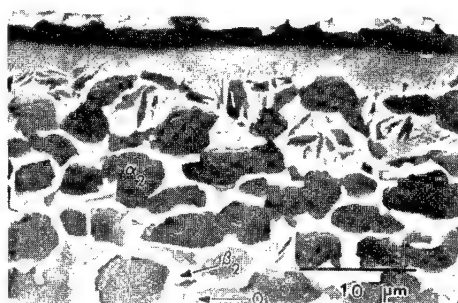


Figure 12. Aluminum denuded zone formed on neat panels of Ti-22Al-23Nb, (a) and data for the oxidation of this alloy with and without this denuded zone.

Figure 11a, a continuous layer of Cr_2O_3 is formed on a Ni-10 wt%Cr alloy that had a recrystallized zone of small grains, Figure 11b, but the Cr_2O_3 formed as discontinuous particles when a recrystallized layer was not present at the alloy surface.

When Ti-Al-Nb neat panels are prepared in the fabrication of titanium matrix composites, the microstructure of this alloy at its surface is changed during processing as shown in Figure 12a. The alloy near its surface becomes denuded of aluminum as indicated by the absence of the α_2 phase. Such conditions affect the oxidation behavior of this alloy as shown by the weight change versus time measurements presented in Figure 12b.

Alloy Homogeneity

In general the oxidation resistance and hot corrosion resistance of homogeneous alloys is better than alloys which are not homogeneous. This usually is the case because some phases have less resistance to attack than others in the alloy, and the attack of the phase with poorer resistance becomes more pronounced with increases in inhomogeneity, Figure 6. Preferential

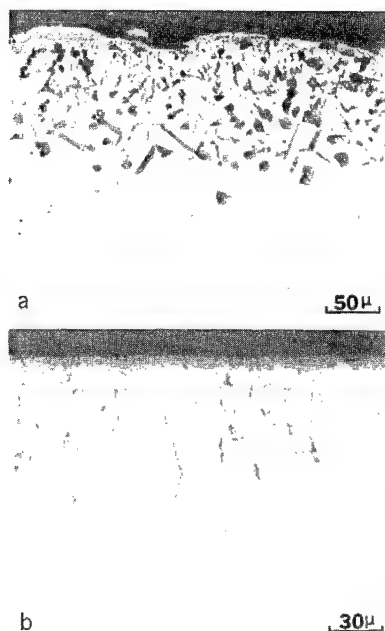


Figure 13. Photomicrographs showing cross-sections of oxidized Co-25Cr-6Al-0.1Y specimens that were fabricated by casting, (a), and by vapor deposition, (b). The as cast specimen was oxidized 500 hours in air at 1100°C whereas the vapor deposited alloy was oxidized 1000 hrs.

attack of the phase with poor oxidation resistance is especially a problem, when this phase forms a continuous network through the alloy, and at low temperatures where diffusion is slow and the more protective oxide cannot be developed over the phase with poor oxidation resistance. In Figure 6 it can be seen even though the yttride phase extended to the surface of the alloy, a diffusion zone (arrows) has developed, the nonprotective yttride is formed as particles (white arrow), and a protective oxide could develop at the base of the oxide pit. This could not occur at low oxidation temperatures. The effects of inhomogeneity can be more subtle than differences in corrosion resistances of different phases. In Figure 13 the cross-sections of oxidized (1100°C, air) CoCrAlY with two different fabrication conditions are presented. In the cast condition the α -Al₂O₃ layer is no longer formed and the aluminum has been oxidized internally after 500 hours of cyclic oxidation, whereas the continuous Al₂O₃ is still present on the specimen prepared by vapor deposition after 1000 hours of cyclic oxidation.

The α -Al₂O₃ scales formed on these alloys after less oxidation are shown in Figure 14. The yttria-rich protrusions are not uniformly distributed on the scale formed on the cast alloy compared to the scale formed on the alloy in the vapor deposited condition. These conditions result from the nonuniform distribution of the yttride phase in the cast alloy compared to the vapor deposited alloy. Even though it is now apparent that oxide protrusions probably do not exert a major influence on oxide scale adherence, the fact that the alloy with the more uniform yttride distribution had better oxidation resistance may indicate that reactive element distribution may be important to effective sulfur gettering, or some other condition that improves the adherence of alumina scales.

Another subtle effect of homogeneity is observed during the oxidation of a CoCrAl alloy that is composed of an α -cobalt solid solution and β -CoAl, Figure 15a, and develops a continuous layer of α -Al₂O₃ during oxidation. This oxide spalls from the alloy upon cooling to room temperature after oxidation. The surface of this oxide that was in contact with the CoCrAl substrate is shown in Figure 15b. The oxide scale has developed a network of voids at areas where the β -CoAl phase had been present in the alloy. Such networks did not develop when the CoCrAl was fabricated by processes that did not produce continuous networks of the β -CoAl. The importance of this condition in regards to oxide scale spalling is not currently obvious, but void formation is a condition that should be avoided.

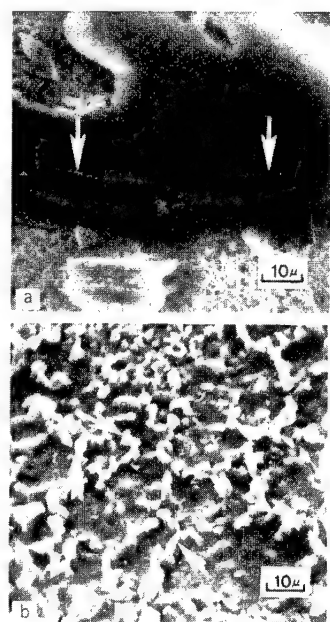


Figure 14. The underside of Al_2O_3 scales formed upon CoCrAlY specimens prepared by casting (a), and by vapor deposition, (b).

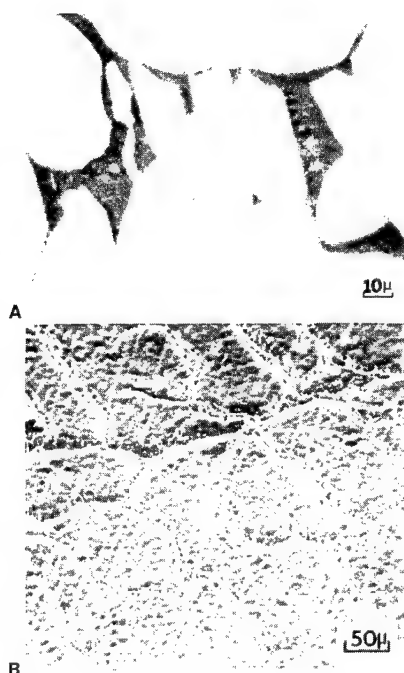


Figure 15. Photomicrographs showing $\beta\text{-CoAl}$ in an alpha-cobalt matrix, (a), and the underside of the Al_2O_3 scale that formed on this alloy after 100 hours of oxidation at 1100°C in air, (b). Voids developed in the Al_2O_3 at those locations where $\beta\text{-CoAl}$ had been present in the alloy.

Concluding Remarks

Processing-environmental interactions are numerous. There is no set pattern. It is necessary to examine and consider each individual case. There are some generalizations that can be made. Homogeneous alloys are more resistant to environmental effects than the same alloys with inhomogeneities. Cracks and pores are always undesirable. Small concentrations of certain elements such as sulfur can produce adverse effects on the environmental resistance of alloys. By carefully investigating processing-environmental interactions it is possible to modify processing conditions to optimize the properties related to the environment.

Acknowledgements

Most of the examples used to illustrate the various processing-environmental interactions represent the efforts of graduate students past and present in the high temperature materials group in the Materials Science and Engineering Department at the University of Pittsburgh. Also, support of these research efforts by the Office of Naval Research and the Air Force Office of Scientific Research is gratefully acknowledged.

References

1. A.W. Funkenbusch, J.G. Smeggel, N.S. Bornestein, "Reactive Element - Sulfur Interaction and Oxide Scale Adherence," Met. Trans. 16A (1985), 1164-1166.
2. J.W. Smialek, "Effect of Sulfur Removal on Al_2O_3 Scale Adhesion," Met. Trans., 22A (1991), 739-752.
3. G.H. Meier, F.S. Pettit and J.L. Smialek, "The effects of Reactive Element Additions and Sulfur Removal on the Adherence of Alumina to Ni-and Fe-Base Alloys," Mat. and Corr., 46 (1995), 232-240.
4. R.W. Bormett et al., "UV Raman Spectroscopy Characterization of CVD Diamond Film Growth and Oxidation," J. App. Phys., 77 (1995), 5916-5923.
5. J. Chen et al., "The Rate-Controlling Processes in the Oxidation of HIPed Si_3N_4 with and without Sintering Additives," J. European Ceramic Soc., 7 (1991), 319-327.
6. Y.G. Gogosti, "Oxidation of Ytria and Alumina-Containing Dense Silicon Nitride Ceramics," J. European Ceramic Soc., 11 (1993), 375-386.
7. D. Cubicciotti and K.L. Lau, "Kinetics of Oxidation of Ytria Hot-Pressed Silicon Nitride," J. Electrochem. Soc., 126 (1979), 1723-1728.
8. B.D. Butler, "Oxidation of Ytria and Alumina Sintered Silicon Nitride and Silicon Carbide Whisker Reinforced Silicon Nitride," (Masters Thesis, University of Pittsburgh, 1994).
9. J.K. Tien and F.S. Pettit, "Mechanism of Oxide Adherence on Fe-25Cr-4Al(Y or Sc) Alloys," Met. Trans. 3 (1972), 1587-1599.
10. T.A. Ramanarayanan et al., "The Influence of Yttrium on Oxide Scale Growth and Adherence," Oxid. Metals, 29 (1988), 445-472.
11. M.C. Stasik et al., "Effects of Reactive Additions and Sulfur Removal on the Oxidation Behavior of FeCrAl Alloys," Scripta Met. and Mat. 31, (12) (1994), 1645-1647.
12. K. Ohmura et al., "Effect of Lanthanoid on Hot-Workability and Foil Oxidation Behavior of Fe-Cr-Al Alloy," Heat Resistant Materials, Proceedings of the First International Conference, September 1991, 505-513.
13. D.A. Berztiss et al., "Oxidation of $MoSi_2$ and Comparison with Other Silicide Materials," Mat. Sci. and Eng., A155 (1992), 165-181.
14. P.J. Meschter, "Low Temperature Oxidation of Molybdenum Disilicide," Met. Trans., 23A (1992), 1763-1772.
15. E. Fitzer, "Molybdandisilized als Hochtemperatur-werkstoffe," F. Benesovsky, ed., Warfeste und Korrosionbistandize Sinterwerkstoffe, Reutte/Tirol, (1995), 56-79.
16. J. Berkowitz-Mattuck, P.E. Blackburn, E.J. Felten, "The Intermediate Temperature Oxidation Behavior of Molybdenum Disilicide," TMS-AIME, 233 (1965), 1093-1099.
17. J. Berkowitz-Mattock, M. Rossetti, and D.W. Lee, "Enhanced Oxidation of Molybdenum Disilicide Under Tensile Stress," Met. Trans. 1 (1970) 479-483.
18. J.H. Westbrook and D.L. Wood, "Pest Degradation in Beryllides Silicides, Aluminides and Related Compounds," J. Nucl. Mater. 12 (1964), 208-215.
19. E. Fitzer and K. Rumuth, "Die Riaktion hochschmelzender Silizide met Stickatoff und Sauerstoff," High Temperature Materials, 6th Plansee Seminar, Reutte Tyrol, June (1968), F. Benesovsky ed., Spring Verlag, Vienna (1969) 767-802.

20. E. Fitzner and W. Remmele, "Possibilities and Limits of Metal Reinforced Refractory Silicides, Especially Molybdenum Disilicides," Fifth International Conference on Composite Materials, AIME, Warrendale, PA (1985), 515.
21. J. Schlichting, "Molybdenum Disilicides als Komponente moderner Hochtemperaturverbundwerkstoffe," High Temperature-High Pressures, 10 (1978), 241-269.
22. D.R. Rishel, F.S. Pettit and G.H. Meier, unpublished research, University of Pittsburgh, March, 1993.
23. C.G. McKamey, et al., "A Study of Pore Oxidation in Polycrystalline MoSi₂," J. Mater. Res., 7 (1992), 2747-2755.
24. N.S. Choudhury, A.C. Graham and J.W. Hinze, "Oxidation Behavior of Titanium Aluminides," in Properties of High Temperature Alloys, Z.A. Foroulis and F.S. Pettit, eds., The Electrochem. Soc., Pennington, N.J. (1976) 668.
25. A. Gil et al., "The Effect of Microstructure on the Oxidation Behavior of TiAl-Based Intermetallics," Corros. Sci., 34 (1993), 615-630.
26. J.M. Rakowski et al., "The Effect of Surface Preparation on the Effect of Surface Preparation on the Oxidation Behavior of Gamma TiAl Base Intermetallic Alloys," Submitted to Scripta Met. and Mater. for publication, February (1996).
27. J.M. Rakowski et al., "The Effect of Nitrogen on the Oxidation of gamma-TiAl," Scripta Met. and Mater., 33 (1995), 997-1003.
28. W.E. Dowling and W.T. Donlon, "The Effect of Surface Film Formation from Thermal Exposure on Ductility of Ti-48Al-1V-0.2 C (at%)" , Scripta Met., 27 (1992) 1663-1668.
29. R. Field et al., Private Communication, G.E. Aircraft Engines, Evandale, OH, November (1995).
30. Y. Cheng et al., "Identification of a New Phase Formed During Oxidation of gamma-Titanium Aluminide," Scripta Met. and Mater. 34 (1996), 707-711.
31. F. Dettenwanger et al., "Microstructure of gamma-TiAl Oxidized in Air," Submitted to Materials and Corrosion for Publication, March (1996).
32. S. Becker et al., "Mechanism of Isothermal Oxidation of the Intermetallic TiAl and TiAl Alloys," Oxid. Metals, 38 (1992), 425-464.
33. R.W. Beyer and R. Gronsky, "Novel Phases in the Oxidation of gamma-Titanium-Aluminum," Acta Met. et Mat., 42 (1994), 1373-1381.
34. N. Zheng et al., "The Significance of Sub-Surface Depletion Layer Composition for the Oxidation Behavior of gamma-Titanium Aluminides," Scripta Met. et Mat., 33 (1995), 47-53.
35. C.S. Giggins and F.S. Pettit, "The Effect of Alloy Grain-Size and Surface Deformation on the Selective Oxidation of Chromium in Ni-Cr Alloys at Temperatures of 900° and 1100°C" , Trans. Met. Soc. AIME, 245 (1969) 2509-2514.

BORON-MODIFIED AND GERMANIUM-DOPED SILICIDE DIFFUSION

COATINGS FOR Ti-Al-Nb, Nb-Ti-Al, Nb-Cr and Nb-base ALLOYS

Brian V. Cockeram¹ and Robert A. Rapp²

¹Westinghouse-Bettis Atomic Power Laboratory
West Mifflin, PA 15122
(412/476-5647; Fax: 412/476-5151)

²Department of Materials Science and Engineering
The Ohio State University
Columbus, OH 43210
(614/292-6178; Fax: 614/292-1537)

Abstract

Many alloys that are based upon intermetallic compounds possess outstanding mechanical properties at high-temperature, but rapid oxide scaling or embrittlement by oxygen dissolution at high temperatures may limit the use of these alloys. Since an acceptable balance of mechanical properties and oxidation resistance has not been achieved by alloy modification, coatings are a viable method for application of these materials.

A halide-activated, pack-cementation method has been used to codeposit either silicon and boron, or else silicon and germanium on Ti-Al-Nb, Nb-Ti-Al, Nb-Cr and Nb-base alloys. Partial diffusive conversion of the substrate into a boron-modified or germanium-doped silicide compound results in the formation of a metallurgically bonded coating. The boron or germanium additions were made to improve the oxidation resistance of the silicide coatings in thermal cycling. The boron additions were generally insoluble in the silicide coating, which results in the formation of an external boride compound. But the germanium additions were fully soluble; thus the microstructures for the two coatings were completely different. Coating variables such as stability of the halide activator, chemical activity of boron, or the silicon to germanium ratio were used to modify the boron or germanium contents in the coatings.

The microstructures of the silicide coatings and interdiffusion zones were characterized. Slow oxidation kinetics were observed for these coatings in isothermal and cyclic oxidation. Microhardness measurements indicated that no oxygen contamination of the substrates occurred, and the coatings were protective. But preliminary load-controlled hot fatigue tests for the Ti-Al-Nb alloys show that the fatigue life of the coated substrates was reduced.

Introduction

The high specific strength of Ti-base alloys and the excellent strength and creep resistance of Nb-base alloys at high temperature are of interest for aerospace applications [1,2]. But engineering use of Ti-base or Nb-base materials at high temperatures in air is prevented by rapid oxide scaling and embrittlement through oxygen dissolution. Brittle aluminide or silicide intermetallic compounds are the only Ti-base or Nb-base materials that form protective, slow growing Al_2O_3 or SiO_2 scales which are needed for high-temperature oxidation resistance in air. An acceptable balance of mechanical properties and high-temperature oxidation resistance has not been achieved by alloy modification. Thus, protective coatings are a viable method for the practical application of Ti-base or Nb-base materials at high temperatures in air.

The modification of silicide diffusion coatings with boron or germanium was developed to protect Ti-base and Nb-base alloys. Boron or germanium additions were intended to dissolve into and improve the SiO_2 scale by: (1) minimizing the mismatch in coefficient of thermal expansion between the substrate/scale to reduce spalling in thermal cycling and (2) increasing the fluidity of the protective glass to heal cracks in the brittle coating. The halide-activated pack cementation (HAPC) method was used to produce a dense, uniform and tightly adherent coating by partial diffusive conversion of the base alloy into a B-modified or Ge-doped silicide coating. Thermodynamic calculations were used to develop HAPC processes for silicide growth with B or Ge additions in a single processing step [3-6].

Halide-Activated Pack Cementation Siliconizing

A source powder, halide activator salt and inert filler are the three components of a powder pack for the HAPC method. The substrates are embedded into these mixed powders in a sealed retort, and during the isothermal heat treatment in an inert atmosphere the halide salt dissociates into volatile halide vapors of the source powder (Si) [3]. Provided the vapor pressures are sufficient, gas-phase diffusion of Si-fluorides to the substrate produces a surface enrichment of Si, and the inward diffusion of Si results in the growth of a tightly adherent silicide compound by partial diffusive conversion of the substrate.

Matching the gas-phase fluxes of the respective halide vapors is required for codeposition of two elements in a single reaction/processing step by the HAPC method [3]. Because the gas-phase flux is proportional to the vapor pressure, thermodynamic calculations have been used to estimate pack compositions for the codeposition of Si and Ge, or Si and B. A pack composed of pure Si and pure Ge powders is predicted to produce Ge-fluoride vapor pressures that are only slightly lower than the Si-fluorides, and Ge-doped Mo-silicide [4] and Ti-silicide [5-7] coatings have been grown on commercial purity (CP) Mo and Ti, respectively. The $\text{Mo}(\text{Si},\text{Ge})_2$ or $\text{Ti}(\text{Si},\text{Ge})_2$ layers generally contain 3-8 atomic% Ge in solution, although Ge is non-uniformly dissolved into the inner $\text{Mo}_3(\text{Si},\text{Ge})_3/\text{Mo}_3(\text{Si},\text{Ge})$ or $\text{Ti}(\text{Si},\text{Ge})/\text{Ti}_3(\text{Si},\text{Ge})/\text{Ti}_3(\text{Si},\text{Ge})/\text{Ti}_3(\text{Si},\text{Ge})$ layers of the coating. Pure Si powder and a boride compound were used to give the required matching in gas phase fluxes for the codeposition of Si and B on CP-Ti [5-7]. TiSi_2 has a low solubility for boron, which resulted in the formation of an external TiB_2 layer on a $\text{TiSi}_2/\text{TiSi}/\text{Ti}_3\text{Si}_2/\text{Ti}_3\text{Si}_3/\text{Ti}_3\text{Si}$ coating. The TiB_2 layer thickness or Ge content was changed by the stability of the boride source compound, the stability of the halide activator, or the Si:Ge ratio in the powder pack.

The isothermal oxidation kinetics for the B-modified and Ge-doped silicide coatings on CP-Ti were slower than those reported for TiSi_2 thin films in air [6,7]. Slow cyclic oxidation kinetics were observed for the B-modified and for Ge-doped coatings on CP-Ti at 500-875 °C in air,

but the coatings were not protective when cycled through the allotropic α -to- β transformation (883°C). Undoped Ti-silicide coatings that did not contain B or Ge were protective at only 500-600°C, which demonstrates that the B or Ge additions are required for good protection. A two-step process was used to protect Nb with the Ge-doped Mo-silicide coatings [3,4]: (1) Mo was preliminarily deposited by sputtering, and (2) the Mo was partially converted into Mo(Si,Ge)₂ by the HAPC method. These coatings provided excellent cyclic oxidation resistance for Nb in air at 900-1540°C. Because Nb-silicides possess poor resistance to high-temperature oxidation, the two-step process was required for a protective coating. However, the direct conversion of the base metal into a silicide layer that possesses excellent high-temperature oxidation resistance is more desirable. The HAPC processes developed for CP-Ti and CP-Mo were extended to complex intermetallic alloy systems in this study.

Experimental Procedure

The previously reported [3-6] HAPC methods were used for Ti-22Al-27Nb, Ti-20Al-22Nb, Ti-24Al-11Nb, Nb-(40, 25 or 10)Ti-15Al, Nb-10Si (at. %) and (Cr-Nb)-base alloys. The compositions of the powder packs are given in Table I. The as-coated and oxidized coupons were analyzed by X-ray diffraction (XRD), metallography and scanning electron microscopy (SEM) with energy dispersive spectroscopy (EDS). The coatings were oxidized in air at 500 to 1000°C by isothermal and cyclic oxidation (1 cycle = 1 hour in the furnace + 1/2 hour of cooling). Microhardness measurements were used to detect for oxygen contamination following oxidation.

Table I Powder Pack Compositions (wt. %) and Process Conditions

Pack #	Masteralloy	Activator	Filler	Temperature	Time
1	16Si, 8Ge	2AlF ₃	Al ₂ O ₃	950-1150°C	6-24h
2	12Si, 6Ge	2MgF ₂	SiC	1150°C	12h
3	7Si, 6TiB ₂	2MgF ₂	Al ₂ O ₃	950-1150°C	6-24h
4	16Si, 6Ge	2NaF	Al ₂ O ₃	1000-1050°C	12h

Results and Discussion

Ti-Al-Nb Alloys (Ti-22Al-27Nb, Ti-20Al-22Nb, Ti-24Al-11Nb)

While the HAPC coating of CP-Ti produces a sequence of single-phase Ti-silicide layers, diffusive conversion of an alloy results in a more complex silicide coating. The (Ti,Nb)(Si,Ge)₂ and (Ti,Nb)(Si,Ge) layers shown in Fig. 1a and 1b were grown on Ti-20Al-22Nb at 950°C for 6 hours using Pack #1 [5-7]. SEM/EDS examination and XRD analysis confirmed that the (Ti,Nb)(Si,Ge)₂ layer in Fig. 1a contained (Nb,Ti)(Si,Ge)₂ precipitates. Ge-rich precipitates were not detected, as Ge dissolved into the silicide layers. The superficial byproduct salt layer at the surface of the coating contained some Al, but the small amount of Al in the TiSi₂ layer was sufficient to stabilize the metastable C49 polymorph (*Cmcm*) rather than the stable C54 polymorph (*Fddd*) that was produced on CP-Ti [5-8]. The coating/substrate interdiffusion zone was depleted of Nb, but the high Al content indicates that one of the layers was probably γ -TiAl, which may also serve as an oxidation resistant layer. Ti-20Al-22Nb was coated below the beta transus temperature, which results in a narrow interdiffusion zone with higher Al content [5]. The morphology of the B-modified silicide coating grown on Ti-20Al-22Nb by pack #3 at 950°C for 6 hours in Fig. 1c was generally similar to the Ge-doped silicide coating. However, boron was not dissolved into the coating;

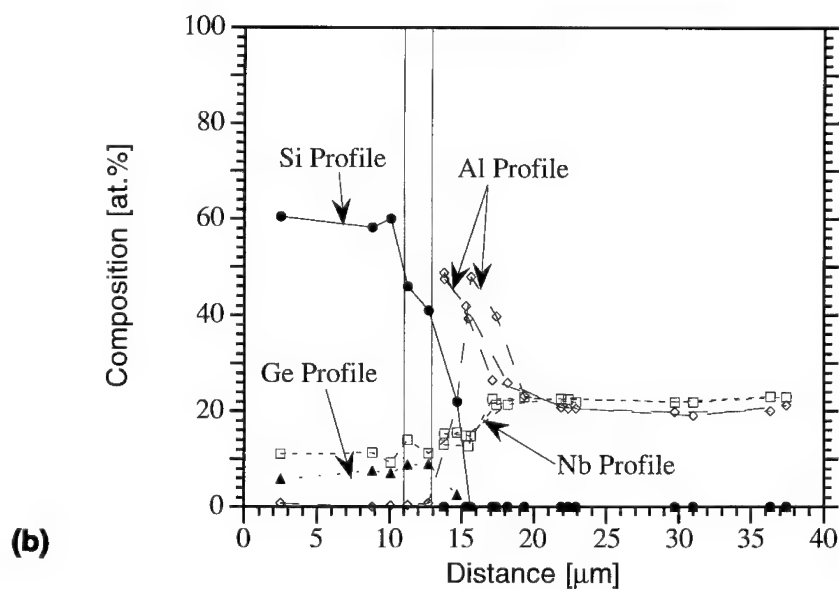
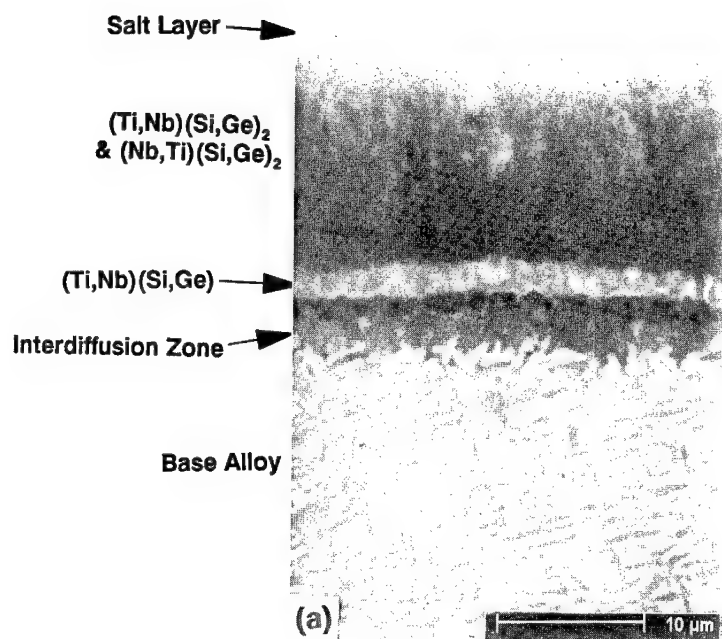


Figure 1 - The growth of Ge-doped and B-modified silicide coatings at 950 °C for 6 hours using Packs #1 and #3, respectively, on Ti-20Al-22Nb (a) SEM/BSE micrograph of Ge-doped silicide coating, (b) EDS profile for Ge-doped coating and (c) SEM/BSE micrograph of B-modified coating that was grown on Ti-20Al-22Nb.

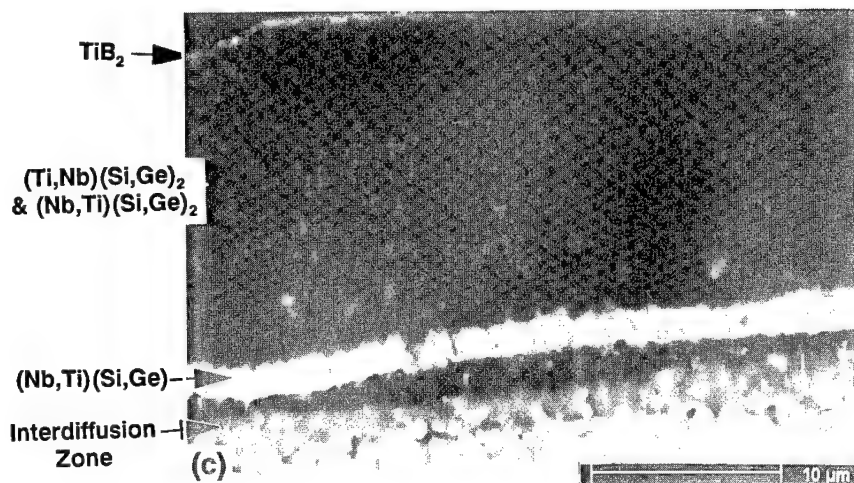
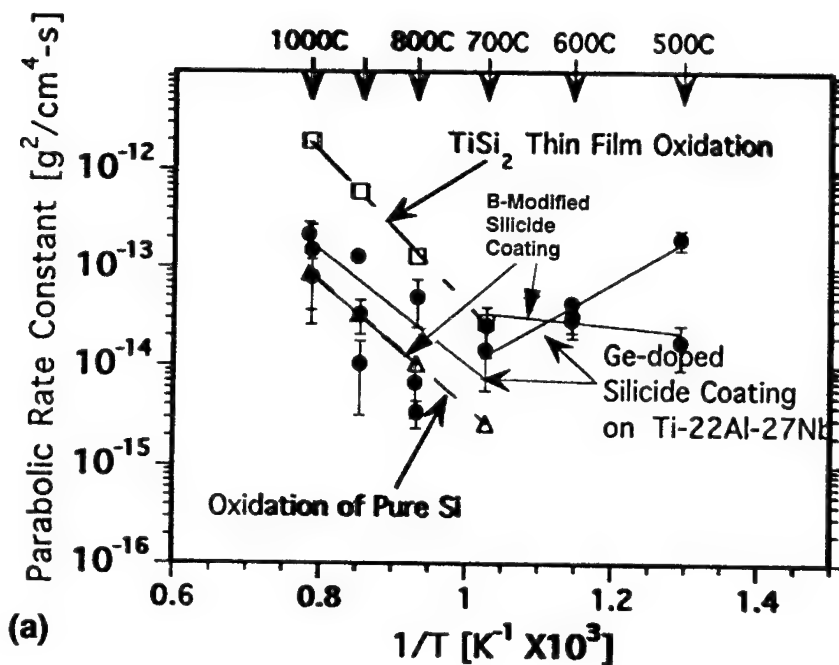


Fig. 1(c).

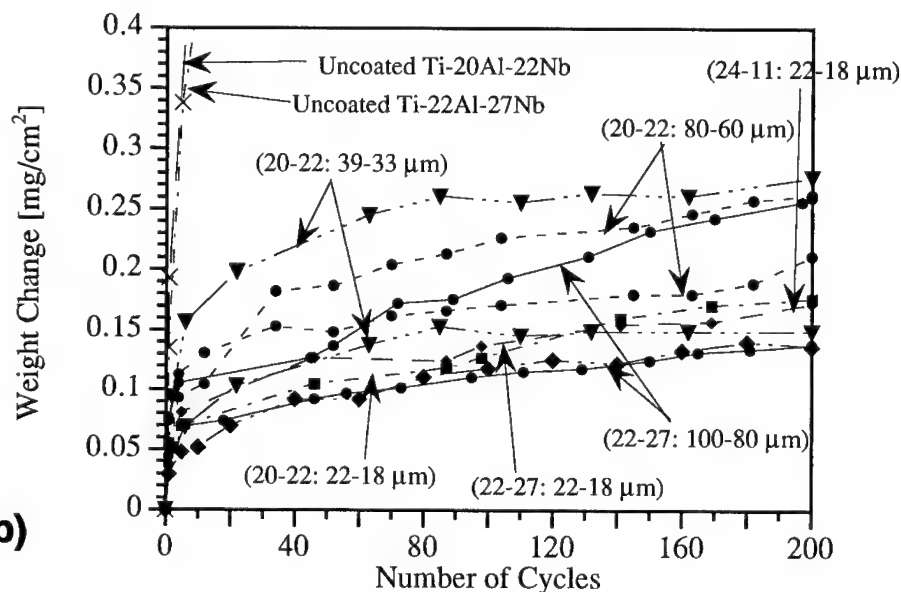
rather, a thin non-continuous layer of TiB_2 was localized at the coating surface, as observed for CP-Ti [5-8]. Both SEM/EDS and microprobe analysis indicated that boron was localized at the surface, and TiB_2 was detected by XRD. Similar features were observed for the B-modified and Ge-doped silicide coatings grown on Ti-22Al-27Nb or Ti-24Al-11Nb.

In Fig. 2a, small parabolic rate constants for isothermal oxidation at 500 to 1000 °C in air are presented for both the B-modified and Ge-doped silicide coatings grown on Ti-22Al-27Nb at 1150 °C for 12 hours using packs #3 and #2, respectively. A change in the oxidation mechanism is represented by the change in slope at 700-800 °C. The activation energies for high temperature oxidation are comparable to pure Si oxidation, and Si-rich oxide scales were observed following coating oxidation, which indicates that SiO_2 scale growth provides the slow oxidation kinetics [6]. Ge or B was also detected by SEM/EDS within the Si-rich oxide scales. The smaller activation energy for low-temperature oxidation is consistent with the observed mixed oxide scales [6]. Coating above the beta transus temperature produced cracks at the corners of the Ge-doped coating that were not filled during low temperature oxidation, which produced the increase in rate constants at 700 to 500 °C. Accelerated oxidation or pitting was not observed for sound B-modified and Ge-doped silicide coatings and small weight gains ($< 0.5 \text{ mg/cm}^2$) were observed following 2000 hours of oxidation at 500 °C [6].

Small cyclic oxidation kinetics at 800 °C in air are shown in Fig. 2b for Ge-doped silicide coatings; coating thickness or base alloy composition has a negligible influence on the kinetics. Fast cyclic oxidation kinetics are shown for the uncoated alloys [6]. Oxygen contamination of the coated substrates in Fig. 2b was not detected by microhardness measurements, which demonstrates that the coatings were protective. Similar results were observed for the B-modified coatings. Thin coatings (20-25 μm) were only protective in cyclic oxidation at 500-900 °C for 200 cycles, but the thicker coatings (40-45 μm) were protective at 500-1000 °C [6]. The thickest coatings (80-100 μm) with cracks that resulted from HAPC processing above the beta transus were protective at 600-1000 °C, but oxide growth was too sluggish to seal cracks for cyclic oxidation at 500 °C. Preliminary fatigue testing at 700 °C in air showed that the fatigue life of coated Ti-22Al-23Nb was reduced by a factor of at least 10, which indicates that the use of silicide coatings for fatigue-limited applications may not be advisable [7].



(a)



(b)

Figure 2 - Oxidation of B-modified and Ge-doped silicide coatings on Ti-Al-Nb alloys in air: (a) Arrhenius plot of parabolic rate constants for isothermal oxidation of coatings grown on Ti-22Al-27Nb at 1150°C for 12 hours by packs #2 and #3 [11,12], and (b) cyclic oxidation kinetics in air at 800°C for Ge-doped silicide coatings of various thicknesses that were grown on Ti-22Al-27Nb, Ti-20Al-22Nb and Ti-24Al-11Nb.

Nb-Base Alloys (Nb-10Si, Nb-(40, 25 or 10)Ti-15Al, Nb-40Ti-15Al-5Cr, Nb-Cr)

B-modified or Ge-doped NbSi₂ coatings were grown on Nb-10Si, but these coatings were not protective and complete substrate oxidation occurred in less than 50 oxidation cycles at 1000°C. Boron or Ge additions did not improve the inherently poor oxidation resistance of NbSi₂, which does not form a protective SiO₂ scale [2]. One of the following possibilities must occur to form a protective coating on a Nb-base alloy by the HAPC method: (1) dissolution of alloying elements into (Nb,M)Si₂ that support the formation of a protective SiO₂ scale, or (2) presence of alloy elements which form a protective silicide coating in preference to NbSi₂, by selective siliciding, analogous to the well known phenomenon of selective oxidation.

The multilayered Ge-doped silicide coating grown on Nb-40Ti-15Al by Pack #1 at 1150°C for 12 hours is shown in Figure 3. The thick outer layer is a mixture of (Ti,Nb)(Si,Ge)₂ and (Nb,Ti)(Si,Ge)₂, but the (Ti,Nb)(Si,Ge)₂ layer is nearly continuous and has the C49 crystal structure that was observed for the Ti-Al-Nb alloys [9]. The inner silicide layers are probably composed of mixed (Ti,Nb)(Si,Ge), (Ti,Nb)₃(Si,Ge)₄, and (Nb,Ti)₃(Si,Ge)₃ phases, and the inner aluminide layers were determined by SEM/EDS analysis to be (Nb,Ti)Al₃, (Ti,Nb)Al and (Nb,Ti)₂Al. The bright precipitates in the (Nb,Ti)Al₃ and (Ti,Nb)Al layers are probably (Nb,Ti)₃(Si,Ge), but the needles at the diffusion zone/alloy interface were not identified. As previously observed for the Ti-Al-Nb alloys, Al was not dissolved in the silicide layers, but underlying aluminide layers were formed that serve as diffusion barriers against Si penetration and inner barriers for oxidation resistance. However, diffusive conversion of the alloy into the Ge-doped silicide coating results in a 20-30 μm Al-rich diffusion zone beneath the aluminide layers. The growth of a B-modified silicide coating by pack #3 at 1150°C for 12 hours produced similar features, but a TiB₂ surface layer was formed and boron was not dissolved into the coating, as previously observed for Ti-Al-Nb [5-7].

Ge-doped silicide coatings were also grown on Nb-25Ti-15Al and Nb-10Ti-15Al by pack #1 at 1150°C for 12 hours. Table II reports low weight changes for the coatings that were grown on the Nb-(40 or 25)Ti-15Al alloys, but fast oxidation was observed for the coating formed on Nb-10Ti-15Al [9]. Titanium additions are known to improve the oxidation resistance of NbSi₂ [2], and at least 25% Ti must be present for the growth of an oxidation-resistant silicide coating by the HAPC method. The Si-rich oxide scale on the Ge-doped coating on Nb-40Ti-15Al following oxidation at 1300°C in Fig. 4 contains Ge and Ti-rich oxide precipitates, which indicates that this is probably a (Si,Ge)O₂ scale with TiO₂-base precipitates. TiO₂ and crystalline SiO₂ were detected by XRD. Both the addition of Ti to (Nb,Ti)(Si,Ge)₂ and the growth of a continuous (Ti,Nb)(Si,Ge)₂ layer on Nb-40Ti-15Al formed the protective (Si,Ge)O₂ scale with excellent high-temperature oxidation resistance.

Massive spalling produced disintegration of uncoated Nb-40Ti-15Al for cyclic oxidation (Figure 5a). Slow cyclic oxidation kinetics were observed at 1100°C in Figure 5a for both the B-modified and Ge-doped silicide coatings grown on Nb-40Ti-15Al with Packs #1, #2 and #3. No oxygen contamination of the substrate was observed or detected using microhardness measurements, which indicates that the coatings were effective barriers against oxygen contamination. Similar results were observed for B-modified and Ge-doped silicide coatings that were grown on Nb-40Ti-15Al-5Cr, and the cyclic oxidation kinetics were even slower. Minor additions of Cr to the silicide coating probably improved the oxidation resistance. B-modified and Ge-doped silicide coatings grown on Nb-40Ti-15Al-(0 or 5)Cr using Packs #1, #2 or #3 also provided excellent protection and slow kinetics for 200 oxidation cycles at 900°C and 760°C. Although some spalling was observed for cyclic oxidation at 1200°C, the same coatings were also protective and showed slow cyclic oxidation kinetics [7]. Furthermore,

Table II Weight Change [mg/cm²] for 24 hours of Isothermal Oxidation at 1300 °C in Air

Coating	Alloy	Mass Gain [mg cm ⁻²]
Uncoated	Nb-40Ti-15Al	60.51
Ge-doped	Nb-40Ti-15Al	1.05, 0.98
B-modified	Nb-40Ti-15Al	1.45
Ge-doped	Nb-25Ti-15Al	1.73
Ge-doped	Nb-10Ti-15Al	-5.30

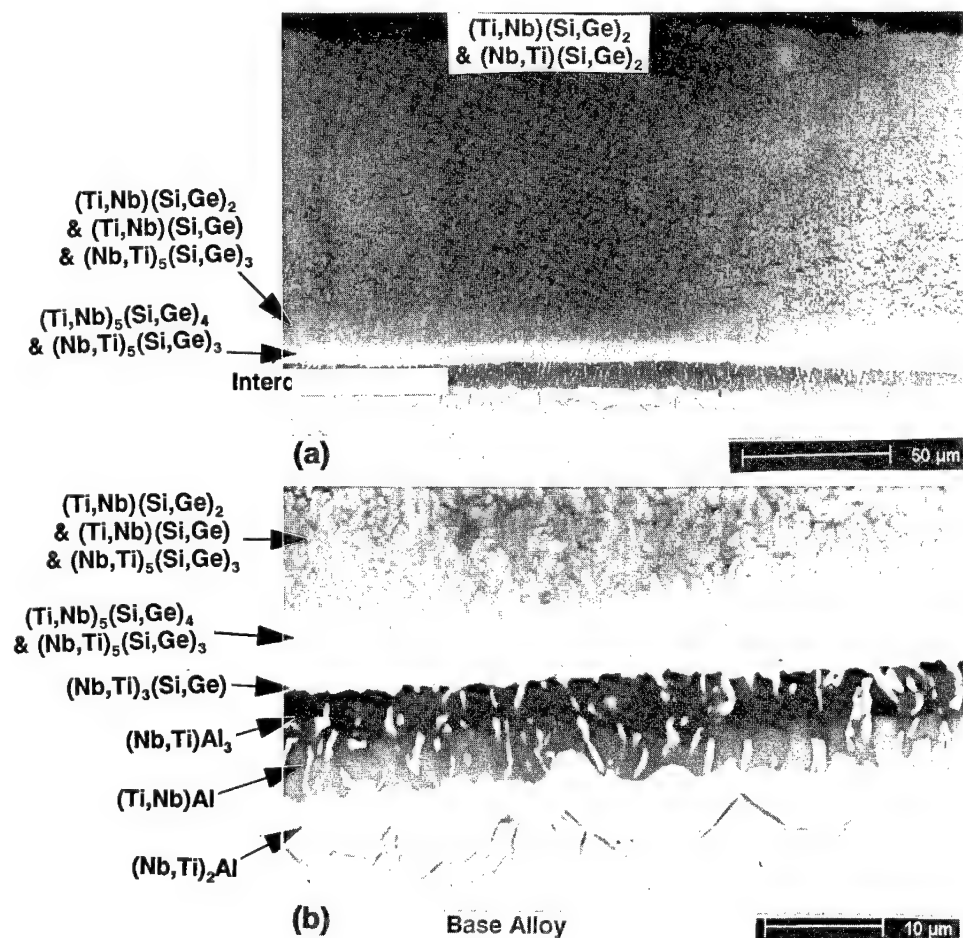


Figure 3 - Ge-doped silicide coating grown on Ti-40Ti-15Al by Pack #1 at 1150 °C for 12 hours (a) SEM/BSE image of coating, (b) SEM/BSE of coating/substrate interface diffusion zone and (c) EDS profile for Nb, Si, Al and Ge.

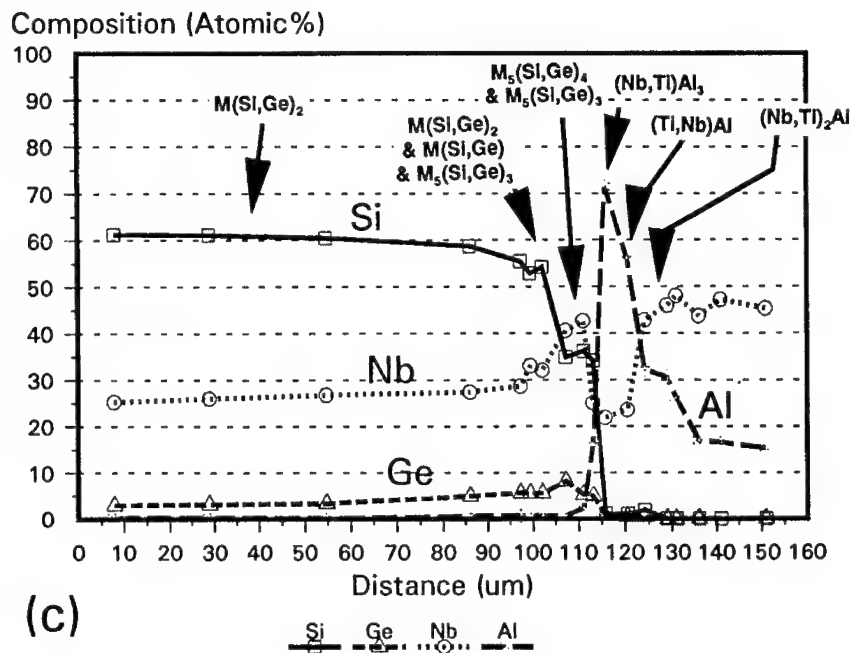


Figure 3(c) - Continued

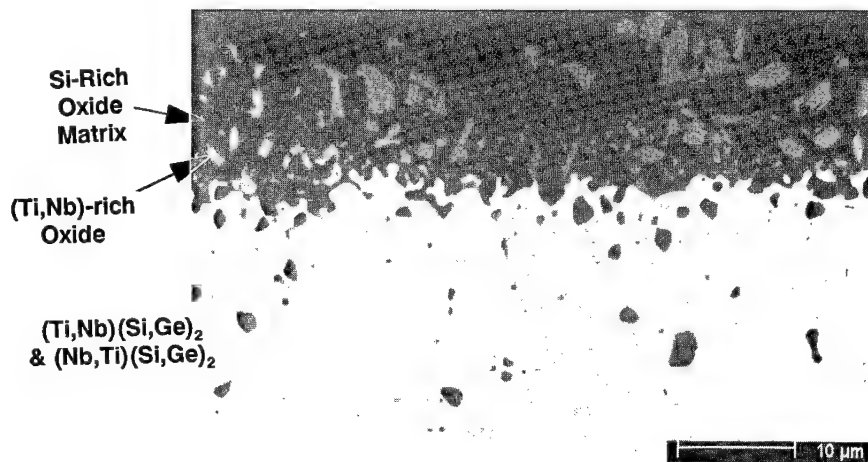


Figure 4 - SEM/BSE micrograph of oxide scale that formed on Ge-doped silicide coating on Nb-40Ti-15Al following 24 hours of isothermal oxidation at 1300°C.

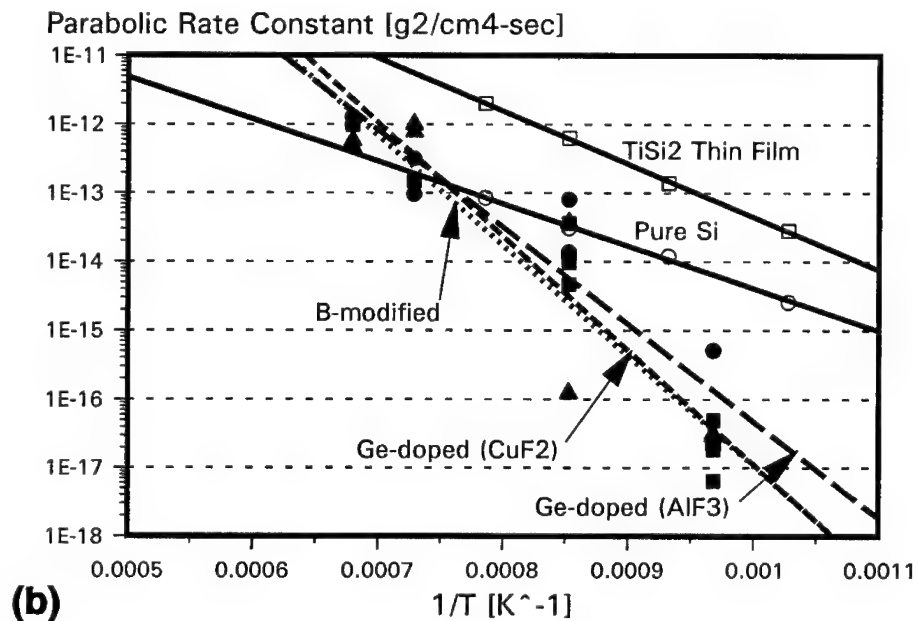
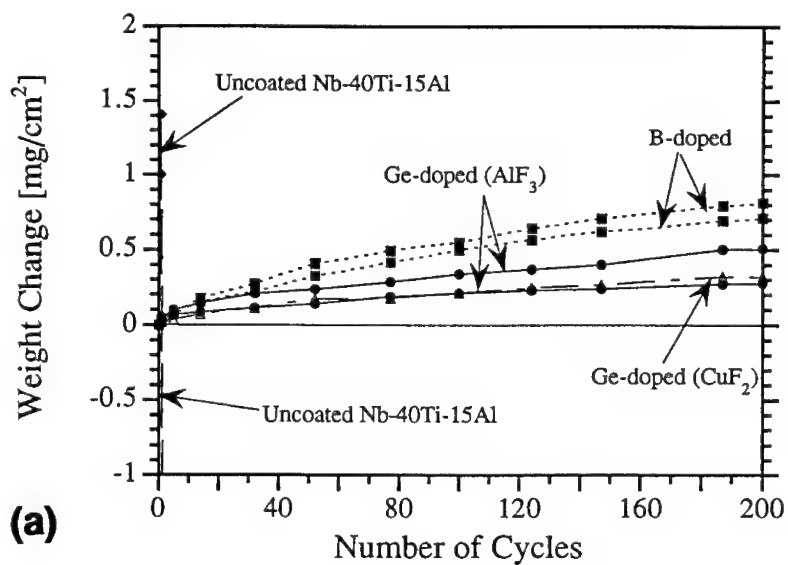


Figure 5 - Oxidation of B-modified (Pack #3) and Ge-doped (Packs #1 and #2) silicide coatings that were grown on Nb-40Ti-15Al at 1150 °C for 12 hours (a) cyclic oxidation kinetics at 1100 °C and (b) Arrhenius plot of parabolic rate constants for cyclic oxidation at 1200, 1100, 900 and 760 °C [11,12].

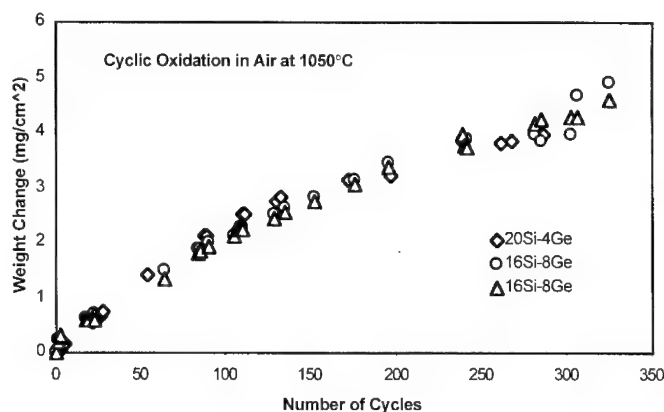


Figure 6 - Cyclic oxidation kinetics at 1050°C in air of Ge-doped silicide coatings that were grown on the (Cr-Nb)-base alloy CN87 using Pack #4 with the Si:Ge ratios of 5:1 and 2:1 [10].

small weight changes and no pesting disintegration was observed for 1200 hours of isothermal oxidation at 500°C for coatings on Nb-40Ti-15Al-(0 or 5)Cr, which indicates that these coatings are resistant to accelerated low-temperature oxidation.

Slow parabolic rate constants were determined in cyclic oxidation for the B-modified and Ge-doped silicide coatings on Nb-40Ti-15Al in Figure 5b. The scatter in the data was produced by spalling, and the measured parabolic rate constants are rough estimates. The oxidation rates and activation energies are comparable to the oxidation of pure Si, which indicates that a protective SiO₂ scale is formed. The protective SiO₂ scale in Figure 4 for isothermal oxidation of the Ge-doped silicide coating at 1300°C is consistent with the kinetic data.

Ge-doped silicide coatings were grown on (Nb-Cr)-base alloys using Pack #4 with different Si:Ge ratios [10]. About 2.9 to 4.1 atom% Ge was dissolved in the silicide layers, but the number of mixed silicide layers was decided by the Si:Ge ratio in the powder pack. Use of a high Si:Ge ratio (5:1) resulted in an outer layer of Nb-rich (Cr,Nb,Mo)(Si,Ge)₂ and Cr-rich (Cr,Mo)(Si,Ge)₂ precipitates in a semi-continuous (Cr,Fe)(Si,Ge) matrix and a mixed inner layer of M(Si,Ge) and (Cr,Mo,Fe)(Si,Ge)₂ [10]. The coating morphology formed with a 2:1 ratio was generally similar to the coating that was grown with a 5:1 pack, but a layer of mixed M₁₁(Si,Ge)₈ and M₅(Si,Ge)₃ phases formed at the coating/substrate interface. The M(Si,Ge)₂ phases were not formed with lower Si:Ge ratio packs (1:1, 0.5:1 and 0.2:1) and the coatings consisted primarily of mixed M(Si,Ge) outer layers, mixed M₁₁(Si,Ge)₈ intermediate layers and mixed M₅(Si,Ge)₃ phases at the coating/substrate interface [10]. Slow cyclic oxidation kinetics at 1050°C are shown in Figure 6 for coatings that were grown on a (Cr-Nb)-base alloy with different Si:Ge ratios. The coatings were observed to be protective following the 325 oxidation cycles at 1050°C. Slow oxidation kinetics were also observed for 912 oxidation cycles at 700°C and for isothermal oxidation at 950 to 1100°C [10]. In every case, a continuous Cr-rich

M(Si,Ge)₂ or M(Si,Ge) layer served as a protective coating over the substrate. Since CrSi₂ and CrSi generally possess good high-temperature oxidation resistance, the excellent protection of these coatings is not surprising.

Summary

The HAPC method was used to form protective B-modified and Ge-doped silicide coatings by partial diffusive conversion of complex intermetallic Ti-base or Nb-base alloys into mixed silicide layers. In each case, the excellent high-temperature oxidation resistance of the coatings was provided by the formation of an alloyed Ti-rich or Cr-rich silicide compound that possessed good oxidation resistance. The coatings exhibited slow oxidation kinetics and were effective barriers to oxygen penetration in thermal cycling.

References

1. G.H. Meier, N. Birks, F.S. Pettit, R.A. Perkins and H.J. Grabke, "Environmental Behavior of Intermetallic Materials", Proceedings of 1st International Conference on Structural Intermetallics, R. Darolia, J.J. Lewandowski, C.T. Liu, P.L. Martin, D.B. Miracle and M.V. Nathal, eds. (Warrendale, PA: TMS, 1994), 861-878.
2. R.A. Perkins and G.H. Meier, "The Oxidation Behavior and Protection of Niobium", JOM, 42(8) (1990) 17-21.
3. R. Bianco, M.A. Harper and R.A. Rapp, "Codepositing Elements by Halide-Activated Pack Cementation", JOM, 43(11) (1991) 20-25.
4. A. Mueller, G. Wang, R.A. Rapp, and E.L. Courtright, "Deposition and Cyclic Oxidation Behavior of a Protective (Mo,W)(Si,Ge)₂ Coating on Nb-base Alloys", J. Electrochem. Soc., 139 (1992) 1266-1275.
5. B.V. Cockeram and R.A. Rapp, "Development and Growth of Boron-Modified and Germanium-Doped Titanium-Silicide Diffusion Coatings by the Halide-Activated, Pack-Cementation Method", Oxid. Met., 45 (1996) 375-425.
6. B.V. Cockeram and R.A. Rapp, "Isothermal and Cyclic Oxidation Resistance of Boron-Modified and Germanium-Doped Silicide Coatings for Titanium Alloys", Oxid. Met., 45 (1996) 427-468.
7. B.V. Cockeram, "Growth and Oxidation Resistance of Boron-Modified and Germanium-Doped Silicide Diffusion Coatings Formed by the Halide-Activated Pack cementation Method", Surf. and Coatings Tech., 76-77 (1995) 20-27.
8. R. Beyers and R. Sinclair, "Metastable Phase Formation in Titanium-Silicon Thin Films", J. Appl. Phys., 57 (1985) 5240-5245.
9. B.V. Cockeram, H.J. Schmutzler, J. Shyue, K. Hoshino, S. Meng, R. Wheeler and H.L. Fraser, "The High-Temperature Oxidation of Nb-40Ti-15Al and the Effect of Cr Alloying and Silicide Diffusion Coatings", MRS Proceed., Fall 1995.
10. Y-R. He, R.A. Rapp and P. Tortorelli, "Oxidation-Resistant Ge-doped Silicide Coating of Cr-Nb Alloys by Pack Cementation", Submitted to Oxid. Met (1996).
11. B.E. Deal and A.S. Grove, "General Relationship for the Thermal Oxidation of Silicon", J. Appl. Phys., 36 (1965) 3770-3778.
11. J-R. Chen, Y-C. Liu and S-D. Chu, "Oxidation of Titanium Disilicide on Polycrystalline Silicon", J. Electronic Mat., 11 (1982) 355-389.

PURITY AND PROCESSING EFFECTS ON THE MICROSTRUCTURE

AND OXIDATION OF MoSi₂

A. Newman, S. Sampath, and H. Herman

Department of Materials Science and Engineering
State University of New York at Stony Brook
Stony Brook, NY 11792-2275

Abstract

Molybdenum disilicide (MoSi₂), due to its high melting point and oxidation resistance, is a candidate for high temperature structural applications. However, its high temperature creep resistance and ambient temperature fracture toughness need to be significantly improved to enable applicability. This study examines the effects of feedstock purity and processing on the resulting microstructure and properties of MoSi₂. Processed MoSi₂ samples were obtained from several laboratories in order to determine the effects of purity and processing. The samples were characterized for their microstructure, hardness, and oxidation. The results indicate that grain size and volume distribution of SiO₂ particles influence the mechanical properties.

Introduction

Intermetallics based on silicides and their composites are currently under examination for potential high temperature structural applications[1]. These silicide- based materials possess enhanced reliability and manufacturability as well as cost over the present generation of structural ceramics[2]. Of the silicides being examined, MoSi₂-based materials have attracted considerable attention due to the high melting point of MoSi₂ (2030°C) and its excellent oxidation resistance[3]. Furthermore, MoSi₂ is electrically conducting, providing the ability for electric-discharge machining. While MoSi₂ is brittle at room temperature, it exhibits dislocation plasticity at high temperatures. An early examination reported the ductile-to-brittle transition temperature (DBTT) for MoSi₂ to be about 1000°C[4]. However, recent examinations of the DBTT, using very low silica samples, have identified the transition point to be between 1300°C and 1400°C[5,6]. Investigators studying single crystal MoSi₂ recently observed slip in several crystal orientations even at temperatures as low as ~173°K[7].

For the silicides to become commercially viable as high temperature structural materials, two important requirements must be satisfied: i.) the intermetallic must have a sufficient ambient temperature fracture toughness; ii.) the high temperature creep properties of the silicides must be improved.

A number of processing approaches are being examined to fabricate monolithic and composite MoSi₂. Included among the processing methods are hot pressing[8], hot isostatic pressing[9], self-propagating high temperature synthesis[10], and plasma spray forming[11]. The extent of mechanical testing of the materials produced was dependant on the experimental program. Due to variations in composition and impurity content, as well as processing and testing protocols, a direct comparison of the results is difficult, especially with respect to fracture toughness values. Indentation fracture toughness measurements reported in the literature show considerable variability from 2.3 to 5.9 Mpam^{1/2} for MoSi₂[12-17] and from 3 to 7.5 MPam^{1/2} for its composites[13,14,16,18,19]. It is important to note that four-point bend and short rod tests generally give a lower fracture toughness value than measurements using indentations[2].

In order to improve the low-temperature toughness and high temperature creep properties of MoSi₂, numerous approaches, primarily based on compositing strategies, have been proposed. The compositing strategies include additions of whiskers or particulates of SiC, ZrO₂, and ductile fibers, such as Nb. The results of the composite studies have shown considerable promise, especially in the area of creep resistance.

As an alternative to, or in conjunction with compositing strategies, microalloying or macroalloying (> 1 wt% alloy addition) have been suggested as a means of improving the mechanical properties[20,21]. Yamaguchi *et al.*[22] have indicated that additions of Cr, Ta, V and Nb may destabilize the C11b structure with respect to the C40 structure. A three atomic percent substitution with chromium in a single crystal produced only minimal compressive ductility at 900-1500°C[23]. Recent work by Stergiou and Tsakiroopoulos[24] has reported lower hardness values with additions of W, Ta, and Al. W forms a solid solution with MoSi₂ in the C11b crystal structure and suppresses formation of Mo₅Si₃. Ta additions result in a lamellar microstructure consisting of the C11b and C40 structures and also suppresses Mo₅Si₃ formation. Al additions lead to the formation of the C40 and C54 structures. In other recent work, silicon atom substitutions in the MoSi₂ lattice with Al, B, and Ge and molybdenum atom substitutions with Hf, Nb, and Re did not result in any effective improvements, yielding DBTTs in the range of 1250°C to 1350°C[25].

The purpose of the present investigation is to examine the physical, mechanical, and oxidation properties of MoSi₂ with respect to purity, grain size, and porosity.

Experimental Procedure

A set of samples produced by various fabrication methods were collected from different laboratories. The various sample processing methods are indicated in Table 1. The concentration of metallic impurities were determined by qualitative spectrographic analysis. Oxygen analysis was performed on a Leco TC-136 analyzer using 5 runs for each sample. The grain size was measured manually using the linear intercept method. Density of the samples was determined by the water immersion method. Hardness measurements were conducted using a 500 and 1000 gram loads on the Buehler Micromet II Microhardness Tester with the load applied for 15 seconds. The Vickers indentation measurements were carried out on samples polished to a one micron diamond finish. Oxidation studies were performed at 500°C for 300 hours, under flowing air with a room temperature relative humidity of 23-35%. The amount of oxide growth and phase composition was determined by X-ray diffraction (XRD).

Results and Discussion

Tables I and II summarize the various MoSi₂ samples, their processing methods, mechanical properties and microstructural features. Samples have been obtained from various laboratories and this has provided the diversity of specimens needed to examine the differences in purity, grain size and porosity, which result from differences in parent materials and processing methods. The present approach enables normalization of the results and allows for a uniform comparison of microstructure and the resulting properties.

Table I. Sample Processing Methods and Microstructure Characteristics

Sample Code	Processing	Grain Size (μm)	Oxygen(wt%)
VPS2	vacuum plasma spraying, as-sprayed[26]	1.0-3.0	4.4
VPS1	vacuum plasma spraying, 24 hrs at 1100°C[11]	1.0-3.0	N/A
SHS	reaction synthesis, hot pressing 1600°C[10]	3.9	2.6
HIP1	hot isostatic pressing at 1350°C, 170 Mpa[27]	4.3	6.3
HIP2	hot isostatic pressing[28]	8.3	0.97
HP1	hot pressing at 1600°C[20,21]	24.2	1.5
EHIP	elemental powders, hot isostatic pressing at 1400°C, 200 MPa[9]	33.2	0.64
HP2	hot pressing at 1800°C, 80 MPa[29]	40.7	0.9

Purity

Spectrographic analysis of impurities has been conducted on consolidated samples. The key impurities, other than oxygen, are identified in Table II. Aluminum is a typical impurity in MoSi₂, substituting for the Si in the C11b crystal structure[30], while W or Cr are commonly

Table II. Hardness, Density, and Impurity Information on the Collected Samples

Sample Code	H _v (1 kg) (GPa)	Density (g/cm ³)	Impurity Levels
VPS2	11.0	5.88	XXX Al, X Ca, X Cr, X Cu, X Ni
VPS1	11.0	6.04	X Al
SHS	11.0	5.96	XX Al, X Fe, X Mn
HIP1	10.2	5.76	XX Al, X Cr, X Fe, X Zn
HIP2	9.2	6.23	XXX Al, X Cu, X Fe
HP1	9.2	5.96	XX Al
EHIP	9.5	6.24	X Al
HP2	8.3	6.21	X Al

note: X = 0.1-1wt%, XX = 0.5-5wt%, XXX = 1-10wt%

observed substitutional elements for Mo[31]. The level of impurities may inhibit grain growth, due to the observation that all the higher impurity samples have a grain size of less than ten microns.

It is widely known that MoSi₂ readily oxidizes in air to form a thin SiO₂ scale. In the case of fine powders, significant oxygen pick-up occurs during particle size reduction and powder handling. For instance, as-reacted powder fragments typically contain 800 - 1000 ppm of oxygen. Upon milling, the <44 micron fraction shows an oxygen level of 2500 - 3000 ppm and further particle size reduction to produce fines increases the oxygen level to > 5000 ppm. Moreover, powder shelf-life is an important factor, because oxygen pick-up is likely during long-term storage. Typically, MoSi₂ fines or the <44 micron fraction are used for consolidating MoSi₂ thus an extensive oxide presence is inevitable unless powder consolidation is conducted in highly controlled environments. The EHIP sample described in Tables 1 and 2, was processed in an argon atmosphere glove-box and shows a significantly lower oxygen content than the other samples.

Microstructural Variations

Figure 1 shows the microstructures of the various MoSi₂ samples. The distinct differences in grain size and oxide content can readily be observed. The effect of processing methods on the consequent microstructure is discussed below.

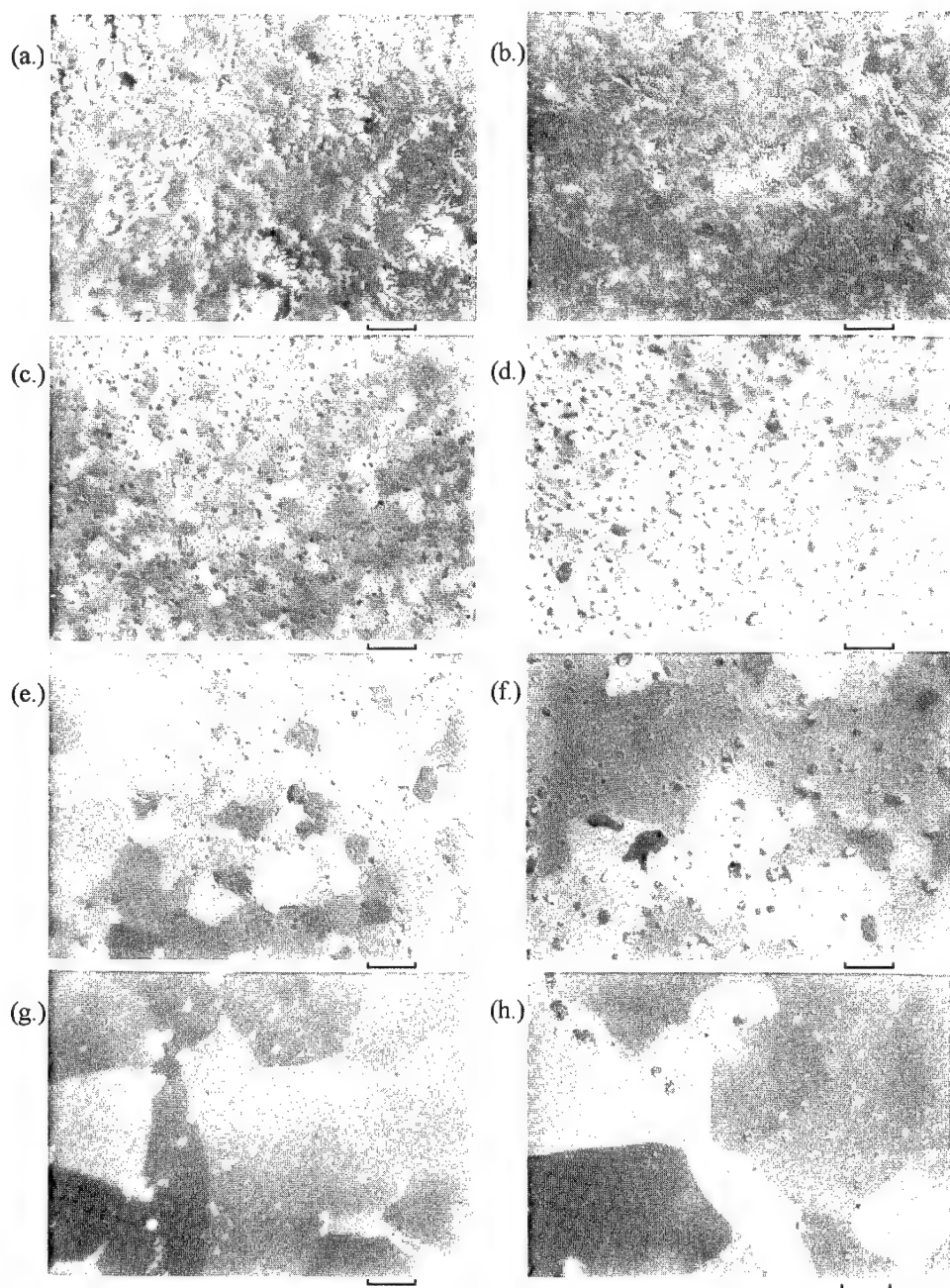


Figure 1. Optical micrographs of MoSi_2 using cross polarized light of the following samples: (a.) VPS2 (b.) VPS1, (c.) SHS, (d.) HIP1, (e.) HIP2, (f.) HP1, (g.) eHIP, (h.) HP2 (Note: All micron markers are 10 microns in length)

In general, the hot pressed (HP) and hot isostatic pressed (HIP) samples show the largest grain sizes, while the reaction synthesis and the plasma sprayed samples show significantly finer grain sizes. The impurities, especially SiO_2 , appear to play a role in retarding grain growth during processing. The impurity effect on grain growth is exemplified by comparing the EHIP sample with the HIP1 samples. In spite of the lower HIP temperatures and finer starting particle sizes of the EHIP sample, the consolidated high purity material exhibited a significantly larger grain size. Furthermore, the HIP1 sample has a high level of oxide, leading to even finer grain size. The EHIP sample shows fine silica inclusions within the grains.

A silica phase is present in all of the samples, as observed by optical microscopy and oxygen analysis. The morphology of the silica depends on the sintering temperature, forming either a thin film of silica between grains at low temperatures or spherical precipitates dispersed trans- or intergranularly at high temperatures. According to Cotton *et al.*[32], silica no longer wets MoSi_2 at high temperatures. The loss in wetting ability may therefore result in the formation of agglomerates. Sadananda *et al.*[33] attribute to the loss in high temperature creep resistance to the glassy film at the grain boundaries, while at low temperatures the silica may facilitate intergranular fracture resulting in a more tortuous crack path.

Rapid solidification of the molten MoSi_2 droplets during vacuum plasma spraying (VPS) produces a fine grained, chemically homogeneous microstructure[34]. In addition to forming polycrystalline regions of MoSi_2 in both the C11b and C40 structures, a secondary phase of Mo_5Si_3 has been confirmed by x-ray diffraction, confirming previous investigations on the processing of MoSi_2 by VPS[13]. The distinct feature resulting from VPS processing is the fine-grained microstructure, with an apparently bimodal grain size distribution. Further, such materials contain silica inclusions that are significantly larger than the grain size.

Self-propagating high temperature synthesis produces very high temperatures for a relatively short period of time (~20 seconds to 1000°C)[10]. The combustion wave, as it propagates through the compact of Mo and Si powders, seems to agglomerate the silica. Liquid phase sintering is enhanced by the heat added to the system by compound formation. Temperatures at the reaction front should be quite high, and may permit the agglomeration of silica during the reaction process.

Elemental hot isostatic pressing of MoSi_2 from low-oxide elemental powders produces a 99% dense product (EHIP sample). Hardwick *et al.*[9] observed that the higher silica level samples experienced less grain growth than the oxygen free samples. Silica is present in the EHIP sample both inter- and transgranularly. The results for the two other HIPped samples are a fine grain size HIP1 sample with an aggregate of silica, predominantly at the grain boundaries, and a larger grain size sample, HIP2, with silica decorating the grain boundaries and within the grains.

The hot pressing of MoSi_2 powder requires higher temperatures to acquire full density than elemental powders. These higher temperatures will produce significantly greater grain growth, and may permit the agglomeration of the silica. The spheroidizing of the silica most likely takes place early in the process because a large fraction of the silica can be found within the grains.

Hardness

There is a 20% variation in hardness from the largest to the finest grain size samples; Table II. Fine grained samples show a higher hardness, which appears to follow a Hall-Petch type relationship, as illustrated in Figure 2. Some of the deviation from linearity is associated with the volume fraction of silica. For the two samples with equivalent grain sizes, HIP1 and SHS, the hardness values are nearly equivalent when the silica volume fraction is accounted for by a rule of

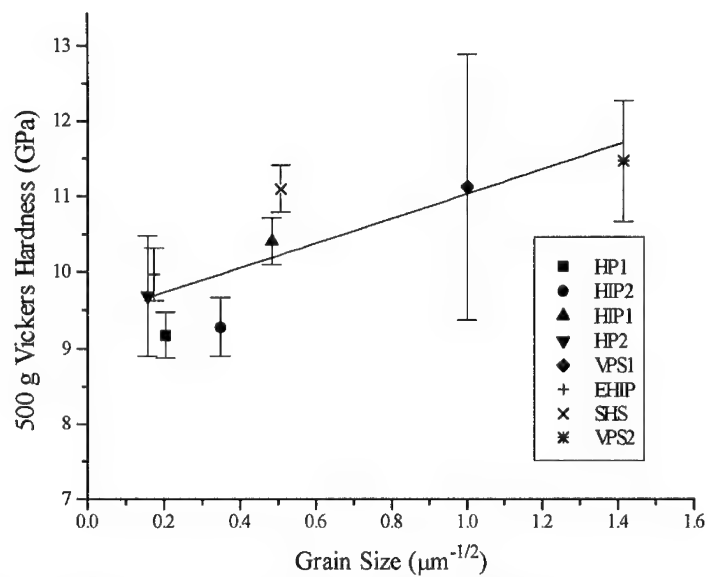


Figure 2 - Hall-Petch type relationship of hardness, applying a linear fit to the measured values



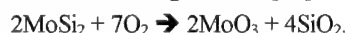
Figure 3. Abundance of slip and/or twin deformation surrounding a 1 kg Vickers indentation for the HIP2 sample.

mixtures, with the silica hardness taken as 4.9 GPa. It is expected that the nonlinearity would be even less if the purity levels, given in Table II, were less variant. A high density of slip lines and/or deformation twins can be seen in Figure 3 surrounding the indentation of the HIP2 specimen. The cross-polarized Nomarski setting on the optical microscope is used to capture these topographical changes. The extent of deformation in this sample is greater than that for the other samples, and this increased deformation is consistent with the observation of its anomalous softness in Figure 2.

Oxidation

Table III provides the results from the pesting oxidation study on the four samples examined. Also included in this table is the silica and Mo₅Si₃ levels, prior to oxidation. Although no clear trend is observed, it appears that volume percent silica and Mo₅Si₃ play a role in the oxidation behavior.

The growth of the oxide surface eventually forms a continuous oxide layer, as demonstrated in the XRD patterns in Figure 4. These four samples have been exposed to identical oxidation conditions prior to x-ray analysis. The HP1 sample produces the least amount of oxide product on its surface, which is demonstrated by the lack of MoO₃ peaks in the XRD pattern, and has the smallest weight change. The sample with the largest weight gain produces a continuous, although porous, oxide layer that eliminates any MoSi₂ peaks in the XRD pattern, so that only MoO₃ peaks remain. The other samples have a mixed pattern of MoSi₂ and MoO₃. In addition, an amorphous SiO₂ background is observed in all of the samples except HP1. There is a significant fraction of SiO₂ in the oxide product due to the following reaction:[35]



Assuming there are not any other oxidation products formed, the volume percent silica, calculated from the molar fractions given in the above reaction, is 64%. Due to its amorphous nature, the volume fraction of silica is not clearly reflected in the XRD pattern.

Table III Flowing Air Oxidation Test At 500°C.

Sample	Calculated Vol% SiO ₂	SEM Image Analysis Vol% SiO ₂	$I(112) \text{ Mo}_5\text{Si}_3 /$ $I(103) \text{ MoSi}_2$	Oxidation Rate (mg/cm ²)
HIP1	24.5%	10.9%	.010	5.6
SHS	11.1%	6.5%	.011	2.4
HP2	4.0%	3.7%	.015	1.9
HP1	6.6%	N/A	.007	.07

The oxidation rate appears to be influenced by the purity levels, oxide content and Mo₅Si₃ levels. The effect of the purity levels is consistent with Meschter's findings that an increase in impurities increases the rate of oxidation.[36] The two samples with a greater number of impurity elements, Table II, and a higher levels of SiO₂ (HIP1 and SHS) appear to have a higher rate of oxidation. The level of silica is apparent from the micrographs in Figure 1, and silica can be present either inter- or transgranularly, as observed by the cross-polarized grain contrast of these optical images. Between the balance two samples (HP1 and HP2), with similar impurities and silica content, the amount of Mo₅Si₃ dominates the rate of oxidation. Other studies have reported that the oxidation resistance of Mo₅Si₃ is much less than that for MoSi₂. [37] HP1 sample has the lowest Mo₅Si₃ content among all samples and clearly superior oxidation behavior.

This trend associated with the secondary phases may be described by the role of nucleating oxides at the surface. The surface morphology is changed by having the oxide and/or Mo₅Si₃

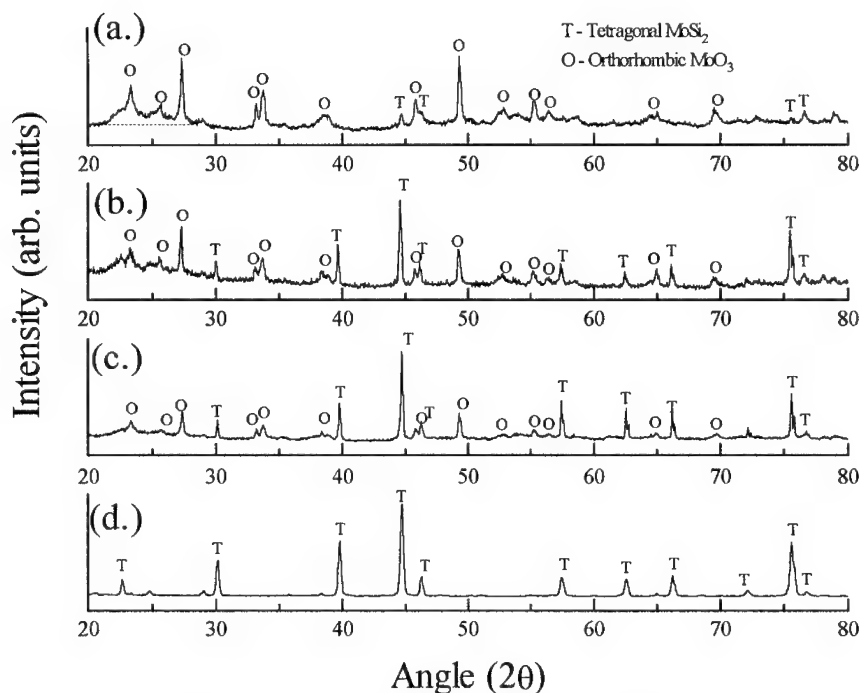


Figure 4. X-ray diffraction patterns of the samples' oxidation surfaces: (a.) HIP1, (b.) SHS, (c.) HP2, (d.) HP1.

particles within the MoSi_2 matrix. These oxide and/or Mo_5Si_3 particles may inhibit the formation of a thin continuous oxide. The lateral growth of silica or silicates is required to produce a continuous oxide barrier which limits further low temperature oxidation in MoSi_2 . [38] The lowest oxidation rate, for the HP2 sample, can be attributed, primarily, to a low level of Mo_5Si_3 and, secondarily, to a lower silica level.

Conclusion

The molybdenum disilicide samples collected for this study have significantly different microstructures. The level of silica, processing temperature, and starting powder size all contribute to the grain size. The samples examined have levels of silica from less than 1 wt% to 4.5 wt%, indicating the susceptibility of oxygen pick-up in MoSi_2 powder. The level of impurities also varied depending on the grade of starting powders and may inhibit grain growth. The hardness values appear to follow a Hall-Petch type relationship. With regard to low temperature oxidation, the pest oxidation rate depends on impurities and phase distribution.

Acknowledgments

This work has been supported by Office of Naval Research (grant no. N000149410553) and AASERT (grant no. N000149511147), supervised by Dr. A. K. Vasudevan. The following individuals are acknowledged for providing samples: D. Alman at the United States Department of the Interior; S. Deevi at the Philip Morris Research Center; D. Hardwick at Rockwell International; J. Petrovic at Los Alamos National Laboratory; and M. Nathal and M. Hebsur at NASA-Lewis Research Center.

References

1. D. M. Shah, D. Berczik, D. L. Anton, and R. Hecht, *Mat. Sci. and Eng.*, A155 (1992) 45-58.
2. A. K. Vasudevan and J. J. Petrovic, *Mat. Sci. and Eng.*, A155 (1992) 1-18.
3. E. Fitzer, Molybdendisilizid als Hochtemperaturwerkstoff, in F. Benesovsky (ed.), *Proc. 2nd Plansee Semin.*, Springer, Berlin (1955) 56-79.
4. Matthias, K., Ph.D Thesis, Universitat Karlsruhe, 1969.
5. D. A. Hardwick, P. L. Martin, and R. J. Moores, *Scripta Metall. Mater.* 27 (1992) 391.
6. R. M. Aikin, Jr., *Scripta Met.*, 26 (1992) 1025-1030.
7. K. Ito, T. Yano, H. Inui, and M. Yamaguchi, *Mat. Res. Soc. Symp. Proc.*, High Temperature Ordered Alloys VI, Eds. J. A. Horton, I. Baker, S. Hanada, R. D. Noebe, D. S. Schwartz, Vol. 364 (1995) 899-904.
8. R. K. Wade and J. J. Petrovic, *J. Am. Ceram. Soc.*, 75(6) (1992) 1682-84.
9. D. A. Hardwick, P. L. Martin, and R. J. Moores, *Scripta Metall. Mater.* 27, 391 (1992).
10. S. C. Deevi, *J. Mat. Sci.*, 26 (1991) 3343-3353.
11. S. Sampath, R. Tiwari, and H. Herman, in *Proceedings of the TMS Symposium on Microstructural Design by Solidification Processes*, E. J. Lavernia and M. N. Gungor, Editors, p. 151, TMS, Warrendale, Pa (1992).
12. J. J. Petrovic and R. E. Honnell, *J. of Mat. Sci.*, 25 (1990) 4453-4456.
13. R. Tiwari, H. Herman, and S. Sampath, *Mat. Sci. and Eng.*, A155 (1992) 95-100.
14. A. K. Bhattacharya and J. J. Petrovic, *J. Am. Ceram. Soc.*, 74(10) (1991) 2700-2703.
15. S. B. Bhaduri and R. Radhakrishnan, *Advances in Powder Metallurgy & Particulate Materials--Vol. 9. Particulate Materials and Processes*, San Francisco, California USA, 21-26 June 1992, p. 369-379.
16. R. G. Castro, R. W. Smith, A. D. Rollett, and P. W. Stanek, *Scripta Metall.*, 26 (1992) 207-212.
17. R. K. Wade and J. J. Petrovic, *J. Am. Ceram. Soc.*, 75(11) (1992) 3160-62.
18. J. J. Petrovic and R. E. Honnell, *J. of Mat. Sci.*, 25 (1990) 4453-4456.
19. Y. L. Jeng, J. Wolfenstine, and E. J. Lavernia, *Scripta Metall.*, 28 (1993) 453-458.
20. I. Baker and P. R. Munroe, *J. of Met.*, 40(2) (1988) 28-31.
21. R. Darolia, D. Lahrman, and R. Field, *Scripta Met.*, 26 (1992) 1007-1012.
22. M. Yamaguchi and Y. Umakoshi, *Prog. Met. Sci.*, 34 (1990) 22,118.
23. Y. Umakoshi, T. Hirano, T. Sakagami, and T. Yamane, *High Temperature Aluminides and Intermetallics*, edited by S. Whang, C. Liu, D. Pope, and J. Stiegler (TMS, Warrendale, PA, 1990) 111-129.
24. A. Stergiou and P. Tsakirooulos, *Mat. Res. Soc. Symp. Proc.*, High Temperature Ordered Alloys VI, Eds. J. A. Horton, I. Baker, S. Hanada, R. D. Noebe, D. S. Schwartz, Vol. 364 (1995) 911-916.
25. S. Chin, D. L. Anton, and A. F. Giamei, *Material Research Society Symp. Proc. High Temperature Structural Applications in High Temperature Silicides and Refractory Alloys*, eds. C. L. Briant, J. J. Petrovic, B. P. Bewlay, A. K. Vasudevan, H. A. Lipsitt, Vol. 322, pp. 423-429, 1994.
26. R. G. Castro, R. W. Smith, A. D. Rollett, and P. W. Stanek, *Mat. Sci. Eng.*, A155, 101-8, 1992.
27. D. Alman, personal communication, Jan., 1995.
28. M. Hebsur, *Intermetallic Matrix Composites III*, MRS Proc. 350, 177-182, 1994.
29. R. Tiwari, H. Herman, S. Sampath, and B. Gedmundsson, *Mat. Sci. Eng.*, A144, 127 (1991).
30. A. Costa e Silva and M. J. Kaufman, *Scripta Met.*, 29, 1141-1145, 1993.
31. Y. Umakoshi, T. Hirano, T. Sakagami, and T. Yamane in *High Temperature Aluminides and Intermetallics*, edited by S. Whang, C. Liu, D. Pope, and J. Stiegler (TMS, Warrendale, PA, 1990), p 111-129.
32. J. D. Cotton, Y. S. Kim, and M. J. Kaufman, *Mat. Sci. and Eng.*, A144 (1991) 287-291.
33. K. Sadananda, C. R. Feng, H. Jones, and J. J. Petrovic, *Mat. Sci. and Eng.*, A155, (1992) 227-240.
34. S. Sampath and H. Herman, D. L. Houch (ed.), *Thermal Spray: Advances in Coating Technology*, American Society for Metals, Metals Park, OH, 1988, p. 1.
35. C. D. Wirkus and D. R. Wilder, *J. Am. Ceram. Soc.*, 49 (1966) 173-177.
36. P. J. Meschter, *Met. Trans. A*, 23A (1992) 1763-17.
37. C. G. McKamey, P. F. Tortorelli, J. H. DeVan, and C. A. Carmichael, *J. Mater. Res.*, 7(10) (1992) 2747-2755.
38. H. J. Grabke and G. H. Meier, *Oxid. of Met.*, 44(1/2) (1995) 147-176.

DESIGN AND SYNTHESIS OF FUNCTIONALLY GRADED COMPOSITES: THE TiB₂/NiAl SYSTEM

R. D. Torres¹, I. E. Reimanis¹, J. J. Moore¹ and G. W. Mustoe²

¹Department of Metallurgical and Materials Engineering

²Engineering Division

Colorado School of Mines

Golden, CO 80401

Abstract

Functionally graded composites have been studied using finite element analysis (FEA) and by synthesizing TiB₂/NiAl compositionally graded specimens. The FEA studies have been used to obtain the distribution of residual stress as a function of the composite architecture (nature of gradation). The combustion synthesis technique in conjunction with hot pressing was employed to obtain the composites. Vickers microhardness at room temperature and 900°C was measured across the graded composite, as a function of volume fraction of TiB₂ (V_{TiB_2}). It was observed that the room temperature hardness varies linearly with V_{TiB_2} but may become nonlinear with V_{TiB_2} at elevated temperature, depending on the microstructure. Specifically, it appears that the hardness at elevated temperature depends sensitively on the distribution of TiB₂ particles. The reasons for this deviation, and the role of residual stresses in governing the mechanical properties are discussed.

Introduction

The efficiency of high temperature applications, such as turbine engines, can be significantly improved if the operating temperatures are increased. This potential increased efficiency drives the development of new materials which are able to withstand higher temperatures. Once a new material has been developed, a second hurdle is joining or attaching the new material to a larger engineering structure. There are many methods of joining structural members [1-5]. A number of these methods utilize an interlayer material which typically has properties intermediate between the two structures to be joined, or which is ductile so that the maximum stresses are limited [3-5]. One potential method of joining two different materials employs a compositionally graded interlayer. As our earlier study demonstrated, the peak stresses in graded joints are significantly lower than in a discrete joint without a graded interlayer [6]. The compositional variation may be implemented so that the appropriate property variation is achieved. In the case of a joint between a metal and a ceramic, the most important property is usually the thermal expansion coefficient, since it determines the magnitude of thermally induced residual stresses.

It is fairly well established that the compositional variation in graded structures determines the distribution and magnitude of thermally induced residual stresses [6-9]. There remain many details concerning the residual stress distribution for different geometries, different material systems, and different microstructures. Experimental studies are required to work out some of these details. For example, it is known that the presence of a ductile phase will affect the residual stress distribution, but it is not known how the phase size and distribution will change that distribution. Because the residual stress distribution may affect crack propagation and/or plastic flow, a complete description of the mechanical response of graded composites must include residual stresses.

The TiB_2/NiAl system has been chosen to examine how the fracture and deformation are influenced by the microstructure, the composite architecture and the residual stress distribution. There are several reasons this system has been chosen. 1) There exists a significant difference in the thermal expansion coefficient between TiB_2 and NiAl (see Table 1); thus, such a composite is a good model system to study the influence of residual stresses. 2) TiB_2 and NiAl are thermodynamically compatible; this eliminates the additional complexity of chemical reactions. Also, because of this thermodynamic compatibility, combustion synthesis is a convenient way in which to produce graded two-phase composites. The Colorado School of Mines has been involved in evaluating the synthesis and design of materials by high temperature combustion synthesis methods [11]. 3) TiB_2/NiAl composites are candidates for high temperature structural applications due to the high melting points and relatively good mechanical properties of the constituents [12,13] (see Table 1).

Table 1. Properties of polycrystalline NiAl and TiB₂. References are indicated.

	NiAl ¹⁰	TiB ₂ ^{14,15}
Melting Point (°C)	1638	3225
Poisson's Ratio	0.31	0.20
Elastic Modulus (GPa)	294	365
Linear Coefficient of Thermal Expansion (10 ⁻⁶ /°C)	15.1	6.4
Yield Strength (MPa)	600-1800	--
Fracture Strength (MPa)	--	130
Fracture Toughness (MPam ^{1/2})	4-7	7

This paper is divided into two sections. The first section presents the results of finite element analyses which have been conducted on several architectures of metal/ceramic graded joints with the purpose of obtaining residual stress distributions. The second section describes the synthesis and characterization of TiB₂/NiAl compositionally graded composites.

Finite Element Analysis (FEA)

FEA Description

The finite element code ALGOR, by ALGOR Inc., was employed with the objective of calculating the thermal residual stress fields in compositionally graded specimens. An isothermal linear elastic material model was used initially to obtain a basic understanding of the stress distributions and to identify any regions which may undergo nonlinear mechanical behavior. Only these linear elastic results are reported here; non-linear results are reported elsewhere [9].

The particular finite element model employed axisymmetrical geometrical discretizations of four noded linear finite elements enriched with incompatible bubble modes [16]. Note that the inclusion of the bubble modes optimizes the accuracy of the stresses computed within the four noded elements. In any spatial regions within the FGM specimen where we expected rapid variations in the stress field we also employed a local fine mesh gradation to model the stresses in an accurate and efficient manner. Such regions included interfaces between different material layers. Zero traction boundary conditions were enforced at ends and on the outer radial surfaces of the FGM specimens. The thermal loading was generated by assuming a uniform cooling of the FGM specimen from its processing temperature down to room temperature. The mechanical and thermal properties of the FGM were assumed to be independent of temperature. The specific values of Young's modulus, Poisson's ratio and coefficient of thermal expansion used in the finite element computations were average values over the temperature range under consideration. A linear rule of mixtures was used to determine the material properties in

the graded regions of the FGM specimens. Some of the relevant properties of NiAl and TiB₂ are listed in table 1. Note that the large variations of the yield strength and the fracture toughness of NiAl depends on factors such as strain rate, stoichiometry, grain size and/or processing technique.

The composition variation across the graded region was represented by

$$V_{TiB_2} = \left(\frac{x}{t}\right)^p$$

where V_{TiB_2} is the volume fraction of TiB₂, x is the distance from the NiAl, t is the thickness of the graded region (t= 24 mm in this study) and p characterizes the nature of gradation. Figure 1 shows the composition profiles for three values of p examined in this work.

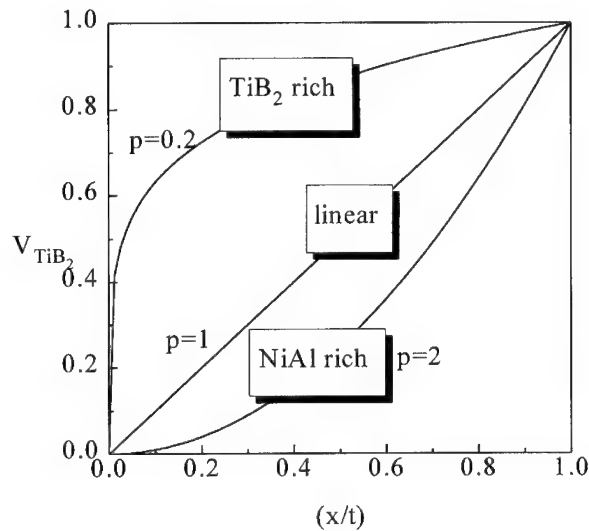


Figure 1. Profile of composition across graded joint, according to equation (1).

FEA Results

Figure 2 shows the distribution of axial and radial stresses for two different values of p from equation (1). It is noted that values of the stresses may not be representative of

actual values in a NiAl/TiB₂ composites; however, here we are concerned with the relative values. The most notable difference between the two specimen types is that

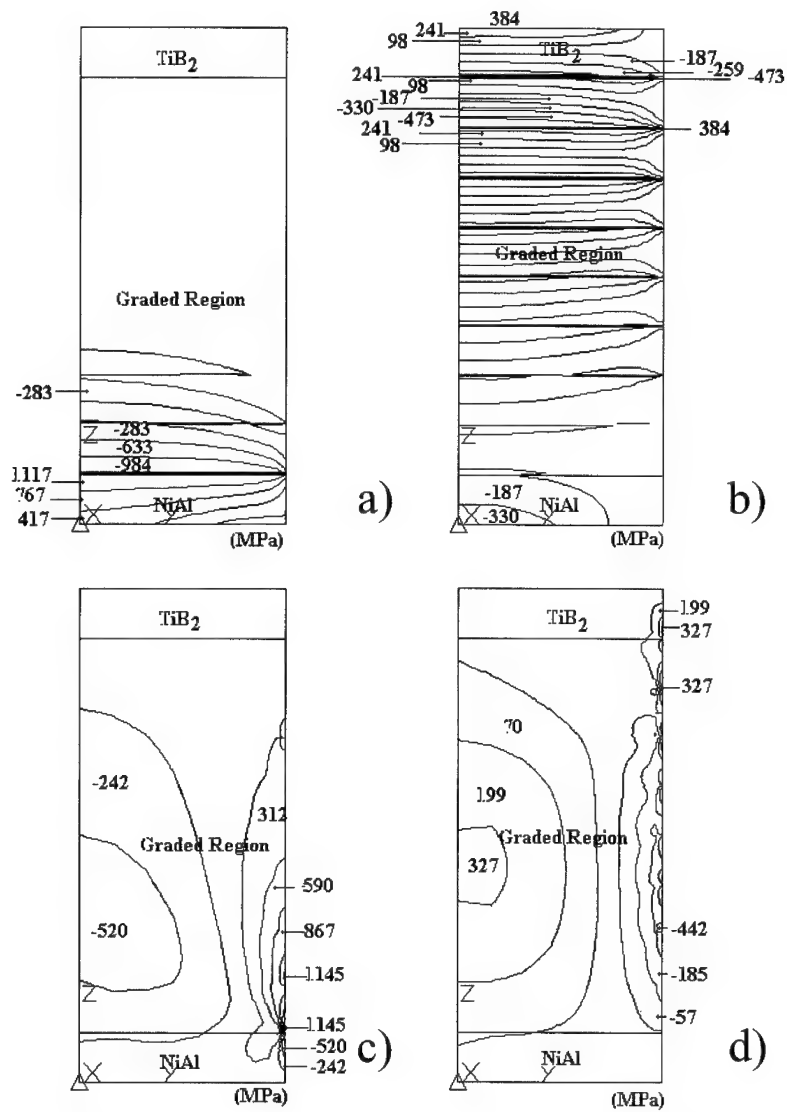


Figure 2. FEA results showing stress contours for a) radial stresses for p=0.2, b) radial stresses for p=2, c) axial stresses for p=0.2, and d) axial stresses for p=2.

the location of the maximum tensile stress is determined by the p -value. For $p=0.2$, where the volume fraction of TiB_2 increases quickly with increasing distance from the NiAl , the maximum of both the axial and the radial stresses occurs within the pure NiAl . In contrast, the maximum stresses for $p=2$, where the volume fraction of TiB_2 increases more slowly with increasing distance from the NiAl , occur in the vicinity of the TiB_2 .

Experimental

Synthesis

The combustion technique has been widely employed in the synthesis of materials [11]. The exact process used in the present study is briefly described below; details may be found elsewhere [6,17]. Briefly, the elements titanium, boron, nickel and aluminum are cleaned with solvents and mixed in a particular ratio depending on the composition desired. These are placed in a graphite die such that the desired composition profile is achieved; the composition profile is described by equation (1). The subsequent composite specimens are called $p=0.2$, $p=1$, $p=2$, depending on the initial ratio of elements. The mixture is heated to the ignition temperature (approximately 1000°C), at which point an exothermic reaction takes place and generates enough heat to insure that all of the elements react. As a result of this reaction, the temperature increases above 2000°C and NiAl is undoubtedly molten.

A pressure of 38 MPa is applied during the combustion reaction to improve the final density of the materials. In the present work, the pressure was applied approximately two seconds after the exothermic chemical reaction. The NiAl rich parts of the composites densified to near theoretical, based on optical microscopy; however, regions with volume fractions of TiB_2 greater than about 0.6 were porous. Future synthesis will be done by applying the pressure prior to the combustion reaction. In the present system, the four elements form two phases: titanium diboride (TiB_2) and nickel aluminide (NiAl). Powder x-ray diffraction was used to determine that only TiB_2 and NiAl were present. Any other phase would be present in a quantity less than approximately 3 %.

Characterization

Cross sections of the synthesized joints were cut, ground and polished by standard metallography techniques using diamond abrasive media. Optical microscopy was used to measure the volume fraction of TiB_2 by a point counting technique; it is noted that some error may be incurred by this technique when the particle size of TiB_2 is very small. The hardness variation across the composite specimens was measured as a function of TiB_2 content. A Nikon QM-2 hot hardness unit[†] was used to measure Vickers hardness at room temperature and at 900°C . For the elevated temperature measurement, the temperature of the indenter was heated to 720°C while the sample was heated to 900°C ;

[†] The authors are grateful to Los Alamos National Laboratory for use of a Nikon QM-2 hot hardness unit.

the lower temperature of the diamond indenter insured that the diamond tip did not decompose substantially. A load of 0.5 kg was applied for 5 seconds in all the tests. The hardness was determined by optical microscopy measurement of the indent diagonals.

Results and Discussion

Optical microscopy on polished specimens after combustion synthesis revealed that approximately the same composition profile of TiB_2/NiAl was achieved, independent of the initial composition profile of Ti/B/Ni/Al . Thus, even though three kinds of samples were produced ($p=0.2$, $p=1$ and $p=2$), they all have the same approximate composition profile (which was equal to $p=2$). There are some differences in the size and distribution of TiB_2 particles in these three samples, as Figure 3 shows for the specimens $p=0.2$ and $p=2$. Figure 4 shows the volume fraction of TiB_2 (V_{TiB_2}) as a function of normalized distance from pure NiAl for the three kinds of specimens.

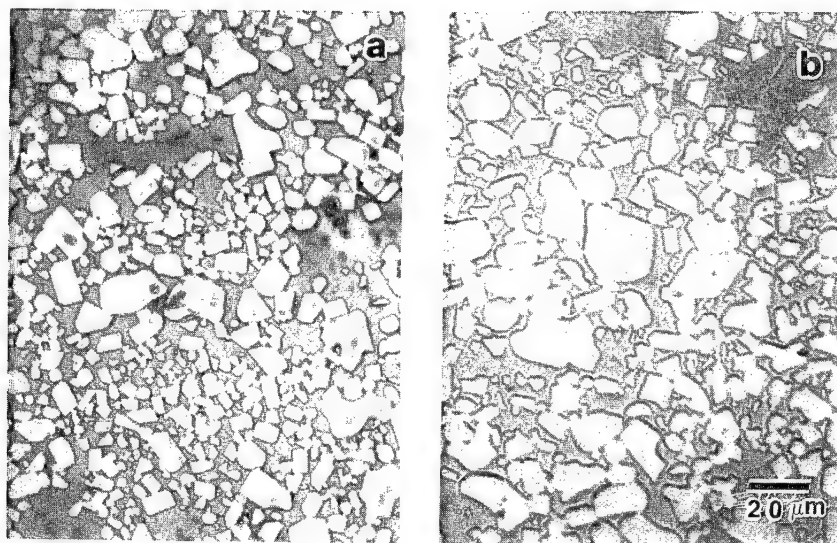


Figure 3. Optical micrograph of composites. Lighter phase is TiB_2 . The approximate composition is 0.5 vol. % TiB_2 . a) $p=0.2$, b) $p=2$.

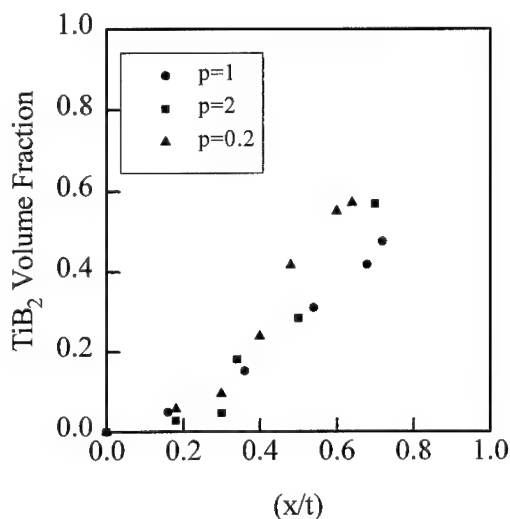


Figure 4. TiB₂ volume fraction measured in the optical microscope as a function of distance from NiAl.

The Vickers microhardness at room temperature increased linearly as a function of TiB₂ content for all three specimens as shown in Figure 5a. This result is consistent with the optical microscopy observation that the composition profile for all three specimen types is the same. The linear variation implies that a linear rule of mixtures for hardness applies to these composites.

The FEA results indicate that for specimens with p=2, the highest tensile stresses (at room temperature) occur near the TiB₂ region. As shown in Figure 2d, compressive axial stresses develop near the NiAl region. Similarly, the average radial stresses are compressive near the NiAl, as figure 2b shows. The presence of these compressive stresses would be expected to increase the room temperature hardness. However, an enhancement in hardness near the NiAl region for specimens with p=2 relative to specimens with p=0.2 is not observed. The influence of these residual stresses on affecting the hardness is yet to be determined; studies on several homogeneous composites with varying compositions will be performed in the future.

The Vickers microhardness at 900°C is substantially lower, as Figure 5b indicates. In addition, the hardness increases nonlinearly as a function of TiB₂ content for the specimen p=0.2. In contrast, the hardness of specimen p=2 appears to increase linearly as a function of TiB₂ content, though the slope is much smaller than for room temperature. This difference between specimen p=0.2 and p=2 suggests that significant microstructural

differences exist between the two types of specimens, even for the same volume fraction of TiB_2 . Figure 3 clearly indicates that the size distribution of TiB_2 particles is different for the two specimens. Based on work on the deformation and fracture of metal matrix composites [18-20], it would be expected that the size and shape of the TiB_2 particles at a given volume fraction would affect the flow of NiAl at higher temperature. In general, the deformation characteristics of metal matrix composites are dependent on a number of factors including the size and shape of the particles, the interparticle spacing and the strength of the interface between the particles and the matrix. In addition, the matrix flow stress may be intrinsically affected if it contains small precipitates which act as obstacles to dislocations. In fact, the observation that the two hardness profiles in Figure 5b (for $p=0.2$ and $p=2$) do not extrapolate to the same value for $V_{\text{TiB}_2} = 0$ suggests that the matrix flow characteristics are indeed different for the two specimens. Further characterization using transmission electron microscopy is required to ascertain the microstructure of these materials.

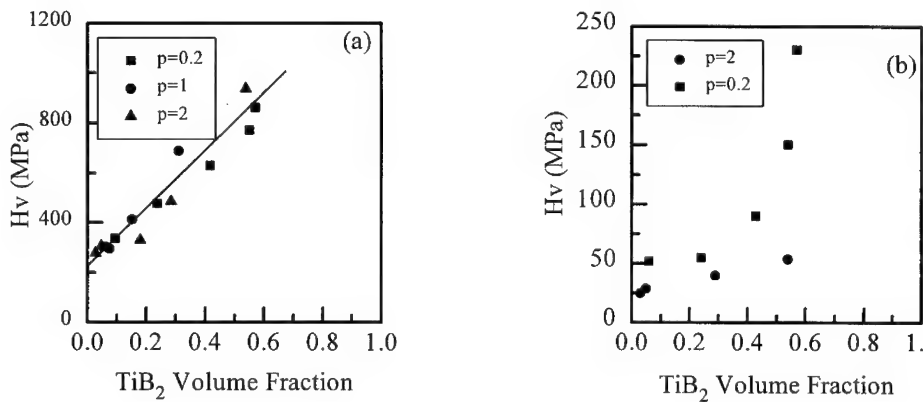


Figure 5. Vickers microhardness as a function of V_{TiB_2} at a) room temperature and b) 900°C.

Summary and Conclusions

In future analysis work, we intend to simulate any nonlinear behavior within the FGM that may occur in localized regions. However, before we conduct this computational study we want to identify the physical nonlinear behavior mechanisms, whether they are ductile or brittle or some combination thereof. It is anticipated that this study will probably require a detailed consideration of the microstructure of the FGM and probably

lead to the development of constitutive models that are based upon the microstructure of the FGM materials.

References

1. R. E. Loehman and A. P. Tomsia. "Joining of Ceramics", *Ceramic Bulletin*, Vol. 67, No. 2 p. 375 (1988).
2. M. L. Santella. "A Review of Techniques for Joining Advanced Ceramics", *Ceram. Bull.* Vol. 71, No. 6, pp. 947-954 (1992).
3. C. H. Bates, M. R. Foley, G. A. Rossi, G. J. Sundberg and F. J. Wu. "Joining Non-Oxide Ceramics for High Temperature Applications", *Ceram. Bull.*, Vol. 69, No. 3 pp. 350-356 (1990).
4. K. Suganuma, T. Okamoto, M. Koizumi and M. Shimada "Joining of Silicon Nitride to Silicon Nitride and to Invar Alloy Using an Aluminum Interlayer", *J. Mater. Sci.* 22, pp. 1359 - 1364 (1987).
5. M. G. Nicholas and R. M. Crispin. "Diffusion Bonding Stainless Steel to Alumina Using Aluminum Layers", *J. Mater. Sci.* 17, p. 3347 (1982).
6. R. D. Torres, J. J. Moore, G. Mustoe and I. E. Reimanis. "Evaluation of Thermal Residual Stresses Developed in a Functionally Graded Material using the Finite Element Technique", in Proceedings of Fourth International Symposium on Processing and Fabrication of Advanced Materials, TMS publication, eds., T. S. Srivatsan and J. J. Moore, in press (1996).
7. R. L. Williamson, B. H. Rabin and J. T. Drake. "Finite Element Analysis of Thermal Residual Stresses at Graded Ceramic-Metal Interfaces. Part 1. Model Description and Geometrical Effects", *J. Appl. Phys.* 74 (2) p. 1310 (1993).
8. J. T. Drake, R. L. Williamson and B. H. Rabin. "Finite Element Analysis of Thermal Residual Stresses at Graded Ceramic-Metal Interfaces. Part 2. Interface Optimization for Residual Stress Reduction", *J. Appl. Phys.* 74 (2) p. 1321 (1993).
9. B. H. Rabin, R. L. Williamson, H. A. Bruck, X. L. Wang, T. R. Watkins, and D. R. Clarke, "Residual Strains in an Al_2O_3 -Ni Joint Bonded with a Composite Interlayer: FEM Predictions and Experimental Measurements" to be published in *J. Amer. Ceram. Soc.*, 1996.
10. R. D. Noebe, R. R. Bowman and M. V. Nathal, "The Physical and Mechanical Metallurgy of NiAl", in Physical Metallurgy and Processing of Intermetallic Compounds, eds. N. S. Stoloff and V. K. Sikka, Chapman & Hall, New York, 212-296 (1996).

11. J. J. Moore and H. J. Feng, "Combustion Synthesis of Advanced Materials: Part 1 and Part 2", *Progress in Materials Science*, Vol. 39, No. 4/5, 243-316 (1995).
12. J. D. Whittenberger, R. Ray, S. C. Jha, and S. Draper, "100-1300 K Slow Strain Rate Properties of NiAl Containing Dispersed TiB_2 and HfB_2 ", *Mat. Sci. Eng. A138*, 83-93 (1991).
13. L. Wang and R. J. Arsenault, "Interfaces in XD Processed TiB_2 /NiAl Composites", *Metall. Trans. A 22A*, 3013-3018 (1991).
14. *Materials Science and Engineering*, CRC Handbook, edited by J. F. Shackelford, W. Alexander and J. S. Park, second edition, CRC Press, Boca Raton (1994).
15. *Engineered Materials Handbook*, Vol. 4, *Ceramics and Glasses*, ASM International, 787, 1991.
16. R. L. Taylor, P. J. Beresford and E. L. Wilson, "A Non-Conforming Element for Stress Analysis," *Int. Journal for Numerical Methods Eng.* Vol. 10, (1976), 1211-1220.
17. R. D. Torres, G. Mustoe, I. E. Reimanis, and J. J. Moore, to be submitted to *Metall. Trans.*
18. M. Manoharan and J. J. Lewandowski, "Crack Initiation and Growth Toughness of an Aluminum Metal-Matrix Composite", *Acta metall. mater.* Vol. 38, No. 3, 489-496 (1990).
19. M. Gupta, F. Mohamed, E. Lavernia and T. S. Srivatsan, "Microstructural Evolution and Mechanical Properties of $\text{SiC}/\text{Al}_2\text{O}_3$ Particulate-Reinforced Spray-Deposited Metal-Matrix Composites", *J. Mater. Sci.* 28, 2245-2259 (1993).
20. F. Zok, S. Jansson, A. G. Evans and V. Nardone, "The Mechanical Behavior of a Hybrid Metal Matrix Composite", *Met. Trans. A*, Vol. 22A, 2107-2117 (1991).

DUCTILITY IMPROVEMENT OF Al-RICH Ni_3Al BY UNIDIRECTIONAL SOLIDIFICATION

T. Hirano and T. Mawari

National Research Institute for Metals
1-2-1, Sengen, Tsukuba, Ibaraki 305, Japan

Abstract

Improvement of the grain boundary brittleness of polycrystalline Ni_3Al can be improved by unidirectional solidification using a floating zone method. The solidified microstructure is dependent on the growth rate and chemical composition of alloys. The relation between the microstructure and the room-temperature tensile properties is studied. This method is effective in improving not only the single phase Ni_3Al but also Al-rich Ni_3Al which has a duplex structure of Ni_3Al and NiAl .

Introduction

Ni₃Al suffers from grain boundary brittleness in polycrystalline form, showing a limited ductility. Since Aoki and Izumi discovered a beneficial effect of microalloying of boron [1,2], macroalloying by Fe, Mn, [3] and Pd [4] has been found to improve the ductility. Unfortunately, the beneficial effect of the micro- and macroalloying occurs only in hypostoichiometric composition, i.e. Ni-rich Ni₃Al, although the reason is not well understood [3-5]. This is not preferable because Al-rich Ni₃Al has greater high-temperature strength than Ni-rich Ni₃Al [6].

Alternatively, we found that unidirectional solidification using a floating zone method extensively improves the room-temperature ductility of stoichiometric Ni₃Al [7-9]. (we call this method FZ-UDS). In this paper, we apply this method to Al-rich Ni₃Al. The relation between the growth rate, the solidification structure, and the mechanical properties is presented.

Experimental

The preparation of the starting rod and the procedure of FZ-UDS were the same as previously reported [7]. Stoichiometric (Ni-25 at% Al) and Al-rich Ni₃Al (Ni-26 and -27 at% Al) rods were unidirectionally grown at growth rates of 25, 50, 75, and 100 mm/h in a flowing argon atmosphere. The starting rod and the grown rod were rotated at 48 rpm in opposite directions during the crystal growth, primarily to make the temperature of the molten zone uniform and secondarily to produce forced convection in the molten zone.

Tensile specimens with a gage section of 0.8x2.7x8 mm were cut along the growth direction by electric discharge machining and the surface was mechanically polished. Tensile tests were performed at room temperature in air with an initial strain rate of $4.2 \times 10^{-3} \text{ s}^{-1}$. The elongation fracture was measured from the tensile specimens. The fracture mode was examined by scanning electron microscopy (SEM).

Results

Microstructure

The microstructure is dependent on the chemical compositions of the alloys and the growth rate. Figure 1 shows the microstructure of Ni-25 at% Al grown at various growth rates. As we previously reported [10], the microstructure is a columnar-grained, single phase Ni₃Al at the growth rate of 25 mm/h, while dendritic NiAl (L1₀ type structure) is present in the columnar-grained Ni₃Al matrix when the growth rate is higher than 50 mm/h. The precipitation of NiAl is due to the peritectic reaction, liquid + NiAl → Ni₃Al. The NiAl is always formed regardless of the growth rate when the alloy solidifies but the morphology is dependent on the growth rate [11]. Below 25 mm/h the NiAl forms simultaneously with Ni₃Al in the form of fine rods similar to a eutectic reaction, but above 50 mm/h it forms dendritically preceding the Ni₃Al. In the former case the NiAl completely dissolves into the Ni₃Al matrix during cooling because the NiAl precipitates are fine rod-like in shape and exposed at high temperatures for a long time. Therefore, the columnar-grained, single phase Ni₃Al is obtained. In the latter case, however, some of the dendritic NiAl is left as a residue because the NiAl precipitates are thick dendrites and are cooled rapidly [11].

Figures 2 and 3 show the microstructures of Ni-26 at% Al and Ni-27 at% Al at various growth rates. In contrast with stoichiometric Ni₃Al the microstructure is a duplex structure of columnar-grained Ni₃Al and dendritic NiAl for all of the growth rate ranges

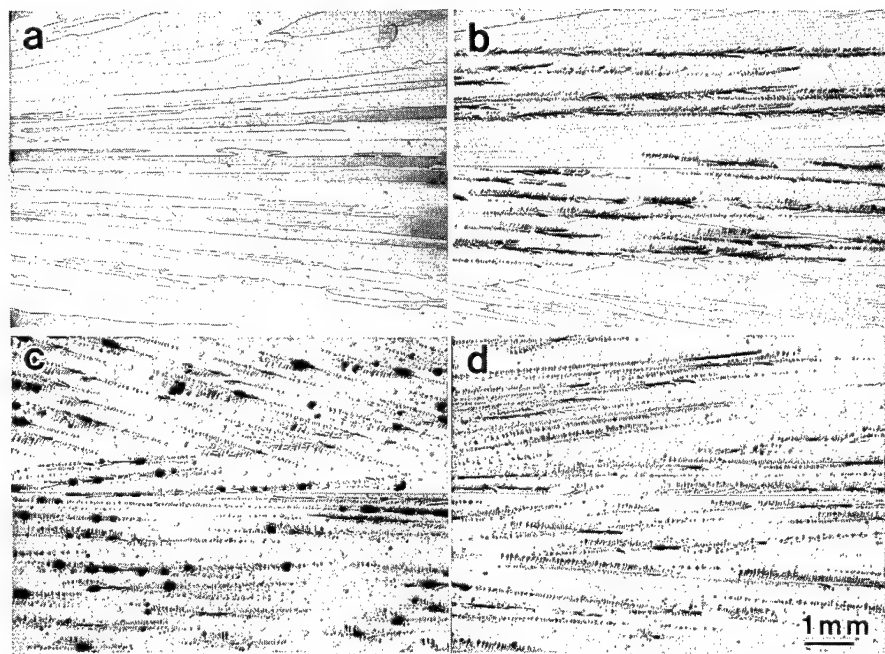


Fig. 1 Optical micrographs of the longitudinal sections of Ni-25 at% Al grown at the growth rate of (a) 25 mm/h, (b) 50 mm/h, (c) 75 mm/h, and (d) 100 mm/h.

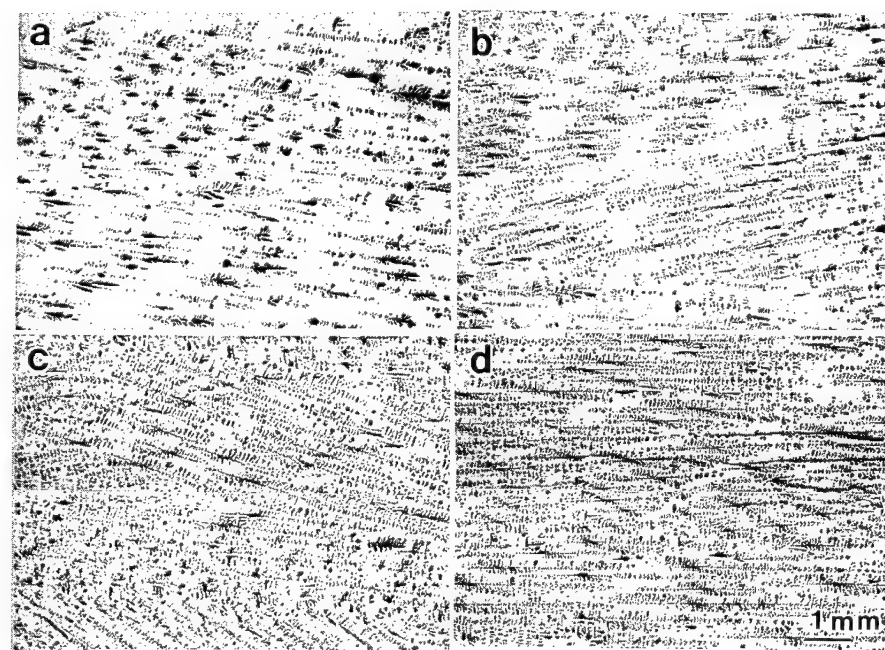


Fig. 2 Optical micrographs of the longitudinal sections of Ni-26 at% Al grown at the growth rates of (a) 25 mm/h, (b) 50 mm/h, (c) 75 mm/h, and (d) 100 mm/h.

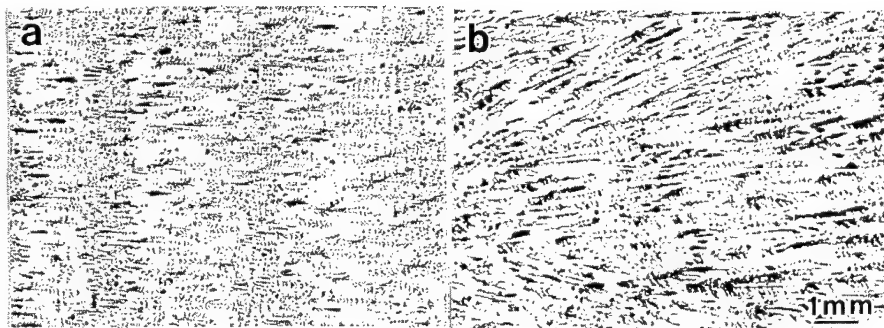


Fig. 3 Optical micrographs of the longitudinal sections of Ni-27 at% Al grown at the growth rates of (a) 25 mm/h and (b) 50 mm/h.

used. There is a tendency that the diameter of the columnar grains is larger than that of the stoichiometric composition. The NiAl dendrites become finer with increasing growth rate. They are stable in these alloys even when heated almost up to the peritectic temperature, indicating that (Ni₃Al+NiAl)/NiAl boundary exists at about 25.4 at% Al in the phase diagram. This phase boundary is slightly shifted to the Al-poor side from the previously reported phase diagram.

Tensile properties

Figure 4 shows the tensile stress-strain curves of Ni-25 at% Al. All the alloys exhibit a large tensile ductility. This markedly differs from that of the conventionally cast alloy which fractures at grain boundaries after yielding, showing almost no ductility. As we previously reported [10], the tensile properties of the current alloys depends markedly on the growth rate and the corresponding microstructure, in particular, elongation decreases with increasing growth rate, while the 0.2% flow stress and the work

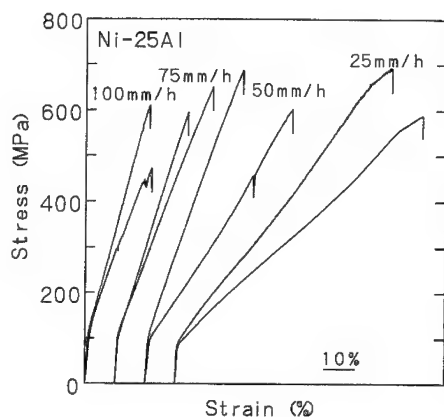


Fig. 4 Tensile stress-strain curves of Ni-25 at% Al grown at various growth rates.

hardening rate increase with increasing growth rate. All the alloys deform uniformly over the entire gage section and fracture without necking, irrespective of growth rate.

Figures 5 shows the SEM micrographs of the fractured surfaces. For the columnar-grained single phase Ni₃Al the fracture mode is transgranular (Fig. 5(a)) and dimpled.

Many slip traces are observed on the surface, indicating that the transgranular fracture occurred after considerable plastic deformation. Intergranular fracture, which is characteristic of brittle polycrystalline Ni_3Al , is suppressed. For the duplex structure the fracture mode is a mixture of transgranular and interphase fractures (Fig. 5(b)). The Ni_3Al matrix fractures transgranularly similar to the columnar-grained single phase Ni_3Al , indicating that the grain boundaries are highly resistant to cracking even in the duplex structure. On the other hand, the $\text{Ni}_3\text{Al}/\text{NiAl}$ phase boundary is less resistant to cracking and cracks initiate there and propagate through the specimens.

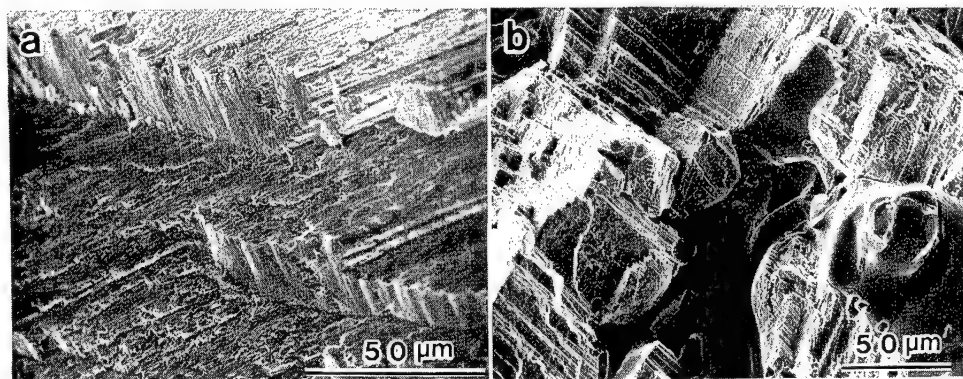


Fig. 5 Fracture surfaces of the tensile-tested specimens of Ni-25 at% Al grown at (a) 25 mm/h, and (b) 50 mm/h.

Figures 6 and 7 show the tensile stress-strain curves of Ni-26 at% Al and Ni-27 at% Al, respectively. The tensile properties show a similar growth rate dependence to those of stoichiometric Ni_3Al , namely the elongation decreases with increasing growth rate, while the 0.2% flow stress and the work hardening rate increase with increasing growth rate. Compared to stoichiometric Ni_3Al , the elongation is lower, the 0.2% flow stress and work hardening rate are higher in Al-rich Ni_3Al . Figure 8 shows the SEM micrographs of the fractured surfaces of Ni-26 at% Al. The fracture mode of Al-rich Ni_3Al is the same as that for the duplex structure of stoichiometric Ni_3Al : cracks initiate at the

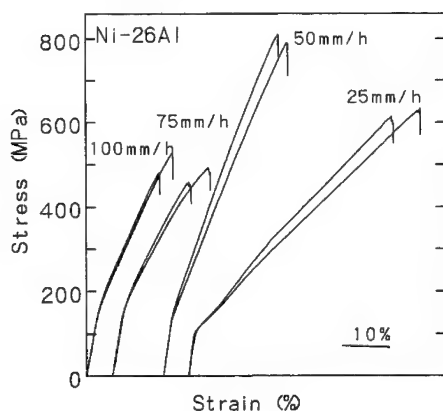


Fig. 6 Tensile stress-strain curves of Ni-26 at% Al grown at various growth rates.

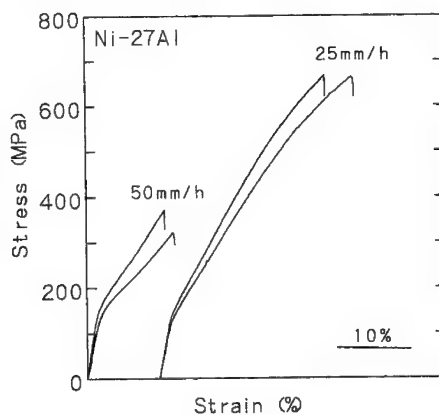


Fig. 7 Tensile stress-strain curves of Ni-27 at% Al grown at various growth rates.

Ni₃Al/NiAl phase boundary (Figs. 8(b)) and the Ni₃Al matrix fractures transgranularly with many slip traces on the fracture surface, indicating that the matrix is still ductile even in Al-rich Ni₃Al. Nevertheless, ductile Al-rich Ni₃Al can be obtained in wide ranges of growth rates and Al concentrations. This is different from both the micro- and macroalloying effects, i.e. Al-rich Ni₃Al cannot be ductilized [1-5].

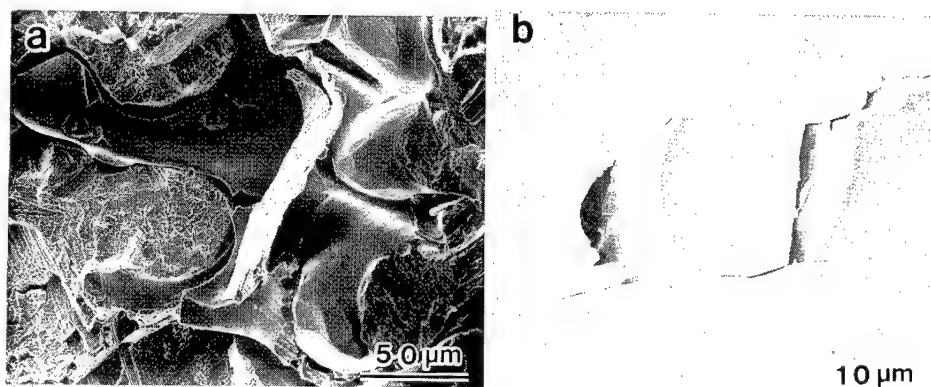


Fig. 8 SEM micrographs of the fractured surface of Ni-26 at% Al. (a) Fracture surface and (b) specimen surface.

Discussion

Figure 9 shows contour maps of the microstructure with fracture mode, tensile elongation, and 0.2% flow stress as functions of growth rate and Al concentration. The largest tensile elongation accompanied by the lowest 0.2% flow stress is obtained for stoichiometric composition grown at the lower growth rates which has columnar-grained, single phase Ni₃Al. Fracture occurs transgranularly (TG) and intergranular fracture is completely suppressed. As we previously reported this is due to the high percentage of low energy grain boundaries, $\Sigma 1$, $\Sigma 3$, and $\Sigma 9$, in this structure [12]. These coincidence boundaries are known to be resistant to cracking. As conditions are changed toward higher growth rate and higher Al concentrations, the microstructure becomes a duplex structure of Ni₃Al and NiAl. This increases 0.2% flow stress but causes interphase fracture (IP), resulting in a decrease in tensile elongation. Nevertheless, the figure proves that FZ-UDS can effectively improve the ductility of Ni₃Al without alloying elements in wide ranges of growth rates and Al concentrations. This is advantageous from the viewpoints of fabrication and high temperature applications as mentioned in the Introduction, namely ductile and high strength Ni₃Al can be fabricated with few limitations.

The results show that duplex intermetallics with proper strength and ductility can be fabricated in-situ by this method.

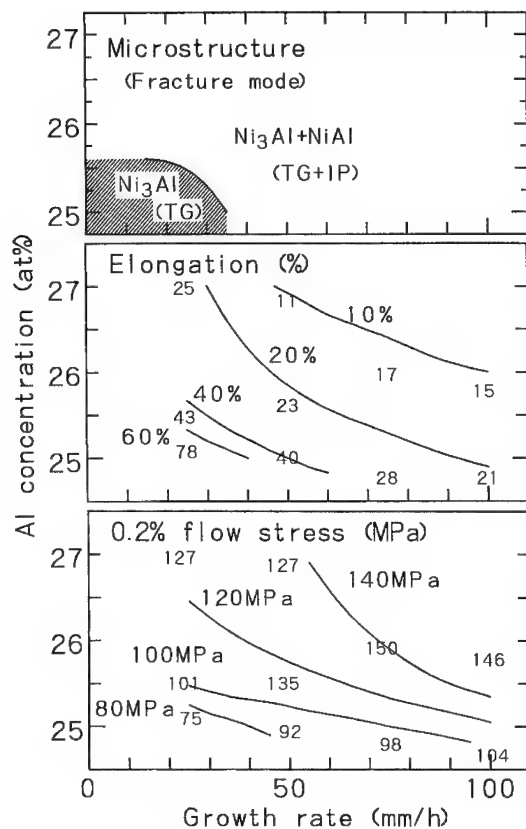


Fig. 9 Contour maps of the microstructure with fracture mode, tensile elongation, and 0.2% flow stress as functions of growth rate and Al concentration. TG and IP represent transgranular fracture and interphase fracture, respectively.

Conclusion

The microstructure of Ni_3Al can be controlled by unidirectional solidification using a floating zone method (FZ-UDS), depending on the growth rate and the chemical composition. As a result, the room-temperature ductility of stoichiometric and even Al-rich Ni_3Al can be significantly improved. The results suggest a possibility that FZ-UDS is applicable to fabricate duplex intermetallics for high temperature applications.

REFERENCES

1. K. Aoki and O. Izumi, "Improvement in Room Temperature Ductility of the Intermetallic Compound Ni_3Al by Ternary Trace Element Addition," *J. Japan Inst. Metals*, 43, (1979), 358-359.
2. K. Aoki and O. Izumi, "Improvement in Room Temperature Ductility of the L_{12} Type Intermetallic Compound Ni_3Al by Boron Addition," *J. Japan Inst. Metals* 43,(1979), 1190-1196.

-
3. T. Takasugi, O. Izumi, and N. Masahashi, "Electronic and Structural Studies of Grain Boundary Strength and Fracture in L1₂ Ordered Alloys - II. On the Effect of Third Elements in Ni₃Al Alloy," Acta metall. 33, (1985), 1259-1269.
 4. A. Chiba, S. Hanada, and S. Watanabe, "Ductilization of Ni₃Al by Macroalloying with Pd," Acta metall. mater. 39, (1991), 1799-1805.
 5. C. T. Liu, C. L. White, and J. A. Horton, "Effect of Boron on Grain-Boundaries in Ni₃Al," Acta metall. 33, (1985), 213-229.
 6. O. Noguchi, Y. Oya, and T. Suzuki, "The Effect of Nonstoichiometry on the Positive Temperature Dependence of Strength of Ni₃Al and Ni₃Ga," Met. Trans. A 12A, (1981), 1647-1653.
 7. T. Hirano, "Improvement of Room Temperature Ductility of Stoichiometric Ni₃Al by Unidirectional Solidification," Acta metall. mater. 38, (1990), 2667-2671.
 8. T. Hirano and T. Kainuma, ISIJ International 31, (1991), 1134.
 9. T. Hirano, "Tensile Ductility of Stoichiometric Ni₃Al Grown by Unidirectional Solidification," Scripta metall. mater. 25, (1991), 1747-1750.
 10. T. Mawari and T. Hirano, "Effects of Unidirectional Solidification Conditions on the Microstructure and Tensile Properties," Intermetallics 3, (1995), 23-33.
 11. T. Hirano and T. Mawari, "Unidirectional Solidification of Ni₃Al by a Floating Zone Method," Acta metall. mater. 41, (1993), 1783-1789.
 12. T. Watanabe, T. Hirano, T. Ochiai, and H. Oikawa, "Texture and Grain Boundary Character Distribution (GBCD) in B-Free Ductile Polycrystalline Ni₃Al," Mater. Sci. Forum, 157-162, (1994), 1103-1108.

FATIGUE LIFE PREDICTION OF TITANIUM MATRIX COMPOSITES UNDER MISSION SPECTRUM LOADING

Theodore Nicholas and Andrew H. Rosenberger

Wright Laboratory Materials Directorate,
WL/MLLN, 2230 Tenth St., Ste. 1
Wright-Patterson AFB, OH 45433, USA

Abstract

Fatigue life predictions are conducted for a high temperature composite for hypersonic vehicle structural applications. A SCS-6/Timetal®21S [0/90]_s composite is evaluated under thermomechanical fatigue (TMF) as well as under typical hypersonic mission profiles and segments of those missions. The fatigue life analysis is based on micromechanical stresses which, in turn, are input into a damage summation model. Spectrum loading is decomposed into a series of in-phase and out-of-phase TMF segments whose lives are predicted from a life fraction model which was developed for isothermal and TMF data. Analytical predictions for the mission spectrum and the simple mission profiles are compared with experimental data obtained here as well as in a previous study. The model is demonstrated to be able to predict fatigue life under mission spectrum loading based solely on calibration under simple isothermal fatigue and TMF conditions.

Introduction

Titanium matrix composites (TMCs) for potential structural applications in advanced aerospace vehicles and gas turbine engines will be exposed to both mechanical and thermal cycling up to high temperatures. These conditions produce a combination of considerations in life prediction modeling which have not existed previously: viscoplastic and time-dependent behavior of the matrix material, environmental degradation and time-dependent behavior, large thermal stresses because of the large thermal coefficient mismatch between fiber and matrix, excursions of both load and temperature commonly referred to as thermomechanical fatigue (TMF), and complex mission spectra which can produce different types of damage.

While the prediction of the fatigue life of continuous fiber reinforced TMCs has been the subject of extensive research efforts over the last several years [1], the conditions which have been addressed have been limited. Early attempts to predict life focused on behavior under isothermal conditions, while subsequent attempts included effects of frequency and stress ratio. Further expansion of the fatigue life modeling concepts focused primarily on TMF under in-phase (IP) and out-of-phase (OP) loading conditions. Limited work has been conducted on addressing life prediction under more general mission spectrum loading where temperature and load excursions have more complicated histories. While some generic conclusions have been drawn on behavior under spectrum loading for specific materials under certain application oriented mission spectra [2,3,4], an approach to the prediction of fatigue life under the most general spectrum loading has been lacking.

Several methods developed for predicting or correlating the fatigue lives of TMCs under isothermal or TMF conditions are discussed by Nicholas [5]. Life prediction has been shown to depend on more than one parameter for general loading conditions, and it appears to be widely

accepted that the parameters should reflect the micromechanical stresses in the composite rather than bulk or applied stresses or strains for the most general applicability [6]. No single correlating parameter seems capable of describing the fatigue process because of the variety of damage mechanisms which may govern life. In this paper, an approach is presented which makes use of knowledge gained in life prediction using damage accumulation, incorporates micromechanical stress computational schemes, and maintains the computational feasibility for complex mission spectra. The applicability of this approach to a generic hypersonic vehicle mission profile as well as to some simplified spectra is demonstrated.

Experimental Program

The fatigue machine consists of a servo hydraulic load frame positioned horizontally and utilizes quartz lamp heating units. Four thermocouples are attached to the specimen providing four active zones of temperature control. Straight sided specimens were diamond cut and ground to a width of 11.2 mm and 110 mm in length. The specimen thickness is that of the fabricated composite panel - typically 0.9 mm. A length of about 30 mm in the center of the specimen is heated uniformly, while the ends of the specimen, clamped in the water-cooled friction grips, remain near room temperature.

In order to perform TMF tests where the minimum temperature of the cycle was room temperature (21°C), a special cooling apparatus was constructed. Active control of specimen cooling was achieved using compressed air that was passed through a coil submerged in a methanol bath held at -50°C. The flow of this chilled air, directed at the specimen, was computer controlled to aid in the temperature control near room temperature.

The simplified mission spectra and OP TMF tests are conducted in load control. Axial strain is monitored throughout the tests using a high temperature extensometer with quartz extension rods placed on the edge of the specimen. Symmetric triangular wave forms are used for both load and temperature for TMF tests.

The experimental data for a hypersonic mission profile, as well as for simplified mission segments, are taken from Mirdamadi and Johnson [7]. In addition to these data, tests are conducted under OP TMF conditions which represent end points in the mission profile. A simple TMF mission is also used which contains a combination of an out-of-phase TMF cycle with a superimposed load spike on the increasing temperature portion of the cycle. The mission is shown in Figs. 1 and 2 as a function of time and in a stress-temperature plot, respectively. The OP cycle has a frequency of 0.001 Hz, maximum and minimum loads of 277 and 75 MPa, respectively, and maximum and minimum temperatures of 816 and 21°C, respectively. The load spike has a maximum value of either 300, 400 or 500 MPa, and is superimposed at a frequency of 0.5 Hz (triangular wave form) at a temperature of 418°C and stress of 176 MPa on the TMF cycle. In addition, several pure OP TMF cycles were evaluated between points RT and ST.

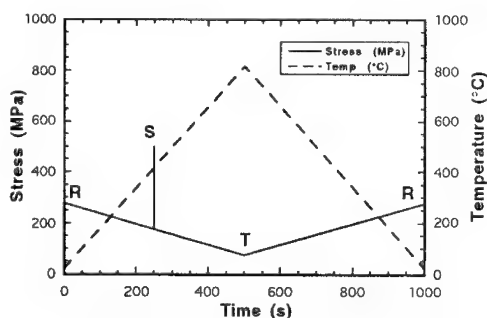


Figure 1 - Time history of out-of-phase spectrum with load spike.

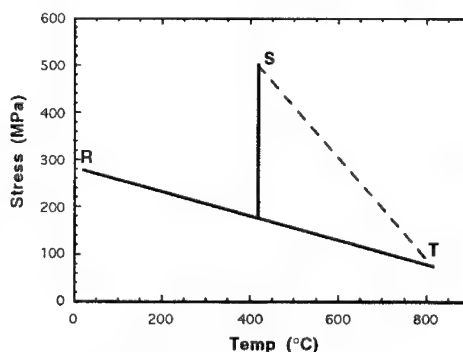


Figure 2 - Stress-temperature plot of spectrum with spike.

Life Fraction Modeling

A description of the life fraction model for predicting elevated temperature fatigue life of TMCs is presented by Nicholas [8]. The analysis utilizes the micromechanical stresses in the constituents as parameters in the model. Experimental data are used as the basis for determining the parameters embedded in the model. The capability to correlate experimental data from a wide variety of test conditions for several versions of a damage summation model was demonstrated in that paper. In general, the model was found to have the capability to capture the general trends in the experimental data over a wide range of conditions.

In the life fraction model, damage is considered to accumulate simultaneously due to independent mechanisms, each represented in the model by a life fraction. When the sum of the damage induced by all mechanisms equals one, failure is predicted. A nonlinear damage summation approach is used where time-dependent damage has a square root dependence, given as

$$\frac{N}{N_c} + \left(\frac{N}{N_t} \right)^{0.5} = 1 \quad \frac{1}{N_c} = \frac{1}{N_f} + \frac{1}{N_m} \quad (1)$$

where N_c represents the cycles to failure due to cyclic damage and N_t is the cycles to failure due to time-dependent damage mechanisms. Further, the cyclic damage term, N_c , is decomposed into fiber (N_f) and matrix (N_m) contributions which, in turn, are given in terms of fiber and matrix micromechanical stresses, respectively,

$$N_f = 10^{N_0} \left(1 - \frac{\sigma_{f, \max} (1-R)^p}{\sigma^*} \right) \quad N_m = B (\Delta \sigma_m)^{-n} \quad (2)$$

where subscripts f and m refer to stresses in the fiber and matrix, respectively, and N_0 , σ^* , B , n and p are empirical constants. The time-dependent term (N_t) is obtained by integrating the incremental damage over a triangular cycle using time to failure, t_c , as a function of stress,

$$t_c = A \sigma^{-m} \quad \frac{1}{N_t} = \frac{1}{f \sigma_{\max}} \frac{1}{(1-R)} \int_{R \sigma_{\max}}^{\sigma_{\max}} \frac{d\sigma}{t_c(\sigma)} \quad (3)$$

where σ is applied stress, f is cycle frequency, R is stress ratio, and A and m are empirical constants. Temperature dependence of the fiber stress term, the matrix stress term, and the time-dependent or environmental term is introduced in the following manner:

$$\sigma^* = \sigma_0^* - C_1 T_{\max} \quad B = B_1 \left(1 + \frac{B_2}{T_{\text{abs}}} \right) \quad A = \frac{A_1}{\exp \left(\frac{-A_2}{T_{\text{abs}}} \right)} \quad (4)$$

where σ^* , B , and A are now the temperature-dependent constants in eqns. (2) and (3), and T_{abs} is absolute temperature ($T_{\text{abs}} = T^\circ\text{C} + 273$). In this modeling, the micromechanical stresses in eqn. (2) are obtained from a concentric cylinder model for the [0] ply using a viscoplastic model for the matrix, but the [90] ply is represented by a thermoviscoplastic model fit to FEM results [9]. The micromechanical stress values used are those calculated in the tenth cycle because it has been found that stress equilibrium is generally approached after ten complete cycles during which creep and stress redistribution take place. This approach produces more consistent results in fatigue life modeling than predictions when the first cycle stresses are used [8].

Application to SCS-6/Timetal®21S [0/90]_s

The modeling described above is applied to experimental data on cycles to failure for SCS-6/Timetal®21S [0/90]_s under isothermal fatigue at 650 and 815°C over a range of frequencies

from 0.01 to 200 Hz, stress ratios (R) from 0.1 to 0.8, as well as under IP and OP TMF from 150 to 650°C. The conditions covered include those where purely time-dependent, purely cycle-dependent, fiber-dominated, and matrix-dominated modes of failure, as well as combinations of these, are observed. A transition under isothermal conditions from cycle-dependent to time-dependent behavior as frequency decreases, has also been observed [10,11].

Data from experiments performed on SCS-6/Timetal®21S [0/90]_S are utilized to determine the constants in this model based on a least squares error minimization scheme. The model is calibrated from a large set of experimental data obtained under isothermal as well as in-phase and out-of-phase TMF conditions and covers a wide range of temperatures and frequencies [12]. The complete data set is tabulated in [11]. The majority of the data are from isothermal tests at 650°C and TMF tests from 150-650°C at a frequency of 0.006 Hz. The constants which are obtained as a best fit to the experimental data used in calibrating the model are as follows: For the fiber term (N_f), $N_0=35.4$, $\sigma_0^*=2482$, $C_1=1.103$, $p=1$; for the matrix term (N_m), $B_1=1.03E+19$, $B_2=29.32$, $n=5.92$; for the time-dependent term (N_t), $A_1=1.28E+04$, $A_2=9457$, $m=1.49$. The capability of the model to represent the entire data base is shown in Fig. 3 where predicted lives are compared with experimental data. The straight line represents perfect correlation. Arrows denote tests which were terminated before failure and are not used in the model calibration. The figure shows that the model does a reasonably good job of representing the fatigue life over the wide range of isothermal and TMF conditions covered in the experimental work. A subset of those data points, those obtained under OP TMF only, are shown in Fig. 4 and are used later in evaluating the capability of the model to predict mission spectra.

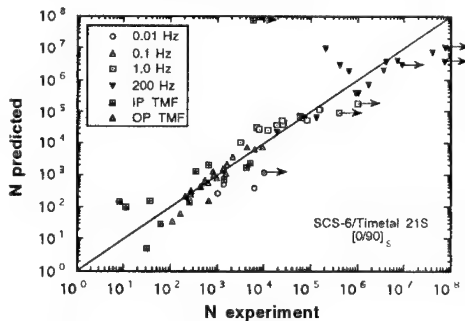


Figure 3 - Predicted vs experimental.

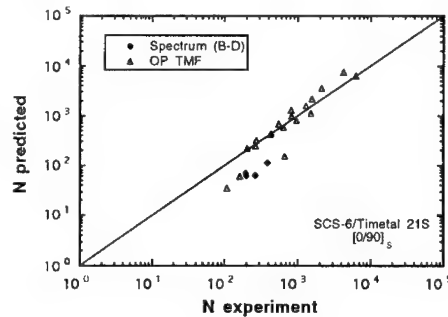


Figure 4 - OP TMF predictions

Application to Mission Profiles

The micromechanical stresses are obtained for the TMF segments as well as for the entire mission profile and compared with each other at the end points of the TMF segments. In addition, simplified missions are also analyzed using the same procedures. In order to analyze a complex mission as depicted in Figs. 5 and 6 [7], or a simplified mission evaluated in the present investigation, Figs. 1 and 2, a methodology is developed which lends itself to analysis using the life fraction model described above. To accomplish this, the complex hypersonic mission profile of Fig. 5 is represented in a load-temperature plane (P-T plot) as shown in Fig. 6. The extremes of load and temperature which are reached are seen easily in this type of plot. The assumption is made that damage accumulation is a function of the extremes of load and temperature which are achieved during a mission, and that the load or temperature path taken in reaching these extremes is of secondary importance. The extremes of the mission are connected by heavy lines in Fig. 6, each line representing a simple in-phase or out-of-phase TMF cycle. For each possible TMF cycle depicted in the figure (IP-1: AC, IP-2: AD, OP-1: BE, OP-2: BD), a fatigue life analysis is conducted using the life fraction model described above. The analysis is conducted using two methods for comparison. First, the micromechanical stresses are computed using the exact mission history. Second, the stresses are computed assuming only the end points for each possibility. The results of the computed micromechanical stresses as well as the predicted lives using the two methods are summarized in Fig. 7 for each of the 4 TMF conditions. The maximum and minimum stress in the fiber and the matrix are shown for each set of end points

using both the spectrum history (sp) and only the end points for a TMF cycle. It can be seen from that figure that the predicted lives, N_{sp} and N_{TMF} , are similar for 3 of the 4 TMF conditions, but condition OP-1 produces predictions which differ by a factor of 2. The stress ranges as well as the maximum stress in the fiber and matrix show some differences between the two computational approaches. The most damaging condition in terms of fatigue life is OP-2. Because of the differences in micromechanical stresses obtained from a simple TMF condition rather than from the actual spectrum, the actual spectrum is used in all cases for the calculation of micromechanical stresses which, in turn, are input into the life prediction model. The model, however, predicts life for a simple OP or IP TMF cycle, and the calculation is based on the stresses at the end points of that cycle.

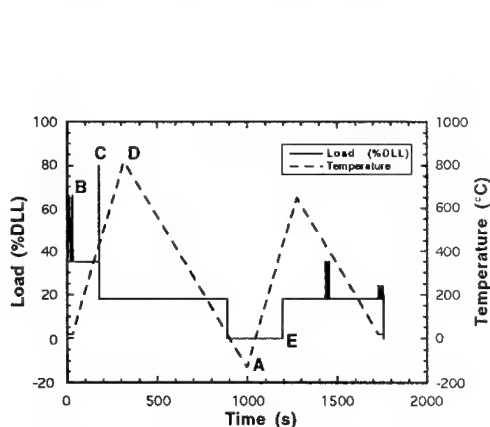


Figure 5 - Time history of hypersonic mission profile

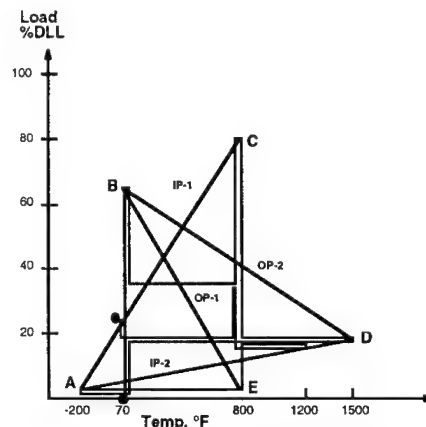


Figure 6 - Load-temperature plot of mission spectrum

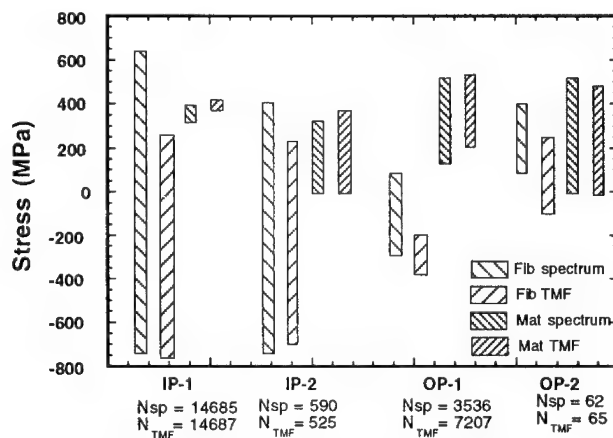


Figure 7 - Micromechanical stresses and predicted cycles to failure

Three mission loading spectra are evaluated in this investigation. The first is the hypersonic mission shown in Figs. 5 and 6. As indicated above, the most damaging segment is OP-2 which goes between end points B and D in Fig. 6. The experimental data for this mission were obtained from Mirdamadi and Johnson [7]. In that investigation, the fatigue life under a portion of a mission cycle was also evaluated. Computations are also carried out to predict the life under that mission segment. Finally, a simple OP cycle with a load spike at an intermediate temperature (Fig. 1) is evaluated experimentally and simulated using the end point approach as depicted in Fig. 2. The cycle with load spike is evaluated for three values of maximum stress at point S.

For reference purposes, experiments and analysis are also carried out for a pure OP cycle, RT, with no load spike and for a pure OP cycle, ST, for values of stress at point S of 300 and 500 MPa. The OP cycle RT represents the most damaging cycle BD in the mission shown in Fig. 6.

Since an out-of-phase TMF cycle is determined to be the life limiting segment of the mission spectrum or the portion of the spectrum (Fig. 7), the comparisons of fatigue life with the model predictions are conducted using only the OP TMF data from the model development. These data, extracted from Fig. 3, are replotted in Fig. 4 along with the mission and mission segment data which were obtained from Mirdamadi and Johnson [7] on a $[0/90]_{2S}$ lay up and the corresponding computational results obtained in this study. It can be seen that the mission data fall very close to some of the baseline data, but this data set deviates somewhat from the general trend of all of the OP TMF data. The three baseline data points which match the mission data in Fig. 4, the mission data, and the remaining tests performed as part of this study are summarized in Fig. 8. The conditions include the portion of Fig. 2 denoted as RT (equivalent to BD in Fig. 6), the cycle ST in Fig. 2, and the cycle with a load spike of Fig. 2 where it was determined that ST was the most damaging combination of end points. In all cases, the frequency of the cycle was 0.001 Hz. It can be seen from Fig. 8 that all of these predictions fall in a narrow band, yet the band is offset from the predictions of the model which was calibrated from the prior data base. None of the data generated in this investigation are used to recalibrate the model or to change any of the constants.

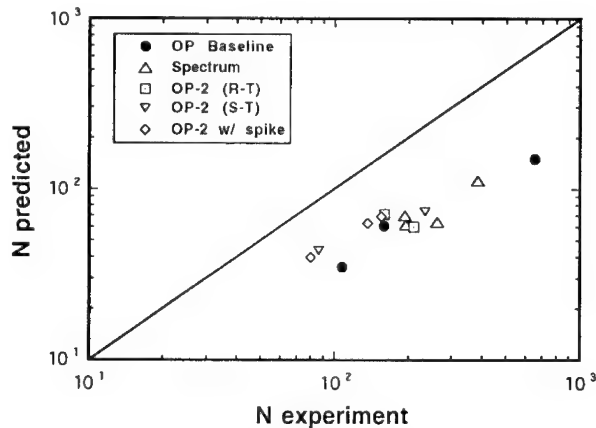


Figure 8 - Correlation of spectrum data.

Discussion of Results

The first question that has to be raised in evaluating the capability of the model as shown in Fig. 4 is why three OP data points in the short life regime differ markedly from the rest of the OP data base which is very well predicted by the model. Further, these 3 points and the spectrum conditions form their own subset of a data base which is used exclusively in the comparisons. Examination of the conditions under which these 3 tests were run reveals that these were the only tests in the OP TMF matrix which were conducted at a very low frequency of 0.0006 Hz. The remaining data for the baseline were obtained at a frequency of 0.006 Hz or higher. Of significance is that the spectrum and modified spectrum tests were all conducted at a frequency of 0.001 Hz, which is very close to the frequency of the 3 outlier tests. It is concluded from this analysis that the model and constants developed from the total data base do not adequately account for time dependent effects at the lowest frequencies where few data exist. Additional data at these low frequencies, and resultant changes in the formulation of the time-dependent term in the model might improve the capability in this regime. Nevertheless, the model was used as developed and calibrated, even though all of the test conditions fall into this low frequency, short life, regime.

An additional observation of the model predictions for the 3 low frequency baseline tests and all of the spectrum tests is that the time dependent term is dominant in all of the computations. This is somewhat unexpected because all of the conditions are based on an OP TMF cycle where matrix fatigue is usually the dominant mechanism. In fact, for all of the other baseline OP TMF conditions, the matrix fatigue term is dominant. Johnson et al. [2], in their evaluation of fatigue life under generic hypersonic vehicle spectrum loading, noted that holding a significant load at temperature was detrimental to the fatigue life and the material accumulated strain in a manner characteristic of classical creep behavior. Recent investigations have shown that hold time at temperature is a very significant contributor to fatigue life under mission spectrum loading [3,4]. As expected, the time-dependent behavior of the material is found to be a dominant factor in the fatigue life under the mission profiles evaluated here.

The data of Fig. 8, which include the 3 low frequency baseline points as well as all of the spectrum conditions seem to consolidate well into a single band, even though this band is not well predicted by the model with its existing constants. The model, however, was able to distinguish between the relevant end points when the spectrum with a load spike, Fig. 2, had no spike or peak stresses at point S of 300, 400, or 500 MPa. For the 300 MPa spike condition, the model predicted that the cycle denoted by RT was the most damaging and the dominant term was the time-dependent one. For the latter two conditions, where the amplitude of the spike is higher, the OP cycle with end points ST became dominant, and the predicted life went down. The experimental data versus predictions form a narrow band of points in Fig. 8. In all these cases, the time-dependent term in the life fraction model was dominant. From these observations, it is concluded that the low frequency spectrum loading conditions are all dominated by time-dependence and that the model does a good job of consolidating all of these data, even though the predictions are all inaccurate by essentially the same amount. In performing the actual experiments, the results were predictable in advance by applying an error factor to the model of approximately three in life. These predictions, in fact, were used in designing the simple spectrum tests.

Conclusions

A methodology for predicting fatigue life of TMCs has been developed which can be applied to complex mission spectra involving combinations of loads and temperatures at different frequencies. The life prediction model is calibrated from isothermal fatigue data as well as TMF data obtained under IP or OP cycling conditions. Micromechanical stresses computed from a computer code which represents the complex material behavior of the cross-ply composite are an integral part of the modeling. When the model is applied to several mission spectra, the predictions match the experimental data equally well as the model is able to match the baseline data from which it was calibrated. The approach, which utilizes the representation of mission profiles in load-temperature space, provides an easy method of decomposing a complex thermo-mechanical (load and temperature) spectrum into simple elements for which fatigue lives are easily calculated.

Acknowledgements

This work was conducted at Wright Laboratory Materials Directorate, Wright-Patterson Air Force Base, Ohio, U.S.A. The support of the U.S. Air Force is gratefully acknowledged.

References

1. W. S. Johnson et al., ed., Life Prediction Methodology for Titanium Matrix Composites, ASTM STP 1253 (Philadelphia: American Society for Testing and Materials, 1996).
2. W. S. Johnson, M. Mirdamadi and J. G. Bakuckas Jr., "Damage Accumulation in Titanium Matrix Composites Under Generic Hypersonic Vehicle Flight Simulation and Sustained Loads," Thermo-Mechanical Fatigue Behavior of Materials, ASTM STP 1263, ed. M. J. Verrilli and M. G. Castelli (Philadelphia: American Society for Testing and Materials, 1996).

3. M. Mirdamadi and W. S. Johnson, "Fatigue of [0/90]_{2s} SCS-6/Ti-15-3 Composite Under Generic Hypersonic Vehicle Flight Simulation," FATIGUE 93, Volume II, ed. J.-P. Bailon and J. I. Dickson (Warley, U.K.: EMAS, 1993), 951-956.
4. M. Mirdamadi, J. G. Bakuckas and W. S. Johnson, "Mechanisms of Strain Accumulation in Titanium Matrix Composites at Elevated Temperatures," Mechanics of Composite Materials - Nonlinear Effects, AMD-Vol. 159, (New York: American Society of Mechanical Engineers, 1993), 245-252.
5. T. Nicholas, "Fatigue Life Prediction in Titanium Matrix Composites," Journal of Engineering Materials and Technology, 117 (1995) 440-447.
6. R. W. Neu and T. Nicholas, "Methodologies for Predicting the Thermomechanical Fatigue Life of Unidirectional Metal Matrix Composites," Advances in Fatigue Lifetime Predictive Techniques: 3rd Volume, ASTM STP 1292, ed. M. R. Mitchell and R. W. Landgraf (Philadelphia: American Society for Testing and Materials, 1996).
7. M. Mirdamadi and W. S. Johnson, "Modeling and Life Predictions for TMC's Subjected to Mission Profiles," Life Prediction Methodology for Titanium Matrix Composites, ASTM STP 1253, ed. W. S. Johnson et al. (Philadelphia: American Society for Testing and Materials, 1996).
8. T. Nicholas, "An Approach to Fatigue Life Modeling in Titanium Matrix Composites," Materials Science and Engineering, A200 (1995) 29-37.
9. R. W. Neu, D. Coker and T. Nicholas, "Cyclic Behavior of Unidirectional and Cross-Ply Titanium Matrix Composites," International Journal of Plasticity, 10 (9) (1996) (in press).
10. T. Nicholas and S. M. Russ, "Fatigue Life Modeling in Titanium Matrix Composites," Proceedings of the American Society for Composites: Ninth Technical Conference, (Lancaster PA: Technomic, 1994) 940-947.
11. R. W. Neu and D. T. Scott, "Effects of Temperature and Frequency on the TMF Mechanisms in Cross-ply Titanium Matrix Composites," Proceedings of the American Society for Composites, 1996, (in press).
12. T. Nicholas, S. M. Russ, Neu, R. W. and Schehl, N., "Life Prediction of a [0/90] Metal Matrix Composite Under Isothermal and Thermomechanical Fatigue," Life Prediction Methodology for Titanium Matrix Composites, ASTM STP 1253, ed. W. S. Johnson et al. (Philadelphia: American Society for Testing and Materials, 1996).

SUBJECT INDEX

- Adhesion, 37-48
- Advanced power plant materials, 123
- Alumina, 236
- B₂ crystal structure, 221, 224
- Blade and vane alloys, 130
- Bonding, 37
- Boron doped, 391
- Boron nitride, 238
- Carbon, 237
 - Carbon interphase layer, 331
- Chemisorption, 38
- Cleavage, 187
- Coatings, 101, 298, 369
 - Silicon nitride, 134
 - Thermal barrier, 132
- Cobalt alloys, 387
- Cohesion, 38
- Combined cycle gas turbines, 409
- Composites, 203, 277-286, 311-318
 - Atomistic calculations, 49-55
- Ceramic matrix, 6, 7, 8, 12, 24, 26, 287-299
- Coatings, 369
- Damage, 315, 316
- Delamination, 24
- Ductility, 3, 11
- Elastic modulus, 369-375
- Embedded atom method, 51
- Environment, 371
- Fracture, 372
- Functionally graded, 413
- High temperature, 3-33
- High resolution TEM, 49, 51
- Interface, 18, 235, 237, 238
- In-situ, 247-262
- Metal matrix, 7, 8, 278
- MoSi₂/Nb, 209
- Mullite/mullite, 235
- NiAl/TiB₂, 413
- NiAl, 49-55
- Notch sensitivity, 8
- Oxide/oxide, 235-245
- SiC/CAS, 19
- SiC/SiC, 1-7, 19, 363, 369-375
- Silicon nitride, 369
- Water vapor effects, 363
- Creep, 237, 248
 - Titanium aluminides, 165
- Creep rupture, 259
- Damage tolerance, 209
 - Ceramics, 209
 - Extrinsic mechanisms, 209
 - Intermetallics, 209
 - Intrinsic mechanisms, 209
- Deformation mechanisms, 225
- Design and life prediction, 219
- Diamond, 301-309
 - Critical resolved shear stress, 302, 307
 - Flow stress, 301-304, 307, 308
 - Grain boundary, 307
 - Impression creep, 301, 303, 307, 308
 - Plastic deformation
- Diffusion, 265, 268, 269, 270
- Directional solidification, 247, 250
- Disc alloys, 131
- Dislocation, 57
- Dislocation pileups, 187
- Displacement reaction, 272
- Ductile phase toughening, 39, 211
- Effective surface energy, 325
- Eutectic, 249, 252
- Exhaust valves, 166
- Extrusion, 170
- Failure, 280-282
- Fatigue, 195-207, 287-299
 - Load ratio effects, 215
 - Power law exponents, 213
- Fatigue life predictions, 433, 435
 - Mission spectrum loading, 434
 - Titanium matrix composites, 433, 435
 - Thermomechanical fatigue, 433
- Fe₃Al, 197
- FeAl, 198

Ferritic steels, 108
 Fiber bridging, 211
 Fibers, 264, 277
 Finite element method, 71
 Finite element modeling, 413, 415
 Forging, 170
 Fracture, 57-64, 195-207, 307, 326
 Mixed mode, 57
 Fracture toughness, 256
 Germanium doped, 391
 Grain bridging, 211
 Grain boundaries, 67, 301
 Grain size, 170
 Halide activation, 392
 Hot corrosion, 75
 Hot isostatic pressing, 160
 Hydrogen effects, 331
 Hypersonic mission profile, 437
 IN, 98, 130
 Interfaces, 37, 57-64, 173
 277, 279-282
 Interfacial energy, 57, 60, 62
 Interfacial shear, 287, 288
 Interphases, 263
 Interstitial sites, 40
 Interstitials, 204
 Isothermal forging, 159
 Isothermal oxidation, 395
 Knudson flow regime, 337
 Larson-Miller parameter, 82, 260
 Laves phase, 248, 253, 258
 Luders band, 190
 Modeling reaction rate, 333
 Molecular flow regime, 337
 MoSi₂
 Hardness, 408-410
 Oxidation, 384, 410, 411
 Processing, 405-407
 Purity, 406
 Mullite, 235
 Nb aluminides, 220, 221
 Ni₃Al, 196, 301-307
 NiAl, 185-194, 196, 197
 Nicalon, 291
 Nucleation, 267
 Ordering tie lines, 223, 224
 Oxidation, 75, 204, 229, 235, 237, 331
 In-situ, 263-273
 Directional solidification, 180
 Oxide volatility, 362
 Silicides, 360-361
 Water vapor effects, 359, 361
 Pack cementation coatings, 391
 Parabolic rate constants, 336
 Phase transformation, 266
 Plasma melting, 169
 Plasticity, 67-72
 Polymer matrix, 8, 12
 Power plant efficiencies, 129
 Pseudo-twinning/stress-induced martensite,
 226, 227, 228
 Refractory based intermetallics, 391
 R-curve behavior, 214
 SiC, 304
 Silica layers, 359
 Silicide, 278
 Silicides, 195, 359
 Silicon nitride, 134
 Single crystals, 75-90, 185
 Sintering
 Fractals, 315, 316
 Grains, 314-317
 Influence on structure, 316, 317
 Interfaces, 315, 316
 Liquid phase, 313, 315
 Slip, 185-194
 Soft impressor method
 Brittle-ductile transition, 301-303, 308
 Mean contact pressure, 302, 304, 306, 307
 Minimum contact pressure, 302, 304, 306
 Spallation, 397
 Steam turbine, 107-122
 Castings, 114, 115
 Creep strength, 111
 Larson-Miller parameter, 113
 Martensite, 110
 Oxidation, 109
 Strength, 313-317
 Stress-rupture properties, 127
 Superalloys, 91-105, 250

- Adherence of Al_2O_3 , 382
- Corrosion, 91
- Cyclic oxidation, 380
- Directional solidification, 94, 96
- Gas turbine, 92
- Oxidation, 91
- Role of yttrium, cerium, and lanthanum, 382
- Single crystals, 96
- Texture, 67, 69, 70, 72, 186
- Ti_2AlNb , 277-286
- Ti_3Al , 57-64, 198, 199
- TiAl , 57-64, 169-174, 175, 177, 199, 200, 209
 - Oxidation, 384
 - Superplastic forming, 179
- TiAl/TiNb , 209
- $\text{TiAl-Al}_2\text{O}_3$, 177

- Titanium alloys, 278
- Titanium aluminide, 159-167, 319
 - θ phase, 320
 - α_2 phase, 319
 - γ phase, 319
 - Hydrogen effect, 319
 - Hydrides, 319, 323
- Titanium matrix, 5, 6, 26
- Toughness, 3
- Turbine, 76
- Turbocharger, 159, 160, 165, 166
- Undirectional solidification, 301-307
- Vacuum induction melting, 79
- Water vapor effects, 363

AUTHOR INDEX

A

Al-Watban, A., 301

B

Bewlay, B.P., 247

Brookes, E.J., 301

Bul, I.A., 185

C

Cawley, J.D., 331

Chawla, K.K., 235, 287

Cockeram, B.V., 391

D

Daw, M.S., 49

Deevi, S.C., 139

Dvorak, G.J., 369

E

Eckel, A.J., 331

Erickson, G.L., 75

Evans, A.G., 3

F

Fishman, S.G., 263

Fraser, H.L., 221

Fu, C.L., 57

G

George, E.P., 139

Gibbons, T.B., 123

Gilbert, C.J., 209

Gundel, D.B., 277

H

Harris, T., 301

Henager, C.H., Jr., 343

Herman, H., 403

Hillig, W.B., 359

Hirano, T., 425

Holmes, J.W., 287

Hou, D.-H., 221

Hu, J., 185

J

Jackson, M.R., 247

Johnson, D.R., 175

Jones, R.H., 343

K

Kaufman, M.J., 185

L

Levit, V.I., 185

Lewinsohn, C.A., 343

Lipetzky, P., 359, 369

Lipsitt, H.A., 247

Liu, C.T., 139

Loretto, M.H., 169

Lund, C.H., 91

M

Mawari, T., 425

Mecking, H., 67

Meier, G.H., 379

Mills, M.J., 49

Miracle, D.B., 277

Mishnaevsky, L.L., Jr., 311

Moore, J.J., 413

Mustoe, G.W., 413

N

Nazmy, M., 159

Newman, A., 403

Nicholas, T., 433

Noseda, C., 159

P

Pettit, F.S., 379

Phillipsen, B., 159

R

Rapp, R.A., 391

Raynolds, J.E., 37

Reimanis, I.E., 413

Ritchie, R.O., 209

Roddick, E.R., 37

Rosenberger, A.H., 433

S

Sampath, S., 403

Scarlin, R.B., 107

Schmauder, S., 311

Schmucker, M., 235

Schneider, H., 235

Sikka, V.K., 139

Smith, J.R., 37

Srolovitz, D.J., 37

Staubli, M., 159

Stoloff, N.S., 195, 369

T

Thompson, A.W., 319

Torres, R.D., 413

V

Venkateswara Rao, K.T., 209

W

Wallis, R.L., 301

Warrier, S., 277

Wheeler, R., IV, 221

Windisch, C.F., Jr., 343

Winton, J.S., 185

X

Xu, Z.R., 235

Y

Yamaguchi, M., 175

Yang, S.S., 221

Yoo, M.H., 57